Stabilized Finite Element Formulations for the Three-Field Viscoelastic Fluid Flow Problem

Ernesto Castillo Del Barrio

Escola Tècnica Superior d'Enginyers de Camins, Canals i Ports de Barcelona
Departament d'Enginyeria Civil i Ambiental
Universitat Politècnica de Catalunya (BarcelonaTECH)

Doctoral Thesis
Structural Analysis Programme

Advisor:

Prof. Ramon Codina Rovira

January 2016

Stabilized Finite Element Formulations for the Three-Field Viscoelastic Fluid Flow Problem

January 2016
Escola Tècnica Superior d'Enginyers de Camins, Canals i Ports de Barcelona
Departament d'Enginyeria Civil i Ambiental
Universitat Politècnica de Catalunya (BarcelonaTECH)
c/ Jordi Girona 1-3, 08034 Barcelona
www.upc.edu

UNIVERSITAT POLITÈCNICA DE CATALUNYA
BARCELONATECH
Escola de Doctorat

Curs acadèmic: 2015/2016

Acta de qualificació de tesi doctoral

Nom i cognoms
Ernesto Francisco Castillo Del Barrio

Programa de doctorat
Anàlisis Estructural

Unitat estructural responsable del programa
Departament d'Enginyeria Civil i Ambiental

Resolució del Tribunal

Reunit el Tribunal designat a l'efecte, el doctorand / la doctoranda exposa el tema de la seva tesi doctoral titulada

_____

_____.

Acabada la lectura i després de donar resposta a les qüestions formulades pels membres titulars del tribunal, aquest atorga la qualificació:

☐ NO APTE ☐ APROVAT ☐ NOTABLE ☐ EXCEL·LENT

(Nom, cognoms i signatura) President/a	(Nom, cognoms i signatura) Secretari/ària	
(Nom, cognoms i signatura) Vocal	(Nom, cognoms i signatura) Vocal	(Nom, cognoms i signatura) Vocal

_____, _____ d'/de _____ de _____

El resultat de l'escrutini dels vots emesos pels membres titulars del tribunal, efectuat per l'Escola de Doctorat, a instància de la Comissió de Doctorat de la UPC, atorga la MENCIÓ CUM LAUDE:

☐ SÍ ☐ NO

(Nom, cognoms i signatura) President de la Comissió Permanent de l'Escola de Doctorat	(Nom, cognoms i signatura) Secretari de la Comissió Permanent de l'Escola de Doctorat

Barcelona, _____ d'/de _____ de _____

To my wife and son
my parents and my sisters

Abstract

The Finite Element Method (FEM) is a powerful numerical tool, that permits the resolution of problems defined by partial differential equations, very often employed to deal with the numerical simulation of multiphysics problems. In this work, we use it to approximate numerically the viscoelastic fluid flow problem, which involves the resolution of the standard Navier-Stokes equations for velocity and pressure, and another tensorial reactive-convective constitutive equation for the elastic part of the stress, that describes the viscoelastic nature of the fluid.

The three-field (velocity-pressure-stress) mixed formulation of the incompressible Navier-Stokes problem, either in the elastic and in the non-elastic case, can lead to two different types of numerical instabilities. The first is associated with the incompressibility and loss of stability of the stress field, and the second with the dominant convection. The first type of instabilities can be overcome by choosing an interpolation for the unknowns that satisfies the two inf-sup conditions that restrict the mixed problem, whereas the dominant convection requires a stabilized formulation in any case. In this work, different stabilized schemes of the Sub-Grid-Scale (SGS) type are proposed to solve the three-field problem, first for quasi Newtonian fluids and then for solving the viscoelastic case.

The proposed methods allow one to use equal interpolation for the problem unknowns and to stabilize dominant convective terms both in the momentum and in the constitutive equation. Starting from a residual based formulation used in the quasi-Newtonian case, a non-residual based formulation is proposed in the viscoelastic case which is shown to have superior behavior when there are numerical or geometrical singularities. The stabilized finite element formulations presented in the work yield a global stable solution, however, if the solution presents very high gradients, local oscillations may still remain. In order to alleviate these local instabilities, a general discontinuity-capturing technique for the elastic stress is also proposed.

The monolithic resolution of the three-field viscoelastic problem could be extremely expensive computationally, particularly, in the threedimensional case with ten degrees of freedom per node. A fractional step approach motivated in the classical pressure segregation algorithms used in the two-field Navier-Stokes problem is presented in the work.The algorithms designed allow one the resolution of the system of equations that define the problem in a fully decoupled manner, reducing in this way the CPU time and memory requirements with respect to the monolithic case.

The numerical simulation of moving interfaces involved in two-fluid flow problems is an important topic in many industrial processes and physical situations. If we solve the problem using a fixed mesh approach, when the interface between both fluids cuts an element, the discontinuity in the material properties leads to discontinuities in the gradients of the unknowns which cannot be captured using a standard finite element interpolation. The method presented in this work features a local enrichment for the pressure unknowns which allows one to capture pressure gradient discontinuities in fluids presenting different density values.

The stability and convergence of the non-residual formulation used for viscoelastic fluids is analyzed in the last part of the work, for a linearized stationary case of the Oseen type and for the semi-discrete time dependent non-linear case. In both cases, it is shown that the formulation is stable and optimally convergent under suitable regularity assumptions.

Resumen

El Método de los Elementos Finitos (MEF) es una herramienta numérica de gran alcance, que permite la resolución de problemas definidos por ecuaciones diferenciales parciales, comúnmente utilizado para llevar a cabo simulaciones numéricas de problemas de multifísica. En este trabajo, se utiliza para aproximar numéricamente el problema del flujo de fluidos viscoelásticos, el cual requiere la resolución de las ecuaciones básicas de Navier-Stokes y otra ecuación adicional constitutiva tensorial de tipo reactiva-convectiva, que describe la naturaleza viscoelástica del fluido.

La formulación mixta de tres campos (velocidad-presión-tensión) del problema de Navier-Stokes, tanto en el caso elástico como en el no-elástico, puede conducir a dos tipos de inestabilidades numéricas. El primer grupo, se asocia con la incompresibilidad del fluido y la pérdida de estabilidad del campo de tensiones, y el segundo con la convección dominante. El primer tipo de inestabilidades, se puede solucionar eligiendo un tipo de interpolación entre las incógnitas que satisfaga las dos condiciones inf-sup que restringen el problema mixto, mientras que la convección dominante requiere del uso de formulaciones estabilizadas en cualquier caso. En el trabajo, se proponen diferentes esquemas estabilizados del tipo SGS (Sub-Grid-Scales) para resolver el problema de tres campos, primero para fluidos del tipo cuasi-newtonianos y luego para resolver el caso viscoelástico.

Los métodos estabilizados propuestos permiten el uso de igual interpolación entre las incógnitas del problema y estabilizan la convección dominante, tanto en la ecuación de momento como en la ecuación constitutiva. Comenzando desde una formulación de tipo residual usada en el caso cuasi-newtoniano, se propone una formulación no-residual para el caso viscoelástico que muestra un comportamiento superior en presencia de singularidades numéricas y geométricas. En general, una formulación estabilizada produce una solución estable global, sin embargo, si la solución presenta gradientes elevados, oscilaciones locales se pueden mantener. Con el objetivo de aliviar este tipo de inestabilidades locales, se propone adicionalmente una técnica general de captura de discontinuidades para la tensión elástica.

La resolución monolítica del problema de tres campos viscoelástico puede llegar a ser extremadamente costosa computacionalmente, sobre todo, en el caso tridimensional donde se tienen diez grados de libertad por nodo. Un enfoque de paso fraccionado motivado en los algorítmos clásicos de segregación de la presión usados en el caso del problema de dos campos de Navier-Stokes, se presenta en el trabajo, el cual permite la resolución del sistema de ecuaciones que definen el problema de una manera completamente desacoplada, lo que reduce los tiempos de cálculo y los requerimientos de memoria, respecto al caso monolítico.

La simulación numérica de interfaces móviles que envuelve los problemas de dos fluidos, es un tópico importante en un gran número de procesos industriales y situaciones físicas. Si se resuelve el problema utilizando un enfoque de mallas fijas, cuando la interfaz que separa los dos fluidos corta un elemento, la discontinuidad en las propiedades materiales da lugar a discontinuidades en los gradientes de las incógnitas que no pueden ser capturados utilizando una formulación estándar de interpolación. Un enriquecimiento local para la presión se presenta en el trabajo, el cual permite la captura de gradientes discontinuos en la presión,

asociados a fluidos de diferentes densidades.

La estabilidad y la convergencia de la formulación no-residual utilizada para fluidos viscoelásticos es analizada en la última parte del trabajo, para un caso linealizado estacionario del tipo Oseen y para un problema transitorio no-lineal semi-discreto. En ambos casos, se logra mostrar que la formulación es estable y de convergencia óptima bajo supuestos de regularidad adecuados.

Acknowledgements

Sin lugar a dudas, cuatro años de trabajo duro pueden ser un periodo de tiempo muy largo si no se disfruta lo que se hace y mas aún si el ambiente de trabajo no es grato. Puedo decir que en mi caso, el tiempo ha volado y el ambiente de trabajo en el que he estado inmerso ha sido el mejor que me pudo haber tocado. Por lo mismo, creo que es necesario decir gracias a un gran número de personas que han sido parte de esta etapa de mi vida.

En primer lugar, gracias Ramon por todo tu apoyo y por la entrega que has tenido a la hora de supervisar cada uno de los trabajos que surgieron de esta tesis. Se que recordarás muy bien cada uno de ellos puesto que has tenido que leerlos una y otra vez corrigiendo mi inglés...De verdad gracias por enseñarme a hacer investigación y siempre intentar resolver las dudas que surgieron. Sigue así!! y espero seguir trabajando juntos por muchos años más, eres una gran persona y un gran investigador.

Marcela, todo esto hubiese sido completamente diferente si no me hubieses recomendado venir a trabajar acá. Claramente no te equivocaste y te lo agradezco enormemente. Espero ahora poder trabajar juntos al otro lado del mundo después de estos cuatro años de doctorado.

Joan, gracias por toda la ayuda que me diste sobre todo en lo que a programación se refiere, sé que no he sido un alumno destacado, pero algunas huellas quedarán plasmadas en Femuss, a menos que las borren todas claro está. Espero seguir trabajando en conjunto por muchos años más.

Team Femuss, gracias por hacer que mi correo esté lleno de mensajes "FemussServer: Tests failed in test server". Ha sido muy gratificante compartir una herramienta de trabajo como Femuss con ustedes. Gracias Héctor por tu ayuda al principio cuando no sabía nada. Gracias Ángel por compartir mazmorra el primero año y por continuar el camino en Femuss. Team Colombia, gracias por darle sabor a café al equipo de trabajo y por la energía que aportaron para que todo avance como ha avanzado. Suerte Ángel, Camilo, Arnau, Alexis y Ricardo en lo que les queda de trabajo. Sé que lo sacarán todo adelante y que continuarán enviándome correos de "FemussServer: Tests failed in test server".

Gabriel, gracias por recibirme en mi estancia doctoral en Glasgow y tener la paciencia que tuviste. Fue una grata experiencia conocerte y trabajar junto a ti. Sin lugar a dudas, me hiciste sentir como en casa y espero que sigamos trabajando en el futuro, ya sea en el Tinderbox o en un café en Chile.

El día a día y la convivencia humana son factores determinantes cuando uno emprende un proyecto lejos de casa. Gracias Ester, Rita, Fermin, Alex, Matías, Arnau, Facundo, Ricardo, Vicent, Victor (Cardoso), Victor (Roldán) y Fei por compartir esos momentos, la verdad, sin ustedes todo hubiese sido diferente y esta etapa de mi vida no la hubiese sentido tan plena. Suerte a todos en lo que se viene, algunos ya son doctores y otros están pronto a serlo, espero que sigan como los conocí y que la vida y la "fama" no los cambie!!. Espero que sigamos en contacto y nos veamos más pronto que tarde.

A pesar que nos separen miles de kilómetros (11170 km), padres y hermanas, ustedes han sido como siempre un apoyo emocional en todo este proceso. La verdad es que es difícil separarse por tantos años de los seres queridos, pero ustedes cada vez que hablábamos me

hicieron sentir como en casa y eso es algo que ayuda sobre todo en los momentos difíciles. Ya no queda nada para el reencuentro!!.

Grace, mi compañera de aventuras y mi compañera de vida, tú sabes que todo esto lo planeamos juntos intentando cumplir nuestros sueños. Gracias por todo tu apoyo y por estar siempre cuando te he necesitado. En un comienzo, fue un sacrificio muy grande dejar todo por mi, pero luego los frutos se dieron y lograste desarrollarte profesionalmente. Ahora tienes cinco meses de embarazo y un hermoso niño viene en camino, y eso es la guinda del pastel, el broche de oro, el mejor final que podríamos haber soñado para cerrar esta etapa de vida en el viejo continente.

Finalmente, agradezco el financiamiento recibido por parte del Gobierno de Chile a través del programa de desarrollo de capital humano avanzado (Becas-Chile), Folio 72120080. También agradezco a la Universidad de Santiago de Chile y al Departamento de Ingieniería Mecánica por confiar en mi para ser parte de él, y al Centro Internacional de Métodos Numéricos en Ingeniería (CIMNE) y a la Universitat Politècnica de Catalunya por la infraestructura prestada en estos cuatro años de trabajo.

Contents

1 Introduction **1**

2 The Three-Field Navier-Stokes Problem **5**
2.1 Abstract . . . 5
2.2 Introduction . . . 5
2.3 The Navier-Stokes problem in a three-field formulation . . . 7
2.3.1 Initial and boundary value problem . . . 7
2.3.2 The variational form . . . 8
2.3.3 Non-Newtonian models . . . 8
2.3.4 Galerkin finite element discretization and time discretization . . . 9
2.4 Design of a stable finite element formulation . . . 10
2.4.1 The sub-scale concept . . . 11
2.4.2 General approach of the sub-scale stabilized formulation . . . 11
2.4.3 Stabilized formulation applied to the three-field Navier-Stokes problem 12
2.4.4 Fully discrete and linearized problem . . . 15
2.5 Numerical results . . . 15
2.5.1 Convergence test . . . 16
2.5.2 Parallel lid-driven cavity problem in non-linear viscosity fluids . . . 20
2.5.3 Transient flow of a power-law fluid over a cylinder . . . 23
2.5.4 Tangential stresses over boundary walls . . . 28
2.6 Conclusions . . . 32

3 The Stationary Viscoelastic Flow Problem **33**
3.1 Abstract . . . 33
3.2 Introduction . . . 33
3.3 The viscoelastic flow problem . . . 36
3.3.1 Boundary value problem . . . 36
3.3.2 Variational form . . . 37
3.3.3 Galerkin finite element discretization . . . 37
3.4 Design of a stable finite element formulation . . . 38
3.4.1 Residual based stabilized finite element methods . . . 38
3.4.2 Split OSGS stabilization . . . 40
3.4.3 Discontinuity capturing technique . . . 42
3.4.4 Linearized problem . . . 43
3.5 Numerical results . . . 46
3.5.1 Convergence test . . . 46
3.5.2 The 4:1 contraction problem . . . 48
3.5.2.1 Oldroyd-B flow at $\mathrm{Re} = 1$ . . . 49
3.5.2.2 Oldroyd-B flow at $\mathrm{Re} = 0.01$ . . . 53
3.5.2.3 Some results for $\mathrm{Re} = 0.01$ and for $\mathrm{Re} = 1$ . . . 55
3.5.3 A threedimensional example . . . 55

3.6 Conclusions . . . 64

4 Fractional Step Methods: Viscoelastic Problem 65
4.1 Abstract . . . 65
4.2 Introduction . . . 65
4.3 The viscoelastic flow problem . . . 68
4.3.1 Initial and boundary value problem . . . 68
4.3.2 Variational form . . . 69
4.4 Numerical approximation . . . 70
4.4.1 Galerkin finite element discretization . . . 70
4.4.2 Monolithic time discretization . . . 70
4.4.3 Algebraic system . . . 71
4.5 Fractional step methods . . . 72
4.5.1 A first algebraic point of view: extrapolation . . . 72
4.5.2 A second algebraic point of view: inexact factorizations . . . 75
4.6 Stabilized finite element formulation . . . 77
4.6.1 Stabilized monolithic formulation . . . 78
4.6.2 Algebraic formulation and fractional step scheme . . . 79
4.6.3 Linearized problem . . . 85
4.7 Numerical results . . . 85
4.7.1 Convergence test . . . 86
4.7.2 Viscoelastic fluid flow past a confined cylinder in a channel . . . 88
4.7.3 Lid-driven cavity flow problem . . . 91
4.7.3.1 2D cavity . . . 91
4.7.3.2 3D cavity . . . 93
4.8 Conclusions . . . 99

5 Approximation of the Two-Fluid Flow Problem 101
5.1 Abstract . . . 101
5.2 Introduction . . . 101
5.3 The viscoelastic flow problem . . . 103
5.3.1 Boundary value problem . . . 103
5.3.2 The variational form . . . 105
5.4 Numerical approximation . . . 106
5.4.1 Galerkin finite element discretization . . . 106
5.4.2 Stabilized finite element formulation . . . 106
5.4.3 Discontinuity-Capturing technique . . . 107
5.4.4 Monolithic time discretization . . . 108
5.4.5 Fractional-step formulation . . . 109
5.5 The level set method . . . 109
5.5.1 The level set equation . . . 109
5.5.2 Discontinuous gradient pressure functions . . . 111
5.6 Numerical results . . . 113
5.6.1 Sloshing of two fluids in a square covered cavity . . . 114
5.6.2 Jet buckling problem . . . 117
5.7 Conclusions . . . 127

6 Numerical Analysis: Linearized Stationary Case 129
6.1 Abstract . . . 129
6.2 Introduction . . . 129
6.3 Problem statement and Galerkin discretization . . . 131
6.3.1 Boundary value problem . . . 131

6.3.2 Variational form of the problem . . . 132
6.3.3 Stability of the Galerkin finite element discretization . . . 133
6.4 Stabilized finite element method . . . 134
6.5 Numerical Analysis . . . 135
6.5.1 Preliminaries . . . 136
6.5.2 Stability and convergence in a mesh-dependent norm . . . 136
6.5.3 Stability and convergence in natural norms . . . 144
6.6 Conclusions . . . 148

7 Numerical Analysis: Nonlinear Time-Dependent Case 149
7.1 Abstract . . . 149
7.2 Introduction . . . 149
7.3 Notation and Preliminaries . . . 151
7.3.1 Notation . . . 151
7.3.2 Preliminaries . . . 151
7.4 Problem statement and Galerkin finite element discretization . . . 152
7.4.1 Boundary Value problem . . . 152
7.4.2 Variational form . . . 153
7.4.3 Galerkin finite element discretization . . . 154
7.5 Stabilized finite element method . . . 155
7.6 Linearized time-dependent case . . . 156
7.6.1 Linearized stabilized Semi-discrete problem . . . 156
7.6.2 Existence and uniqueness of the semi-discrete solution . . . 157
7.6.3 Stability of the linearized semi-discrete problem . . . 159
7.7 Analysis of the nonlinear problem . . . 163
7.8 Conclusions . . . 175

8 Conclusions 177
8.1 Achievements . . . 177
8.2 Future work . . . 178

List of Figures

2.1 Schematic representation: (a) mixing cavity and (b) flow over a cylinder. . . 17
2.2 Mesh used in problems: mixing cavity (a) and flow over a cylinder (b). . . . 17
2.3 Contours of viscosity obtained in the convergence test problem in dilatant fluid ($n = 1.5$) and pseudo-plastic fluid ($n = 0.5$). 18
2.4 Convergence of the velocity-pressure-stress fields, in linear triangular elements for the different power-law indexes analyzed: (a) $n = 0.5$, (b) $n = 1$ y (c) $n = 1.5$. 19
2.5 Convergence of the velocity-pressure-stress fields, in quadratic triangular elements for the different power-law indexes analyzed. 20
2.6 Contours of the normal stress component σ_{xx}, obtained in the convergence test problem for the different power-law fluids analyzed. 20
2.7 Streamlines in Carreau-Yasuda fluids: (a) Shear-thinning, (b) Shear-thickening. 24
2.8 Pressure isolines in Newtonian fluid ($\mathrm{Re} = 5000$), left: ASGS formulation; right: OSS formulation. 25
2.9 Influence of the power-law index (n), in the drag coefficient (C_D), the lift coefficient (C_L) and the Strouhal number (St). 26
2.10 Wave scheme to define some comparison points. 27
2.11 Evolution of the streamlines close to the cylinder, from the input condition to the output condition in the problem of flow over a cylinder in pseudoplastic ($n = 0.4$) and dilatant ($n = 1.8$) fluids. 27
2.12 Contours of stress σ_{xx} in the cylinder problem for the case $n = 0.4$ and $\mathrm{Re}_{\mathrm{PL}} = 140$. 28
2.13 Viscosity contours, in the cylinder problem, for the case $n = 1.8$ and $\mathrm{Re}_{\mathrm{PL}} = 140$. 29
2.14 Shear stress (σ_{xy}) in the straight pipe with in the Carreau-Yasuda blood flow. 29
2.15 Schematic representation of threedimensional poblems: (a) arterial stenosis (b) vessel elbow. 30
2.16 Contour of pressure (PRESS) and velocity magnitude (VELOC) in the stenosis problem (a) and in the elbow problem (b). Both cases correspond to the mid section. 31
2.17 Shear stress modulus in the arterial stenosis problem (a) and in the vessel elbow problem (b). 31

3.1 Discrete L^2errors using Q_1 (left) and Q_2 (right) elements, for the manufactured exact solution. a) $L^2_{\boldsymbol{u}}$ (velocity error), b) L^2_p (pressure error) and c) $L^2_{\boldsymbol{\sigma}}$ (stress error). 47
3.2 Geometry description of the two-dimensional 4:1 contraction problem. 48
3.3 Typical mesh used in the two-dimensional 4:1 contraction problem. 48
3.4 Close-up view of streamlines near the corner for Re = 1: a) We = 0, b) We = 0.5, c) We = 2.5, d) We = 3, e) We = 4 and f) We = 5. 50

3.5 Vortex size validation at different Weissenberg numbers for Re = 1. 51
3.6 Pressure in a cut line near the contraction corner for Re = 1: a) Q_1 elements, b) Q_2 elements. 51
3.7 Pressure isolines near the contraction corner: a) We = 0, b) We = 1, c) We = 3, d) We = 5. 52
3.8 Normal elastic stress component σ_{xx} near the contraction corner: a) We = 0, b) We = 1, c) We = 3, d) We = 5. 53
3.9 Normal elastic stress component σ_{yy} near the contraction corner: a) We = 0, b) We = 1, c) We = 3, d) We = 5. 54
3.10 Elastic stress component σ_{xy} near the contraction corner: a) We = 0, b) We = 1, c) We = 3, d) We = 5. 55
3.11 Elastic stress components along the horizontal line $y = -1$ for Re = 1 : a) σ_{xx}, b) σ_{yy}, c) σ_{xy}. 57
3.12 Velocity profiles: a) u_x along $y = 0$ (symmetry axis), b) u_y along $y = -1$ (bottom wall of the narrow region). 58
3.13 Vortex size validation at different Weissenberg numbers for Re = 0.01. 58
3.14 Close-up view of streamlines near the corner for Re = 0.01: a) We = 0, b) We = 1, c) We = 2, d) We = 4, e) We = 5, f) We = 6.5. 59
3.15 Typical oscillation in a stress component: a) without discontinuity capturing technique, b) with discontinuity capturing technique. 59
3.16 Secondary vortex size at different Weissenberg numbers for Re = 0.01 and Re = 1. 60
3.17 Sketch of the 3D 4:1 contraction problem. 60
3.18 Mesh used in the 3D 4:1 contraction problem. 61
3.19 Streamlines in the 3D 4:1 contraction problem (Re = 0.01 and We = 1): a) Isometric view, b) Cuts with the planes $y = 0$ (left) and a plane $x =$ constant close to the contraction plane (right). 62
3.20 Contours of transverse velocity components on the planes $y = 0.5$ and $z = 0.5$: a) u_y, b) u_z. 63
3.21 Pressure around the corner: a) contour lines, b) along a cut line across the corner. 63
3.22 Normal elastic stress component σ_{zz} across the corner: a) without discontinuity-capturing technique, b) with discontinuity-capturing technique. 63

4.1 Schematic representation of the flow past a cylinder. 86
4.2 Computational mesh (M2) used in the flow past a cylinder. 86
4.3 Schematic representation of the 2D lid-driven cavity flow problem. 87
4.4 Schematic representation of the 3D lid-driven cavity flow problem. 87
4.5 Converge test: a) First order scheme, b) Second order scheme and c) third order scheme. 88
4.6 Drag coefficient validation. 90
4.7 Stress profile along the cylinder wall and downstream the plane $y = 0$ for: a) We = 0.6, b) We = 0.7 and c) $\mathrm{We} = 0.9$. 91
4.8 Results for the flow over a cylinder for the case We = 1.3. From the top to the bottom: isolines of u_x, p, σ_{xx} and σ_{xy}. 95
4.9 Streamlines in the lid-driven cavity problem using the third order fractional step algorithm. From the top to the bottom and from the left to the right: $t = 0.5$, 1, 1.5 and 2.0. 96
4.10 σ_{xy} component of the elastic stress tensor in the lid-driven cavity problem using the third order fractional step algorithm. From the top to the bottom and from the left to the right: $t = 0.5$, 1, 1.5 and 2.0. 97

4.11 Lid-driven cavity in 3D: a) pressure isolines and b) σ_{xx} component of the elastic stress tensor. 98
4.12 Lid-driven cavity in 3D: some streamlines at $t = 2$. 98

5.1 Enriched element sketch and modified integration rule. 112
5.2 Tetrahedral element cut: three intersection points (left) and four intersection points (right). 113
5.3 Three-dimensional hydrostatic pressure problem: without enriched functions (left) and using enriched functions (right). 114
5.4 Two-fluids cavity problem: Initial condition, mesh used in 2D and mesh used in 3D (from left to right ,respectively). 115
5.5 two-dimensional sloshing: a) without enriched functions and b) using enriched functions ($t = 0$, $t = 0.7$ and $t = 30$ for both cases from left to right). 116
5.6 Temporal history of the bottom right corner of the stress magnitude without (left) and with (right) a discontinuity-capturing term. 116
5.7 Three-dimensional sloshing: a) without enriched functions and b) using enriched functions ($t = 0$, $t = 0.7$ and $t = 15$ in both cases from left to right). . 117
5.8 Jet buckling problem and mesh used. 118
5.9 Jet buckling in Newtonian fluids. From left to right: Re = 0.25, Re = 0.50, Re = 0.55 and Re = 0.60 (all at $t = 1.5$) 120
5.10 Jet buckling in a 2D rectangular cavity (Re = 0.25). First row We = 0 , second row We = 10 and third row We = 100, at time $t = 0.6$ (first column), $t = 0.8$ (second column), $t = 0.9$ (third column) and $t = 1.5$ (fourth column). 121
5.11 Contour line in the jet buckling problem for We = 10: σ_{xx} (first row), σ_{yy} (second row) and p (third row). For $t = 0.6$, $t = 0.8$, $t = 0.9$ and $t = 1.5$ (from left to right). 122
5.12 Contour line in the jet buckling problem for We = 100: σ_{xx} (first row), σ_{yy} (second row) and p (third row). For $t = 0.6$, $t = 0.8$, $t = 0.9$ and $t = 1.5$ (from left to right). 123
5.13 Jet buckling in a 3D prismatic cavity using a Newtonian fluid (Re = 0.25, We = 0). Top ($t = 1.25$ and $t = 1.5$), bottom ($t = 1.75$ and $t = 2$). 124
5.14 Jet buckling in a 3D prismatic cavity using a non-Newtonian (Re = 0.25, We = 100). Top ($t = 1.25$ and $t = 1.5$), bottom ($t = 1.75$ and $t = 2$). 125
5.15 Velocity vectors in the jet buckling problem for We = 100 in $t = 0.2$, $t = 1.0$ and $t = 2.0$ (from left to right). 126

List of Tables

2.1 Viscosity limit values obtained in the convergence test problem, in pseudoplastic fluid ($n = 0.5$) and dilatant fluid ($n = 1.5$), using the stabilized formulations ASGS and OSS. . . . 18
2.2 Mesh refinement study in the parallel lid-driven cavity problem for different power law indexes in the location of the upper vortex (x-coordinate/y-coordinate). The number of nodes / number of elements is indicated below each mesh label. . . . 21
2.3 Location of primary vortex mixing cavity problem for the different power indexes analyzed (reference [116]/present work): (a) $n = 1.0$, (b) $n = 0.5$ and (c) $n = 1.5$. . . . 22
2.4 Constants of the Carreau-Yasuda model in the mixing cavity problem (SI units). . . . 23
2.5 Location of primary vortexes, number of iterations and peaks of viscosity-pressure in Carreau-Yasuda fluis, for the ASGS and the OSS formulations. . 23
2.6 Iterations required for convergence in the mixing cavity problem with a power-law fluid for the two proposed stabilized formulations. . . . 24
2.7 Mesh dependency study for $C_{\overline{D}}$ (mean drag coefficient), $C_{L,m}$ (maximum lift coefficient), and St for the flow over a cylinder problem using different power law indexes and $Re_{PL} = 140$. Mesh M1 (31710 nodes, 61211 elements) and mesh M2 (43182 nodes, 82588 elements). . . . 25
2.8 Comparison of macroscopic parameters in the flow over a cylinder problem. $C_{\overline{D}}$: mean drag coefficient, $C_{L,max}$: maximum lift coefficient in time. . . . 26
2.9 Blood properties with the Carreau-Yasuda model (SI units). . . . 28
2.10 Meshes used in the shear stresses problems. . . . 28

3.1 Meshes used in the 4:1 contraction problem. . . . 49
3.2 Maximum peak values for each elastic stress component corresponding to Fig. 6. 52
3.3 Pressure drop for different Weissenberg and Reynolds numbers using bilinear (Q_1) and biquadratic (Q_2) elements. . . . 56

4.1 Meshes used in the flow over a cylinder problem. . . . 89
4.2 Drag force coefficient for the flow over a confined cylinder. . . . 90
4.3 Vortex location in lid driven cavity problem. . . . 92
4.4 Saves in CPU time of the fractional step schemes over the monolithic formulations. . . . 92
4.5 Comparison between the number of iterations of the monolithic and of the second order fractional step algorithm using the BDF2 time integrator. . . . 93
4.6 Saves in CPU time of the fractional step schemes over the monolithic formulations in the 3D case (second order schemes). . . . 93
4.7 Comparison between the number of iterations of the monolithic and the second order fractional step algorithm in the 3D case. . . . 94

5.1 Fluid properties in the sloshing problem. 114
5.2 Comparison of computational requirements: monolithic approach v/s fractional step approach. 117
5.3 Fluid properties for the buckling problem. 118
5.4 Mesh convergence analysis in jet-buckling problem. 119
5.5 Non-linear iterations for the jet buckling-problem. 126

List of Algorithms

2.1 Stabilized formulations: ASGS and OSS 16
3.1 Fully discrete and linearized problem at each iteration. 44
3.2 General algorithm. 45
4.1 First and second order fractional step schemes $(k = 1, 2)$. 74
4.2 Third order fractional step scheme. 76
4.3 Inexact factorization of the first order fractional step method. 81
4.4 Inexact factorization second order fractional step method. 82
4.5 Inexact factorization third order fractional step method. 83
4.6 Stabilized FEM: Inexact factorization third order fractional step method. . . 84
5.1 Fractional step approach: intermediate steps. 110
5.2 Fractional step approach: final steps. 110

Chapter 1

Introduction

This research work is devoted to the numerical approximation of the flow of viscoelastic (non-Newtonian) fluids using the Finite Element Method (FEM). It is well known that, for real problems, a wide variety of fluids can be modeled by the Navier-Stokes equations for Newtonian fluids under suitable conditions. Water and air are the typical examples. However, several experiments have shown that this behavior is not possible for all fluids and for this reason, a large variety of constitutive models have been developed. Fluids that cannot be modeled by a linear constitutive law equation are called non-Newtonian fluids. The viscosity of this type of fluids may be dependent on the rate of strain as well as on the state variables, such as temperature and pressure or total deformation. Typical cases can be found in biological fluids, adhesives, food products, greases and lubricants, polymers and molten metals, among others [142].

Viscoelastic fluids are a specific type of non-Newtonian fluids. They are characterized by having complex and high-molecular-weight molecules with many internal degrees of freedom [23]. The classical examples of this type of fluids are the polymer solutions and molten polymers. The basic feature of polymeric fluids is the presence of long chain molecules. In a flow, these chain molecules are stretched out by the drag forces exerted on them by the surrounding fluid [139]. The natural tendency of the molecule to retract from this stretched configuration generates an elastic force which contributes to the macroscopic stress tensor, and for this reason they are called viscoelastic fluids. The interest for fluids of this kind has increased in the last years, due to the connections with the industrial applications, and motivates the numerical and mathematical analysis of the governing equations [82].

The finite element method is a tool very often employed to deal with the numerical simulation of multiphysics problems, but many times the direct application of the Galerkin method is not possible and the design of new methods is needed. The finite element approximation of the flow of viscoelastic fluids presents several numerical difficulties. It inherits obviously the problems associated with the approximation of the incompressible Navier-Stokes equations, mainly the compatibility between the velocity-pressure approximation and the treatment of the nonlinear advective term. But, on top of that, now the constitutive equation is highly nonlinear, with an advective term that may lead to both global and local oscillations in the numerical approximation. Moreover, even in the case of smooth solutions it is necessary to meet some additional compatibility conditions between the velocity and the stress interpolation in order to control velocity gradients. Elements that satisfy the compatibility requirements velocity-pressure and stress-velocity are scarce and complex.

The objective of this work, is the development of new numerical schemes to solve viscolelastic fluid flows, that are based in the finite element method and can be framed in the context of Sub-Grid-Scales (SGS) methods, also termed Variational Multi-Scale (VMS), al-

lowing to use the same interpolation for the three-fields (velocity-pressure-stress), even in problems where the convection component is dominant both in the momentum and in the constitutive equations.

The starting point of a sub-grid scale approach is to split the unknowns of the problem into two components, namely, the component that can be approximated by the finite element mesh and the unresolvable one, called sub-grid scale or simply sub-scale. The latter needs to be approximated in a simple manner in terms of the former, so as to capture its main effect and yield a stable formulation for the finite element unknown. The number of degrees of freedom is therefore the same as for the Galerkin method. There are different ways to approximate the sub-scale and, in particular, to choose the (finite dimensional) space where it is taken. In this work two different choices are used to define the sub-grid-scale space. In the first one, it is equal to the space of finite element residuals, whereas in the second the space for the sub-scales it is taken as orthogonal to the finite element space, which is a key ingredient in the design of accurate non-residual formulations.

The monolithic resolution of the system of equations that is obtained after discretization of the continuous problem is the most straightforward option. However, solving this system is computationally very expensive, specially in 3D. In this case, the degrees of freedom of the spatial discretization are the six independent elastic stress components, the three velocity components and the pressure. Furthermore, all these variables are coupled, some of them through nonlinear terms. Instead of solving the monolithic system, an alternative is to use a fractional step method in time, in which different equations need to be solved for the different variables in an uncoupled way. The splitting of the equations introduced in fractional step methods has an additional temporal error, that has to be at least of the order of the time integration scheme used to approximate time derivatives if this order is to be preserved. In this work, three different fractional step methods of first, second and third order error in time, are designed for the three-field viscoelastic flow problem.

The numerical solution of incompressible flows involving more than one fluid is a real challenge in computational fluid dynamics, and an important topic in many industrial processes and physical situations. The problems of tracing the interfaces and the discontinuity in the gradients of the unknowns generated by the different material properties of the fluids on a time dependent domain are a hard numerical task. When the interface cuts an element, the discontinuity in the material properties leads to discontinuities in the gradients of the unknowns, which cannot be captured using standard interpolation functions. A local enrichment for the pressure unknowns is presented in the work, which allows one to capture pressure gradient discontinuities in fluids presenting different density values.

Stability and convergence is an important topic in numerical analysis for all kind of problems. For the non-linear nature of the system of equations that defines the viscoelastic fluid flow problem, and the possible time-dependent regime of the flow, a complete study requires advanced knowledge of functional analysis. The objective of the last part of the work is to start with this analysis, knowing that this is only a brushstroke. Stability and convergence is proved both in the stationary as in the time-dependent case for a linearized problem. For the semi-discrete time-dependent case, a fixed point theorem is used to prove the existence of the numerical approximation.

The work has been organized in eight chapters, where the different topics mentioned above are treated.

The Second chapter of the work, *The Three-Field Navier-Stokes Problem*, is devoted to solve numerically quasi-Newtonian fluids flows. In this chapter, two residual based stabilized schemes of the SGS type are proposed, differing in the definition of the space of the sub-grid scales. Both schemes allow one the use of equal interpolation for the variables (velocity-pressure-stress), even in problems where the convection component is dominant and the velocity-pressure-stress gradients are high. This chapter includes a detailed description of

both proposed methods, some of their implementation issues and a discussion about benefits and drawbacks of a three-field formulation. Several numerical examples are tested to show the accuracy and robustness of the formulations.

In the third chapter of the thesis, *The Stationary Viscoelastic Flow Problem*, starting from residual based stabilized formulations, a term-by-term stabilized one is proposed, which is shown to have superior behavior when there are stress and pressure singularities. The proposed methods allow one to use equal interpolation for the problem unknowns and to stabilize the dominant convective terms both in the momentum and constitutive equations. The formulations are tested in the classical benchmarks used for this kind of fluids showing accuracy and robustness.

The fourth chapter of the work, *Fractional Step Methods for the Viscoelastic Problem*, is dedicated to the design of fractional step methods that permit the resolution of the viscoelastic flow problem in a fully decoupled manner. Three different fractional step methods of first, second and third order are presented. The starting point of the methods is the same as for the classical pressure segregation algorithms used in the Newtonian incompressible Navier-Stokes problem. These methods can be understood as an inexact LU block factorization of the original system matrix of the fully discrete problem and are designed at the pure algebraic level. Some classical benchmark problems are used to evaluate the computational improvements in the resolution of the problem, using a fractional step approach.

In the fifth chapter of the thesis, *Approximation of the Two-Fluid Flow Problem*, the different numerical ingredients proposed in the above chapters are used to solve a two fluid flow problem. When the interface between both fluids cuts an element, the discontinuity in the material properties leads to discontinuities in the gradients of the unknowns which cannot be captured using a standard finite element interpolation. In this chapter, a method based on a local enrichment for the pressure unknowns is implemented, that allows one to capture pressure gradient discontinuities in fluids presenting different density values.

The last two chapters, *Numerical Analysis: Stationary Linearized Problem* and *Numerical Analysis: Time-Dependent Problem*, are devoted to the numerical analysis of the proposed non-residual formulation. In the sixth chapter, it is shown that the formulation proposed is stable and optimally convergent independently of the interpolation used. In the seventh chapter, based on a fixed point theorem, the existence of the numerical approximation for a semi-discrete non-linear problem is proved .

We close the work with chapter 8, where conclusions and further possible research lines are summarized.

Chapters are quite self contained even if this implies the need of repeating some information. This is due to the fact that each chapter is based on the following publications:

1. Chapter 2. Stabilized stress-velocity-pressure finite element formulation of the Navier-Stokes problem for fluids with non-linear viscosity. Ernesto Castillo and Ramon Codina. *Computer methods in applied mechanics and engineering*, 279 (2014) 554-578.

2. Chapter 3. Variational multi-scale stabilized formulations for the stationary three-field incompressible viscoelastic flow problem. Ernesto Castillo and Ramon Codina. *Computer methods in applied mechanics and engineering*, 279 (2014) 579-605.

3. Chapter 4. First, second and third order fractional step methods for the three-field viscoelastic flow problem. E. Castillo and R. Codina. *Journal of Computational Physics*, 296 (2015) 113-137.

4. Chapter 5. Approximation of the two-fluid flow problem for viscoelastic fluids using the level set method and pressure enriched finite element shape functions. E. Castillo, J. Baiges and R. Codina. *Journal of Non-Newtonian Fluid Mechanics*, 225 (2015) 37-53.

5. Chapter 6. Numerical analysis of a stabilized finite element approximation for the three-field linearized viscoelastic fluid problem using arbitrary interpolations. E. Castillo and R. Codina. *Submitted*, (2016).

6. Chapter 7. Time-dependent semi-dicrete analysis of the viscoelastic fluid flow problem using a variational multi-scale stabilized formulation. G. Barrenechea, E. Castillo and R. Codina. *in preparation*, (2016).

Additionally, another short article derived from this work, that summarizes some of the key ideas, is:

- Finite element approximation of the viscoelastic flow problem: a non-residual based stabilized formulation. Ernesto Castillo and Ramon Codina. *Computers and Fluids*, *accepted for publication*, (2015).

Chapter 2

The Three-Field Navier-Stokes Problem

2.1 Abstract

The three-field (stress-velocity-pressure) mixed formulation of the incompressible Navier-Stokes problem can lead to two different types of numerical instabilities. The first is associated with the incompressibility and loss of stability in the calculation of the stress field, and the second with the dominant convection. The first type of instabilities can be overcome by choosing an interpolation for the unknowns that satisfies the appropriate inf-sup conditions, whereas the dominant convection requires a stabilized formulation in any case. In this chapter, two stabilized schemes of Sub-Grid Scale (SGS) type are proposed, differing in the definition of the space of the sub-grid scales, and both allowing to use the same interpolation for the variables $\boldsymbol{\sigma}$-$\boldsymbol{u}$-p (deviatoric stress, velocity and pressure), even in problems where the convection component is dominant and the velocity-stress gradients are high. Another aspect considered in this part of the work is the non-linearity of the viscosity, modeled with constitutive models of quasi-Newtonian type. The chapter includes a description of the proposed methods, some of their implementation issues and a discussion about benefits and drawbacks of a three-field formulation. Several numerical examples serve to justify our claims.

2.2 Introduction

Fluids, depending on their behavior under the action of shear-stress, can be classified as Newtonian and non-Newtonian. The last group is predominant in the petroleum industry, in chemical-pharmaceutical processes and in food products [15, 67, 120, 107]. The non-Newtonian behavior is caused by the complex microstructure present in these fluids, in some cases originated by a mixture of different components, which in turn can be found in different states. For example, blood is a complex fluid composed of red cells, white cells, platelets and plasma, which at different shear stresses can pass from a fluid exhibiting Newtonian behavior to one exhibiting pseudoplastic non-Newtonian behavior in high shear stress ranges [100].

There are specific texts devoted to rheology [23, 34] where we can find detailed descriptions of classical models. The simplest of them of quasi-Newtonian type is the Ostwald de Waele or power-law model. More specific for example is the Walburn-Schneck model [171] for modelling blood flow, which includes among its parameters the amount of hematocrit H or fraction of red cells in the blood. The polymeric models consider other factors that modify the viscosity, such as the molecular weight, the polymeric concentration and the changes in the shape of

the polymer chain [119]. Within the quasi-Newtonian classical models, the four parameter Carreau model and the five parameter Carreau-Yasuda model allows one to constrain the limit values in the viscosity when the power-law model predicts non-physical values at high and low shear stresses.

In this part of the work we are interested in the finite element approximation of this type of problems. In particular, we aim to explore the possibilities and benefits of using a three-field formulation, having as unknowns the deviatoric stress, the velocity and the pressure. These mixed approximations can lead to different types of numerical instabilities inherent to the mathematical structure of the equations to be solved when the classical Galerkin approach is used. On the one hand, pressure and velocity are out of control unless appropriate inf-sup conditions are satisfied by the interpolation spaces. Conditions of this type need to be fulfilled also for the velocity and stress interpolation spaces. On the other hand, small viscosity values can lead to the classical instabilities found in convection dominated flows.

Referring to the compatibility conditions (see e.g. [30]), for the three-field approximation they consist of two restrictions, one between pressure and velocity and the other between velocity and stress [56]. These two restrictions reduce the choices of stable finite element spaces that allow one to discretize the unknowns. For example, in [145, 143] it is shown as to design elements that satisfy the inf-sup condition between velocities and stresses through the addition of bubble functions. Another way to satisfy this restriction is using discontinuous finite element spaces for the stress, as shown in [84]. In the viscoelastic fluid context, a well-known stable interpolation in the two-dimensional case consists of using biquadratic elements for the velocity field, bilinear pressure interpolation and a multi-bilinear interpolation for the stresses, which is the popular Marchal-Crochet element [111]. The mathematical analysis of this element can be found in [85]. It is a clear example of the difficulties to satisfy the inf-sup conditions associated to the three-field formulation of flow problems.

When convection becomes dominant, it is necessary to use a stabilized formulation in any case. Among the methods that serve this purpose one can use the Streamline-Upwind/Petrov-Galerkin (SUPG) method [31], the Galerkin-Least Square (GLS) method [98], the Characteristics Galerkin method [74] or the Taylor-Galerkin method [72] (see [50]).

The two stabilized formulations proposed in this chapter are framed in the context of sub-grid scale (SGS) methods (also termed variational multi-scale methods) introduced by Hughes et al. [97] for the scalar convection-diffusion-reaction problem, and extended later to the vectorial Stokes problem in [51], where the space of the sub-grid scales is taken as orthogonal to the finite element space. The purpose of the present chapter is to extend and test numerically the formulation presented in [56] for the Stokes problem with constant viscosity to a three-field formulation $\boldsymbol{\sigma}$-$\boldsymbol{u}$-p (deviatoric stress, velocity and pressure) of the Navier-Stokes problem with non-linear viscosity.

The starting point of a sub-grid scale approach is to split the unknowns of the problem into two components, namely, the component that can be approximated by the finite element mesh and the unresolvable one, called sub-grid scale or simply sub-scale in what follows. The latter needs to be approximated in a simple manner in terms of the former, so as to capture its main effect and yield a stable formulation for the finite element unknown. The number of degrees of freedom is therefore the same as for the Galerkin method. There are different ways to approximate the sub-scale and, in particular, to choose the (finite dimensional) space where it is taken. In this chapter we will describe two formulations which precisely differ in this choice. In the first one, it will be equal to the space of finite element residuals (in a sense to be made precise in what follows), whereas in the second the space for the sub-scales will be taken as orthogonal to the finite element space. Both formulations will allow one to deal with the instabilities of the three-field formulation described earlier. There will be no need to meet the inf-sup conditions for the interpolation spaces and it will be possible to solve convection dominated problems.

We have performed a rather complete numerical testing of the formulations presented. The numerical results shown in this chapter can be separated into four groups. The first (section 2.5.1) corresponds to the study of the convergence of the formulations proposed for the stationary case with non-linear viscosity, more precisely for a power-law fluid with a power-law index in the range $0.5 \leq n \leq 1.5$ and in the range of Reynolds number $0.3 \leq \mathrm{Re} \leq 400$, using linear and quadratic triangular elements. To perform this test we manufacture the solution by introducing a force term computed with a predetermined stress-velocity-pressure solution. The second group of results corresponds to a stationary lid-driven square cavity, where the fluid is subject to a parallel flow and it is modeled by the Ostwald de Waele constitutive model, for a power-law index in the range $0.5 \leq n \leq 1.5$ and with a regime of flow in the range of $100 \leq \mathrm{Re} \leq 5000$. We compare our results with those published by Mendu and Das [116]. The third group of numerical results corresponds to the classical problem of the flow over a cylinder for a highly convected case ($\mathrm{Re} = 140$) of a fluid with non-linear viscosity in the power-law range of $0.4 \leq n \leq 1.8$. We compare some characteristic parameters of the flow obtained with our formulation, like the Strouhal number (St), the drag coefficient ($\mathrm{C_D}$) and the lift coefficient ($\mathrm{C_L}$), with those published by Patnana et al. [131]. This example closes the evaluation of the two formulations in the cases of nonlinear viscosity and dominant convection, in stationary and transient problems. The section with numerical examples concludes with an analysis of the shear stresses over walls computed with the three-field formulation and a classical two-field (velocity-pressure) one, showing the accuracy improvement obtained with the former. This suggests the interest of using the three-field approach in situations in which the accurate evaluation of the shear stresses may be crucial, such as in blood flow or in some fluid-structure interaction problems. Furthermore, it gives confidence in its use in more complex rheological behavior, such as that of viscoelastic fluids, in which the introduction of stresses as unknowns is almost a must.

This chapter is organized as follows. Section 2.3 contains the presentation of the problem, with the three-field continuous Navier-Stokes equations, its variational form, the description of some non-Newtonian constitutive models and the straightforward Galerkin finite element discretization in space and finite difference discretization in time. Section 2.4 presents our stabilized finite element approach, with the description of the general idea and its application to the present problem. The linearization of the problem is also discussed. Section 2.5 contains the numerical results described above and, finally, in Section 2.6 conclusions are summarized.

2.3 The Navier-Stokes problem in a three-field formulation

2.3.1 Initial and boundary value problem

Let Ω be the computational domain of $\mathbb{R}^d$ (d =2 or 3) occupied by the fluid in the time interval $[0, T]$, assumed to be bounded and polyhedral, and let $\partial\Omega$ be its boundary. The incompressible Navier-Stokes equations formulated in terms of stress-velocity-pressure can be written as:

$$\begin{aligned} \rho\left(\frac{\partial \boldsymbol{u}}{\partial t} + \boldsymbol{u}\cdot\nabla\boldsymbol{u}\right) - \nabla\cdot\boldsymbol{\sigma} + \nabla p = \boldsymbol{f} \ \text{ in } \Omega, t \in]0,T[\,, \\ \nabla\cdot\boldsymbol{u} = 0 \ \text{ in } \Omega, t \in]0,T[\,, \\ \frac{1}{2\eta}\boldsymbol{\sigma} - \nabla^s\boldsymbol{u} = \boldsymbol{0} \ \text{ in } \Omega, t \in]0,T[\,, \end{aligned}$$

where $\boldsymbol{u}$ is the velocity field, p the pressure, $\boldsymbol{\sigma}$ the deviatoric component of the stress field, $\boldsymbol{f}$ the vector of body forces, η corresponds to the apparent viscosity of the fluid, which in

the Newtonian case is identical to the dynamic viscosity (μ), ρ is the fluid density and $\nabla^s \boldsymbol{u}$ is the symmetrical part of $\nabla \boldsymbol{u}$.

The equations above need to be solved together with initial conditions of the form $\boldsymbol{u} = \boldsymbol{u}^0$ and appropriate boundary conditions. For the sake of simplicity in the exposition, we will consider homogeneous boundary conditions $\boldsymbol{u} = \boldsymbol{0}$ on $\partial\Omega$.

2.3.2 The variational form

In order to write the weak form of the problem, let us introduce some notation. As usual, the space of square integrable functions in a domain Ω is denoted by $L^2(\Omega)$, while the space of functions whose first derivative is square integrable is denoted by $H^1(\Omega)$. The space $H_0^1(\Omega)$ consists of functions in $H^1(\Omega)$ vanishing on $\partial\Omega$. Using this notation, the finite element spaces used in the continuous three-field problem are $L^2\left(0,\ T;\ \boldsymbol{\mathcal{V}}_0\right)$ for the velocity field, $\mathcal{D}'\left(0,\ T;\ Q\right)$ for the pressure, and $\mathcal{D}'\left(0,\ T;\ \boldsymbol{\Upsilon}\right)$ for the stress field, where $\boldsymbol{\mathcal{V}}_0 = \left(H_0^1\left(\Omega\right)\right)^{\mathrm{d}}$, $Q = L^2\left(\Omega\right)/\mathbb{R}$, $\boldsymbol{\Upsilon} = \left(L^2\left(\Omega\right)\right)^{d\times d}_{\mathrm{sym}}$ (symmetric second order tensors with square-integrable components) and $\mathcal{D}'$ is used to denote distributions in time.

For constant viscosity, the weak form of the problem consists in finding $\boldsymbol{U} = [\boldsymbol{u}, p, \boldsymbol{\sigma}] \in \boldsymbol{\mathcal{X}}_T$ such that:

$$\begin{aligned}\left(\rho\frac{\partial \boldsymbol{u}}{\partial t}, \boldsymbol{v}\right) + \langle \rho\boldsymbol{u}\cdot\nabla\boldsymbol{u}, \boldsymbol{v}\rangle + (\boldsymbol{\sigma}, \nabla^s\boldsymbol{v}) - (p, \nabla\cdot\boldsymbol{v}) &= \langle \boldsymbol{f}, \boldsymbol{v}\rangle\,,\\ (\nabla\cdot\boldsymbol{u}, q) &= 0,\\ \left(\frac{1}{2\eta}\boldsymbol{\sigma}, \boldsymbol{\tau}\right) - (\nabla^s\boldsymbol{u}, \boldsymbol{\tau}) &= 0,\end{aligned}$$

for all $\boldsymbol{V} = [\boldsymbol{v}, q, \boldsymbol{\tau}] \in \boldsymbol{\mathcal{X}} = \boldsymbol{\mathcal{V}}_0 \times Q \times \boldsymbol{\Upsilon}$, where $\boldsymbol{\mathcal{X}}_T = L^2\left(0,\ T;\ \boldsymbol{\mathcal{V}}_0\right) \times \mathcal{D}'\left(0,\ T;\ Q\right) \times \mathcal{D}'\left(0,\ T;\ \boldsymbol{\Upsilon}\right)$, $(\cdot,\cdot)$ stands for the L^2 inner product and $\langle\cdot,\cdot\rangle$ is the integral of the product of the functions in the two arguments, whenever it makes sense. In particular, it is the duality pairing between $\boldsymbol{\mathcal{V}}_0$ and its dual $(H^{-1}(\Omega))^d$, where $\boldsymbol{f}$ is assumed to belong.

In compact form, the problem can be written as:

$$\left(\rho\frac{\partial \boldsymbol{u}}{\partial t}, \boldsymbol{v}\right) + B\left(\boldsymbol{U}, \boldsymbol{V}\right) = \langle \boldsymbol{f}, \boldsymbol{v}\rangle\,, \tag{2.1}$$

where

$$B\left(\boldsymbol{U}, \boldsymbol{V}\right) = \langle \rho\boldsymbol{u}\cdot\nabla\boldsymbol{u}, \boldsymbol{v}\rangle + (\boldsymbol{\sigma}, \nabla^s\boldsymbol{v}) - (p, \nabla\cdot\boldsymbol{v}) + (\nabla\cdot\boldsymbol{u}, q) + \left(\frac{1}{2\eta}\boldsymbol{\sigma}, \boldsymbol{\tau}\right) - (\nabla^s\boldsymbol{u}, \boldsymbol{\tau})\,.$$

Equation (2.1) needs to be completed with the initial condition satisfied in a weak sense.

In the case on nonlinear viscosity, more regularity on the stresses and the velocities might be required depending on the constitutive model. This is however outside the scope of this part of the work.

2.3.3 Non-Newtonian models

In many fluids the viscosity may be dependent on the rate of strain as well as on the state variables, such as temperature and pressure or total deformation (see for example [173]). Typical cases can be found in biological fluids (blood, saliva, synovial fluid), adhesives, food products (pureed fruits/vegetables, sauces), greases and lubricants, polymers and molten metals, among others. The non-Newtonian models abound in the literature and the formulations can vary from a simple two-parameter power-law model to complex models designed for

specific fluids. In the simplest case, the constitutive law of a non-Newtonian fluid is written in terms of the second invariant of the strain rate tensor, which we will denote as I_2.

In this chapter, two non-Newtonian models have been implemented to characterize the non-linear viscosity of the fluid, both based on I_2. These are the two-parameter power law model and the five-parameter Carreau-Yasuda model, respectively given by

$$\eta = m\left(\frac{I_2}{2}\right)^{\frac{n-1}{2}}, \tag{2.2}$$

$$\eta = \mu_\infty + (\mu_0 - \mu_\infty)\left(1 + \left(\lambda\sqrt{I_2}\right)^b\right)^{\frac{n-1}{b}}, \tag{2.3}$$

where

$$I_2 = 2\left(\dot{\boldsymbol{\varepsilon}} : \dot{\boldsymbol{\varepsilon}}\right), \qquad \dot{\boldsymbol{\varepsilon}} = \frac{1}{2}\left(\nabla\boldsymbol{u} + (\nabla\boldsymbol{u})^T\right) =: \nabla^s\boldsymbol{u}.$$

In (2.2)-(2.3), m represents the consistency index, n the power-law index, μ_0 and μ_∞ the limit values of the viscosity in the Carreau-Yasuda model, and λ and b are constants of this model. When $b = 2$, the Carreau-Yasuda model tends to the classical Carreau model.

The two-parameter power-law model is the simplest of the models that allow one to introduce a nonlinear relationship between viscosity and shear rate. The major drawback of this model is seen at low and high shear rates, where the apparent viscosity value can tend to singular values. With respect to this problem, the Carreau-Yasuda model is superior, allowing to control the range of viscosities, with the disadvantage of requiring a larger number of parameters to be implemented.

Even though we will use the described models in the numerical examples, the stabilized formulation presented in the Section 2.4 is completely general and any generalized Newtonian model can be easily implemented.

2.3.4 Galerkin finite element discretization and time discretization

The standard Galerkin approximation for the variational problem defined by (2.1) can be performed by considering a finite element partition $\mathcal{T}_h$ of the domain Ω. The diameter of an element domain $K \in \mathcal{T}_h$ is denoted by h_K and the diameter of the element partition is defined by $h = \max\{h_K \mid K \in \mathcal{T}_h\}$. Under the above considerations, we can construct conforming finite element spaces, $\boldsymbol{\mathcal{V}}_{h,0} \subset \boldsymbol{\mathcal{V}}_0$, $Q_h \subset Q$ and $\boldsymbol{\Upsilon}_h \subset \boldsymbol{\Upsilon}$ in the usual manner. If $\boldsymbol{\mathcal{X}}_h = \boldsymbol{\mathcal{V}}_{h,0} \times Q_h \times \boldsymbol{\Upsilon}_h$ and $\boldsymbol{U}_h = [\boldsymbol{u}_h, p_h, \boldsymbol{\sigma}_h]$, the Galerkin finite element approximation consists in finding $\boldsymbol{U}_h \in C^0(0, T; \boldsymbol{\mathcal{X}}_h)$ such that

$$\left(\rho\frac{\partial\boldsymbol{u}_h}{\partial t}, \boldsymbol{v}_h\right) + B\left(\boldsymbol{U}_h, \boldsymbol{V}_h\right) = \langle\boldsymbol{f}, \boldsymbol{v}_h\rangle, \tag{2.4}$$

for all $\boldsymbol{V}_h = [\boldsymbol{v}_h, q_h, \boldsymbol{\tau}_h] \in \boldsymbol{\mathcal{X}}_h$

The term involving the time derivative can be discretized in different ways. A possible option is to use a space-time finite element formulation, although we will use the most common option of discretizing in time using finite differences. In particular, we have implemented first and second order backward differencing schemes, based respectively on the approximations

$$\frac{\partial\boldsymbol{u}_h^{j+1}}{\partial t} = \frac{\boldsymbol{u}_h^{j+1} - \boldsymbol{u}_h^j}{\delta t} + \mathcal{O}\left(\delta t\right),$$
$$\frac{\partial\boldsymbol{u}_h^{j+1}}{\partial t} = \frac{3\boldsymbol{u}_h^{j+1} - 4\boldsymbol{u}_h^j + \boldsymbol{u}_h^{j-1}}{2\delta t} + \mathcal{O}\left(\delta t^2\right).$$

In both cases, δt corresponds to the size of a uniform partition of the time interval $[0, T]$, while $\mathcal{O}(\cdot)$ represents the approximation order of the scheme. The superscript indicates the time step where the variable is being approximated, so that $\boldsymbol{u}^j$ is an approximation to $\boldsymbol{u}$ at time $t^j = j\delta t$.

So far, no restrictions have been imposed on the choice of the finite element spaces. However, there are restrictions that must be satisfied explicitly in the discrete formulation used. To see this, consider the stationary Stokes problem with constant viscosity, which can be written as: find $\boldsymbol{U}_h = [\boldsymbol{u}_h, p_h, \boldsymbol{\sigma}_h] \in \boldsymbol{\mathcal{X}}_h$ such that

$$B_0(\boldsymbol{U}_h, \boldsymbol{V}_h) = \langle \boldsymbol{f}, \boldsymbol{v}_h \rangle,$$

for all $\boldsymbol{V}_h = [\boldsymbol{v}_h, q_h, \boldsymbol{\tau}_h] \in \boldsymbol{\mathcal{X}}_h$, with

$$\begin{aligned} B_0(\boldsymbol{U}_h, \boldsymbol{V}_h) = &(\boldsymbol{\sigma}_h, \nabla^s \boldsymbol{v}_h) - (p_h, \nabla \cdot \boldsymbol{v}_h) + (\nabla \cdot \boldsymbol{u}_h, q_h) \\ &+ \frac{1}{2\eta}(\boldsymbol{\sigma}_h, \boldsymbol{\tau}_h) - (\nabla^s \boldsymbol{u}_h, \boldsymbol{\tau}_h). \end{aligned} \tag{2.5}$$

Taking $\boldsymbol{V}_h = \boldsymbol{U}_h$ it is easily seen that the Galerkin formulation only provides control over the stress field:

$$B_0(\boldsymbol{U}_h, \boldsymbol{U}_h) = \frac{1}{2\eta} \|\boldsymbol{\sigma}_h\|^2.$$

The three-field Stokes problem has been studied by a large number of authors (see for example [29, 95]). It can be shown that the classical inf-sup condition:

$$\inf_{\boldsymbol{U}_h \in \boldsymbol{\mathcal{X}}_h} \sup_{\boldsymbol{V}_h \in \boldsymbol{\mathcal{X}}_h} \frac{B_0(\boldsymbol{U}_h, \boldsymbol{V}_h)}{\|\boldsymbol{U}_h\|_{\boldsymbol{\mathcal{X}}_h} \|\boldsymbol{V}_h\|_{\boldsymbol{\mathcal{X}}_h}} \geq \beta$$

is not satisfied for any positive constant β, unless the following two conditions hold:

$$\inf_{q_h \in \mathcal{Q}_h} \sup_{\boldsymbol{v}_h \in \boldsymbol{\mathcal{V}}_h} \frac{(q_h, \nabla \cdot \boldsymbol{v}_h)}{\|\boldsymbol{v}_h\|_{\boldsymbol{\mathcal{V}}_h} \|q_h\|_{\mathcal{Q}_h}} \geq C_1, \tag{2.6}$$

$$\inf_{\boldsymbol{v}_h \in \boldsymbol{\mathcal{V}}_h} \sup_{\boldsymbol{\tau}_h \in \boldsymbol{\Upsilon}_h} \frac{(\boldsymbol{\tau}_h, \nabla^s \boldsymbol{v}_h)}{\|\boldsymbol{\tau}_h\|_{\boldsymbol{\Upsilon}_h} \|\boldsymbol{v}_h\|_{\boldsymbol{\mathcal{V}}_h}} \geq C_2, \tag{2.7}$$

where C_1 and C_2 represent two positive constants independent of h, while $\|\cdot\|_Y$ stands for the appropriate norm in space Y. A stable numerical formulation is obtained if the finite element spaces satisfy (7.21)-(7.22). However, from the numerical point of view, the spaces that fulfill these conditions are limited, particularly when the problem needs to be solved in three dimensions. The alternative is to use a stabilized formulation allowing any interpolation for the variables. In general, a stabilized formulation consists of replacing (2.5) by another bilinear form B_h, possibly mesh dependent, with enhanced stability properties. In the Navier-Stokes equations, it has to be also capable of dealing with the instabilities generated in the case of dominant convection. The two stabilized formulations presented below satisfy these conditions.

2.4 Design of a stable finite element formulation

In the following we present two stabilized formulations for the three-field Navier-Stokes problem analyzed. Both formulations are based on the variational multi-scale approach introduced by Hughes et al. [97] for the scalar convection-diffusion problem. The basic idea is to approximate the effect of the components of the solution of the continuous problem that cannot be resolved by the finite element mesh. Here we present the general idea in the case

of a general nonlinear evolution problem, and then particularize it to the problem of interest. The presentation is formal, avoiding technicalities and trying to describe the essential ideas and simplifications.

Consider a differential equation of the form:

$$\boldsymbol{M}\left(\boldsymbol{U}\right)\frac{\partial \boldsymbol{U}}{\partial t}+\mathcal{L}\left(\boldsymbol{U},\boldsymbol{U}\right)=\boldsymbol{F}, \tag{2.8}$$

where $\boldsymbol{U}$ contains the unknowns of the problem (which in our particular case are $[\boldsymbol{u}, p, \boldsymbol{\sigma}]$), $\mathcal{L}(\boldsymbol{U},\cdot)$ corresponds to an operator associated with the specific problem assumed to be linear in the second argument, $M(\boldsymbol{U})$ is a mass matrix and $\boldsymbol{F}$ a force vector.

The weak form of the generic problem (2.8), can be formally written as

$$\left(\boldsymbol{M}\left(\boldsymbol{U}\right)\frac{\partial \boldsymbol{U}}{\partial t},\boldsymbol{V}\right)+\left\langle \mathcal{L}\left(\boldsymbol{U},\boldsymbol{U}\right),\boldsymbol{V}\right\rangle =\left\langle \boldsymbol{F},\boldsymbol{V}\right\rangle , \tag{2.9}$$

for an appropriate "duality" and considering $\boldsymbol{V}$ as a test function. The boundary conditions of the problem have to be taken into account, and are understood to be incorporated in the duality $\langle\cdot,\cdot\rangle$. Likewise, when considering finite element functions the duality has to be understood as the element-wise integral with appropriate inter-element jumps.

2.4.1 The sub-scale concept

The basic idea of the formulation applied to the generic problem is to split the unknown as $\boldsymbol{U}=\boldsymbol{U}_h+\boldsymbol{U}'$, where $\boldsymbol{U}_h\in\boldsymbol{\mathcal{X}}_h$ is the component of the solution that belongs to the finite element space and $\boldsymbol{U}'\in\boldsymbol{\mathcal{X}}'$ is the remainder, referred to as sub-grid scale or sub-scale. The spaces $\boldsymbol{\mathcal{X}}_h$ and $\boldsymbol{\mathcal{X}}'$ are such that $\boldsymbol{\mathcal{X}}=\boldsymbol{\mathcal{X}}_h\bigoplus\boldsymbol{\mathcal{X}}'$. Under the above considerations, the original problem (2.9), is exactly equivalent to:

$$\left(\boldsymbol{M}\left(\boldsymbol{U}\right)\frac{\partial \boldsymbol{U}}{\partial t},\boldsymbol{V}_h\right)+\left\langle \mathcal{L}\left(\boldsymbol{U},\boldsymbol{U}\right),\boldsymbol{V}_h\right\rangle =\left\langle \boldsymbol{F},\boldsymbol{V}_h\right\rangle \quad\forall\boldsymbol{V}_h\in\boldsymbol{\mathcal{X}}_h, \tag{2.10}$$

$$\left(\boldsymbol{M}\left(\boldsymbol{U}\right)\frac{\partial \boldsymbol{U}}{\partial t},\boldsymbol{V}'\right)+\left\langle \mathcal{L}\left(\boldsymbol{U},\boldsymbol{U}\right),\boldsymbol{V}'\right\rangle =\left\langle \boldsymbol{F},\boldsymbol{V}'\right\rangle \quad\forall\boldsymbol{V}'\in\boldsymbol{\mathcal{X}}'. \tag{2.11}$$

In essence, the goal of all sub-scale methods, including the approximation of the sub-scale with bubble functions, is to approximate $\boldsymbol{U}'$ in one way or another and end up with a problem for $\boldsymbol{U}_h$ alone.

2.4.2 General approach of the sub-scale stabilized formulation

There are different approximations for the sub-scale component $\boldsymbol{U}'$ that allow writing it as a function of the finite element component, $\boldsymbol{U}_h$.

We call the sub-scales *dynamic* if their temporal derivative is taken into account, whereas if it is neglected we call them *quasi-static*. Another possible simplification is to consider that they vanish on the inter-element boundaries, as it is done for example when bubble functions are used to approximate the sub-scales. We will assume this, although this restriction could be relaxed (see [56]). A third possible simplification, explained in more detail below, is to neglect the sub-scale effect on the non-linear terms of the equation.

Apart from the simplifications described, another important ingredient in the construction of the stabilized formulation is the choice of the space where the sub-scales belong. The most common choice is to take it equal to the space generated by the operator associated with the problem, applied to the finite element space [53]. Another possibility is to take it orthogonal

to the finite element space, that is, $\boldsymbol{\mathcal{X}}' = \boldsymbol{\mathcal{X}}_h^{\perp}$, resulting in the so called orthogonal sub-scales (OSS) method [54].

Equations (2.10)-(2.11), after an appropriate integration by parts, can be written as follows:

$$\left(\boldsymbol{M}\left(\boldsymbol{U}\right)\frac{\partial \boldsymbol{U}}{\partial t},\boldsymbol{V}_h\right)+\left\langle \mathcal{L}\left(\boldsymbol{U},\boldsymbol{U}_h\right),\boldsymbol{V}_h\right\rangle+\left\langle \boldsymbol{U}^{'},\mathcal{L}^{*}\left(\boldsymbol{U},\boldsymbol{V}_h\right)\right\rangle=\left\langle \boldsymbol{F},\boldsymbol{V}_h\right\rangle \quad \forall \boldsymbol{V}_h\in\boldsymbol{\mathcal{X}}_h, \tag{2.12}$$

$$\left(\boldsymbol{M}\left(\boldsymbol{U}\right)\frac{\partial \boldsymbol{U}}{\partial t},\boldsymbol{V}^{'}\right)+\left\langle \mathcal{L}\left(\boldsymbol{U},\boldsymbol{U}_h\right),\boldsymbol{V}^{'}\right\rangle+\left\langle \boldsymbol{U}^{'},\mathcal{L}^{*}\left(\boldsymbol{U},\boldsymbol{V}^{'}\right)\right\rangle=\left\langle \boldsymbol{F},\boldsymbol{V}^{'}\right\rangle \quad \forall \boldsymbol{V}^{'}\in\boldsymbol{\mathcal{X}}^{'}, \tag{2.13}$$

where we have introduced the formal adjoint $\mathcal{L}^{*}(\boldsymbol{U},\cdot)$ of operator $\mathcal{L}(\boldsymbol{U},\cdot)$, which is defined through the relationship

$$\left\langle \mathcal{L}\left(\boldsymbol{U},\boldsymbol{W}\right),\boldsymbol{V}\right\rangle=\left\langle \boldsymbol{W},\mathcal{L}^{*}\left(\boldsymbol{U},\boldsymbol{V}\right)\right\rangle,$$

for all $\boldsymbol{U}$, $\boldsymbol{W}$, $\boldsymbol{V}\in\boldsymbol{\mathcal{X}}$. Again, the duality might involve inter-element jump terms when finite element functions are considered. However, if these inter-element terms are neglected and P' denotes the L^2 projection onto the space of sub-scales, Eq. (2.13) can be formally written as

$$P^{'}\left[\boldsymbol{M}\left(\boldsymbol{U}\right)\frac{\partial \boldsymbol{U}^{'}}{\partial t}+\mathcal{L}\left(\boldsymbol{U},\boldsymbol{U}^{'}\right)\right]=P^{'}\left[\boldsymbol{R}_{\boldsymbol{U}}\right],$$

where $\boldsymbol{R}_{\boldsymbol{U}}$ represents the residual of the finite element approximation, that is to say,

$$\boldsymbol{R}_{\boldsymbol{U}}=\boldsymbol{F}-\boldsymbol{M}\left(\boldsymbol{U}\right)\frac{\partial \boldsymbol{U}_h}{\partial t}-\mathcal{L}\left(\boldsymbol{U},\boldsymbol{U}_h\right).$$

At this point additional approximations are required and different methods may be devised according to the approximations chosen. A particular case of the sub-scale method described above is an algebraic approximation of the sub-scales [96]. The approximation of the problem in this case is:

$$\mathcal{L}\left(\boldsymbol{U},\boldsymbol{U}^{'}\right)\approx\boldsymbol{\alpha}^{-1}\left(\boldsymbol{U}\right)\boldsymbol{U}^{'},$$

where $\boldsymbol{\alpha}^{-1}\left(\boldsymbol{U}\right)$ is a matrix defined within each element domain that has to be determined. We shall refer to it has the matrix of stabilization parameters.

With the above approximation, for an adequate projection onto the sub-scale space P', $\boldsymbol{U}'$ needs to be calculated from the following ordinary nonlinear differential equation in each element:

$$\boldsymbol{M}\left(\boldsymbol{U}_h+\boldsymbol{U}^{'}\right)\frac{\partial \boldsymbol{U}^{'}}{\partial t}+\boldsymbol{\alpha}^{-1}\left(\boldsymbol{U}_h+\boldsymbol{U}^{'}\right)\boldsymbol{U}^{'}=P^{'}\left[\boldsymbol{F}-\boldsymbol{M}\left(\boldsymbol{U}_h+\boldsymbol{U}^{'}\right)\frac{\partial \boldsymbol{U}_h}{\partial t}-\mathcal{L}\left(\boldsymbol{U}_h+\boldsymbol{U}^{'},\boldsymbol{U}_h\right)\right], \tag{2.14}$$

where we have assumed for simplicity that the term on the left is in the space of sub-scales.

It is important to note that the calculation of $\boldsymbol{U}'$ needs to be made at the integration points, that is to say, Eq. (2.14) is in fact a nonlinear ordinary differential equation.

2.4.3 Stabilized formulation applied to the three-field Navier-Stokes problem

Let us apply the general procedure described to the three-field form of the incompressible Navier-Stokes equations. The key point is the approximation of matrix $\boldsymbol{\alpha}(\boldsymbol{U})$. We shall not motivate it here, but simply use the same heuristic arguments as in [56]. Taking this matrix

diagonal, of the form $\boldsymbol{\alpha} = \text{diag}(\alpha_1 \boldsymbol{I_u}, \alpha_2, \alpha_3 \boldsymbol{I_\sigma})$, with $\boldsymbol{I_u}$ and $\boldsymbol{I_\sigma}$ the identity matrices on velocities and stresses, respectively, Eq. (2.14) reads

$$\rho \frac{\partial \boldsymbol{u}'}{\partial t} + \frac{1}{\alpha_1} \boldsymbol{u}' = P' \left(\boldsymbol{R_u} \right), \tag{2.15}$$

$$\frac{1}{\alpha_2} p' = P' \left(R_p \right), \tag{2.16}$$

$$\frac{1}{\alpha_3} \boldsymbol{\sigma}' = P' \left(\boldsymbol{R_\sigma} \right), \tag{2.17}$$

where $\boldsymbol{R_u}$ corresponds to the residual of the momentum equation, R_p the residual of the continuity equation and $\boldsymbol{R_\sigma}$ the residual of the constitutive equation.

Problem (2.15)-(2.17) (with initial conditions for the sub-scale velocity) is in fact a differential-algebraic system. Taking into account the time derivative of the sub-scale velocity leads to improved numerical behavior that we have exploited for example in [54, 60, 58, 13]. However, when the time step of the time discretization is not much smaller than $\rho\alpha_1$, this time derivative can be neglected, leading to what we call *quasi-static* sub-scales, which is the approach used in this work. In this case, problem (2.15)-(2.17) reduces to

$$\begin{aligned} \boldsymbol{u}' &= \alpha_1 P' \left(\boldsymbol{R_u} \right), \\ p' &= \alpha_2 P' \left(R_p \right), \\ \boldsymbol{\sigma}' &= \alpha_3 P' \left(\boldsymbol{R_\sigma} \right). \end{aligned}$$

All the approximations used heretofore will be used in our formulation. It remains only to define the space of sub-scales or, what is equivalent, the projection P'. As in previous works, two possibilities will be explored. In the first case, P' will be taken as the adequate identity I when applied to finite element residuals. We will refer to this approach as the ASGS (Algebraic Sub-Grid Scale) formulation. The sub-scales are then given by

$$\boldsymbol{u}' = \alpha_1 \boldsymbol{R_u}, \tag{2.18}$$

$$p' = \alpha_2 R_p, \tag{2.19}$$

$$\boldsymbol{\sigma}' = \alpha_3 \boldsymbol{R_\sigma}. \tag{2.20}$$

The second formulation that we will test, which we will refer to as OSS (Orthogonal Sub-scale Stabilization) method, considers that the space of sub-scales is orthogonal to the finite element space ($\boldsymbol{\mathcal{X}}' = \boldsymbol{\mathcal{X}}_h^\perp$), and then the expression of the sub-scales is

$$\boldsymbol{u}' = \alpha_1 P_h^\perp \left(\boldsymbol{R_u} \right) = \alpha_1 \left(\boldsymbol{R_u} - P_h \left(\boldsymbol{R_u} \right) \right), \tag{2.21}$$

$$p' = \alpha_2 P_h^\perp \left(R_p \right) = \alpha_2 \left(R_p - P_h \left(R_p \right) \right), \tag{2.22}$$

$$\boldsymbol{\sigma}' = \alpha_3 P_h^\perp \left(\boldsymbol{R_\sigma} \right) = \alpha_3 \left(\boldsymbol{R_\sigma} - P_h \left(\boldsymbol{R_\sigma} \right) \right), \tag{2.23}$$

where P_h is the L^2 projection onto the appropriate finite element space.

A simple dimensional analysis reveals that the units of α_1 must be time divided by density (TL^3/M, if T is time, L is length and M is mass), whereas the units of α_2 and α_3 must be those of viscosity (M/LT). In this case, $\boldsymbol{u}'$ will be a velocity, p' a pressure and $\boldsymbol{\sigma}'$ a stress.

A discussion about the construction of the stabilizing parameter matrix for the Stokes problem can be found in [56]. In our case, we can follow a similar approach, now considering

the existence of the convective term in the momentum equations and the fact that the viscosity is variable. The expression of matrix $\boldsymbol{\alpha}$ we will use is [51, 55]:

$$\boldsymbol{\alpha} = \begin{bmatrix} \left[c_1 \frac{\eta}{h_1^2} + c_2 \frac{\rho \left| \boldsymbol{u}_h \right|}{h_2} \right]^{-1} & 0 & 0 \\ 0 & c_3 2\eta & 0 \\ 0 & 0 & c_4 2\eta \end{bmatrix}. \tag{2.24}$$

Here, η corresponds to the apparent viscosity of the fluid that in the Newtonian case is identical to the dynamic viscosity (μ), h_1 corresponds to a characteristic length calculated as the square root of the element area in the 2D case, and as the cube root of the element volume in the 3D case, and h_2 corresponds to another characteristic length, calculated as the element length in the direction of the streamline. The constants c_i, $i = 1, 4$, are algorithmic parameters in the formulation. The values used in this part of the work are $c_1 = 4.0$, $c_2 = 2.0$ and $c_3 = c_4 = 0.1$. In the case of higher order elements, the element lengths h_1 and h_2 in (2.24) are respectively divided by k^2 and k, k being the order of the finite element interpolation.

The two proposed stabilized formulations can be defined as residual-based. Consistency is ensured by construction. The stability constant depends on the value of the algorithmic constants c_i, $i = 1, 2, 3, 4$. The numerical analysis indicates that they have to be of order one (see [56]), and that $c_4 < 1$ (note that they are all dimensionless, and independent of the dimensionless numbers that govern the problem). The value $c_4 = 0.1$ has been found to give good results in the tests presented in this chapter, whereas $c_1 = 4.0$, $c_2 = 2.0$ are the optimal values for the approximation of the one-dimensional convection-diffusion equation.

We are now in a position to write the stabilized finite element formulations we will test. The abstract equation for the finite element component (2.12), which replaces the Galerkin finite element equation (2.4), now reads

$$\left(\rho \frac{\partial \boldsymbol{u}_h}{\partial t}, \boldsymbol{v}_h \right) + B\left(\boldsymbol{U}_h, \boldsymbol{V}_h \right) + \sum_K \left(\mathcal{L}^* \left(\boldsymbol{u}_h; \boldsymbol{V}_h \right), \boldsymbol{\alpha} \boldsymbol{R}_{\boldsymbol{U}} \right)_K = \left\langle \boldsymbol{f}, \boldsymbol{v}_h \right\rangle, \tag{2.25}$$

for the ASGS case, and:

$$\left(\rho \frac{\partial \boldsymbol{u}_h}{\partial t}, \boldsymbol{v}_h \right) + B\left(\boldsymbol{U}_h, \boldsymbol{V}_h \right) + \sum_K \left(\mathcal{L}^* \left(\boldsymbol{u}_h; \boldsymbol{V}_h \right), \boldsymbol{\alpha} \left(\boldsymbol{R}_{\boldsymbol{U}} - P_h \left(\boldsymbol{R}_{\boldsymbol{U}} \right) \right) \right)_K = \left\langle \boldsymbol{f}, \boldsymbol{v}_h \right\rangle, \tag{2.26}$$

in the case of orthogonal sub-scales (OSS), $\sum_K$ denoting summation for all elements of the finite element partition and $(\cdot, \cdot)_K$ the $L^2(K)$ inner product. In both formulations (2.25) and (2.26), the following term is added to the standard Galerkin formulation:

$$\left(\mathcal{L}^* \left(\boldsymbol{a}; \boldsymbol{V}_h \right), \boldsymbol{\alpha} \boldsymbol{R}_{\boldsymbol{U}} \right)_K = \int_K \begin{bmatrix} \nabla \cdot \boldsymbol{\tau}_h - \rho \boldsymbol{a} \cdot \nabla \boldsymbol{v}_h - \nabla q_h \\ -\nabla \cdot \boldsymbol{v}_h \\ \frac{1}{2\eta} \boldsymbol{\tau}_h + \nabla^s \boldsymbol{v}_h \end{bmatrix}^T \boldsymbol{\alpha} \begin{bmatrix} \boldsymbol{f} - \left(\rho \left(\frac{\partial \boldsymbol{u}_h}{\partial t} + \boldsymbol{a} \cdot \nabla \boldsymbol{u}_h \right) - \nabla \cdot \boldsymbol{\sigma}_h + \nabla p_h \right) \\ -\nabla \cdot \boldsymbol{u}_h \\ -\frac{1}{2\eta} \boldsymbol{\sigma}_h + \nabla^s \boldsymbol{u}_h \end{bmatrix} dK, \tag{2.27}$$

with η computed with the velocity field $\boldsymbol{a}$. In the case of the OSS method, the contribution from the projection P_h in (2.26) needs also to be added.

The velocity field $\boldsymbol{a}$ appearing in (2.27) may be computed in several ways, depending on the linearization strategy and on whether the velocity sub-scales are taken into account or not in the advection velocity. If $\boldsymbol{a} = \boldsymbol{u}_h + \boldsymbol{u}'$, we call the sub-scales non-linear, in the sense that they are not neglected in the nonlinear terms. Even if this option has shown its superior

performance, particularly in thermally coupled flows (see [6]) and can be shown to mimic the dissipative structure of the continuous problem (see [136]), we will approximate $\boldsymbol{a} \approx \boldsymbol{u}_h$. The iteration where this velocity is evaluated is indicated below.

Regarding the qualitative comparison between (2.25) and (2.26), it has to be noted that both formulations are consistent, and that the latter introduces less dissipation, in the sense that only the component of (part of) the finite element residual orthogonal to the finite element space appears as dissipation when the test function is taken equal to the finite element unknown.

2.4.4 Fully discrete and linearized problem

The Navier-Stokes problem to be solved has two sources of nonlinearity, namely, the convective term and the constitutive law. When the equations are discretized using the finite element method described, other nonlinearities appear because of the dependence of the stabilizing terms on the velocity.

For the sake of conciseness, we will consider only a fixed-point iterative scheme and the second order BDF scheme for the time integration, since this linearization is stable for divergence free velocities (another possibility would be to use a Newton-Raphson scheme or variants of it). In particular, the stabilization parameters in (2.24) are assumed to be computed with a given velocity guess and iteratively updated, also neglecting the velocity sub-scale. If we denote with a double superscript the time step and iteration counter, the problem to be solved at time step $j+1$ to find the $i+1$ iterate of the unknowns is given by:

$$\begin{aligned}
&\left(\rho\frac{3\boldsymbol{u}_h^{j+1,i+1}}{2\delta t},\boldsymbol{v}_h\right)+\left(\nabla^s\boldsymbol{v}_h,\boldsymbol{\sigma}_h^{j+1,i+1}\right)+\left(\rho\boldsymbol{u}_h^{j+1,i}\cdot\nabla\boldsymbol{u}_h^{j+1,i+1},\boldsymbol{v}_h\right)\\
&\quad-\left(p_h^{j+1,i+1},\nabla\cdot\boldsymbol{v}_h\right)+\sum_K\left(-\rho\boldsymbol{u}_h^{j+1,i}\cdot\nabla\boldsymbol{v}_h,\alpha_1P'\left(\boldsymbol{R_u}\right)\right)_K\\
&\quad+\sum_K\left(-\nabla\cdot\boldsymbol{v}_h,\alpha_2P'\left(R_p\right)\right)_K+\sum_K\left(\nabla^s\boldsymbol{v}_h,\alpha_3P'\left(\boldsymbol{R_\sigma}\right)\right)_K=\langle\boldsymbol{f},\boldsymbol{v}_h\rangle\\
&\qquad\qquad+\left(\rho\frac{4\boldsymbol{u}_h^{j}-\boldsymbol{u}_h^{j-1}}{2\delta t},\boldsymbol{v}_h\right),
\end{aligned}\tag{2.28}$$

$$\left(q_h,\nabla\cdot\boldsymbol{u}_h^{j+1,i+1}\right)+\sum_K\left(-\nabla q_h,\alpha_1P'\left(\boldsymbol{R_u}\right)\right)_K=0,\tag{2.29}$$

$$\begin{aligned}
&\left(\frac{1}{2\eta^{j+1,i}}\boldsymbol{\sigma}_h^{j+1,i+1},\boldsymbol{\tau}_h\right)-\left(\nabla^s\boldsymbol{u}_h^{j+1,i+1},\boldsymbol{\tau}_h\right)\\
&+\sum_K\left(\nabla\cdot\boldsymbol{\tau}_h,\alpha_1P'\left(\boldsymbol{R_u}\right)\right)_K+\sum_K\left(\frac{1}{2\eta^{j+1,i}}\boldsymbol{\tau}_h,\alpha_3P'\left(\boldsymbol{R_\sigma}\right)\right)_K=0,
\end{aligned}\tag{2.30}$$

for all $[\boldsymbol{v}_h,q_h,\boldsymbol{\tau}_h]\in\boldsymbol{\mathcal{X}}_h$, where converged values at a given time step have only the time step superscript and P' is the identity in the ASGS formulation and $P_h^\perp$ in the OSS method.

Algorithm 2.1 describes the flow of calculations to solve the problem. The possibility of using under-relaxation is taken into account through the parameter β, with $0<\beta\leq 1$.

2.5 Numerical results

This section shows the different test cases used to evaluate the performance of the stabilized formulations proposed in this chapter, both in the cases of non-linear viscosity and of dominant convection, in steady-state and in transient problems.

Algorithm 2.1 Stabilized formulations: ASGS and OSS

READ $\boldsymbol{u}_h^0$ (initial condition)
SET $p_h^0 = 0$, $\boldsymbol{\sigma}_h^0 = 0$
FOR, $j = 0, ..., N-1$ DO (temporal loop, N number of time steps):
  SET $i = 0$
  SET $\boldsymbol{u}_h^{j+1,0} = \boldsymbol{u}_h^j$, $p_h^{j+1,0} = p_h^j$ and $\boldsymbol{\sigma}_h^{j+1,0} = \boldsymbol{\sigma}_h^j$
  WHILE not converged DO:
    $i \leftarrow i + 1$
    SET $\boldsymbol{a}^{j+1,i} = \boldsymbol{u}_h^{j+1,i-1}$
    COMPUTE $\eta^{j+1,i}$ (from the constitutive equation)
    IF(OSS case)
      COMPUTE $P_h\left(\boldsymbol{R}_{\boldsymbol{U}}^{j+1,i}\right)$
    END IF
    COMPUTE α_1, α_2 and α_3 (stabilization parameters) from (2.24)
    SOLVE FOR $\boldsymbol{u}_h^{j+1,i}$, $p_h^{j+1,i}$ and $\boldsymbol{\sigma}_h^{j+1,i}$ from (2.28)-(2.30)
    $\boldsymbol{u}_h^{j+1,i} \leftarrow \beta \boldsymbol{u}_h^{j+1,i} + (1-\beta)\, \boldsymbol{u}_h^{j+1,i-1}$
    $p_h^{j+1,i} \leftarrow \beta p_h^{j+1,i} + (1-\beta)\, p_h^{j+1,i-1}$
    $\boldsymbol{\sigma}_h^{j+1,i} \leftarrow \beta \boldsymbol{\sigma}_h^{j+1,i} + (1-\beta)\, \boldsymbol{\sigma}_h^{j+1,i-1}$
    CHECK convergence
  END WHILE
  SET converged values
  $\boldsymbol{u}_h^{j+1} = \boldsymbol{u}_h^{j+1,i}$
  $p_h^{j+1} = p_h^{j+1,i}$
  $\boldsymbol{\sigma}_h^{j+1} = \boldsymbol{\sigma}_h^{j+1,i}$
END DO (temporal loop)

We will first present a convergence test (in sub-section 2.5.1) and then move to two 2D examples. Fig. 2.1 schematizes the problems considered in this case, namely, (a) the parallel flow mixing cavity and (b) the flow over a cylinder, discussed in sub-sections 2.5.2 and 2.5.3, respectively. The spatial discretization can be seen in Fig. 2.2. A structured triangular mesh of 12961 nodes and 25600 linear elements will be used in the mixing cavity problem (Fig. 2.1(a)) for all cases, whereas a triangular mesh of 43183 nodes and 82588 linear elements will be used for the flow over a cylinder. A zoom of this mesh is shown in Fig. 2.1(b). This section will conclude with the evaluation of the formulation to compute shear stresses on walls using two 3D examples (sub-section 2.5.4).

The discrete linearized problem is solved in all cases by using an iterative solver based on the Generalized Minimal Residual Method (GMRES) of Saad and Schultz [144], with an incomplete-LU (ILU) factorization as a preconditioner.

2.5.1 Convergence test

The first set of results shown corresponds to the convergence analysis of the stabilized formulations used in the three-field Navier-Stokes problem with non-linear viscosity, where the fluid is characterized by a quasi-Newtonian Ostwald de Waele model. The range of the power-law indexes is $0.5 \leq n \leq 1.5$ and the range of Reynolds numbers $0.3 \leq \mathrm{Re} \leq 400$. A force term is introduced in the momentum equation so that the exact solution is given by

$$u(x,y) = 2x^2 y\,(x-1)^2\,(y-1)\,(2y-1)\,,$$

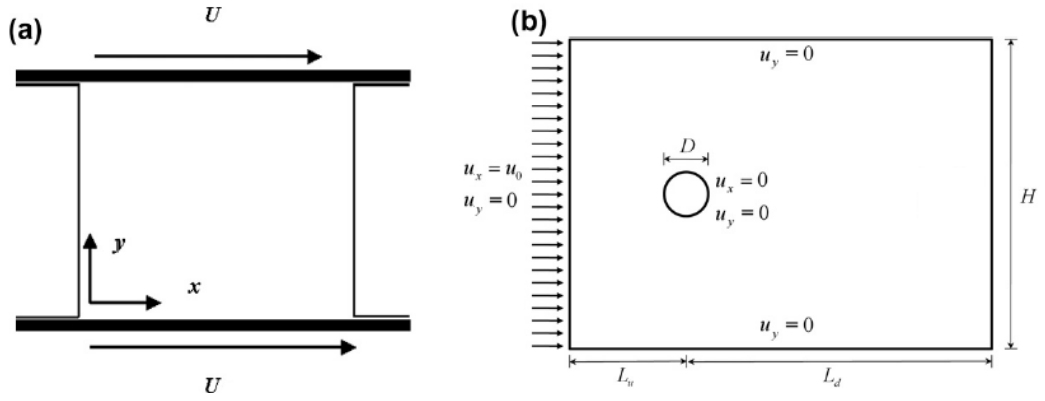

Figure 2.1: Schematic representation: (a) mixing cavity and (b) flow over a cylinder.

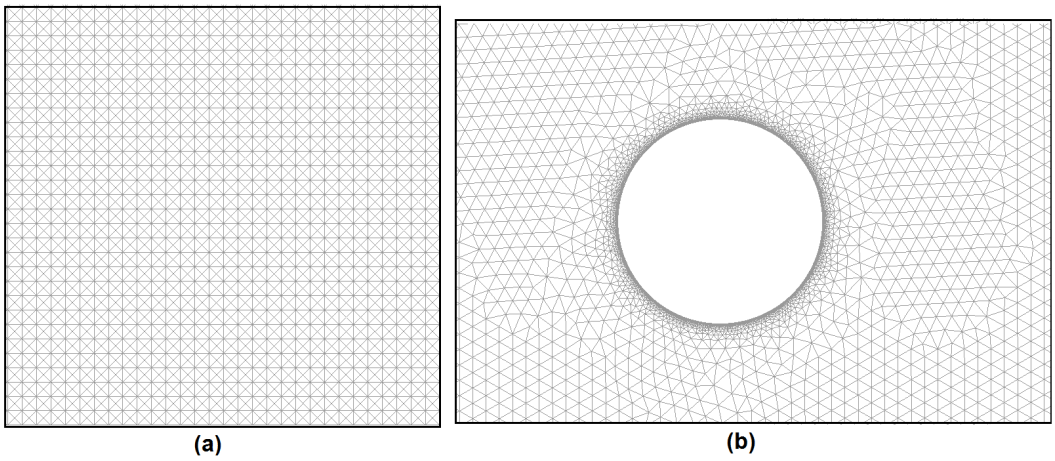

Figure 2.2: Mesh used in problems: mixing cavity (a) and flow over a cylinder (b).

$$v(x,y) = -2xy^2\,(x-1)\,(y-1)^2\,(2y-1)\,,$$
$$p(x,y) = \sin(2\pi x)\cos(2\pi y)\,,$$

$u(x,y)$ and $v(x,y)$ being the x- and y-velocity components, respectively.

The stress field is derived from the constitutive equation that relates the stress tensor with the symmetrical velocity gradient, including therefore the non-Newtonian effect of the viscosity. The stresses in this 2D case are explicitly given by

$$\sigma_{xx}(x,y) = 2\eta\frac{\partial u_x}{\partial x}, \qquad \sigma_{yy}(x,y) = 2\eta\frac{\partial u_y}{\partial y}, \qquad \sigma_{xy}(x,y) = \eta\left(\frac{\partial u_x}{\partial y} + \frac{\partial u_y}{\partial x}\right).$$

The computational domain is the unit square, discretized using uniform structured meshes of linear and quadratic triangular elements, the range of element sizes being $0.005 \leq h \leq 0.1$. From the physical point of view, the complexity of the test relies on the non-linearity of the viscosity modeled as a power law. In Fig. 2.3 one can see the viscosity field for pseudo-plastic and dilatant fluids, respectively. It is worth noting that in both cases there are singularities in the viscosity field, both at the four corners and at the central point of the domain. In the dilatant fluid ($n = 1.5$), the minimum viscosity value is zero, while in the pseudo-plastic case ($n = 0.5$), the maximum viscosity value tends to infinity.

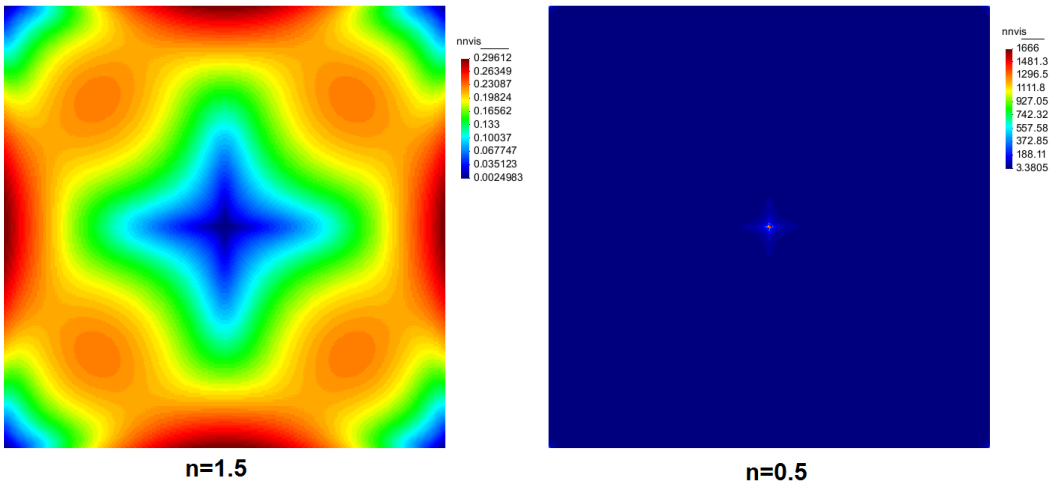

Figure 2.3: Contours of viscosity obtained in the convergence test problem in dilatant fluid ($n = 1.5$) and pseudo-plastic fluid ($n = 0.5$).

The maximum viscosity values obtained at the numerical integration points for the two numerical formulations studied are detailed in the Table 2.1. It can be noted that in both fluids the OSS method captures better the limit values of viscosity, both the maximum and the minimum values. In the pseudo-plastic case we obtain a difference between the OSS and the ASGS formulations (Dif(OSS-ASGS)) equal to 10.04% and in the dilatant case a difference equal to 22.99%, in both cases using as a reference value the OSS estimation (see Table 2.1).

$n = 0.5$	ASGS	OSS	Dif(OSS-ASGS)
$\eta_{\max}$	1498.7	1666	10.04%
$\eta_{\min}$	3.4169	3.3805	1.07%
$n = 1.5$	ASGS	OSS	Dif(OSS-ASGS)
$\eta_{\max}$	0.29569	0.29612	0.145%
$\eta_{\min}$	0.0030626	0.00249	22.99%

Table 2.1: Viscosity limit values obtained in the convergence test problem, in pseudoplastic fluid ($n = 0.5$) and dilatant fluid ($n = 1.5$), using the stabilized formulations ASGS and OSS.

The optimal convergence rate expected when the mesh size is reduced using linear triangular elements is two in velocity and one in pressure and stress in the L^2-norm, while using quadratic triangular elements it is three in velocity and two in pressure and stress. The graphs in Figures 2.4 and 2.5 show the obtained results using the ASGS formulation and the OSS method in the three-field problem, also compared with the analogue in the two-field case using the ASGS formulation [53]. Regarding the nomenclature used in the graphs, L2_U_2C corresponds to the L^2-norm in the two-field case, while L2_U_ASGS and L2_U_OSS, corresponds to the ASGS and OSS cases in the proposed three-field formulation, where U is the variable whose convergence is evaluated. The reference lines, Slope_(1, 2 and 3), allow one to evaluate the behavior of the schemes, where 1, 2 and 3 are the values of the slope in each of them.

We remark that the two-field approach follows simply changing the space of stresses so that $\boldsymbol{\sigma}_h = 2\eta\nabla^s\boldsymbol{u}_h$, with the viscosity evaluated at the integration points, and setting

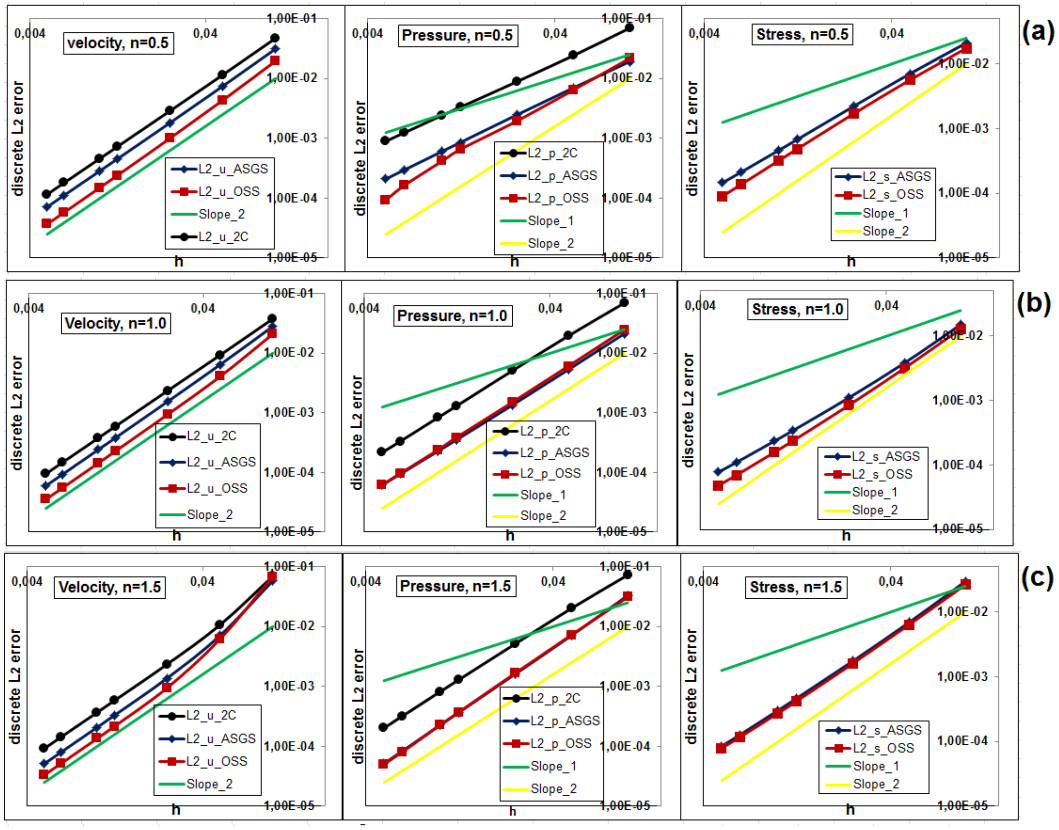

Figure 2.4: Convergence of the velocity-pressure-stress fields, in linear triangular elements for the different power-law indexes analyzed: (a) $n = 0.5$, (b) $n = 1$ y (c) $n = 1.5$.

$\alpha_3 = 0$ (no stress stabilization is required). The rest of parameters of both formulations are the same. Likewise, in the numerical examples we have used the same convergence tolerance in the discrete L^2 norm of velocities.

Independently of the power index employed, both stabilized formulations of three fields show better accuracy properties than their counterpart in two fields, yielding in all cases optimal slopes in the convergence curves. It is also worth noting that the OSS method generates a smaller error for all the cases analyzed, both in velocity and stress, and it behaves almost like the ASGS formulation in pressure. For quadratic elements (Fig. 2.5) only the ASGS case is shown. Optimal convergence rates are found for all variables.

The expected convergence orders are those of the interpolation error in the adequate norm. This is the best one can expect and what is proved in [56]. However, for smooth solutions as the one considered in our convergence test, a super-convergent behavior can be observed, and this is what happens for the pressure and the stress using linear elements. For quadratic elements, the asymptotic convergence rate is the theoretical one. Note that the convergence analysis is intended to be valid *in all situations*, and thus it does not seem possible to expect more than convergence of order k (interpolation order) for pressure and stresses.

The non-Newtonian effect can be appreciated in the stress field. Fig. 2.6 shows the σ_{xx} component for the three fluids analyzed.

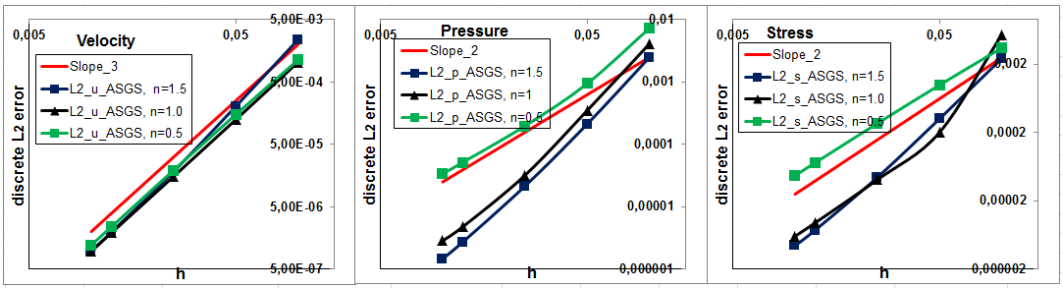

Figure 2.5: Convergence of the velocity-pressure-stress fields, in quadratic triangular elements for the different power-law indexes analyzed.

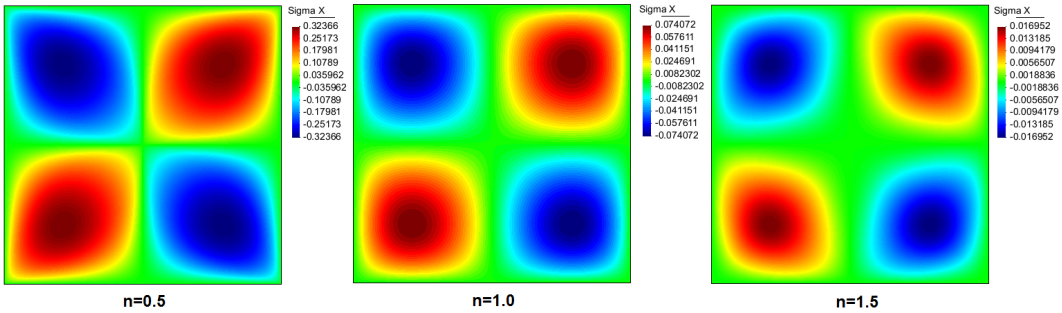

Figure 2.6: Contours of the normal stress component σ_{xx}, obtained in the convergence test problem for the different power-law fluids analyzed.

2.5.2 Parallel lid-driven cavity problem in non-linear viscosity fluids

The problem of the mixing cavity is a recurrent test in the approximation of non-Newtonian fluid flows. The results shown below correspond specifically to a unit square, subjected to a unidirectional velocity field in the parallel horizontal faces and zero velocity in the vertical faces (Fig. 2.1(a)). The results obtained are compared with those published by Mendu and Das [116] for a power-law fluid. In addition, a more convective case than those in the cited reference is also considered, using now Carreau-Yasuda models of shear-thinning and shear-thickening types.

It is important to define the power-law Reynolds number:

$$\mathrm{Re}_{\mathrm{PL}} = \frac{\rho U^{2-n} L_c^n}{m},$$

where ρ is the fluid density, U the mixing velocity (see Fig. 2.1(a)), L_c a characteristic length ($L_c = 1$ in this problem), n the power-law index and m the consistency index in the power-law. The Newtonian case is reproduced when $n = 1$ and $m = \mu$, obtaining the standard expression of the Reynolds number Re. In the Carreau-Yasuda fluid, the Reynolds number is calculated in the standard manner, using the minimum value of the viscosity ($\eta_{\min}$), that is, $\mathrm{Re} = \dfrac{\rho U L_c}{\eta_{\min}}$.

Before comparing the results obtained with our formulations, we present in Table 2.2 the results of a mesh refinement study conducted to select the working mesh. For different values of exponent n, we show the location of the upper vortex for the higher Reynolds number obtained using three different meshes with increasing number of elements. It is observed from Table 2.2 that the differences observed when using mesh M2 and mesh M3 are negligible,

and results agree with those presented in [116]. We have used mesh M2 in all the results to be described next.

$\mathrm{Re_{PL}} = 1000$	mesh M1	mesh M2	mesh M3
n	3281/6400	12961/25600	20201/40000
$n = 0.5$	0.5125/0.75	0.5625/0.75	0.56/0.75
$n = 1.0$	0.55/0.75	0.5375/0.75	0.54/0.75
$n = 1.5$	0.55/0.75	0.54375/0.75625	0.545/0.755

Table 2.2: Mesh refinement study in the parallel lid-driven cavity problem for different power law indexes in the location of the upper vortex (x-coordinate/y-coordinate). The number of nodes / number of elements is indicated below each mesh label.

Table 2.3 shows and compares the results obtained with those published in [116]. It is noteworthy that in [116] the lattice Boltzmann scheme was used for the calculation, employing a mesh of 257×257 points, while in the present work the structured mesh used was composed of 12961 linear triangular elements (Fig. 2.2(a)). In the two proposed formulations the location of the primary vortex is identical.

The results published by Mendu and Das [116] comprise the range of Reynolds numbers $100 \leq \mathrm{Re_{PL}} \leq 1000$. As an additional test, we considered a more convective problem ($\mathrm{Re_{PL}} = 5000$) to show the stabilizing properties of the two presented formulations.

The excellent correlation of our results with those published in [116] can be observed from Table 2.3. The maximum difference in coordinates in the location of the primary vortexes is 1.87% for a fixed mesh five times coarser than that used in [116], independently of the power-law index and the Reynolds number considered, thus showing the robustness of both VMS schemes proposed, in dominant convection and in the case of nonlinear viscosity.

For the Carreau-Yasuda fluid, the constants that define if the fluid is shear-thinning or shear-thickening are presented in Table 2.4.

The results of primary vortexes location and number of iterations for each of the formulations are shown in Table 2.5 for the Carreau-Yasuda fluid. The minimum and maximum viscosity and pressure values obtained are also indicated. The location of vortexes is identical in both formulations, and only results for the OSS method are shown. Viscosity peaks differ slightly and are given for both the ASGS and the OSS formulations.

Regarding the results presented in Table 2.5, it can be observed that always a greater pressure difference between pressure peaks is found in the OSS formulation, although the location of primary vortexes is the same in the two formulations. The viscosity peaks are practically identical and are bounded by the limit values indicated in Table 2.4, thus regulating the behavior of the model independently of the value of the second invariant of the strain rate tensor in the constitutive model. This eliminates any singularity in the viscosity field, as it occurs with the power-law model. Figure 2.7 show the streamlines for the Carreau-Yasuda fluids in the two cases considered.

Since the projection of the residual in the OSS method is evaluated in the previous iteration, it is important to compare the number of iterations required to reach convergence for the ASGS and the OSS formulations. Table 2.6 indicates this number of iterations necessary to achieve a convergence error smaller that 10^{-8} in the discrete L^2 norm of the unknowns. In general it can be observed that a slightly higher number of iterations is required in the OSS formulation. This however may be compensated by a higher accuracy, as observed in the convergence test and in the better reproduction of peaks of the unknowns using the OSS method.

From the physical standpoint, the flow presents pressure peaks at the corners of the computational domain. Fig. 2.8 shows the pressure isolines for the case $\mathrm{Re} = 5000$ in the case of a Newtonian fluid, where it can be seen that the pressure peaks are greater in the

	Upper	($n = 1.0$)			Lower	($n = 1.0$)		**(a)**
$\mathrm{Re_{PL}}$	x_coord	y_coord	dif_x	dif_y	x_coord	y_coord	dif_x	dif_y
100	0.6187/0.6131	0.7937/0.7964	0.92%	0.33%	0.6187/0.6131	0.2062/0.2059	0.92%	0.17%
400	0.5937/0.5863	0.7562/0.7607	1.27%	0.58%	0.5937/0.5863	0.2437/0.2396	1.27%	1.73%
1000	0.5375/0.5364	0.75/0.7544	0.21%	0.58%	0.5375/0.5364	0.25/0.248	0.21%	0.81%
5000	0.5125	0.75	-	-	0.5125	0.25	-	-
	Upper	($n = 0.5$)			Lower	($n = 0.5$)		**(b)**
$\mathrm{Re_{PL}}$	x_coord	y_coord	dif_x	dif_y	x_coord	y_coord	dif_x	dif_y
100	0.7187/0.7186	0.8250/0.8196	0.02%	0.66%	0.7187/0.7186	0.1812/0.1807	0.02%	0.30%
400	0.65/0.6419	0.75/0.7523	1.26%	0.31%	0.65/0.6419	0.25/0.2459	1.26%	1.67%
1000	0.5625/0.5732	0.75/0.7503	1.87%	0.04%	0.5625/0.5732	0.25/0.2522	1.87%	0.87%
5000	0.55625	0.74375	-	-	0.55625	0.25625	-	-
	Upper	($n = 1.5$)			Lower	($n = 1.5$)		**(c)**
$\mathrm{Re_{PL}}$	x_coord	y_coord	dif_x	dif_y	x_coord	y_coord	dif_x	dif_y
100	0.5437/0.5499	0.7812/0.7859	1.12%	0.59%	0.5437/0.5499	0.2187/0.2164	1.12%	1.09%
400	0.5812/0.5805	0.7687/0.7691	0.13%	0.05%	0.5812/0.5805	0.2312/0.2312	0.13%	0.02%
1000	0.5437/0.5422	0.7562/0.7586	0.29%	0.31%	0.5437/0.5422	0.2437/0.2438	0.29%	0.02%
5000	0.5125	0.75	-	-	0.5125	0.25	-	-

Table 2.3: Location of primary vortex mixing cavity problem for the different power indexes analyzed (reference [116]/present work): (a) $n = 1.0$, (b) $n = 0.5$ and (c) $n = 1.5$.

Fluid type	μ_0	μ_∞	λ	n	a	ρ
Shear-thinning	0.056	0.00345	1.902	0.22	1.25	1.0
Shear-thickening	0.00345	0.056	1.902	0.22	1.25	1.0

Table 2.4: Constants of the Carreau-Yasuda model in the mixing cavity problem (SI units).

Upper	$x_$coord	$y_$coord	**Viscosity peaks**	$\eta_{\min}$	$\eta_{\max}$
S.-thining	0.5125	0.75	S.-thinning ASGS	0.00345	0.05862
S.-thickening	0.6125	0.7625	S.-thinning OSS	0.00345	0.05434
Lower	$x_$coord	$y_$coord	S.-thickening ASGS	0.009115	0.05599
S.-thining	0.5125	0.25	S.-thickening OSS	0.00919	0.05599
S.-thickening	0.6125	0.2375	**Pressure peaks**	$p_{\min}$	$p_{\max}$
NÂº of iterations	ASGS	OSS	S.-thinning ASGS	-38.715	98.497
S.-thining	141	138	S.-thinning OSS	-38.806	100.29
S.-thickening	53	53	S.-thickening ASGS	-40.722	385.6
			S.-thickening OSS	-41.657	386.73

Table 2.5: Location of primary vortexes, number of iterations and peaks of viscosity-pressure in Carreau-Yasuda fluis, for the ASGS and the OSS formulations.

OSS formulation. Similar results were presented in Table 2.5 for the Carreau-Yasuda fluid, in addition to the maximum and minimum values of the viscosity (Table 2.1) obtained in the previous sub-section. As it can be observed, the capability to represent in a better manner the singular points by the OSS formulation is a general tendency.

2.5.3 Transient flow of a power-law fluid over a cylinder

The problem of flow over a cylinder has been studied by a great number of authors over the years, both in the stationary case and in the transient regime. The fluid dynamics that develops when the flow collides with the solid cylinder varies considerably with the Reynolds number, going from a steady state to a periodically time varying state, presenting in the latter case the characteristic von Karman vortexes. The critical Reynolds number that determines the beginning of the oscillatory behavior lies in the range $40 \leq \mathrm{Re} \leq 50$ in Newtonian fluids.

In the case of non-linear viscosity, results are more scarce, especially at high Reynolds numbers, where the dominant convection is combined with the non-linearity of the viscosity. Patnana et al. analyzed in [131] the problem of the flow of a power-law fluid over a cylinder in the range of Reynolds numbers $40 \leq \mathrm{Re_{PL}} \leq 140$ with a commercial software. They found different correlations between macroscopic parameters, as the coefficients of drag-lift and the Strouhal number, with the power-law index that characterizes the fluid for a fixed Reynolds number.

When a transient problem is analyzed, an important parameter that defines the dimensionless frequency of the fluid dynamics is the Strouhal number, which is defined as

$$\mathrm{St} = \frac{fD}{u_0},$$

where f corresponds to the oscillatory frequency of the problem, D represents the diameter of the cylinder and u_0 is a characteristic velocity, which in the present case corresponds to the inlet velocity u_0 (Fig. 2.1(b)).

Let F_D and F_L be the drag and lift forces, respectively. The dimensionless drag and lift

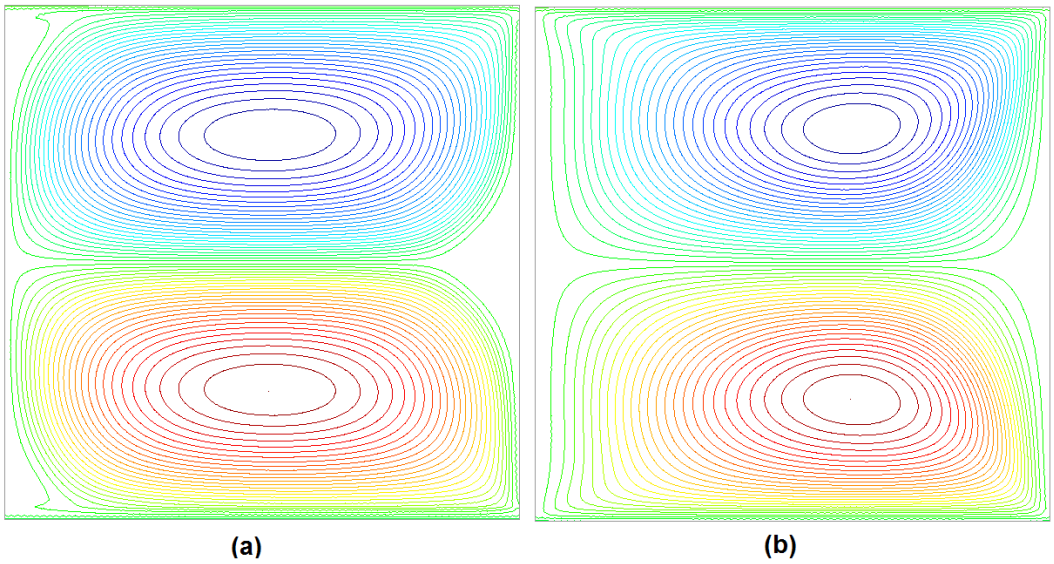

Figure 2.7: Streamlines in Carreau-Yasuda fluids: (a) Shear-thinning, (b) Shear-thickening.

Power-law index	$n = 0.5$	$n = 1.0$	$n = 1.5$
Iterations	ASGS/OSS	ASGS/OSS	ASGS/OSS
$\mathrm{Re_{PL}} = 100$	35/37	17/17	23/24
$\mathrm{Re_{PL}} = 400$	83/90	38/38	47/47
$\mathrm{Re_{PL}} = 1000$	94/113	45/44	58/58
$\mathrm{Re_{PL}} = 5000$	131/141	104/130	62/82

Table 2.6: Iterations required for convergence in the mixing cavity problem with a power-law fluid for the two proposed stabilized formulations.

coefficients are computed as

$$\mathrm{C_D} = \frac{F_\mathrm{D}}{(1/2)\,\rho u_0^2 D}, \qquad \mathrm{C_L} = \frac{F_\mathrm{L}}{(1/2)\,\rho u_0^2 D}.$$

If we increase the size of the computational domain, the boundary conditions are less influential on the velocity, pressure and stress fields, but of course at a higher computational cost. Patnana et al. [131], studied the influence of the dimensions of the domain around the cylinder in the macroscopic parameters, without encountering important variations in the value of the drag-lift coefficients and in the Strouhal number for domains larger than the one we have chosen. It is a rectangle of dimensions $[0, 16] \times [0, 8]$, with a cylinder of unitary diameter centred at point $(4, 4)$. The mesh used in this problem consists of 82588 linear triangular elements and 43183 nodes, mostly concentrated in the area close to the cylinder (Fig. 2.2(b)). Regarding the boundary conditions applied to the problem, the inlet condition (at $x = 0$) corresponds to a constant velocity field with components $\boldsymbol{u} = (u_0, 0)$, the boundaries $y = 0,\ y = 8$ are left free in the horizontal component and the vertical velocity is prescribed to zero, while on the outlet ($x = 16$) both velocity components are left free.

From the physical standpoint, the lift coefficient C_L oscillates between two extreme values with zero mean because of symmetry. The first order backward Euler scheme is able to capture the oscillation frequency (St), but yields a poor approximation to the maximum values of C_L. On the other hand, the second order BDF2 scheme yields a much better approximation

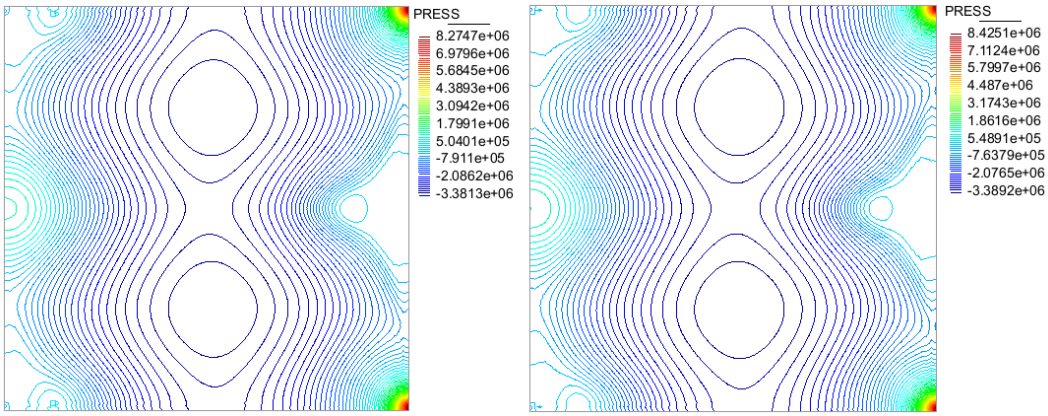

Figure 2.8: Pressure isolines in Newtonian fluid (Re = 5000), left: ASGS formulation; right: OSS formulation.

to the amplitude of C_L. The results shown below were calculated using this second order scheme.

We present in Table 2.7 the values computed of different coefficients for two meshes and different time step sizes. In fact, we have computed these coefficients with more time step sizes. The results presented are only intended to show as they are influenced by mesh refinement. Even if the difference is not very important, the results presented next have been obtained using the small time step size δt_2 (which varies according to power n) and the refined mesh M2.

			M1,δt_1			M2,δt_1			M2,δt_2		
n	δt_1	δt_2	$C_{\overline{D}}$	$C_{L,m}$	St	$C_{\overline{D}}$	$C_{L,m}$	St	$C_{\overline{D}}$	$C_{L,m}$	St
0.4	0.005	0.0025	1.264	0.814	0.227	1.268	0.818	0.227	1.266	0.855	0.230
0.6	0.005	0.0025	1.292	0.633	0.217	1.293	0.634	0.214	1.296	0.634	0.214
1.0	0.001	0.0005	1.427	0.501	0.193	1.427	0.501	0.192	1.425	0.500	0.192
1.4	0.001	0.0005	1.623	0.446	0.180	1.623	0.448	0.180	1.623	0.448	0.180
1.8	0.001	0.0005	1.779	0.425	0.166	1.770	0.425	0.165	1.770	0.420	0.165

Table 2.7: Mesh dependency study for $C_{\overline{D}}$ (mean drag coefficient), $C_{L,m}$ (maximum lift coefficient), and St for the flow over a cylinder problem using different power law indexes and $Re_{PL} = 140$. Mesh M1 (31710 nodes, 61211 elements) and mesh M2 (43182 nodes, 82588 elements).

Table 2.8 has the purpose of validating the results in the transient problem for the power-law fluid. Since transient non-Newtonian results are scarce, it also includes a stationary sub-case for a Reynolds number $Re_{PL} = 40$, with the purpose of comparing the results with others authors [20, 154].

As shown in Table 2.8, results are in a reasonable agreement between the different sources. The most important differences occur for high values of the power-law index. Let us remark that the transient values published by Patnana et al. in [131] were obtained with the Finite Volume Method, using a second order upwind scheme for the convective term, the SIMPLE algorithm and a second order time integration scheme with a mesh with 212323 cells, three times more than in the mesh used in the present work.

In general, for a fixed Reynolds number the drag coefficient is increased when the power-law index is increased. The opposite happens with the lift coefficient and the Strouhal number. Fig. 2.9 shows the correlation between these parameters for the case $Re_{PL} = 140$. This agrees with the tendency shown in [131]. The normalization of results in Fig. 2.9 is performed by

Source	$C_{\bar{\mathrm{D}}}$	Source	$C_{\bar{\mathrm{D}}}$	$C_{\mathrm{L,max}}$	St
Re = 40, $n = 0.6$		Re = 140, $n = 0.4$			
Present study	1.4316	Present study	1.2667	0.855	0.2300
Patnana et al. [131]	1.3576	Patnana et al. [131]	1.2514	0.9983	0.2262
Bharti et al. [20]	1.3717	Re = 140, $n = 0.6$			
Soares et al. [154]	1.3900	Present study	1.2960	0.6342	0.2142
Re = 40, $n = 1.4$		Patnana et al. [131]	1.2560	0.7453	0.2128
Present study	1.6792	Re = 140, $n = 1.0$			
Patnana et al. [131]	1.6541	Present study	1.4250	0.5005	0.1920
Bharti et al. [20]	1.6429	Patnana et al. [131]	1.3579	0.4936	0.1851
Soares et al. [154]	1.6200	Re = 140, $n = 1.4$			
Re = 40, $n = 1.8$		Present study	1.6230	0.4480	0.1800
Present study	1.9437	Patnana et al. [131]	1.49369	0.4072	0.1721
Patnana et al. [131]	1.8726	Re = 140, $n = 1.8$			
Bharti et al. [20]	1.9556	Present study	1.7701	0.4235	0.1650
		Patnana et al. [131]	1.6265	0.3436	0.1529

Table 2.8: Comparison of macroscopic parameters in the flow over a cylinder problem. $C_{\bar{\mathrm{D}}}$: mean drag coefficient, $C_{\mathrm{L,max}}$: maximum lift coefficient in time.

dividing the value obtained for the specific variable computed with the power index that defines the problem, say $g(n)$, by the value of the same variable in the Newtonian case, that is to say, $g(n = 1)$, where function $g(\cdot)$ corresponds to the Strouhal number or the drag-lift coefficients, depending on the case.

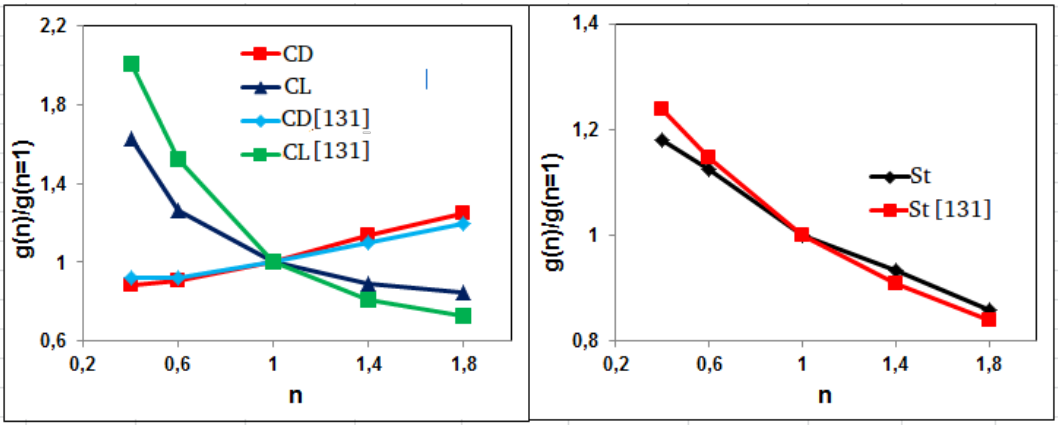

Figure 2.9: Influence of the power-law index (n), in the drag coefficient (C_D), the lift coefficient (C_L) and the Strouhal number (St).

Let us show now some results obtained with the proposed three-field stabilized formulations for the pseudo-plastic fluid ($n = 0.4$) and for the dilatant fluid ($n = 1.8$). It is noteworthy that both in the ASGS and in the OSS formulations these results are very similar, so that the contours and the isolines of some of the variables are displayed without indicating the formulation employed.

In order to compare the physical behavior of pseudo-plastic and dilatant fluids, we plot in Fig. 2.11 the streamlines corresponding to the solution obtained using $n = 0.4$ (pseudo-plastic case) and $n = 1.8$ (dilatant case). The time instants correspond to positions (1), (2),

(3) and (4) in Fig. 2.10.

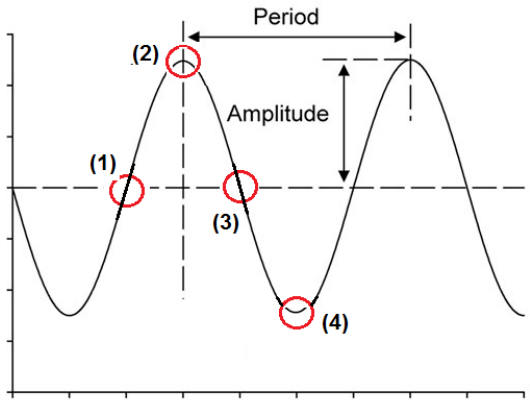

Figure 2.10: Wave scheme to define some comparison points.

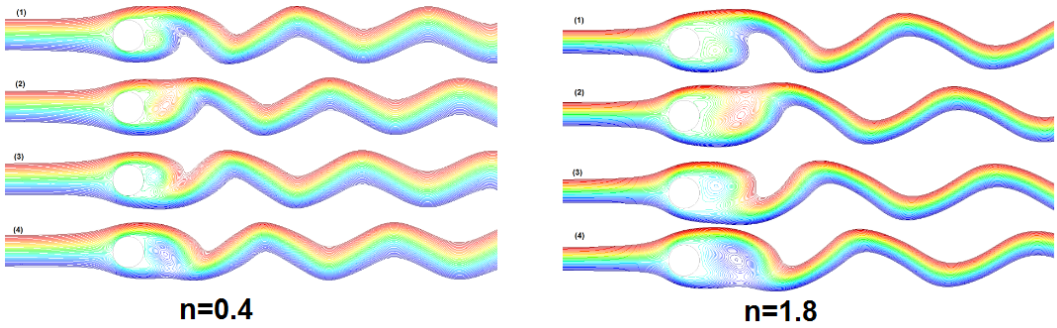

Figure 2.11: Evolution of the streamlines close to the cylinder, from the input condition to the output condition in the problem of flow over a cylinder in pseudoplastic ($n = 0.4$) and dilatant ($n = 1.8$) fluids.

From Fig. 2.11 it can be observed that the recirculation zone is bigger in the case of a dilatant fluid. This gives rise to a higher period of oscillations, that is to say, the oscillation frequency is higher for pseudo-plastic fluids. This agrees with the Strouhal numbers obtained in each case.

The contour plots of the stress component σ_{xx} are depicted in Fig. 2.12 in the case of a pseudo-plastic fluid. Once again, the snapshots correspond to the time instants indicated in Fig. 2.10.

Finally, Fig. 2.13 illustrates the nonlinearity and dynamic behavior in the viscosity field for $\mathrm{Re}_{\mathrm{PL}} = 140$ and $n = 1.8$. Note that the consistency index used for the dilatant case $n = 1.8$ is $m = 0.02$, with a maximum value for the viscosity in the vicinity of the cylinder of 6.28 (314 times greater than 0.02). The problem is thus convection dominated and with a high non-linear variation in the viscosity, and the numerical formulations proposed are able to cope with this problem, which is what we intend to demonstrate in this part of the work.

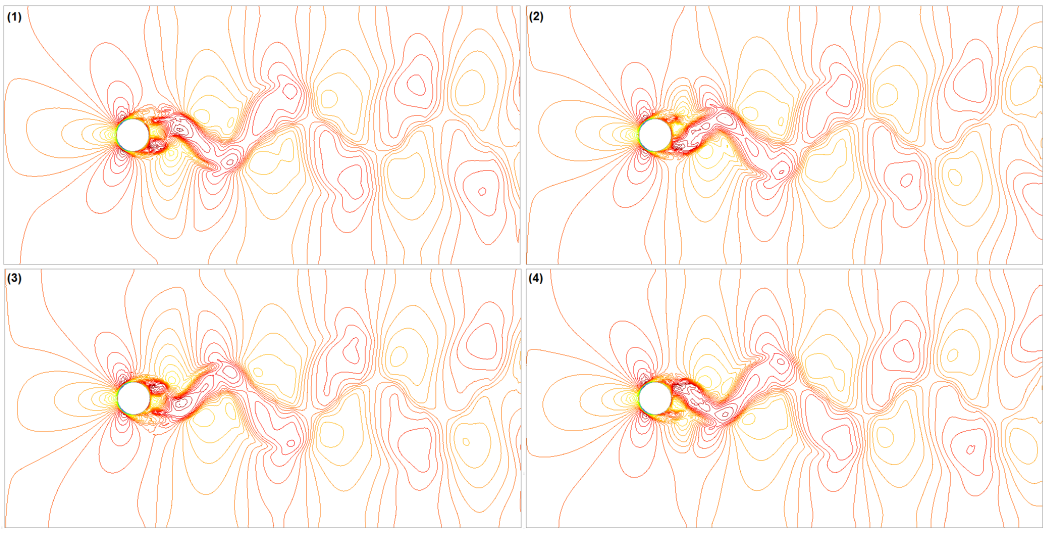

Figure 2.12: Contours of stress σ_{xx} in the cylinder problem for the case $n = 0.4$ and $\mathrm{Re}_{\mathrm{PL}} = 140$.

2.5.4 Tangential stresses over boundary walls

The evaluation of stresses over boundaries is an important need in some biomechanical applications that involve blood flow, for example (see [166, 42]). In order to evaluate the performance of the three-field formulation to compute these stresses, and compare it with the corresponding two-field method, we will present the results obtained in the calculation of shear stresses first on a 2D straight pipe and then over curved walls in two 3D examples, that we shall refer to as arterial stenosis and arterial elbow. In all the results, the blood properties of a Carreau-Yasuda model with the parameters shown in the Table 2.9 are used. Since our intention is to compare the two-field and the three-field approaches, the OSS method will be used in all cases.

Fluid type	μ_0	μ_∞	λ	n	a	ρ
Shear-thinning	0.022	0.0022	0.392	0.11	0.624	1410

Table 2.9: Blood properties with the Carreau-Yasuda model (SI units).

The number of elements and mesh nodes used in each problem are indicated in Table 2.10. Unstructured meshes of linear triangles in 2D and linear tetrahedra in 3D are used. Also, the Reynolds numbers that define each problem are $\mathrm{Re} = 2000$ in the straight pipe, $\mathrm{Re} = 113$ in the arterial stenosis and $\mathrm{Re} = 227$ in the arterial elbow.

Meshes	straight pipe	arterial stenosis	arterial elbow
M1	2111n/4000e	97517n/583033e	112331n/524981e
M2	8221n/16000e	168770n/1150852e	175273n/838841e
M3	22345n/43956e		

Table 2.10: Meshes used in the shear stresses problems.

Let us start discussing the results obtained for the 2D straight pipe. Fig. 2.14 shows the distribution of shear stresses σ_{xy}. A parabolic velocity profile is prescribed at the inlet of the pipe, and it varies along its axis until reaching the constant value corresponding to the

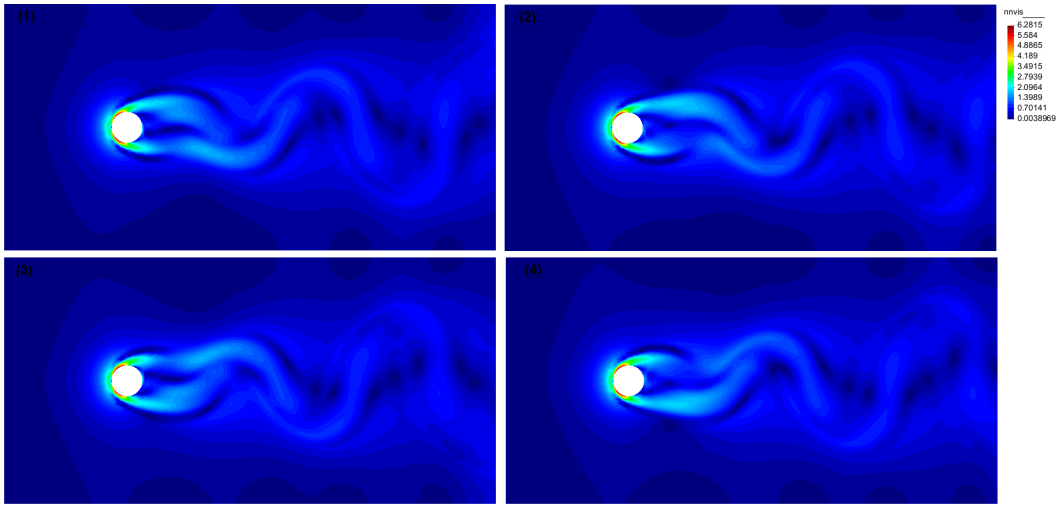

Figure 2.13: Viscosity contours, in the cylinder problem, for the case $n = 1.8$ and $\mathrm{Re}_{\mathrm{PL}} = 140$.

constitutive model. In Figure 14 it is observed that the results obtained with mesh M3 (with 43956 elements) using the two-field approach are almost the same as those obtained with mesh M2 (with 16000 elements) using the three-field approach. The gain in accuracy using the three-field formulation is clearly demonstrated. Note that mesh M2 with the three-field approach has $8221 \times 6 = 49326$ degrees of freedom, whereas mesh M3 with the two-field one has $22345 \times 3 = 67035$ degrees of freedom, 35% more than the former.

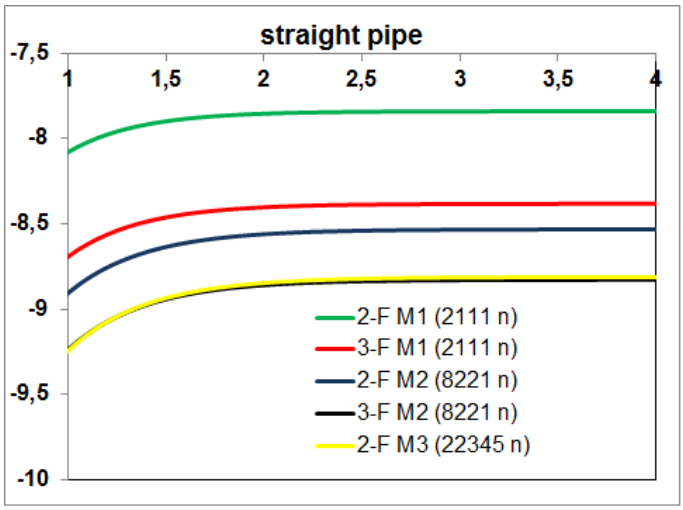

Figure 2.14: Shear stress (σ_{xy}) in the straight pipe with in the Carreau-Yasuda blood flow.

The extension to the 3D case is shown in two problems. The first corresponds to an arterial stenosis occlusion of 50% and the second an arterial elbow, both represented in Fig. 2.15. Fig. 2.16 shows the contour of velocity magnitude and pressure, both for the stenosis and the elbow problems. These contours are plotted for the mid planes in both cases.

In order to compare the stress calculation in the two-field and the three-field formulations,

we will plot the modulus of the stress along a line. In the stenosis problem, this line will be the intersection of the boundary with the mid plane between the two cross sections indicated in Fig. 2.15(a), so that the stenosis is located approximately at the middle of this line. In the case of the elbow, this line is the external intersection of the boundary with the mid plane between the two cross sections closest to the elbow indicated in Fig. 2.15(b). In both cases, the curves to plot the stresses will be developed in a straight line.

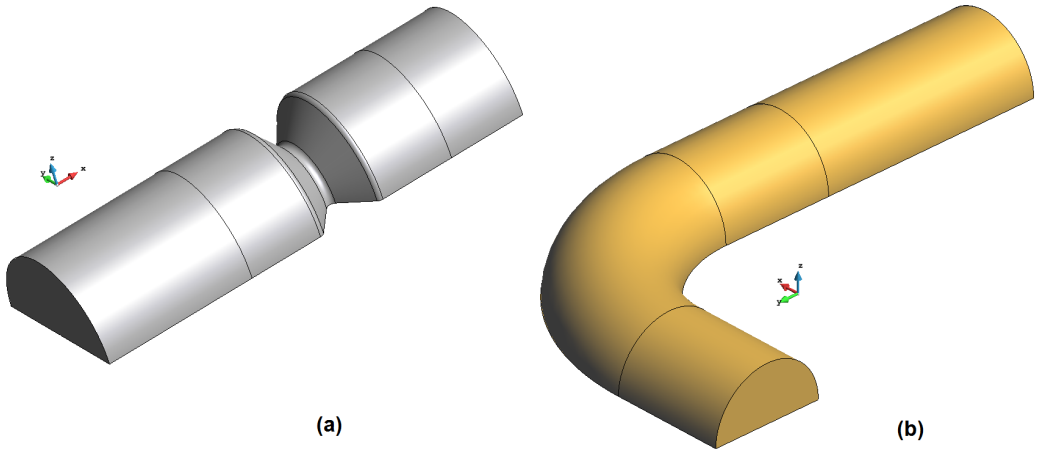

Figure 2.15: Schematic representation of threedimensional poblems: (a) arterial stenosis (b) vessel elbow.

Results are shown in Fig. 2.17. In both problems we have used meshes M1 and M2 for the two-field approach and only mesh M1 for the three-field formulation (see Table 2.10 for the description of these meshes). It is clearly observed that the results with M1 in the three-field approach are similar to those obtained with M2 in the two-field one. In fact, in the stenosis problem the three-field formulation is even able to reproduce a higher stress peak at the stenosis with mesh M1 than the two-field one with mesh M2.

The better accuracy of the three-field approach over the two-field one is a general trend that we attribute to the fact that the former has more degrees of freedom than the latter, even if the interpolation order and consequently the convergence rates are the same. The continuous solution can be approximated with better accuracy simply because the constraint $\boldsymbol{\sigma}_h = 2\eta\nabla^s \boldsymbol{u}_h$ at interpolation level is replaced by an additional equation for the stresses.

Obviously, the computational cost of the three-field approach is much higher than for the two-field one. For equal interpolation for all variables, six additional degrees of freedom per node are required in the 3D case. To partially alleviate this problem, one can design block-iterative schemes to segregate the calculation of the stresses from that of the velocity and the pressure, as those proposed in [41] for the strain-displacement approach in solid mechanics. Whether the additional computational cost is compensated or not by the increased accuracy observed is problem dependent, and depends also on the variables we wish to analyze, as this example has demonstrated. Without using any stress segregation scheme, the calculation using the two-field formulation on mesh M3 took 18% more CPU time than the calculation using the three-field one on mesh M2, for a similar accuracy, but using mesh M2 in both cases the former took 56% less CPU time. However, the interest of the three-field approach relies on applications where it is not a choice, but a need, as in the case of viscoelastic flows.

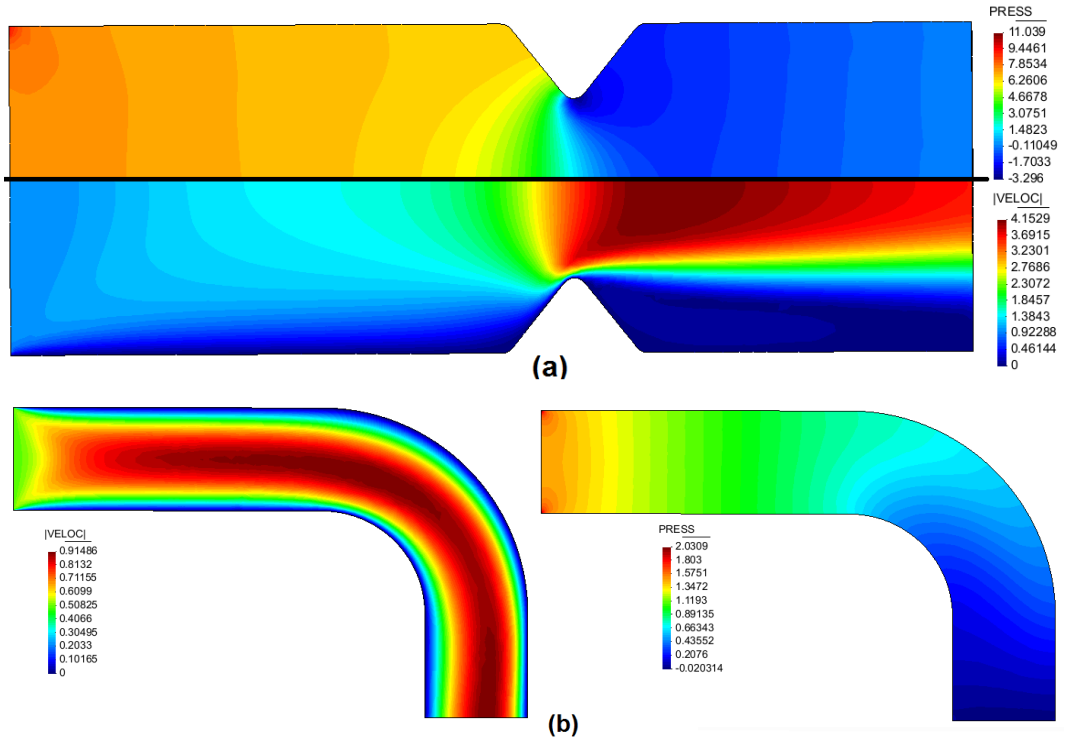

Figure 2.16: Contour of pressure (PRESS) and velocity magnitude (VELOC) in the stenosis problem (a) and in the elbow problem (b). Both cases correspond to the mid section.

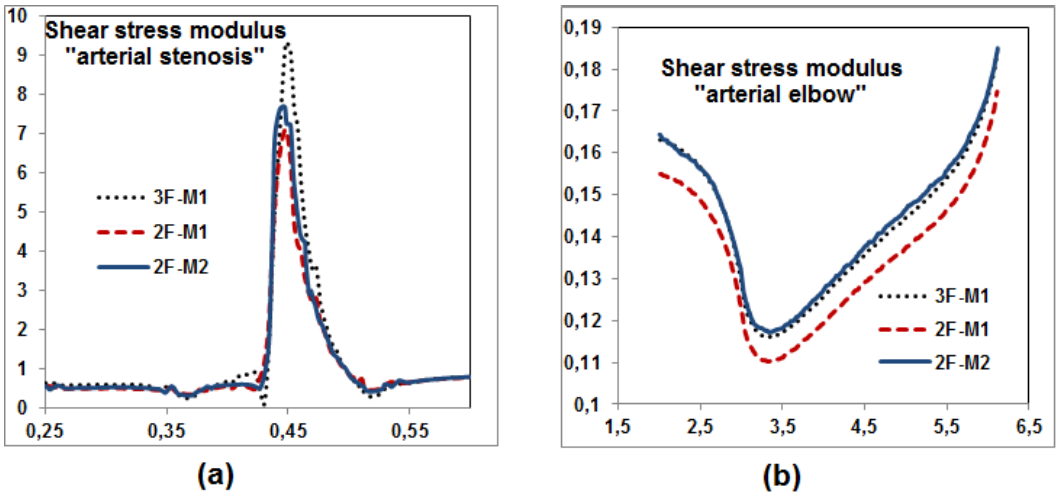

Figure 2.17: Shear stress modulus in the arterial stenosis problem (a) and in the vessel elbow problem (b).

2.6 Conclusions

In this chapter we have proposed two stabilized numerical formulations (ASGS and OSS) of SGS type for the three-field (stress-velocity-pressure) Navier-Stokes problem with non-linear viscosity models. It has been tested numerically that both formulations have optimal convergence properties for linear and quadratics elements, also evidencing a clear reduction in the L^2-norm of the error when approximating a problem with analytical solution with respect to the two-field (velocity-pressure) formulation. Likewise, for a fixed mesh the OSS method tends to perform better than the ASGS approach, introducing less numerical dissipation.

The proposed schemes were tested in different numerical test cases available in the literature. The range of $100 \leq \mathrm{Re}_{\mathrm{PL}} \leq 5000$ was considered in the mixed cavity problem with non-Newtonian power-law and Carreau-Yasuda fluids, and the range of $40 \leq \mathrm{Re}_{\mathrm{PL}} \leq 140$ in the classical flow over a cylinder. In both cases, results compare satisfactorily with reference solutions found in the literature, both in the location of primary vortexes and in the value of macroscopic parameters, namely the Strouhal number and the drag and lift coefficients, for a power-law fluid with power index in the range $0.4 \leq n \leq 1.8$. In the calculation of shear stresses over the boundaries of the domain the three-field formulation is superior to its two-fields counterpart with a fixed mesh.

The numerical results presented serve to demonstrate the feasibility of the finite element formulation proposed to approximate the three-field Navier-Stokes problem, both in situations in which the viscosity is non-linear and in convection dominated flows, using *equal interpolation for all the unknowns*. In the problem considered, introducing the stresses as unknowns is not mandatory. However, there are situations in which this is a must, notably in the case of viscoelastic fluid flows. The methods proposed are promising tools to attempt this problem.

Chapter 3

The Stationary Viscoelastic Flow Problem

3.1 Abstract

In this chapter, three-field finite element stabilized formulations are proposed for the numerical solution of incompressible viscoelastic flows. These methods allow one to use equal interpolation for the problem unknowns $\boldsymbol{\sigma}$-$\boldsymbol{u}$-p (elastic deviatoric stress-velocity-pressure) and to stabilize dominant convective terms. Starting from residual-based stabilized formulations, the proposed method introduces a term-by-term stabilization which is shown to have a superior behavior when there are stress singularities. A general discontinuity-capturing technique for the elastic stress component is also proposed, which allows one to eliminate the local oscillations that can appear when the Weissenberg number We is high and the fluid flow finds an abrupt change in the geometry. The formulations are tested in the classical 4:1 planar contraction benchmark up to We = 5 in the inertial case, with Reynolds number Re = 1, and up to We = 6.5 in the quasi non-inertial case, with Re = 0.01. The standard Oldroyd-B constitutive model is used for the rheological behavior and linear and quadratic elements for the spatial approximation.

3.2 Introduction

The finite element approximation of the flow of viscoelastic fluids presents several numerical difficulties. It inherits obviously the problems associated with the approximation of the incompressible Navier-Stokes equations, mainly the compatibility between the velocity-pressure approximation and the treatment of the nonlinear advective term. But, on top of that, now the constitutive equation is highly nonlinear, with an advective term that may lead to both global and local oscillations in the numerical approximation. Moreover, even in the case of smooth solutions it is necessary to meet some additional compatibility conditions between the velocity and the stress interpolation in order to control velocity gradients. Elements that satisfy the compatibility requirements velocity-pressure and stress-velocity are rare.

The treatment of the nonlinearity is another aspect that deserves to be studied in detail. Apart from the nonlinearity in the convective term of the momentum equation, the constitutive equation has two additional nonlinear terms, namely, the convective one and the rotational one. Fixed point type schemes are robust, but with a very low convergence rate when the elastic component increases [106]. Newton-Raphson schemes are the most ex-

tensively used in the literature [103, 148], although they often need to be complemented with additional numerical tools, such as continuation methods or relaxation schemes. The results obtained in this part of the work have been obtained using the Newton-Raphson method, which has produced good results in all the range of Weissenberg numbers analyzed ($0 \leq \mathrm{We} \leq 6.5$).

Once the equations have been properly linearized, the advective nature of the constitutive equation, which becomes dominant when the Weissenberg number increases, makes it necessary to use a stabilized finite element formulation to avoid global oscillations. The most widespread method to account for the convective term in the constitutive equation is the so-called SUPG method of Brooks and Hughes [31], first applied to viscoelastic flows by Marchal and Crochet [111]. In a more recent work, Masud et al. [103] use a Variational Multi-Scale (VMS) stabilized method for the momentum-continuity equations and the same SUPG method for the constitutive equation. Other stabilized methods for the viscoelastic fluid problem are the GLS-type methods used for example by Fan et al. [79] and Coronado et al. [64]. Different families of stabilized formulations can also be found in the literature. For example, Li et al. [108] proposed the so-called I-PS-DEVSS-CNBS scheme to stabilize the viscoelastic problem, based on the finite incremental calculus (FIC) pressure stabilization process, the discrete elastic-viscous stress-splitting method (DEVSS), the use of the Crank-Nicolson-based-splitting (CNBS) scheme, and the use of the non-consistent SU method to stabilize the viscoelastic equation. Other two options to circumvent the dominant convective nature of the problem are the fully explicit characteristic based split (CBS) scheme (see [172]) proposed by Nithiarasu [123], with a good performance for a wide range of Weissenberg numbers, and the nonlinear weighted least-squares finite element method proposed by Lee [106]. In this part of the work, we apply two stabilized formulations based on the VMS framework to control the convective nature of the viscoelastic constitutive equation, different to those just described.

The use of discontinuity-capturing (DC) techniques is not a popular topic in the analysis of viscoelastic flows, but the high elastic stress gradients that appear when the Weissenberg number is increased make it a typical situation where the application of a DC scheme can help. Carew et al. [33] have shown that the inclusion of such a DC technique in a stabilized formulation can improve the stability properties and permits to analyze fluids with a higher elasticity. In the work cited, the numerical diffusion of the discontinuity-capturing term is based on the finite element residual of the constitutive equation, in a similar way to that used by Codina [49] (see also [124]). In the present chapter we propose a numerical diffusion based on the orthogonal projection of the elastic stress gradient, which represents the *non-captured* part in the finite element approximation.

Referring to the compatibility conditions of inf-sup type for the viscoelastic three-field approximation, they consist of two restrictions on the interpolation spaces, one between pressure and velocity and the other between velocity and the elastic stress (see e.g [29, 147] and [30] for background). These two restrictions reduce drastically the choices of stable finite element spaces that allow one to discretize the unknowns. For example, in the work of Marchal and Crochet [111] one can find different inf-sup stable elements capable to solve the viscoelastic problem. In this classical reference, the authors propose a family of biquadratic velocity and bilinear pressure elements with a multi-bilinear (2×2 or 3×3 or 4×4) stress element for the 2D case. The mathematical analysis of these elements can be found in [84]. It is a clear example of the difficulties to satisfy the two inf-sup conditions associated to the three-field formulation needed in the viscoelastic flow problem. For the threedimensional case, Bogaerds et al. [25] propose a DEVSS-DG stable spatial discretization using tri-quadratic interpolation for velocity, tri-linear interpolation for both pressure and discrete rate of deformation, while the viscoelastic stresses are approximated by discontinuous tri-linear polynomials. In [8] one can find a good review of mixed methods that satisfy the two compatibility conditions

required.

The stabilized formulations proposed in this part of the work have their roots in the context of VMS methods introduced by Hughes et al. [97] for the scalar convection-diffusion-reaction problem, and extended later to the vectorial Stokes problem in [51], where the space of the sub-grid scales is taken as orthogonal to the finite element space. As we shall see, this is an important ingredient in the design of our formulations. The purpose of the present chapter is precisely to design and test numerically stabilized formulations for the viscoelastic fluid flow problem, permitting the use of equal interpolation between the unknowns (deviatoric elastic stress, velocity and pressure) even in cases where the elastic stress gradients and the elastic component of the fluid are important.

The starting point of a VMS approach is to split the unknowns of the problem into two components, namely, the component that can be approximated by the finite element mesh and the unresolvable one, called sub-grid scale or simply sub-scale in what follows. The latter needs to be approximated in a simple manner in terms of the former, so as to capture its main effect and yield a stable formulation for the finite element unknown. The number of degrees of freedom is therefore the same as for the Galerkin method. There are different ways to approximate the sub-scale and, in particular, to choose the (finite dimensional) space where it is taken. We will describe two formulations which precisely differ in this choice. Both formulations will allow one to deal with the instabilities of the three-field viscoelastic formulation described earlier. There will be no need to meet the inf-sup conditions for the interpolation spaces and it will be possible to solve convection dominated problems both in the momentum and in the constitutive equation. For the latter, these methods have been found to work well. However, for the momentum equation we have observed that *they are not robust in the presence of high gradients of the unknowns*, and therefore we have had to modify them. The modification consists in designing a sort of *term-by-term stabilization based on the choice of subscales orthogonal to the finite element space*. We will describe in detail this method and the need for it.

The numerical results shown in this chapter can separated into three groups. The first (Section 3.5.1) corresponds to the study of the h-convergence of the formulations proposed for a stationary Oldroyd-B fluid, using linear and quadratic quadrilateral elements. To perform this test we manufacture the solution by introducing a force term computed with a predetermined elastic stress-velocity-pressure solution. The second group (Section 3.5.2) of results corresponds to the classical 4:1 planar contraction for an Oldroyd-B fluid in the range of Weissenberg numbers $0 \leq \mathrm{We} \leq 5.0$ for a Reynolds number $\mathrm{Re} = 1.0$, and in the range of $0 \leq \mathrm{We} \leq 6.5$ for the quasi non-inertial case $\mathrm{Re} = 0.01$. We compare our results with those published by different authors. The section with numerical examples concludes with a threedimensional example (Section 3.5.3), only to show that the formulations introduced are immediately extended to the 3D case.

The chapter is organized as follows. Section 3.3 contains the presentation of the problem, with the viscoelastic three-field continuous problem, its variational form and the straightforward Galerkin finite element discretization. Section 3.4 presents our stabilized finite element approach, with the description of the general idea and its application to the present problem. The linearization of the problem and a discontinuity-capturing technique are also discussed. Section 3.5 contains the numerical results and, finally, in Section 3.6 conclusions are summarized.

3.3 The viscoelastic flow problem

3.3.1 Boundary value problem

Let Ω be the computational domain of $\mathbb{R}^d (d = 2 \text{ or } 3)$ occupied by the fluid, assumed to be bounded and polyhedral, and let $\partial\Omega$ be its boundary. Only stationary problems will be considered in this part of the work. In this case, for incompressible and isothermal viscoelastic flows, the conservation equations for momentum and mass may be expressed as

$$\begin{aligned} -\nabla \cdot \boldsymbol{T} + \rho \boldsymbol{u} \nabla \cdot \boldsymbol{u} + \nabla p &= \boldsymbol{f} \text{ in } \Omega, \\ \nabla \cdot \boldsymbol{u} &= 0 \text{ in } \Omega, \end{aligned}$$

where ρ denotes the constant density, $p : \Omega \to \mathbb{R}$ the pressure field, $\boldsymbol{u} : \Omega \to \mathbb{R}^d$ the velocity field, $\boldsymbol{f} : \Omega \to \mathbb{R}^d$ the force field and $\boldsymbol{T} : \Omega \to \mathbb{R}^d \otimes \mathbb{R}^d$ the deviatoric extra stress tensor. In general, $\boldsymbol{T}$ is defined in terms of a viscous and a viscoelastic contribution as

$$\boldsymbol{T} = 2\eta_e \nabla^s \boldsymbol{u} + \boldsymbol{\sigma},$$

where η_e represents the effective viscosity (or solvent viscosity), $\nabla^s \boldsymbol{u}$ is the symmetrical part of the velocity gradient and $\boldsymbol{\sigma}$ is the viscoelastic or elastic stress tensor. For viscoelastic fluids, the problem is incomplete without the definition of a constitutive equation for this viscoelastic stress tensor. A large variety of approaches exist to define it. One the one hand, we have closed integral and differential constitutive models [21] and, on the other, kinetic and molecular dynamics theories [22], that do not yield a closed form constitutive expression. In this chapter, only the differential Oldroyd-B model is considered. It reads:

$$\boldsymbol{\sigma} + \lambda \overset{\nabla}{\boldsymbol{\sigma}} - 2\eta_p \nabla^s \boldsymbol{u} = \boldsymbol{0},$$

where λ is the relaxation time, η_p represents the polymeric viscosity and $\overset{\nabla}{\boldsymbol{\sigma}}$ is the upper convected time derivative of the elastic stress tensor. The sum of the effective and polymeric viscosities give the total viscosity η_0. We can introduce an additional parameter $\beta \in [0, 1]$ and write η_e and η_p as $\eta_e = \beta\eta_0$ and $\eta_p = (1 - \beta)\eta_0$.

The system of equations can be written only in terms of the total viscosity η_0 and β as follows:

$$-\nabla \cdot \boldsymbol{\sigma} - 2\beta\eta_0 \nabla \cdot (\nabla^s \boldsymbol{u}) + \rho \boldsymbol{u} \cdot \nabla \boldsymbol{u} + \nabla p = \boldsymbol{f} \text{ in } \Omega, \tag{3.1}$$

$$\nabla \cdot \boldsymbol{u} = 0 \text{ in } \Omega, \tag{3.2}$$

$$\frac{1}{2\eta_0}\boldsymbol{\sigma} - (1 - \beta)\nabla^s \boldsymbol{u} + \frac{\lambda}{2\eta_0}\left(\boldsymbol{u} \cdot \nabla\boldsymbol{\sigma} - \boldsymbol{\sigma} \cdot \nabla\boldsymbol{u} - (\nabla\boldsymbol{u})^T \cdot \boldsymbol{\sigma}\right) = \boldsymbol{0} \text{ in } \Omega, \tag{3.3}$$

where the unknowns are the velocity, the pressure and the viscoelastic stress tensor.

Calling $\boldsymbol{U} = [\boldsymbol{u}, p, \boldsymbol{\sigma}]$, $\boldsymbol{F} = [\boldsymbol{f}, 0, \boldsymbol{0}]$ and defining

$$\mathcal{L}(\hat{\boldsymbol{u}}; \boldsymbol{U}) = \begin{pmatrix} -\nabla \cdot \boldsymbol{\sigma} - 2\beta\eta_0 \nabla \cdot (\nabla^s \boldsymbol{u}) + \rho\hat{\boldsymbol{u}} \cdot \nabla\boldsymbol{u} + \nabla p \\ \nabla \cdot \boldsymbol{u} \\ \frac{1}{2\eta_0}\boldsymbol{\sigma} - (1 - \beta)\nabla^s \boldsymbol{u} + \frac{\lambda}{2\eta_0}\left(\hat{\boldsymbol{u}} \cdot \nabla\boldsymbol{\sigma} - \boldsymbol{\sigma} \cdot \nabla\hat{\boldsymbol{u}} - (\nabla\hat{\boldsymbol{u}})^T \cdot \boldsymbol{\sigma}\right) \end{pmatrix}, \tag{3.4}$$

we may write (3.1)-(3.3) as $\mathcal{L}(\boldsymbol{u}; \boldsymbol{U}) = \boldsymbol{F}$.

Boundary conditions have to be appended to problem (3.1)-(3.3). For simplicity in the exposition, we will consider the simplest condition $\boldsymbol{u} = \boldsymbol{0}$ on $\partial\Omega$, and no boundary conditions for $\boldsymbol{\sigma}$. However, in some of the numerical examples we shall specify the viscoelastic stress on inflow boundaries. To avoid this and still get adequate approximations, we would need excessively large computational domains.

For a complete description of the mathematical structure of the problem we refer to [82].

3.3.2 Variational form

In order to write the weak form of the problem, let us introduce some notation. The space of square integrable functions in a domain ω is denoted by $L^2(\omega)$, and the space of functions whose distributional derivatives of order up to $m \geq 0$ (integer) belong to $L^2(\omega)$ by $H^m(\omega)$. The space $H_0^1(\omega)$ consists of functions in $H^1(\omega)$ vanishing on $\partial\omega$. The topological dual of $H_0^1(\Omega)$ is denoted by $H^{-1}(\Omega)$, the duality pairing being $\langle\cdot,\cdot\rangle$. The L^2 inner product in ω (for scalar, vectors and tensors) is denoted by $(\cdot,\cdot)_\omega$ and the integral over ω of the product of two general functions is written as $\langle\cdot,\cdot\rangle_\omega$, the subscript being omitted when $\omega = \Omega$. The norm in a space X is denoted by $\|\cdot\|_X$, except in the case $X = L^2(\Omega)$, case in which the subscript is omitted.

Using this notation, the stress, velocity and pressure finite element spaces for the continuous problem are $\boldsymbol{\Upsilon} = H^1(\Omega)^{d\times d}_{\text{sym}}$ (symmetric second order tensors with components in $H^1(\Omega)$), $\boldsymbol{\mathcal{V}}_0 = H_0^1(\Omega)^d$ and $\mathcal{Q} = L^2(\Omega)/\mathbb{R}$, respectively. The weak form of the problem consists in finding $\boldsymbol{U} = [\boldsymbol{u}, p, \boldsymbol{\sigma}] \in \boldsymbol{\mathcal{X}} := \boldsymbol{\mathcal{V}}_0 \times \mathcal{Q} \times \boldsymbol{\Upsilon}$, such that:

$$
\begin{aligned}
(\boldsymbol{\sigma}, \nabla^s \boldsymbol{v}) - (2\beta\eta_0 \nabla^s \boldsymbol{u}, \nabla^s \boldsymbol{v}) + \langle \rho \boldsymbol{u}\cdot\nabla\boldsymbol{u}, \boldsymbol{v}\rangle - (p, \nabla\cdot\boldsymbol{v}) &= \langle \boldsymbol{f}, \boldsymbol{v}\rangle, \\
(\nabla\cdot\boldsymbol{u}, q) &= 0, \\
\left(\frac{1}{2\eta_0}\boldsymbol{\sigma} - (1-\beta)\nabla^s\boldsymbol{u}, \boldsymbol{\tau}\right) + \frac{\lambda}{2\eta_0}\left(\boldsymbol{u}\cdot\nabla\boldsymbol{\sigma} - \boldsymbol{\sigma}\cdot\nabla\boldsymbol{u} - (\nabla\boldsymbol{u})^T\cdot\boldsymbol{\sigma}, \boldsymbol{\tau}\right) &= 0,
\end{aligned}
$$

for all $\boldsymbol{V} = [\boldsymbol{v}, q, \boldsymbol{\tau}] \in \boldsymbol{\mathcal{X}}$, where $\boldsymbol{f} \in H^{-1}(\Omega)^d$ is assumed.

In a compact form, the problem can be written as: find $\boldsymbol{U} \in \boldsymbol{\mathcal{X}}$ such that

$$
B(\boldsymbol{u}; \boldsymbol{U}, \boldsymbol{V}) = \langle \boldsymbol{f}, \boldsymbol{v}\rangle, \tag{3.5}
$$

for all $\boldsymbol{V} \in \boldsymbol{\mathcal{X}}$, where

$$
\begin{aligned}
B(\hat{\boldsymbol{u}}; \boldsymbol{U}, \boldsymbol{V}) = {} & (\boldsymbol{\sigma}, \nabla^s\boldsymbol{v}) - (2\beta\eta_0\nabla^s\boldsymbol{u}, \nabla^s\boldsymbol{v}) + \langle\rho\hat{\boldsymbol{u}}\cdot\nabla\boldsymbol{u}, \boldsymbol{v}\rangle - (p, \nabla\cdot\boldsymbol{v}) + (\nabla\cdot\boldsymbol{u}, q) \\
& + \left(\frac{1}{2\eta_0}\boldsymbol{\sigma} - (1-\beta)\nabla^s\boldsymbol{u}, \boldsymbol{\tau}\right) + \frac{\lambda}{2\eta_0}\left(\hat{\boldsymbol{u}}\cdot\nabla\boldsymbol{\sigma} - \boldsymbol{\sigma}\cdot\nabla\hat{\boldsymbol{u}} - (\nabla\hat{\boldsymbol{u}})^T\cdot\boldsymbol{\sigma}, \boldsymbol{\tau}\right).
\end{aligned} \tag{3.6}
$$

3.3.3 Galerkin finite element discretization

Let $\mathcal{T}_h = \{K\}$ be a finite element partition of the domain Ω. For the sake of conciseness, we consider it quasi-uniform, of diameter h. From this we may construct conforming finite element spaces for the velocity, the pressure and the viscoelastic stress, $\boldsymbol{\mathcal{V}}_{h,0} \subset \boldsymbol{\mathcal{V}}_0$, $\mathcal{Q}_h \subset \mathcal{Q}$ and $\boldsymbol{\Upsilon}_h \subset \boldsymbol{\Upsilon}$, in the usual manner. The Galerkin finite element approximation consist in finding $\boldsymbol{U}_h = [\boldsymbol{u}_h, p_h, \boldsymbol{\sigma}_h] \in \boldsymbol{\mathcal{X}}_h := \boldsymbol{\mathcal{V}}_{h,0} \times \mathcal{Q}_h \times \boldsymbol{\Upsilon}_h$ such that:

$$
B(\boldsymbol{u}_h; \boldsymbol{U}_h, \boldsymbol{V}_h) = \langle \boldsymbol{f}, \boldsymbol{v}_h\rangle, \tag{3.7}
$$

for all $\boldsymbol{V}_h = [\boldsymbol{v}_h, q_h, \boldsymbol{\tau}_h] \in \boldsymbol{\mathcal{X}}_h$.

In principle, we have posed no restrictions on the choice of the finite element spaces. However, there are conditions on these interpolation spaces that must be satisfied in the discrete formulation used. These are the same as for the three-field formulation of the Stokes problem (see for example [56] and references therein), and read as follows: there exist positive constants C_1 and C_2 such that

$$
\inf_{q_h\in\mathcal{Q}_h}\sup_{\boldsymbol{v}_h\in\boldsymbol{\mathcal{V}}_{h,0}} \frac{(q_h, \nabla\cdot\boldsymbol{v}_h)}{\|q_h\|_{\mathcal{Q}_h}\|\boldsymbol{v}_h\|_{\boldsymbol{\mathcal{V}}_{h,0}}} \geq C_1, \tag{3.8}
$$

$$
\inf_{\boldsymbol{v}_h\in\boldsymbol{\mathcal{V}}_{h,0}}\sup_{\boldsymbol{\tau}_h\in\boldsymbol{\Upsilon}_h} \frac{(\boldsymbol{\tau}_h, \nabla^s\boldsymbol{v}_h)}{\|\boldsymbol{\tau}_h\|_{\boldsymbol{\Upsilon}_h}\|\boldsymbol{v}_h\|_{\boldsymbol{\mathcal{V}}_{h,0}}} \geq C_2. \tag{3.9}
$$

Let us see as to use these conditions for the viscoelastic problem. Using expression (3.6) and considering that $\boldsymbol{u}_h$ vanishes on $\partial\Omega$, it is readily checked that

$$B\left(\boldsymbol{u}_h;\left[\boldsymbol{u}_h,p_h,\boldsymbol{\sigma}_h\right],\left[\left(1-\beta\right)\boldsymbol{u}_h,\left(1-\beta\right)p_h,\boldsymbol{\sigma}_h\right]\right) = 2\beta\eta_0\left(1-\beta\right)\left\|\nabla^s\boldsymbol{u}_h\right\|^2+\frac{1}{2\eta_0}\left\|\boldsymbol{\sigma}_h\right\|^2 - \frac{\lambda}{2\eta_0}\left(\boldsymbol{\sigma}_h\cdot\nabla\boldsymbol{u}_h+\left(\nabla\boldsymbol{u}_h\right)^T\cdot\boldsymbol{\sigma}_h,\boldsymbol{\sigma}_h\right).$$

Assuming $\lambda\nabla\boldsymbol{u}_h$ to be small enough (in fact, it is only $\lambda\nabla^s\boldsymbol{u}_h$ that needs to be small), this expression provides only control on $\|\boldsymbol{\sigma}_h\|^2$ for all β. One has then to make use of (3.9) to control $\nabla^s\boldsymbol{u}_h$ and then of (3.8) to control p_h. It is therefore required that the finite element spaces satisfy (3.8)-(3.9) (for more details, see [29, 148], for example).

Choosing equal order approximations for $\boldsymbol{\sigma}$, $\boldsymbol{u}$ and p does not yield a stable scheme. A possible remedy to this situation is to enrich the finite element spaces for the velocity and the stress in order to satisfy both restrictions [111, 84]. Another possibility is to use stabilized formulations permitting any interpolation for the variables [108, 103, 64], which is the approach we pursue in this chapter for the viscoelastic fluid flow problem. In general, a stabilized formulation consists of replacing B in (3.5) by another semilinear form B_h, possibly mesh dependent, with better stabilities properties.

3.4 Design of a stable finite element formulation

3.4.1 Residual based stabilized finite element methods

In the following we present two stabilized finite element formulations for computing viscoelastic flows using the Olrdroyd-B constitutive model. They are based on the splitting of the unknowns $\boldsymbol{U}$ in a component $\boldsymbol{U}_h$ which can be resolved by the finite element space, and the remainder $\tilde{\boldsymbol{U}}$, that will be called sub-grid scale. The framework we use is based on [97].

We will omit the details of the derivation of the method. In the context of a three-field formulation for flow problems, they can be found in Chapter 2 (also in [36]). Here we just state the method for the particular case of stationary viscoelastic flows. After some approximations, this method consists in finding $\boldsymbol{U}_h\in\boldsymbol{\mathcal{X}}_h$ such that

$$B\left(\boldsymbol{u};\boldsymbol{U}_h,\boldsymbol{V}_h\right)+\sum_K\left\langle\tilde{\boldsymbol{U}},\mathcal{L}^*\left(\boldsymbol{u}_h;\boldsymbol{V}_h\right)\right\rangle_K=\left\langle\boldsymbol{f},\boldsymbol{v}_h\right\rangle, \tag{3.10}$$

for all $\boldsymbol{V}_h\in\boldsymbol{\mathcal{X}}_h$, where $\mathcal{L}^*(\hat{\boldsymbol{u}};\boldsymbol{V})$ is the formal adjoint of the operator in (3.4) without considering boundary conditions, which is given by

$$\mathcal{L}^*\left(\hat{\boldsymbol{u}};\boldsymbol{V}\right)=\begin{pmatrix}-\left(1-\beta\right)\nabla\cdot\boldsymbol{\tau}-2\beta\eta_0\nabla\cdot\left(\nabla^s\boldsymbol{v}\right)-\rho\hat{\boldsymbol{u}}\cdot\nabla\boldsymbol{v}-\nabla q\\ -\nabla\cdot\boldsymbol{v}\\ \frac{1}{2\eta_0}\boldsymbol{\tau}+\nabla^s\boldsymbol{v}-\frac{\lambda}{2\eta_0}\left(\hat{\boldsymbol{u}}\cdot\nabla\boldsymbol{\tau}+\boldsymbol{\tau}\cdot\left(\nabla\hat{\boldsymbol{u}}\right)^T+\nabla\hat{\boldsymbol{u}}\cdot\boldsymbol{\tau}\right)\end{pmatrix},$$

and $\tilde{\boldsymbol{U}}$ is the sub-grid scale, which needs to be approximated. If $\tilde{P}$ is the L^2 projection onto the space of sub-grid scales, the approximation we consider within each element is

$$\tilde{\boldsymbol{U}}=\boldsymbol{\alpha}\tilde{P}\left[\boldsymbol{F}-\mathcal{L}\left(\boldsymbol{u}_h;\boldsymbol{U}_h\right)\right], \tag{3.11}$$

where $\boldsymbol{\alpha}$ is a matrix computed within each element, which we take as

$$\boldsymbol{\alpha}=\operatorname{diag}\left(\alpha_1\boldsymbol{I}_d,\alpha_2,\alpha_3\boldsymbol{I}_{d\times d}\right), \tag{3.12}$$

with $\boldsymbol{I}_d$ the identity on vectors of $\mathbb{R}^d$, $\boldsymbol{I}_{d\times d}$ the identity on second order tensors and the parameters α_i, $i=1,2,3$, are computed as (see [56, 36])

$$\begin{aligned}
\alpha_1 &= \left[c_1\frac{\eta_0}{h_1^2}+c_2\frac{\rho\,|\boldsymbol{u}_h|}{h_2}\right]^{-1},\\
\alpha_2 &= \frac{h_1^2}{c_1\alpha_1},\\
\alpha_3 &= \left[c_3\frac{1}{2\eta_0}+c_4\left(\frac{\lambda}{2\eta_0}\frac{|\boldsymbol{u}_h|}{h_2}+\frac{\lambda}{\eta_0}\,|\nabla\boldsymbol{u}_h|\right)\right]^{-1}.
\end{aligned}$$

In these expressions, h_1 corresponds to a characteristic length calculated as the square root of the element area in the 2D case and the cubic root of the element volume in 3D, and h_2 corresponds to another characteristic length calculated as the element length in the streamline direction. The term $|\boldsymbol{u}_h|$ is the Euclidean norm of the velocity, and $|\nabla\boldsymbol{u}_h|$ the Frobenius norm of the velocity gradient (another possibility for this last term is to take the maximum eigenvalue of the velocity gradient matrix). The constants c_i, $i=1,4$ are algorithmic parameters in the formulation. The values used in this chapter for linear elements are $c_1=4.0$, $c_2=2.0$, $c_3=4.0$ and $c_4=0.25$. For higher order elements, the characteristic lengths h_1 and h_2 are respectively divided by k^2 and k, k being the order of the finite element interpolation, and we keep the value of the constants used for linear elements.

Inserting (3.11) with $\boldsymbol{\alpha}$ given in (3.12) in (3.10) we get the following method: find $\boldsymbol{U}_h\in\boldsymbol{\mathcal{X}}_h$ such that

$$B\left(\boldsymbol{u}_h;\boldsymbol{U}_h,\boldsymbol{V}_h\right)+S_1\left(\boldsymbol{u}_h;\boldsymbol{U}_h,\boldsymbol{V}_h\right)+S_2\left(\boldsymbol{U}_h,\boldsymbol{V}_h\right)+S_3\left(\boldsymbol{u}_h;\boldsymbol{U}_h,\boldsymbol{V}_h\right)=\langle\boldsymbol{f},\boldsymbol{v}_h\rangle+R_1\left(\boldsymbol{u}_h;\boldsymbol{V}_h\right), \tag{3.13}$$

for all $\boldsymbol{V}_h\in\boldsymbol{\mathcal{X}}_h$, where

$$\begin{aligned}
S_1\left(\hat{\boldsymbol{u}}_h;\boldsymbol{U}_h,\boldsymbol{V}_h\right) &= \sum_K \alpha_1\Big\langle\tilde{P}\left[-\nabla\cdot\boldsymbol{\sigma}_h-2\beta\eta_0\nabla\cdot\left(\nabla^s\boldsymbol{u}_h\right)+\rho\hat{\boldsymbol{u}}_h\cdot\nabla\boldsymbol{u}_h+\nabla p_h\right], \qquad (3.14)\\
&\quad -(1-\beta)\,\nabla\cdot\boldsymbol{\tau}_h+2\beta\eta_0\nabla\cdot\left(\nabla^s\boldsymbol{v}_h\right)+\rho\hat{\boldsymbol{u}}_h\cdot\nabla\boldsymbol{v}_h+\nabla q_h\rangle_K,\\
S_2\left(\boldsymbol{U}_h,\boldsymbol{V}_h\right) &= \sum_K \alpha_2\Big\langle\tilde{P}\left[\nabla\cdot\boldsymbol{u}_h\right],\nabla\cdot\boldsymbol{v}_h\Big\rangle_K, \qquad (3.15)\\
S_3\left(\hat{\boldsymbol{u}}_h;\boldsymbol{U}_h,\boldsymbol{V}_h\right) &= \sum_K \alpha_3\Big\langle\tilde{P}\left[\frac{1}{2\eta_0}\boldsymbol{\sigma}_h-(1-\beta)\,\nabla^s\boldsymbol{u}_h+\frac{\lambda}{2\eta_0}\left(\hat{\boldsymbol{u}}_h\cdot\nabla\boldsymbol{\sigma}_h-g\left(\hat{\boldsymbol{u}}_h,\boldsymbol{\sigma}_h\right)\right)\right], \qquad (3.16)\\
&\quad -\frac{1}{2\eta_0}\boldsymbol{\tau}_h-\nabla^s\boldsymbol{v}_h+\frac{\lambda}{2\eta_0}\left(\hat{\boldsymbol{u}}_h\cdot\nabla\boldsymbol{\tau}_h+\boldsymbol{\tau}_h\cdot\left(\nabla\hat{\boldsymbol{u}}_h\right)^T+\nabla\hat{\boldsymbol{u}}_h\cdot\boldsymbol{\tau}_h\right)\Big\rangle_K,\\
R_1\left(\hat{\boldsymbol{u}}_h;\boldsymbol{V}_h\right) &= \sum_K \alpha_1\Big\langle\tilde{P}\left[\boldsymbol{f}\right],-(1-\beta)\,\nabla\cdot\boldsymbol{\tau}_h+2\beta\eta_0\nabla\cdot\left(\nabla^s\boldsymbol{v}_h\right)+\rho\hat{\boldsymbol{u}}_h\cdot\nabla\boldsymbol{v}_h+\nabla q_h\Big\rangle_K, \qquad (3.17)
\end{aligned}$$

where $g\left(\hat{\boldsymbol{u}}_h,\boldsymbol{\sigma}_h\right)=\boldsymbol{\sigma}_h\cdot\nabla\hat{\boldsymbol{u}}_h+\left(\nabla\hat{\boldsymbol{u}}_h\right)^T\cdot\boldsymbol{\sigma}_h$.

In these equations, $\tilde{P}$ is the projection restricted to the appropriate space of the components of the finite element residual $\boldsymbol{R}_h:=\boldsymbol{F}-\mathcal{L}(\boldsymbol{u}_h;\boldsymbol{U}_h)$. It remains only to define this projection, for which we consider two possible choices as in chapter 2:

- Algebraic sub-grid scale (ASGS) method: $\tilde{P}=I$ (the identity) when applied to finite element residuals.

- Orthogonal sub-grid scale (OSGS) method: $\tilde{P} = P_h^\perp = I - P_h$, where P_h is the L^2 projection onto the appropriate finite element space.

For the analysis of the ASGS and the OSGS methods for the linearized Navier-Stokes equations using the classical velocity-pressure formulation, see [53] and [55], respectively.

Independently of the choice of the projection $\tilde{P}$, method (3.13) is consistent, since the terms added to the Galerkin ones are proportional to the finite element residual $\boldsymbol{R}_h$. Thus, they vanish if the finite element solution is replaced by the solution of the continuous problem $\boldsymbol{U}$. It is in this sense that we call (3.13) a *residual based* method.

3.4.2 Split OSGS stabilization

For smooth solutions, method (3.13) is stable and displays optimal order of convergence, both for $\tilde{P} = I$ and for $\tilde{P} = P_h^\perp$. In our experience for Newtonian and quasi-Newtonian flows, the OSGS method is in general more accurate, whereas the ASGS is cheaper, since projections are not needed, and sometimes more robust. Note that the OSGS will be, by construction, less dissipative.

If we consider the case $\tilde{P} = P_h^\perp$, from (3.13) we can design *a simplified method*, which consists in *neglecting the cross local inner-product terms* in (3.13), as well as some other terms that do not contribute to stability. In particular, the term $S_1(\hat{\boldsymbol{u}}_h; \boldsymbol{U}_h, \boldsymbol{V}_h)$ in (3.14) can in principle be replaced by

$$(1-\beta)\sum_K \alpha_1 \left\langle P_h^\perp \left[\nabla\cdot\boldsymbol{\sigma}_h\right], \nabla\cdot\boldsymbol{\tau}_h\right\rangle_K - \beta^2 \sum_K \alpha_1 \left\langle P_h^\perp \left[2\eta_0 \nabla\cdot(\nabla^s \boldsymbol{u}_h)\right], 2\eta_0 \nabla\cdot(\nabla^s \boldsymbol{v}_h)\right\rangle_K$$
$$+ \sum_K \alpha_1 \left\langle P_h^\perp \left[\rho\hat{\boldsymbol{u}}_h\cdot\nabla\boldsymbol{u}_h\right], \rho\hat{\boldsymbol{u}}_h\cdot\nabla\boldsymbol{v}_h\right\rangle_K + \sum_K \alpha_1 \left\langle P_h^\perp \left[\nabla p_h\right], \nabla q_h\right\rangle_K, \quad (3.18)$$

and, since the second term does not contribute to stability, it can be also deleted, like the term $R_1(\boldsymbol{u}_h; \boldsymbol{V}_h)$ in the right-hand-side of (3.13). The three remaining terms in (3.18) help to improve stability, the first giving control on the divergence of the viscoelastic stress, the third on the convective term and the fourth on the pressure gradient. This term-by-term stabilization point of view is in fact previous to the OSGS method, based on the approximation of the sub-grid scales. It is proposed in [51] and analyzed in [55].

The key point that allows one to add (3.18) to the Galerkin terms is the orthogonal projection $P_h^\perp$. Obviously, (3.18) is not zero when the finite element solution is replaced by the continuous solution, and therefore the method is not consistent in the sense used in the finite element context. However, *the consistency error is of optimal order*, since for any smooth enough function f, $P_h(f)$ is an optimal approximation to f in the finite element space, and therefore $P_h^\perp(f)$ goes to zero with h at the optimal rate permitted by the finite element interpolation (and the smoothness of f).

The method in (3.13) is consistent for any projection $\tilde{P}$, and therefore there we might consider $\tilde{P} = I - P_{h,0}$ for the projection applied to the residual of the momentum equation, where $P_{h,0}$ is the L^2 projection onto the velocity finite element space *incorporating* boundary conditions, i.e., the L^2 projection onto $\boldsymbol{\mathcal{V}}_{h,0}$. However, in (3.18) we need to take $P_h^\perp = I - P_h$, P_h being the L^2 projection *without* boundary conditions, since otherwise $P_h^\perp(f)$ would not converge to zero at the optimal order mentioned before. The price to be paid is that the finite element mesh needs to satisfy a mild compatibility condition, as explained in [55], which is easily fulfilled for most meshes.

Apart from $P_h^\perp$, other projections can be used in (3.18), as soon as one can guarantee that they provide enough stability and that the consistency error introduced has optimal order. Among these, let us mention those associated to the Local Projection Stabilization (see for

example [18, 114] and references therein) or the method proposed in [10] for the Stokes problem. These local projections avoid the global projection P_h that we have used, which requires to solve a linear system (trivial to solve, though). This might seem an advantage of local projections. However, the bottleneck of these methods is that they all increase the sparsity of the final matrix. This is usually unaffordable, and therefore an iterative strategy is needed anyway. In our case, we solve the problem by lagging the projection one iteration in the iterative process, as described below. This is for free in nonlinear problems as the one considered in this work. Furthermore, it is shown in [55] that the Galerkin method already gives control on the finite element component of the different terms of the equation, and therefore only control on the component orthogonal to the finite element space is required. Thus, *any* projection different to the L^2 one will introduce more numerical dissipation for the same stability.

Similar considerations can be applied to modify the term $S_3(\hat{\boldsymbol{u}}_h;\boldsymbol{U}_h,\boldsymbol{V}_h)$ in (3.16), now taking into account that $P_h^\perp(\boldsymbol{\sigma}_h)=\mathbf{0}$ ($P_h^\perp$ being now the orthogonal projection to the space of viscoelastic stresses). Therefore, the modified method we propose, that we call *split OSGS method*, is: find $\boldsymbol{U}_h\in\boldsymbol{\mathcal{X}}_h$ such that

$$B\left(\boldsymbol{u}_h;\boldsymbol{U}_h,\boldsymbol{V}_h\right)+S_1^\perp\left(\boldsymbol{u}_h;\boldsymbol{U}_h,\boldsymbol{V}_h\right)+S_2^\perp\left(\boldsymbol{U}_h,\boldsymbol{V}_h\right)+S_3^\perp\left(\boldsymbol{u}_h;\boldsymbol{U}_h,\boldsymbol{V}_h\right)=\left\langle\boldsymbol{f},\boldsymbol{v}_h\right\rangle, \tag{3.19}$$

for all $\boldsymbol{V}_h\in\boldsymbol{\mathcal{X}}_h$, where

$$\begin{aligned}
S_1^\perp\left(\hat{\boldsymbol{u}}_h;\boldsymbol{U}_h,\boldsymbol{V}_h\right)=&(1-\beta)\sum_K\alpha_1\left\langle P_h^\perp\left[\nabla\cdot\boldsymbol{\sigma}_h\right],\nabla\cdot\boldsymbol{\tau}_h\right\rangle_K+\sum_K\alpha_1\left\langle P_h^\perp\left[\nabla p_h\right],\nabla q_h\right\rangle_K \qquad (3.20)\\
&+\sum_K\alpha_1\left\langle P_h^\perp\left[\rho\hat{\boldsymbol{u}}_h\cdot\nabla\boldsymbol{u}_h\right],\rho\hat{\boldsymbol{u}}_h\cdot\nabla\boldsymbol{v}_h\right\rangle_K,\\
S_2^\perp\left(\boldsymbol{U}_h,\boldsymbol{V}_h\right)=&\sum_K\alpha_2\left\langle P_h^\perp\left[\nabla\cdot\boldsymbol{u}_h\right],\nabla\cdot\boldsymbol{v}_h\right\rangle_K, \qquad (3.21)\\
S_3^\perp\left(\hat{\boldsymbol{u}}_h;\boldsymbol{U}_h,\boldsymbol{V}_h\right)=&(1-\beta)\sum_K\alpha_3\left\langle P_h^\perp\left[\nabla^s\boldsymbol{u}_h\right],\nabla^s\boldsymbol{v}_h\right\rangle_K \qquad (3.22)\\
&+\left(\frac{\lambda}{2\eta_0}\right)^2\sum_K\alpha_3\left\langle P_h^\perp\left[\hat{\boldsymbol{u}}_h\cdot\nabla\boldsymbol{\sigma}_h\right],\hat{\boldsymbol{u}}_h\cdot\nabla\boldsymbol{\tau}_h\right\rangle_K\\
&-\left(\frac{\lambda}{2\eta_0}\right)^2\sum_K\alpha_3\left\langle P_h^\perp\left[\boldsymbol{\sigma}_h\cdot\nabla\hat{\boldsymbol{u}}_h+\left(\nabla\hat{\boldsymbol{u}}_h\right)^T\cdot\boldsymbol{\sigma}_h\right],\boldsymbol{\tau}_h\cdot\left(\nabla\hat{\boldsymbol{u}}_h\right)^T+\nabla\hat{\boldsymbol{u}}_h\cdot\boldsymbol{\tau}_h\right\rangle_K.
\end{aligned}$$

The stabilizing mechanism introduced by the different terms in these expressions is clear. Term $S_1^\perp$ has already been discussed. Regarding term $S_3^\perp$ in (3.22) it is observed that the first part has an EVSS-like structure (see [89]), that now has been derived from a simplification of the OSGS method, whereas the second part has a streamline-upwind structure, but the introduction of the orthogonal projection $P_h^\perp$ makes it have an optimal consistency error.

Method (3.19) is not just a simplification of (3.13). *For smooth solutions*, both have an optimal convergence rate in h. However, *in problems where the solution has strong gradients*, we have found (3.19) more robust. The split form of the OSGS formulation in the continuity and in the momentum equation has been applied and chosen after a large number of numerical tests. This method shows better response than the non-split formulation in the solution of pressure and stress, and gives the possibility to resolve problems where the elastic component is higher. When using (3.14), the terms that we have identified as "problematic" are the cross-terms $\alpha_1\left\langle\nabla p_h,-(1-\beta)\nabla\cdot\boldsymbol{\tau}_h\right\rangle_K$ and $\alpha_1\left\langle-\nabla\cdot\boldsymbol{\sigma}_h,\nabla q_h\right\rangle_K$. In the presence of high derivatives of pressure and stresses, such as in the corner of the 4:1 contraction example in Section 5.2, they lead to convergence difficulties for high Weissenberg numbers and to inaccurate localization of pressure and stress peaks.

We have not observed important differences in the use of either $S_3(\hat{\boldsymbol{u}}_h; \boldsymbol{U}_h, \boldsymbol{V}_h)$ in (3.16) or the modification $S_3^{\perp}(\hat{\boldsymbol{u}}_h; \boldsymbol{U}_h, \boldsymbol{V}_h)$ in (3.22). The former allows us to consider $\tilde{P} = I$ or $\tilde{P} = P_h^{\perp}$, and this is what we will compare in the numerical examples. So, in these examples we will use the terminology S-ASGS when (3.16) is used with $\tilde{P} = I$ and S-OSGS when (3.16) is used with $\tilde{P} = P_h^{\perp}$, but in both cases we will use (3.20) and (3.21) instead of (3.14) and (3.15).

3.4.3 Discontinuity capturing technique

The stabilized finite element formulation presented above yields a *globally* stable solution, i.e., norms of the unknowns over the whole domain Ω are bounded. However, if the solution displays very high gradients, local oscillations may still remain. In order to avoid this, or at least to alleviate this problem, we have introduced a discontinuity-capturing (DC) or shock-capturing term in our numerical formulation. In general, the main idea of any DC technique is to increase the amount of numerical dissipation in the neighbourhood of layers (see [49], for example).

In viscoelastic flow problems, we can find local instabilities or very high gradients in the pressure and in the viscoelastic stress components when the fluid flow finds an abrupt change in the geometry. This gradient can be especially strong when the amount of elastic component in the fluid is important.

The constitutive equation is of convective-reactive nature. The advection velocity is $\boldsymbol{u}_h$ (in the discrete problem) and the reactive terms are proportional to the velocity gradient $\nabla \boldsymbol{u}_h$. Therefore, if a non-consistent artificial diffusion is to be introduced, it must be of the form

$$k_\sigma = c_a h_1 \left|\boldsymbol{u}_h\right| + c_b h_1^2 \left|\nabla \boldsymbol{u}_h\right|. \tag{3.23}$$

The characteristic lengths give dimensional consistency, and the parameters C_a and C_b are algorithmic constants.

If an artificial diffusion term is added to problem (3.19), with the diffusion given by (3.23), the consistency error would make the method converge at most with an order $\mathcal{O}(h^{1/2})$. In order to design a method that can yield optimal convergence, at least when the solution is smooth, a possible option is to multiply the diffusion in (3.23) by a term proportional to the residual of the equation being solved properly normalized (see [49] and references therein). In this case, the residual would be that of the constitutive equation, as in [33]. However, in this work we have used another switch to activate the numerical diffusion, which is to make it proportional to the component of the viscoelastic stress orthogonal to the finite element space, that is to say, we take as diffusion coefficient

$$k_\sigma = \left(c_a h_1 \left|\boldsymbol{u}_h\right| + c_b h_1^2 \left|\nabla \boldsymbol{u}_h\right|\right) \frac{\left|P_h^{\perp}\left(\nabla \boldsymbol{\sigma}_h\right)\right|}{\left|\nabla \boldsymbol{\sigma}_h\right|}, \tag{3.24}$$

instead of (3.23). The way to introduce the DC dissipation is to add the term

$$\sum_K k_\sigma \left\langle \nabla \boldsymbol{\sigma}_h, \nabla \boldsymbol{\tau}_h \right\rangle_K,$$

to the left-hand-side of (3.19), where $\boldsymbol{\tau}_h$ is the test function of the constitutive equation.

The values used in this part of the work for the constants appearing in the numerical diffusion are $C_a = 0.1$ and $C_b = 0.5$.

3.4.4 Linearized problem

The equations for incompressible viscoelastic flows have several non-linear terms, both in the momentum and in the constitutive equations. In the former we have the convective term, and in the latter we have the term corresponding to convection of stresses and the rotational terms arising from the objective derivative of stresses. On top of that, the stabilization terms depend also on the velocity, introducing therefore additional nonlinearities.

As it is usual for incompressible flow problems, for the convective term of the momentum equation we can use a fixed point scheme, taking the advection velocity of the previous iteration. This leads only to first order convergence, but it is a robust option. However, for the nonlinear terms in the constitutive equation we have found crucial to use a Newton-Raphson linearization. This has allowed us to reach higher Weissenberg numbers.

The equations to be solved at each iteration are written in Algortihm 3.1. To understand them, let us make the following remarks:

- The nonlinear term in the momentum equation can be linearized with the fixed point scheme or with Newton-Raphson's method. This corresponds respectively to $N_u = 0$ and $N_u = 1$. Newton's iterations are only considered for the Galerkin contribution in the constitutive equation.
- Only a fixed point scheme is considered for the stabilization terms of the constitutive equation.
- The stabilization parameters are computed with values of the unknowns at the previous iterations. This is why a superscript $i-1$ has been used for them.
- The orthogonal projection of any function f has been approximated as $P_h^{\perp}(f^i) \approx f^i - P_h(f^{i-1})$. The iterative treatment of the orthogonal projection is thus coupled to the linearization of the whole system.
- The ASGS method for the constitutive equation corresponds to $\tilde{P} = I$, whereas the OSS method corresponds to $\tilde{P} = P_h^{\perp}$. In this case, the same strategy as for the rest of orthogonal projections is used.
- The DC dissipation is linearized using a fixed point strategy.

The equations in Algortihm 3.1 need to be embedded in a general algorithm which defines the nonlinear strategy to be used. In this respect, apart from the linearization of the different terms just described, we have found useful to use two more numerical ingredients, namely, an under-relaxation scheme and a continuation method in terms of the relaxation time λ. Concerning the former, we always use a relaxation parameter $\varepsilon = 0.5$, which we have found useful to set by default (even when it might not be necessary). Referring to the continuation method, we use when needed a simple continuation technique, consisting in N_λ continuation steps of equal size $\delta\lambda = \lambda/N_\lambda$. Moreover, we couple the continuation loop with the linearization loop, although both loops could also be treated in a nested way.

With these comments in mind, the final algorithm is presented in Algorithm 3.2.

Algorithm 3.1 Fully discrete and linearized problem at each iteration.

Given $\boldsymbol{u}_h^{i-1}$, $\boldsymbol{\sigma}_h^{i-1}$ $(i \geq 1)$, solve $\boldsymbol{u}_h^i$, p_h^i and $\boldsymbol{\sigma}_h^{i-1}$ from :

$$
\begin{aligned}
&\left(\boldsymbol{\sigma}_h^i, \nabla^s \boldsymbol{v}_h\right) + \left(2\beta\eta_0 \nabla^s \boldsymbol{u}_h^i, \nabla^s \boldsymbol{v}_h\right) + \left\langle \rho \boldsymbol{u}_h^{i-1} \cdot \nabla \boldsymbol{u}_h^i, \boldsymbol{v}_h \right\rangle + N_u \left\langle \rho \boldsymbol{u}_h^i \cdot \nabla \boldsymbol{u}_h^{i-1}, \boldsymbol{v}_h \right\rangle \\
&\quad - \left(p_h^i, \nabla \cdot \boldsymbol{v}_h\right) + \left(\nabla \cdot \boldsymbol{u}_h^i, q_h\right) + \left(\frac{1}{2\eta_0}\boldsymbol{\sigma}_h^i - (1-\beta)\nabla^s \boldsymbol{u}_h^i, \boldsymbol{\tau}_h\right) \\
&\quad + \frac{\lambda}{2\eta_0}\left(\boldsymbol{u}_h^{i-1} \cdot \nabla \boldsymbol{\sigma}_h^i - \boldsymbol{\sigma}_h^i \cdot \nabla \boldsymbol{u}_h^{i-1} - \left(\nabla \boldsymbol{u}_h^{i-1}\right)^T \cdot \boldsymbol{\sigma}_h^i, \boldsymbol{\tau}_h\right) \\
&\quad + \frac{\lambda}{2\eta_0}\left(\boldsymbol{u}_h^i \cdot \nabla \boldsymbol{\sigma}_h^{i-1} - \boldsymbol{\sigma}_h^{i-1} \cdot \nabla \boldsymbol{u}_h^i - \left(\nabla \boldsymbol{u}_h^i\right)^T \cdot \boldsymbol{\sigma}_h^{i-1}, \boldsymbol{\tau}_h\right) \\
&\quad + (1-\beta)\sum_K \alpha_1^{i-1} \left\langle \nabla \cdot \boldsymbol{\sigma}_h^i, \nabla \cdot \boldsymbol{\tau}_h \right\rangle_K \\
&\quad + \sum_K \alpha_1^{i-1} \left\langle \rho \boldsymbol{u}_h^{i-1} \cdot \nabla \boldsymbol{u}_h^i, \rho \boldsymbol{u}_h^{i-1} \cdot \nabla \boldsymbol{v}_h \right\rangle_K + \sum_K \alpha_1^{i-1} \left\langle \nabla p_h^i, \nabla q_h \right\rangle_K \\
&\quad + \sum_K \alpha_2^{i-1} \left\langle \nabla \cdot \boldsymbol{u}_h^i, \nabla \cdot \boldsymbol{v}_h \right\rangle_K \\
&\quad + \sum_K \alpha_3^{i-1} \left\langle \tilde{P}\left[\frac{1}{2\eta_0}\boldsymbol{\sigma}_h^i - (1-\beta)\nabla^s \boldsymbol{u}_h^i + \frac{\lambda}{2\eta_0}\left(\boldsymbol{u}_h^{i-1} \cdot \nabla \boldsymbol{\sigma}_h^i - g(\boldsymbol{u}_h^{i-1}, \boldsymbol{\sigma}_h^i)\right)\right], \right. \\
&\quad \left. -\frac{1}{2\eta_0}\boldsymbol{\tau}_h - \nabla^s \boldsymbol{v}_h + \frac{\lambda}{2\eta_0}\left(\boldsymbol{u}_h^{i-1} \cdot \nabla \boldsymbol{\tau}_h + \boldsymbol{\tau}_h \cdot \left(\nabla \boldsymbol{u}_h^{i-1}\right)^T + \nabla \boldsymbol{u}_h^{i-1} \cdot \boldsymbol{\tau}_h\right)\right\rangle_K, \\
&\quad + \sum_K k_\sigma^{i-1} \left\langle \nabla \boldsymbol{\sigma}_h^i, \nabla \boldsymbol{\tau}_h \right\rangle_K \\
&= \left\langle \boldsymbol{f}, \boldsymbol{v}_h \right\rangle + N_u \left\langle \rho \boldsymbol{u}_h^{i-1} \cdot \nabla \boldsymbol{u}_h^{i-1}, \boldsymbol{v}_h \right\rangle + \frac{\lambda}{2\eta_0}\left(\boldsymbol{u}_h^{i-1} \cdot \nabla \boldsymbol{\sigma}_h^{i-1} - g(\boldsymbol{u}_h^{i-1}, \boldsymbol{\sigma}_h^{i-1}), \boldsymbol{\tau}_h\right) \\
&\quad + (1-\beta)\sum_K \alpha_1^{i-1} \left\langle P_h\left[\nabla \cdot \boldsymbol{\sigma}_h^{i-1}\right], \nabla \cdot \boldsymbol{\tau}_h \right\rangle_K \\
&\quad + \sum_K \alpha_1^{i-1} \left\langle P_h\left[\rho \boldsymbol{u}_h^{i-1} \cdot \nabla \boldsymbol{u}_h^{i-1}\right], \rho \boldsymbol{u}_h^{i-1} \cdot \nabla \boldsymbol{v}_h \right\rangle_K + \sum_K \alpha_1^{i-1} \left\langle P_h\left[\nabla p_h^{i-1}\right], \nabla q_h \right\rangle_K \\
&\quad + \sum_K \alpha_2^{i-1} \left\langle P_h\left[\nabla \cdot \boldsymbol{u}_h^{i-1}\right], \nabla \cdot \boldsymbol{v}_h \right\rangle_K
\end{aligned}
$$

for all test functions $\boldsymbol{v}_h$,$\boldsymbol{\tau}_h$ and q_h.

Algorithm 3.2 General algorithm.

SET $\boldsymbol{u}_h^0 = \mathbf{0}$, $\boldsymbol{\sigma}_h^0 = \mathbf{0}$ and $p_h^0 = 0$
SET $\lambda^0 = 0$ and $k_\sigma^0 = 0$
  SET $i = 0$
  WHILE not converged DO:
    $i \leftarrow i + 1$
    SET the relaxation time to $\lambda^i = \max\left(\lambda^{i-1} + \lambda/N_\lambda, \lambda\right)$
    COMPUTE projections $P_h\left(\rho \boldsymbol{u}_h^{i-1} \cdot \nabla \boldsymbol{u}_h^{i-1}\right)$, $P_h\left(\nabla \cdot \boldsymbol{\sigma}_h^{i-1}\right)$,$P_h\left(\nabla p_h^{i-1}\right)$ and $P_h\left(\nabla \cdot \boldsymbol{u}_h^{i-1}\right)$
      IF $\tilde{P} = P_h^{\perp}$ THEN
        COMPUTE projection
        $$P_h\left[\frac{1}{2\eta_0}\boldsymbol{\sigma}_h^{i-1} - (1-\beta)\nabla^s \boldsymbol{u}_h^{i-1} + \frac{\lambda}{2\eta_0}\left(\boldsymbol{u}_h^{i-1} \cdot \nabla \boldsymbol{\sigma}_h^{i-1} - g\left(\boldsymbol{u}_h^{i-1}, \boldsymbol{\sigma}_h^{i-1}\right)\right)\right]$$
      END IF
    COMPUTE stabilization parameters α_1^{i-1}, α_2^{i-1} and α_3^{i-1}
    COMPUTE shock capturing term k_σ^{i-1} from (3.24), if needed
    SOLVE the equations in the Algorithm 3.1
    UPDATE unknowns:
      $\boldsymbol{u}_h^i \leftarrow \varepsilon \boldsymbol{u}_h^i + (1-\varepsilon)\,\boldsymbol{u}_h^{i-1}$
      $p_h^i \leftarrow \varepsilon p_h^i + (1-\varepsilon)\,p_h^{i-1}$
      $\boldsymbol{\sigma}_h^i \leftarrow \varepsilon \boldsymbol{\sigma}_h^i + (1-\varepsilon)\,\boldsymbol{\sigma}_h^{i-1}$
    CHECK convergence
  END WHILE

3.5 Numerical results

In this section, some tests are conducted to show the numerical performance of the proposed stabilized formulations and the benefits of the inclusion of a DC technique in the constitutive equation for the viscoelastic stress.

The first example is a convergence test with a manufactured solution. It serves to show that in the case of smooth solutions the formulations presented are optimally convergent. In fact, in this case also the original residual-based formulations yield optimal convergence. However, these formulations perform poorly in the example of subsection 3.5.2, where the classical 4:1 flow contraction problem is solved. Peaks of stresses and pressure at the corner are not properly captured, and this is precisely the reason that has led us to the split OSGS formulation. This section concludes with a threedimensional extension of the contraction problem in subsection 3.5.3.

3.5.1 Convergence test

The first set of results shown corresponds to the convergence study of the stabilized formulations presented for the viscoelastic fluid problem. A force term is introduced both in the momentum and constitutive equations so that the exact solution is given by:

$$\begin{aligned}
u_x(x,y) =& 2x^2 y (x-1)^2 (y-1)(2y-1), \\
u_y(x,y) =& -2xy^2 (x-1)(y-1)^2 (2x-1), \\
p(x,y) =& \sin(2\pi x)\sin(2\pi y), \\
\sigma_{xx}(x,y) =& 5\sin(2\pi x)\sin(2\pi y), \\
\sigma_{yy}(x,y) =& -5\sin(2\pi x)\sin(2\pi y), \\
\sigma_{xy}(x,y) =& \sin(2\pi x)\sin(2\pi y),
\end{aligned}$$

where the x and y components of the velocity and the stress have been indicated with a subscript.

Of course these velocity and stress fields do not satisfy the constitutive equation (3.3), with a zero right-hand-side. We have added a forcing term in this equation given by

$$\boldsymbol{f_c} = \frac{1}{2\eta_0}\boldsymbol{\sigma} - (1-\beta)\nabla^s \boldsymbol{u} + \frac{\lambda}{2\eta_0}\left(\boldsymbol{u}\cdot\nabla\boldsymbol{\sigma} - \boldsymbol{\sigma}\cdot\nabla\boldsymbol{u} - (\nabla\boldsymbol{u})^T\cdot\boldsymbol{\sigma}\right) \text{ in } \Omega,$$

with $\boldsymbol{u}$ and $\boldsymbol{\sigma}$ the manufactured solution given above.

The computational domain is the unit square, discretized using uniform structured meshes of bilinear and biquadratic quadrilateral elements, the range of element sizes being $0.0030625 < h < 0.0125$ in the bilinear case (Fig. 3.1, left), and $0.005 < h < 0.025$ in the biquadratic case (see Fig. 3.1, right). For each mesh, we have solved the problem for We $= 0$, We $= 1.0$ and We $= 2.0$, both for the S-OSGS and the S-ASGS formulations. The Weissenberg number for this case is calculated using the maximum value of the velocity taking the unit side of the computational domain as characteristic length.

The optimal convergence rate expected when the mesh size is reduced using linear elements is two in velocity and one in pressure-elastic stress in the L^2-norm, while using quadratic elements it is three in velocity and two in pressure-stress in the same norm. For both element types the S-OSGS formulation and the S-ASGS formulation show optimal convergence for all fields $\boldsymbol{\sigma}$, $\boldsymbol{u}$ and p.

From the quantitative point of view, if we compare the discrete L^2 errors for the same mesh, the S-OSGS formulation is more accurate that the S-ASGS formulation, showing at least the same error. This is a general trend that we have observed in several numerical

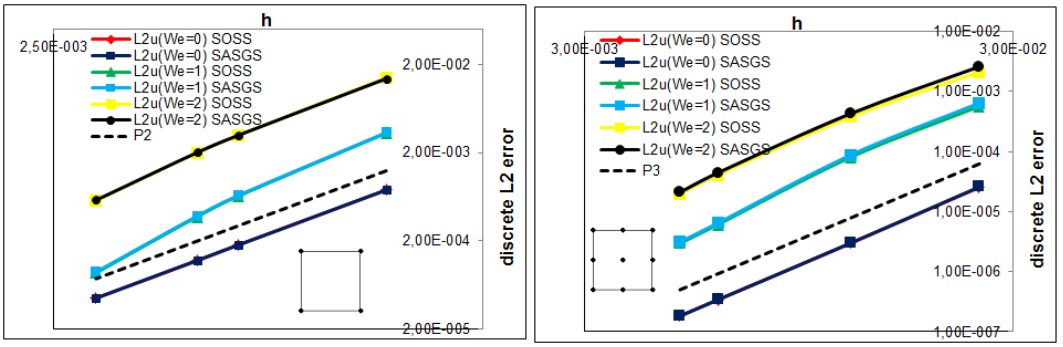

a)

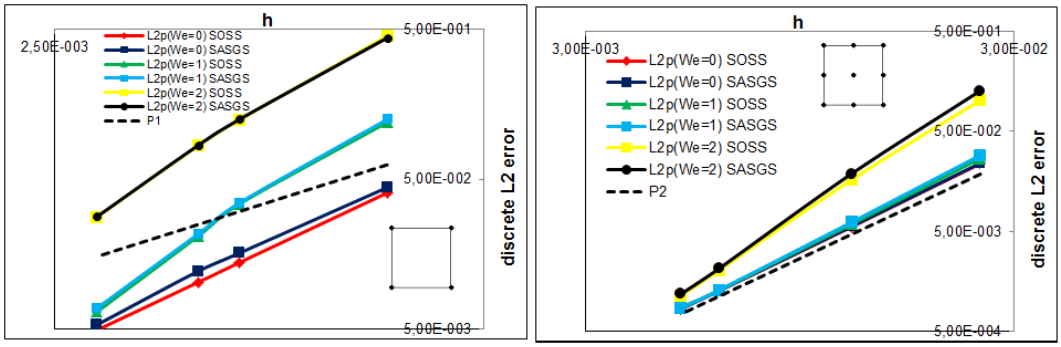

b)

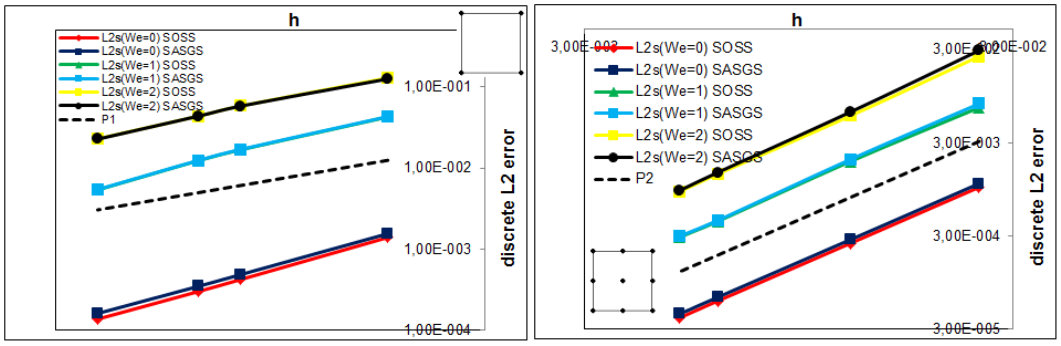

c)

Figure 3.1: Discrete L^2errors using Q_1 (left) and Q_2 (right) elements, for the manufactured exact solution. a) $L^2_{\boldsymbol{u}}$ (velocity error), b) L^2_p (pressure error) and c) $L^2_{\boldsymbol{\sigma}}$ (stress error).

examples: the S-OSGS formulation is less dissipative and this leads in general to better accuracy.

3.5.2 The 4:1 contraction problem

We present in the following the results we have obtained for the classical 4:1 contraction problem in the 2D case. The geometry of the problem is depicted in Fig. 3.2. Since the problem is symmetric, only half of the domain is considered. To discretize this computational domain we have used finite element meshes that are isotropic in the region surrounding the corner and anisotropic and unstructured further way. One of the meshes used for this problem is shown in Fig. 3.3.

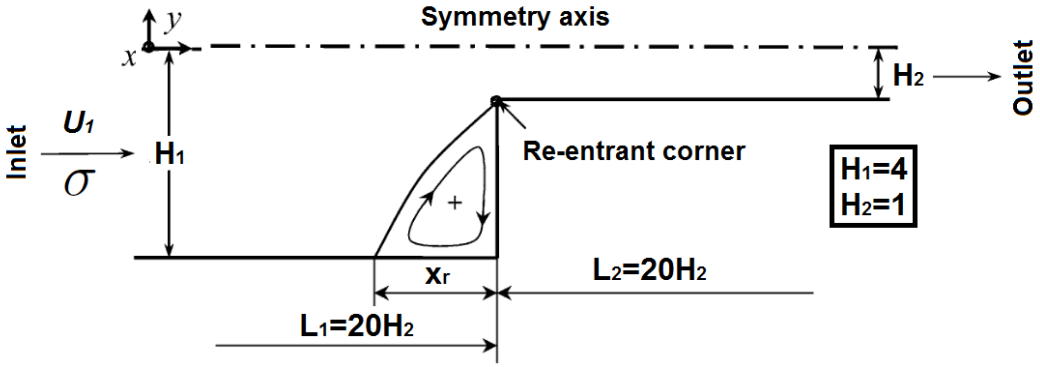

Figure 3.2: Geometry description of the two-dimensional 4:1 contraction problem.

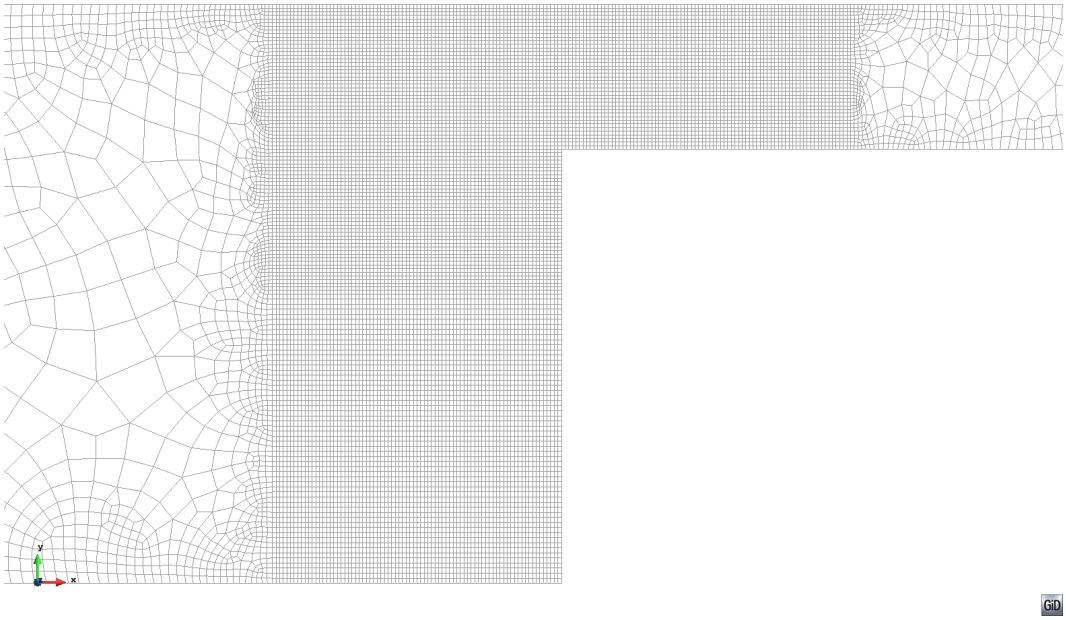

Figure 3.3: Typical mesh used in the two-dimensional 4:1 contraction problem.

The characteristic lengths of the problem are detailed in Fig. 3.2, where in addition we can see the definition of the vortex length X_r used to compare our results with those published by other authors.

Let us describe the boundary conditions of the problem. For the velocity, no-slip conditions are imposed on the solid walls and symmetry conditions are prescribed along the axis $y = 0$,

which in this case mean the y-velocity is set to zero. A fully developed parabolic velocity profile and the stress profile associated the Newtonian behavior are prescribed at the inlet. These are given by

$$u_x = \frac{3Q}{2H_1}\left(1 - \frac{y^2}{H_1^2}\right), \qquad u_y = 0,$$
$$\sigma_{xx} = 2\lambda\,(1-\beta)\,\eta_0\left(\frac{3Q}{H_1^3}y\right)^2, \qquad \sigma_{yy} = 0, \qquad \sigma_{xy} = -\,(1-\beta)\,\eta_0\left(\frac{3Q}{H_1^3}y\right),$$

where Q is the flow rate, taken as $Q = 1$. As already explained, the boundary conditions for the stresses are required to avoid an excessively large computational domain.

For the outlet, the horizontal velocity is left free, the vertical velocity is taken to be zero and pressure is prescribed to zero, constant. Altogether, the x-component of the normal component of the total Cauchy stress tensor (i.e., the x-component of the boundary traction) is taken to be zero.

We have solved the problem for two different Reynolds numbers (Re = 1 and Re = 0.01), with a total viscosity of value $\eta_0 = 1$ and with two different values of density ($\rho = 0.01$ and $\rho = 1$, respectively). The parameter β is taken as $\beta = 1/9$ and the relaxation time λ is fixed in terms of the required Weissenberg number. For this example, and using the above definitions, the Weissenberg number is defined in terms of the relaxation time as follows:

$$\mathrm{We} = \frac{\lambda \bar{u}_2}{H_2} = \lambda,$$

where $\bar{u}_2$ represents the average velocity at the outflow ($\bar{u}_2 = 1$) and we have taken $H_2 = 1$. The Reynolds number is calculated also using the outflow values, i.e.:

$$\mathrm{Re} = \frac{\rho \bar{u}_2 H_2}{\eta_0} = \rho.$$

To verify the mesh size dependency of the results, we have used three different meshes of bilinear elements (Q_1) and two meshes of biquadratic elements (Q_2). The most significant difference in the results obtained is in the secondary lip vortex that appears in the vertical wall, which is only well captured in the finest mesh.

The most important details of the meshes used are summarized in Table 3.1. There, $\Delta x_{\min} = \Delta y_{\min}$ is the minimum element size (not node-spacing) in the x- and y-directions, respectively. All the results shown below correspond to mesh M2 for bilinear elements and to mesh M5 for biquadratic elements, unless otherwise indicated.

Q_1	nº elements	nº nodes	$\Delta x_{\min} = \Delta y_{\min}$
M1	27258	27667	0.05
M2	39894	40501	0.025
M3	105816	106671	0.01
Q_2	nº elements	nº nodes	$\Delta x_{\min} = \Delta y_{\min}$
M4	17573	71211	0.075
M5	28859	116519	0.035

Table 3.1: Meshes used in the 4:1 contraction problem.

3.5.2.1 Oldroyd-B flow at Re = 1

Let us start considering the case with significant inertial effects, i.e., Re = 1 (in the context of viscoelastic flows). The maximum Weissenberg number that we have been able to

reach is We = 5, which is higher than what is usually reported in the literature. For We = 5.5 we have found some instabilities of the iterative scheme, and for We = 6 we have failed to obtain a converged solution. Note that we are considering the stationary problem, and we have attempted to solve it directly. Higher values of the Weissenberg number could probably be reached by integrating in time the transient problem until a steady-state is reached.

Fig. 3.4 shows distributions of streamlines for all the Weissenberg numbers considered in this case. It is observed that the size of the vortex appearing in the bottom corner decreases as We increases. This is consistent with the results reported in the literature [108, 123, 133, 150].

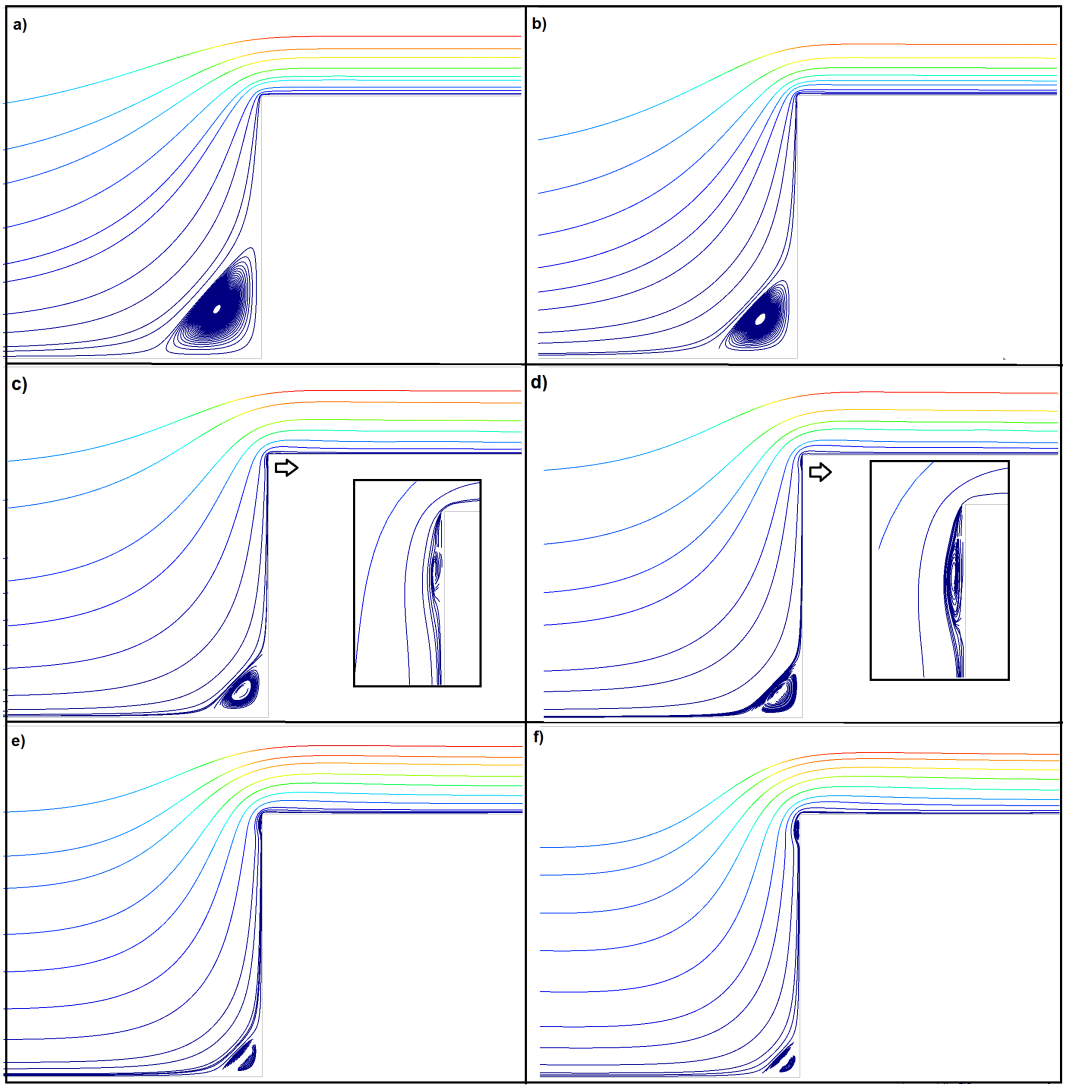

Figure 3.4: Close-up view of streamlines near the corner for Re = 1: a) We = 0, b) We = 0.5, c) We = 2.5, d) We = 3, e) We = 4 and f) We = 5.

Using the finest mesh (M3) the secondary lip vortex emerges as We > 2.0. For We > 2.5 it appears clearly defined (both in the M3 and in the M2-M5 meshes) with a bigger size in the more elastic cases. This is perfectly consistent with the results published by Li et al. [108] and the sizes of the vortex are very close to the values reported by Nithiarasu [123].

Fig. 3.5 shows a comparison of the vortex length obtained as a function of the Weissenberg number with other results that can be found in the literature. The agreement between our results and those presented in the references mentioned in the figure label is good up to We = 2.5, both using bilinear and biquadratic elements. For more elastic cases, i.e. We > 2.5, we did not find results reported in the case Re = 1. From Fig. 3.5 it is observed that the size of the vortex keeps decreasing as We increases.

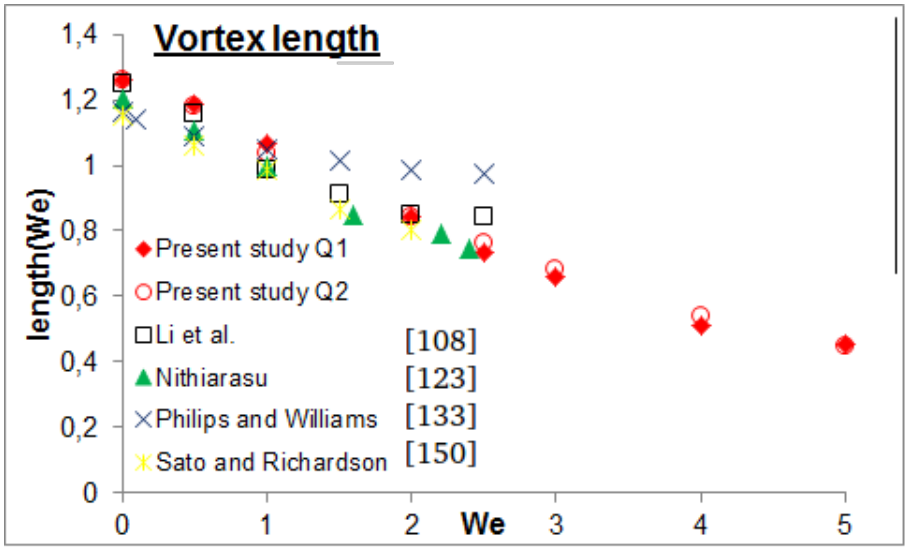

Figure 3.5: Vortex size validation at different Weissenberg numbers for Re = 1.

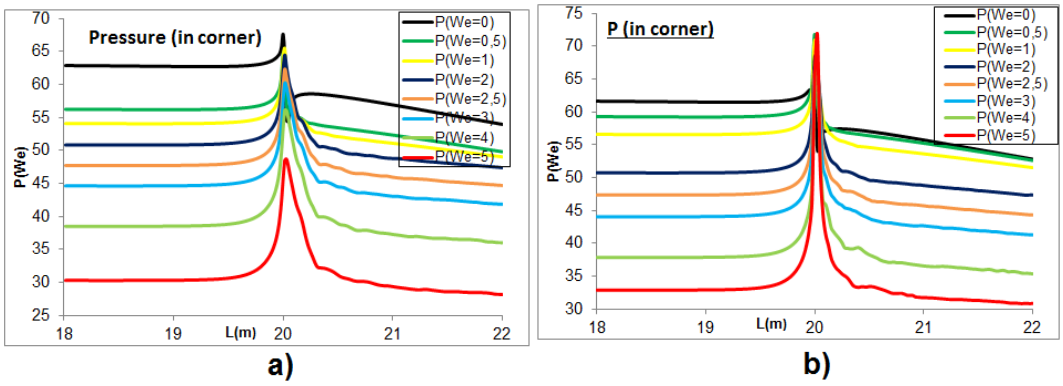

Figure 3.6: Pressure in a cut line near the contraction corner for Re = 1: a) Q_1 elements, b) Q_2 elements.

Fig. 3.6 shows a cut line near the contraction corner where pressure is plotted. The contours of pressure and of elastic stress components provided by the proposed formulations for the different Weissenberg numbers analyzed in the case Re = 1 are presented in Figs. 3.7-3.10. It is noteworthy that both in the S-ASGS and in the S-OSGS formulations these results are very similar, so that the isolines of the variables are displayed without indicating the formulation employed. The patterns of the results obtained are smooth, without oscillations, and in a good agreement with the results reported in [108, 123].

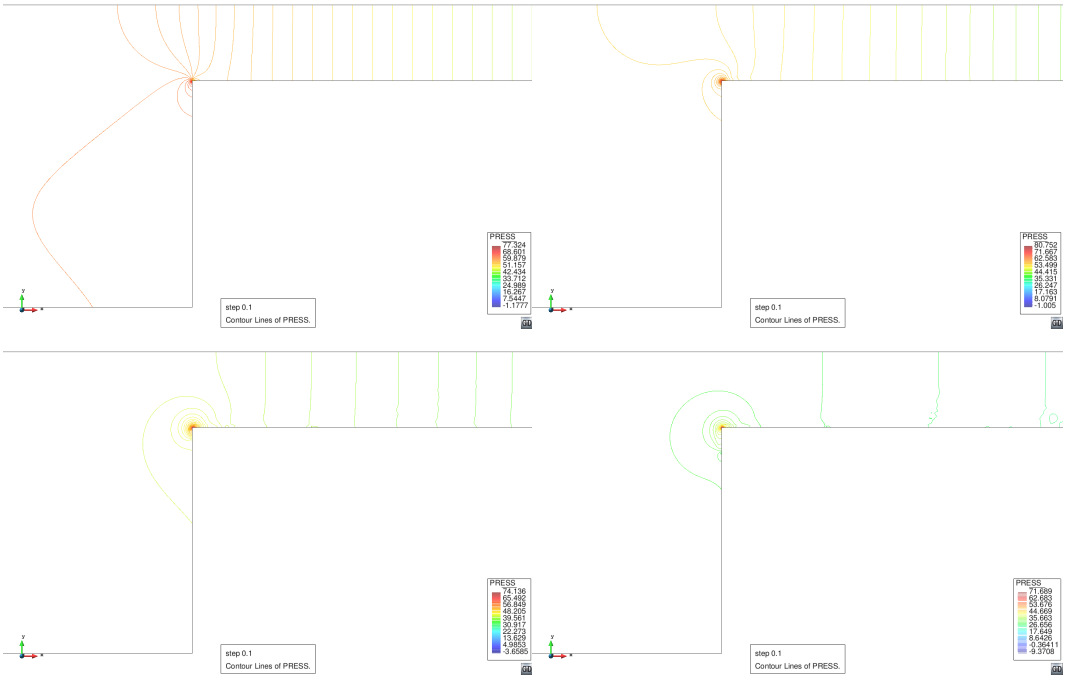

Figure 3.7: Pressure isolines near the contraction corner: a) We = 0, b) We = 1, c) We = 3, d) We = 5.

The elastic stress contours are given in Figs. 3.8-3.10. We can note that the elastic stress gradients in the vicinity of the contraction corner are higher with increasing Weissenberg number. The same occurs for the maximum values.

Fig. 3.11 shows the elastic stress distribution along the horizontal line $y = -1$. It is observed that the peak values of the viscoelastic stresses increase strongly as We increases and no oscillations are observed. We have not encountered any numerical difficulty in capturing it, neither in the nonlinear iterative loop nor in the numerical integration. These values are in accordance with the results presented in [108] (for a proper scaling). Table 3.2 collects the maximum peak values for each stress component shown in Fig. 6.

We	σ_{xx}	σ_{xy}	σ_{yy}
We = 0.0	7.722	8.766	7.305
We = 0.5	58.174	18.483	12.003
We = 1.0	98.377	30.049	18.321
We = 2.0	162.04	51.16	34.551
We = 2.5	194.6	60.929	41.641
We = 3.0	229.53	71.375	49.208
We = 4.0	301.69	89.128	59.979
We = 5.0	375.02	104.77	67.609

Table 3.2: Maximum peak values for each elastic stress component corresponding to Fig. 6.

To further demonstrate the quality of the results and the absence of oscillations, even in the vicinity of the contraction corner, Fig. 3.12 shows the horizontal velocity u_x along the symmetry axis $y = 0$ and the vertical velocity u_y along the line $y = -1$, which corresponds to

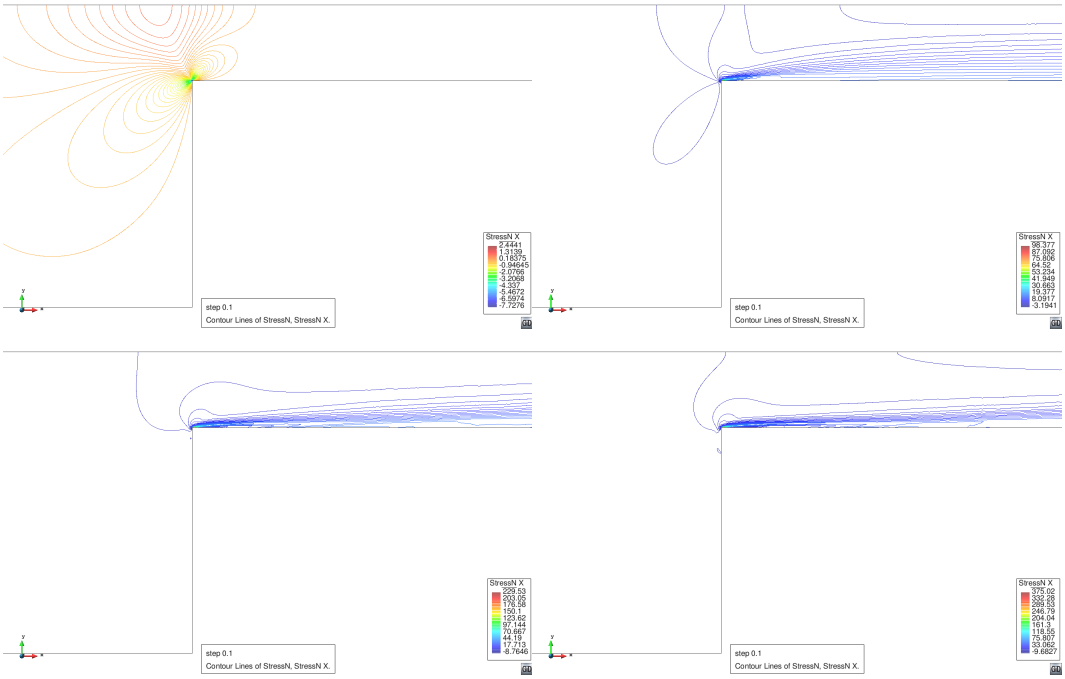

Figure 3.8: Normal elastic stress component σ_{xx} near the contraction corner: a) We = 0, b) We = 1, c) We = 3, d) We = 5.

the bottom wall of the narrow region of the domain. The results obtained are in agreement with those reported in [106, 5].

3.5.2.2 Oldroyd-B flow at Re = 0.01

The study of creeping flows in the 4:1 planar contraction problem has proven to be a non-trivial benchmark. In the works of Alves et al. [3, 5] the dispersion in the results using different methods of the vortex length was analyzed in detail. In [3], the authors showed that the use of high order order schemes (HOS) in a finite volume formulation can significantly improve the accuracy of the numerical solution in the analysis of viscoelastic flows. They found that the first-order upwind differencing scheme (UDS) is unable to predict accurately the flow pattern in the 4:1 planar contraction even in very fine meshes and for moderate Weissenberg numbers (up to We = 3.0). In an exhaustive analysis of the 4:1 benchmark flow using Oldroyd-B and Phan-Thien-Tanner (PTT) fluids, Alves et al. [5] proposed recommended and non-recommended values for the vortex length in creeping flows of viscoelastic fluids. To get an example of wrong values they used a first order UDS and coarse meshes, and for the recommended values they used a successive mesh refinement and a Richardson extrapolation to predict the vortex sizes in conjunction with a high-resolution scheme (MINMOD) to represent the stress derivatives in the constitutive equation. For the non-recommended case, the authors obtained a decrease in the vortex size with increasing Weissenberg number up to We = 1.5, and an increase in the size for more elastic cases. However, for the recommended results, the decrease of the vortex length remains up to We = 3.0 (the most elastic case that the authors could solve).

As it can be seen from the studies of Sato and Richardson [150] and Matallah et al. [113], the solutions for the Oldroyd-B fluid with Re = 0.01 in the 4:1 planar contraction flow

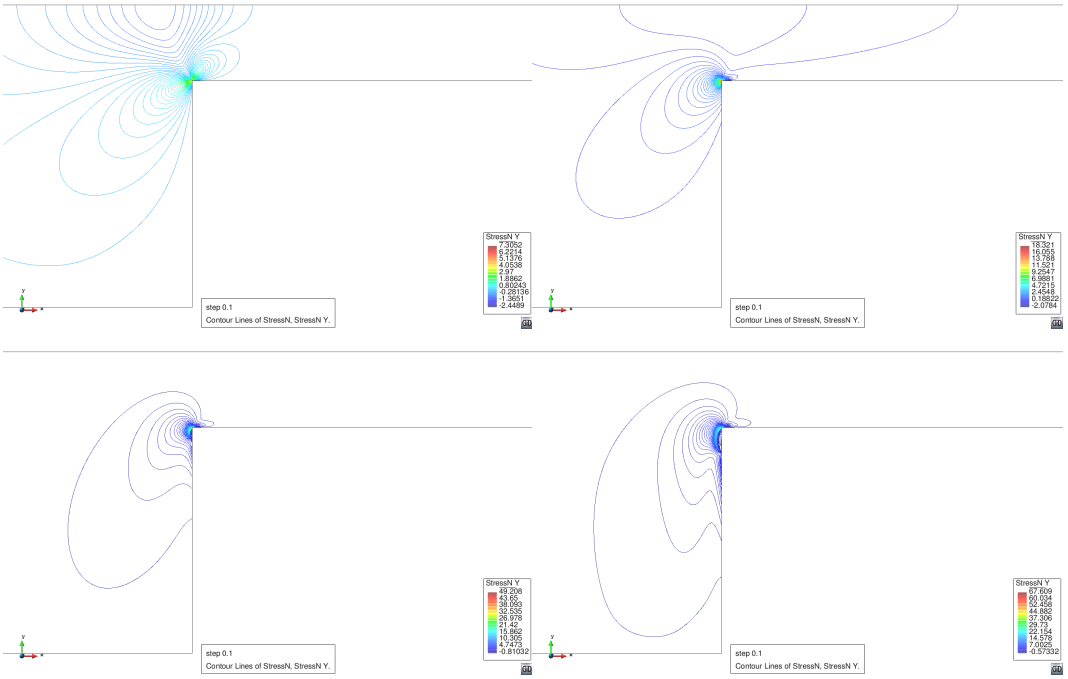

Figure 3.9: Normal elastic stress component σ_{yy} near the contraction corner: a) We = 0, b) We = 1, c) We = 3, d) We = 5.

problem are almost identical to those for the non-inertial or creeping flow case (Re = 0), so in the comparison we use both cases to validate our results.

Fig. 3.13, shows the comparison of the vortex length distribution in terms of the Weissenberg number. These results show the behavior recommended by [5] (with a four times coarser mesh in our case), and are in agreement with the results published by [3, 1, 101] up to We = 5 which is the highest elastic value for which we could find results reported for this case, even though we could reach We = 6.5 with our formulations.

The stress distribution patterns for Re = 0.01 are very similar to those of the Re = 1 case, and therefore not repeated here. Only the streamlines are shown in Fig. 3.14 to compare them with the results of other authors. In the Re = 1 case, the secondary lip vortex appears for We > 2. However, for Re = 0.01, this secondary vortex is already clearly defined for We = 2. This value is comparable to those found in [108, 123], although the Weissenberg number at which the vortex appears is clearly mesh-dependent.

The final result that we present for the case Re = 0.01 is intended to demonstrate the benefits of using a DC technique as the one proposed in subsection 3.4.3. In the example we are considering, when the elasticity of the fluid is increased, the elastic stress gradients in the vicinity of the contraction corner are higher the higher the Weissenberg number is. If the finite element mesh is not fine enough to resolve these gradients, node-to-node oscillations may appear. Fig. 3.15 shows an example of these oscillations in a stress component, and how they are corrected when the DC technique is used. The curve shown corresponds to the σ_{yy} stress component along $y = -1$ computed with a Weissenberg number We = 3 using mesh M1, but the same behavior is observed in all cases where there is a peak in one of the unknowns.

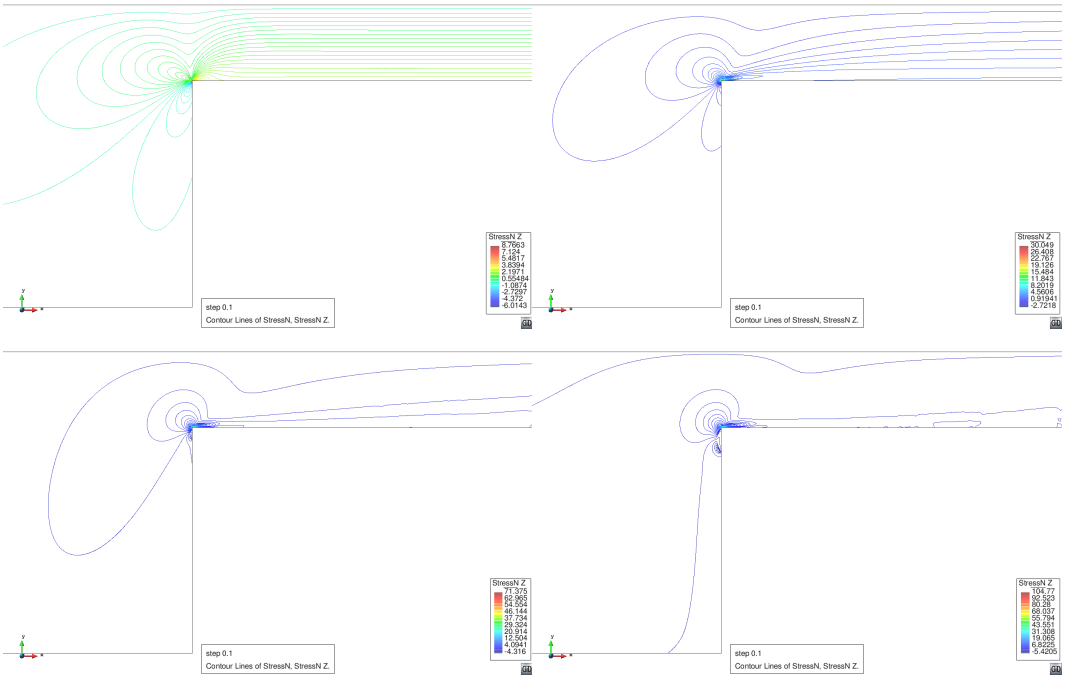

Figure 3.10: Elastic stress component σ_{xy} near the contraction corner: a) We = 0, b) We = 1, c) We = 3, d) We = 5.

3.5.2.3 Some results for Re = 0.01 and for Re = 1

As for the primary vortex, we can show the length variation for the secondary vortex. For this case, we have not found results reported in the literature against which we could compare our results. From Fig. 3.16 it is seen that the growth in the vortex size with the Weissenberg number is smooth. We show there both the results obtained for Re = 0.01 and for Re = 1.

Table 3.3 shows the pressure drop ($\Delta p = p_{\text{inlet}} - p_{\text{outlet}}$) for all the Weissenberg numbers analyzed. As we can see, Δp is very similar using bilinear and biquadratic elements, even though the pressure peak is better captured by the biquadratic elements. Both in the inertial (Re = 1) and in the quasi non-inertial (Re = 0.01) cases, we can see that Δp decreases when the Weissenberg number is increased, which is what is expected from the physical point of view. In viscoelastic flows the velocity profile is more blunt than for Newtonian fluids, and the pressure drop increases much less rapidly with the mass flow rate than in the Newtonian case. This is why polymers, which provide elasticity to the fluid, are often used as *drag-reducing agents* [23].

3.5.3 A threedimensional example

To show that the formulation proposed in this chapter can be applied to the 3D case without any difficulty, we extend the 4:1 contraction problem of the previous subsection to three dimensions. The problem geometry is shown in Fig. 3.17, and the mesh to discretize it is shown in Fig. 3.18. It is a unstructured mesh composed of 528396 linear tetrahedral elements and 98814 nodes.

The $y = 0$ and $z = 0$ planes (see Fig. 3.18) are considered to be symmetry planes, and thus

Re = 1	Δp (Q_1)	Δp (Q_2)	Re = 0.01	Δp (Q_1)
We = 0	63.793	62.539	We = 0	63.067
We = 0.5	58.69	60.47	We = 0.5	60.449
We = 1.0	56.05	57.78	We = 1.0	57.124
We = 2.0	52.198	52.12	We = 2.0	50.414
We = 2.5	48.252	48.539	We = 2.5	47.158
We = 3.0	45.207	45.637	We = 3.0	43.994
We = 4.0	42.166	41.294	We = 4.0	38.648
We = 5.0	37.52	37.22	We = 5.0	33.934
-	-	-	We = 6.0	29.842
-	-	-	We = 6.5	29.236

Table 3.3: Pressure drop for different Weissenberg and Reynolds numbers using bilinear (Q_1) and biquadratic (Q_2) elements.

the normal velocity to these planes is set to zero. The domain of Fig. 3.17 can be considered one fourth of the flow domain. In the same way as for the 2D case, the half-width of the shorter square channel, $H_2 = 1$, is taken as the characteristic length scale and the average velocity in that channel $\bar{u}_2 = 1$ is the characteristic velocity scale. The boundary conditions employed are the straightforward extension of those used in the 2D case.

The discrete and linearized problem is solved by using an iterative solver based on the BiCGStab (Stabilized version of BiConjugate Gradient Squared) method of van der Vorst [165], with the additive Schwarz preconditioner.

As for the 2D case, the constitutive model is Oldroyd-B. The dimensionless numbers that govern the problem have been taken Re = 0.01 and We = 1. Higher values of the Weissenberg number would require finer meshes, particularly when the secondary lip vortex appears. However, it is not our purpose in this example to analyze complex physics, but only to assess the feasibility of the 3D extension of the formulation.

Some streamlines are shown in 3.19. A general isometric view is depicted in Fig. 3.19-a), whereas two cuts with perpendicular planes are shown in Fig. 3.19-b). The primary vortex can be clearly appreciated, as well as the emergence of the secondary lip vortex. From Fig. 3.19-b) it is also observed that the solution develops a symmetry with respect to the plane $y = z$. Three-dimensional flow patterns can also be clearly observed.

Fig. 3.20 shows the contours of the two transverse velocity components u_y and u_z in two perpendicular planes $y = 0.5$ and $z = 0.5$, both parallel to the symmetry axis $y = z = 0$. Note that, despite having a non-structured mesh, the results show the symmetry of the problem.

One of the most difficult results to obtain in a problem with an abrupt change in geometry is the pressure field. Fig. 3.21 shows the pressure contour lines around the corner zone (Fig. 3.21-a), and the pressure variation along a cut line on the wall in one of the symmetry planes in the contraction zone (Fig. 3.21-b)). In both cases we can see that no oscillations appear, and the solution is smooth. If we compare the pressure variation along a line in the corner between the 2D case (Fig. 3.6) and the 3D case (Fig. 3.21-b)), we can appreciate that the rate at which pressure diminishes after the corner peak is greater in the latter.

Both in the 2D and in the 3D cases DC techniques need to be used to avoid node-to-node oscillations in the elastic stress components. Fig. 3.22 shows the variation of the σ_{zz} component across the corner in the line $y = 0.5$, $z = 0.5$ without (Fig. 3.22-a)) and with (Fig. 3.22-b)) the introduction of the DC dissipation. The spurious secondary peak observed in the first case is removed by the introduction of the DC term, even if the solution in Fig. 3.22-b) is not perfectly smooth. Note that the mesh used in the calculation is rather coarse for the complexity of the problem being solved.

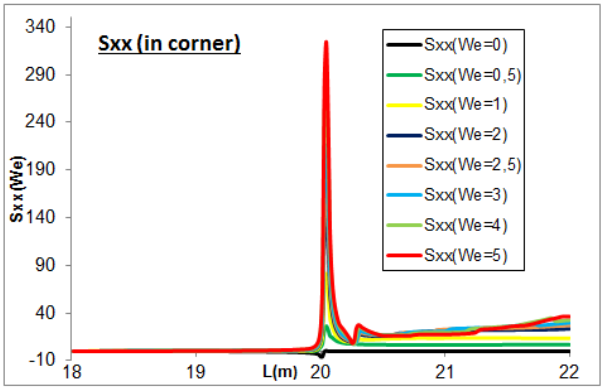

a)

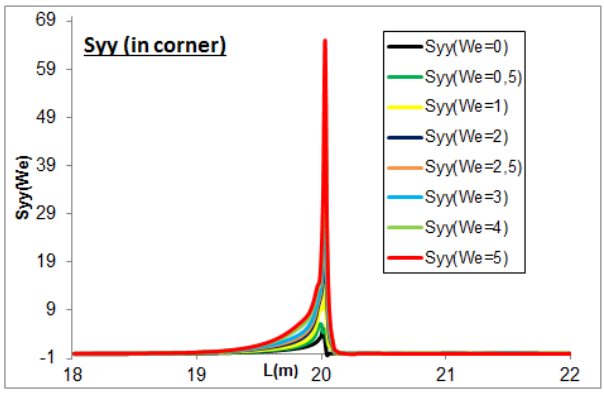

b)

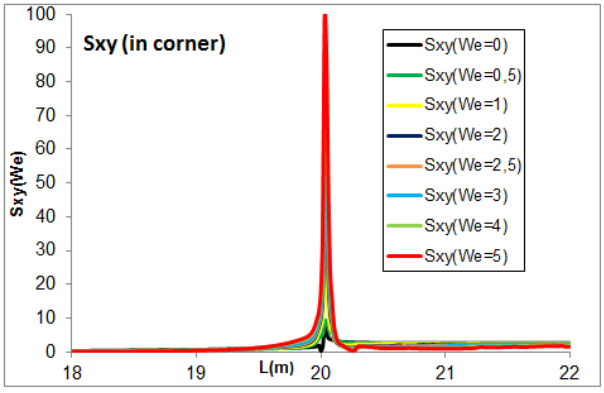

c)

Figure 3.11: Elastic stress components along the horizontal line $y = -1$ for $\mathrm{Re} = 1$: a) σ_{xx}, b) σ_{yy}, c) σ_{xy}.

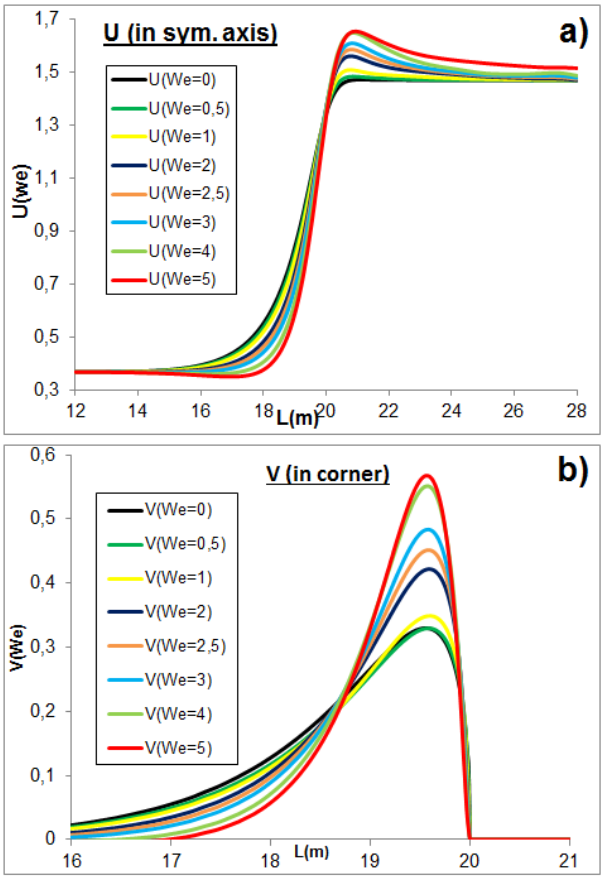

Figure 3.12: Velocity profiles: a) u_x along $y = 0$ (symmetry axis), b) u_y along $y = -1$ (bottom wall of the narrow region).

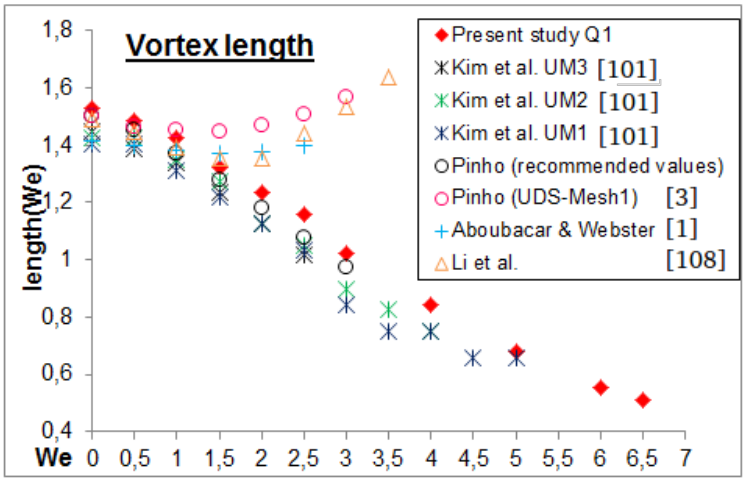

Figure 3.13: Vortex size validation at different Weissenberg numbers for $\mathrm{Re} = 0.01$.

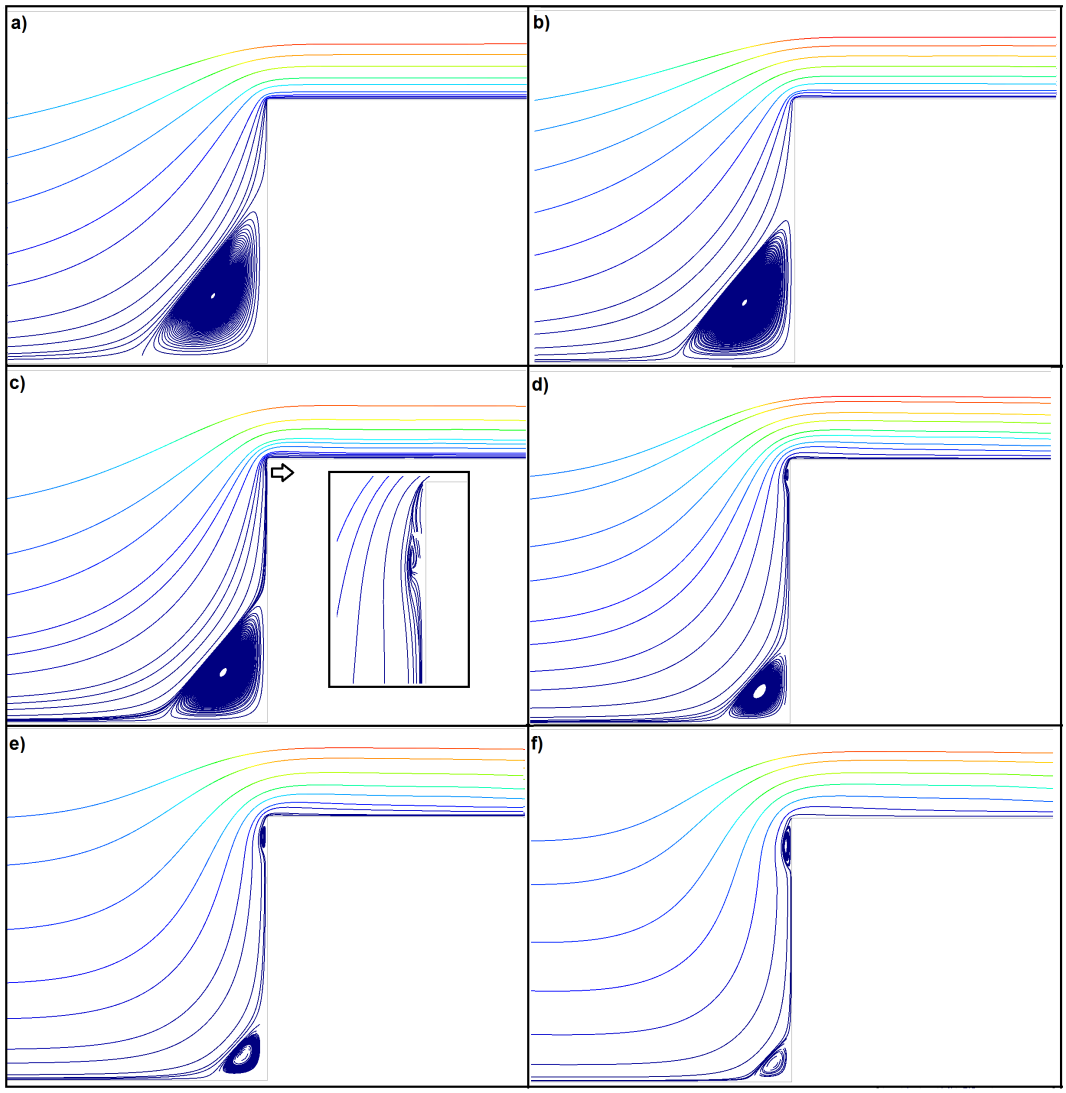

Figure 3.14: Close-up view of streamlines near the corner for Re = 0.01: a) We = 0, b) We = 1, c) We = 2, d) We = 4, e) We = 5, f) We = 6.5.

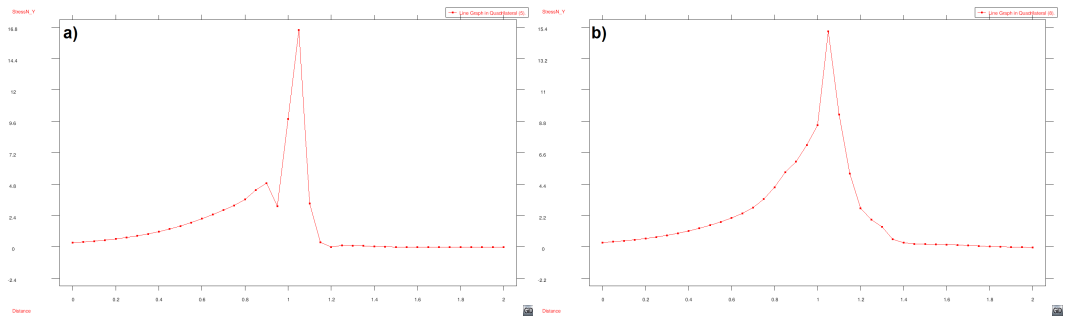

Figure 3.15: Typical oscillation in a stress component: a) without discontinuity capturing technique, b) with discontinuity capturing technique.

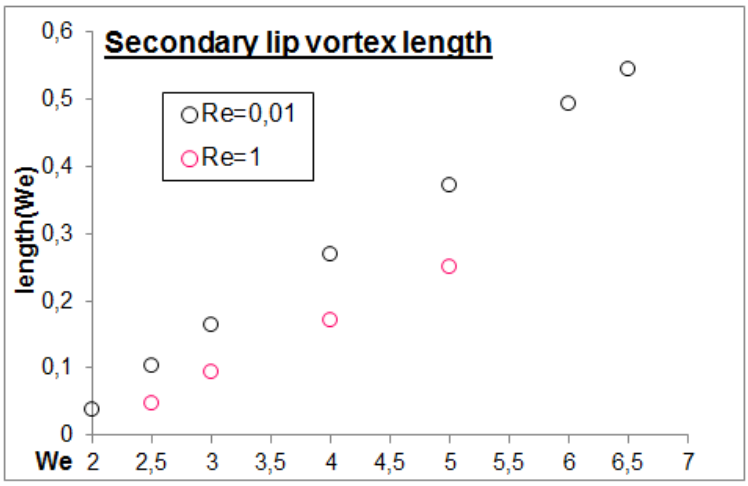

Figure 3.16: Secondary vortex size at different Weissenberg numbers for Re = 0.01 and Re = 1.

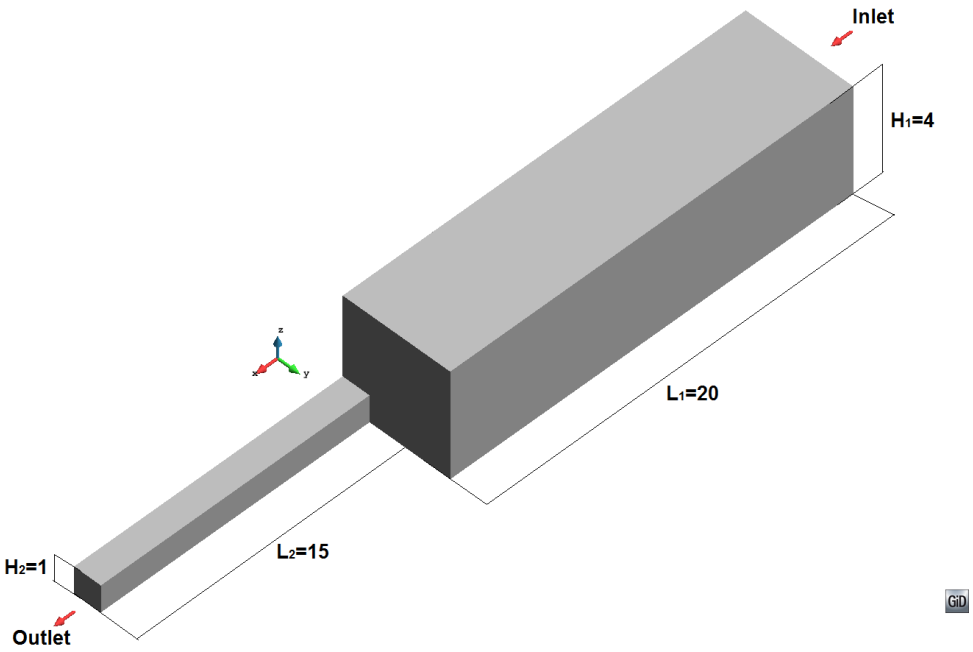

Figure 3.17: Sketch of the 3D 4:1 contraction problem.

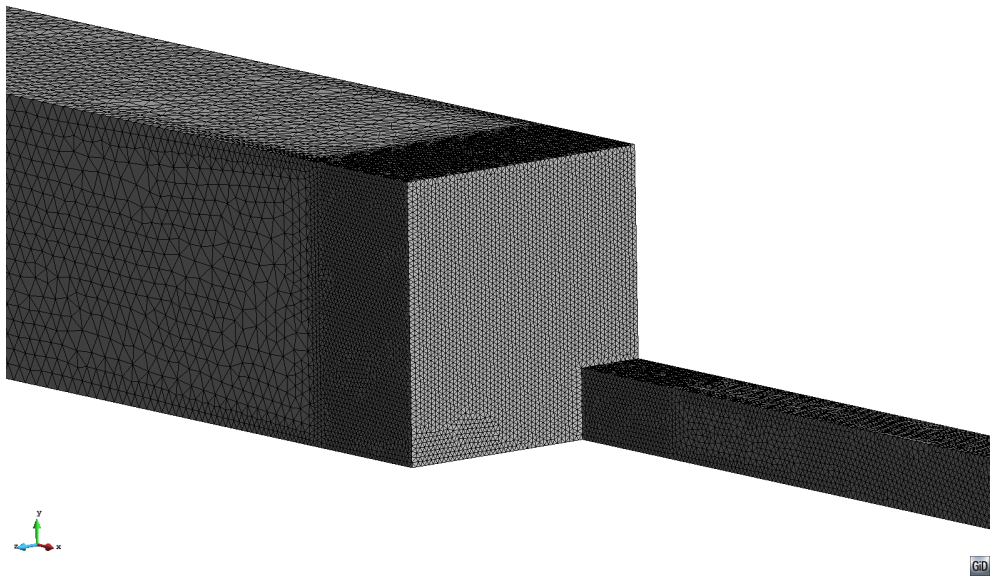

Figure 3.18: Mesh used in the 3D 4:1 contraction problem.

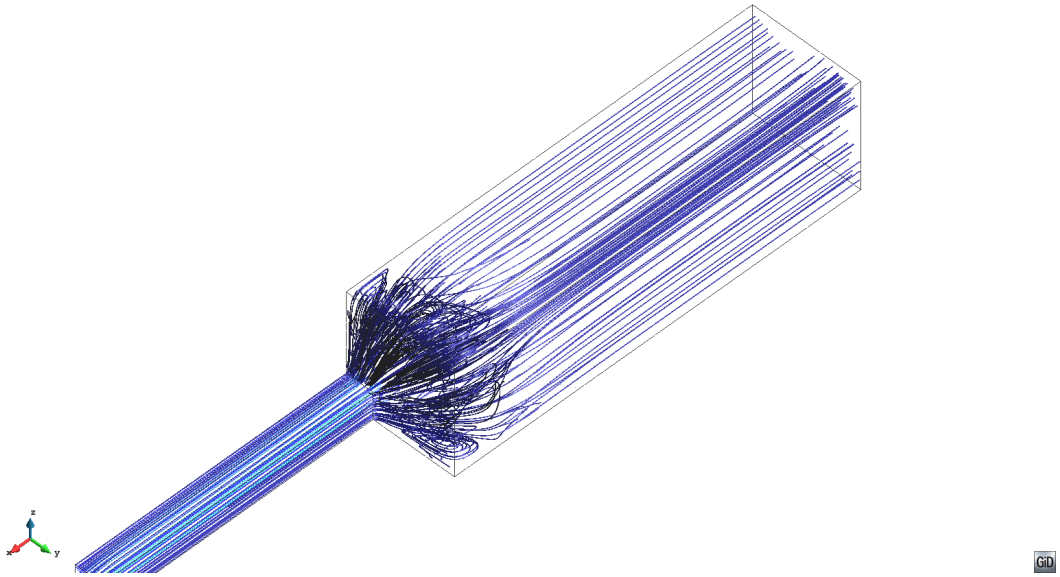

a)

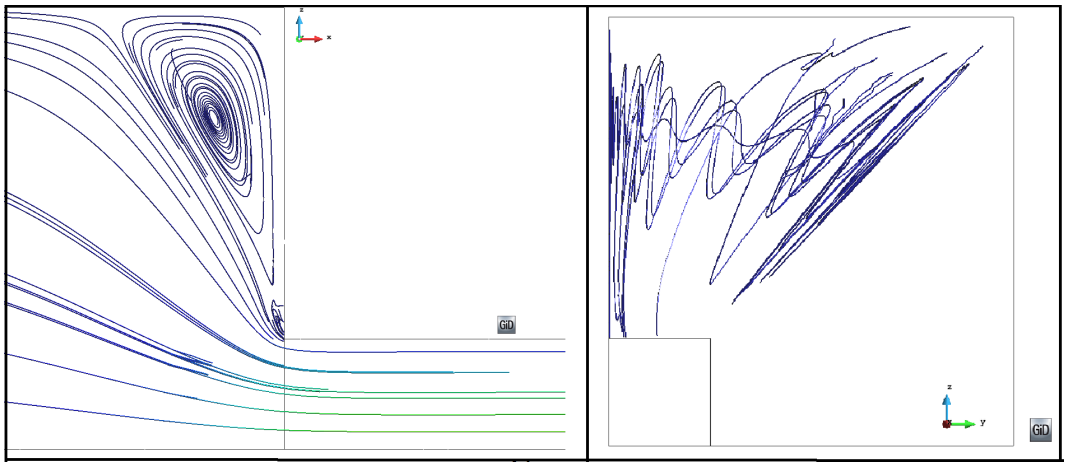

b)

Figure 3.19: Streamlines in the 3D 4:1 contraction problem (Re = 0.01 and We = 1): a) Isometric view, b) Cuts with the planes $y = 0$ (left) and a plane $x =$ constant close to the contraction plane (right).

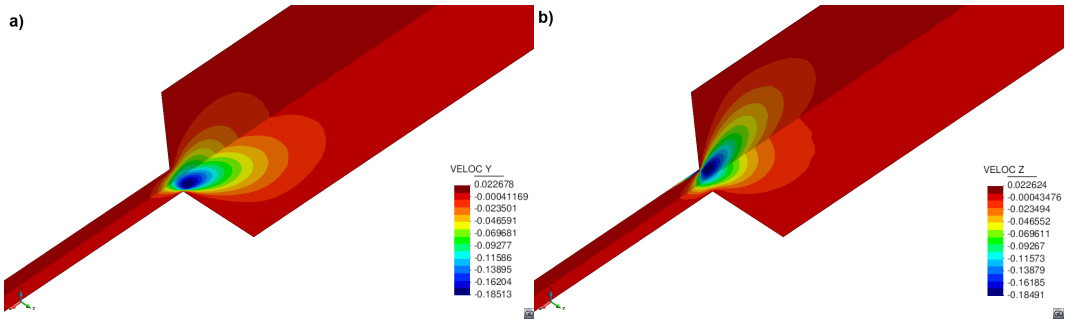

Figure 3.20: Contours of transverse velocity components on the planes $y = 0.5$ and $z = 0.5$: a) u_y, b) u_z.

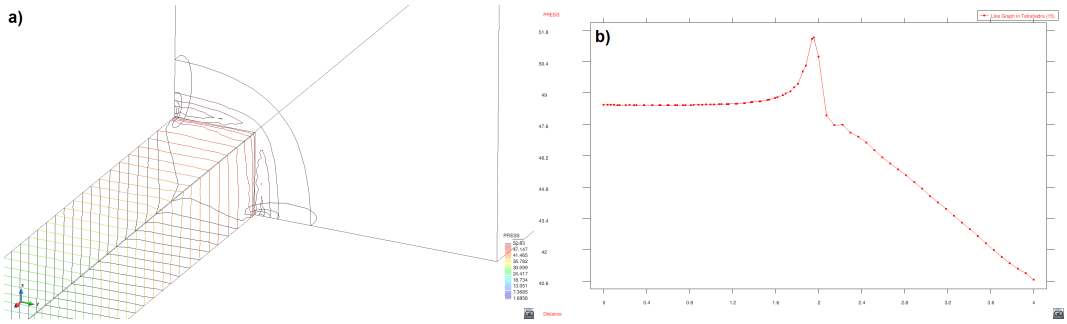

Figure 3.21: Pressure around the corner: a) contour lines, b) along a cut line across the corner.

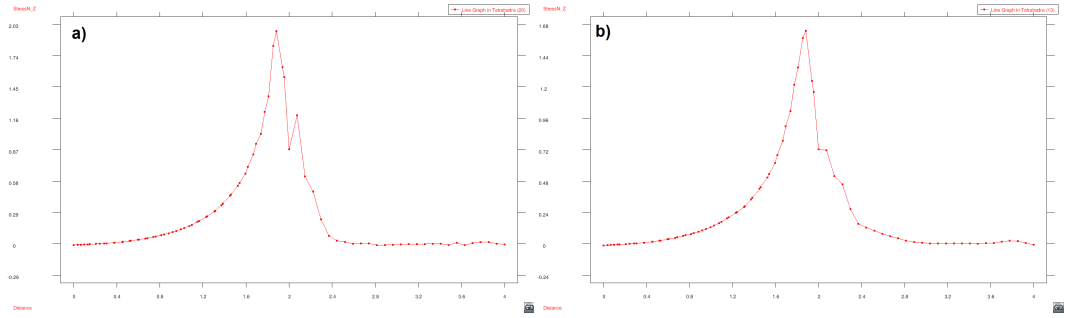

Figure 3.22: Normal elastic stress component σ_{zz} across the corner: a) without discontinuity-capturing technique, b) with discontinuity-capturing technique.

3.6 Conclusions

In this Chapter of the work we have introduced stabilized finite element methods for the viscoelastic flow problem based on the VMS concept. Starting from residual-based formulation for the momentum and the continuity equations, we have moved to the use of a split orthogonal sub-grid scale technique for them. This is not a residual based stabilization, but introduces stabilization for pressure, stress and velocity in independent terms. We have observed a better behavior of this approach in regions where the solution displays high gradients. For the approximation of the constitutive equation, classical residual-based stabilization works well.

The method finally designed allows one to obtain globally stable solutions using equal interpolation for all the unknowns and to treat convection-dominated problems. However, node-to-node oscillations in the viscoelastic stress components and the pressure in regions of high gradients may still remain. A discontinuity-capturing technique has been introduced to remove them.

The resulting formulation is accurate, showing optimal convergence properties for smooth solutions, and robust, able to deal with high gradients of the unknowns appearing at corners in viscoelastic flow problems. We have presented here the results obtained for a simple manufactured solution and for the 4:1 contraction problem, both in the classical 2D version and in a 3D extension. An indication of the robustness of the formulation is that we have been able to solve problems with Weissenberg numbers significantly higher than those reported in the literature we have consulted, even solving directly the stationary problem.

Chapter 4

Fractional Step Methods: Viscoelastic Problem

4.1 Abstract

In this chapter, three different fractional step methods are designed for the three-field viscoelastic flow problem, whose variables are velocity, pressure and elastic stress. The starting point of our methods is the same as for classical pressure segregation algorithms used in the Newtonian incompressible Navier-Stokes problem. These methods can be understood as an inexact LU block factorization of the original system matrix of the fully discrete problem and are designed at the pure algebraic level. The final schemes allow one to solve the problem in a fully decoupled form, where each equation (for velocity, pressure and elastic stress) is solved separately. The first order scheme is obtained from a straightforward segregation of pressure and elastic stress in the momentum equation, whereas the key point for the second order scheme is a first order extrapolation of these variables. The third order fractional step method relies on Yosida's scheme. Referring to the spatial discretization, either the Galerkin method or a stabilized finite element formulation can be used. We describe the fractional step methods first assuming the former, and then we explain the modifications introduced by the stabilized formulation proposed in chapter 3. This discretization in space shows very good stability, permitting in particular the use of equal interpolation for all variables.

4.2 Introduction

The viscoelastic behavior of fluids can be a dominant feature in the flow of polymeric fluids, and in the injection molding flows where moving boundaries are present and the unsteady regime defines the problem [117, 93]. Many applications in viscoelastic flows where the dynamics of the fluid are crucial can be found in the industry. Jets of these flows are quite broad, and include areas such as micro-dispensing of bioactive fluids through high throughput injection devices, scaffolds for tissue engineering, ink jet processes or viscoelastic blood flow past valves [169].

The flow patterns in viscoelastic fluids can be highly dynamic and in some cases chaotic, due to the elastic component of the fluid and the convective nature of the constitutive equation, even in quasi non-inertial flows. In [155], the effect of the contraction ratio in the dynamic response of the flow in square-square three-dimensional contractions is analyzed using experimental and numerical results. In [104] the instabilities and the asymmetry of flow in a symmetric domain is analyzed for flows with high Deborah number using the Leonov

constitutive equations to characterize the fluid. The turbulent flow of a viscoelastic solution is a new challenge from the numerical approximation perspective, partially due to the reduced friction drag properties of this type of fluids. In [112], the four-field model proposed in [109] is modified in order to model turbulence in the channel flow of dilute polymer solutions. In all the above mentioned cases, the transient simulation is a must and the generation of efficient algorithms to solve the problem, with the unknowns highly coupled, is an important task which motivates this part of the work.

The monolithic resolution of the system of equations that is obtained after discretization of the continuous problem is the most straightforward option. However, solving this system is computationally very expensive, specially in 3D. In this case, the degrees of freedom of the spatial discretization are the six independent elastic stress components, the three velocity components and the pressure. Furthermore, all these variables are coupled, some of them through nonlinear terms.

Instead of solving the monolithic system, an alternative is to use a fractional step method in time, in which different equations need to be solved for the different variables in an uncoupled way, perhaps with correction steps. The splitting of the equations introduced in fractional step methods has an additional temporal error, that has to be at least of the order of the time integration scheme used to approximate time derivatives if this order is to be preserved.

Fractional step methods can be either introduced at the continuous or at the purely algebraic levels. For overviews of both strategies in the case of the incompressible Navier-Stokes equations for Newtonian fluids, see [90] and [11], respectively. In this chapter we will follow the second alternative, and show how to apply it to the viscoelastic flow problem. In this case, it is necessary not only to uncouple the velocity from the pressure in the momentum equation, but also from the elastic stress. Additional equations need to be solved for these variables, followed by correction steps. We will propose three schemes of this type, of first, second and third order of (formal) accuracy in time. The first will consist of four steps, whereas five steps will be required for the second and the third order schemes.

In the viscoelastic flow context, several fractional step schemes have been proposed. One of the most popular is the Θ-method, originally proposed in [88] for Newtonian fluids and later extended to viscoelastic flows in [153, 149]. In this method the problem is split in three steps: a Stokes-like system with an explicit stress value, a transport problem involving the constitutive equation and another Stokes problem which enhances the stability of the method. This Θ-method was reported as being second order in time for a proper Θ value. In [47] a priori error estimates for this Θ-method using the Oldroyd-B constitutive model were derived, and theoretical and numerical computations to demonstrate the capability of this scheme were provided. A second order in time two-step decoupling method for modelling inertialess viscoelastic fluids was presented in [70]. In [71] the two-step method was extended to solve fluid flows with inertia. In the first step of this method the elastic stress is computed at the new time level by using the velocity field at the previous time step. In the second step the viscoelastic stress just calculated is used as a force term in the momentum balance equation, which can be regarded together with the continuity equation as a Stokes system. For the two-step method, second order accuracy in time is reported in the previous references, recommending the second order semi-implicit Gear scheme instead of the Crank-Nicolson scheme to discretize the temporal derivatives. In the same fractional step context, in [101] an extension is presented of the fourth step fractional step method proposed in [45] for the standard Navier-Stokes problem, now using the Oldroyd-B constitutive model and the DEVSS-G/DG stabilization technique.

Typical applications in viscoelastic fluid flows where an efficient scheme is needed for the resolution of a large number of degrees of freedoms are, for example, the modelling of a free surface evolution and the sedimentation of particles. The first case is classical for polymeric

injections and mould filling [28, 160], and the second is found in the investigation of microstructure in flowing suspensions, sedimentation columns, fluidized beds, slurry transport and hydraulic fracturing [152, 170]. In [28] a splitting time discretization method for free surface flows is proposed, where the interface of the fluid is solved in addition to the viscoelastic Navier-Stokes problem. The problem is solved in two steps; in the first (prediction) step the three advection problems are solved separately, and in the second (correction) step, a Stokes and constitutive Oldroyd-B problem is solved sequentially. For the case of sedimentation, in [170] an extended version of the method proposed by in [170] is described. The authors use the Marchuk-Yanenko operator splitting scheme to deal with the effect of the viscoelastic stress on the velocity, the incompressibility condition, the advection term, the constitutive equation and the constraint of rigid-body motion inside the particles.

The viscoelastic fluid flow problem presents several numerical difficulties, particularly for the spatial approximation. On the one hand, the finite element approximation used must satisfy two inf-sup conditions: the first between the interpolation of the velocity and of the pressure to control the pressure and the second between the interpolation of the velocity and of the elastic stress to control the symmetrical gradient of the velocity. On the other hand, the convective term in the momentum and in the constitutive equations require to use methods to deal with convection. Many algorithms have been developed to solve this problem: the classical SUPG method and its non-consistent counterpart, the SU method [111], the GLS method [79], and the stabilization based on the discontinuous Galerkin method [84, 7], among others in the context of finite element methods. Similarly, the upwind difference scheme (UDS) [168], the second order linear upwinding scheme (LUDS) [126], the sharp and monotonic algorithm for realistic transport (SMART) the and MINMOD method [3] were introduced for the finite volume method.

The highly nonlinear nature of the constitutive equation requires proper linearization strategies, and the possibility of local peaks in the elastic stress components when the amount of elasticity is important needs to be taken into account by methods with some type of monotonicity to avoid local oscillations. A standard numerical treatment to alleviate the nonlinear iterative process is the implementation of continuation methods (see [95] for more details) clearly more used in steady state problems [95, 37]. The addition of discontinuity-capturing techniques is another interesting tool, overcoat when the Weissenberg number is increased [37].

The formulation we use for the spatial approximation is a variational multiscale (VMS) stabilized finite element method detailed in chapter 3 (also in [37]) (which in turn relies on [36]), and we will only briefly describe it here, since our interest is the time discretization using fractional step schemes. Nevertheless, let us mention that in some cases fractional step methods have been used to obtain stable pressure interpolations, as explained in [52]. We will not consider at all the possible pressure stability provided by the splitting methods we will describe. Other stabilization methods applied to the viscoelastic flow problem can be found in [103, 79, 64, 108, 106], among others.

In this chapter we present three fractional step methods with first, second and third order splitting errors. The first step in all cases is the momentum equation to calculate an intermediate velocity. For the first order method the intermediate velocity is obtained without any pressure and elastic stress contribution. For the second order scheme, we use extrapolated values of pressure and elastic stresses to obtain a better approximation of the intermediate value of the velocity, and likewise for the third order scheme. In the second step we obtain the intermediate elastic stress values using the intermediate velocity approximation. The third step has the structure of a discrete pressure Poisson equation. The fourth step corresponds to the velocity correction step. For the first and second order schemes this step can be understood as a projection step, whereas for the third order case we use the Yosida approximation [137]. Finally, the fifth step is a projection step to obtain the final elastic

stresses. In all cases, when we refer to the order of accuracy of a scheme the arguments we use are completely formal. A rigorous numerical analysis of the formulations presented is outside the scope of this paper.

The chapter is organized as follows. In Section 4.3 we introduce the continuous viscoelastic fluid flow problem. Section 4.4 is devoted to its numerical approximation with the Galerkin approximation and a monolithic time discretization. In Section 4.5, the fractional step methods we propose are presented for the Galerkin case following two approaches, namely, one based on variable extrapolation and the other on an inexact LU decomposition. In Section 4.6 we describe the stabilized finite element method we use and explain which are the modifications that need to be made to the fractional step schemes introduced earlier. Numerical results are presented in Section 4.7 and, finally, conclusions are drawn in Section 4.8.

4.3 The viscoelastic flow problem

4.3.1 Initial and boundary value problem

Let us consider a viscoelastic fluid moving in a domain Ω of $\mathbb{R}^d$ ($d = 2, 3$) during the time interval $[0, t_\mathrm{f}]$. Considering the flow incompressible and isothermal, the governing equations are the conservation of momentum and mass, which can be written as

$$\rho\frac{\partial \boldsymbol{u}}{\partial t} + \rho\boldsymbol{u}\cdot\nabla\boldsymbol{u} - \nabla\cdot\boldsymbol{T} + \nabla p = \boldsymbol{f} \text{ in } \Omega,\ t \in]0, t_f[, \tag{4.1}$$

$$\nabla\cdot\boldsymbol{u} = 0 \text{ in } \Omega,\ t \in]0, t_f[, \tag{4.2}$$

where ρ denotes the constant density, $p : \Omega\times]0, t_\mathrm{f}[\to \mathbb{R}$ is the pressure, $\boldsymbol{u} : \Omega\times]0, t_\mathrm{f}[\to \mathbb{R}^d$ is the velocity field, $\boldsymbol{f} : \Omega\times]0, t_\mathrm{f}[\to \mathbb{R}^d$ is the force vector and $\boldsymbol{T} : \Omega\times]0, t_\mathrm{f}[\to \mathbb{R}^d \otimes \mathbb{R}^d$ the deviatoric extra stress tensor, which can be defined in terms of a viscous and a viscoelastic or elastic contribution as

$$\boldsymbol{T} = 2\beta\eta_0\nabla^s\boldsymbol{u} + \boldsymbol{\sigma}, \tag{4.3}$$

where ∇^s is the symmetrical gradient operator and $\beta \in [0, 1]$ is a parameter to define the amount of viscous or solvent viscosity $\beta\eta_0$ and elastic or polymeric viscosity $(1-\beta)\,\eta_0$. The constitutive behavior of the fluid needs to be completed with the expression of the elastic part of the extra stress, $\boldsymbol{\sigma}$. A large variety of approaches exist to define it (see [21, 22] for a complete description). In this chapter, only the differential Oldroyd-B model is considered, which reads

$$\left(\frac{1}{2\eta_0}\boldsymbol{\sigma} - (1-\beta)\,\nabla^s\boldsymbol{u}\right) + \frac{\lambda}{2\eta_0}\left(\frac{\partial\boldsymbol{\sigma}}{\partial t} + \boldsymbol{u}\cdot\nabla\boldsymbol{\sigma} - \boldsymbol{\sigma}\cdot\nabla\boldsymbol{u} - (\nabla\boldsymbol{u})^T\cdot\boldsymbol{\sigma}\right) = \boldsymbol{0} \text{ in } \Omega,\ t \in]0, t_f[, \tag{4.4}$$

where λ is the relaxation time.

Let us introduce some notation. Calling $\boldsymbol{U} = [\boldsymbol{u}, \boldsymbol{\sigma}, p]$, $\boldsymbol{F} = [\boldsymbol{f}, 0, 0]$ and defining

$$\mathcal{L}(\hat{\boldsymbol{u}}; \boldsymbol{U}) := \begin{pmatrix} \rho\hat{\boldsymbol{u}}\cdot\nabla\boldsymbol{u} - 2\beta\eta_0\nabla\cdot(\nabla^s\boldsymbol{u}) - \nabla\cdot\boldsymbol{\sigma} + \nabla p \\ \nabla\cdot\boldsymbol{u} \\ \frac{1}{2\eta_0}\boldsymbol{\sigma} - (1-\beta)\,\nabla^s\boldsymbol{u} + \frac{\lambda}{2\eta_0}\left(\hat{\boldsymbol{u}}\cdot\nabla\boldsymbol{\sigma} - \boldsymbol{\sigma}\cdot\nabla\hat{\boldsymbol{u}} - (\nabla\hat{\boldsymbol{u}})^T\cdot\boldsymbol{\sigma}\right) \end{pmatrix},$$

and

$$\mathcal{D}_t\left(\boldsymbol{U}\right) := \begin{pmatrix} \rho\dfrac{\partial \boldsymbol{u}}{\partial t} \\ 0 \\ \dfrac{\lambda}{2\eta_0}\dfrac{\partial \boldsymbol{\sigma}}{\partial t} \end{pmatrix},$$

we may write (6.1), (6.2) and (6.4) using definition

$$\mathcal{D}_t\left(\boldsymbol{U}\right) + \mathcal{L}(\hat{\boldsymbol{u}}; \boldsymbol{U}) = \boldsymbol{F}. \tag{4.5}$$

These equations need to be complemented with initial and boundary conditions to close the problem. The conservation laws (6.1)-(6.2) and the Oldroyd-B constitutive equation (6.4) are a mixed parabolic-hyperbolic problem. The characteristic lines are the streamlines, and the components of the elastic stress tensor $\boldsymbol{\sigma}$ may be considered as quantities conveyed along these characteristics.

For the sake of simplicity in the exposition, we will consider the simplest boundary condition $\boldsymbol{u} = \boldsymbol{0}$ on $\partial\Omega$ for all time, even if in the numerical examples we will leave part of the boundary free, i.e., zero traction will be prescribed there, and a non-homogeneous velocity will be prescribed on a certain part of $\partial\Omega$.

The boundary conditions for the elastic stresses are more delicate. In principle, they do not need to be prescribed, but that can imply an excessively large computational domain to obtain the correct value of these stresses (see [82] for a complete description of the mathematical structure of the problem and the boundary conditions required). Therefore, in numerical applications they are often prescribed. Due to the hyperbolic nature of Eq. (6.4), in principle they can be fixed only on the inflow part of the boundary, $\Gamma_{\text{in}} = \{\boldsymbol{x} \in \partial\Omega \ |(\boldsymbol{u} \cdot \boldsymbol{n})(\boldsymbol{x}) < 0\}$, where $\boldsymbol{n}$ is the outward unit normal vector to $\partial\Omega$. However, in some numerical works there are examples in which elastic stresses are prescribed not only on Γ_{in}, but on the whole $\partial\Omega$ [167, 156]. We will explicitly indicate in our examples where are the elastic stresses prescribed.

The problem is completely defined with the initial conditions for the velocity and the elastic stress, which are of the form $\boldsymbol{u} = \boldsymbol{u}^0$ and $\boldsymbol{\sigma} = \boldsymbol{\sigma}^0$ at time $t = 0$, with $\boldsymbol{u}^0$ and $\boldsymbol{\sigma}^0$ functions defined on the whole domain Ω.

4.3.2 Variational form

Let us introduce some notation in order to write the weak form of the problem. The space of square integrable functions in a domain ω will be denoted by $L^2(\omega)$ and the space of functions whose distributional derivatives of order up to $m \geq 0$ (integer) belong to $L^2(\omega)$ by $H^m(\omega)$. The space of functions in $H^1(\omega)$ vanishing on $\partial\omega$ will be written as $H_0^1(\omega)$. We shall use the symbol $\langle \cdot, \cdot \rangle_\omega$ to denote the integral of the product of two functions on ω, assuming this is well defined; subscript ω will be omitted when $\omega = \Omega$. The L^2 inner product in Ω (for scalar, vectors and tensors) will be denoted by $(\cdot, \cdot)$.

Let $\boldsymbol{\Upsilon} = H^1\left(\Omega\right)^{d\times d}_{\text{sym}}$ (symmetric second order tensors with components in $H^1\left(\Omega\right)$), $\boldsymbol{\mathcal{V}} = H_0^1\left(\Omega\right)^d$ and $\mathcal{Q} = L^2\left(\Omega\right)/\mathbb{R}$, which are the spaces where we may seek the elastic stress, the velocity and the pressure, respectively, for each fixed time t. The weak form of the problem is obtained by testing (4.5) against an arbitrary test function $\boldsymbol{V}$ with appropriate regularity. It can be written as: find $[\boldsymbol{u}, p, \boldsymbol{\sigma}] :]0, t_{\text{f}}[\longrightarrow \boldsymbol{\mathcal{X}} := \boldsymbol{\mathcal{V}} \times \mathcal{Q} \times \boldsymbol{\Upsilon}$ such that the initial conditions are satisfied and

$$\left(\rho\frac{\partial \boldsymbol{u}}{\partial t}, \boldsymbol{v}\right) + 2\left(\beta\eta_0\nabla^s\boldsymbol{u}, \nabla^s\boldsymbol{v}\right) + \langle \rho\boldsymbol{u}\cdot\nabla\boldsymbol{u}, \boldsymbol{v}\rangle + \left(\boldsymbol{\sigma}, \nabla^s\boldsymbol{v}\right) - \left(p, \nabla\cdot\boldsymbol{v}\right) = \langle \boldsymbol{f}, \boldsymbol{v}\rangle, \tag{4.6}$$

$$(q, \nabla \cdot \boldsymbol{u}) = 0, \quad (4.7)$$

$$\frac{1}{2\eta_0}(\boldsymbol{\sigma}, \boldsymbol{\tau}) - (1-\beta)(\nabla^s \boldsymbol{u}, \boldsymbol{\tau}) + \frac{\lambda}{2\eta_0}\left(\frac{\partial \boldsymbol{\sigma}}{\partial t} + \boldsymbol{u}\cdot\nabla\boldsymbol{\sigma} - \boldsymbol{\sigma}\cdot\nabla\boldsymbol{u} - (\nabla\boldsymbol{u})^T\cdot\boldsymbol{\sigma}, \boldsymbol{\tau}\right) = 0, \quad (4.8)$$

for all $\boldsymbol{V} = [\boldsymbol{v}, q, \boldsymbol{\tau}] \in \boldsymbol{\mathcal{X}}$, where it is assumed that $\boldsymbol{f}$ is such that $\langle \boldsymbol{f}, \boldsymbol{v}\rangle$ is well defined.

In a compact form, problem (6.6)-(4.8) can be written as:

$$(\mathcal{D}_t(\boldsymbol{U}), \boldsymbol{V}) + B(\boldsymbol{u}; \boldsymbol{U}, \boldsymbol{V}) = \langle \boldsymbol{f}, \boldsymbol{v}\rangle, \quad (4.9)$$

for all $\boldsymbol{V} \in \boldsymbol{\mathcal{X}}$, where

$$B(\hat{\boldsymbol{u}}; \boldsymbol{U}, \boldsymbol{V}) = 2(\beta\eta_0 \nabla^s \boldsymbol{u}, \nabla^s \boldsymbol{v}) + \langle \rho\hat{\boldsymbol{u}}\cdot\nabla\boldsymbol{u}, \boldsymbol{v}\rangle + (\boldsymbol{\sigma}, \nabla^s\boldsymbol{v}) - (p, \nabla\cdot\boldsymbol{v}) + (q, \nabla\cdot\boldsymbol{u}) + \frac{1}{2\eta_0}(\boldsymbol{\sigma}, \boldsymbol{\tau}) - (1-\beta)(\nabla^s\boldsymbol{u}, \boldsymbol{\tau}) + \frac{\lambda}{2\eta_0}\left(\hat{\boldsymbol{u}}\cdot\nabla\boldsymbol{\sigma} - \boldsymbol{\sigma}\cdot\nabla\hat{\boldsymbol{u}} - (\nabla\hat{\boldsymbol{u}})^T\cdot\boldsymbol{\sigma}, \boldsymbol{\tau}\right).$$

4.4 Numerical approximation

4.4.1 Galerkin finite element discretization

Let us consider a finite element partition $\mathcal{T}_h$ of the computational domain Ω. The diameter of an element domain $K \in \mathcal{T}_h$ is denoted by h_K and the diameter of the partition is defined as $h = \max\{h_K \mid K \in \mathcal{T}_h\}$. From $\mathcal{T}_h$ we may construct conforming finite element spaces for the velocity, the pressure and the elastic stress, $\boldsymbol{\mathcal{V}}_h \subset \boldsymbol{\mathcal{V}}$, $\mathcal{Q}_h \subset \mathcal{Q}$ and $\boldsymbol{\Upsilon}_h \subset \boldsymbol{\Upsilon}$, respectively. Calling $\boldsymbol{\mathcal{X}}_h := \boldsymbol{\mathcal{V}}_h \times \mathcal{Q}_h \times \boldsymbol{\Upsilon}_h$, the Galerkin finite element approximation of problem (4.9) consist in finding $\boldsymbol{U}_h :]0, t_f[\longrightarrow \boldsymbol{\mathcal{X}}_h$, such that:

$$(\mathcal{D}_t(\boldsymbol{U}_h), \boldsymbol{V}_h) + B(\boldsymbol{u}_h; \boldsymbol{U}_h, \boldsymbol{V}_h) = \langle \boldsymbol{f}, \boldsymbol{v}_h\rangle, \quad (4.10)$$

for all $\boldsymbol{V}_h = [\boldsymbol{v}_h, q_h, \boldsymbol{\tau}_h] \in \boldsymbol{\mathcal{X}}_h$, and satisfying the appropriate initial conditions.

In principle, we have posed no restrictions on the choice of the finite element spaces. However, there are restrictions that must be satisfied explicitly in the discrete formulation used. These are the same as for the three-field formulation of the Stokes problem (see [29, 56] and references therein), and read as follows: there exist positive constants C_1 and C_2 such that

$$\inf_{q_h \in \mathcal{Q}_h} \sup_{\boldsymbol{v}_h \in \boldsymbol{\mathcal{V}}_h} \frac{(q_h, \nabla\cdot\boldsymbol{v}_h)}{\|q_h\|_{\mathcal{Q}_h}\|\boldsymbol{v}_h\|_{\boldsymbol{\mathcal{V}}_h}} \geq C_1, \qquad \inf_{\boldsymbol{v}_h \in \boldsymbol{\mathcal{V}}_h} \sup_{\boldsymbol{\tau}_h \in \boldsymbol{\Upsilon}_h} \frac{(\boldsymbol{\tau}_h, \nabla^s\boldsymbol{v}_h)}{\|\boldsymbol{\tau}_h\|_{\boldsymbol{\Upsilon}_h}\|\boldsymbol{v}_h\|_{\boldsymbol{\mathcal{V}}_h}} \geq C_2, \quad (4.11)$$

where $\|\cdot\|_{\boldsymbol{\mathcal{Y}}}$ denotes the norm in space $\boldsymbol{\mathcal{Y}}$. Finite element interpolations that satisfy these conditions are scarce (see [111] for a 2D example and [25] for the 3D case). However, for most of our exposition we will assume that they hold, and thus that the Galerkin formulation is stable. We will explain in Section 4.5 the stabilized finite element formulation we favor and that allows one to use arbitrary interpolations.

4.4.2 Monolithic time discretization

Let us explain as to discretize in time problem (6.11) using a monolithic approach, i.e., solving for all the components of $\boldsymbol{U}_h$ at the same time. Any time discretization is possible, although for the sake of conciseness we will restrict ourselves to the classical backward-difference (BDF) approximations. The fractional step formulations to be presented will be based on this time discretization.

Let us consider a partition of the time interval $]0, t_f[$ into time steps of size δt, for simplicity constant. If $t^n = n\delta t$, $n = 0, 1, 2, \ldots$, the approximation of a time dependent function $g(t)$

at t^n will be denoted by g^n. The BDF approximation to the time derivative of g of order $k = 1, 2, \ldots$, is given by $\dfrac{\delta_k g^{n+1}}{\delta t}$, which we also write $\dfrac{\delta_k}{\delta t} g^{n+1}$, where

$$\delta_k \mathrm{g}^{n+1} = \frac{1}{\gamma_k} \left(\mathrm{g}^{n+1} - \sum_{i=0}^{k-1} \varphi_k^i \mathrm{g}^{n-i} \right), \tag{4.12}$$

where γ_k and φ_k^i are parameters. In particular, for the cases $k = 1$, 2 and 3 we have:

$$\begin{aligned}
\delta_1 \mathrm{g}^{n+1} \equiv & \delta \mathrm{g}^{n+1} = \mathrm{g}^{n+1} - \mathrm{g}^n, \\
\delta_2 \mathrm{g}^{n+1} = & \frac{3}{2} \left(\mathrm{g}^{n+1} - \frac{4}{3} \mathrm{g}^n + \frac{1}{3} \mathrm{g}^{n-1} \right), \\
\delta_3 \mathrm{g}^{n+1} = & \frac{11}{6} \left(\mathrm{g}^{n+1} - \frac{18}{11} \mathrm{g}^n + \frac{9}{11} \mathrm{g}^{n-1} - \frac{2}{11} \mathrm{g}^{n-2} \right),
\end{aligned}$$

We will also use the extrapolation operators of order k, defined as $\widehat{g}_k^{n+1} = g^{n+1} + \mathcal{O}(\delta t^k)$, which for $k = 1$, 2 and 3 are given by

$$\hat{\mathrm{g}}_1^{n+1} = \mathrm{g}^n, \tag{4.13}$$

$$\hat{\mathrm{g}}_2^{n+1} = 2\mathrm{g}^n - \mathrm{g}^{n-1}, \tag{4.14}$$

$$\hat{\mathrm{g}}_3^{n+1} = 3\mathrm{g}^n - 3\mathrm{g}^{n-1} + \mathrm{g}^{n-2}. \tag{4.15}$$

Using BDF schemes, the time discretization of problem (6.11) can be written, in expanded form, as: for $n = 1, 2, \ldots$, find $[\boldsymbol{u}_h^{n+1}, p_h^{n+1}, \boldsymbol{\sigma}_h^{n+1}] \in \boldsymbol{\mathcal{X}}_h$ such that

$$\begin{aligned}
\rho \left(\frac{\delta_k \boldsymbol{u}_h^{n+1}}{\delta t}, \boldsymbol{v}_h \right) + 2 \left(\beta \eta_0 \nabla^s \boldsymbol{u}_h^{n+1}, \nabla^s \boldsymbol{v}_h \right) + \left\langle \rho \boldsymbol{u}_h^{n+1} \cdot \nabla \boldsymbol{u}_h^{n+1}, \boldsymbol{v}_h \right\rangle \\
+ \left(\boldsymbol{\sigma}_h^{n+1}, \nabla^s \boldsymbol{v}_h \right) - \left(p_h^{n+1}, \nabla \cdot \boldsymbol{v}_h \right) = \left\langle \boldsymbol{f}_h^{n+1}, \boldsymbol{v}_h \right\rangle, \qquad (4.16) \\
\left(q_h, \nabla \cdot \boldsymbol{u}_h^{n+1} \right) = 0, \qquad (4.17) \\
\frac{\lambda}{2\eta_0} \left(\frac{\delta_k \boldsymbol{\sigma}_h^{n+1}}{\delta t}, \boldsymbol{\tau}_h \right) + \frac{1}{2\eta_0} \left(\boldsymbol{\sigma}_h^{n+1}, \boldsymbol{\tau}_h \right) - (1 - \beta) \left(\nabla^s \boldsymbol{u}_h^{n+1}, \boldsymbol{\tau}_h \right) \\
+ \frac{\lambda}{2\eta_0} \left(\boldsymbol{u}_h^{n+1} \cdot \nabla \boldsymbol{\sigma}_h^{n+1} - \boldsymbol{\sigma}_h^{n+1} \cdot \nabla \boldsymbol{u}_h^{n+1} - \left(\nabla \boldsymbol{u}_h^{n+1} \right)^T \cdot \boldsymbol{\sigma}_h^{n+1}, \boldsymbol{\tau}_h \right) = 0, \qquad (4.18)
\end{aligned}$$

for all $[\boldsymbol{v}_h, q_h, \boldsymbol{\tau}_h] \in \boldsymbol{\mathcal{X}}_h$.

The first order (BDF1) and the second order (BDF2) schemes are $\mathcal{A}$-stable. Higher order BDF methods do not keep this property, a limitation known as the *second Dahlquist barrier*. Nevertheless, BDF3 has a mild $\mathcal{A}$-stability restriction. We will use it in the numerical examples without discussing about its stability. For the time steps used, we have never observed unstable behaviors.

4.4.3 Algebraic system

Problem (4.16)-(4.18) yields an algebraic system for the nodal unknowns of the finite element functions $\left[\boldsymbol{u}_h^{n+1}, p_h^{n+1}, \boldsymbol{\sigma}_h^{n+1}\right] \in \boldsymbol{\mathcal{X}}_h$. The arrays of nodal unknowns will be identified by an upright case symbol, boldface for $\boldsymbol{u}_h$ and $\boldsymbol{\sigma}_h$ and light case for p_h. Matrices will be written with light case italic characters. In the case of elastic stresses, the Voight notation will be employed, so that the components of the nodal values of $\boldsymbol{\sigma}_h$ at a node a will be Σ_I^a,

I running from 1 to $d_V = 3$ if $d = 2$ and from 1 to $d_V = 6$ if $d = 3$. Having this notation in mind, the algebraic structure of problem (4.16)-(4.18) is

$$M_{\boldsymbol{u}} \frac{\delta_k}{\delta t} \mathbf{U}^{n+1} + K_{\boldsymbol{u}} \left(\mathbf{U}^{n+1} \right) \mathbf{U}^{n+1} + G\mathrm{P}^{n+1} - D_{\boldsymbol{\sigma}} \boldsymbol{\Sigma}^{n+1} = \mathbf{F}^{n+1}, \tag{4.19}$$

$$D\mathbf{U}^{n+1} = \mathbf{0}, \tag{4.20}$$

$$M_{\boldsymbol{\sigma}} \frac{\delta_k}{\delta t} \boldsymbol{\Sigma}^{n+1} + K_{\boldsymbol{\sigma}} \left(\mathbf{U}^{n+1} \right) \boldsymbol{\Sigma}^{n+1} - S\mathbf{U}^{n+1} = \mathbf{0}. \tag{4.21}$$

The dependence of matrices $K_{\boldsymbol{u}}$ and $K_{\boldsymbol{\sigma}}$ on $\mathbf{U}$ has been explicitly displayed. The identification of the different terms in (4.16)-(4.18) that contribute to the matrices in these expressions is straightforward.

System (4.19)-(4.21) can be written as

$$\begin{bmatrix} A_{11} & A_{12} & A_{13} \\ A_{21} & A_{22} & 0 \\ A_{31} & 0 & 0 \end{bmatrix} \begin{bmatrix} \mathbf{U}^{n+1} \\ \boldsymbol{\Sigma}^{n+1} \\ \mathrm{P}^{n+1} \end{bmatrix} = \begin{bmatrix} \mathbf{F}_1^{n+1} \\ \mathbf{F}_2^{n+1} \\ \mathrm{F}_3^{n+1} \end{bmatrix}, \tag{4.22}$$

where

$$A_{11} = \frac{1}{\gamma_k \delta t} M_{\boldsymbol{u}} + K_{\boldsymbol{u}} \left(\mathbf{U}^{n+1} \right), \qquad A_{12} = -D_{\sigma}, \qquad A_{13} = G,$$

$$A_{21} = -S, \quad A_{22} = \frac{1}{\gamma_k \delta t} M_{\boldsymbol{\sigma}} + K_{\boldsymbol{\sigma}} \left(\mathbf{U}^{n+1} \right), \quad A_{31} = D,$$

$$\mathbf{F}_1 = \mathbf{F}^{n+1} + \frac{1}{\gamma_k \delta t} \left(\sum_{i=0}^{k-1} \varphi_k^i \mathbf{U}^{n-i} \right), \qquad \mathbf{F}_2 = \frac{1}{\gamma_k \delta t} \left(\sum_{i=0}^{k-1} \varphi_k^i \boldsymbol{\Sigma}^{n-i} \right), \qquad \mathrm{F}_3 = 0.$$

The ordering of the equations chosen is consistent with the steps of the splitting algorithm proposed below.

4.5 Fractional step methods

The three fractional step methods proposed next can be viewed as extensions of pressure-segregation or pressure-correction schemes applied to the viscoelastic fluid flow problem. Instead of calculating the velocity with a guess of the pressure only, now we will need a guess of the elastic stresses as well. After computing these two fields, velocities will be corrected. We will not discuss extensions of velocity-correction methods, in which the guess is the velocity to compute the pressure instead of the opposite. Nevertheless, the ideas to be presented could also be used to design velocity-correction-type methods, or to the momentum-pressure Poisson equation formulation of the problem (see [11, 57] and references therein).

Our approach here is to present the splitting at the pure algebraic level, as in [132], rather than at the space continuous level as it done in the original works of Chorin [46] and Temam [159] and which is still the most common approach [90]. The algebraic viewpoint, discussed in detail in [11], obviates the discussion on pressure boundary conditions.

4.5.1 A first algebraic point of view: extrapolation

A first possibility to design fractional step methods is to extrapolate the variable that needs to be segregated from a certain equation, and correct the result once this variable has been computed somehow. In our case, we extrapolate the pressure and the stress in

the momentum equation to compute a velocity guess, we compute these variables with this velocity guess and finally we correct the velocity.

To derive the methods we propose, let us start writing (4.19)-(4.21) in the *equivalent* form

$$M_{\boldsymbol{u}}\frac{\delta_k}{\delta t}\tilde{\mathbf{U}}^{n+1}+K_{\boldsymbol{u}}\left(\tilde{\mathbf{U}}^{n+1}\right)\tilde{\mathbf{U}}^{n+1}+G\hat{\mathrm{P}}_{k'-1}^{n+1}-D_{\boldsymbol{\sigma}}\hat{\boldsymbol{\Sigma}}_{k'-1}^{n+1}=\mathbf{F}^{n+1}, \tag{4.23}$$

$$M_{\boldsymbol{u}}\frac{1}{\gamma_k\delta t}\left(\mathbf{U}^{n+1}-\tilde{\mathbf{U}}^{n+1}\right)+\mathbf{N}_{\boldsymbol{u}}^{n+1}+G\left(\mathrm{P}^{n+1}-\hat{\mathrm{P}}_{k'-1}^{n+1}\right)-D_{\boldsymbol{\sigma}}\left(\boldsymbol{\Sigma}^{n+1}-\hat{\boldsymbol{\Sigma}}_{k'-1}^{n+1}\right)=\mathbf{0}, \tag{4.24}$$

$$M_{\boldsymbol{\sigma}}\frac{\delta_k}{\delta t}\tilde{\boldsymbol{\Sigma}}^{n+1}+K_{\boldsymbol{\sigma}}\left(\tilde{\mathbf{U}}^{n+1}\right)\tilde{\boldsymbol{\Sigma}}^{n+1}-S\tilde{\mathbf{U}}^{n+1}=\mathbf{0}, \tag{4.25}$$

$$M_{\boldsymbol{\sigma}}\frac{1}{\gamma_k\delta t}\left(\boldsymbol{\Sigma}^{n+1}-\tilde{\boldsymbol{\Sigma}}^{n+1}\right)+\mathbf{N}_{\boldsymbol{\sigma}}^{n+1}-S\left(\mathbf{U}^{n+1}-\tilde{\mathbf{U}}^{n+1}\right)=\mathbf{0}, \tag{4.26}$$

$$\begin{aligned}-D\tilde{\mathbf{U}}^{n+1}+\gamma_k\delta tDM_{\boldsymbol{u}}^{-1}\mathbf{N}_{\boldsymbol{u}}^{n+1}+\gamma_k\delta tDM_{\boldsymbol{u}}^{-1}G\left(\mathrm{P}^{n+1}-\hat{\mathrm{P}}_{k'-1}^{n+1}\right)\\ -\gamma_k\delta tDM_{\boldsymbol{u}}^{-1}D_{\boldsymbol{\sigma}}\left(\boldsymbol{\Sigma}^{n+1}-\hat{\boldsymbol{\Sigma}}_{k'-1}^{n+1}\right)=\mathbf{0},\end{aligned} \tag{4.27}$$

where

$$\begin{aligned}\mathbf{N}_{\boldsymbol{u}}^{n+1}=&K_{\boldsymbol{u}}\left(\mathbf{U}^{n+1}\right)\mathbf{U}^{n+1}-K_{\boldsymbol{u}}\left(\tilde{\mathbf{U}}^{n+1}\right)\tilde{\mathbf{U}}^{n+1},\\ \mathbf{N}_{\boldsymbol{\sigma}}^{n+1}=&K_{\boldsymbol{\sigma}}\left(\mathbf{U}^{n+1}\right)\boldsymbol{\Sigma}^{n+1}-K_{\boldsymbol{\sigma}}\left(\tilde{\mathbf{U}}^{n+1}\right)\tilde{\boldsymbol{\Sigma}}^{n+1}.\end{aligned}$$

In these equations, $\tilde{\mathbf{U}}^{n+1}$ and $\tilde{\boldsymbol{\Sigma}}^{n+1}$ are auxiliary variables, $\hat{g}_{k'-1}^{n+1}$ is the extrapolation of order $k'-1$ at t^{n+1} of a function g (see (4.13)-(4.15) for the cases $k'-1=1,2,3$), taking $\hat{g}_0^{n+1}=0$, and it is understood that the difference $\delta_k\tilde{g}^{n+1}$ is computed from $\tilde{g}^{n+1}$ and g^m, for time steps m previous to $n+1$, g now being either $\mathbf{U}$ or $\boldsymbol{\Sigma}$. Note that adding up (4.23) and (4.24) we recover (4.19), adding up (4.25) and (4.26) we recover (4.21), and that (4.24) is obtained multiplying (4.24) by $\gamma_k\delta tDM_{\boldsymbol{u}}^{-1}$ and using (4.20). This last equation (4.27) is a Poisson-type equation for the pressure. Note also that k gives the order of the time integration, whereas k' determines the order of the variables that are extrapolated.

In the previous equations, k determines the order of the time integration scheme and k' the order of the extrapolations to uncouple variables. They can be chosen independently, but need to be properly balanced to achieve a certain order of the final approximation. In principle, fractional step methods of order k could be designed *taking* $k'=k$ as follows:

1. Compute $\tilde{\mathbf{U}}^{n+1}$ from (4.23).
2. Compute $\tilde{\boldsymbol{\Sigma}}^{n+1}$ from (4.25).
3. Compute *an approximation* to P^{n+1} by solving (4.27) *neglecting* $\mathbf{N}_{\boldsymbol{u}}^{n+1}$ and *replacing* $\boldsymbol{\Sigma}^{n+1}$ by $\tilde{\boldsymbol{\Sigma}}^{n+1}$.
4. Compute an approximation to $\mathbf{U}^{n+1}$ from (4.24) neglecting $\mathbf{N}_{\boldsymbol{u}}^{n+1}$.
5. Compute an approximation to $\boldsymbol{\Sigma}^{n+1}$ from (4.26) neglecting $\boldsymbol{\sigma}^{n+1}$.

Several remarks are in order:

- Steps 1 to 5 above allow one to uncouple the calculation of the different variables, which is the objective of fractional step methods.

- Matrix $DM_{\boldsymbol{u}}^{-1}G$, appearing in the pressure Poisson equation (4.27), has a wide stencil. Since it approximates the continuous Laplacian operator, it is often approximated by the matrix resulting from the direct approximation of this Laplacian, with a narrower stencil.

- Formally, it is easy to see that the resulting scheme is of order $\mathcal{O}(\delta t^k)$ for a given spatial discretization (if the spatial discretization is considered, the error will depend on both δt and the mesh size h). Assuming this to be true up to time step n and assuming that the scheme is stable (see next remark), from the approximation to (4.23)-(4.27) it follows that it is also true at time step $n+1$. If the order of extrapolation is higher than $k-1$, i.e $k' > k$, the order of the error would be dominated by the time integration scheme.

- Unfortunately, the resulting scheme is only stable for $k' = 1, 2$. For $k' = 3$, the extrapolation $\hat{\mathrm{P}}_2^{n+1} = 2\mathrm{P}^n - \mathrm{P}^{n-1}$ is known to yield an unstable scheme (see [11, 12] and references therein).

- For $k = 1$ we have an extension to viscoelastic flows of the classical first order fractional step method, whereas for $k = 2$ we have an extension of the second order method that keeps the pressure gradient at the previous time step in the momentum equation, sometimes known as the incremental projection method and whose continuous version is analyzed in [151].

The final algorithm for the first and second order schemes is displayed in Algorithm 4.1, where two remarks need to be made. The first is that for the first order scheme the fifth step is not needed to obtain the first order accuracy in time, and the second is that the sixth step is written only for formal reasons, with the objective of identifying this scheme with the inexact block LU-decomposition described in the next subsection.

Algorithm 4.1 First and second order fractional step schemes ($k = 1, 2$).

Intermediate Steps:

$$
\begin{aligned}
M_{\boldsymbol{u}}\frac{\delta_k}{\delta t}\tilde{\mathbf{U}}^{n+1} + K_{\boldsymbol{u}}\left(\tilde{\mathbf{U}}^{n+1}\right)\tilde{\mathbf{U}}^{n+1} + G\hat{\mathrm{P}}_{k-1}^{n+1} - D_{\boldsymbol{\sigma}}\hat{\boldsymbol{\Sigma}}_{k-1}^{n+1} &= \mathbf{F}^{n+1} \to \tilde{\mathbf{U}}^{n+1},\\
M_{\boldsymbol{\sigma}}\frac{\delta_k}{\delta t}\tilde{\boldsymbol{\Sigma}}^{n+1} + K_{\boldsymbol{\sigma}}\left(\tilde{\mathbf{U}}^{n+1}\right)\tilde{\boldsymbol{\Sigma}}^{n+1} - S\tilde{\mathbf{U}}^{n+1} &= \mathbf{0} \to \tilde{\boldsymbol{\Sigma}}^{n+1},\\
-D\tilde{\mathbf{U}}^{n+1} + \gamma_k\delta t D M_{\boldsymbol{u}}^{-1}G\left(\tilde{\mathrm{P}}^{n+1} - \hat{\mathrm{P}}_{k-1}^{n+1}\right) - \gamma_k\delta t D M_{\boldsymbol{u}}^{-1}D_\sigma\left(\tilde{\boldsymbol{\Sigma}}^{n+1} - \hat{\boldsymbol{\Sigma}}_{k-1}^{n+1}\right) &= \mathbf{0} \to \tilde{\mathrm{P}}^{n+1}.
\end{aligned}
$$

Correction steps:

$$
\begin{aligned}
\frac{1}{\gamma_k\delta t}M_{\boldsymbol{u}}\left(\mathbf{U}^{n+1} - \tilde{\mathbf{U}}^{n+1}\right) + G\left(\tilde{\mathrm{P}}^{n+1} - \hat{\mathrm{P}}_{k-1}^{n+1}\right) - D_\sigma\left(\tilde{\boldsymbol{\Sigma}}^{n+1} - \hat{\boldsymbol{\Sigma}}_{k-1}^{n+1}\right) &= \mathbf{0} \to \mathbf{U}^{n+1},\\
\frac{1}{\gamma_k\delta t}M_{\boldsymbol{\sigma}}\left(\boldsymbol{\Sigma}^{n+1} - \tilde{\boldsymbol{\Sigma}}^{n+1}\right) - S\left(\mathbf{U}^{n+1} - \tilde{\mathbf{U}}^{n+1}\right) &= \mathbf{0} \to \boldsymbol{\Sigma}^{n+1},\\
\mathrm{P}^{n+1} &= \tilde{\mathrm{P}}^{n+1} \to \mathrm{P}^{n+1}.
\end{aligned}
$$

Since the third order fractional step version ($k = 3$) of Algorithm 4.1 is unstable, a third other scheme needs to be designed by other means. This third order method can be obtained by using only first order extrapolations but *without* neglecting $\mathbf{N}_{\boldsymbol{u}}^{n+1}$ in (4.24). As we shall

see in the next subsection, this can be interpreted as a *Yosida scheme*. The steps are thus as follows:

1. Compute $\tilde{\mathbf{U}}^{n+1}$ from (4.23) with $k=3$ and $k'=2$.
2. Compute $\tilde{\boldsymbol{\Sigma}}^{n+1}$ from (4.25) with $k=3$ and $k'=2$.
3. Compute *an approximation* to P^{n+1} by solving (4.27) *neglecting* $\mathbf{N}_{\boldsymbol{u}}^{n+1}$, *replacing* $\boldsymbol{\Sigma}^{n+1}$ by $\tilde{\boldsymbol{\Sigma}}^{n+1}$ and taking $k=3$ and $k'=2$.
4. Compute an approximation to $\mathbf{U}^{n+1}$ from (4.24) *without neglecting* $\mathbf{N}_{\boldsymbol{u}}^{n+1}$.
5. Compute an approximation to $\boldsymbol{\Sigma}^{n+1}$ from (4.26) neglecting $\boldsymbol{\sigma}^{n+1}$.

The resulting scheme is displayed in Algorithm 4.2. Even if only a first order extrapolation is used for the pressure and the elastic stresses in the momentum equation, including $\mathbf{N}_{u}^{n+1}$ in the fourth step allows one to obtain third order accuracy. This will be clearly seen in the next subsection, but it can also be formally guessed by inspecting Algorithm 4.2 and comparing the different steps with the exact equations (4.23)-(4.27). From the first step it is seen that $\tilde{\mathbf{U}}^{n+1}$ is expected to be a second order approximation to the exact nodal velocities at time step $n+1$, from the second step it then follows that $\tilde{\boldsymbol{\Sigma}}^{n+1}$ is a second order approximation to the exact vector of nodal stresses, and from the fourth step that $\tilde{\mathrm{P}}^{n+1}$ is a second order approximation to the nodal pressures. Then, adding up the first and the fourth steps it is seen that the error in $\tilde{\mathbf{U}}^{n+1}$ does not affect the error in $\mathbf{U}^{n+1}$, which happens to be a third order approximation to the exact nodal velocities. Taking into account $\mathbf{N}_{u}^{n+1}$ in the fourth step has also some advantages for the first order scheme, particularly regarding boundary conditions when it is considered at the continuous level. This is precisely the formulation whose mathematical analysis is presented in [24].

Let us remark that another alternative to obtain a third order fractional step method is to change the approach to velocity segregation methods [12, 129], which permit second order extrapolation of the velocity, thus avoiding the unstable pressure extrapolation. Finally, let us mention that a third order scheme in time only makes sense for a higher order spatial approximation, since error estimates will couple spatial and temporal errors. Nevertheless, both the Galerkin approximation and the stabilized formulation presented later allow one to use any interpolation order in space.

4.5.2 A second algebraic point of view: inexact factorizations

An interesting approach in fractional step methods is the reinterpretation of the splitting process as an inexact LU block factorization of the matrix of the system after discretization in time and space. High order algebraic pressure segregation algorithms can be designed using this methodology. In [86] for example the authors apply this approach to solve the Navier-Stokes problem using the spectral element method.

The starting point to apply this idea is the original system (4.22). Let us write it as $A\mathbf{X}^{n+1}=\mathbf{B}^{n+1}$, with the obvious identifications. If we consider the LU-decomposition of A, with L a lower triangular and U an upper triangular matrix, the original system $LU\mathbf{X}^{n+1}=\mathbf{B}^{n+1}$ can be split into two systems that can be solved sequentially:

$$L\tilde{\mathbf{X}}^{n+1}=\mathbf{B}^{n+1}, \qquad U\mathbf{X}^{n+1}=\tilde{\mathbf{X}}^{n+1},$$

and each of which is easy to solve by backward or forward substitution. The array $\tilde{\mathbf{X}}^{n+1}$ represents the intermediate value of the unknown. The problem of course is that both L and U involve the inversion of the block matrix A_{11}, which is computationally unaffordable. The idea of inexact factorizations is to approximate A_{11}^{-1}, this yielding approximations to L and

Algorithm 4.2 Third order fractional step scheme.

Intermediate Steps:

$$
\begin{aligned}
M_{\boldsymbol{u}}\frac{\delta_3}{\delta t}\tilde{\mathbf{U}}^{n+1}+K_{\boldsymbol{u}}\left(\tilde{\mathbf{U}}^{n+1}\right)\tilde{\mathbf{U}}^{n+1}+G\mathrm{P}^{n}-D_{\boldsymbol{\sigma}}\boldsymbol{\Sigma}^{n}&=\mathbf{F}^{n+1}\rightarrow\tilde{\mathbf{U}}^{n+1},\\
M_{\boldsymbol{\sigma}}\frac{\delta_3}{\delta t}\tilde{\boldsymbol{\Sigma}}^{n+1}+K_{\boldsymbol{\sigma}}\left(\tilde{\mathbf{U}}^{n+1}\right)\tilde{\boldsymbol{\Sigma}}^{n+1}-S\tilde{\mathbf{U}}^{n+1}&=\mathbf{0}\rightarrow\tilde{\boldsymbol{\Sigma}}^{n+1},\\
-D\tilde{\mathbf{U}}^{n+1}+\gamma_3\delta tDM_{\boldsymbol{u}}^{-1}G\left(\tilde{\mathrm{P}}^{n+1}-\mathrm{P}^{n}\right)-\gamma_3\delta tDM_{\boldsymbol{u}}^{-1}D_{\sigma}\left(\tilde{\boldsymbol{\Sigma}}^{n+1}-\boldsymbol{\Sigma}^{n}\right)&=\mathbf{0}\rightarrow\tilde{\mathrm{P}}^{n+1}.
\end{aligned}
$$

Correction steps:

$$
\begin{aligned}
\frac{1}{\gamma_3\delta t}M_{\boldsymbol{u}}\left(\mathbf{U}^{n+1}-\tilde{\mathbf{U}}^{n+1}\right)+K_{\boldsymbol{u}}\left(\mathbf{U}^{n+1}\right)\mathbf{U}^{n+1}-K_{\boldsymbol{u}}\left(\tilde{\mathbf{U}}^{n+1}\right)\tilde{\mathbf{U}}^{n+1}&\\
+G\left(\tilde{\mathrm{P}}^{n+1}-\mathrm{P}^{n}\right)-D_{\sigma}\left(\tilde{\boldsymbol{\Sigma}}^{n+1}-\boldsymbol{\Sigma}^{n}\right)&=\mathbf{0}\rightarrow\mathbf{U}^{n+1},\\
\frac{1}{\gamma_3\delta t}M_{\boldsymbol{\sigma}}\left(\boldsymbol{\Sigma}^{n+1}-\tilde{\boldsymbol{\Sigma}}^{n+1}\right)-S\left(\mathbf{U}^{n+1}-\tilde{\mathbf{U}}^{n+1}\right)&=\mathbf{0}\rightarrow\boldsymbol{\Sigma}^{n+1},\\
\mathrm{P}^{n+1}=\tilde{\mathrm{P}}^{n+1}&\rightarrow\mathrm{P}^{n+1}.
\end{aligned}
$$

U respectively denoted by L^* and U^*. Thus, the matrix of the approximate factorization is $A^*=L^*U^*$, and the error matrix is $E^*=A-A^*$.

The first, second and third order schemes introduced in the previous subsection, with slight modifications of higher order, are recast as inexact LU factorizations in Algorithms 4.3, 4.4 and 4.5. We identify there the approximate matrix A^* and the error matrix E^* of each case. The splitting error in the first order fractional step method (Algorithm 4.3) is first order in time and does not affect the continuity equation, i.e., the scheme preserves the mass conservation equation.

For the second and the third order schemes it is more convenient to work with the increments of the variables. Suppose that we know the exact solution of the problem up to time step n and we want to compute an approximation to the solution of system $A\mathbf{X}^{n+1}=\mathbf{B}^{n+1}$, at time step $n+1$. Assume for the moment that the problem is linear and A does not depend on $\mathbf{X}$. Let $A^*\mathbf{X}^{*,n+1}=\mathbf{B}^{*,n+1}$ be the approximate system. We may write both the exact and the approximate systems as $A\delta\mathbf{X}^{n+1}=\delta\mathbf{B}^{n+1}:=\mathbf{B}^{n+1}-A\mathbf{X}^{n}$ and $A^*\delta\mathbf{X}^{*,n+1}=\delta\mathbf{B}^{*,n+1}:=\mathbf{B}^{*,n+1}-A^*\mathbf{X}^{n}$, respectively, where $\delta\mathbf{X}^{*,n+1}=\mathbf{X}^{*,n+1}-\mathbf{X}^{n}$. It is easily found that

$$
\mathbf{X}^{n+1}-\mathbf{X}^{*,n+1}=(A^*)^{-1}\left(\delta\mathbf{B}^{n+1}-\delta\mathbf{B}^{*,n+1}\right)-(A^*)^{-1}E^*\delta\mathbf{X}^{n+1}.
$$

Therefore, if $(A^*)^{-1}$ has a bounded norm (i.e., the approximate scheme is stable), $\delta\mathbf{B}^{n+1}-\delta\mathbf{B}^{*,n+1}=\mathcal{O}(\delta t^k)$ (in an appropriate norm) and $E^*=\mathcal{O}(\delta t^{k-1})$, the scheme can be formally expected to be of order k. In the case the solution up to time step n is not exact, but approximate up to the adequate order, and A depends on $\mathbf{X}$, we may proceed by induction and show (formally) the same result.

For the second and third order ($k=2,3$) fractional step schemes we propose, we will be able to write the problem in incremental form with right-hand-sides whose difference with the exact ones will be of order k, assuming this is the order of the error up to time step n. Therefore, if we show that the error matrix E^* is of order $k-1$, the solution at time step $n+1$ will have an error of order k. Again, the dependence of A on the unknown has

to be treated by assuming this unknown has a certain order of approximation and then checking it a posteriori. As mentioned earlier, these arguments are merely formal, but serve to understand why the methods have the order we claim and that is observed in numerical experiments.

The inexact factorization point of view of the second and third order schemes is presented in Algorithm 4.4 and Algorithm 4.5 respectively. Considering first the second order case, it is seen from Algorithm 4.4 that the splitting error for the momentum equation is the dominant error. The splitting error for the constitutive equation is formally of third order in time, and the splitting error in the continuity equation is also of third order, because the inversion of A^* introduces a factor $1/\delta t$ (the matrix multiplying the pressure increments has a factor δt). From this observation it follows that in order to design a third order scheme in fact it is only necessary to improve the accuracy of the splitting of the momentum equation. This is precisely what can be accomplished with the Yosida scheme introduced in the previous subsection. From Algorithm 4.5 it is observed that in fact in this case there is no error in the momentum equation. That the third order scheme can be interpreted as a Yosida factorization (with an extrapolation of the pressure and the elastic stresses in the momentum equation) comes from the expression of matrices L^* and U^* in Algorithm 4.5.

Let us finally remark that the second and third order schemes proposed in this subsection are not identical to those proposed in the previous one. The equations for the intermediate variables are exactly the same, and the intermediate pressure is taken in all cases as the end-of-step pressure. The difference is in the order of calculation of the end-of-step velocities and elastic stresses. In Algorithms 4.1 (for $k = 2$) and 4.2, the end-of-step velocities are first computed and then the elastic stresses are updated, whereas in Algorithm 4.4 and Algorithm 4.5 the order is reversed. This change in the order is given by the LU decomposition structure. Note that solving for the elastic stresses without knowing the end-of-step velocities implies solving two systems, with matrices $M_{\boldsymbol{u}}$ and $M_{\boldsymbol{\sigma}}$, and is therefore computationally more expensive. Nevertheless, the difference can be shown to be of fourth order by using Maclaurin expansions in terms of δt, and thus the splitting error is the same for the methods of this subsection and of the previous one.

4.6 Stabilized finite element formulation

Up to this point, we have assumed that the spatial approximation has been carried out using the Galerkin finite element method or, in fact, any spatial discretization that yields the same matrix structure as this method. However, apart from methods to stabilize convection dominated flows, it may be convenient to use formulations that allow one to use arbitrary interpolations, not necessarily satisfying the inf-sup conditions (4.11). Let us remark that sometimes pressure stability can be obtained from the pressure splitting, even if that implies a proper selection of the time step size and it cannot be used in methods of order higher than one. See [52] for a discussion about this point and the analysis of pressure stability for first and second order fractional step schemes for Newtonian flows.

In this section we present the stabilized finite element formulation that we use, which is described in detail in chapter 3 (also in [36]) for the stationary problem. Here we will only write the resulting discrete equations, and after this we will present the final algebraic structure and the linearization of the problem. The essential difference with respect to (4.22) is the appearance of a non-zero A_{33} block in matrix A. We will explain how this modifies the fractional step methods presented heretofore.

4.6.1 Stabilized monolithic formulation

Stabilized finite element methods consist in modifying the discrete Galerkin formulation of the problem by adding terms designed to enhance stability without upsetting accuracy. The method we propose, and that replaces (6.11), consist in finding $\boldsymbol{U}_h :]0, t_{\mathrm{f}}[\longrightarrow \boldsymbol{\mathcal{X}}_h$, such that:

$$\left(\mathcal{D}_t\left(\boldsymbol{U}_h\right), \boldsymbol{V}_h\right) + B\left(\boldsymbol{u}_h; \boldsymbol{U}_h, \boldsymbol{V}_h\right) + S_1^{\perp}(\boldsymbol{u}_h; \boldsymbol{U}_h, \boldsymbol{V}_h) + S_2^{\perp}(\boldsymbol{U}_h, \boldsymbol{V}_h) + S_3(\boldsymbol{u}_h; \boldsymbol{U}_h, \boldsymbol{V}_h) = \langle \boldsymbol{f}, \boldsymbol{v}_h \rangle, \tag{4.28}$$

for all $\boldsymbol{V}_h = [\boldsymbol{v}_h, q_h, \boldsymbol{\tau}_h] \in \boldsymbol{\mathcal{X}}_h$, and satisfying the appropriate initial conditions.

In order to give the expression of the stabilization terms $S_1^{\perp}$, $S_2^{\perp}$ and S_3 in (4.28), let P_h denote the L^2 projection onto the appropriate finite element space, either of velocities, elastic stresses or pressures (the case will be clear by the argument of this projection), *without* boundary conditions. Let also $P_h^{\perp} = I - P_h$ be the orthogonal projection, I being now the identity. We then define

$$\begin{aligned} S_1^{\perp}(\hat{\boldsymbol{u}}_h; \boldsymbol{U}_h, \boldsymbol{V}_h) = & \sum_K \alpha_1 \left\langle P_h^{\perp}\left[\rho \hat{\boldsymbol{u}}_h \cdot \nabla \boldsymbol{u}_h\right], \rho \hat{\boldsymbol{u}}_h \cdot \nabla \boldsymbol{v}_h \right\rangle_K + \sum_K \alpha_1 \left\langle P_h^{\perp}\left[\nabla p_h\right], \nabla q_h \right\rangle_K \\ & + (1-\beta) \sum_K \alpha_1 \left\langle P_h^{\perp}\left[\nabla \cdot \boldsymbol{\sigma}_h\right], \nabla \cdot \boldsymbol{\tau}_h \right\rangle_K, \end{aligned} \tag{4.29}$$

$$S_2^{\perp}(\boldsymbol{U}_h, \boldsymbol{V}_h) = \sum_K \alpha_2 \left\langle P_h^{\perp}\left[\nabla \cdot \boldsymbol{u}_h\right], \nabla \cdot \boldsymbol{v}_h \right\rangle_K, \tag{4.30}$$

$$\begin{aligned} S_3(\hat{\boldsymbol{u}}_h; \boldsymbol{U}_h, \boldsymbol{V}_h) = & \sum_K \alpha_3 \left\langle \tilde{P}_h \left[\frac{1}{2\eta_0} \boldsymbol{\sigma}_h - (1-\beta) \nabla^s \boldsymbol{u}_h + \frac{\lambda}{2\eta_0} \left(\frac{\partial \boldsymbol{\sigma}_h}{\partial t} + \hat{\boldsymbol{u}}_h \cdot \nabla \boldsymbol{\sigma}_h - g\left(\hat{\boldsymbol{u}}_h, \boldsymbol{\sigma}_h\right) \right) \right] \right. \\ & \left. - \frac{1}{2\eta_0} \boldsymbol{\tau}_h - \nabla^s \boldsymbol{v}_h + \frac{\lambda}{2\eta_0} \left(\hat{\boldsymbol{u}}_h \cdot \nabla \boldsymbol{\tau}_h + \boldsymbol{\tau}_h \cdot \left(\nabla \hat{\boldsymbol{u}}_h\right)^T + \nabla \hat{\boldsymbol{u}}_h \cdot \boldsymbol{\tau}_h \right) \right\rangle_K, \end{aligned} \tag{4.31}$$

where $g\left(\hat{\boldsymbol{u}}_h, \boldsymbol{\sigma}_h\right) = \boldsymbol{\sigma}_h \cdot \nabla \hat{\boldsymbol{u}}_h + \left(\nabla \hat{\boldsymbol{u}}_h\right)^T \cdot \boldsymbol{\sigma}_h$.

In (4.31) the projection $\tilde{P}_h$ can be taked as the identity or the orthogonal projection $P_h^{\perp}$, and the parameters $\alpha_i, i = 1, 2, 3$, are computed within each element K as

$$\begin{aligned} \alpha_1 = & \left[c_1 \frac{\eta_0}{h_1^2} + c_2 \frac{\rho \left|\boldsymbol{u}_h\right|}{h_2} \right]^{-1}, \\ \alpha_2 = & \frac{h_1^2}{c_1 \alpha_1}, \\ \alpha_3 = & \left[c_3 \frac{1}{2\eta_0} + c_4 \left(\frac{\lambda}{2\eta_0} \frac{\left|\boldsymbol{u}_h\right|}{h_2} + \frac{\lambda}{\eta_0} \left|\nabla \boldsymbol{u}_h\right| \right) \right]^{-1}. \end{aligned}$$

In these expressions, h_1 corresponds to a characteristic element length calculated as the square root of the element area in the 2D case and the cubic root of the element volume in 3D, and h_2 corresponds to another characteristic length calculated as the element length in the streamline direction. The term $\left|\boldsymbol{u}_h\right|$ is the Euclidean norm of the velocity, and $\left|\nabla \boldsymbol{u}_h\right|$ the Frobenius norm of the velocity gradient. The constants c_i, $i = 1, 2, 3, 4$, are algorithmic parameters in the formulation. The values used in this chapter are $c_1 = 12.0$, $c_2 = 2.0$, $c_3 = 4.0$ and $c_4 = 0.125$. We have found better convergence in the nonlinear iterative scheme described later using the modified values c_1 and c_4, with respect to the values used in chapter 3 and chapter 2 (also in [36, 37]) ($c_1 = 4.0$ and $c_4 = 0.25$), with similar accuracy (the values of the algorithmic constants affect the results, but not the mesh convergence rate to be expected). For higher order elements, the characteristic lengths h_1 and h_2 should be divided respectively by r^2 and r, r being the order of the finite element interpolation.

The stabilizing mechanism introduced by the terms $S_1^\perp$, $S_2^\perp$ and S_3 are the following. The first component of the $S_1^\perp$ gives control on the convective term, the second component gives control on the pressure gradient, and the third term gives control on the divergence of the viscoelastic stress. The term $S_2^\perp$ is not a must but in some cases it improves stability of the problem. Finally, the term S_3 ensures stability of the constitutive equation. Note that some of the components of this last term are the convective-convective term of the viscoelastic stress tensor and an equivalent EVSS-structure component, among others cross local inner-product terms (see chapter 3 for more details of this spatial stabilized formulation). The addition of these three terms permit the resolution of convection dominant problems both in velocity and in stress, and the implementation of equal order interpolation for all the unknowns. The orthogonal projections introduce consistency errors, but of optimal order. For stationary problems, the resulting formulation turns out to have optimal order of convergence, as checked numerically in chapter 3 and proved in some simpler settings, for example in [56]. If r is the order of the finite element interpolation, velocity convergence in $L^2(\Omega)$ turns out to be of order $r+1$, whereas pressure and stress convergence in $L^2(\Omega)$ and velocity convergence in $H^1(\Omega)$ are of order r.

The time discretization of (4.28) can be performed as for the Galerkin method. Using BDF schemes of order k, partial time derivatives have to be replaced by incremental quotients $\delta_k/\delta t$ and all unknowns need to be evaluated at time step $n+1$. We consider the resulting fully discrete problem in the following.

4.6.2 Algebraic formulation and fractional step scheme

From Eq. (4.28) it is easy to see that the algebraic system to be solved at each time step will be of the form

$$\begin{bmatrix} A_{s,11} & A_{s,12} & A_{13} \\ A_{s,21} & A_{s,22} & 0 \\ A_{31} & 0 & A_{s,33} \end{bmatrix} \begin{bmatrix} \mathbf{U}^{n+1} \\ \mathbf{\Sigma}^{n+1} \\ \mathrm{P}^{n+1} \end{bmatrix} = \begin{bmatrix} \mathbf{F}_1 \\ \mathbf{F}_2 \\ \mathrm{F}_3 \end{bmatrix}, \tag{4.32}$$

where subscript s has been introduced in the matrices that have contributions from the stabilization terms. Comparing this system with (4.22), we see that:

- From the point of view of the algebraic structure, the only difference between Eq. (4.32) and (4.22) is the presence of the term $A_{s,33}$, which comes from $\sum_K \alpha_1 \left\langle P_h^\perp \left[\nabla p_h\right], \nabla q_h \right\rangle_K$. We will write it as $A_{s,33} = L_s^\perp$.

- The fact that $A_{s,23} = A_{s,32} = 0$ simplifies the introduction of fractional step methods. The orthogonal projections $P_h^\perp$ in (4.29) and (4.30) (and maybe also in (4.31)) allows one to introduce a sort of term-by-term stabilization while maintaining optimal accuracy. This is also why matrices A_{13} and A_{31} of the Galerkin method are unaltered. See [51, 55] for the analysis in the Newtonian case.

- The time derivative of the velocity does not appear in the stabilization terms, and therefore the only matrix which is multiplied by $1/\delta t$ in the first row of (4.32) is $M_{\boldsymbol{u}}$, which is symmetric and positive definite. An analogous comment can be made about the second row if $\tilde{P}_h = P_h^\perp$, since the orthogonal projection of the time derivative is zero. On the other hand, if $\tilde{P}_h = I$ there is a contribution of the elastic stress time derivative in the stabilization terms of the constitutive equation, which may deteriorate the behavior of iterative solvers.

- All stabilization terms are nonlinear, as the stabilization parameters depend on the velocity $\boldsymbol{u}_h$.

With these observations in mind, the first, second and third order fractional step methods proposed for the Galerkin method can be easily extended to the stabilized finite element method. The only difference will be to take into account that matrices may have a contribution coming from the stabilization terms and that there will be a new contribution to the discrete equation for the pressure. For example, the third order scheme is given in Algorithm 4.6. Matrices with a contribution from the stabilization terms have been identified with a subscript s. The resulting matrix L^* is as in Algorithm 4.5, only adding $L_s^{\perp}$ in the 33-block and accounting for the stabilization contributions. This is also the only difference in matrix A^*, while matrices U^* and E^* are the same as in Algorithm 4.5, except for the modification in the matrices due to stabilization. This in particular implies that the splitting error will be of the same order in both the Galerkin and the stabilized finite element formulations.

Algorithm 4.3 Inexact factorization of the first order fractional step method.

L-steps:

$$\begin{aligned}
\frac{1}{\delta t} M_{\boldsymbol{u}} \tilde{\mathbf{U}}^{n+1} + K_{\boldsymbol{u}} \left(\tilde{\mathbf{U}}^{n+1} \right) \tilde{\mathbf{U}}^{n+1} &= \mathbf{F}_1^{n+1} \rightarrow \tilde{\mathbf{U}}^{n+1}, \\
\frac{1}{\delta t} M_{\boldsymbol{\sigma}} \tilde{\boldsymbol{\Sigma}}^{n+1} + K_{\boldsymbol{\sigma}} \left(\tilde{\mathbf{U}}^{n+1} \right) \tilde{\boldsymbol{\Sigma}}^{n+1} - S \tilde{\mathbf{U}}^{n+1} &= \mathbf{F}_2^{n+1} \rightarrow \tilde{\boldsymbol{\Sigma}}^{n+1}, \\
-D \tilde{\mathbf{U}}^{n+1} + \delta t D M_{\boldsymbol{u}}^{-1} G \tilde{\mathrm{P}}^{n+1} - \delta t D M_{\boldsymbol{u}}^{-1} D_\sigma \tilde{\boldsymbol{\Sigma}}^{n+1} &= \mathrm{F}_3^{n+1} \rightarrow \tilde{\mathrm{P}}^{n+1}.
\end{aligned}$$

L-matrix associated:

$$L^* = \begin{bmatrix}
\frac{1}{\delta t} M_{\boldsymbol{u}} + K_{\boldsymbol{u}} \left(\tilde{\mathbf{U}}^{n+1} \right) & 0 & 0 \\
-S & \frac{1}{\delta t} M_{\boldsymbol{\sigma}} + K_{\boldsymbol{\sigma}} \left(\tilde{\mathbf{U}}^{n+1} \right) & 0 \\
-D & -\delta t D M_{\boldsymbol{u}}^{-1} D_\sigma & \delta t D M_{\boldsymbol{u}}^{-1} G
\end{bmatrix}$$

U-steps:

$$\begin{aligned}
\mathrm{P}^{n+1} &= \tilde{\mathrm{P}}^{n+1} \rightarrow \mathrm{P}^{n+1}, \\
\boldsymbol{\Sigma}^{n+1} &= \tilde{\boldsymbol{\Sigma}}^{n+1} \rightarrow \boldsymbol{\Sigma}^{n+1}, \\
\mathbf{U}^{n+1} + \delta t M_{\boldsymbol{u}}^{-1} G \mathrm{P}^{n+1} - \delta t M_{\boldsymbol{u}}^{-1} D_\sigma \boldsymbol{\Sigma}^{n+1} &= \tilde{\mathbf{U}}^{n+1} \rightarrow \mathbf{U}^{n+1}.
\end{aligned}$$

U-matrix associated:

$$U^* = \begin{bmatrix}
\boldsymbol{I} & -\delta t M_{\boldsymbol{u}}^{-1} D_\sigma & \delta t M_{\boldsymbol{u}}^{-1} G \\
0 & \boldsymbol{I} & 0 \\
0 & 0 & I
\end{bmatrix}$$

Approximate resultant matrix ($L^* U^* = A^*$):

$$A^* = \begin{bmatrix}
\frac{1}{\delta t} M_{\boldsymbol{u}} + K_{\boldsymbol{u}} \left(\tilde{\mathbf{U}}^{n+1} \right) & -D_\sigma - \delta t K_{\boldsymbol{u}} \left(\tilde{\mathbf{U}}^{n+1} \right) M_{\boldsymbol{u}}^{-1} D_\sigma & G + \delta t K_{\boldsymbol{u}} \left(\tilde{\mathbf{U}}^{n+1} \right) M_{\boldsymbol{u}}^{-1} G \\
-S & \frac{1}{\delta t} M_{\boldsymbol{\sigma}} + K_{\boldsymbol{\sigma}} \left(\tilde{\mathbf{U}}^{n+1} \right) + \delta t S M_{\boldsymbol{u}}^{-1} D_\sigma & -\delta t S M_{\boldsymbol{u}}^{-1} G \\
-D & 0 & 0
\end{bmatrix}$$

Splitting error matrix ($E^* = A - A^*$):

$$E^* = \begin{bmatrix}
0 & \delta t K_{\boldsymbol{u}} \left(\tilde{\mathbf{U}}^{n+1} \right) M_{\boldsymbol{u}}^{-1} D_\sigma & -\delta t K_{\boldsymbol{u}} \left(\tilde{\mathbf{U}}^{n+1} \right) M_{\boldsymbol{u}}^{-1} G \\
0 & -\delta t S M_{\boldsymbol{u}}^{-1} D_\sigma & \delta t S M_{\boldsymbol{u}}^{-1} G \\
0 & 0 & 0
\end{bmatrix}$$

Algorithm 4.4 Inexact factorization second order fractional step method.

L-steps:

$$\begin{aligned}
\frac{1}{\gamma_2\delta t}M_{\boldsymbol{u}}\delta\tilde{\mathbf{U}}^{n+1}+K_{\boldsymbol{u}}\left(\tilde{\mathbf{U}}^{n+1}\right)\delta\tilde{\mathbf{U}}^{n+1} =& \mathbf{F}_1^{n+1}-\frac{1}{\gamma_2\delta t}M_{\boldsymbol{u}}\mathbf{U}^n-K_{\boldsymbol{u}}\left(\tilde{\mathbf{U}}^{n+1}\right)\mathbf{U}^n\\
&-G\mathrm{P}^n+D_{\boldsymbol{\sigma}}\boldsymbol{\Sigma}^n\rightarrow\delta\tilde{\mathbf{U}}^{n+1},\\
\frac{1}{\gamma_2\delta t}M_{\boldsymbol{\sigma}}\delta\tilde{\boldsymbol{\Sigma}}^{n+1}+K_{\boldsymbol{\sigma}}\left(\tilde{\mathbf{U}}^{n+1}\right)\delta\tilde{\boldsymbol{\Sigma}}^{n+1}-S\delta\tilde{\mathbf{U}}^{n+1} =& \mathbf{F}_2^{n+1}-\frac{1}{\gamma_2\delta t}M_{\boldsymbol{\sigma}}\boldsymbol{\Sigma}^n-K_{\boldsymbol{\sigma}}\left(\tilde{\mathbf{U}}^{n+1}\right)\boldsymbol{\Sigma}^n\\
&+S\mathbf{U}^n\rightarrow\delta\tilde{\boldsymbol{\Sigma}}^{n+1},\\
-D\delta\tilde{\mathbf{U}}^{n+1}+\gamma_2\delta tDM_{\boldsymbol{u}}^{-1}G\delta\tilde{\mathrm{P}}^{n+1}-\gamma_2\delta tDM_{\boldsymbol{u}}^{-1}D_\sigma\delta\tilde{\boldsymbol{\Sigma}}^{n+1} =& \mathrm{F}_3^{n+1}+D\mathbf{U}^n\rightarrow\delta\tilde{\mathrm{P}}^{n+1}.
\end{aligned}$$

L-matrix associated:

$$L^*=\begin{bmatrix}
\frac{1}{\gamma_2\delta t}M_{\boldsymbol{u}}+K_{\boldsymbol{u}}\left(\tilde{\mathbf{U}}^{n+1}\right) & 0 & 0\\
-S & \frac{1}{\gamma_2\delta t}M_{\boldsymbol{\sigma}}+K_{\boldsymbol{\sigma}}\left(\tilde{\mathbf{U}}^{n+1}\right) & 0\\
-D & -\gamma_2\delta tDM_{\boldsymbol{u}}^{-1}D_\sigma & \gamma_2\delta tDM_{\boldsymbol{u}}^{-1}G
\end{bmatrix}$$

U-steps:

$$\begin{aligned}
\delta\mathrm{P}^{n+1}=\delta\tilde{\mathrm{P}}^{n+1}&\rightarrow\delta\mathrm{P}^{n+1},\\
\left(\boldsymbol{I}-\left(\gamma_2\delta t\right)^2\left(M_{\boldsymbol{\sigma}}^{-1}S\right)\left(M_{\boldsymbol{u}}^{-1}D_\sigma\right)\right)\delta\boldsymbol{\Sigma}^{n+1}+\left(\gamma_2\delta t\right)^2\left(M_{\boldsymbol{\sigma}}^{-1}S\right)\left(M_{\boldsymbol{u}}^{-1}G\right)\delta\mathrm{P}^{n+1}&=\delta\tilde{\boldsymbol{\Sigma}}^{n+1}\rightarrow\delta\boldsymbol{\Sigma}^{n+1},\\
\delta\mathbf{U}^{n+1}+\gamma_2\delta tM_{\boldsymbol{u}}^{-1}G\delta\mathrm{P}^{n+1}-\gamma_2\delta tM_{\boldsymbol{u}}^{-1}D_\sigma\delta\boldsymbol{\Sigma}^{n+1}&=\delta\tilde{\mathbf{U}}^{n+1}\rightarrow\delta\mathbf{U}^{n+1}.
\end{aligned}$$

U-matrix associated:

$$U^*=\begin{bmatrix}
\boldsymbol{I} & -\gamma_2\delta tM_{\boldsymbol{u}}^{-1}D_\sigma & \gamma_2\delta tM_{\boldsymbol{u}}^{-1}G\\
0 & \left(\boldsymbol{I}-\left(\gamma_2\delta t\right)^2\left(M_{\boldsymbol{\sigma}}^{-1}S\right)\left(M_{\boldsymbol{u}}^{-1}D_\sigma\right)\right) & \left(\gamma_2\delta t\right)^2\left(M_{\boldsymbol{\sigma}}^{-1}S\right)\left(M_{\boldsymbol{u}}^{-1}G\right)\\
0 & 0 & I
\end{bmatrix}$$

Approximate resultant matrix ($L^*U^*=A^*$):

$$A^*=\begin{bmatrix}
\frac{1}{\gamma_2\delta t}M_{\boldsymbol{\sigma}}+K_{\boldsymbol{\sigma}}\left(\tilde{\mathbf{U}}^{n+1}\right) & -D_\sigma-\gamma_2\delta tK_{\boldsymbol{u}}\left(\tilde{\mathbf{U}}^{n+1}\right)M_{\boldsymbol{u}}^{-1}D_\sigma & G+\gamma_2\delta tK_{\boldsymbol{u}}\left(\tilde{\mathbf{U}}^{n+1}\right)M_{\boldsymbol{u}}^{-1}G\\
-S & A_{22}^* & A_{23}^*\\
-D & A_{32}^* & A_{33}^*
\end{bmatrix}$$

with the following components

$$\begin{aligned}
A_{22}^*=&\frac{1}{\gamma_2\delta t}M_{\boldsymbol{\sigma}}+K_{\boldsymbol{\sigma}}\left(\tilde{\mathbf{U}}^{n+1}\right)-\left(\gamma_2\delta t\right)^2K_{\boldsymbol{\sigma}}\left(\tilde{\mathbf{U}}^{n+1}\right)\left(M_{\boldsymbol{\sigma}}^{-1}S\right)\left(M_{\boldsymbol{u}}^{-1}D_\sigma\right)\\
A_{23}^*=&\left(\gamma_2\delta t\right)^2K_{\boldsymbol{\sigma}}\left(\tilde{\mathbf{U}}^{n+1}\right)\left(M_{\boldsymbol{\sigma}}^{-1}S\right)\left(M_{\boldsymbol{u}}^{-1}G\right)\\
A_{32}^*=&\left(\gamma_2\delta t\right)^3\left(DM_{\boldsymbol{u}}^{-1}D_\sigma\right)\left(M_{\boldsymbol{\sigma}}^{-1}S\right)\left(M_{\boldsymbol{u}}^{-1}D_\sigma\right)\\
A_{33}^*=&-\left(\gamma_2\delta t\right)^3\left(DM_{\boldsymbol{u}}^{-1}D_\sigma\right)\left(M_{\boldsymbol{\sigma}}^{-1}S\right)\left(M_{\boldsymbol{u}}^{-1}G\right)
\end{aligned}$$

Splitting error matrix ($E^*=A-A^*$):

$$E^*=\begin{bmatrix}
0 & \gamma_2\delta tK_{\boldsymbol{u}}\left(\tilde{\mathbf{U}}^{n+1}\right)M_{\boldsymbol{u}}^{-1}D_\sigma & -\gamma_2\delta tK_{\boldsymbol{u}}\left(\tilde{\mathbf{U}}^{n+1}\right)M_{\boldsymbol{u}}^{-1}G\\
0 & \left(\gamma_2\delta t\right)^2K_{\boldsymbol{\sigma}}\left(\tilde{\mathbf{U}}^{n+1}\right)\left(M_{\boldsymbol{\sigma}}^{-1}S\right)\left(M_{\boldsymbol{u}}^{-1}D_\sigma\right) & -\left(\gamma_2\delta t\right)^2K_{\boldsymbol{\sigma}}\left(\tilde{\mathbf{U}}^{n+1}\right)\left(M_{\boldsymbol{\sigma}}^{-1}S\right)\left(M_{\boldsymbol{u}}^{-1}G\right)\\
0 & -\left(\gamma_2\delta t\right)^3\left(DM_{\boldsymbol{u}}^{-1}D_\sigma\right)\left(M_{\boldsymbol{\sigma}}^{-1}S\right)\left(M_{\boldsymbol{u}}^{-1}D_\sigma\right) & \left(\gamma_2\delta t\right)^3\left(DM_{\boldsymbol{u}}^{-1}D_\sigma\right)\left(M_{\boldsymbol{\sigma}}^{-1}S\right)\left(M_{\boldsymbol{u}}^{-1}G\right)
\end{bmatrix}$$

Algorithm 4.5 Inexact factorization third order fractional step method.

L-steps:

$$\begin{aligned}
\frac{1}{\gamma_3\delta t}M_{\boldsymbol{u}}\delta\tilde{\mathbf{U}}^{n+1}+K_{\boldsymbol{u}}\left(\tilde{\mathbf{U}}^{n+1}\right)\delta\tilde{\mathbf{U}}^{n+1} &= \mathbf{F}_1^{n+1}-\frac{1}{\gamma_3\delta t}M_{\boldsymbol{u}}\mathbf{U}^n-K_{\boldsymbol{u}}\left(\tilde{\mathbf{U}}^{n+1}\right)\mathbf{U}^n \\
&\quad -G\mathrm{P}^n+D_{\boldsymbol{\sigma}}\boldsymbol{\Sigma}^n\rightarrow\delta\tilde{\mathbf{U}}^{n+1}, \\
\frac{1}{\gamma_3\delta t}M_{\boldsymbol{\sigma}}\delta\tilde{\boldsymbol{\Sigma}}^{n+1}+K_{\boldsymbol{\sigma}}\left(\tilde{\mathbf{U}}^{n+1}\right)\delta\tilde{\boldsymbol{\Sigma}}^{n+1}-S\delta\tilde{\mathbf{U}}^{n+1} &= \mathbf{F}_2^{n+1}-\frac{1}{\gamma_3\delta t}M_{\boldsymbol{\sigma}}\boldsymbol{\Sigma}^n \\
&\quad -K_{\boldsymbol{\sigma}}\left(\tilde{\mathbf{U}}^{n+1}\right)\boldsymbol{\Sigma}^n+S\mathbf{U}^n\rightarrow\delta\tilde{\boldsymbol{\Sigma}}^{n+1}, \\
-D\delta\tilde{\mathbf{U}}^{n+1}+\gamma_3\delta tDM_{\boldsymbol{u}}^{-1}G\delta\tilde{\mathrm{P}}^{n+1}-\gamma_3\delta tDM_{\boldsymbol{u}}^{-1}D_\sigma\delta\tilde{\boldsymbol{\Sigma}}^{n+1} &= \mathrm{F}_3^{n+1}+D\mathbf{U}^n\rightarrow\delta\tilde{\mathrm{P}}^{n+1},
\end{aligned}$$

L-matrix associated:

$$L^*=\begin{bmatrix} C_{\boldsymbol{u}} & 0 & 0 \\ -S & C_{\boldsymbol{\sigma}} & 0 \\ -D & -\gamma_3\delta tDM_{\boldsymbol{u}}^{-1}D_\sigma & \gamma_3\delta tDM_{\boldsymbol{u}}^{-1}G \end{bmatrix}.$$

U-steps:

$$\begin{aligned}
\delta\mathrm{P}^{n+1}=\delta\tilde{\mathrm{P}}^{n+1}&\rightarrow\delta\mathrm{P}^{n+1}, \\
\left[\boldsymbol{I}-(\gamma_3\delta t)^2\left(M_{\boldsymbol{\sigma}}^{-1}S\right)\left(M_{\boldsymbol{u}}^{-1}D_\sigma\right)\right]\delta\boldsymbol{\Sigma}^{n+1}+(\gamma_3\delta t)^2\left(M_{\boldsymbol{\sigma}}^{-1}S\right)\left(M_{\boldsymbol{u}}^{-1}G\right)\delta\mathrm{P}^{n+1}&=\delta\tilde{\boldsymbol{\Sigma}}^{n+1}\rightarrow\delta\boldsymbol{\Sigma}^{n+1}, \\
\delta\mathbf{U}^{n+1}+\left[\frac{1}{\gamma_3\delta t}M_{\boldsymbol{u}}+K_{\boldsymbol{u}}\left(\tilde{\mathbf{U}}^{n+1}\right)\right]^{-1}G\delta\mathrm{P}^{n+1}& \\
-\left[\frac{1}{\gamma_3\delta t}M_{\boldsymbol{u}}+K_{\boldsymbol{u}}\left(\tilde{\mathbf{U}}^{n+1}\right)\right]^{-1}D_\sigma\delta\boldsymbol{\Sigma}^{n+1}&=\delta\tilde{\mathbf{U}}^{n+1}\rightarrow\delta\mathbf{U}^{n+1},
\end{aligned}$$

where

$$C_{\boldsymbol{u}}=\frac{1}{\gamma_3\delta t}M_{\boldsymbol{u}}+K_{\boldsymbol{u}}\left(\tilde{\mathbf{U}}^{n+1}\right)\text{ and }C_{\boldsymbol{\sigma}}=\frac{1}{\gamma_3\delta t}M_{\boldsymbol{\sigma}}+K_{\boldsymbol{\sigma}}\left(\tilde{\mathbf{U}}^{n+1}\right).$$

U-matrix associated:

$$U^*=\begin{bmatrix} \boldsymbol{I} & -C_{\boldsymbol{u}}^{-1}D_\sigma & C_{\boldsymbol{u}}^{-1}G \\ 0 & \left(\boldsymbol{I}-(\gamma_3\delta t)\left(M_{\boldsymbol{\sigma}}^{-1}S\right)\left(C_{\boldsymbol{u}}^{-1}D_\sigma\right)\right) & (\gamma_3\delta t)\left(M_{\boldsymbol{\sigma}}^{-1}S\right)\left(C_{\boldsymbol{u}}^{-1}G\right) \\ 0 & 0 & I \end{bmatrix}.$$

Approximate resultant matrix($L^*U^*=A^*$):

$$A^*=\begin{bmatrix} C_{\boldsymbol{u}} & -D_\sigma & G \\ -S & C_{\boldsymbol{\sigma}}-(\delta t_3)^2\left(K_{\boldsymbol{\sigma}}\left(\tilde{\mathbf{U}}^{n+1}\right)M_{\boldsymbol{\sigma}}^{-1}S\right)\left(M_{\boldsymbol{u}}^{-1}D_\sigma\right) & (\delta t_3)^2\left(K_{\boldsymbol{\sigma}}\left(\tilde{\mathbf{U}}^{n+1}\right)M_{\boldsymbol{\sigma}}^{-1}S\right)\left(M_{\boldsymbol{u}}^{-1}G\right) \\ -D & (\delta t_3)^3\left(DM_{\boldsymbol{u}}^{-1}D_\sigma\right)\left(M_{\boldsymbol{\sigma}}^{-1}S\right)\left(M_{\boldsymbol{u}}^{-1}D_\sigma\right) & -(\delta t_3)^3\left(DM_{\boldsymbol{u}}^{-1}D_\sigma\right)\left(M_{\boldsymbol{\sigma}}^{-1}S\right)\left(M_{\boldsymbol{u}}^{-1}G\right) \end{bmatrix}.$$

where $\gamma_3\delta t=\delta t_3$ Splitting error matrix ($E^*=A-A^*$):

$$E^*=\begin{bmatrix} 0 & 0 & 0 \\ 0 & (\gamma_3\delta t)^2\left(K_{\boldsymbol{\sigma}}\left(\tilde{\mathbf{U}}^{n+1}\right)M_{\boldsymbol{\sigma}}^{-1}S\right)\left(M_{\boldsymbol{u}}^{-1}D_\sigma\right) & -(\gamma_3\delta t)^2\left(K_{\boldsymbol{\sigma}}\left(\tilde{\mathbf{U}}^{n+1}\right)M_{\boldsymbol{\sigma}}^{-1}S\right)\left(M_{\boldsymbol{u}}^{-1}G\right) \\ 0 & -(\gamma_3\delta t)^3\left(DM_{\boldsymbol{u}}^{-1}D_\sigma\right)\left(M_{\boldsymbol{\sigma}}^{-1}S\right)\left(M_{\boldsymbol{u}}^{-1}D_\sigma\right) & (\gamma_3\delta t)^3\left(DM_{\boldsymbol{u}}^{-1}D_\sigma\right)\left(M_{\boldsymbol{\sigma}}^{-1}S\right)\left(M_{\boldsymbol{u}}^{-1}G\right) \end{bmatrix}.$$

Algorithm 4.6 Stabilized FEM: Inexact factorization third order fractional step method.

L-steps:

$$\begin{aligned}
\frac{1}{\gamma_3\delta t}M_{\boldsymbol{u}}\delta\tilde{\mathbf{U}}^{n+1}+K_{s,\boldsymbol{u}}\left(\tilde{\mathbf{U}}^{n+1}\right)\delta\tilde{\mathbf{U}}^{n+1} &= \mathbf{F}_1^{n+1}-\frac{1}{\gamma_3\delta t}M_{\boldsymbol{u}}\mathbf{U}^n-K_{s,\boldsymbol{u}}\left(\tilde{\mathbf{U}}^{n+1}\right)\mathbf{U}^n\\
&\quad -G\mathrm{P}^n+D_{s,\boldsymbol{\sigma}}\boldsymbol{\Sigma}^n\rightarrow\delta\tilde{\mathbf{U}}^{n+1},\\
\frac{1}{\gamma_3\delta t}M_{s,\boldsymbol{\sigma}}\delta\tilde{\boldsymbol{\Sigma}}^{n+1}+K_{s,\boldsymbol{\sigma}}\left(\tilde{\mathbf{U}}^{n+1}\right)\delta\tilde{\boldsymbol{\Sigma}}^{n+1}-S_s\delta\tilde{\mathbf{U}}^{n+1} &= \mathbf{F}_2^{n+1}-\frac{1}{\gamma_3\delta t}M_{s,\boldsymbol{\sigma}}\boldsymbol{\Sigma}^n\\
&\quad -K_{s,\boldsymbol{\sigma}}\left(\tilde{\mathbf{U}}^{n+1}\right)\boldsymbol{\Sigma}^n+S_s\mathbf{U}^n\rightarrow\delta\tilde{\boldsymbol{\Sigma}}^{n+1},\\
-D\delta\tilde{\mathbf{U}}^{n+1}+\left(\gamma_3\delta tDM_{\boldsymbol{u}}^{-1}G+L_s^{\perp}\right)\delta\tilde{\mathrm{P}}^{n+1} &\\
-\gamma_3\delta tDM_{\boldsymbol{u}}^{-1}D_{s,\boldsymbol{\sigma}}\delta\tilde{\boldsymbol{\Sigma}}^{n+1} &= \mathrm{F}_3^{n+1}+D\mathbf{U}^n-L_s^{\perp}\mathrm{P}^n\rightarrow\delta\tilde{\mathrm{P}}^{n+1}.
\end{aligned}$$

U-steps:

$$\begin{aligned}
\delta\mathrm{P}^{n+1} &= \delta\tilde{\mathrm{P}}^{n+1}\rightarrow\delta\mathrm{P}^{n+1},\\
\left(\boldsymbol{I}-(\gamma_3\delta t)^2\left(M_{s,\boldsymbol{\sigma}}^{-1}S\right)\left(M_{\boldsymbol{u}}^{-1}D_{s,\sigma}\right)\right)\delta\boldsymbol{\Sigma}^{n+1} &\\
+(\gamma_3\delta t)^2\left(M_{s,\boldsymbol{\sigma}}^{-1}S_s\right)\left(M_{\boldsymbol{u}}^{-1}G\right)\delta\mathrm{P}^{n+1} &= \delta\tilde{\boldsymbol{\Sigma}}^{n+1}\rightarrow\delta\boldsymbol{\Sigma}^{n+1},\\
\delta\mathbf{U}^{n+1}+\left(\frac{1}{\gamma_3\delta t}M_{\boldsymbol{u}}+K_{s,\boldsymbol{u}}\left(\tilde{\mathbf{U}}^{n+1}\right)\right)^{-1}G\delta\mathrm{P}^{n+1} &\\
-\left(\frac{1}{\gamma_3\delta t}M_{\boldsymbol{u}}+K_{s,\boldsymbol{u}}\left(\tilde{\mathbf{U}}^{n+1}\right)\right)^{-1}D_{s,\sigma}\delta\boldsymbol{\Sigma}^{n+1} &= \delta\tilde{\mathbf{U}}^{n+1}\rightarrow\delta\mathbf{U}^{n+1}.
\end{aligned}$$

4.6.3 Linearized problem

The equations to be solved in the methods proposed are nonlinear and an iterative scheme is required to deal with this nonlinearity. In the case of the stabilized finite element formulation, it is also important to explain how to treat the orthogonal projections $P_h^\perp$. Let us consider for example the third order method in Algorithm 4.6. The three ingredients we use to design an iterative scheme are the following:

- A fixed-point-type method is used to evaluate all the stabilization terms. They need to be calculated with a known velocity $\boldsymbol{u}_h$, which may taken either as the velocity of the previous iteration of the iterative scheme (the intermediate or the end-of-step one) or as the velocity of the previous time step. This does not affect the order of convergence of the formulation, neither in space nor in time, but only the stability and the nonlinear convergence behavior. We have found effective both choices, and used the former in the numerical examples.

- The nonlinearity in $K_{s,\boldsymbol{\sigma}}(\tilde{\mathbf{U}}^{n+1})\delta\tilde{\mathbf{U}}^{n+1}$ due to the convective term may be treated using either a fixed-point or a Newton-Raphson method. As in any fractional step scheme, δt cannot be taken very large for the method to be effective, compared for example to the critical time step of an explicit time integration scheme. Thus, only a few nonlinear iterations are required and the fixed-point option is usually enough. Note that the term $K_{s,\boldsymbol{\sigma}}\left(\tilde{\mathbf{U}}^{n+1}\right)\delta\tilde{\boldsymbol{\Sigma}}^{n+1}$ does not need to be linearized, as $\tilde{\mathbf{U}}^{n+1}$ is already known when $\delta\tilde{\boldsymbol{\Sigma}}^{n+1}$ needs to be computed.

- The treatment of $P_h^\perp$ deserves a special comment. For any function g, we may compute $P_h^\perp(g)$ as $P_h^\perp(g) = g - P_h(g)$. Matrices resulting from the orthogonal projection of the unknowns have a wider stencil, when compared to that of the Galerkin method. In order to avoid this, at the i-th iteration of the n-th time step we may approximate $P_h^\perp(g^{n,i}) \approx g^{n,i} - P_h(g^{n,i-1})$ or $P_h^\perp(g^{n,i}) \approx g^{n,i} - P_h(g^{n-1})$. Numerical experiments show that both options are effective, the former being chosen in the numerical examples presented next.

4.7 Numerical results

In this section, some numerical tests are conducted to show the numerical performance of the proposed fractional step methods, and to compare them with the monolithic approach. The first example (subsection 4.7.1) is a convergence test with a manufactured solution to check the time integration errors associated with each of the fractional steps algorithms. The second example (subsection 4.7.2) is the typical flow over a confined cylinder, which serves to show that the proposed methods converge accurately to a steady state solution. Finally, in subsection 4.7.3 we present the numerical results of a dynamic lid-driven cavity flow problem in 2D and 3D, and we discuss the efficiency of the stabilized fractional step methods. In all cases, either linear (P_1) or multilinear (Q_1) elements are used, and the same continuous interpolation is employed for all variables. All the results are obtained using the proposed fractional step methods and the stabilized formulation presented in Section 4.6.

The geometry of the viscoelastic fluid flow past a confined cylinder in a channel problem is shown in Fig. 4.1, whereas the unstructured mesh used to discretize this domain with linear triangles is shown in Fig. 4.2. For the lid-driven cavity problem, the geometry and the mesh, formed by bi-linear elements in 2D and by tri-linear elements in 3D, are presented in Fig. 4.3 for the 2D case and in Fig. 4.4 for the 3D case.

In all the numerical examples the discrete and linearized problem is solved by using an iterative solver based on the BiCGStab (Stabilized version of BiConjugate Gradient Squared)

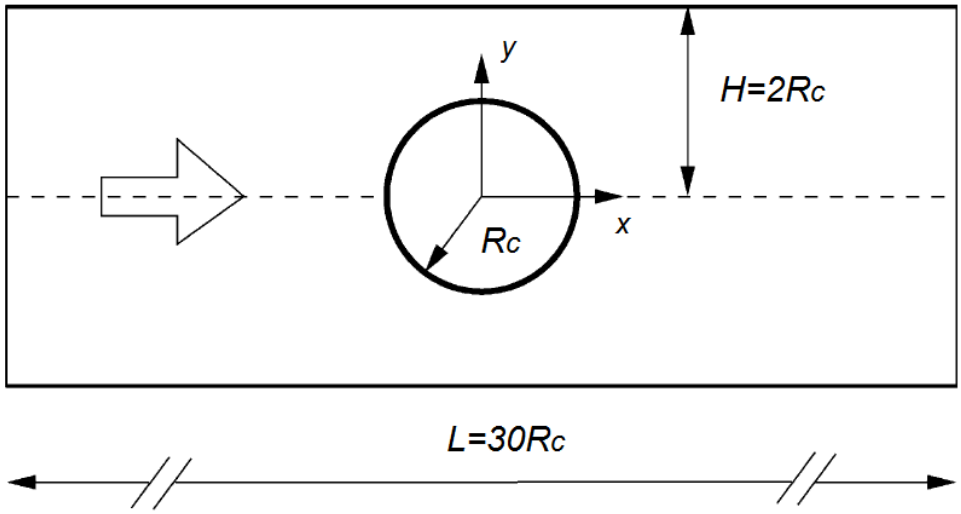

Figure 4.1: Schematic representation of the flow past a cylinder.

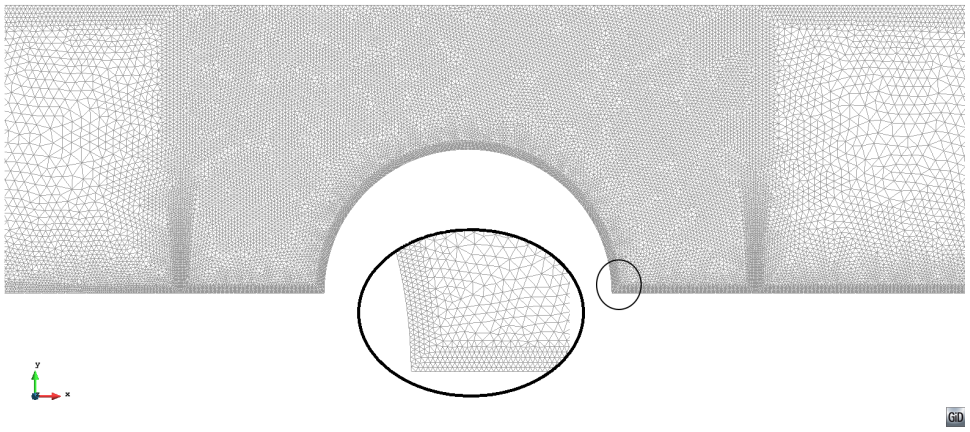

Figure 4.2: Computational mesh (M2) used in the flow past a cylinder.

method of van der Vorst [165], with the additive Schwarz preconditioner. The version of the second and third order splitting schemes used is the one presented in Algortihms 4.1 (for $k = 2$) and 4.2.

4.7.1 Convergence test

In this first example we consider a simple convergence test whose goal is to check numerically the rate of convergence in time for the three proposed fractional step algorithms. We recall that as time integration scheme we use backward differences, of the same order as the fractional step to be tested.

The computational domain is the unit square, discretized using a uniform triangular mesh with 2500 linear elements. The boundary and initial conditions and the force term are prescribed so that the analytical solution is given by:

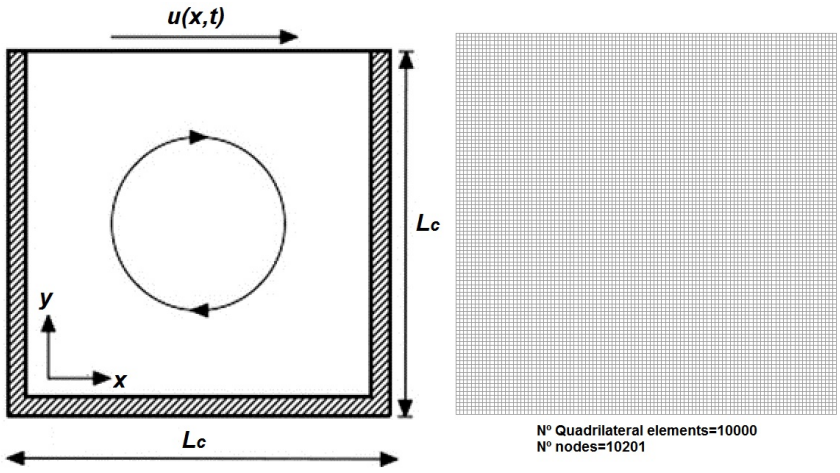

Figure 4.3: Schematic representation of the 2D lid-driven cavity flow problem.

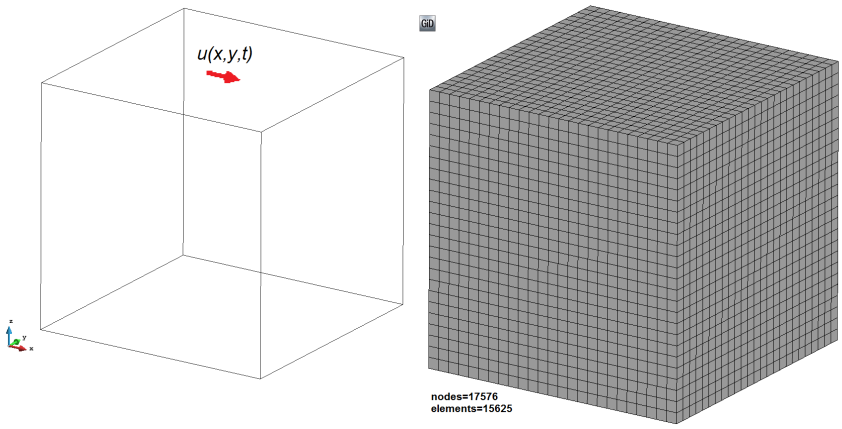

Figure 4.4: Schematic representation of the 3D lid-driven cavity flow problem.

$$
\begin{aligned}
u_x(x,y) &= (4x+6)\, f(t)\,, & u_y(x,y) &= -(4y-6)\, f(t)\,,\\
\sigma_{xx}(x,y) &= (2x+3)\, f(t)\,, & \sigma_{xy}(x,y) &= (x+y)\, f(t)\,,\\
\sigma_{yy}(x,y) &= (2y+3)\, f(t)\,, & p(x,y) &= x,
\end{aligned}
$$

with $f(t) = \cos(4\pi t)\exp(-t)$ and subscripts x and y referring to the Cartesian axes. Obviously these velocity and elastic stress fields do not satisfy the constitutive equation (6.4) with a zero right-hand-side. We have added a forcing term in this equation given by

$$
\boldsymbol{f}_c = \frac{1}{2\eta_0}\boldsymbol{\sigma} - (1-\beta)\nabla^s\boldsymbol{u} + \frac{\lambda}{2\eta_0}\left(\frac{\partial\boldsymbol{\sigma}}{\partial t} + \boldsymbol{u}\cdot\nabla\boldsymbol{\sigma} - \boldsymbol{\sigma}\cdot\nabla\boldsymbol{u} - (\nabla\boldsymbol{u})^T\boldsymbol{\sigma}\right) \text{ in } \Omega.
$$

Similarly, the force term in the momentum equation is computed so that the solution is the one given above.

Note that for each time t the exact solution belongs to the finite element space, and thus the only source of numerical error is the time discretization, avoiding this way the possibility

of a mix of space and time errors. The stabilized finite element formulation used in this chapter was already tested in chapter 3 (also in [37]) for the stationary problem using linear and quadratic elements, and it is not the objective of this part of the work to test it again, but to check the performance of the fractional step schemes we propose.

Results are shown in Fig. 4.5. The error E is measured in two different norms, $\ell^\infty(L^2(\Omega))$ (maximum of the sequence of spatial L^2-norms of the solution) and $\ell^2(H^1(\Omega))$ (ℓ^2-norm of the sequence of spatial H^1-norms of the solutions). It is seen that the three methods show the expected rate of convergence. In all cases shown in Fig. 4.5 we use the same nomenclature: Linf(L2)z corresponds to the $\ell^\infty(L^2(\Omega))$-error, where z represents the measured variable, L2(H1)z corresponds to the $\ell^2(H^1(\Omega))$-error and P_i, $i = 1, 2, 3$, is the reference line with slope equal to i in logarithmic scale.

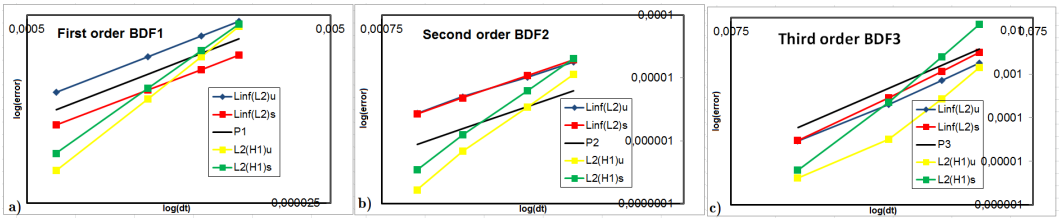

Figure 4.5: Converge test: a) First order scheme, b) Second order scheme and c) third order scheme.

4.7.2 Viscoelastic fluid flow past a confined cylinder in a channel

The flow over a cylinder is a classical benchmark to prove the accuracy of new formulations in viscoelastic fluid flows. We use it here to check the behavior of the proposed fractional step methods to reach a steady state. Note that this steady state has also an error of the order of the scheme itself, it is not independent of the time step size δt.

Let us describe the boundary conditions of the problem. For the velocity, no-slip conditions are imposed on the top wall $y = H$, and symmetry conditions are prescribed along the axis $y = 0$, which in this case means that the y-velocity is set to zero. A fully developed parabolic velocity profile and the associated elastic stress profile are prescribed at the inlet $y = 0$. These are given by

$$u_x = \frac{3Q}{2R_c}\left(1 - \frac{y^2}{(2R_c)^2}\right), \qquad u_y = 0,$$
$$\sigma_{xx} = 2\lambda\,(1-\beta)\,\eta_0\left(\frac{\partial u_x}{\partial y}\right)^2, \qquad \sigma_{xy} = (1-\beta)\,\eta_0\left(\frac{\partial u_x}{\partial y}\right), \qquad \sigma_{yy} = 0,$$

where Q is the flow rate, taken as $Q = 1$, $\eta_0 = 1$, $\beta = 0.59$ and R_c is the cylinder radius. For the outlet, the horizontal velocity is left free, the vertical velocity is taken equal to zero and the pressure is prescribed to zero, constant. The boundary term that comes from integration by parts of the divergence of the elastic stress, and that now is not zero on the outlet because the test function is not zero there, is evaluated using the elastic stresses of the time step previous to the one in which the solution is computed.

As initial condition, we start with a Newtonian ($\lambda = 0$) stationary solution, and then we solve the problem for different increasing Weissenberg numbers We $= \lambda U/L_0$ (U characteristic velocity, taken as $U = 3Q/2R_c$, L_0 characteristic length of the problem, taken as $L_0 = R_c$). The initial condition for one case is taken as the stationary solution of the previous

one. In all the calculations, the convective term in the momentum equation is neglected, the standard option in this benchmark problem.

In viscoelastic fluids the high Weissenberg number problem (HWNP) has been the major stumbling block in computational rheology for the last decades. The term HWNP refers to the empirical observation that all numerical methods break down when the Weissenberg number exceeds a critical value. The precise critical value at which computations break down varies with the problem (including the constitutive model), the method and the mesh used [99].

The viscoelastic problem can be solved using the standard constitutive equation given by (6.4) or a log-conformation formulation, permitting the latter to solve fluids with higher elasticity. In this work we use the former, but the log-conformation formulation could also be used with the fractional step schemes we have presented. Using (6.4), in the literature one finds important differences in the obtention of drag coefficient values in fluids with We > 0.6. In [4] the authors solve the flow over a cylinder problem with the simplest upwind differencing scheme (UDS) and with high order resolution schemes (SMART and MINMOD) to evaluate the elastic stress derivatives in the constitutive equation. A finite volume formulation is employed in that work. The authors find that the UDS fails to obtain converged solutions for We > 0.43 on fine meshes, whereas they could go up to We $= 1.5$ using "moderate" meshes (mesh M60 in that article). Using the high resolution schemes the authors found more accuracy, but a lower range of working values of Weissenberg numbers (We ≤ 1.0). In general, what can be found in the literature is that standard formulations can solve the problem for We up to a value between 0.7 and 1.0, depending on the reference [4, 56, 103], whereas the log-conformation formulation allows one to obtain solutions for We up to a value between 2.0 and 2.5, depending on the source [69, 99, 2]. In all cases mentioned, the Oldroyd-B constitutive model is used and the width of the channel is twice the radius of the cylinder. Using our formulations, we have been able to solve the problem up to We $= 1.3$, both using the second order and the third order fractional step schemes we have proposed.

We have used three meshes in order to check the independency of the results with respect to the spatial approximation. The number of elements and nodes and the minimum element size $h_{\min}$ of these meshes are detailed in Table 4.1. All the results to be presented have been computed with mesh M2, unless otherwise stated.

Mesh	Nodes	Elements	$h_{\min}$
M1	21330	41514	0.025
M2	29152	56905	0.015
M3	35167	67856	0.005

Table 4.1: Meshes used in the flow over a cylinder problem.

In Fig.4.6, the drag coefficients obtained with our formulations are compared with the values that can be found in the literature [99, 4, 69, 73]. The agreement is good up to We $= 1.0$, with differences lower than 1% with respect to the accepted values of reference, both for the second and for the third order fractional step methods. For more elastic cases the differences with respect to the log-conformation approach begin to increase, which is possibly associated to the HWNP. The results obtained with meshes M1 and M2 are very close.

Table 4.2 presents some published drag coefficients and the values obtained in the present work with the second and third order fractional step schemes. It is important to note that in some cases the references use the log-conformation elastic stress tensor formulation, and are identified with the label "log". In [2] the authors use the standard and the log-conformation formulation to solve the same problem using a finite volume method. With our formulations the problem can be solved with the same accuracy as the high order finite volume methods

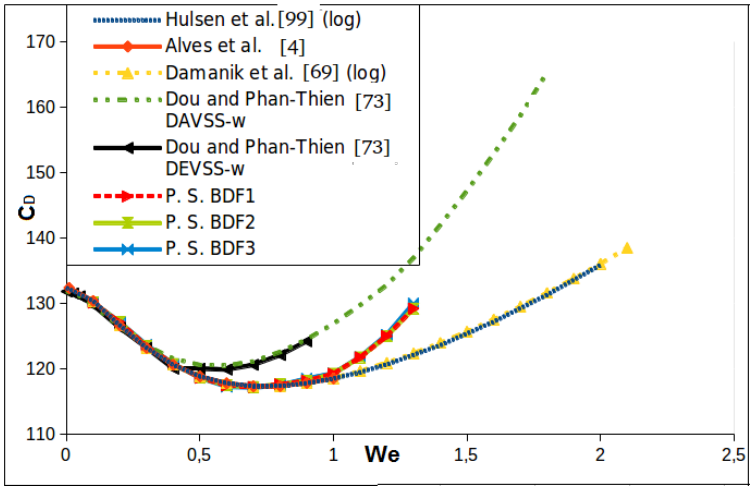

Figure 4.6: Drag coefficient validation.

(SMART and MINMOD), but with the possibility to solve more elastic cases. However, for We > 1.0 the accuracy could be questioned, as we have seen.

We	[4]	[99] (log)	[2]	[2] (log)	P. S. BDF2-M2	P. S. BDF3-M2
0.1	130.355	130.363	–	–	130.1	130.128
0.2	126.632	126.626	–	–	127.01	127.003
0.3	123.210	123.193	–	–	123.48	123.437
0.4	120.607	120.596	–	–	120.74	120.742
0.5	118.838	118.836	118.821	118.818	118.626	118.598
0.6	117.797	117.792	117.776	117.774	117.438	117.446
0.7	117.323	117.340	117.324	117.323	117.222	117.229
0.8	117.357	117.373	117.370	117.364	117.62	117.504
0.9	117.851	117.787	not solved	117.817	118.15	118.28
1.0	118.518	118.501	not solved	118.680	119.25	119.27
1.1	not solved	119.466	not solved	119.780	122.07	121.8
1.2	not solved	120.650	not solved	121.051	125.02	125.2
1.3	not solved	–	not solved	–	129.2	130.02
1.4	not solved	123.801	not solved	124.092	not solved	not solved

Table 4.2: Drag force coefficient for the flow over a confined cylinder.

In terms of the elastic stress convergence for We ≥ 0.7, significant discrepancies are encountered among the results found in the literature (see [2] and references therein), especially in the maximum peak of normal elastic stresses at the rear of the wake. In Fig. 4.7, we show a comparison of the elastic stress profile of the component σ_{xx} along the cylinder wall and downstream the plane $y = 0$ that we obtained against other published results (once again, results obtained with the log-conformation formulation are labelled "log"). For the We $= 0.6$ case the agreement with the reported values is very good independently of the used mesh. For the others two cases, the results of the mesh M3 are also presented, showing a better approximation to the log-conformation formulations, especially in the wake region of the cylinder. A similar behavior was reported by Alves et al. in [4] using an extremely refined mesh behind the cylinder. Is important to note that the drag coefficients presented above are practically identical using the mesh M2 or the mesh M3. In [99] the authors do not find

any sign of convergence of the elastic stress in the wake beyond the cylinder as the mesh is refined, even using the log-conformation formulation and the Oldroyd-B model for We ≈ 1.0. The authors relate this phenomenon to the behavior of the constitutive model, which models an unlimited extension of the fluid at finite extension rates.

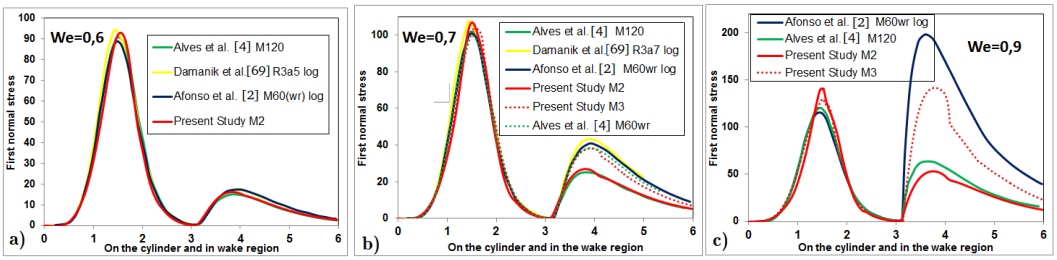

Figure 4.7: Stress profile along the cylinder wall and downstream the plane $y = 0$ for: a) We $= 0.6$, b) We $= 0.7$ and c) $\mathrm{W_e} = 0.9$.

Fig. 4.8 shows the contour lines for the We $= 1.3$ case of velocity, pressure and elastic stress. The convective nature of the constitutive equation can be appreciated clearly. Furthermore, no oscillations appear, neither in pressure nor in elastic stress components, which are the most difficult results to obtain in this problem.

4.7.3 Lid-driven cavity flow problem

4.7.3.1 2D cavity

A viscoelastic fluid can exhibit quite different flow behavior from a Newtonian one in many aspects, such as rod climbing, siphoning, and secondary flows. The elastic stresses of the viscoelastic fluid depend not only on the actual stresses, but also on all the stresses to which they have been subjected during their previous deformation history. The lid-driven cavity flow is a clear example of the differences that can be generated by the viscoelastic contribution in the fluid, even in non-inertial (Stokes) flows.

In the following example, the fluid is confined in the unit square $[0, 1]^2$, bounded by solid walls, with the top boundary moving to the x^+ axis. For Newtonian fluids, a discontinuity of the flow field at the upper corners causes the pressure to diverge, without affecting the well-posedness of the problem. A viscoelastic fluid cannot sustain deformations at a stagnation point, and therefore the motion of the lid needs to be smooth, so that $\nabla \boldsymbol{u}$ vanishes at the corners [81]. To satisfy this condition, we use the following horizontal velocity profile at the lid of the cavity ($y = 1$) as boundary condition for the velocity [81, 130]:

$$u_x(x, 1, t) = 8\left[1 + \tanh\left(8\left(t - 0.5\right)\right)\right] x^2 \left(1 - x\right)^2 .$$

Function $1 + \tanh(8(t - 0.5))$ has a smooth transition, being almost zero at $t = 0$ and growing rapidly up to two. The lid velocity attains its maximum ($u_x = 1$) at the center of the wall ($x = 0.5$). The inflow boundary conditions for the elastic stress tensor are not needed since there is no inflow boundary in this problem.

In Table 4.3 the location of the primary vortex of the Stokes viscoelastic flow that we have obtained is compared with the result published in [130]. In this reference the authors use the log-conformation tensor instead of the elastic stress tensor with a first order accurate operator-splitting technique to solve the system of equations in a finite element formulation. In our results the mesh used for all the cases is a structured mesh with 10000 (100×100) bilinear elements (Q_1), with a constant time step $\delta t = 0.0025$.

	Pan et al. [130]	Present study
We	(x, y)	(x, y)
0.0	–	$(0.50, 0.765)$
0.5	$(0.4692383, 0.7981873)$	$(0.47, 0.80)$
1.0	$(0.4395693, 0.8159704)$	$(0.44, 0.82)$
1.5	–	$(0.41, 0.83)$

Table 4.3: Vortex location in lid driven cavity problem.

The lid-driven cavity flow problem without inertia leads to a symmetrical horizontal location of the vortex for a Newtonian fluid. From Table 4.3 one can see how the symmetry is broken when the Weissenberg number is increased. It is observed that the vortex is displaced in the direction opposite to the one expected when we increase the Reynolds number in a flow with inertia.

The cases considered so far yield stationary solutions, even for higher values of the Weissenberg number [81]. We have started with them to compare our results with those existing in the literature. In order to solve a truly dynamic problem, we force the lid velocity to be time dependent. In particular, let us consider now that it is given by

$$u_x(x, 1, t) = 16x^2 (1 - x)^2 \sin(\pi t) .$$

Using this lid velocity we obtain again a smooth initial boundary condition, as well as a time dependent behavior. The time interval used in all the simulations presented next is $[0, 2]$, which represents a complete period in the boundary condition. The time step size has been taken as $\delta t = 0.0025$.

We wish to compare now the performance of the monolithic time integration against the fractional step methods we have proposed, particularly in terms of CPU time. We take the Weissenberg number $\mathrm{We} = 1$ and two values of the Reynolds number, $\mathrm{Re} = UL_0/\beta\eta_0 = 1$ (quasi non-inertial case) and $\mathrm{Re} = 100$ (convective case). The characteristic velocity to compute Re and We has been taken as the maximum lid velocity and the characteristic length as $L_0 = 1$. Figs. 4.9 and 4.10 show the flow patterns obtained by the third order fractional step method in the convective case (both the other two fractional step schemes and the monolithic case give practically identical results).

Table 4.4 shows the saves in CPU time of the fractional step algorithms using the different temporal integrators with respect to the monolithic formulation. A simple sequential implementation has been used in all cases. The saves are presented as the quotient between the CPU time of the fractional step scheme over the CPU time of the corresponding monolithic scheme. The mesh used is the same as in the stationary problem.

$\mathrm{M}_1 = 100 \times 100$	FS-BDF1	FS-BDF2	FS-BDF3
$\mathrm{We} = 1.0$, $\mathrm{Re} = 1.0$	0.64	0.57	0.88
$\mathrm{We} = 1.0$, $\mathrm{Re} = 100$	0.338	0.1818	0.2589

Table 4.4: Saves in CPU time of the fractional step schemes over the monolithic formulations.

For the quasi non-inertial problem the saves obtained are not very important, particularly for the third order fractional step scheme. However, these saves are more relevant for the convective case. Apart from the fact that the linear systems to be solved in the fractional step method are smaller, the drawback of the monolithic formulation is that the total number of iterations of the linear system solver is driven by the slowest variable. In fractional step schemes, each variable requires a different number of iterations to solve the corresponding linear system. As for Newtonian flows, the slowest variable in incompressible flows is the

pressure. Table 4.5 illustrates this point. There, $\overline{\text{nni}}$ is the average number of nonlinear iterations and $\overline{\text{nsi}}$ is the average number of solver iterations. Subscripts are used in the fractional step case to identify the variable.

	Monolithic	Fractional-Step		
case	$\overline{\text{nni}}/\overline{\text{nsi}}$	$\overline{\text{nni}}_{\boldsymbol{u}}/\overline{\text{nsi}}_{\boldsymbol{u}}$	$\overline{\text{nni}}_{\boldsymbol{\sigma}}/\overline{\text{nsi}}_{\boldsymbol{\sigma}}$	$\overline{\text{nsi}}_{p}$
We = 1.0, Re = 1.0	13/57	11/2	9/2	108
We = 1.0, Re = 100	22/107	13/3	12/3	115

Table 4.5: Comparison between the number of iterations of the monolithic and of the second order fractional step algorithm using the BDF2 time integrator.

From the information of the Table 4.5 we observe that the number of nonlinear iterations needed for the monolithic approaches is always greater than when using fractional step methods, and that in this last case the number of solver iterations in the momentum and in the constitutive equations is drastically smaller than for the pressure equation, as expected. This fact is a general trend, also encountered in Newtonian flows. Moreover, the subsystems to be solved when using fractional step methods are in general better conditioned, and solvers specifically designed for each of them can be used. Even if in our examples we have used the same solver for all subsystems, specific solvers could be exploited to improve the performance of fractional step schemes.

4.7.3.2 3D cavity

To check the efficiency of fractional step algorithms in the 3D case, we consider now the three-dimensional lid-driven cavity problem, only using the second order algorithm and its monolithic counterpart for the sake of brevity. The problem is an extension of the 2D case presented above, now solved in the unit cube $[0,1]^3$. On the lid $z = 1$ the x-component of the velocity is prescribed to

$$u_x(x, y, 1, t) = 256x^2 \left(1 - x\right)^2 y^2 \left(1 - y\right)^2 \sin\left(\pi t\right),$$

and $u_y = u_z = 0$, whereas $\boldsymbol{u} = \boldsymbol{0}$ is prescribed on the rest of the boundaries. No boundary conditions are required for the elastic stress tensor. Two cases are analyzed, one with Reynolds number Re = 0 (Stokes flow) and the other with Re = 100, and in both cases We = 0.5. The time interval of analysis is $[0, 2]$.

Referring to the numerical discretization, a mesh of 15625 linear hexahedral elements (Q_1) is employed. The time step size has been taken as $\delta t = 0.01$.

The comparison between the monolithic and fractional step methods is made in terms of the total CPU time ($\text{T}_{\text{cputime}}$), the CPU time used to build the algebraic system ($\text{B}_{\text{cputime}}$) and the time needed by the solver ($\text{S}_{\text{cputime}}$), all given in Table 4.6, as well as in terms of the number of iterations needed by the solver to solve the system of equations and by the number of nonlinear iterations used to obtain converged results, which are given in Table 4.7.

	$\text{T}_{\text{cputime}}$	$\text{B}_{\text{cputime}}$	$\text{S}_{\text{cputime}}$
We = 0.5, Re = 0.0	0.2439	0.3817	0.1072
We = 0.5, Re = 100	0.0673	0.156	0.0129

Table 4.6: Saves in CPU time of the fractional step schemes over the monolithic formulations in the 3D case (second order schemes).

	Monolithic	Fractional-Step		
case	$\overline{\text{nni}}/\overline{\text{nsi}}$	$\overline{\text{nni}}_{\boldsymbol{u}}/\overline{\text{nsi}}_{\boldsymbol{u}}$	$\overline{\text{nni}}_{\boldsymbol{\sigma}}/\overline{\text{nsi}}_{\boldsymbol{\sigma}}$	$\overline{\text{nsi}}_p$
We = 0.5, Re = 100	70/36	18/2	17/2	48

Table 4.7: Comparison between the number of iterations of the monolithic and the second order fractional step algorithm in the 3D case.

As for the 2D case, the reduction in the CPU time needed to solve the same problem with respect to the monolithic approach is very important and justifies the design of accurate fractional step algorithms. In terms of the number of iterations needed by each scheme (Table 4.7), the same comments as for the 2D case can be made for this 3D problem. The number of iterations needed by the monolithic method is greater both for the linear solver and for the nonlinear algorithm. Again we can see as the pressure equation is the bottleneck of the problem, with the greatest number of solver iterations, which in the monolithic case delays the convergence of the total system of equations. Likewise, the greater number of nonlinear iterations needed by the monolithic method confirms the better treatment of the nonlinearity when the problem is solved in a decoupled manner.

Fig. 4.11 shows some graphical results of the 3D cavity at time $t = 1.5$. Figs. 4.11a) and 4.11b) show respectively the pressure isolines and the isolines of the σ_{xx} component of the elastic stress tensor. No oscillations appear in neither of these variables. Finally, some streamlines at $t = 2$ are shown in Fig. 4.12 to visualize the flow pattern.

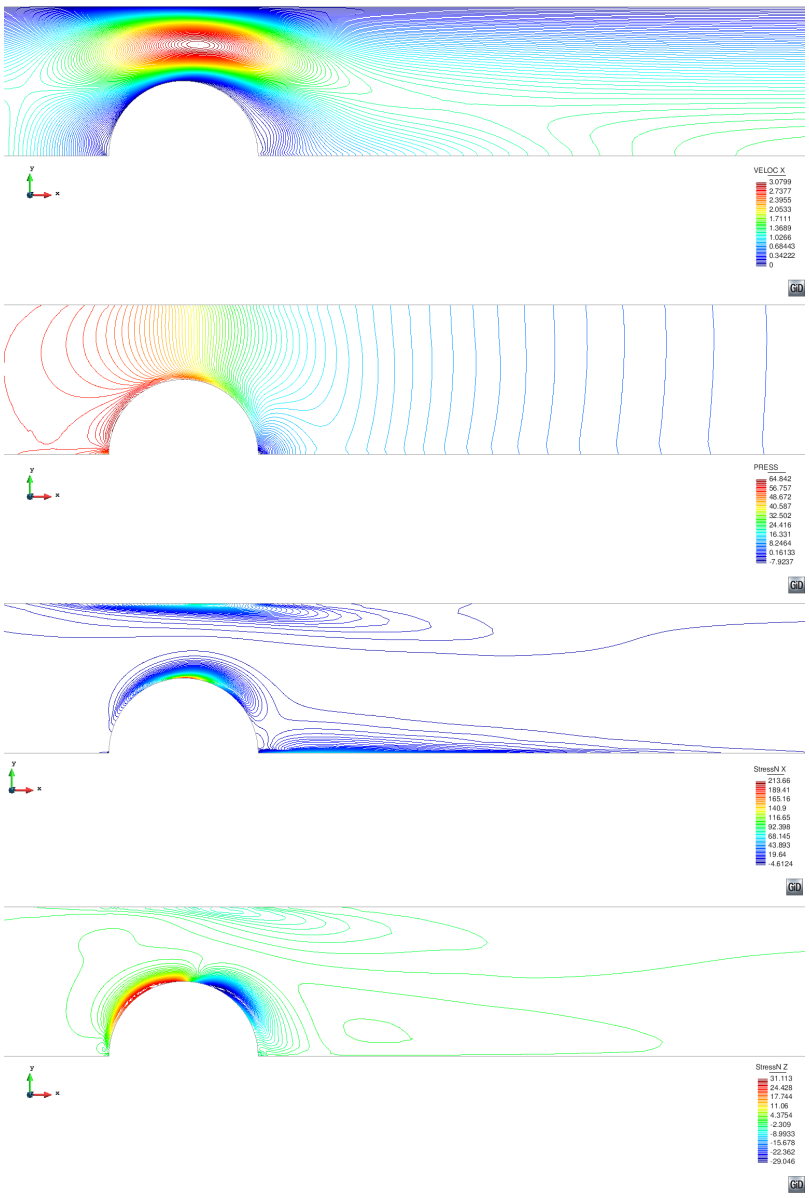

Figure 4.8: Results for the flow over a cylinder for the case We = 1.3. From the top to the bottom: isolines of u_x, p, σ_{xx} and σ_{xy}.

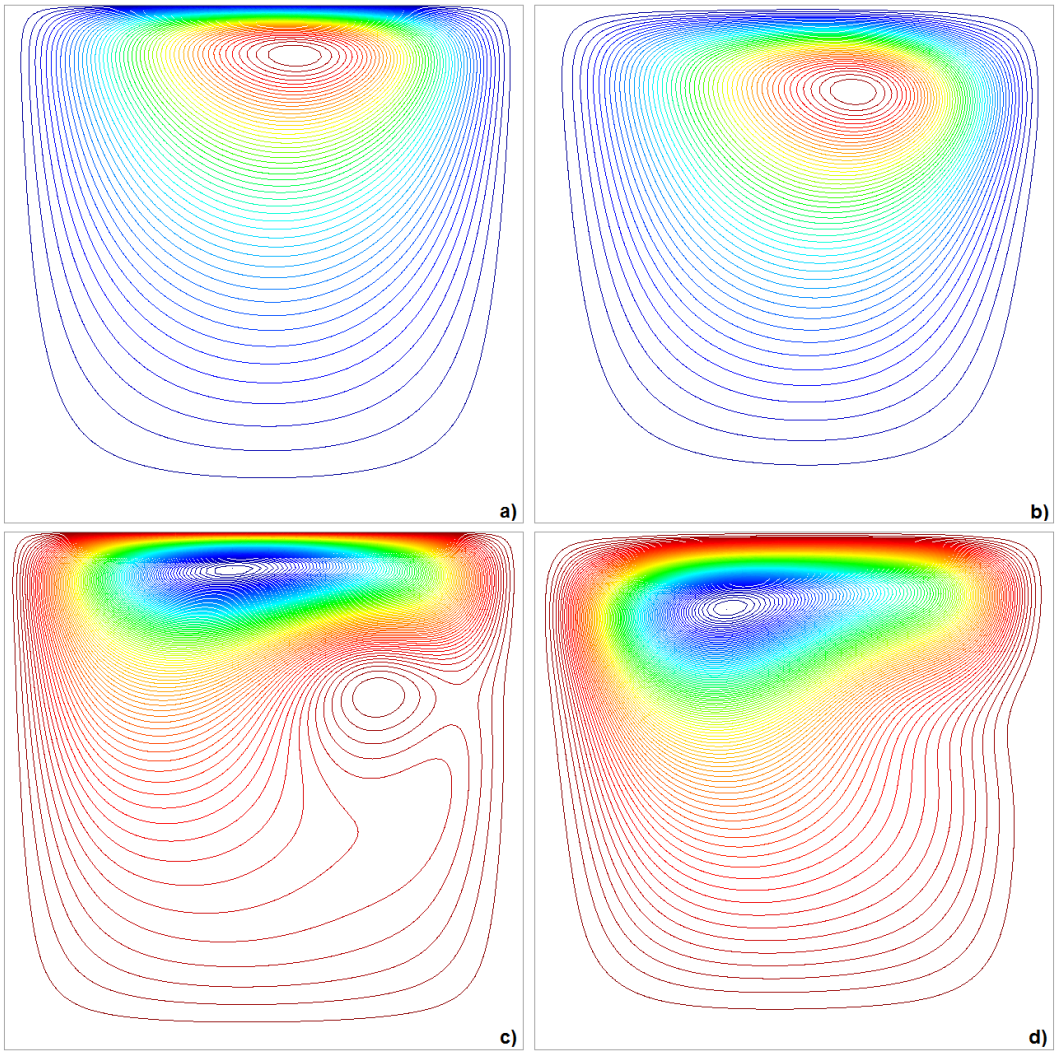

Figure 4.9: Streamlines in the lid-driven cavity problem using the third order fractional step algorithm. From the top to the bottom and from the left to the right: $t = 0.5$, 1, 1.5 and 2.0.

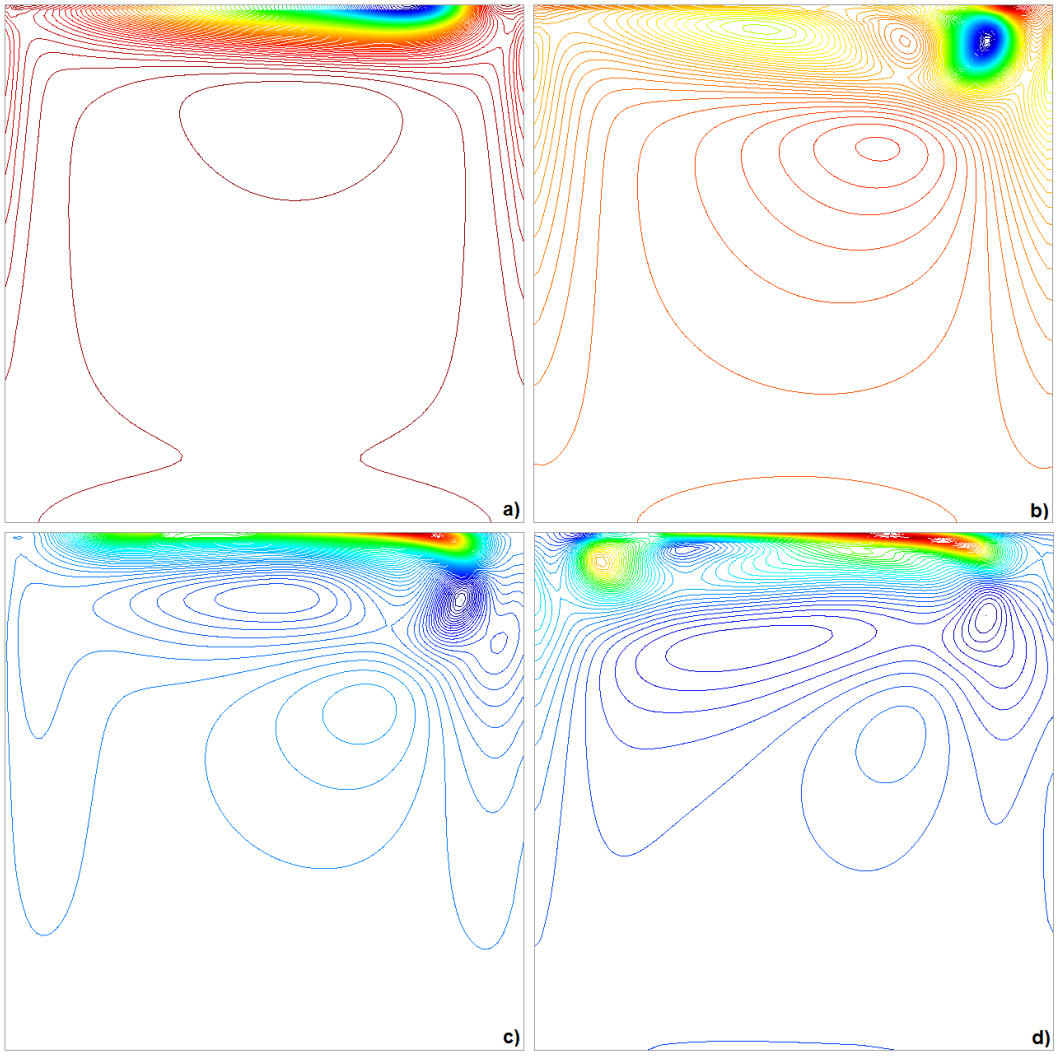

Figure 4.10: σ_{xy} component of the elastic stress tensor in the lid-driven cavity problem using the third order fractional step algorithm. From the top to the bottom and from the left to the right: $t = 0.5$, 1, 1.5 and 2.0.

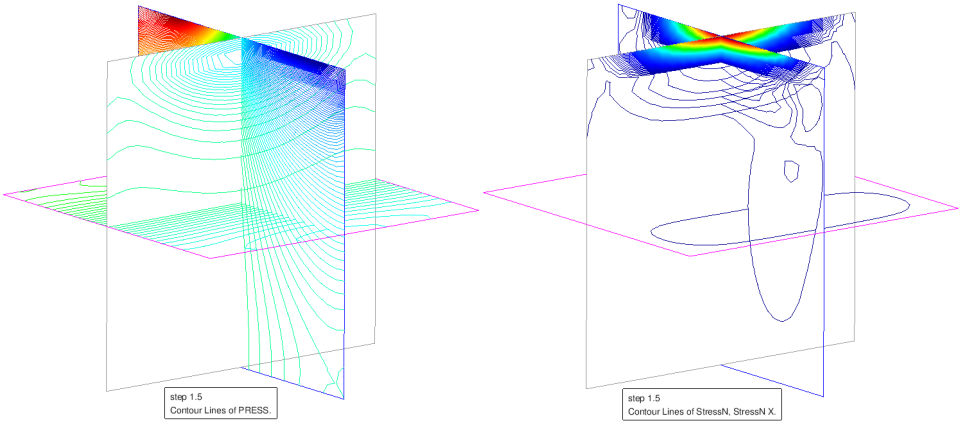

Figure 4.11: Lid-driven cavity in 3D: a) pressure isolines and b) σ_{xx} component of the elastic stress tensor.

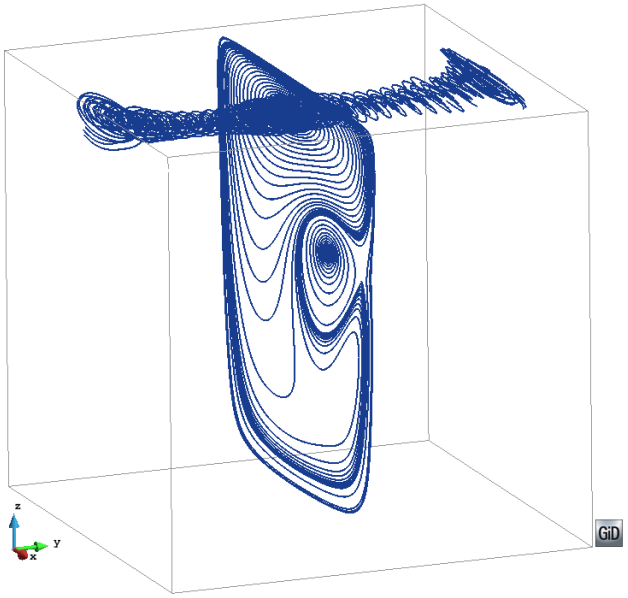

Figure 4.12: Lid-driven cavity in 3D: some streamlines at $t = 2$.

4.8 Conclusions

In this chapter we have presented three different fractional step methods of first, second and third order in time to solve the viscoelastic fluid flow problem. The three methods have been constructed at the pure algebraic level, presenting in all cases the formal design via extrapolation and the associated approximate LU decomposition, with the corresponding matrix errors. The third order scheme, which to our knowledge had not been tested before even for Newtonian flows, has been obtained by applying a Yosida splitting to the problem written in terms of the increments of the variables from one time step to the next. The accuracy of all the resulting methods has been checked numerically using an analytical manufactured solution, showing optimal convergence properties for smooth solutions.

Both the Galerkin and the stabilized finite element formulation presented in chapter 3 (also in [37]) have been considered for the spatial discretization. It has been shown that the latter introduces slight modifications of the former when applied in conjunction with the fractional step schemes. The resulting formulation has been found to be very robust, reaching Weissenberg numbers greater than those found for other formulations using the standard form of the constitutive equation, and close to those reached using the log-conformation version of it.

The efficiency of the fractional step formulations has been tested in a dynamic problem in 2D and 3D, showing an important reduction in the CPU time with respect to the monolithic case for the three formulations, particularly in problems where convection is more important. The splitting of the equations yields a problem that requires less nonlinear iterations per time step than the monolithic method, and the maximum number of linear solver iterations is only needed for the slowest variable, pressure in the incompressible flows considered.

As a general comment, the methods we have proposed for the viscoelastic flow problem inherit the properties of fractional step methods for Newtonian flows, and can be in fact designed by extending the same conceptual ingredients. Likewise, they could also be used as preconditioners of the monolithic problem, or as the starting point of predictor-corrector schemes, topics not touched in this work.

Chapter 5

Approximation of the Two-Fluid Flow Problem

5.1 Abstract

The numerical simulation of complex flows has been a subject of intense research in the last years with important industrial applications in many fields. In this chapter we present a finite element method to solve the two immiscible fluid flow problems using the level set method. When the interface between both fluids cuts an element, the discontinuity in the material properties leads to discontinuities in the gradients of the unknowns which cannot be captured using a standard finite element interpolation. The method presented in this part of the work features a local enrichment for the pressure unknowns which allows one to capture pressure gradient discontinuities in fluids presenting different density values. The method is tested on two problems: the first example consists of a sloshing case that involves the interaction of a Giesekus and a Newtonian fluid. This example shows that the enriched pressure functions permit the exact resolution of the hydrostatic rest state. The second example is the classical jet buckling problem used to validate our method. To permit the use of equal interpolation between the variables, we use the variational multiscale formulation proposed in chapter 3, that has shown very good stability properties, permitting also the resolution of the jet buckling flow problem in the the range of Weissenberg number $0 < \mathrm{We} < 100$, using the Oldroyd-B model without any sign of numerical instability. Additional features of the chapter are the inclusion of a discontinuity capturing technique for the constitutive equation and some comparisons between the monolithic resolution and the fractional step approach proposed in chapter 4 to solve the viscoelastic fluid flow problem from the point of view of computational requirements.

5.2 Introduction

The numerical simulation of moving interfaces involved in two-fluid flow problems is an important topic in many industrial processes and physical situations. Dam break, sloshing in tanks, shallow waters, mould filling or inkjet analysis, are recurrent applications that involve the treatment of a surface evolution problem.

Viscoelastic fluid flows are present in several industrial processes involving paints, plastics, food or adhesives, but also in geophysical applications such as mud flows or avalanches. Accurate modelling of this type of flows can have a critical role in the optimization of the operational parameters of different processes or in the prediction of physical phenomena.

The classification of the methods used for free surface and two-fluid flows is not an easy task, mainly because of the wide range of numerical schemes that exist. However, one of the most general classifications depends on the nature of the mesh used, which can be fixed or not. In this chapter we use a fixed mesh approach based on the level set method [128], which has been successfully used to validate experimental results that involve an interface evolution both in Newtonian and non-Newtonian fluids (see for example the review of Cruchaga et al. [65]). In the context of viscoelastic fluids the level set method has been used in the works of Yu et al. [169] and Pillapakkam and Singh [135]. Another common possibility is to use the volume of fluid approach (VOF) to evaluate the position of the moving interface, as in the work of Bonito et al. [28] where in addition, the authors use the SLIC post-processing algorithm (Simple Linear Interface Calculation) [125] to reduce numerical diffusion. The GENSMAC method (GENeralized Simplified Marker-And- Cell) [162] and its three-dimensional extension GENSMAC3D [161] is another possibility to follow the interface as shown in the works of Tomé et al. [160] and Figueiredo et al. [83]. See the work of McKee et al. [115] for a comprehensive review of the Marker and Cell (MAC) method.

The numerical solution of incompressible flows involving more than one fluid is one of the most challenging tasks in computational fluid dynamics [118]. The problems of tracing the interfaces and the discontinuity in the unknowns (velocity-stress-pressure) generated by the different material properties of the fluids on a time dependent domain are hard numerical tasks, which requires a great number of numerical ingredients in order to reach an accurate solution for this physical phenomenon. When the interface cuts an element, the discontinuity in the material properties leads to discontinuities in the gradients of the unknowns, which cannot be captured using standard interpolation functions. For instance, for two different density fluids at rest, the interpolation errors in pressure give rise to spurious velocities, which in turn give rise to spurious values in the elastic stresses. The combination of these errors causes the solution to lose physical sense. Also, viscosity discontinuities can lead to discontinuous velocity gradients that give rise to spurious stress and pressure values. Enriched methods add degrees of freedom at elements cut by the interface in order to reduce interpolation errors. Minev et al. [118] use a local enrichment of the bases for the velocity and pressure fields in a finite element formulation, which is used in the elements cut by the interface to improve the mass conservation properties; Newtonian fluids using the $P2$-$P1$ Taylor-Hood element are considered in this article. Chessa and Belytschko [43] use an enriched method based on the extended finite element method (XFEM), which is able to treat the material discontinuities. Coppola and Codina [63] propose a very easy-to-implement solution based on enriching the pressure shape functions on the elements cut by the interface to improve the ability to simulate the behavior of fluids with different densities under a gravitational force. The enrichment is used to enable the pressure gradient to be discontinuous at the interface, which could otherwise not be captured by the standard finite element shape functions and which can also be condensed prior to matrix assembly, thereby maintaining the number of degrees of freedom of the original problem.

The level set method may fail to preserve the total mass in applications that involve the interaction of immiscible fluids. A large number of publications exist in this context [157, 164, 127, 61]. A known approach to improve mass conservation properties of a level set method involves solving a continuity equation for the volume fraction of one phase of the problem. In this context hybrid level set/VOF methods [158] have been designed with important improvements in the mass conservation properties. Minev et al. [118] show that using local enrichment of the bases for the velocity and the pressure unknowns contributes to improving the mass conservation properties in the case of numerical simulations involving the effect of surface tension in Newtonian fluids.

The viscoelastic fluid flow problem presents several numerical difficulties, particularly for the spatial approximation. On the one hand, the finite element interpolation used must

satisfy two inf-sup conditions, the same ones appearing in the Stokes or the Navier-Stokes problem written in a three field formulation [56, 36]. On the other hand, the convective term in the momentum and in the constitutive equations requires the use of methods to deal with convection related instabilities. Many algorithms have been developed to solve this problem: see for example the works [111, 84, 79] in the finite element context, and [168, 3] for the finite volume method. In this chapter we use the finite element variational multiscale formulation proposed in chapter 3 (see also [37]). In the present context, multiscale refers to the scales of the unknown that can be resolved by the numerical approximation and those that cannot. This discretization in space shows excellent stability properties, permitting in particular the use of equal interpolation spaces for all variables.

The inability to simulate viscoelastic flows at high Weissenberg numbers is currently one of the major challenges in computational rheology in the past few years and is known as the High Weissenberg Number Problem (HWNP). The log-conformation formulation for the elastic stress tensor proposed by Fattal and Kupfermann [80] is a common approach to solve highly elastic fluids and has been used for the free surface evolution problem successfully with different numerical methods [160, 92]. Continuation methods are another numerical tool to increase the Weissenberg number limit that can be solved by a standard formulation, as shown in the work of Howell [94]. For the treatment of local oscillations, discontinuity-capturing techniques have proved to produce good results in [33, 37]. In this chapter we use a standard formulation for the elastic stress tensor with an additional discontinuity-capturing technique based on the orthogonal projection of the elastic stress tensor gradient as proposed in chapter 3. The formulation allows one to solve the jet buckling problem in the range of Weissenberg number $0 < \mathrm{We} < 100$ using the Oldroyd-B model.

We present here two numerical simulations to illustrate the capability of our finite element formulation to simulate moving interfaces using the Oldroyd-B and the Giesekus constitutive models. The first example consists in the resolution of a sloshing case that involves the interaction between a Giesekus fluid and a Newtonian one. Secondly, the jet buckling problem is solved to compare the results using the proposed methodology with previously published works using the Oldroyd-B constitutive model. Both examples are solved both in the two-dimensional and in the three-dimensional case.

The chapter is organized as follows. In Section 5.3 we introduce the continuous viscoelastic fluid flow problem. Section 5.4 is devoted to its numerical approximation with the Galerkin approximation and the stabilized formulations used. In Section 5.5, the level set method and the enriched pressure shape functions are presented. Numerical results are shown in Section 5.6 and, finally, conclusions are drawn in Section 5.7.

5.3 The viscoelastic flow problem

5.3.1 Boundary value problem

To simulate the transient incompressible and isothermal flow of viscoelastic fluids, one needs to solve the momentum balance equation, the continuity equation and a constitutive equation that defines the viscoelastic contribution of the fluid.

The conservation equations for momentum and mass may be expressed for each fluid as:

$$\rho_i \frac{\partial \boldsymbol{u}_i}{\partial t} + \rho_i \boldsymbol{u}_i \cdot \nabla \boldsymbol{u}_i - \nabla \cdot \boldsymbol{T}_i + \nabla p_i = \boldsymbol{f}_i \quad \text{in } \Omega_i,\ t \in]0, t_\mathrm{f}[, \tag{5.1}$$

$$\nabla \cdot \boldsymbol{u}_i = 0 \quad \text{in } \Omega_i,\ t \in]0, t_\mathrm{f}[, \tag{5.2}$$

where Ω_i is the computational domain of $\mathbb{R}^d$ occupied by the fluid $i = 1$ or 2, $d = 2$ or 3 being the space dimensions. The whole domain Ω is defined as $\Omega = \Omega_1 \cup \Omega_2$, $]0, t_\mathrm{f}[$ is the

time interval in which the problem is solved, ρ_i denotes the density, $p_i : \Omega_i \times]0, t_\mathrm{f}[\longrightarrow \mathbb{R}$ the pressure, $\boldsymbol{u}_i : \Omega_i \times]0, t_\mathrm{f}[\longrightarrow \mathbb{R}^d$ the velocity field, $\boldsymbol{f}_i : \Omega_i \to \mathbb{R}^d$ the force vector, taken as the gravity force $\rho_i \boldsymbol{g}$, and $\boldsymbol{T}_i : \Omega_i \times]0, t_\mathrm{f}[\longrightarrow \mathbb{R}^d \otimes \mathbb{R}^d$ is the deviatoric extra stress tensor, which can be defined in terms of a viscous and a viscoelastic or elastic contribution as:

$$\boldsymbol{T}_i = 2\beta_i \eta_{0,i} \nabla^s \boldsymbol{u}_i + \boldsymbol{\sigma}_i, \tag{5.3}$$

where $\beta_i \in [0, 1]$ is a real parameter to define the amount of viscous or solvent viscosity $\eta_{s,i} = \beta_i \eta_{0,i}$ and elastic or polymeric viscosity $\eta_{p,i} = (1 - \beta_i)\, \eta_{0,i}$ in the fluid. For viscoelastic fluids, the problem is incomplete without the definition of a constitutive equation for the elastic part of the extra stress tensor ($\boldsymbol{\sigma}_i$). A large variety of approaches exist to define it (see [21, 22] for a complete description). In this part of the work, we use the Oldroyd-B and the Giesekus constitutive models to define the fluid. Both models can be defined using the equation

$$\begin{aligned} \frac{\lambda_i}{2\eta_{0,i}} \frac{\partial \boldsymbol{\sigma}_i}{\partial t} - (1 - \beta_i) \nabla^s \boldsymbol{u}_i + \frac{\lambda_i}{2\eta_{0,i}} \left(\boldsymbol{u}_i \cdot \nabla \boldsymbol{\sigma}_i - \boldsymbol{\sigma}_i \cdot \nabla \boldsymbol{u}_i - (\nabla \boldsymbol{u}_i)^T \cdot \boldsymbol{\sigma}_i \right) \\ + \frac{1}{2\eta_{0,i}} (1 + h(\boldsymbol{\sigma}_i)) \cdot \boldsymbol{\sigma}_i = \boldsymbol{0} \quad \text{in } \Omega,\ t \in]0, t_\mathrm{f}[. \end{aligned} \tag{5.4}$$

The Giesekus model is obtained replacing $h(\boldsymbol{\sigma}_i) = \dfrac{\varepsilon_i \lambda_i}{\eta_{p,i}} \boldsymbol{\sigma}_i$ in (6.4), where λ_i is the relaxation time and ε_i the mobility factor. When $\varepsilon_i = 0$, the Giesekus model reduces to the Oldroyd-B rheological model. Note that $h(\boldsymbol{\sigma})$ is a tensor, and thus $1 + h$ should be understood as identity plus h.

The non-linear term $(\boldsymbol{\sigma}_i \cdot \boldsymbol{\sigma}_i)$ of the Giesekus model enables simply qualitative descriptions of a number of well-known properties of viscoelastic fluids, namely, shear thinning, the non-zero second normal stress coefficient, and stress overshoot in transient shear flows [122].

To avoid excessive nomenclature we will omit the subindex i that defines each fluid in the exposition of the methods, unless the expression needs explicitly this definition.

Let us introduce some notation used in the next subsections. Calling $\boldsymbol{U} = [\boldsymbol{u}, \boldsymbol{\sigma}, p]$, $\boldsymbol{F} = [\boldsymbol{f}, 0, 0]$ and defining

$$\mathcal{L}(\hat{\boldsymbol{u}}, \hat{\boldsymbol{\sigma}}; \boldsymbol{U}) := \begin{pmatrix} \rho \hat{\boldsymbol{u}} \cdot \nabla \boldsymbol{u} - 2\beta\eta_0 \nabla \cdot (\nabla^s \boldsymbol{u}) - \nabla \cdot \boldsymbol{\sigma} + \nabla p \\ \nabla \cdot \boldsymbol{u} \\ -(1 - \beta) \nabla^s \boldsymbol{u} + \dfrac{\lambda}{2\eta_0} \left(\hat{\boldsymbol{u}} \cdot \nabla \boldsymbol{\sigma} - \boldsymbol{\sigma} \cdot \nabla \hat{\boldsymbol{u}} - (\nabla \hat{\boldsymbol{u}})^T \cdot \boldsymbol{\sigma} \right) + \dfrac{1}{2\eta_0} (1 + h(\hat{\boldsymbol{\sigma}})) \cdot \boldsymbol{\sigma} \end{pmatrix},$$

and

$$\mathcal{D}_t(\boldsymbol{U}) := \begin{pmatrix} \rho \dfrac{\partial \boldsymbol{u}}{\partial t} \\ 0 \\ \dfrac{\lambda}{2\eta_0} \dfrac{\partial \boldsymbol{\sigma}}{\partial t} \end{pmatrix},$$

we may write (5.1), (5.2) and (5.4) using the definition (5.3) as:

$$\mathcal{D}_t(\boldsymbol{U}) + \mathcal{L}(\boldsymbol{u}, \boldsymbol{\sigma}; \boldsymbol{U}) = \boldsymbol{F}. \tag{5.5}$$

These equations are a mixed parabolic-hyperbolic system. Additionally to the three equations defined by (5.5), the problem needs initial and boundary conditions both in the velocity and the elastic stress fields to close the problem. In principle the elastic stresses can be fixed only on the inflow part of the boundary $\Gamma_\mathrm{in} = \{\boldsymbol{x} \in \partial\Omega \mid (\boldsymbol{u} \cdot \boldsymbol{n})(\boldsymbol{x}) < 0\}$, where $\boldsymbol{n}$ is the outward unit normal vector to $\partial\Omega$. For a complete description of the mathematical structure

of the problem and the boundary conditions required, see for example the work of Fernández-Cara et al. [82]. For the sake of conciseness, the boundary conditions for the velocity will be taken of homogeneous Dirichlet type, even if zero traction boundary conditions will also be used in the numerical simulations. Note that pressure will be determined up to a constant.

5.3.2 The variational form

Let us introduce some notation in order to write the weak form of the problem. The space of square integrable functions in a domain ω is denoted by $L^2(\omega)$, and the space of functions whose distributional derivatives of order up to $m \geq 0$ (integer) belong to $L^2(\omega)$ by $H^m(\omega)$. The space $H_0^m(\omega)$ consists of functions in $H^1(\omega)$ vanishing on $\partial\omega$. The topological dual of $H_0^1(\Omega)$ is denoted by $H^{-1}(\Omega)$, the duality pairing by $\langle\cdot,\cdot\rangle$, and the L^2 inner product in Ω (for scalar, vectors and tensors) is denoted by $(\cdot,\cdot)$. The integral of the product of two functions in a domain ω is denoted as $\langle\cdot,\cdot\rangle_\omega$. When $\omega = \Omega$, the subscript or the domain information are omitted.

Let $\boldsymbol{\Upsilon} = H^1(\Omega)^{d\times d}_{\text{sym}}$ (symmetric second order tensors with components in $H^1(\Omega)$), $\boldsymbol{\mathcal{V}} = H_0^1(\Omega)^d$ and $\mathcal{Q} = L^2(\Omega)/\mathbb{R}$, be the spaces where we may seek the elastic stress, the velocity and the pressure, respectively, for each fixed time t. Let also $\boldsymbol{U} = [\boldsymbol{u}, p, \boldsymbol{\sigma}]$. The weak form of the problem is obtained by testing (5.5) against an arbitrary test function $\boldsymbol{V} = [\boldsymbol{v}, q, \boldsymbol{\tau}]$ with appropriate regularity. It can be written as: find $[\boldsymbol{u}, p, \boldsymbol{\sigma}] :]0, t_{\text{f}}[\longrightarrow \boldsymbol{\mathcal{X}} := \boldsymbol{\mathcal{V}} \times \mathcal{Q} \times \boldsymbol{\Upsilon}$ such that the initial conditions are satisfied and

$$\left(\rho\frac{\partial \boldsymbol{u}}{\partial t}, \boldsymbol{v}\right) + 2\left(\beta\eta_0\nabla^s\boldsymbol{u}, \nabla^s\boldsymbol{v}\right) + \langle\rho\boldsymbol{u}\cdot\nabla\boldsymbol{u}, \boldsymbol{v}\rangle + (\boldsymbol{\sigma}, \nabla^s\boldsymbol{v}) - (p, \nabla\cdot\boldsymbol{v}) = \langle\boldsymbol{f}, \boldsymbol{v}\rangle, \quad (5.6)$$

$$(q, \nabla\cdot\boldsymbol{u}) = 0, \quad (5.7)$$

$$\left(\frac{\lambda}{2\eta_0}\frac{\partial\boldsymbol{\sigma}}{\partial t}, \boldsymbol{\tau}\right) - \left(\left(1-\beta\right)\nabla^s\boldsymbol{u}, \boldsymbol{\tau}\right) + \frac{\lambda}{2\eta_0}\left(\boldsymbol{u}\cdot\nabla\boldsymbol{\sigma} - \boldsymbol{\sigma}\cdot\nabla\boldsymbol{u} - (\nabla\boldsymbol{u})^T\cdot\boldsymbol{\sigma}, \boldsymbol{\tau}\right) + \left(\frac{1}{2\eta_0}\boldsymbol{\sigma}, \boldsymbol{\tau}\right) + \left(\frac{\lambda\varepsilon}{2(1-\beta)\eta_0^2}\boldsymbol{\sigma}\cdot\boldsymbol{\sigma}, \boldsymbol{\tau}\right) = 0, \quad (5.8)$$

for all $\boldsymbol{V} = [\boldsymbol{v}, q, \boldsymbol{\tau}] \in \boldsymbol{\mathcal{X}}$, where it is assumed that $\boldsymbol{f}$ is such that $\langle\boldsymbol{f}, \boldsymbol{v}\rangle$ is well defined. The last term of the constitutive equation appears only in the Giesekus model but it is always included to avoid more definitions.

In a compact form, the problem (5.6)-(5.8) can be written as:

$$(\mathcal{D}_t(\boldsymbol{U}), \boldsymbol{V}) + B(\boldsymbol{u}, \boldsymbol{\sigma}; \boldsymbol{U}, \boldsymbol{V}) = \langle\boldsymbol{f}, \boldsymbol{v}\rangle, \quad (5.9)$$

for all $\boldsymbol{V} \in \boldsymbol{\mathcal{X}}$, where

$$\begin{aligned} B(\hat{\boldsymbol{u}}, \hat{\boldsymbol{\sigma}}; \boldsymbol{U}, \boldsymbol{V}) = {} & 2\left(\beta\eta_0\nabla^s\boldsymbol{u}, \nabla^s\boldsymbol{v}\right) + \langle\rho\hat{\boldsymbol{u}}\cdot\nabla\boldsymbol{u}, \boldsymbol{v}\rangle + (\boldsymbol{\sigma}, \nabla^s\boldsymbol{v}) - (p, \nabla\cdot\boldsymbol{v}) + (q, \nabla\cdot\boldsymbol{u}) \\ & - \left(\left(1-\beta\right)\nabla^s\boldsymbol{u}, \boldsymbol{\tau}\right) + \frac{\lambda}{2\eta_0}\left(\hat{\boldsymbol{u}}\cdot\nabla\boldsymbol{\sigma} - \boldsymbol{\sigma}\cdot\nabla\hat{\boldsymbol{u}} - (\nabla\hat{\boldsymbol{u}})^T\cdot\boldsymbol{\sigma}, \boldsymbol{\tau}\right) \\ & + \left(\frac{1}{2\eta_0}\boldsymbol{\sigma}, \boldsymbol{\tau}\right) + \left(\frac{\lambda\varepsilon}{2(1-\beta)\eta_0^2}\hat{\boldsymbol{\sigma}}\cdot\boldsymbol{\sigma}, \boldsymbol{\tau}\right). \end{aligned} \quad (5.10)$$

It is understood that integrals involved in this expression extend either over Ω_1 or over Ω_2, according to the fluid that occupies a certain region, with its physical properties. Appropriate transmission conditions (continuity of velocity and of the normal component of the total stress) are ensured by writing the problem in this global form.

5.4 Numerical approximation

5.4.1 Galerkin finite element discretization

The standard Galerkin approximation for the variational problem can be performed by considering a finite element partition $\mathcal{T}_h$ of the domain Ω. The diameter of an element domain $K \in \mathcal{T}_h$ is denoted by h_K and the diameter of the element partition is defined by $h = \max\{h_K \mid K \in \mathcal{T}_h\}$. Under the above considerations, we can construct conforming finite elements spaces, $\boldsymbol{\mathcal{V}}_h \subset \boldsymbol{\mathcal{V}}$, $\mathcal{Q}_h \subset \mathcal{Q}$ and $\boldsymbol{\Upsilon}_h \subset \boldsymbol{\Upsilon}$ in the usual manner. If $\boldsymbol{\mathcal{X}}_h = \boldsymbol{\mathcal{V}}_h \times \mathcal{Q}_h \times \boldsymbol{\Upsilon}_h$, and $\boldsymbol{U}_h = [\boldsymbol{u}_h, p_h, \boldsymbol{\sigma}_h]$, the Galerkin finite element approximation consists in finding $\boldsymbol{U}_h :]0, t_\mathrm{f}[\longrightarrow \boldsymbol{\mathcal{X}}_h$ such that:

$$(\mathcal{D}_t(\boldsymbol{U}_h), \boldsymbol{V}_h) + B(\boldsymbol{u}_h, \boldsymbol{\sigma}_h; \boldsymbol{U}_h, \boldsymbol{V}_h) = \langle \boldsymbol{f}, \boldsymbol{v}_h \rangle, \tag{5.11}$$

for all $\boldsymbol{V}_h = [\boldsymbol{v}_h, q_h, \boldsymbol{\tau}_h] \in \boldsymbol{\mathcal{X}}_h$.

5.4.2 Stabilized finite element formulation

Choosing equal order approximations for $\boldsymbol{\sigma}$, $\boldsymbol{u}$ and p does not yield a stable scheme. A possible remedy to this situation is to enrich the finite element spaces for the velocity and the stress in order to satisfy the two compatibility conditions associated with the viscoelastic problem (see for example [29] and references therein). Another possibility is to use stabilized formulations permitting any interpolation of the variables, which is the approach we use in this work. In general, a stabilized formulation consists of replacing B in (5.11) by another semi-linear form B_h, possibly mesh dependent, with better stability properties.

Stabilized finite element methods consist in modifying the discrete Galerkin formulation of the problem by adding terms designed to enhance stability without upsetting accuracy. In this chapter we use the split orthogonal sub-grid (Split OSGS) method proposed in chapter 3 (also in [37]) for the stationary viscoelastic problem using the Oldroyd-B constitutive model, and tested in transient problems in chapter 4 (also in [38]) in the context of fractional step methods. The theoretical foundations of the method, applied to linearized Newtonian flows, are presented in [55].

The method consists in replacing (5.11) by the following problem: find $\boldsymbol{U}_h :]0, t_\mathrm{f}[\rightarrow \boldsymbol{\mathcal{X}}_h$, such that

$$\begin{aligned}(\mathcal{D}_t(\boldsymbol{U}_h), \boldsymbol{V}_h) + B(\boldsymbol{u}_h, \boldsymbol{\sigma}_h; \boldsymbol{U}_h, \boldsymbol{V}_h) + S_1^{\perp}(\boldsymbol{u}_h; \boldsymbol{U}_h, \boldsymbol{V}_h) \\ + S_2^{\perp}(\boldsymbol{U}_h, \boldsymbol{V}_h) + S_3^{\perp}(\boldsymbol{u}_h, \boldsymbol{\sigma}_h; \boldsymbol{U}_h, \boldsymbol{V}_h) = \langle \boldsymbol{f}, \boldsymbol{v}_h \rangle,\end{aligned} \tag{5.12}$$

for all $\boldsymbol{V}_h \in \boldsymbol{\mathcal{X}}_h$, where

$$\begin{aligned}S_1^{\perp}(\hat{\boldsymbol{u}}_h; \boldsymbol{U}_h, \boldsymbol{V}_h) &= \sum_K \alpha_1 \left\langle P_h^{\perp}\left[\rho \hat{\boldsymbol{u}}_h \cdot \nabla \boldsymbol{u}_h\right], \rho \hat{\boldsymbol{u}}_h \cdot \nabla \boldsymbol{v}_h \right\rangle_K + \sum_K \alpha_1 \left\langle P_h^{\perp}\left[\nabla p_h - \rho \boldsymbol{g}\right], \nabla q_h \right\rangle_K \\ &\quad + (1-\beta) \sum_K \alpha_1 \left\langle P_h^{\perp}\left[\nabla \cdot \boldsymbol{\sigma}_h\right], \nabla \cdot \boldsymbol{\tau}_h \right\rangle_K, \\ S_2^{\perp}(\boldsymbol{U}_h, \boldsymbol{V}_h) &= \sum_K \alpha_2 \left\langle P_h^{\perp}\left[\nabla \cdot \boldsymbol{u}_h\right], \nabla \cdot \boldsymbol{v}_h \right\rangle_K, \\ S_3^{\perp}(\hat{\boldsymbol{u}}_h, \hat{\boldsymbol{\sigma}}_h; \boldsymbol{U}_h, \boldsymbol{V}_h) &= \sum_K \alpha_3 \Big\langle P_h^{\perp}\left[\boldsymbol{R}_{\sigma,h}(\hat{\boldsymbol{u}}_h, \hat{\boldsymbol{\sigma}}_h; \boldsymbol{U}_h)\right], \\ &\quad - \frac{1}{2\eta_0} h(\hat{\boldsymbol{\sigma}_h})^T \boldsymbol{\tau}_h - \nabla^s \boldsymbol{v}_h + \frac{\lambda}{2\eta_0}\left(\hat{\boldsymbol{u}}_h \cdot \nabla \boldsymbol{\tau}_h + \boldsymbol{\tau}_h \cdot (\nabla \hat{\boldsymbol{u}}_h)^T + \nabla \hat{\boldsymbol{u}}_h \cdot \boldsymbol{\tau}_h\right) \Big\rangle_K,\end{aligned}$$

where $P_h^{\perp} = I - P_h$ is the orthogonal projection, with P_h the L^2 projection onto the appropriate finite element space. In the last expression, $\boldsymbol{R}_{\sigma,h}$ represents the residual of the

constitutive equation without the local temporal derivative and without the term $\frac{1}{2\eta_0}\boldsymbol{\sigma}_h$:

$$\boldsymbol{R}_{\sigma,h}(\hat{\boldsymbol{u}}_h,\hat{\boldsymbol{\sigma}}_h;\boldsymbol{U}_h) = -(1-\beta)\nabla^s\boldsymbol{u}_h + \frac{\lambda}{2\eta_0}\left(\hat{\boldsymbol{u}}_h\cdot\nabla\boldsymbol{\sigma}_h - \boldsymbol{\sigma}_h\cdot\nabla\hat{\boldsymbol{u}}_h - (\nabla\hat{\boldsymbol{u}}_h)^T\cdot\boldsymbol{\sigma}_h\right) \quad (5.13)$$
$$+\frac{1}{2\eta_0}h(\hat{\boldsymbol{\sigma}}_h)\cdot\boldsymbol{\sigma}_h.$$

The orthogonal projection of all these terms converges to zero at the optimal rate allowed by the finite element interpolation. In particular, this is why the temporal term has been neglected even if it is not exactly zero for non-constant physical properties (note that the orthogonal projection of the temporal derivative of $\boldsymbol{\sigma}_h$ is exactly zero). For the same reason, the last term in (5.13) could be neglected.

The parameters α_j, $j=1,2,3$ represent the components of the stabilizing parameter matrix presented in [37], computed within each element K as

$$\alpha_1 = \left[c_1\frac{\eta_0}{h_1^2} + c_2\frac{\rho\,|\boldsymbol{u}_h|}{h_2}\right]^{-1}, \quad \alpha_2 = \frac{h_1^2}{c_1\alpha_1}$$
$$\alpha_3 = \left[c_3\frac{1}{2\eta_0} + c_4\left(\frac{\lambda}{2\eta_0}\frac{|\boldsymbol{u}_h|}{h_2} + \frac{\lambda}{\eta_0}|\nabla\boldsymbol{u}_h|\right)\right]^{-1}.$$

In these expressions, h_1 corresponds to a characteristic element length calculated as the square root of the element area in 2D case and the cubic root of the element volume in 3D, and h_2 corresponds to another characteristic length calculated as the element length in the streamline direction. The constants c_j,$j=1,2,3,4$ are algorithmic parameters in the formulation. The values used (for linear elements) are $c_1=12.0$, $c_2=2.0$, $c_3=4.0$ and $c_4=1.0$. For higher order elements, the characteristic lengths h_1 and h_2 should be divided respectively by r^2 and r, r being the order of the finite element interpolation. The stabilization parameters need to be computed at each integration point, and thus the physical properties to be employed in their evaluation depend on the fluid (1 or 2) that occupies each point.

The stabilizing mechanisms introduced by terms $S_1^\perp$, $S_2^\perp$ and $S_3^\perp$ are the following. The first component of the $S_1^\perp$ gives control on the convective term, the second component gives control on the pressure gradient and *includes the gravity force term*, and the third term gives control on the divergence of the viscoelastic stress. The term $S_2^\perp$ is not always necessary but in some cases it improves stability of the problem. Finally, the term $S_3^\perp$ ensures stability of the constitutive equation. Note that some of the components of this last term are the convective-convective term of the viscoelastic stress tensor and an equivalent EVSS-structure component (see [89]) obtained when testing the orthogonal component of the first term in (5.13) with $\nabla^s\boldsymbol{v}_h$, among other cross local inner-product terms.

The addition of $S_1^\perp$, $S_2^\perp$ and $S_3^\perp$ permit the approximation of convection-dominated problems both in velocity and in stress, and the implementation of equal order interpolation for all the unknowns (see chapter 3 or [37] for more details on the stabilized formulation used).

5.4.3 Discontinuity-Capturing technique

The previously described stabilized finite element formulation yields a globally stable solution, i.e., norms of the unknowns over the whole domain are bounded. However, if the solution displays large gradients, local oscillations may still remain.

In the case of viscoelastic flow problems, local instabilities or very high gradients in the pressure and in the viscoelastic stress components can be found when the fluid flow finds an abrupt change in the geometry. In order to overcome these instabilities, we use the discontinuity capturing term proposed in chapter 3 based on the orthogonal projection of

the elastic stress tensor gradient. The implementation is very easy and standard for any type of formulation, and consists in adding to the left hand side of the constitutive equation the following term:

$$\sum_K \langle \kappa_\sigma \nabla \boldsymbol{\sigma}_h, \nabla \boldsymbol{\tau}_h \rangle_K ,$$

where the diffusion coefficient κ_σ is defined as

$$\kappa_\sigma = \left(C_a h_1 \left| \boldsymbol{u}_h \right| + C_b h_1^2 \left| \nabla \boldsymbol{u}_h \right| \right) \frac{|P_h^\perp(\nabla \boldsymbol{\sigma}_h)|}{|\nabla \boldsymbol{\sigma}_h|}.$$

Note that this term converges to zero at the optimal rate permitted by the finite element interpolation, at least when the solution is smooth. The values used in this part of the work for the constants appearing in the numerical diffusion are $C_a = 1.0$ and $C_b = 1.0$, but they can be tuned depending on the properties of the particular flow.

5.4.4 Monolithic time discretization

Let us explain as to discretize in time problem (5.11) using a monolithic approach. Any time discretization is possible, although for the sake of conciseness we will restrict the explanation to the classical backward-difference (BDF) approximation, even if in some parts of the work we use the Crank Nicolson scheme.

The time interval $]0, t_\mathrm{f}[$ can be partitioned into time steps of size δt, which are considered to be constant for simplicity. Let us use a superscript to denote the time step counter. The BDF approximation to the time derivative of a time dependent function $y(t)$ of order $k = 1, 2, ..,$ is given by $\delta_k y^{n+1}/\delta t$, with

$$\delta_k y^{n+1} = \frac{1}{\gamma_k} \left(y^{n+1} - \sum_{i=0}^{k-1} \varphi_k^i y^{n-i} \right),$$

where γ_k and φ_k^i are numerical parameters. In particular, for the cases $k = 1$ and 2 (BDF1 and BDF2) we have:

$$\begin{aligned} \delta_1 y^{n+1} &= y^{n+1} - y^n, \\ \delta_2 y^{n+1} &= \frac{3}{2} \left(y^{n+1} - \frac{4}{3} y^n + \frac{1}{3} y^{n-1} \right). \end{aligned}$$

We will also use the extrapolation of order 1, defined as $\hat{y}_1^{n+1} = y^n + \mathcal{O}(\delta t)$.

To simplify the description of the time integration, let us consider the Galerkin method. Using a BDF scheme, the time discretization of problem (5.11) can be written, in expanded form, as: given the initial conditions, for $n = 1, 2, ...,$ find $\left[\boldsymbol{u}_h^{n+1}, p_h^{n+1}, \boldsymbol{\sigma}_h^{n+1} \right] \in \boldsymbol{\mathcal{X}}_h$, such that:

$$\begin{aligned} &\left(\rho \frac{\delta_k \boldsymbol{u}_h^{n+1}}{\delta t}, \boldsymbol{v}_h \right) + 2 \left(\beta \eta_0 \nabla^s \boldsymbol{u}_h^{n+1}, \nabla^s \boldsymbol{v}_h \right) + \left\langle \rho \boldsymbol{u}_h^{n+1} \cdot \nabla \boldsymbol{u}_h^{n+1}, \boldsymbol{v}_h \right\rangle + \left(\boldsymbol{\sigma}_h^{n+1}, \nabla^s \boldsymbol{v}_h \right) \\ &\quad - \left(p_h^{n+1}, \nabla \cdot \boldsymbol{v}_h \right) = \left\langle \boldsymbol{f}_h^{n+1}, \boldsymbol{v}_h \right\rangle, \qquad (5.14) \\ &\left(q_h, \nabla \cdot \boldsymbol{u}_h^{n+1} \right) = 0, \qquad (5.15) \\ &\left(\frac{\lambda}{2\eta_0} \frac{\delta_k \boldsymbol{\sigma}_h^{n+1}}{\delta t}, \boldsymbol{\tau}_h \right) + \left(\frac{1}{2\eta_0} \boldsymbol{\sigma}_h^{n+1}, \boldsymbol{\tau}_h \right) - \left((1-\beta) \nabla^s \boldsymbol{u}_h^{n+1}, \boldsymbol{\tau}_h \right) \\ &\quad + \frac{\lambda}{2\eta_0} \left(\boldsymbol{u}_h^{n+1} \cdot \nabla \boldsymbol{\sigma}_h^{n+1} - \boldsymbol{\sigma}_h^{n+1} \cdot \nabla \boldsymbol{u}_h^{n+1} - \left(\nabla \boldsymbol{u}_h^{n+1} \right)^T \cdot \boldsymbol{\sigma}_h^{n+1}, \boldsymbol{\tau}_h \right) \end{aligned}$$

$$+\left(\frac{\lambda\varepsilon}{2(1-\beta)\eta_0^2}\boldsymbol{\sigma}_h^{n+1}\cdot\boldsymbol{\sigma}_h^{n+1},\boldsymbol{\tau}_h\right)=0, \tag{5.16}$$

for all $\boldsymbol{V}_h \in \boldsymbol{\mathcal{X}}_h$. The fully discrete stabilized problem can be defined in the same way (see chapter 4 or [38]).

5.4.5 Fractional-step formulation

The monolithic resolution of the system of equations that is obtained after discretization of the continuous problem is the most straightforward option. However, solving this system is computationally very expensive, specially in 3D. In some of the numerical examples, we have uses a fractional step approach to solve the two immiscible fluid flow problem. This fractional step algorithm was proposed in chapter 4 (also in [38]) and gives second order accuracy in time, even if a third order scheme is also proposed in this article. For a review of fractional step schemes designed at the pure algebraic level, see [11].

Problem (5.14)-(5.16) can be written in the following algebraic form:

$$M_{\boldsymbol{u}}\frac{\delta_k}{\delta t}\mathbf{U}^{n+1}+K_{\boldsymbol{u}}\left(\mathbf{U}^{n+1}\right)\mathbf{U}^{n+1}+G\mathrm{P}^{n+1}-D_\sigma\boldsymbol{\Sigma}^{n+1}=\boldsymbol{F}^{n+1}, \tag{5.17}$$

$$D\mathbf{U}^{n+1}=\mathbf{0}, \tag{5.18}$$

$$M_{\boldsymbol{\sigma}}\frac{\delta_k}{\delta t}\boldsymbol{\Sigma}^{n+1}+K_{\boldsymbol{\sigma}}\left(\mathbf{U}^{n+1}\right)\boldsymbol{\Sigma}^{n+1}-S\mathbf{U}^{n+1}=\mathbf{0}, \tag{5.19}$$

where $\mathbf{U}$, P and $\boldsymbol{\Sigma}$ are arrays of the nodal unknowns for $\boldsymbol{u}$, p and $\boldsymbol{\sigma}$. $K_{\boldsymbol{u}}$ and $K_{\boldsymbol{\sigma}}$ are the stiffness matrices of the momentum and constitutive equation, G represent the gradient operator, D is the divergence of the velocity, D_σ the divergence of the elastic stress tensor and S the symmetrical part of the velocity gradient. $M_{\boldsymbol{u}}$ and $M_{\boldsymbol{\sigma}}$ represent the mass matrices of the momentum and the constitutive equation. We are using the same notation used in [38] to facilitate the explanation. Additional terms coming from stabilization can be easily treated, as explained in this article.

Roughly speaking, a fractional step method consists in the resolution of the full problem in different algorithmic steps that permit the calculation of all the variables in a sequential way. The different steps can be separated in steps where intermediate values are obtained, denoted by $\tilde{()}^{n+1}$, and steps where the final values $()^{n+1}$ are determined correcting the intermediate values.

The fractional step algorithm used in this chapter is of formal second order accuracy in time and can be written in matrix form in terms of intermediate and final steps, as it is shown in algorithms (5.1) and (5.2) (see chapter 4 for more details). The extrapolated first order values $\hat{\boldsymbol{\Sigma}}_1^{n+1}$ and $\hat{\mathrm{P}}_1^{n+1}$ allow us to obtain the second order accuracy of the fractional step algorithm.

The stabilized version can be written in the same way as the Galerkin formulation. For more details see chapter 4 (also [38]) where the fractional step algorithm for viscoelastic fluids used in this chapter was developed.

5.5 The level set method

5.5.1 The level set equation

The level set method is based on the pure advection of a smooth function, say $\phi(\boldsymbol{x},t)$, over the whole computational domain $\Omega=\Omega_1\cup\Omega_2$. This function defines the position of the front or the interface, by the isovalue $\phi(\boldsymbol{x},t)=\phi_c$ where ϕ_c is a critical value defined a

Algorithm 5.1 Fractional step approach: intermediate steps.

1. Intermediate velocity using the pressure and the elastic stress values extrapolated:

$$\frac{\delta_k}{\delta t} M_{\boldsymbol{u}} \tilde{\mathbf{U}}^{n+1} + K_{\boldsymbol{u}} \left(\tilde{\mathbf{U}}^{n+1} \right) \tilde{\mathbf{U}}^{n+1} = \boldsymbol{f} - G \hat{\mathrm{P}}_1^{n+1} + D_{\boldsymbol{\sigma}} \hat{\boldsymbol{\Sigma}}_1^{n+1} \rightarrow \tilde{\mathbf{U}}^{n+1}$$

2. Intermediate elastic stress values using the intermediate velocity:

$$\frac{\delta_k}{\delta t} M_{\boldsymbol{\sigma}} \tilde{\boldsymbol{\Sigma}}^{n+1} + K_{\boldsymbol{\sigma}} \left(\tilde{\mathbf{U}}^{n+1} \right) \tilde{\boldsymbol{\Sigma}}^{n+1} - S \tilde{\mathbf{U}}^{n+1} = \boldsymbol{f_c} \rightarrow \tilde{\boldsymbol{\Sigma}}^{n+1}$$

3. Intermediate pressure calculation using the intermediate velocity and elastic stress:

$$-D \tilde{\mathbf{U}}^{n+1} + \gamma_k \delta t D M_{\boldsymbol{u}}^{-1} G \left(\tilde{\mathrm{P}}^{n+1} - \hat{\mathrm{P}}_1^{n+1} \right) - \gamma_k \delta t D M_{\boldsymbol{u}}^{-1} D_\sigma \left(\tilde{\boldsymbol{\Sigma}}^{n+1} - \hat{\boldsymbol{\Sigma}}_1^{n+1} \right) = \mathbf{0} \rightarrow \tilde{\mathrm{P}}^{n+1}$$

Algorithm 5.2 Fractional step approach: final steps.

4. Velocity correction:

$$\frac{1}{\gamma_k \delta t} M_{\boldsymbol{u}} \left(\mathbf{U}^{n+1} - \tilde{\mathbf{U}}^{n+1} \right) + G \left(\tilde{\mathrm{P}}^{n+1} - \hat{\mathrm{P}}_1^{n+1} \right) - D_\sigma \left(\tilde{\boldsymbol{\Sigma}}^{n+1} - \hat{\boldsymbol{\Sigma}}_1^{n+1} \right) = \mathbf{0} \rightarrow \mathbf{U}^{n+1}$$

5. Elastic stress correction:

$$\frac{1}{\gamma_k \delta t} M_{\boldsymbol{\sigma}} \left(\boldsymbol{\Sigma}^{n+1} - \tilde{\boldsymbol{\Sigma}}^{n+1} \right) - S \left(\mathbf{U}^{n+1} - \tilde{\mathbf{U}}^{n+1} \right) = \mathbf{0} \rightarrow \boldsymbol{\Sigma}^{n+1}$$

6. Pressure correction (formally):

$$\mathrm{P}^{n+1} = \tilde{\mathrm{P}}^{n+1} \rightarrow \mathrm{P}^{n+1}$$

priori; in this work we have taken $\phi_c = 0$. Thereby, the domain of the first fluid (Ω_1) can be associated with $\phi(\boldsymbol{x}, t) > 0$, while that of the second fluid (Ω_2), is defined by $\phi(\boldsymbol{x}, t) \leq 0$.

The conservation of ϕ in any control volume $V_t \subset \Omega$ which is moving with the divergence-free velocity field $\boldsymbol{u}$, can be defined by the following hyperbolic equation

$$\frac{\partial \phi}{\partial t} + (\boldsymbol{u} \cdot \nabla) \phi = 0 \quad \text{in } \Omega, \ t \in]0, t_{\mathrm{f}}[, \tag{5.20}$$

with the corresponding initial and boundary conditions:

$$\begin{aligned} \phi &= \overline{\phi} \quad \text{on } \Gamma_{\mathrm{in}}, \ t \in]0, t_{\mathrm{f}}[, \\ \phi &= \phi_0 \quad \text{in } \Omega, \ t = 0. \end{aligned}$$

The initial condition ϕ_0, is chosen in order to define the initial position of the interface, and at the same time provide a smooth field which can be easily advected. The boundary condition $\overline{\phi}$ determines an inflow boundary when it is needed. Usually an initial condition field ϕ_0 such that $|\phi| = 1$ is chosen. We use standard numerical techniques to approximate the level set equation (5.20), solving this equation at the end of each time step to define the interface between both fluids which is then used in the next time step. Due to its pure convective nature it requires some type of stabilization. In this work we use the classical SUPG technique for this purpose [31], which corresponds to a standard variational multiscale (VMS) one in a pure convection problem. Time is discretized using second order finite difference schemes (Crank-Nicolson in the examples). From time to time, re-distancing is needed to preserve

the condition $|\phi| = 1$, for example, when interfaces merge or by the advection nature of the equation (5.20), which we do using a direct calculation of the distance to $\phi = 0$ of each node (see [61] for examples of alternatives).

5.5.2 Discontinuous gradient pressure functions

Using fixed meshes, the standard Lagrangian finite element approximation of an unknown ψ within each element K of the finite element partition can be written as:

$$\psi_h \mid_K = \sum_{I=1}^{n_{\text{nod}}} N_K^I \psi_K^I,$$

where n_{nod} is the number of element nodes, N_K^I the shape function of node I and ψ_K^I the nodal value at this node. In typical finite element methods, the gradient of the shape functions is continuous within each element and therefore the gradient of the unknown is also continuous. If the interface cuts an element, the discontinuity in the material properties when solving a two immiscible fluid flow problems leads to discontinuities in the gradients of the unknowns which cannot be captured with standard finite element interpolation.

In this work we use the enriched gradient pressure method proposed in [63] to treat different density fluids. If an element is crossed by the interface, the pressure can be interpolated as

$$p_h \mid_K = \sum_{I=1}^{n_{\text{nod}}} N_K^I p_K^I + N_K^* p_K^*.$$

The enriched shape function N_K^* has a constant gradient on each side of the interface, its value is zero at the element nodes and it is C^0 continuous in K. The added degree of freedom is local to the element and can therefore be condensed after the element matrix has been computed and before the assembly step. As a consequence, the number of nodes of the problem remains constant. It is worth noting that this is the main difference between our approach and that of a XFEM-strategy [43], in which the enriching function would be multiplied by the standard shape functions (making use of the fact that they are a partition of unity). This would introduce new pressure degrees of freedom at the nodes of the elements cut by the interface.

In our approach, the resulting pressure finite element space is defined by discontinuous functions across the inter-element boundaries, and thus it is a subspace of $L^2(\Omega)$, but not of $H^1(\Omega)$, as would be the case using $P1$-$P1$ elements. However, the method is still conforming [63].

Figure 5.1 (left) shows a sketch of the enriched pressure used for an element crossed by the interface in a $P1$ element. In the same figure (right) the modified integration rule used to ensure a good representation of the discontinuities in the cut elements is shown. *This modified integration rule was used in all numerical examples, independently of whether the enriched pressure functions were used or not.* In the 2D case the element is subdivided into three sub-elements (for $P1$ elements) while in the 3D case for linear elements it can be subdivided into four or six sub-elements (sub-tetrahedra), depending on the cut type. For each sub-element the same integration rule as for the original elements is used.

Let us consider linear triangles in 2D first. The enriched shape functions can be constructed using the standard shape functions and the position of the intersection points (A and B in Figure 5.1) as

$$N_K^* = \begin{cases} \theta_1 N_K^1, \text{ on } K_1 := \Omega_1 \cap \Omega_K, \\ \theta_2 N_K^2 + \theta_3 N_K^3, \text{ on } K_2 := \Omega_2 \cap \Omega_K, \end{cases}$$

were θ_i, $i = 1, 2, 3$, are parameters to be determined. To construct each component of the enriched function we can follow the next three steps:

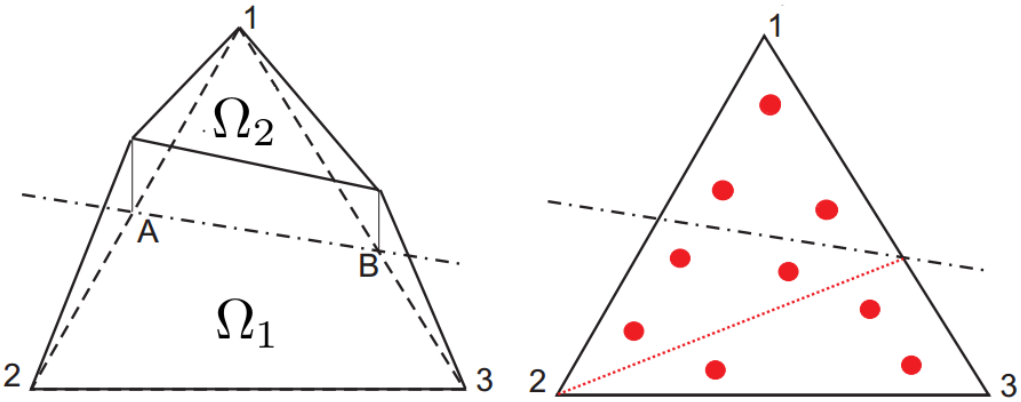

Figure 5.1: Enriched element sketch and modified integration rule.

- Assume that $N_K^* (\boldsymbol{x}_A) = 1$ (the other case $N_K^* (\boldsymbol{x}_B) = 1$ is also possible).
- Use this definition to evaluate each component of the enriched function, i.e., $N_K^* (\boldsymbol{x}_A) \mid_{K_1} = N_K^* (\boldsymbol{x}_A) \mid_{K_2} = 1$, and the fact that $N_K^3 (\boldsymbol{x}_A) = 0$.
- The enriched function must be continuous in Ω_K, so $N_K^* (\boldsymbol{x}_B) \mid_{K_1} = N_K^* (\boldsymbol{x}_B) \mid_{K_2}$. In the same way as in the above step, $N_K^2 (\boldsymbol{x}_B) = 0$.

Using the above three points and based on the cut element showed in Figure 5.1, the parameters θ_i, $i = 1, 2, 3$, are:

$$\theta_1 = \frac{1}{N_K^1 (\boldsymbol{x}_A)}, \; \theta_2 = \frac{1}{N_K^2 (\boldsymbol{x}_A)}, \; \theta_3 = \theta_1 \frac{N_K^1 (\boldsymbol{x}_B)}{N_K^3 (\boldsymbol{x}_B)}.$$

The same ideas can be used to obtain N_K^* for 3D linear elements or for other element types. In the tetrahedral case we have two possibilities, depending on the number of intersection points (3 or 4) as we can see in figure 5.2, where the intersection cut plane is defined by the green area.

For the three intersection points case, the enriched pressure function takes the following form:

$$N_K^* = \begin{cases} \theta_1 N_K^1, \text{ on } K_1 = \Omega_1 \cap \Omega_K, \\ \theta_2 N_K^2 + \theta_3 N_K^3 + \theta_4 N_K^4, \text{ on } K_2 = \Omega_2 \cap \Omega_K, \end{cases}$$

where

$$\theta_1 = \frac{1}{N_K^1 (\boldsymbol{x}_A)}, \; \theta_2 = \frac{1}{N_K^2 (\boldsymbol{x}_A)}, \; \theta_3 = \theta_1 \frac{N_K^1 (\boldsymbol{x}_B)}{N_K^3 (\boldsymbol{x}_B)}, \; \theta_4 = \theta_1 \frac{N_K^1 (\boldsymbol{x}_C)}{N_K^4 (\boldsymbol{x}_C)}.$$

In the case of four intersection points we have:

$$N_K^* = \begin{cases} \theta_1 N_K^1 + \theta_2 N_K^2, \text{ on } K_1 = \Omega_1 \cap \Omega_K, \\ \theta_3 N_K^3 + \theta_4 N_K^4, \text{ on } K_2 = \Omega_2 \cap \Omega_K, \end{cases}$$

with

$$\theta_1 = \frac{1}{N_K^1 (\boldsymbol{x}_A)}, \; \theta_2 = \theta_3 \frac{N_K^3 (\boldsymbol{x}_C)}{N_K^2 (\boldsymbol{x}_C)}, \; \theta_3 = \frac{1}{N_K^3 (\boldsymbol{x}_A)}, \; \theta_4 = \theta_2 \frac{N_K^2 (\boldsymbol{x}_D)}{N_K^4 (\boldsymbol{x}_D)}.$$

From the numerical point of view, when the cut is extremely near to a nodal point, bad or poor conditioning of the additional degrees of freedom can occur, causing the new shape

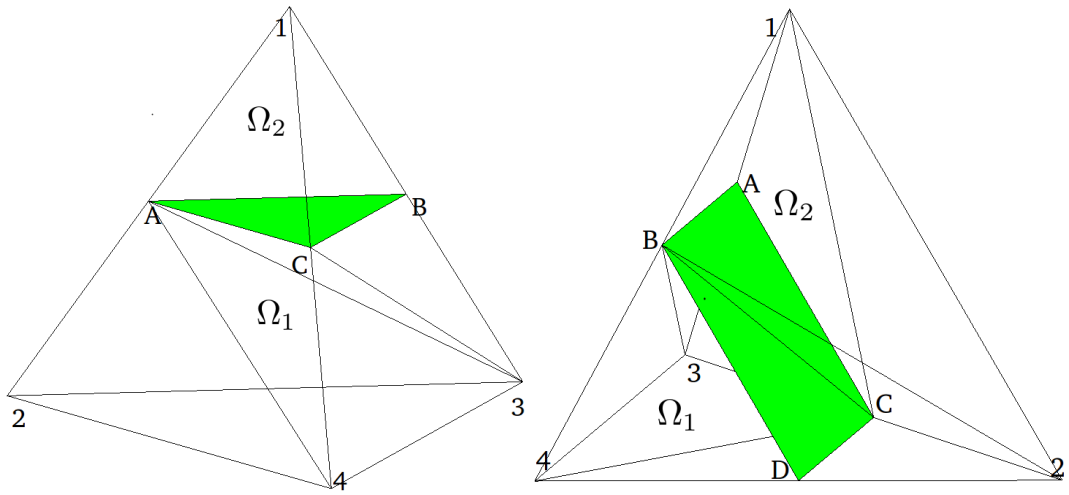

Figure 5.2: Tetrahedral element cut: three intersection points (left) and four intersection points (right).

functions to have large gradients. In order to minimize this problem, an external numerical parameter can be defined to "move" the fluid-interface over the node, for example, if the distance between the geometric centre of the intersection surface (line in 2d) to a nodal point is smaller than $\epsilon = 0.02h$ (where h is the element diameter). In this case, the interface is moved over the node. This numerical treatment is sufficient to solve ill-conditioning problems when dealing with free surface. However, the ill-conditioning present in the two-fluid flow problem is independent of the cut criteria and is truly associated to the ratio between the properties of the fluids. The larger this ratio is, the more ill-conditioned the final problem will be. No remedies for this type of ill-conditioning can be applied, and the linear system solver preconditioner will be in charge of improving the condition number of the system to be solved.

The most illustrative example where the need of some kind of enrichment is crucial is in fact, not a flow, but two different density fluids at rest (the lighter one on top) inside a closed cavity. The hydrostatic pressure gradient is discontinuous at the interface, and therefore this cannot be correctly represented by the standard finite element shape functions. Since the problem is coupled in velocities, stresses and pressure, the error in the representation of the pressure gives rise to spurious velocities that in turn give rise to spurious stresses. Figure 5.3 shows the interface solution of a two-fluid flow problem using a Giesekus fluid and a Newtonian fluid on top. The Newtonian fluid is one hundred times lighter than the Giesekus fluid in the bottom.

Remark: A fully enriched method for a viscoelastic two-fluid flow problem, should include *enrichment for the three fields* (velocity-stress-pressure). In this work we use the pressure enrichment as a first approach to show that the two-fluid flow problem cannot be solved accurately without enrichment.

5.6 Numerical results

In this section, some numerical tests are conducted to show the performance of the proposed methods. In subsection 5.6.1 a classical sloshing of a Giesekus fluid inside a covered square cavity with a one hundred times lighter Newtonian fluid on top is numerically mod-

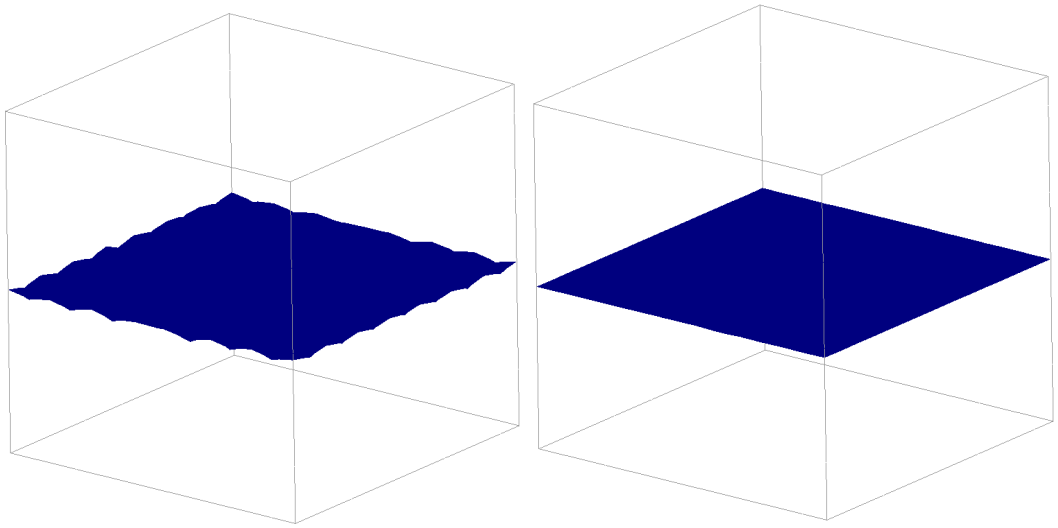

Figure 5.3: Three-dimensional hydrostatic pressure problem: without enriched functions (left) and using enriched functions (right).

eled. Subsection 5.6.2 is devoted to the jet buckling problem of an Oldroyd-B fluid. In both examples we solve the two-dimensional and the three-dimensional cases.

In all the numerical examples the discrete and linearized problem is solved using an iterative solver based on the BiCGStab (Stabilized version of BiConjugate Gradient Squared) method of van der Vorst [165], with the additive Schwarz preconditioner.

5.6.1 Sloshing of two fluids in a square covered cavity

The sloshing problem is a typical benchmark to test the accuracy of new numerical methods widely used in Newtonian fluids and less explored in the non-Newtonian case [66, 121]. In this case we solve the sloshing of a Giesekus fluid inside a square covered cavity with a Newtonian fluid on top with the properties detailed in table 5.1. The initial condition is an unstable inclined plane, as shown in Figure 5.4, under the influence of gravitational forces. For the time discretization both in the two-dimensional and in the three-dimensional case we use the BDF2 scheme for the momentum and constitutive equations, and the Crank Nicolson scheme for the level set equation. The time step has been taken constant with a value $\delta t = 0.01$ in all the cases.

Fluid type	$\eta_{0,i}$	β_i	λ_i	ε_i	ρ_i
Giesekus	1.0	0.111	1.0	0.01	100.0
Newtonian	1.0	0.111	0.0	0.0	1.0

Table 5.1: Fluid properties in the sloshing problem.

The space discretization used in the sloshing case is shown in Figure 5.4. The meshes used are very coarse, but enough for our purposes. For the 2D case, the mesh is defined by 890 linear elements, while in the three-dimensional case 76742 linear tetrahedral elements are used. The coordinates of points A and B detailed in Figure 5.4 are $(0.78; 0)$ and $(0.87; 0)$ respectively.

The objective of this subsection is to show that a standard formulation cannot be used to solve accurately a two-fluid flow problem without the addition of some type of enrichment.

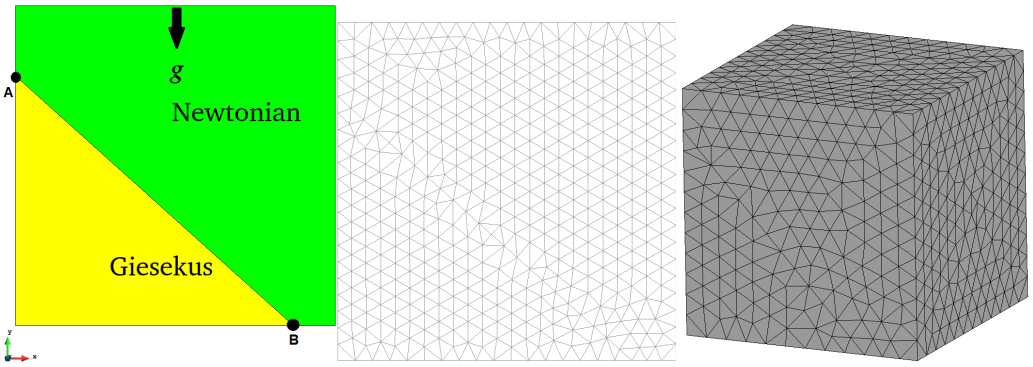

Figure 5.4: Two-fluids cavity problem: Initial condition, mesh used in 2D and mesh used in 3D (from left to right ,respectively).

The enrichment used here is added only to the pressure field, although the problem has different properties also in the "viscoelastic" parameters.

The dimensionless numbers of the problem based on the maximum obtained velocity ($|\boldsymbol{u}|_{\max} \approx 3.5$) and the characteristic length of the cavity ($L_c = 1$), are for the 2D case:

$$\mathrm{Re} \approx 350, \ \mathrm{We} \approx 3.5, \ \mathrm{Fr} \approx 1.1$$

and for the three-dimensional case based on the maximum velocity ($|\boldsymbol{u}|_{\max} \approx 4.5$):

$$\mathrm{Re} \approx 450, \ \mathrm{We} \approx 4.5, \ \mathrm{Fr} \approx 1.43$$

where Re represents the Reynolds number, We the Weissenberg number and Fr the Froude number. Note that the velocity decreases as the flow becomes stationary, and so do these numbers.

In Figure 5.5 we have the results obtained with and without enriched pressure functions for the 2D case. The most important point of these results is the final state of both cases. Without pressure enrichment, in addition to a greater amount of mass losses, the state of rest, where the interface must be completely horizontal is not satisfied. In the case of enriched pressure the lost mass is around 9%, while in the non-enriched case a mass loss of 38.5% is obtained. It is important to note that the mesh used is coarse and the time step large, but we think that this is the best scenario to compare both methods.

The inclusion of a discontinuity-capturing term is necessary according to our experience in the flow of viscoelastic fluids. In Figure 5.6 the temporal history of the bottom right corner of the stress magnitude in the time interval $[0, 3]$ is shown, with and without a discontinuity-capturing term for the two-dimensional case of the sloshing problem. It is clear from this figure that a discontinuity-capturing term can help to eliminate possible non-physical peaks. For all the cases shown in this work we use the discontinuity-capturing term summarized in subsection 5.4.3.

For the three-dimensional case, the tendency is maintained with less mass loss in the enriched pressure case (13% v/s 35%), and with the capability to solve the hydrostatic steady state. The same that in the 2D case, respect to the mesh and time step size. In both cases the loss mass could be reduced upon mesh refinement or reducing the time step size.

In viscoelasticity the number of degrees of freedom per node can be a bottleneck from the computational point of view, especially in the three-dimensional case. In table 5.2 a comparison of total CPU time and the maximum memory required to solve the problem both in the two-dimensional and in the three-dimensional cases are shown. It can be observed that

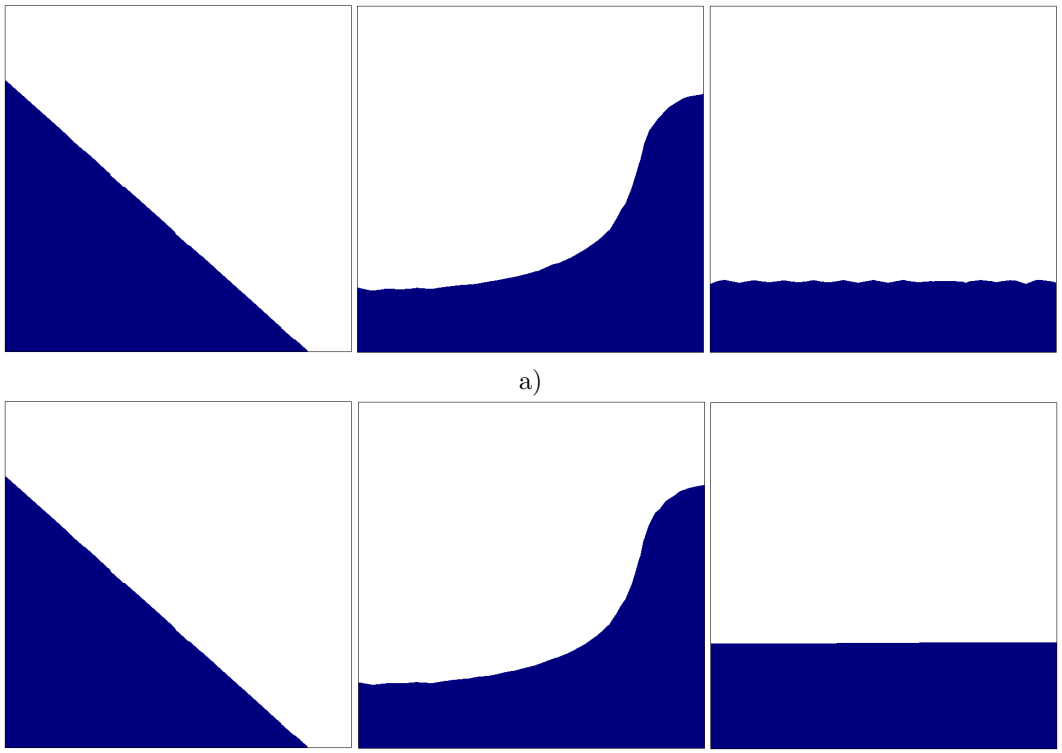

Figure 5.5: two-dimensional sloshing: a) without enriched functions and b) using enriched functions ($t = 0$, $t = 0.7$ and $t = 30$ for both cases from left to right).

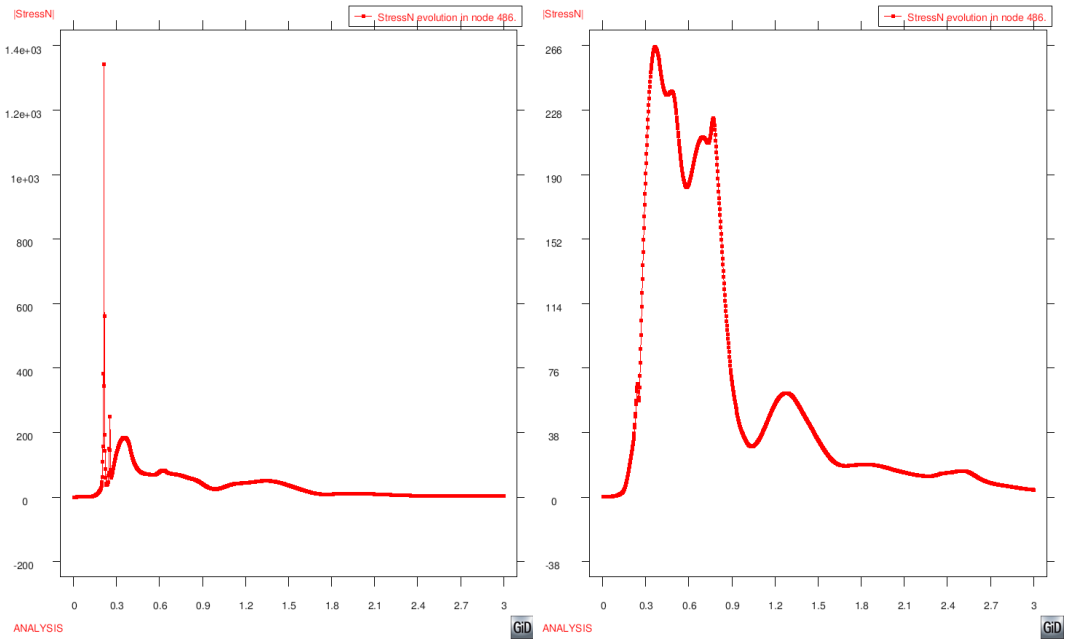

Figure 5.6: Temporal history of the bottom right corner of the stress magnitude without (left) and with (right) a discontinuity-capturing term.

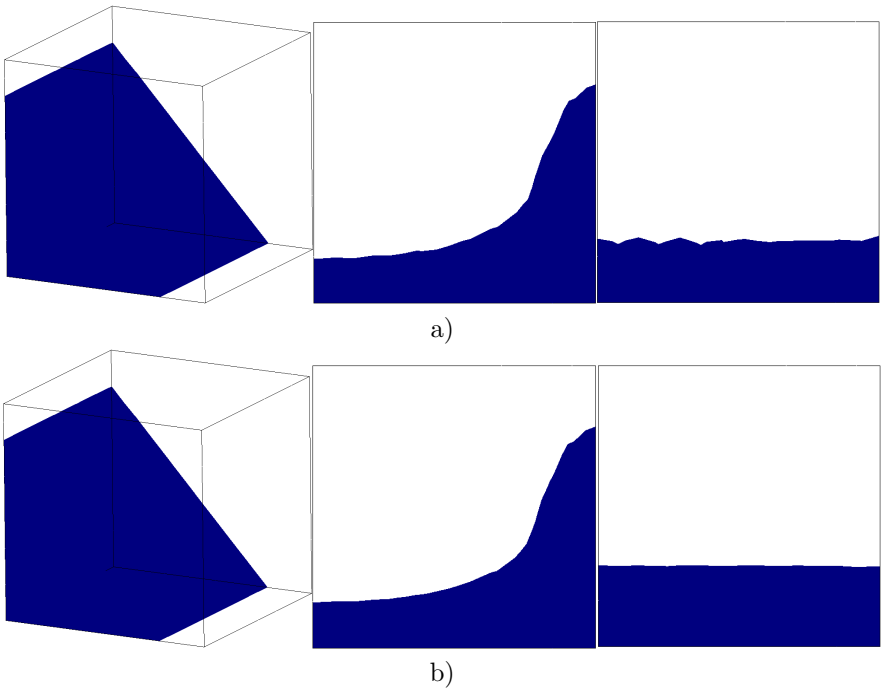

Figure 5.7: Three-dimensional sloshing: a) without enriched functions and b) using enriched functions ($t = 0$, $t = 0.7$ and $t = 15$ in both cases from left to right).

the use of a fractional step scheme is critical, especially in the three-dimensional case. The CPU time is reduced by a factor of three and the maximum memory requirements by a half. Regarding the accuracy of the numerical solution, the results obtained by the fractional step approach are practically identical to those of the monolithic approach.

	Monolithic	Fractional	Fractional/Monolithic
$2D - CPU_{time}$	1828.1s	1267.14s	0.6931
$3D - CPU_{time}$	158747s	61861s	0.3896
2D – Memory	16.7Mb	14.04Mb	0.84
3D – Memory	547Mb	301Mb	0.55

Table 5.2: Comparison of computational requirements: monolithic approach v/s fractional step approach.

5.6.2 Jet buckling problem

The jet buckling problem is the typical benchmark of free surface problems in viscoelastic fluids. In this subsection we use the two-fluid flow approach with enriched pressure shape functions to solve it. The buckling phenomena of viscous flows is a known physical instability, that depends in Newtonian fluids on the Reynolds number and the height from which the jet falls. Tomé and McKee [163] give a complete analysis of planar jets in Newtonian fluids. The authors propose an empirical relationship to evaluate the critical Reynolds number that defines the beginning of buckling which depends on the characteristic lengths that define the problem in the two-dimensional case. Another important work in viscous buckling analysis from the experimental and theoretical points of view is due to Cruickshank and Munson [68],

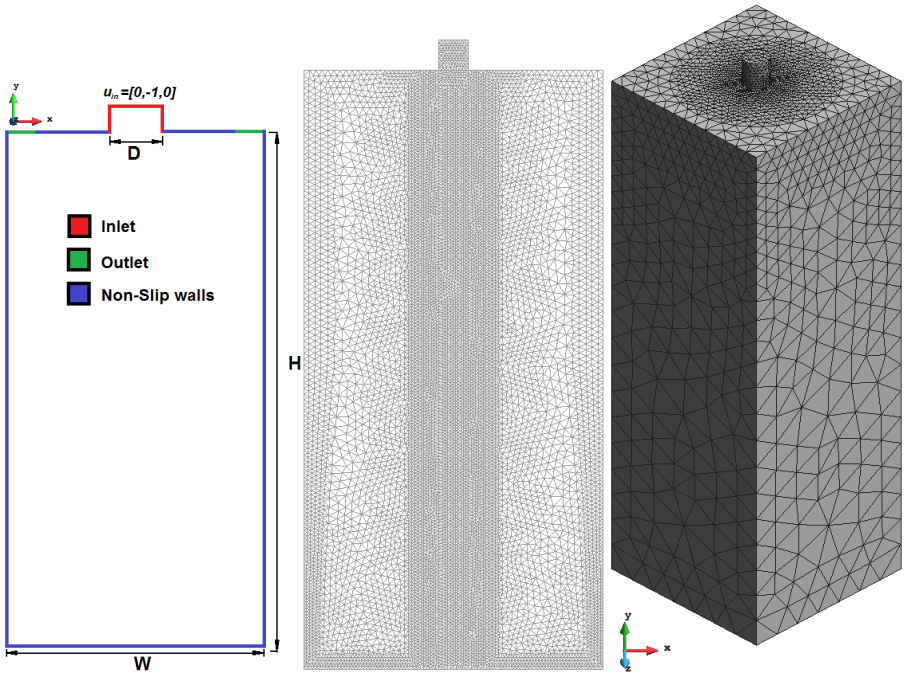

Figure 5.8: Jet buckling problem and mesh used.

where the authors show that a necessary condition for a jet buckling is $\mathrm{Re} \leq 1.2$. In the work of Bonito et al. [28] the authors use the relationship of Tomé and McKee to compare the flow patterns in viscoelastic and Newtonian fluids.

In Figure 5.8 the problem definition and the meshes used are shown for the two-dimensional and the three-dimensional cases. For rigid boundaries we employ slip walls (no-slip walls is another used option). The aspect ratios selected for the planar jet are $W/D = 10$ and $H/D = 20$ to ensure the occurrence of buckling (according to [163] buckling occurs for $H/D > 8.8$ in Newtonian fluids). The fluid properties are defined with respect to the Reynolds number (Re), the Weissenberg number (We), the inflow diameter (D_H) and the inflow velocity ($\boldsymbol{u}_{\text{in}}$) in Table 5.3.

D_H	$\boldsymbol{u}_{\text{in}}$	ρ	β	η_0	λ
0.05	1.0	1000.0	0.111	$\dfrac{\mathrm{Re}}{\rho \lvert\boldsymbol{u}_{\text{in}}\rvert D_H}$	$\dfrac{\mathrm{We} D_H}{\lvert\boldsymbol{u}_{\text{in}}\rvert}$

Table 5.3: Fluid properties for the buckling problem.

Figure 5.8 shows a sketch of the jet buckling problem and the meshes used for the two-dimensional and the three-dimensional cases. The 2D mesh is composed by 19209 linear elements and the three-dimensional case by 544548 linear tetrahedral elements. The buckling problem is by definition non-symmetric; therefore, the three-dimensional case must be solved for the full domain. It is important to note that we solve a two incompressible fluid flow problem and then, outlets are needed to ensure the mass conservation. For the time discretization both in the two-dimensional and in the three-dimensional cases we use the BDF2 scheme for the momentum and the constitutive equations, and the BDF1 scheme for the level set equation. The time step was taken constant with a value $\delta t = 0.005$ in all cases.

In general, the jet buckling problem is solved as a free surface case, i.e., the external flow

is not solved. In this work we use the two-fluid flow approach (the real physical problem) to emulate the free surface-approach used in the literature. To do this, we use a ratio relationship between the densities and the viscosities, of the order of a water-air interaction problem. The values used for all the simulations are $\rho_{\text{jet}} = 1000\,\rho_{\text{external}}$ and $\eta_{0,\text{jet}} = 500\,\eta_{0,\text{external}}$. Obviously, in a two-fluid problem, the outer fluid affects the dynamics of the internal fluid. In our simulations we found that a density ratio $\rho_{\text{jet}} \geqslant 1000\,\rho_{\text{external}}$ and a viscosity ratio $\eta_{0,\text{jet}} \geqslant 250\,\eta_{0,\text{external}}$, can be associated to a free-surface case. The real profit of a two fluid formulation is the capability to solve problems where the influence of the external flow is important, and therefore needs to be solved, which is not possible using a free surface approach.

With respect to mesh convergence, an analysis to ensure that the results are independent of the discretization used to perform the simulation is shown in Table 5.4. In this table, the exact time for the impact of different fluids in the case Re=0.25 is shown. The differences between mesh M2 and mesh M3 are negligible and, therefore, the selected mesh for all the calculations was mesh M2. In Table 5.4, t^* represents the instant of impact, $\text{E}_{\%}$ the percentual error using as reference the values obtained using mesh M3 and n_e the number of elements of the respective mesh. In this results, we can see as the shear-thinning effect of the fluid causes the impact to happen earlier than in the Newtonian case.

case Re = 0.25	M1 ($\text{n}_\text{e} = 6463$) $\Delta x_{\min} = 0.0075$	M2 ($\text{n}_\text{e} = 19209$) $\Delta x_{\min} = 0.005$	M3 ($\text{n}_\text{e} = 58683$) $\Delta x_{\min} = 0.00333$
	$t^*/\text{E}_{\%}$	t^*	$t^*/\text{E}_{\%}$
We = 0.0	0.725/3.33%	0.745/0.666%	0.75
We = 10.0	0.635/3.05%	0.65/0.763%	0.655
We = 100.0	0.615/3.14%	0.63/0.787%	0.635

Table 5.4: Mesh convergence analysis in jet-buckling problem.

The first set of results is devoted to the validation of our formulation in the jet buckling for Newtonian fluids. From [163], the condition for a Newtonian jet to buckle is:

$$\text{Re}\left(\frac{H}{D}\right) \leq \sqrt{\frac{1}{\pi}\frac{\left(\frac{H}{D}\right)^{2.6} - 8.8^{2.6}}{\left(\frac{H}{D}\right)^{2.6}}},$$

where the Reynolds number is defined in terms of the inlet velocity and the total viscosity (i.e. $\text{Re} = \rho\,|\boldsymbol{u}_{\text{in}}|\,D_H\eta_0^{-1}$). For the ratio $H/D = 20$, the critical Reynolds number for buckling is $\text{Re} \approx 0.53$. The critical Reynolds number obtained in our work for Newtonian fluids is $\text{Re} \approx 0.55$; for $\text{Re} \geqslant 0.6$ no sign of buckling exists (see Figure 5.9).

In Figure 5.10 the interface evolution of three cases was solved for Re = 0.25. This Reynolds number was selected to show the differences between Newtonian and viscoelastic fluid flows and the influence of the elastic properties in the buckling phenomena. The first row represents the Newtonian fluid while the second and third row are Oldroyd-B fluids defined by We = 10 and We = 100, respectively. In the first column, $t = 0.6$, we can see as the elastic part of the fluid convects the flow, even in a fixed Reynolds number, advancing the instant of the impact point. For this Reynolds number case, the Newtonian fluid presents the classical buckling flow while the more elastic flow is completely different, showing that the fluid has an elastic resistance that prevents buckling at the beginning, generating an unstable fluid pile ($t = 0.8$ and $t = 0.9$) that collapses later as we can see in Figure 5.10. Similar results were reported by Bonito et al. in [28] for the same case.

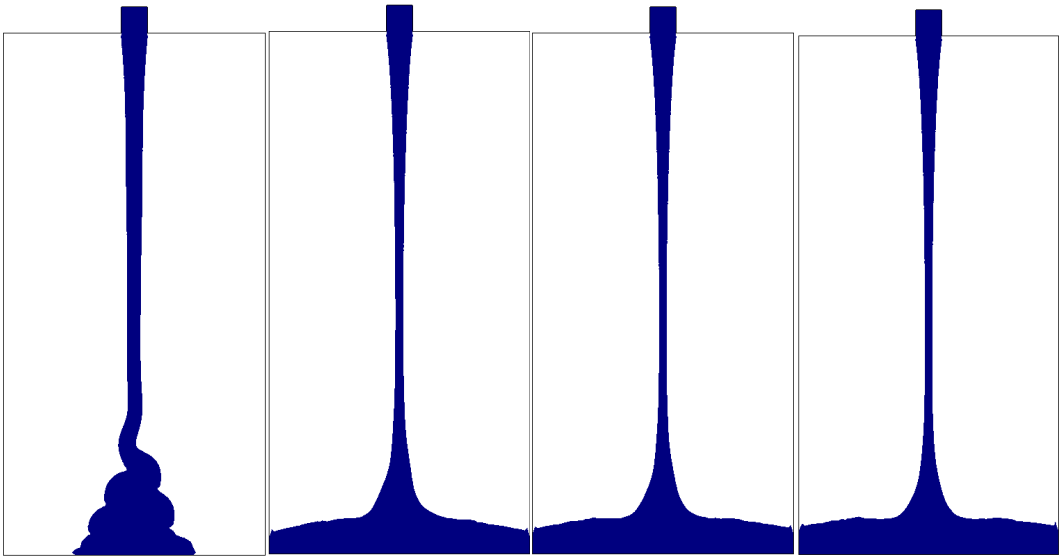

Figure 5.9: Jet buckling in Newtonian fluids. From left to right: Re = 0.25, Re = 0.50, Re = 0.55 and Re = 0.60 (all at $t = 1.5$)

In Figures 5.11 and 5.12 we can see the contour lines for the normal stresses and for the pressure for the same steps shown in Figure 5.10 for both viscoelastic cases. The normal component σ_{xx} reaches its maximum value when the flow strikes the ground and tries to slip. In this moment, the elastic properties of the fluid prevent slippage and the fluid begins to pile up. Later, the pile of fluid collapses and the other normal component of the stress tensor σ_{yy} reaches its highest value. The pressure field reaches its highest value when the fluid hits the ground. In all the figures we can see the interface between both fluids clearly defined by a zone of high gradients characterized by a large concentration of contour lines.

For the three-dimensional case, the two limit cases used in the two-dimensional case were solved. For the Newtonian fluid case (Figure 5.13), the buckling occurs from the beginning in the same way as in the two-dimensional case. For the viscoelastic case (Figure 5.14), the flow hits the base in conditions similar to a more inertial flow, contrary to what is observed in the the Newtonian case ($t = 1.0$). Then, the elastic stresses become apparent by stopping the slipping of the jet and preventing buckling, and beginning the stacking of the fluid ($t = 1.25$, $t = 1.5$). Finally, the stack begins to collapse ($t = 2.0$). Similar results were published by Bonito et al. in [28] using a free surface approach.

The resolution of a two-fluid flow problem gives the possibility to evaluate the interaction of both flows. Figure 5.15 gives a good graphical visualization of this point. This figure corresponds to the viscoelastic case where the outlets and the vortex zone near the jet are clearly defined.

The viscoelastic fluid flow problem is defined by a nonlinear system of equations, which is linearized and solved iteratively to reach an accepted convergence error value (10^{-6} in our simulations) defined as

$$E_{CV}^{i+1} = \frac{\left|\mathbf{U}^{i+1} - \mathbf{U}^{i}\right|}{\left|\mathbf{U}^{i+1}\right|},$$

where i represents the iteration counter. For the pressure and the stresses, the error is defined in the same way.

In each iteration the BiCGStab method is used to solve the system of equations. The

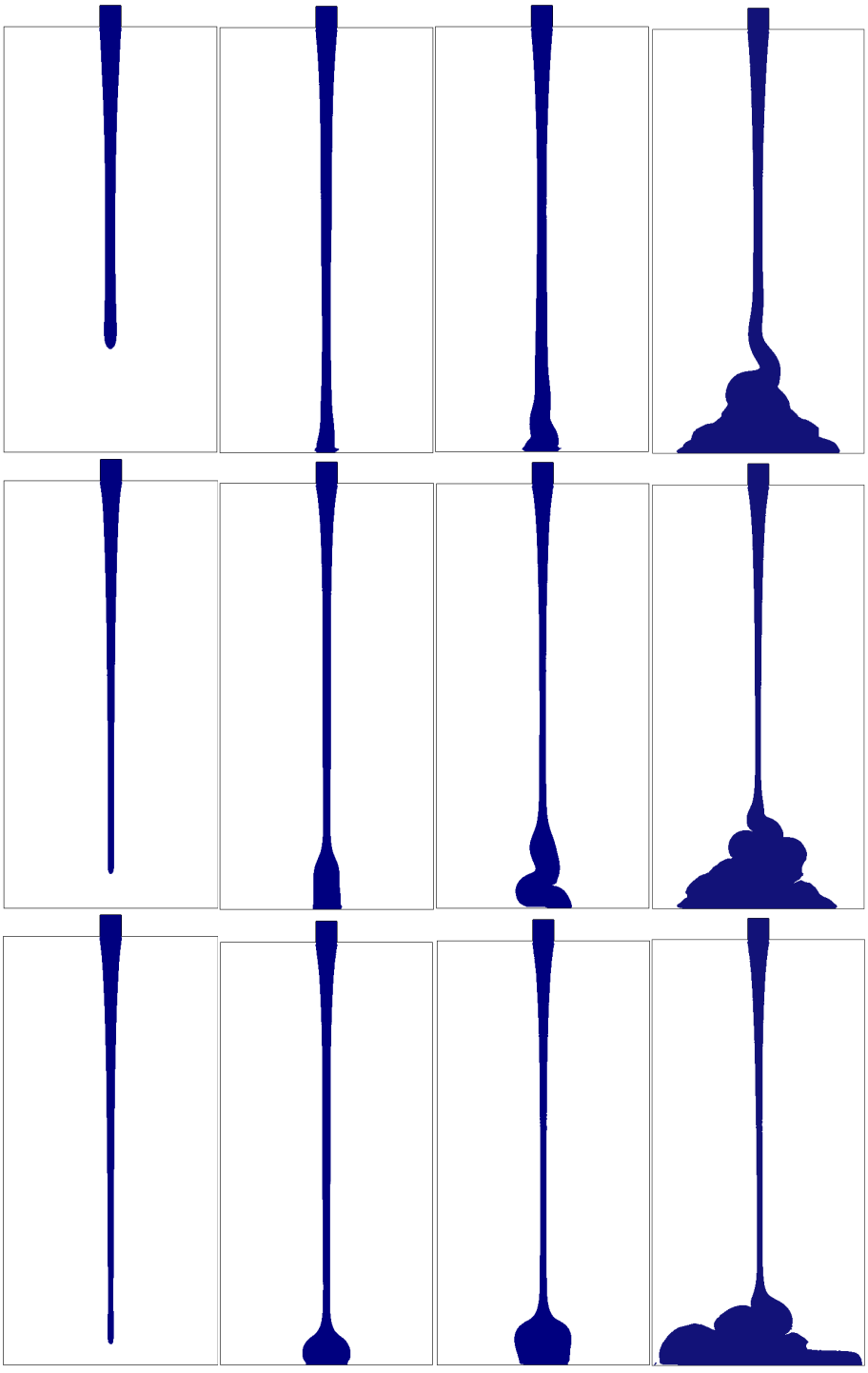

Figure 5.10: Jet buckling in a 2D rectangular cavity (Re = 0.25). First row We = 0 , second row We = 10 and third row We = 100, at time $t = 0.6$ (first column), $t = 0.8$ (second column), $t = 0.9$ (third column) and $t = 1.5$ (fourth column).

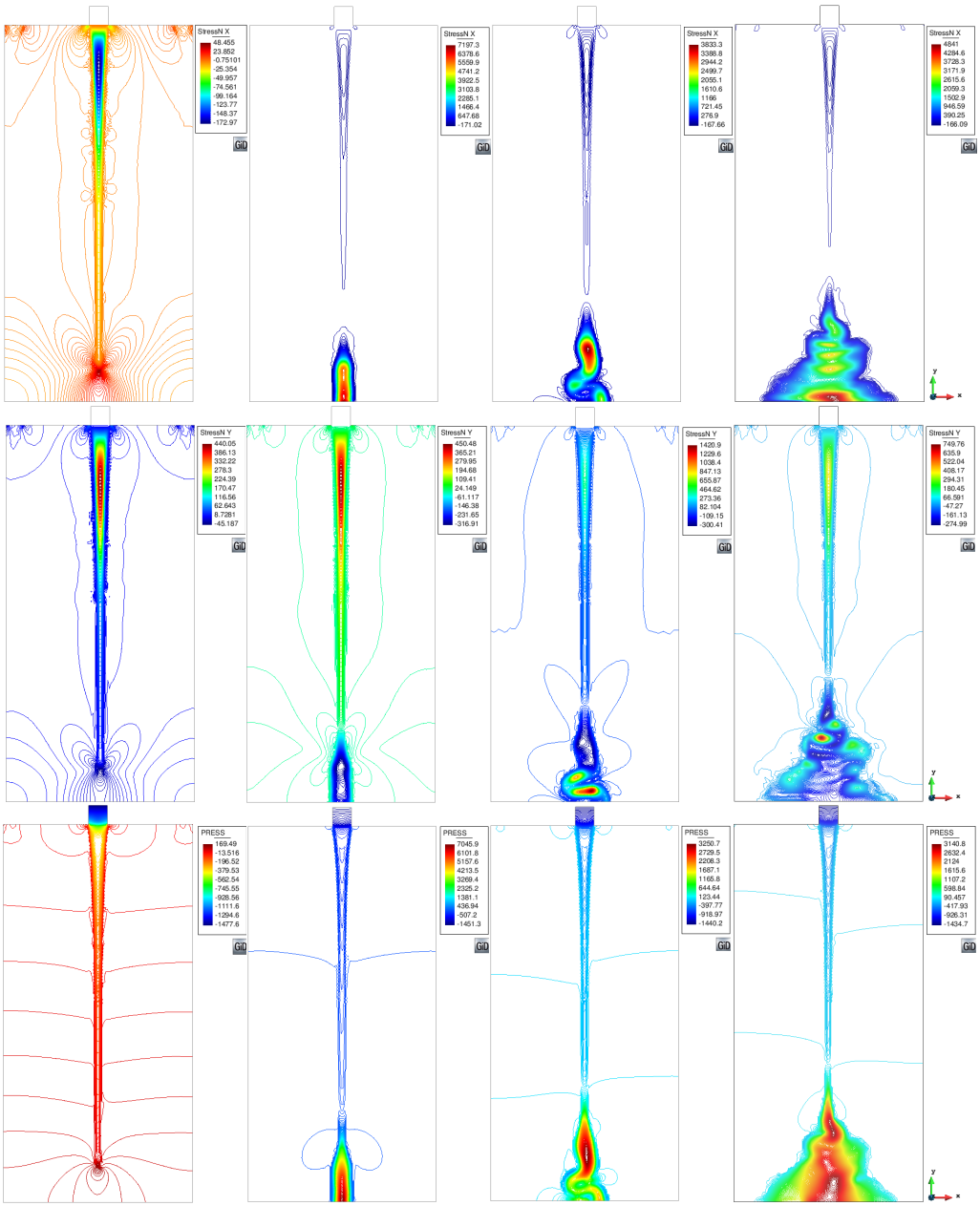

Figure 5.11: Contour line in the jet buckling problem for We = 10: σ_{xx} (first row), σ_{yy} (second row) and p (third row). For $t = 0.6$, $t = 0.8$, $t = 0.9$ and $t = 1.5$ (from left to right).

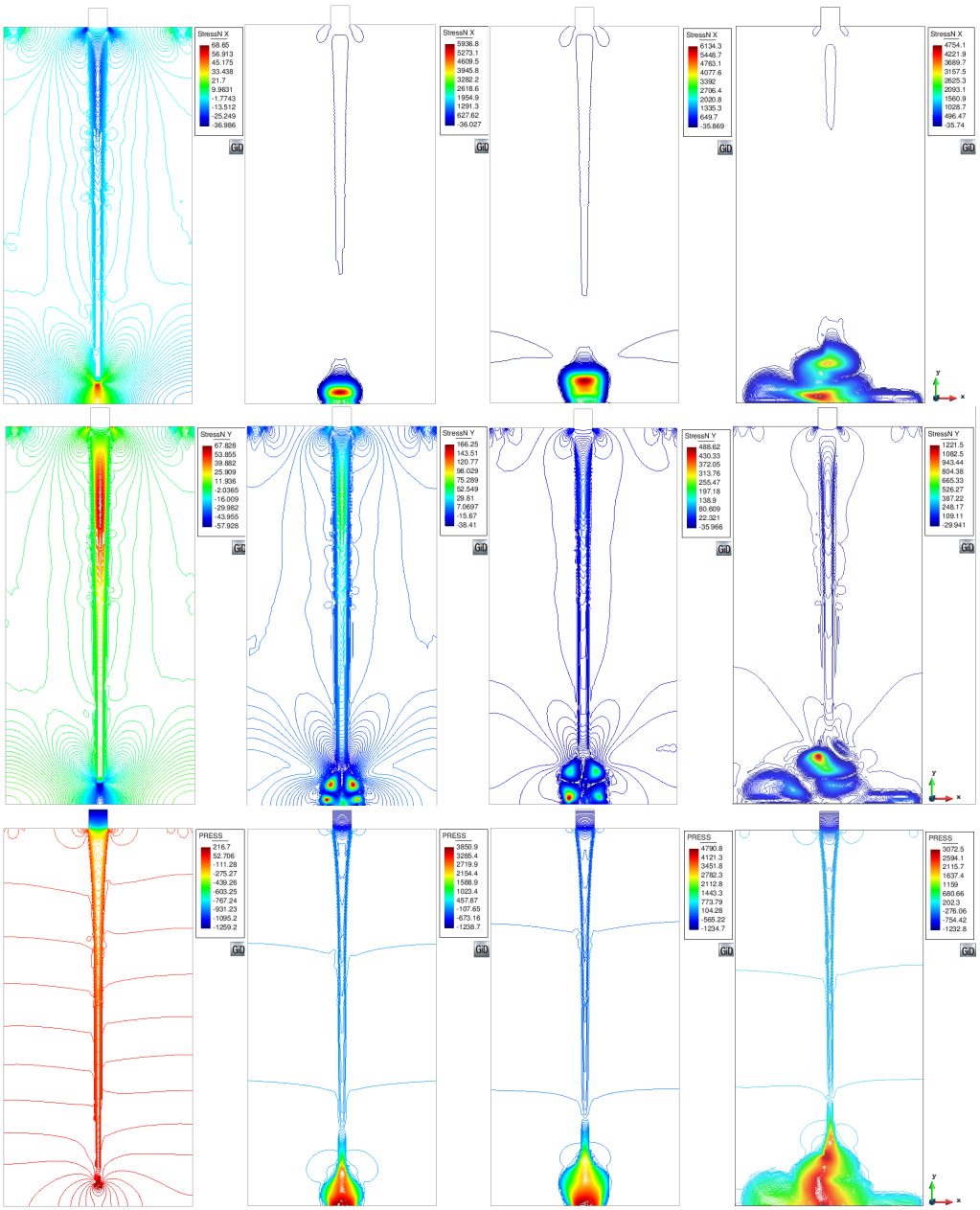

Figure 5.12: Contour line in the jet buckling problem for We = 100: σ_{xx} (first row), σ_{yy} (second row) and p (third row). For $t = 0.6$, $t = 0.8$, $t = 0.9$ and $t = 1.5$ (from left to right).

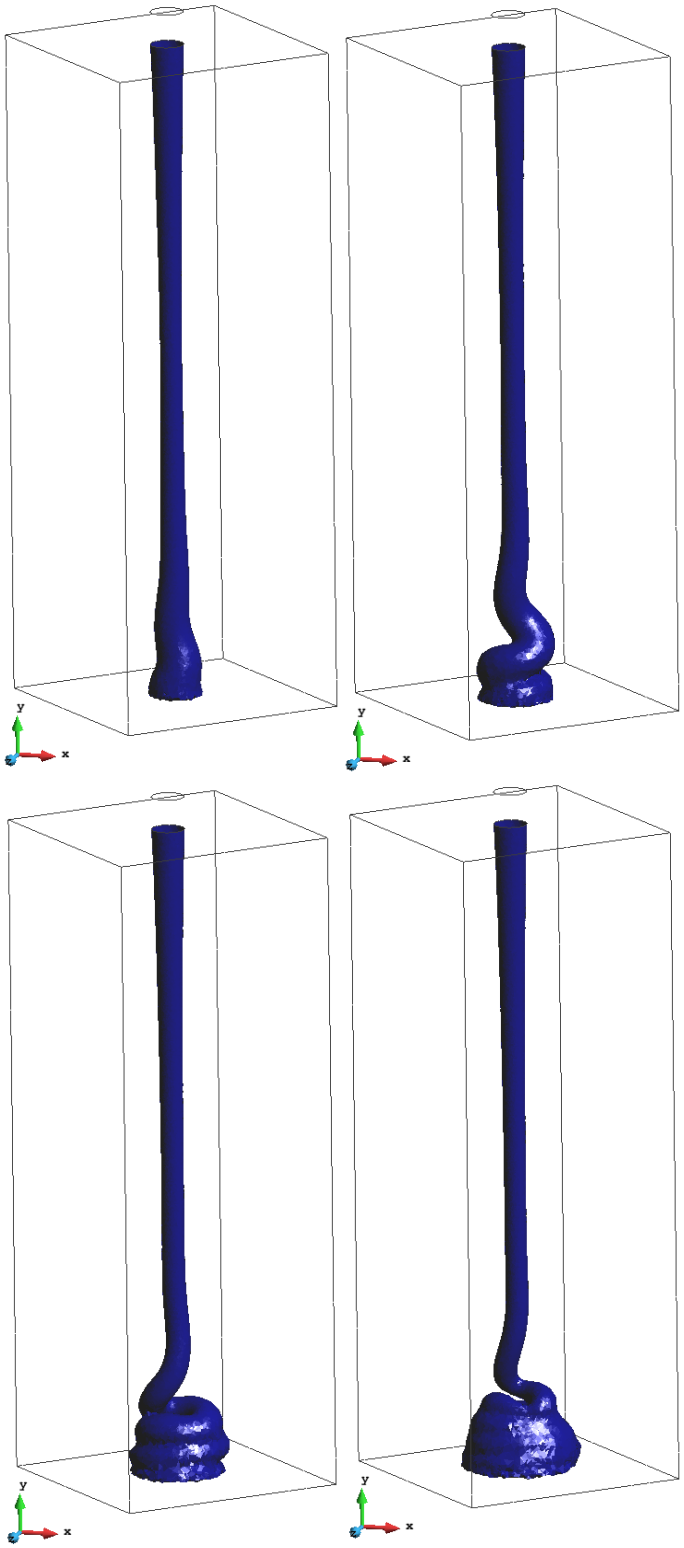

Figure 5.13: Jet buckling in a 3D prismatic cavity using a Newtonian fluid ($\mathrm{Re} = 0.25, \mathrm{We} = 0$). Top ($t = 1.25$ and $t = 1.5$), bottom ($t = 1.75$ and $t = 2$).

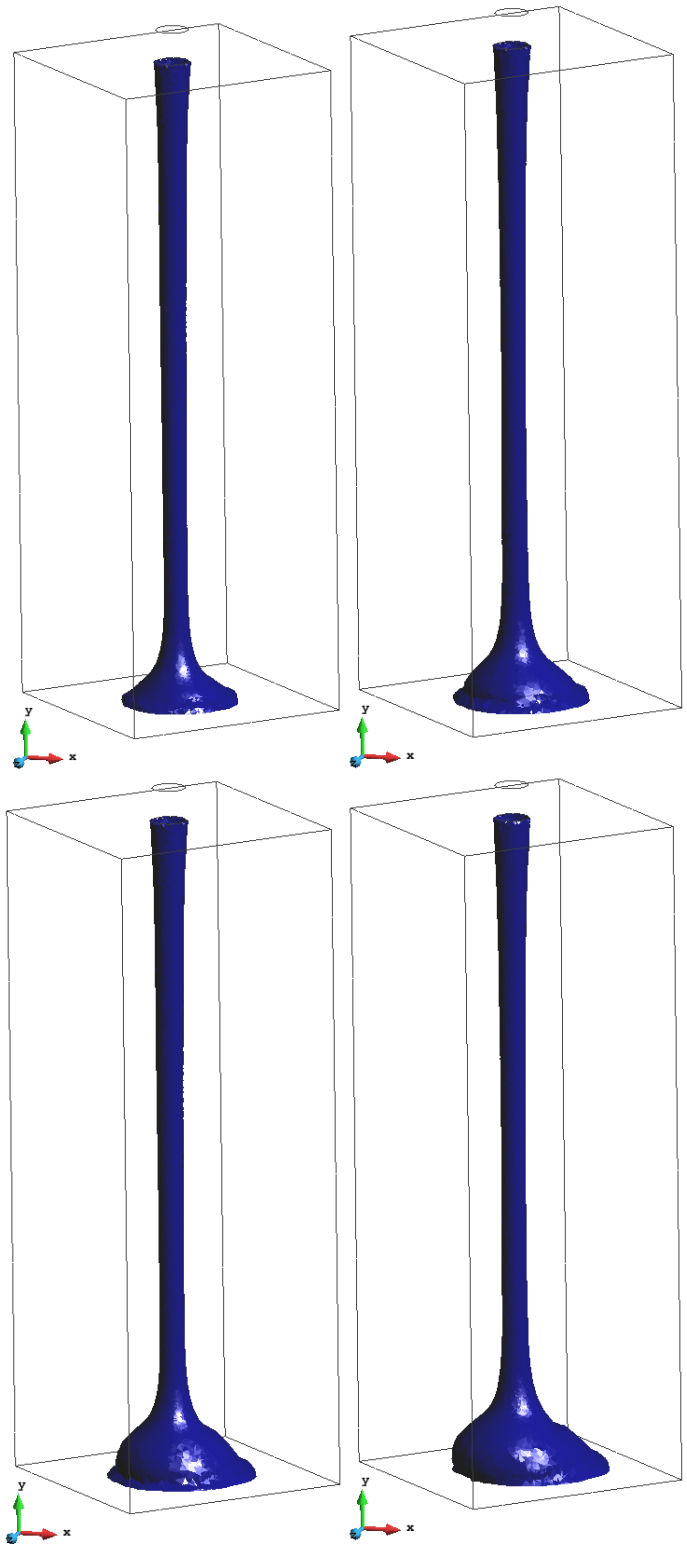

Figure 5.14: Jet buckling in a 3D prismatic cavity using a non-Newtonian ($\mathrm{Re} = 0.25, \mathrm{We} = 100$). Top ($t = 1.25$ and $t = 1.5$), bottom ($t = 1.75$ and $t = 2$).

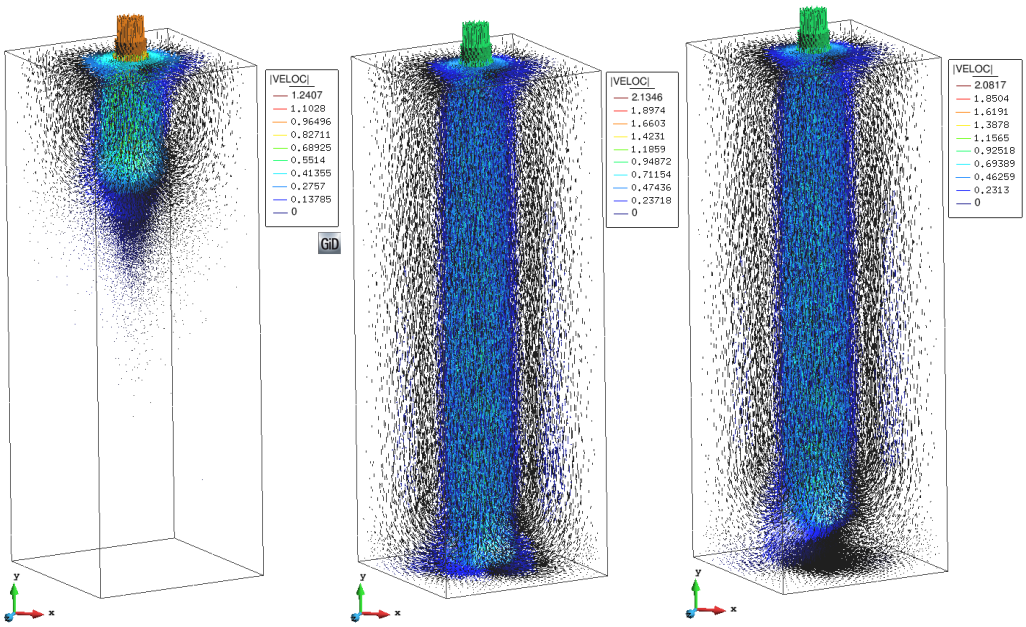

Figure 5.15: Velocity vectors in the jet buckling problem for We = 100 in $t = 0.2$, $t = 1.0$ and $t = 2.0$ (from left to right).

Weissenberg number is the non-dimensional number that defines the non-linear nature of the fluid. In Table 5.5, the mean number of non-linear iterations required in each of the simulations is detailed and represented by $\bar{\text{nn}}_{it}$. In this table we can see how the number of nonlinear iterations increases when the elastic behavior becomes dominant.

Re = 0.25	2D-Case	3D-Case
	$\bar{\text{nn}}_{it}$	$\bar{\text{nn}}_{it}$
We = 0.0	9	8
We = 10	18	-
We = 100	39	37

Table 5.5: Non-linear iterations for the jet buckling-problem.

5.7 Conclusions

In this chapter we have presented a stabilized finite element method to solve the two immiscible fluid flow problem by the level set method for Oldroyd-B and Giesekus fluids. The method shows very good stability and robustness even using the standard formulation of the elastic stress tensor. The buckling problem was solved up to We = 100 without any sign of instability both in the two-dimensional and three-dimensional cases. The enriched pressure formulation permits the resolution even of *free surface* problems and gives the possibility to solve real two-fluid problems that a free surface formulation cannot represents.

For the case of two immiscible fluids, the discontinuity in the material properties when the interface cuts an element leads to discontinuities in the gradients of the unknowns that standard interpolations cannot capture. A local pressure enriched function was tested to solve the interaction of viscoelastic and Newtonian fluids with very good results, correcting the amount of lost mass, and permitting the exact resolution of the hydrostatic rest state that standard formulations cannot solve.

The ten degrees of freedom per node in a three-dimensional case of the viscoelastic fluid flow problem requires efficient algorithms to resolve the coupled system of equations. In this chapter a fractional step approach to solve the two immiscible fluid flow problem was tested which shows an important reduction in computational resources with respect to the monolithic approach, both in the total CPU time required to solve the problem and in the total memory necessary to store the matrices.

A discontinuity-capturing technique for the constitutive equation was tested in order to eliminate non-physical peaks that can appear when the flow finds an abrupt change in the geometry with very satisfactory results.

Chapter 6

Numerical Analysis: Linearized Stationary Case

6.1 Abstract

In this Chapter we present the numerical analysis of the three-field stabilized finite element formulation proposed in chapter 3 to approximate viscoelastic flows. The three-field viscoelastic fluid flow problem may suffer from two types of numerical instabilities: on the one hand we have the two inf-sup conditions related to the mixed nature problem and, on the other, the convective nature of the momentum and constitutive equations may produce global and local oscillations in the numerical approximation. Both can be overcome by resorting from the standard Galerkin method to a stabilized formulation. The one presented here is based on the subgrid scale concept, in which unresolvable scales of the continuous solution are approximately accounted for. In particular, the approach developed herein is based on the decomposition into their finite element component and a subscale, which is approximated properly to yield a stable formulation. The analyzed problem corresponds to a linearized version of the Navier-Stokes/Oldroyd-B case where the advection velocity of the momentum equation and the non-linear terms in the constitutive equation are treated using a fixed point strategy for the velocity and the velocity gradient. The proposed method permits the resolution of the problem using arbitrary interpolations for all the unknowns. We describe some important ingredients related to the design of the formulation and present the results of its numerical analysis. It is shown that the formulation is stable and optimally convergent independently of the interpolation used.

6.2 Introduction

The numerical approximation of viscoelastic fluid flows is a current line of research due to the wide range of industrial applications where these materials are found [44]. The mathematical structure of the equations that define the problem presents different types of numerical instabilities and difficulties in which intensive research has been done in recent years (see for example [139, 82, 9] for a review about this topic).

When using finite elements, the numerical approximation of the flow of viscoelastic fluids presents basically two types of instabilities. The first is associated with the two compatibility or inf-sup conditions that restrict the possible choices of interpolation spaces. The second is related to the convective terms in both the momentum and the hyperbolic constitutive equation, in both cases nonlinear.

Referring to the compatibility conditions, many authors have studied the problem, considering first simplified model problems such as the three-field Stokes problem [134, 29, 56] or the three-field Navier-Stokes problem [19, 36], which have the same interpolation requirements as the viscoelastic case. For these simplified problems the classical compatibility condition between velocity and pressure [30] is not sufficient, and an additional condition that relates the interpolation of the velocity with that of the elastic stress must be added. The convective terms have been treated using the extension of classical methods used for the Navier-Stokes problem, such as the SUPG method [111], the Galerkin/Least-Squares (GLS) method [79] or approaches based on the Variational Multiscale (VMS) concept (see [103, 37], among others).

Concerning the mathematical analysis, the existence of a slow steady viscoelastic flow solution has been proved by Renardy in [138]. For the time-dependent case, existence of solutions locally in time, and for small data globally in time, have been proved by Guillopé and Saut [91]. These analysis have been performed in Hilbert spaces. The extension to Banach spaces and a complete review of uniqueness, regularity, well-posedness and stability results can be found in the work of Fernández-Cara et al. [82]. The existence of global weak solutions for general initial conditions using a co-rotational Oldroyd model has been proved by Lions and Masmoudi in [110].

In the context of the finite element approximation, for the steady state case one of the first works where the existence of approximate solutions and error analysis were presented is that of Baranger and Sandri in [16]. The authors used a discontinuous interpolation (Lesaint-Raviart method) to treat the viscoelastic stresses. Later, Sandri in [146] showed by using a fixed point method that the discrete approximate problem using a $P1$(continuous)-$P2$(continuous)-$P1$(continuous) interpolation for stress, velocity and pressure, respectively, and the SUPG method to treat the convective term in the constitutive equation, has an unique solution for which error bounds were given, supposing that the continuous problem admits sufficiently smooth and small solutions. Picasso and Rappaz [134] analyzed a stationary non-linear Stokes problem (Stokes/Oldroyd-B model without convective term), and they proved a priori and a posteriori error estimates for the finite element approximation for small Weissenberg numbers using a GLS method and an Elastic Viscous Split Stress (EVSS) scheme. The extension to the time-dependent case was treated in [27] for the same non-linear Stokes problem, proving global existence in time in Banach spaces provided the data are small enough. For a Stokes/Oldroyd-B linearized problem, Bonito and Burman presented in [26] optimal a priori error estimates using the Interior-Penalty method. In this work the authors showed that adding some type of artificial viscosity in the constitutive equation, the problem can be solved for a large range of Weissenberg numbers. A similar problem was studied by Ervin et al. in [76] for the steady state case, but using the Johnson-Segalman linearized constitutive model, proving existence and uniqueness of the continuous problem and of a finite element approximation under small data assumption. Ervin and Miles in [77] analyzed the Oldroyd-B time-dependent case both in the semi-discrete and in the fully discrete cases using the SUPG method, proving existence and deriving a priori error estimates for the numerical approximation, assuming a Taylor-Hood pair approximation for the velocity and pressure and a continuous approximation for the viscoelastic stresses.

The stabilized finite element formulation analyzed in this work has its roots in the VMS framework introduced by Hughes et al. [97] for the scalar convection-diffusion-reaction problem, and extended later to the vectorial Stokes problem in [51], where the space of the sub-grid scales is taken orthogonal to the finite element space. As we shall see, this is an important ingredient in the design of the formulation analyzed herein. The starting point of a VMS approach is to split the unknowns of the problem in two scales, the finite element one and the unresolvable one, called sub-grid scale or simply subscale in what follows. The latter needs to be approximated in a simple manner in terms of the former, so as to capture its main effect and yield a stable formulation for the finite element unknown, keeping therefore

the number of degrees of freedom of the Galerkin method.

One of the most common viscoelastic constitutive models used in the rheological community is the Oldroyd-B model. When this model is approximated numerically, the most challenging problem associated to it is the High Weissenberg Number Problem (HWNP), a phenomenon related to the inability of the numerical algorithms to converge to a solution when the Weissenberg (or Deborah) number is high (see for example [140, 99] and the references therein). Some numerical tools have been proved to increase the limits of the numerical formulations to solve more elastic fluids. The log-conformation formulation presented by Fattal and Kupferman [80] is a common possibility to deal with the exponential growth of stresses when the Weissenberg number is increased. Continuation methods are another numerical tool used to increase the Weissenberg number limits that can be reached by a standard formulation, as we can see in the work of Howell [94]. For the treatment of local oscillations, discontinuity-capturing techniques have proved to produce good results in [26, 37].

The objective of this part of the work is to analyze numerically the stabilized finite element formulation presented in chapter 3 and tested numerically with very good accuracy and robustness properties, both in stationary (chapter 3 and also in [37]) and time dependent cases (chapter 4 and 5 or [38, 35]). The analysis is standard and follows a classical approach to prove stability and convergence, first using a mesh-dependent or working norm, and then extending the results to natural norms, that is to say, to the norms of the spaces where the continuous problem is posed.

The chapter is organized as follows. In the following section we present the problem to be solved and its Galerkin finite element approximation, explaining the sources of numerical instability. Then, in Section 6.4 we present our stabilized finite element formulation. In Section 6.5, we present the numerical analysis performed, and finally, conclusions and remarks are given in Section 6.6.

6.3 Problem statement and Galerkin discretization

6.3.1 Boundary value problem

The stationary linearized viscoelastic fluid flow problem is defined by the following equations. First we have the conservation equations for momentum and mass

$$\rho \boldsymbol{a} \cdot \nabla \boldsymbol{u} - \nabla \cdot \boldsymbol{T} + \nabla p = \boldsymbol{f} \quad \text{in } \Omega, \tag{6.1}$$

$$\nabla \cdot \boldsymbol{u} = 0 \quad \text{in } \Omega, \tag{6.2}$$

where $\boldsymbol{a}$ is the advection velocity vector, Ω represents the computational domain of $\mathbb{R}^d$ occupied by the fluid, $d = 2$ or 3 being the space dimensions, ρ denotes the density of the fluid, $p : \Omega \longrightarrow \mathbb{R}$ the pressure, $\boldsymbol{u} : \Omega \longrightarrow \mathbb{R}^d$ the velocity field, $\boldsymbol{f} : \Omega \to \mathbb{R}^d$ the force vector and $\boldsymbol{T} : \Omega \longrightarrow \mathbb{R}^d \otimes \mathbb{R}^d$ the deviatoric extra stress tensor, which can be defined in terms of a viscous and a viscoelastic or elastic contribution as:

$$\boldsymbol{T} = 2\beta\mu\nabla^{\mathrm{s}}\boldsymbol{u} + \boldsymbol{\sigma}, \tag{6.3}$$

where μ represents the total viscosity, $\beta \in [0, 1]$ is a real parameter to define the amount of viscous or solvent viscosity $\mu_s = \beta\mu$ and elastic or polymeric viscosity $\mu_p = (1 - \beta)\,\mu$ in the fluid, and $\nabla^{\mathrm{s}}\boldsymbol{u}$ is the symmetrical part of the gradient of $\boldsymbol{u}$. We will consider that both the density ρ and the total viscosity μ are constants. For viscoelastic fluids, the problem is incomplete without the definition of a constitutive equation for the elastic part of the extra stress tensor ($\boldsymbol{\sigma}$). A large variety of approaches exist to define it (see [21, 22] for a

description). In this part of the work, we use the classical Oldroyd-B constitutive model to describe the fluid, which is defined as

$$\frac{1}{2\mu}\boldsymbol{\sigma} - (1-\beta)\nabla^{\mathrm{s}}\boldsymbol{u} + \frac{\lambda}{2\mu}\left(\boldsymbol{a}\cdot\nabla\boldsymbol{\sigma} - \boldsymbol{\sigma}\cdot\nabla\boldsymbol{a} - (\nabla\boldsymbol{a})^{T}\cdot\boldsymbol{\sigma}\right) = \mathbf{0} \quad \text{in } \Omega, \tag{6.4}$$

where λ is the relaxation time. This equation can be viewed as a convection-reaction equation.

Equations (6.1)-(6.4) are a mixed parabolic-hyperbolic system which additionally needs boundary conditions both in the velocity and in the stress fields to close the problem. In principle the elastic stresses can be fixed only on the inflow part of the boundary $\Gamma_{\mathrm{in}} = \{\boldsymbol{x}\in\partial\Omega \mid (\boldsymbol{u}\cdot\boldsymbol{n})(\boldsymbol{x}) < 0\}$, where $\boldsymbol{n}$ is the outward unit normal vector to $\partial\Omega$. For simplicity in the exposition, we shall consider the simplest boundary condition $\boldsymbol{u} = \mathbf{0}$ on $\partial\Omega$ for the velocity.

Calling $\boldsymbol{U} = [\boldsymbol{u}, p, \boldsymbol{\sigma}]$, $\boldsymbol{F} = [\boldsymbol{f}, 0, \mathbf{0}]$ and defining

$$\mathcal{L}(\boldsymbol{U}) := \begin{pmatrix} -2\beta\mu\nabla\cdot\nabla^{\mathrm{s}}\boldsymbol{u} + \rho\boldsymbol{a}\cdot\nabla\boldsymbol{u} - \nabla\cdot\boldsymbol{\sigma} + \nabla p \\ \nabla\cdot\boldsymbol{u} \\ \frac{1}{2\mu}\boldsymbol{\sigma} - (1-\beta)\nabla^{\mathrm{s}}\boldsymbol{u} + \frac{\lambda}{2\mu}\left(\boldsymbol{a}\cdot\nabla\boldsymbol{\sigma} - \boldsymbol{\sigma}\cdot\nabla\boldsymbol{a} - (\nabla\boldsymbol{a})^{T}\cdot\boldsymbol{\sigma}\right) \end{pmatrix}, \tag{6.5}$$

we may write (6.1), (6.2) and (6.4) as $\mathcal{L}(\boldsymbol{U}) = \boldsymbol{F}$.

This linearized problem can be viewed as a viscoelastic Oseen problem that represents a linearization of the stationary Navier-Stokes/Oldroyd-B problem. It also appears as one of the steps of some multilevel or multi-grid methods (see for example [105] in the context of viscoelastic flows). This is why it is often used as a first step towards the analysis of the full nonlinear problem, both to obtain a priori and posteriori error estimates. With respect to the advection velocity, in particular, we will take it in $\mathcal{C}^0\left(\overline{\Omega}\right)$, weakly divergence free and with bounded derivatives (see assumption **H1** in the following section).

6.3.2 Variational form of the problem

Let us introduce some notation in order to write the weak form of the problem. The space of square integrable functions in a domain ω is denoted by $L^2(\omega)$, and the space of functions whose distributional derivatives of order up to $m \geq 0$ (integer) belong to $L^2(\omega)$ by $H^m(\omega)$. The space $H_0^m(\omega)$ consists of functions in $H^m(\omega)$ vanishing on $\partial\omega$. The topological dual of $H_0^1(\Omega)$ is denoted by $H^{-1}(\Omega)$, the duality pairing by $\langle\cdot,\cdot\rangle$, and the L^2 inner product in Ω (for scalar, vectors and tensors) is denoted by $(\cdot,\cdot)$. The integral of the product of two functions in a domain ω is denoted as $\langle\cdot,\cdot\rangle_\omega$. The subscript ω is omitted when $\omega = \Omega$. The norm in a space X is written as $\|\cdot\|_X$, with the subscript omitted when $X = L^2(\Omega)$. When $X = L^2(\omega)$ we denote the norm by $\|\cdot\|_\omega$.

Let $\boldsymbol{\Upsilon} := \left\{\boldsymbol{\tau} \mid \boldsymbol{\tau}\in\left(L^2(\Omega)\right)^{d\times d},\ \tau_{ij} = \tau_{ji},\ \boldsymbol{a}\cdot\nabla\boldsymbol{\tau}\in\left(L^2(\Omega)\right)^{d\times d}\right\}$, $\boldsymbol{\mathcal{V}} := H_0^1(\Omega)^d$ and $\mathcal{Q} := L^2(\Omega)/\mathbb{R}$, which are the spaces where we may seek the elastic stress, the velocity and the pressure, respectively. The weak form of the problem is obtained by testing (6.5) against an arbitrary test function $\boldsymbol{V} = [\boldsymbol{v}, q, \boldsymbol{\tau}]$ with appropriate regularity. It can be written as: find $\boldsymbol{U} = [\boldsymbol{u}, p, \boldsymbol{\sigma}] \in \boldsymbol{\mathcal{X}} := \boldsymbol{\mathcal{V}}\times\mathcal{Q}\times\boldsymbol{\Upsilon}$ such that

$$2\beta\mu\left(\nabla^{\mathrm{s}}\boldsymbol{u}, \nabla^{\mathrm{s}}\boldsymbol{v}\right) + \langle\rho\boldsymbol{a}\cdot\nabla\boldsymbol{u}, \boldsymbol{v}\rangle + (\boldsymbol{\sigma}, \nabla^{\mathrm{s}}\boldsymbol{v}) - (p, \nabla\cdot\boldsymbol{v}) = \langle\boldsymbol{f}, \boldsymbol{v}\rangle, \tag{6.6}$$

$$(q, \nabla\cdot\boldsymbol{u}) = 0, \tag{6.7}$$

$$\frac{1}{2\mu}(\boldsymbol{\sigma}, \boldsymbol{\tau}) - ((1-\beta)\nabla^{\mathrm{s}}\boldsymbol{u}, \boldsymbol{\tau}) + \frac{\lambda}{2\mu}\left(\boldsymbol{a}\cdot\nabla\boldsymbol{\sigma} - \boldsymbol{\sigma}\cdot\nabla\boldsymbol{a} - (\nabla\boldsymbol{a})^{T}\cdot\boldsymbol{\sigma}, \boldsymbol{\tau}\right) = 0, \tag{6.8}$$

for all $\boldsymbol{V} = [\boldsymbol{v}, q, \boldsymbol{\tau}] \in \boldsymbol{\mathcal{X}}$, where it is assumed that $\boldsymbol{f}$ is such that $\langle\boldsymbol{f}, \boldsymbol{v}\rangle$ is well defined.

In a compact form, problem (6.6)-(6.8) can be written as:

$$B\left(\boldsymbol{U},\boldsymbol{V}\right)=\left\langle \boldsymbol{f},\boldsymbol{v}\right\rangle , \tag{6.9}$$

for all $\boldsymbol{V}\in\boldsymbol{\mathcal{X}}$, where

$$\begin{aligned} B\left(\boldsymbol{U},\boldsymbol{V}\right)=&2\beta\mu\left(\nabla^{\mathrm{s}}\boldsymbol{u},\nabla^{\mathrm{s}}\boldsymbol{v}\right)+\left\langle \rho\boldsymbol{a}\cdot\nabla\boldsymbol{u},\boldsymbol{v}\right\rangle +\left(\boldsymbol{\sigma},\nabla^{\mathrm{s}}\boldsymbol{v}\right)-\left(p,\nabla\cdot\boldsymbol{v}\right)+\left(q,\nabla\cdot\boldsymbol{u}\right)+\frac{1}{2\mu}\left(\boldsymbol{\sigma},\boldsymbol{\tau}\right)\\ &-\left(1-\beta\right)\left(\nabla^{\mathrm{s}}\boldsymbol{u},\boldsymbol{\tau}\right)+\frac{\lambda}{2\mu}\left(\boldsymbol{a}\cdot\nabla\boldsymbol{\sigma}-\boldsymbol{\sigma}\cdot\nabla\boldsymbol{a}-\left(\nabla\boldsymbol{a}\right)^{T}\cdot\boldsymbol{\sigma},\boldsymbol{\tau}\right). \end{aligned} \tag{6.10}$$

To guarantee the well-posedness of problem (6.9), the advection velocity must satisfy **H1** below. Note that this assumption is consistent with those used in previous works [141, 82, 76], and it is obviously inherited by the discrete problem:

H1 $\boldsymbol{a}\in\boldsymbol{\mathcal{V}}$, $\nabla\cdot\boldsymbol{a}=0$, $\left\|\boldsymbol{a}\right\|_{L^{\infty}(\Omega)}\leq M_{a}<\infty$, $\left\|\nabla\boldsymbol{a}\right\|_{L^{\infty}(\Omega)}\leq M_{g}<\infty$.

6.3.3 Stability of the Galerkin finite element discretization

Let us consider a finite element partition $\mathcal{P}_h$ of the domain Ω of diameter h. For simplicity, we will consider quasi-uniform refinements, and thus all the element diameters can be bounded above and below by constants multiplying h. Under the above considerations, we can construct conforming finite elements spaces, $\boldsymbol{\mathcal{V}}_h\subset\boldsymbol{\mathcal{V}}$, $\mathcal{Q}_h\subset\mathcal{Q}$ and $\boldsymbol{\Upsilon}_h\subset\boldsymbol{\Upsilon}$ in the usual manner. If $\boldsymbol{\mathcal{X}}_h=\boldsymbol{\mathcal{V}}_h\times\mathcal{Q}_h\times\boldsymbol{\Upsilon}_h$, and $\boldsymbol{U}_h=[\boldsymbol{u}_h,p_h,\boldsymbol{\sigma}_h]$, the Galerkin finite element approximation consists in finding $\boldsymbol{U}_h\in\boldsymbol{\mathcal{X}}_h$ such that:

$$B\left(\boldsymbol{U}_h,\boldsymbol{V}_h\right)=\left\langle \boldsymbol{f},\boldsymbol{v}_h\right\rangle , \tag{6.11}$$

for all $\boldsymbol{V}_h=[\boldsymbol{v}_h,q_h,\boldsymbol{\tau}_h]\in\boldsymbol{\mathcal{X}}_h$.

At the moment, we have posed no restrictions on the choice of the finite element spaces. However, there are restriction that must be satisfied. For example, it is readily checked that

$$\begin{aligned} B\left(\boldsymbol{U}_h,[\left(1-\beta\right)\boldsymbol{u}_h,\left(1-\beta\right)p_h,\boldsymbol{\sigma}_h]\right)=&2\left(1-\beta\right)\beta\mu\left\|\nabla^{s}\boldsymbol{u}_h\right\|^{2}+\frac{1}{2\mu}\left\|\boldsymbol{\sigma}_h\right\|^{2}\\ &-\frac{\lambda}{2\mu}\left(\boldsymbol{\sigma}_h\cdot\nabla\boldsymbol{u}_h+\left(\nabla\boldsymbol{u}_h\right)^{T}\cdot\boldsymbol{\sigma}_h,\boldsymbol{\sigma}_h\right). \end{aligned}$$

Assuming $\lambda\nabla\boldsymbol{a}_h$ to be small enough, this expression provides only control on $\left\|\boldsymbol{\sigma}_h\right\|^2$ for all $\beta\in[0,1]$. To control the other two fields one has then to make use of the two inf-sup conditions that restrict the possible interpolations:

$$\inf_{q_h\in\mathcal{Q}_h}\sup_{\boldsymbol{v}_h\in\boldsymbol{\mathcal{V}}_h}\frac{\left(q_h,\nabla\cdot\boldsymbol{v}_h\right)}{\left\|\boldsymbol{v}_h\right\|_{\boldsymbol{\mathcal{V}}_h}\left\|q_h\right\|_{\mathcal{Q}_h}}\geq C_1, \tag{6.12}$$

to control p_h, and

$$\inf_{\boldsymbol{v}_h\in\boldsymbol{\mathcal{V}}_h}\sup_{\boldsymbol{\tau}_h\in\boldsymbol{\Upsilon}_h}\frac{\left(\boldsymbol{\tau}_h,\nabla^{\mathrm{s}}\boldsymbol{v}_h\right)}{\left\|\boldsymbol{\tau}_h\right\|_{\boldsymbol{\Upsilon}_h}\left\|\boldsymbol{v}_h\right\|_{\boldsymbol{\mathcal{V}}_h}}\geq C_2, \tag{6.13}$$

to control $\nabla^{\mathrm{s}}\boldsymbol{u}_h$, where C_1 and C_2 are positive constants. It is therefore required that the finite element spaces satisfy (6.12)-(6.13). These two conditions pose stringent requirements on the choice of the finite element spaces (see for example [111] for the 2D case and [25] for the 3D case). Our intention in this work is to analyze a stabilized finite element formulation that avoids the need for such conditions and, in particular, allows one to use equal interpolation for all the unknowns, including the possibility to use discontinuous interpolations.

Let us introduce some notation. The finite element partition will be denoted by $\mathcal{P}_h = \{K\}$, and summation over all the elements will be indicated as $\sum_K$. The collection of all edges (faces, for $d = 3$) will be denoted by $\mathcal{E}_h = \{E\}$ and, as for the elements, summation over all these edges will be indicated as $\sum_E$. Suppose now that elements K_1 and K_2 share an edge E, and let $\boldsymbol{n}_1$ and $\boldsymbol{n}_2$ be the normals to E exterior to K_1 and K_2, respectively. For a scalar function g, possibly discontinuous across E, we define its jump as $[\![\boldsymbol{n} g]\!]_E := \boldsymbol{n}_1 g|_{\partial K_1 \cap E} + \boldsymbol{n}_2 g|_{\partial K_2 \cap E}$, and for a vector or tensor $\boldsymbol{v}$, $[\![\boldsymbol{n} \cdot \boldsymbol{v}]\!]_E := \boldsymbol{n}_1 \cdot \boldsymbol{v}|_{\partial K_1 \cap E} + \boldsymbol{n}_2 \cdot \boldsymbol{v}|_{\partial K_2 \cap E}$. When $E \subset \partial\Omega$ and $\boldsymbol{n}$ is the external normal, these definitions reduce to $[\![\boldsymbol{n} g]\!]_E := \boldsymbol{n} g|_E$ and $[\![\boldsymbol{n} \cdot \boldsymbol{v}]\!]_E := \boldsymbol{n} \cdot \boldsymbol{v}|_E$. Generic positive constants will be denoted by C, possibly with subscripts and with different values in different appearances. The symbol $\lesssim$ will be used for $\leq$ up to constants.

6.4 Stabilized finite element method

In the following section we summarize the stabilized formulation analyzed. This formulation was proposed in chapter 3 (also in [37]) and tested numerically in chapters 3, 4 and 5 (also in [37, 38, 35]), but the numerical analysis was not performed yet. As a novelty of this part of the work, we will introduce an additional stabilizing term for the subscales on the element boundaries that the original works do not include, which allows us to consider discontinuous pressure and stress interpolations.

The method consist in replacing (6.11) by the following problem: find $\boldsymbol{U}_h \in \boldsymbol{\mathcal{X}}_h$ such that

$$B_{\text{stab}}\left(\boldsymbol{U}_h, \boldsymbol{V}_h\right) = B\left(\boldsymbol{U}_h, \boldsymbol{V}_h\right) + B^*\left(\boldsymbol{U}_h, \boldsymbol{V}_h\right) = \left\langle \boldsymbol{f}, \boldsymbol{v}_h \right\rangle, \tag{6.14}$$

for all $\boldsymbol{V}_h \in \boldsymbol{\mathcal{X}}_h$, where B^* represent the stabilizing part of the model, defined as

$$B^*\left(\boldsymbol{U}_h, \boldsymbol{V}_h\right) = S_1^{\perp}\left(\boldsymbol{U}_h, \boldsymbol{V}_h\right) + S_2^{\perp}\left(\boldsymbol{U}_h, \boldsymbol{V}_h\right) + S_3^{\perp}\left(\boldsymbol{U}_h, \boldsymbol{V}_h\right)$$

where the three additional terms that define $B^*\left(\boldsymbol{U}_h, \boldsymbol{V}_h\right)$ are associated to the stabilized terms of each equation and are defined as

$$\begin{aligned} S_1^{\perp}\left(\boldsymbol{U}_h, \boldsymbol{V}_h\right) = & \sum_K \alpha_u \left\langle P_u^{\perp}\left(\rho \boldsymbol{a} \cdot \nabla \boldsymbol{u}_h\right), P_h^{\perp}\left(\rho \boldsymbol{a} \cdot \nabla \boldsymbol{v}_h\right) \right\rangle_K + \sum_K \alpha_u \left\langle P_u^{\perp}\left(\nabla p_h\right), P_h^{\perp}\left(\nabla q_h\right) \right\rangle_K \\ & + (1-\beta) \sum_K \alpha_u \left\langle P_u^{\perp}\left(\nabla \cdot \boldsymbol{\sigma}_h\right), P_u^{\perp}\left(\nabla \cdot \boldsymbol{\tau}_h\right) \right\rangle_K \\ & + \sum_E \alpha_{[u]} \left\langle [\![\left(\boldsymbol{n} q_h - (1-\beta)\, \boldsymbol{n} \cdot \boldsymbol{\tau}_h\right) + 2\beta\mu \boldsymbol{n} \cdot \nabla^{\mathrm{s}} \boldsymbol{v}_h]\!], [\![\left(\boldsymbol{n} p_h - \boldsymbol{n} \cdot \boldsymbol{\sigma}_h\right) - 2\beta\mu \boldsymbol{n} \cdot \nabla^{\mathrm{s}} \boldsymbol{u}_h]\!] \right\rangle_E, \end{aligned} \tag{6.15}$$

$$S_2^{\perp}\left(\boldsymbol{U}_h, \boldsymbol{V}_h\right) = \sum_K \alpha_p \left\langle P_p^{\perp}\left(\nabla \cdot \boldsymbol{u}_h\right), P_p^{\perp}\left(\nabla \cdot \boldsymbol{v}_h\right) \right\rangle_K, \tag{6.16}$$

$$S_3^{\perp}\left(\boldsymbol{U}_h, \boldsymbol{V}_h\right) = \sum_K \alpha_\sigma \left\langle P_\sigma^{\perp}\left(\boldsymbol{\mathcal{R}}_\sigma\right), P_\sigma^{\perp}\left(\nabla^{\mathrm{s}} \boldsymbol{v}_h - \frac{\lambda}{2\mu}\left(\boldsymbol{a}_h \cdot \nabla \boldsymbol{\tau}_h + \boldsymbol{\tau}_h \cdot \left(\nabla \boldsymbol{a}_h\right)^T + \nabla \boldsymbol{a}_h \cdot \boldsymbol{\tau}_h\right)\right) \right\rangle_K. \tag{6.17}$$

In the last expression, $\boldsymbol{\mathcal{R}}_\sigma$ represents the residual of the constitutive equation without the stress, given by

$$\boldsymbol{\mathcal{R}}_\sigma = (1-\beta)\, \nabla^{\mathrm{s}} \boldsymbol{u}_h - \frac{\lambda}{2\mu}\left(\boldsymbol{a}_h \cdot \nabla \boldsymbol{\sigma}_h - \boldsymbol{\sigma}_h \cdot \nabla \boldsymbol{a}_h - \left(\nabla \boldsymbol{a}_h\right)^T \cdot \boldsymbol{\sigma}_h\right),$$

In the numerical analysis below we will also use the notation

$$\boldsymbol{\sigma}_h \cdot \nabla \boldsymbol{a}_h + \left(\nabla \boldsymbol{a}_h\right)^T \cdot \boldsymbol{\sigma}_h = \dot{\boldsymbol{\sigma}}_h^* + \dot{\boldsymbol{\sigma}}_h^{**} \quad \text{and} \quad \boldsymbol{\sigma}_h \cdot \left(\nabla \boldsymbol{a}_h\right)^T + \nabla \boldsymbol{a}_h \cdot \boldsymbol{\sigma}_h = \dot{\boldsymbol{\sigma}}_h^* - \dot{\boldsymbol{\sigma}}_h^{**},$$

where $\dot{\boldsymbol{\sigma}}_h^* = \boldsymbol{\sigma}_h \cdot \nabla^{\rm s}\boldsymbol{a}_h + \nabla^{\rm s}\boldsymbol{a}_h \cdot \boldsymbol{\sigma}_h$ and $\dot{\boldsymbol{\sigma}}_h^{**} = \boldsymbol{\sigma}_h \cdot \nabla^{\rm as}\boldsymbol{a}_h - \nabla^{\rm as}\boldsymbol{a}_h \cdot \boldsymbol{\sigma}_h$. In these expressions, $\nabla^{\rm as}\boldsymbol{a}_h$ represents the skew-symmetric part of the velocity gradient.

In (6.15)-(6.17), $P_u^\perp$ represents the projection L^2-orthogonal to the velocity space, $P_p^\perp$ the projection L^2-orthogonal to the pressure space and $P_\sigma^\perp$ the projection L^2-orthogonal to the stress space. For example $P_u^\perp = I - P_u$, where P_u is the L^2 projection onto the velocity finite element space. The last term in $S_1^\perp$ is an approximation to the subscales on the element boundaries and allows us to consider discontinuous interpolations for the pressure and the stress. The design of the stabilized terms without the boundary term was presented in chapter 3 for the stationary three-field viscoelastic case. For the design of the boundary term we refer to [56], where a three-field Stokes problem was analyzed in detail. The extension to the Oldroyd-B viscoelastic case is trivial.

The stabilization parameters α_i, $i = u$ or $i = p$ or $i = \sigma$, are computed within each element K as

$$\alpha_u = \left(c_1 \frac{\mu}{h^2} + c_2 \frac{\rho\,|\boldsymbol{a}_h|}{h} \right)^{-1}, \tag{6.18}$$

$$\alpha_p = \frac{h^2}{c_1 \alpha_1}, \tag{6.19}$$

$$\alpha_\sigma = \left(c_3 \frac{1}{2\mu} + c_4 \frac{\lambda}{2\mu} \frac{|\boldsymbol{a}_h|}{h} + c_5 \frac{\lambda}{\mu} |\nabla \boldsymbol{a}_h| \right)^{-1}. \tag{6.20}$$

A possible justification for these parameters is the Fourier analysis presented in [56] for the three-field Stokes problem or in [54] for the transient Navier-Stokes problem. The constants c_i, $i = 1, 2, 3, 4, 5$, are algorithmic parameters. As a reference, the values used in the numerical experiments in [37, 38, 35] for linear elements were $c_1 = 4.0$ or 12.0 , $c_2 = 2.0$, $c_3 = 4.0$ and $c_4 = c_5 = 0.25$ or 1.0. For higher order elements these values should be modified in terms of the interpolation order used (more details can be found in the numerical references where the method was tested).

The boundary stabilization parameter in $S_1^\perp$ can be defined as $\alpha_{[u]} = \dfrac{\delta_0 h}{2\mu}$, as in [59, 56], where δ_0 is an algorithmic parameter that can be taken as $\delta_0 = \dfrac{1}{10}$.

The method presented is a mix of an orthogonal-term-by-term formulation for the momentum and continuity equations and a residual-based formulation for the constitutive equation. The term-by-term part is not just a simplification of a standard residual based one. For smooth solutions, both have an optimal convergence rate in h. However, in problems where the solution has strong gradients, we have found the term-by-term formulation more robust than the residual-based one, which can be explained using numerical analysis as we will show below. The method we analyze permits a term-by-term control of the orthogonal projections of the pressure gradient, the convective term of the momentum equation and the divergence of the elastic stress which is not possible using the residual-based formulation.

6.5 Numerical Analysis

The numerical analysis performed in this section follows a more less standard approach. First we prove stability in the form of inf-sup condition in a mesh dependent norm that depends on the stabilized formulation used. Next we prove convergence in the same norm. Stability and convergence in natural norms, that is to say, the norms where the continuous problem is posed, and then proved. Finally, we obtain an L^2-error estimate for the velocity using a duality argument.

6.5.1 Preliminaries

As it has been mentioned in Section 6.4, we will consider for the sake of conciseness quasi-uniform finite element partitions. Therefore, we assume that there is a constant c_{inv}, independent of the mesh size h (the maximum of all the element diameters), such that

$$\|\nabla v_h\|_K \leq c_{\text{inv}} h^{-1} \|v_h\|_K ,$$

for all finite element functions v_h defined on $K \in \mathcal{P}_h$, which can be either scalars, vectors or tensors. Similarly, the trace inequality

$$\|v\|^2_{\partial K} \leq c_{\text{tr}} \left(h^{-1} \|v\|^2_K + h \|\nabla v\|^2_K \right),$$

is assumed to hold for functions $v_h \in H^1(K)$, $K \in \mathcal{P}_h$. The last term can be dropped if v_h is a polynomial on the element domain K. Thus, if φ_h is a piecewise discontinuous polynomial and ψ_h a continuous one, it follows that

$$\sum_E \|[\![\boldsymbol{n} \varphi_h]\!]\|^2_E \leq 2 c_{\text{tr}} h^{-1} \sum_K \|\varphi_h\|^2_K , \qquad \sum_E \|\psi_h\|^2_E \leq \frac{c_{\text{tr}}}{2} h^{-1} \sum_K \|\psi_h\|^2_K . \tag{6.21}$$

We will also make use of Korn's inequality, which holds for the conforming approximation that we consider:

$$\|\boldsymbol{v}_h\|^2_{H^1(\Omega)} \leq c \|\nabla^{\text{s}} \boldsymbol{v}_h\|^2 .$$

Let $\mathcal{W}_h$ be a finite element space of degree k_v. For any function $v \in H^{k'_v+1}(\Omega)$ and for $i = 0, 1$, we define the interpolation errors $\varepsilon_i(v)$ from the interpolation estimates

$$\inf_{v_h \in \mathcal{W}_h} \sum_K \|v - v_h\|_{H^i(K)} \leq C h^{k''_v+1-i} \sum_K \|v\|_{H^{k''_v+1}(K)} =: \sum_K \varepsilon_{i,K}(v) =: \varepsilon_i(v) ,$$

where $k''_v = \min(k_v, k'_v)$. We will denote by $\tilde{v}_h$ the best approximation of v in $\mathcal{W}_h$. Clearly, we may take $\varepsilon_0(v) = h\varepsilon_1(v)$.

6.5.2 Stability and convergence in a mesh-dependent norm

The norm in which the results will be first presented is

$$\begin{aligned}
\|\boldsymbol{V}_h\|^2_W = {} & 2\beta\mu(1-\beta) \sum_K \|\nabla^{\text{s}} \boldsymbol{v}_h\|^2_K + \frac{1}{2\mu} \sum_K \|\boldsymbol{\tau}_h\|^2_K + \sum_K \alpha_u \|\rho \boldsymbol{a}_h \cdot \nabla \boldsymbol{v}_h + \nabla q_h - \nabla \cdot \boldsymbol{\tau}_h\|^2_K \\
& + \sum_K \alpha_u \left\| P^\perp_u (\rho \boldsymbol{a}_h \cdot \nabla \boldsymbol{v}_h) \right\|^2_K + (1-\beta) \sum_K \alpha_u \left\| P^\perp_u (\nabla \cdot \boldsymbol{\tau}_h) \right\|^2_K \\
& + \sum_K \alpha_u \left\| P^\perp_u (\nabla q_h) \right\|^2_K + \sum_K \alpha_p \|\nabla \cdot \boldsymbol{v}_h\|^2_K \\
& + \sum_K \alpha_\sigma \left\| -(1-\beta) \nabla^{\text{s}} \boldsymbol{v}_h + \frac{\lambda}{2\mu} (\boldsymbol{a}_h \cdot \nabla \boldsymbol{\tau}_h - \dot{\boldsymbol{\tau}}^{**}_h) \right\|^2_K \\
& + (1-\beta) \sum_E \alpha_{[u]} \|[\![\boldsymbol{n} q_h - \boldsymbol{n} \cdot \boldsymbol{\tau}_h]\!]\|^2_E ,
\end{aligned} \tag{6.22}$$

although later on we will transform our results to natural norms under the assumption of small elasticity and large viscosity. Note that the term multiplied by α_p is unnecessary, since it is already contained in the first right hand side term. However, we will keep it to see

the effect of the subscale associated to the pressure. It can also be helpful for some non-conforming elements (not considered in this work) for which the discrete Korn's inequality does not hold (see e.g. [102]).

If β is very small (or $\beta = 0$) control on velocity gradient can be obtained from the term multiplied by α_σ. However, to simplify a little the analysis we will consider $\beta > 0$, and the stability provided by the first term relevant enough.

Note that the stabilization term $S_1^\perp$ allows us to have a term-by-term control of the orthogonal projections of the convective term, the pressure gradient and the divergence of the elastic stress tensor.

This fact may be an explanation of why we have found the term-by-term stabilization more robust than the residual based in the presence of high gradients.

Our first result states the the formulation we consider is stable in the working norm (6.22):

Theorem 1 (Stability) *For λ small enough, there is a constant $C > 0$ such that*

$$\inf_{\boldsymbol{U}_h \in \boldsymbol{\mathcal{X}}_h} \sup_{\boldsymbol{V}_h \in \boldsymbol{\mathcal{X}}_h} \frac{B_{\text{stab}}\left(\boldsymbol{U}_h, \boldsymbol{V}_h\right)}{\|\boldsymbol{U}_h\|_W \|\boldsymbol{V}_h\|_W} \geq C,$$

provided δ_0 is taken small enough and the constants c_i, $i = 1, 2, 3, 4, 5$ in (6.18)-(6.20) are large enough.

Proof. Given $\boldsymbol{U}_h \in \boldsymbol{\mathcal{X}}_h$, consider $\boldsymbol{U}_{h1} = ((1-\beta)\,\boldsymbol{u}_h, (1-\beta)\,p_h, \boldsymbol{\sigma}_h)$. Using only Schwarz's inequality we obtain

$$\begin{aligned}
B_{\text{stab}}\left(\boldsymbol{U}_h, \boldsymbol{U}_{h1}\right) \geq\ & 2\beta\,(1-\beta)\,\mu\,\|\nabla^{\text{s}}\boldsymbol{u}_h\|^2 + \frac{1}{2\mu}\sum_K \left(1 - 2\lambda\,\|\nabla \boldsymbol{a}_h\|_K\right)\|\boldsymbol{\sigma}_h\|_K^2 \\
& - \frac{1}{2\mu}\sum_K \left(4\lambda\alpha_\sigma \frac{\lambda}{2\mu}\,\|\nabla^{\text{s}}\boldsymbol{a}_h\|_K^2\right)\|\boldsymbol{\sigma}_h\|_K^2 + (1-\beta)\sum_K \alpha_p \left\|P_p^\perp\left(\nabla\cdot\boldsymbol{u}_h\right)\right\|_K^2 \\
& + (1-\beta)\sum_K \alpha_u \left\|P_u^\perp\left(\rho\boldsymbol{a}_h\cdot\nabla\boldsymbol{u}_h\right)\right\|_K^2 + (1-\beta)\sum_K \alpha_u \left\|P_u^\perp\left(\nabla p_h\right)\right\|_K^2 \\
& + (1-\beta)\sum_K \alpha_u \left\|P_u^\perp\left(\nabla\cdot\boldsymbol{\sigma}_h\right)\right\|_K^2 \\
& + \sum_K \alpha_\sigma \left\|P_\sigma^\perp\left(-(1-\beta)\,\nabla^{\text{s}}\boldsymbol{u}_h + \frac{\lambda}{2\mu}\left(\boldsymbol{a}_h\cdot\nabla\boldsymbol{\sigma}_h - \dot{\boldsymbol{\sigma}}_h^{**}\right)\right)\right\|_K^2 \\
& + (1-\beta)\sum_E \frac{\delta_0 h}{2\mu}\,\|[\![\,\boldsymbol{n}p_h - \boldsymbol{n}\cdot\boldsymbol{\sigma}_h\,]\!]\|_E^2 - (1-\beta)\sum_E \frac{\delta_0 h}{2\mu}\,\|[\![\,2\beta\mu\boldsymbol{n}\cdot\nabla^{\text{s}}\boldsymbol{u}_h\,]\!]\|_E^2\,.
\end{aligned}$$

Using now (6.21) we obtain

$$\begin{aligned}
B_{\text{stab}}\left(\boldsymbol{U}_h, \boldsymbol{U}_{h1}\right) \geq\ & 2\beta\,(1-\beta)\,\mu\sum_K \left(1 - 2\beta\delta_0 c_{\text{tr}}\right)\|\nabla^{\text{s}}\boldsymbol{u}_h\|_K^2 + (1-\beta)\sum_K \alpha_u \left\|P_u^\perp\left(\rho\boldsymbol{a}_h\cdot\nabla\boldsymbol{u}_h\right)\right\|_K^2 \\
& + (1-\beta)\sum_K \alpha_p \left\|P_p^\perp\left(\nabla\cdot\boldsymbol{u}_h\right)\right\|_K^2 + \frac{1}{2\mu}\sum_K \left(1 - 2\lambda\,\|\nabla\boldsymbol{a}_h\|_K - 4\lambda\alpha_\sigma\frac{\lambda}{2\mu}\,\|\nabla^{\text{s}}\boldsymbol{a}_h\|_K^2\right)\|\boldsymbol{\sigma}_h\|_K^2 \\
& + \alpha_u\,(1-\beta)\sum_K \left\|P_u^\perp\left(\nabla p_h\right)\right\|_K^2 + (1-\beta)\sum_K \alpha_u \left\|P_u^\perp\left(\nabla\cdot\boldsymbol{\sigma}_h\right)\right\|_K^2 \\
& + \alpha_\sigma \left\|P_\sigma^\perp\left(-(1-\beta)\,\nabla^{\text{s}}\boldsymbol{u}_h + \frac{\lambda}{2\mu}\left(\boldsymbol{a}_h\cdot\nabla\boldsymbol{\sigma}_h - \dot{\boldsymbol{\sigma}}_h^{**}\right)\right)\right\|_K^2 + (1-\beta)\sum_E \frac{\delta_0 h}{2\mu}\,\|[\![\,\boldsymbol{n}p_h - \boldsymbol{n}\cdot\boldsymbol{\sigma}_h\,]\!]\|_E^2\,.
\end{aligned} \tag{6.23}$$

An important restriction inherited from the continuous case is that the stability of the elastic stresses can be ensured only for small Weissenberg numbers. In the above expression the factor of the term $\|\boldsymbol{\sigma}_h\|^2$ must be strictly positive to guarantee the stability. In this factor we have two negative components, the first $2\lambda\|\nabla \boldsymbol{a}_h\|$ comes from the Galerkin method, and the second $4\lambda\alpha_\sigma \dfrac{\lambda}{2\mu}\|\nabla^{\mathrm{s}}\boldsymbol{a}_h\|^2$ from the stabilized formulation. All the analysis carried out assumes that

$$1 - 2\lambda\|\nabla \boldsymbol{a}_h\|_K - 4\lambda\alpha_\sigma \frac{\lambda}{2\mu}\|\nabla^{\mathrm{s}}\boldsymbol{a}_h\|_K^2 \geq C > 0.$$

The basic idea to prove Theorem 1 is to obtain control on the components on the finite element space for the terms whose orthogonal component appears in the above expression. The key point is that this control comes from the Galerkin terms of B_{stab} (6.14).

Let us start considering $\boldsymbol{V}_{h1} = \alpha_u(1-\beta)\left(P_u\left(\rho\boldsymbol{a}_h\cdot\nabla\boldsymbol{u}_h + \nabla p_h - \nabla\cdot\boldsymbol{\sigma}_h\right), 0, \boldsymbol{0}\right)$. Recalling that P_u is defined based on elementwise integrals, $P_u\left(\rho\boldsymbol{a}_h\cdot\nabla\boldsymbol{u}_h + \nabla p_h - \nabla\cdot\boldsymbol{\sigma}_h\right)$ is well defined. We will use the abbreviation $\boldsymbol{v}_1 \equiv P_u\left(\rho\boldsymbol{a}_h\cdot\nabla\boldsymbol{u}_h + \nabla p_h - \nabla\cdot\boldsymbol{\sigma}_h\right)$. Using Young's inequality, inverse estimates and (6.21), we obtain

$$\begin{aligned}
&B_{\mathrm{stab}}(\boldsymbol{U}_h, \boldsymbol{V}_{h1}) = B(\boldsymbol{U}_h, \boldsymbol{V}_{h1}) + B^*(\boldsymbol{U}_h, \boldsymbol{V}_{h1}) \\
&\quad \geq B^*(\boldsymbol{U}_h, \boldsymbol{V}_{h1}) + (1-\beta)\left(1 - \frac{\varepsilon_1}{2} - \frac{c_{\mathrm{tr}}}{2}\frac{\varepsilon_2}{2}\right)\sum_K \alpha_u \|P_u\left(\rho\boldsymbol{a}_h\cdot\nabla\boldsymbol{u}_h + \nabla p_h - \nabla\cdot\boldsymbol{\sigma}_h\right)\|_K^2 \\
&\quad - \mu(1-\beta)(2\beta)^2\frac{c_{\mathrm{inv}}^2}{2\varepsilon_1}\sum_K \alpha_u\frac{\mu}{h^2}\|\nabla^{\mathrm{s}}\boldsymbol{u}_h\|_K^2 \\
&\quad - (1-\beta)\frac{1}{2\varepsilon_2}\sum_E \frac{\alpha_u}{h}\|[\![(\boldsymbol{n}p_h - \boldsymbol{n}\cdot\boldsymbol{\sigma}_h) - 2\beta\mu\boldsymbol{n}\cdot\nabla^{\mathrm{s}}\boldsymbol{u}_h]\!]\|_E^2 \\
&\quad \geq B^*(\boldsymbol{U}_h, \boldsymbol{V}_{h1}) + (1-\beta)\left(1 - \frac{\varepsilon_1}{2} - \frac{c_{\mathrm{tr}}}{2}\frac{\varepsilon_2}{2}\right)\sum_K \alpha_u \|P_u\left(\rho\boldsymbol{a}_h\cdot\nabla\boldsymbol{u}_h + \nabla p_h - \nabla\cdot\boldsymbol{\sigma}_h\right)\|_K^2 \\
&\quad - \mu(1-\beta)(2\beta)^2\left(\frac{c_{\mathrm{inv}}^2}{2\varepsilon_1} + 4\frac{c_{\mathrm{tr}}}{2\varepsilon_2}\right)\sum_K \alpha_u\frac{\mu}{h^2}\|\nabla^{\mathrm{s}}\boldsymbol{u}_h\|_K^2 \\
&\quad - 2(1-\beta)\frac{1}{2\varepsilon_2}\sum_E \frac{\alpha_u}{h}\|[\![\boldsymbol{n}p_h - \boldsymbol{n}\cdot\boldsymbol{\sigma}_h]\!]\|_E^2,
\end{aligned} \tag{6.24}$$

for any ε_1, ε_2. On the other hand, the stabilizing part leads to

$$\begin{aligned}
B^*(\boldsymbol{U}_h, \boldsymbol{V}_{h1}) \geq &-(1-\beta)\frac{1}{2\varepsilon_4}\sum_K\left(\alpha_u^2\frac{\rho\|\boldsymbol{a}_h\|_K}{h}\right)\left\|P_u^{\perp}\left(\rho\boldsymbol{a}_h\cdot\nabla\boldsymbol{u}_h\right)\right\|_K^2 \\
&- (1-\beta)(c_{\mathrm{inv}})^2\sum_K \alpha_u^2\left(\frac{\alpha_p}{h^2}\frac{\varepsilon_3}{2} + \frac{\rho\|\boldsymbol{a}_h\|_K}{h}\frac{\varepsilon_4}{2} + \frac{2\mu}{h^2}\beta^2\delta_0 c_{\mathrm{tr}}\frac{\varepsilon_5}{2} + \frac{\alpha_\sigma}{h^2}\frac{\varepsilon_6}{2}\right)\|\boldsymbol{v}_1\|_K^2 \\
&- (1-\beta)\frac{1}{2\varepsilon_3}\sum_K \alpha_p\left\|P_p^{\perp}\left(\nabla\cdot\boldsymbol{u}_h\right)\right\|_K^2 \\
&- 2(1-\beta)\frac{1}{2\varepsilon_6}\sum_K \alpha_\sigma\left\|P_\sigma^{\perp}\left(-(1-\beta)\nabla^{\mathrm{s}}\boldsymbol{u}_h + \frac{\lambda}{2\mu}\left(\boldsymbol{a}_h\cdot\nabla\boldsymbol{\sigma}_h - \dot{\boldsymbol{\sigma}}_h^{**}\right)\right)\right\|_K^2 \\
&- 2(1-\beta)\frac{1}{2\varepsilon_6}\left(\frac{\lambda}{2\mu}\right)^2\sum_K \alpha_\sigma\|\dot{\boldsymbol{\sigma}}_h^*\|_K^2
\end{aligned}$$

$$- 2\left(1-\beta\right)\frac{1}{2\varepsilon_5}\sum_E \alpha_{[u]}\left\|\left[\!\left[\boldsymbol{n}p_h - \boldsymbol{n}\cdot\boldsymbol{\sigma}_h\right]\!\right]\right\|_E^2 - 8\beta^2\left(1-\beta\right)\mu c_{\mathrm{tr}}\frac{1}{2\varepsilon_5}\sum_K \delta_0\left\|\nabla^{\mathrm{s}}\boldsymbol{u}_h\right\|_K^2, \tag{6.25}$$

for any ε_i, $i = 3,4,5,6$. Using (6.25) in (6.24) we get

$$\begin{aligned}
B_{\mathrm{stab}}\left(\boldsymbol{U}_h,\boldsymbol{V}_{h1}\right) \geq{}& \left(1-\beta\right)\sum_K \alpha_u C_u\left\|\boldsymbol{v}_1\right\|_K^2 \\
&- \mu\left(1-\beta\right)\left(2\beta\right)^2\left(\frac{c_{\mathrm{inv}}^2}{2\varepsilon_1} + 4\frac{c_{\mathrm{tr}}}{2\varepsilon_2} + 2\frac{c_{\mathrm{tr}}\delta_0}{2\varepsilon_5}\right)\sum_K \alpha_u\frac{\mu}{h^2}\left\|\nabla^{\mathrm{s}}\boldsymbol{u}_h\right\|_K^2 \\
&- \left(1-\beta\right)\frac{1}{2\varepsilon_3}\sum_K \alpha_p\left\|P_p^{\perp}\left(\nabla\cdot\boldsymbol{u}_h\right)\right\|_K^2 - \left(1-\beta\right)\frac{1}{2\varepsilon_4}\sum_K \alpha_u^2\frac{\rho\left\|\boldsymbol{a}_h\right\|_K}{h}\left\|P_u^{\perp}\left(\rho\boldsymbol{a}_h\cdot\nabla\boldsymbol{u}_h\right)\right\|_K^2 \\
&- \left(1-\beta\right)2\frac{1}{2\varepsilon_6}\sum_K \alpha_\sigma\left\|P_\sigma^{\perp}\left(-\left(1-\beta\right)\nabla^{\mathrm{s}}\boldsymbol{u}_h + \frac{\lambda}{2\mu}\left(\boldsymbol{a}_h\cdot\nabla\boldsymbol{\sigma}_h - \dot{\boldsymbol{\sigma}}_h^{**}\right)\right)\right\|_K^2 \\
&- \frac{1}{2\mu}2\left(1-\beta\right)\frac{1}{2\varepsilon_6}\sum_K \frac{\alpha_\sigma}{2\mu}\left(\lambda\left\|\nabla^{\mathrm{s}}\boldsymbol{a}_h\right\|_K\right)^2\left\|\boldsymbol{\sigma}_h\right\|_K^2 \\
&- 2\left(1-\beta\right)\left(\frac{\delta_0 h}{\mu}\left(\alpha_u\frac{\mu}{\delta_0 h^2}\frac{1}{2\varepsilon_2} + \frac{1}{2\varepsilon_5}\right)\right)\sum_E\left\|\left[\!\left[\boldsymbol{n}p_h - \boldsymbol{n}\cdot\boldsymbol{\sigma}_h\right]\!\right]\right\|_E^2,
\end{aligned} \tag{6.26}$$

with

$$C_u := 1 - \frac{\varepsilon_1}{2} - \frac{\varepsilon_2}{4}c_{\mathrm{tr}} - \alpha_u\left(\frac{\alpha_p}{h^2}\frac{\varepsilon_3}{2} + \frac{\rho\left\|\boldsymbol{a}_h\right\|_K}{h}\frac{\varepsilon_4}{2} + \frac{2\mu}{h^2}\beta^2\delta_0 c_{\mathrm{tr}}\frac{\varepsilon_5}{2} + \frac{\alpha_\sigma}{h^2}\frac{\varepsilon_6}{2}\right)c_{\mathrm{inv}}^2. \tag{6.27}$$

Let us consider now the test function $\boldsymbol{V}_{h2} = \alpha_p\left(1-\beta\right)\left(\boldsymbol{0}, P_p\left(\nabla\cdot\boldsymbol{u}_h\right),\boldsymbol{0}\right)$. We will use the abbreviation $q_2 \equiv P_p\left(\nabla\cdot\boldsymbol{u}_h\right)$. Proceeding as before we get

$$\begin{aligned}
B_{\mathrm{stab}}\left(\boldsymbol{U}_h,\boldsymbol{V}_{h2}\right) \geq{}& \left(1-\beta\right)\sum_K \alpha_p C_p\left\|P_p\left(\nabla\cdot\boldsymbol{u}_h\right)\right\|_K^2 \\
&- \left(1-\beta\right)\frac{\varepsilon_7}{2}\sum_K \alpha_u\left\|P_u^{\perp}\left(\nabla p_h\right)\right\|_K^2 - 2\frac{\delta_0 h}{2\mu}\left(1-\beta\right)\varepsilon_8\sum_E\frac{\alpha_p}{\mu}\left\|\left[\!\left[\boldsymbol{n}p_h - \boldsymbol{n}\cdot\boldsymbol{\sigma}_h\right]\!\right]\right\|_E^2 \\
&- 2\frac{\delta_0 h}{2\mu}\left(1-\beta\right)\left(2\beta\mu\right)^2\frac{2c_{\mathrm{tr}}}{h}\varepsilon_8\sum_K\frac{\alpha_p}{\mu}\left\|\nabla^{\mathrm{s}}\boldsymbol{u}_h\right\|_K^2,
\end{aligned} \tag{6.28}$$

for any ε_7, ε_8, with

$$C_p := 1 - \frac{c_{\mathrm{inv}}^2}{2\varepsilon_7}\frac{\alpha_u\alpha_p}{h^2} - \frac{\delta_0 c_{\mathrm{tr}}}{2\varepsilon_8}. \tag{6.29}$$

The last step is to consider as test function $\boldsymbol{V}_{h3} = \alpha_\sigma(\boldsymbol{0},0,\boldsymbol{\sigma}_3)$, with

$$\boldsymbol{\sigma}_3 := P_\sigma\left(-\left(1-\beta\right)\nabla^{\mathrm{s}}\boldsymbol{u}_h + \frac{\lambda}{2\mu}\left(\boldsymbol{a}_h\cdot\nabla\boldsymbol{\sigma}_h - \boldsymbol{\sigma}_h\cdot\nabla\boldsymbol{a}_h - \left(\nabla\boldsymbol{a}_h\right)^T\cdot\boldsymbol{\sigma}_h\right)\right).$$

Using the same tools as in the previous cases we now obtain

$$\begin{aligned}
B_{\mathrm{stab}}\left(\boldsymbol{U}_h,\boldsymbol{V}_{h3}\right) \geq{}& -\frac{1}{2\mu}\frac{1}{2\varepsilon_9}\left\|\boldsymbol{\sigma}_h\right\|^2 - 2\frac{\delta_0 h}{2\mu}\frac{1}{2\varepsilon_{12}}\left(1-\beta\right)\sum_E\left\|\left[\!\left[\boldsymbol{n}p_h - \boldsymbol{n}\cdot\boldsymbol{\sigma}_h\right]\!\right]\right\|_E^2 \\
&- \left(1-\beta\right)^2\frac{1}{2\varepsilon_{11}}\sum_K \alpha_u\left\|P_u^{\perp}\left(\nabla\cdot\boldsymbol{\sigma}_h\right)\right\|_K^2 - 2\frac{\delta_0 h}{2\mu}\frac{1}{2\varepsilon_{12}}\left(1-\beta\right)\left(2\beta\mu\right)^2\frac{2c_{\mathrm{tr}}}{h}\sum_K\left\|\nabla^{\mathrm{s}}\boldsymbol{u}_h\right\|_K^2
\end{aligned}$$

$$
\begin{aligned}
&+\sum_K \alpha_\sigma C_\sigma \left\| P_\sigma \left(-(1-\beta)\,\nabla^{\mathrm{s}}\boldsymbol{u}_h + \frac{\lambda}{2\mu}\left(\boldsymbol{a}_h\cdot\nabla\boldsymbol{\sigma}_h - \dot{\boldsymbol{\sigma}}_h^{**}\right)\right)\right\|_K^2 \\
&+\sum_K \alpha_\sigma \left[1 - 2\frac{1}{2\varepsilon_{10}} - 2\left(\frac{\alpha_\sigma}{2\mu}\frac{\varepsilon_9}{2} + \alpha_u \frac{\alpha_\sigma}{h^2} c_{\mathrm{inv}}^2 \frac{\varepsilon_{11}}{2} + 2c_{\mathrm{tr}}\delta_0 \frac{\alpha_\sigma}{2\mu}\frac{\varepsilon_{12}}{2}\right)\right. \\
&\left. -2\left(\frac{\alpha_\sigma}{2\mu}\right)^2 \left(4\left(\frac{\lambda\left\|\boldsymbol{a}_h\right\|_K}{h}\right)^2 + 4\left(\lambda\left\|\nabla^{\mathrm{s}}\boldsymbol{a}_h\right\|_K\right)^2 + 2\left(\lambda\left\|\nabla^{\mathrm{as}}\boldsymbol{a}_h\right\|_K\right)^2\right)\frac{\varepsilon_{13}}{2}\right] \left\| P_\sigma\left(\frac{\lambda}{2\mu}\dot{\boldsymbol{\sigma}}_h^*\right)\right\|_K^2 \\
&-2\frac{1}{2\varepsilon_{13}}\sum_K \alpha_\sigma \left\| P_\sigma^\perp \left(-(1-\beta)\,\nabla^{\mathrm{s}}\boldsymbol{u}_h + \frac{\lambda}{2\mu}\left(\boldsymbol{a}_h\cdot\nabla\boldsymbol{\sigma}_h - \dot{\boldsymbol{\sigma}}_h^{**}\right)\right)\right\|_K^2 \\
&-2\frac{1}{2\varepsilon_{13}}\sum_K \alpha_\sigma \left\| P_\sigma^\perp \left(\frac{\lambda}{2\mu}\dot{\boldsymbol{\sigma}}_h^*\right)\right\|_K^2, \qquad (6.30)
\end{aligned}
$$

for any ε_i, $i = 9, 10, 11, 12, 13$, with

$$
\begin{aligned}
C_\sigma :=\ & 1 - 2\frac{\varepsilon_{10}}{2} - 2\left(\frac{\alpha_\sigma}{2\mu}\frac{\varepsilon_9}{2} + \alpha_u\frac{\alpha_\sigma}{h^2}c_{\mathrm{inv}}^2\frac{\varepsilon_{11}}{2} + 2c_{\mathrm{tr}}\delta_0\frac{\alpha_\sigma}{2\mu}\frac{\varepsilon_{12}}{2}\right) \\
& - 2\left(\frac{\alpha_\sigma}{2\mu}\right)^2\left(4\left(\frac{\lambda\left\|\boldsymbol{a}_h\right\|_K}{h}\right)^2 + 4\left(\lambda\left\|\nabla^{\mathrm{s}}\boldsymbol{a}_h\right\|_K\right)^2 + 2\left(\lambda\left\|\nabla^{\mathrm{as}}\boldsymbol{a}_h\right\|_K\right)^2\right)\frac{\varepsilon_{13}}{2}. \qquad (6.31)
\end{aligned}
$$

It can be checked that the constants ε_i, $i = 1, \ldots, 13$, can be taken such that

$$C_u > 0, \quad C_p > 0, \quad C_\sigma > 0,$$

where C_u, C_p and C_σ are given by (6.27), (6.29) and (6.31), respectively.

Let $\boldsymbol{V}_h = \boldsymbol{U}_{h1} + \theta_1\boldsymbol{V}_{h1} + \theta_2\boldsymbol{V}_{h2} + \theta_3\boldsymbol{V}_{h3}$. It is trivially verified that the parameters θ_i can be chosen small enough so as to obtain:

$$
\begin{aligned}
B_{\mathrm{stab}}\left(\boldsymbol{U}_h, \boldsymbol{V}_h\right) \geq\ & 2\beta\left(1-\beta\right)\mu\sum_K C_1\left\|\nabla^{\mathrm{s}}\boldsymbol{u}_h\right\|^2 + \frac{1}{2\mu}\sum_K C_2\left\|\boldsymbol{\sigma}_h\right\|^2 \\
& + (1-\beta)\sum_K \alpha_u C_3\left\|P_u\left(\rho\boldsymbol{a}_h\cdot\nabla\boldsymbol{u}_h + \nabla p_h - \nabla\cdot\boldsymbol{\sigma}_h\right)\right\|^2 \\
& + (1-\beta)\sum_K \alpha_u C_4\left\|P_u^\perp\left(\rho\boldsymbol{a}_h\cdot\nabla\boldsymbol{u}_h\right)\right\|^2 + (1-\beta)\sum_K \alpha_u C_5\left\|P_u^\perp\left(\nabla p_h\right)\right\|^2 \\
& + (1-\beta)\sum_K \alpha_u C_6\left\|P_u^\perp\left(\nabla\cdot\boldsymbol{\sigma}_h\right)\right\|^2 \\
& + (1-\beta)\sum_K \alpha_p C_7\left\|P_p^\perp\left(\nabla\cdot\boldsymbol{u}_h\right)\right\|^2 + (1-\beta)\sum_K \alpha_p C_8\left\|P_p\left(\nabla\cdot\boldsymbol{u}_h\right)\right\|^2 \\
& + \sum_K \alpha_\sigma C_9\left\|P_\sigma\left(-(1-\beta)\,\nabla^{\mathrm{s}}\boldsymbol{u}_h + \frac{\lambda}{2\mu}\left(\boldsymbol{a}_h\cdot\nabla\boldsymbol{\sigma}_h - \dot{\boldsymbol{\sigma}}_h^{**}\right)\right)\right\|^2 \\
& + \sum_K \alpha_\sigma C_{10}\left\|P_\sigma^\perp\left(-(1-\beta)\,\nabla^{\mathrm{s}}\boldsymbol{u}_h + \frac{\lambda}{2\mu}\left(\boldsymbol{a}_h\cdot\nabla\boldsymbol{\sigma}_h - \dot{\boldsymbol{\sigma}}_h^{**}\right)\right)\right\|^2 \\
& + \frac{\delta_0 h}{2\mu}\sum_E C_{11}\left\|[\![\boldsymbol{n}p_h - \boldsymbol{n}\cdot\boldsymbol{\sigma}_h]\!]\right\|^2 + \frac{1}{2\mu}\sum_K \alpha_\sigma C_{12}\left\|\lambda P_\sigma\left(\dot{\boldsymbol{\sigma}}_h^*\right)\right\|^2, \qquad (6.32)
\end{aligned}
$$

with the various constants appearing in this expression given by

$$C_1 = 1 - \theta_1 2\beta c_{\mathrm{inv}}^2\alpha_u\frac{\mu}{h^2}\left(\frac{1}{2\varepsilon_1} + \frac{4c_{\mathrm{tr}}}{2\varepsilon_2} + \frac{2c_{\mathrm{tr}}\delta_0}{2\varepsilon_5}\right) - \theta_2\frac{\alpha_p}{\mu}\left(4\delta_0\beta c_{\mathrm{tr}}\varepsilon_8\right) - \theta_3 2\delta_0\beta c_{\mathrm{tr}}\frac{1}{2\varepsilon_{12}},$$

$$
\begin{aligned}
C_2 =& 1 - 2\lambda \left\|\nabla \boldsymbol{a}_h\right\|_K - 4\lambda\alpha_\sigma \frac{\lambda}{2\mu} \left\|\nabla^{\mathrm{s}} \boldsymbol{a}_h\right\|_K^2 - \theta_3 \frac{1}{2\varepsilon_9} \\
& - \left(\alpha_\sigma \frac{\lambda}{2\mu} \left\|\nabla^{\mathrm{s}} \boldsymbol{a}_h\right\|_K\right)^2 \left(\theta_1 \left(2\left(1-\beta\right) \frac{2\mu}{\alpha_\sigma} \frac{1}{2\varepsilon_6}\right) + \theta_3 \left(2 \frac{2\mu}{\alpha_\sigma} \frac{1}{2\varepsilon_{13}}\right)\right), \\
C_3 =& \theta_1 \left(1 - \frac{\varepsilon_1}{2} - \frac{\varepsilon_2}{4} c_{\mathrm{tr}} - \left(\alpha_u \frac{\alpha_p}{h^2} \frac{\varepsilon_3}{2} + \alpha_u \frac{\rho \left\|\boldsymbol{a}_h\right\|_K}{h} \frac{\varepsilon_4}{2} + \alpha_u \frac{2\mu}{h^2} \beta^2 \delta_0 c_{\mathrm{tr}} \frac{\varepsilon_5}{2} + \alpha_u \frac{\alpha_\sigma}{h^2} \frac{\varepsilon_6}{2}\right) c_{\mathrm{inv}}^2\right), \\
C_4 =& 1 - \theta_1 \alpha_u \frac{\mu}{h^2} \frac{\rho \left\|\boldsymbol{a}_h\right\|_K h}{\mu} \frac{1}{2\varepsilon_4}, \\
C_5 =& 1 - \theta_2 \frac{\varepsilon_7}{2}, \\
C_6 =& 1 - \theta_3 \left(1-\beta\right) \frac{1}{2\varepsilon_{11}}, \\
C_7 =& 1 - \theta_1 \frac{1}{2\varepsilon_3}, \\
C_8 =& \theta_2 \left(1 - c_{\mathrm{inv}}^2 \alpha_u \frac{\alpha_p}{h^2} \frac{1}{2\varepsilon_7} - \delta_0 c_{\mathrm{tr}} \frac{1}{2\varepsilon_8}\right), \\
C_9 =& \theta_3 \left(1 - 2\frac{\varepsilon_{10}}{2} - 2\left(\frac{\alpha_\sigma}{2\mu} \frac{\varepsilon_9}{2} + \alpha_u \frac{\alpha_\sigma}{h^2} c_{\mathrm{inv}}^2 \frac{\varepsilon_{11}}{2} + 2c_{\mathrm{tr}} \delta_0 \frac{\alpha_\sigma}{2\mu} \frac{\varepsilon_{12}}{2}\right)\right. \\
& \left. -2\left(\frac{\alpha_\sigma}{2\mu}\right)^2 \left(4\left(\frac{\lambda \left\|\boldsymbol{a}_h\right\|_K}{h}\right)^2 + 4\left(\lambda \left\|\nabla^{\mathrm{s}} \boldsymbol{a}_h\right\|_K\right)^2 + 2\left(\lambda \left\|\nabla^{\mathrm{as}} \boldsymbol{a}_h\right\|_K\right)^2\right) \frac{\varepsilon_{13}}{2}\right), \\
C_{10} =& 1 - \theta_1 2\left(1-\beta\right) \frac{1}{2\varepsilon_6} - \theta_3 2 \frac{1}{2\varepsilon_{13}}, \\
C_{11} =& 1 - 2\theta_1 2\left(1-\beta\right) \left(\alpha_u \frac{\mu}{\delta_0 h^2} \frac{1}{2\varepsilon_2} + \frac{1}{2\varepsilon_5}\right) - \theta_2 \left(1-\beta\right) \frac{\alpha_p}{\mu} \varepsilon_8 - \theta_3 \frac{1}{2\varepsilon_{12}}, \\
C_{12} =& \theta_3 \frac{\alpha_\sigma}{2\mu} \left(1 - 2\frac{1}{2\varepsilon_{10}} - 2\left(\frac{\alpha_\sigma}{2\mu} \frac{\varepsilon_9}{2} + \alpha_u \frac{\alpha_\sigma}{h^2} c_{\mathrm{inv}}^2 \frac{\varepsilon_{11}}{2} + 2c_{\mathrm{tr}} \delta_0 \frac{\alpha_\sigma}{2\mu} \frac{\varepsilon_{12}}{2}\right)\right. \\
& \left. -2\left(\frac{\alpha_\sigma}{2\mu}\right)^2 \left(4\left(\lambda \frac{\left\|\boldsymbol{a}_h\right\|_K}{h}\right)^2 + 4\left(\lambda \left\|\nabla^{\mathrm{s}} \boldsymbol{a}_h\right\|_K\right)^2 + 2\left(\lambda \left\|\nabla^{\mathrm{as}} \boldsymbol{a}_h\right\|_K\right)^2\right) \frac{\varepsilon_{13}}{2}\right),
\end{aligned}
$$

all positive *for λ (or the Weissenberg number) small enough* and the constants c_i, $i = 1,2,3,4,5$ in (6.18)-(6.20) large enough. Therefore, for each $\boldsymbol{U}_h$ we have found $\boldsymbol{V}_h$ such that

$$
B_{\mathrm{stab}}\left(\boldsymbol{U}_h, \boldsymbol{V}_h\right) \geq C \|\boldsymbol{U}_h\|_W^2.
$$

In fact, it is seen from (6.32) that we could have included the term $\frac{1}{2\mu} C_{12} \left\|\lambda P_\sigma\left(\dot{\boldsymbol{\sigma}}_h^*\right)\right\|^2$ in the working norm, which gives control on the finite element part of $\boldsymbol{\sigma}_h \cdot \nabla^{\mathrm{s}} \boldsymbol{a}_h + \nabla^{\mathrm{s}} \boldsymbol{a}_h \cdot \boldsymbol{\sigma}_h$.

On the other hand, it is easily checked that $\|\boldsymbol{V}_h\|_W \leq C \|\boldsymbol{U}_h\|_W$. Using this fact we have shown that for each $\boldsymbol{U}_h \in \boldsymbol{\mathcal{X}}_h$ there exist $\boldsymbol{V}_h \in \boldsymbol{\mathcal{X}}_h$ such that $B_{\mathrm{stab}}\left(\boldsymbol{U}_h, \boldsymbol{V}_h\right) \geq C \left\|\boldsymbol{U}_h\right\|_W \left\|\boldsymbol{V}_h\right\|_W$, from where the theorem follows. □

Once stability is established, a more or less standard procedure leads to convergence. The objective is to show that the error function of the method is

$$
\begin{aligned}
E\left(h\right) :=& \sqrt{\mu} \varepsilon_1\left(\boldsymbol{u}\right) + \sqrt{\mu} \sum_K \sqrt{\frac{\rho \left\|\boldsymbol{a}_h\right\|_K h}{\mu}} \varepsilon_{1,K}\left(\boldsymbol{u}\right) + \frac{1}{\sqrt{\mu}} \varepsilon_0\left(\boldsymbol{\sigma}\right) \\
& + \frac{1}{\sqrt{\mu}} \sum_K \frac{\lambda \left\|\boldsymbol{a}_h\right\|_K}{h} \varepsilon_{0,K}\left(\boldsymbol{\sigma}\right) + \frac{1}{\sqrt{\mu}} \varepsilon_0\left(p\right).
\end{aligned} \tag{6.33}
$$

This expression allows us to see how the error will deteriorate in terms of the local Reynolds number and the local Weissenberg number, defined on the factor that multiply $\varepsilon_{1,K}(\boldsymbol{u})$ and $\varepsilon_{0,K}(\boldsymbol{\sigma})$ respectively.

The first preliminary result we need concerns the consistency of the formulation:

Lemma 1 (Consistency) *Let $\boldsymbol{U} \in \boldsymbol{\mathcal{X}}$ be the solution of the continuous problem and $\boldsymbol{U}_h \in \boldsymbol{\mathcal{X}}_h$ the finite element solution. If $\boldsymbol{f} \in \boldsymbol{\mathcal{V}}_h$ and $\boldsymbol{U}$ is regular enough, so that $B_{\text{stab}}(\boldsymbol{U}, \boldsymbol{V}_h)$ is well defined, there holds*

$$B_{\text{stab}}(\boldsymbol{U} - \boldsymbol{U}_h, \boldsymbol{V}_h) \leq CE(h) \|\boldsymbol{V}_h\|_W, \tag{6.34}$$

for all $\boldsymbol{V}_h \in \boldsymbol{X}_h$, where $E(h)$ is given by (6.33).

Proof. Obviously, the Galerkin terms do not contribute to the consistency error. In the constitutive equation the stabilized term is residual based and the consistency is also satisfy by construction, the same as in the continuity equation. It only remains to show that $S_1^{\perp}$ has a consistency error bounded as (6.34) indicates. This easily follows from the fact that the orthogonal projection $P^{\perp}$ onto an appropriate finite element space satisfies $\|P^{\perp}(v)\| \leq C\varepsilon_0(v)$ for any function v. □

The second preliminary lemma provides an interpolation error in terms of the working norm $\|\cdot\|_W$ and the stabilized form B_{stab} for the continuous solution $\boldsymbol{U} = (\boldsymbol{u}, p, \boldsymbol{\sigma}) \in \boldsymbol{\mathcal{X}}$, assumed to have enough regularity:

Lemma 2 (Interpolation error) *Let $\boldsymbol{U} \in \boldsymbol{\mathcal{X}}$ be the solution of the continuous problem, assumed to be regular enough, and $\tilde{\boldsymbol{U}}_h \in \boldsymbol{\mathcal{X}}_h$ its best finite element approximation. Then, for λ small enough the following inequalities hold:*

$$B_{\text{stab}}\left(\boldsymbol{U} - \tilde{\boldsymbol{U}}_h, \boldsymbol{V}_h\right) \leq CE(h) \|\boldsymbol{V}_h\|_W, \tag{6.35}$$

$$\left\|\boldsymbol{U} - \tilde{\boldsymbol{U}}_h\right\|_W \leq CE(h). \tag{6.36}$$

Proof. Set $\boldsymbol{e}_u = \boldsymbol{u} - \tilde{\boldsymbol{u}}_h$, $e_p = p - \tilde{p}_h$ and $\boldsymbol{e}_\sigma = \boldsymbol{\sigma} - \tilde{\boldsymbol{\sigma}}_h$. The proof of (6.36) follows from a repeated application of Schwarz's inequality and then Young's inequality for scalars. Boundary terms can be treated using (6.21). One gets

$$\begin{aligned}
\left\|\boldsymbol{U} - \tilde{\boldsymbol{U}}_h\right\|_W^2 \leq\ & 2\mu \sum_K \left(\beta + \beta\frac{\varepsilon_1}{2} + \frac{\alpha_p}{2\mu} + \frac{\alpha_\sigma}{2\mu}\beta^2\frac{1}{2\varepsilon_3} + \frac{\alpha_\sigma}{\mu}\left(1 + \frac{\varepsilon_3}{2}\right) + 2\delta_0 c_{\text{tr}}\beta^2\left(1 + 2\beta\frac{\varepsilon_4}{2}\right)\right) \|\nabla^{\text{s}}\boldsymbol{e}_u\|_K^2 \\
& + 2\mu \sum_K \alpha_u \frac{\rho\|\boldsymbol{a}_h\|_K}{h} \frac{\rho\|\boldsymbol{a}_h\|_K h}{2\mu} \|\nabla^{\text{s}}\boldsymbol{e}_u\|_K^2 \\
& + \frac{1}{2\mu}\sum_K \left(1 + \beta\frac{1}{2\varepsilon_1} + \frac{1}{2\varepsilon_2} + 4\lambda^2\|\nabla\boldsymbol{a}_h\|_K^2\frac{\varepsilon_2}{2} + (1-\beta)\alpha_u\frac{2\mu}{h^2} + 2c_{\text{tr}}\delta_0(2+\beta)\right)\|\boldsymbol{e}_\sigma\|_K^2 \\
& + \frac{1}{2\mu}\sum_K \frac{\alpha_\sigma}{2\mu}\left(2\left(\frac{\lambda\|\boldsymbol{a}_h\|_K}{h} - \lambda\|\nabla^{\text{as}}\boldsymbol{a}_h\|_K\right)^2(1+\varepsilon_3) + \lambda\|\nabla^{\text{s}}\boldsymbol{a}_h\|_K^2\left(\frac{1}{2} - \varepsilon_3\right)\right)\|\boldsymbol{e}_\sigma\|_K^2 \\
& + \frac{1}{2\mu}\sum_K \left(\alpha_u\frac{2\mu}{h^2} + 2c_{\text{tr}}\delta_0\left(1 + 2\beta\frac{\varepsilon_4}{2}\right)\right)\|e_p\|_K^2,
\end{aligned}$$

for any constants ε_i, $i = 1, 2, 3$ (not to be confused with the interpolation errors). Estimate (6.36) follows from the definition of the error function in (6.33) and assuming λ to be small enough (this assumption allows us not to include the gradient of $\boldsymbol{a}_h$ in the error function).

To prove (6.35) one needs to apply repeatedly Young's inequality and use the expression of the stabilization parameters, as well as classical interpolation estimates. To treat the boundary terms, note that according to (6.21) we may write

$$\sum_K \|v - \tilde{v}_h\|_{\partial K}^2 \leq C\left(h^{-1}\varepsilon_0^2(v) + h\varepsilon_1^2(v)\right) = Ch^{-1}\varepsilon_0^2(v),$$

for both continuous and discontinuous functions v.

The bound one finally obtains is

$$
\begin{aligned}
&B_{\text{stab}}\left(\boldsymbol{U}-\tilde{\boldsymbol{U}}_h,\boldsymbol{V}_h\right)\\
&\leq \sqrt{\mu}\varepsilon_1(\boldsymbol{u})\left(\sum_K\left(2\beta\sqrt{\mu}\left\|\nabla^{\text{s}}\boldsymbol{v}_h\right\|_K+\frac{h}{\sqrt{\mu}}\left\|-\nabla q_h+(1-\beta)\nabla\cdot\boldsymbol{\tau}_h\right\|_K+\frac{\rho\left\|\boldsymbol{a}_h\right\|h}{\mu}\frac{\sqrt{\mu}}{c_{\text{inv}}}\left\|\nabla\boldsymbol{v}_h\right\|_K\right)\right.\\
&\quad\left.+\sum_E\sqrt{c_{\text{tr}}}\frac{\sqrt{h}}{\sqrt{\mu}}\left\|[\![\boldsymbol{n}q_h-(1-\beta)\boldsymbol{n}\cdot\boldsymbol{\tau}_h]\!]\right\|_E\right)\\
&+\frac{1}{\sqrt{\mu}}\varepsilon_0(\boldsymbol{\sigma})\sum_K\left(\sqrt{\mu}\left\|\nabla^{\text{s}}\boldsymbol{v}_h\right\|_K+\frac{1}{2\sqrt{\mu}}\left\|\boldsymbol{\tau}_h\right\|_K+\frac{\lambda\left\|\boldsymbol{a}_h\right\|_K}{h}c_{\text{inv}}\frac{1}{2\sqrt{\mu}}\left\|\boldsymbol{\tau}_h\right\|_K+\lambda\left\|\nabla\boldsymbol{a}_h\right\|_K\frac{\lambda}{\sqrt{\mu}}\left\|\boldsymbol{\tau}_h\right\|_K\right)\\
&+(1-\beta)\frac{c_{\text{inv}}}{\sqrt{\mu}}\varepsilon_0(\boldsymbol{\sigma})\sum_K\alpha_u\frac{\mu}{h^2}\frac{c_{\text{inv}}}{\sqrt{\mu}}\left\|\boldsymbol{\tau}_h\right\|\\
&+\sqrt{\mu}\varepsilon_1(\boldsymbol{u})\sum_K\left(\frac{\alpha_p}{\mu}\sqrt{\mu}\left\|\nabla\cdot\boldsymbol{v}_h\right\|_K+\alpha_u\frac{\mu}{h^2}\left(\frac{\rho\left\|\boldsymbol{a}_h\right\|_K h}{\mu}\right)^2\sqrt{\mu}\left\|\nabla\boldsymbol{v}_h\right\|_K+(1-\beta)\frac{\alpha_\sigma}{\mu}\sqrt{\mu}\left\|\nabla^{\text{s}}\boldsymbol{v}_h\right\|_K\right)\\
&+\frac{1}{\sqrt{\mu}}\varepsilon_0(p)\left(\sqrt{\mu}\left\|\nabla\cdot\boldsymbol{v}_h\right\|\right)+\frac{1}{\sqrt{\mu}}\varepsilon_0(p)\sum_K\left(\alpha_u\frac{\mu}{h^2}\frac{c_{\text{inv}}^2}{\sqrt{\mu}}\left\|q_h\right\|_K\right)\\
&+\frac{\delta_0}{2}\frac{1}{\sqrt{\mu}}\left(\varepsilon_0(p)+\varepsilon_0(\boldsymbol{\sigma})+2\beta\mu\varepsilon_1(\boldsymbol{u})\right)\sum_E\frac{\sqrt{h}}{\sqrt{\mu}}\left\|[\![\boldsymbol{n}q_h-(1-\beta)\boldsymbol{n}\cdot\boldsymbol{\tau}_h+2\beta\mu\boldsymbol{n}\cdot\nabla^{\text{s}}\boldsymbol{v}_h]\!]\right\|_E\\
&+(1-\beta)\sqrt{\mu}\varepsilon_1(\boldsymbol{u})\sum_K\frac{\alpha_\sigma}{\mu}\frac{1}{2\sqrt{\mu}}\left\|\lambda\left(\boldsymbol{a}_h\cdot\nabla\boldsymbol{\tau}_h+\boldsymbol{\tau}_h\cdot(\nabla\boldsymbol{a}_h)^T+\nabla\boldsymbol{a}_h\cdot\boldsymbol{\tau}_h\right)\right\|\\
&+\frac{1}{2\sqrt{\mu}}\varepsilon_0(\boldsymbol{\sigma})\sum_K\sqrt{\mu}\frac{\alpha_\sigma}{\mu}\left(\left\|\nabla^{\text{s}}\boldsymbol{v}_h\right\|_K+\left\|\frac{\lambda}{2\mu}\left(\boldsymbol{a}_h\cdot\nabla\boldsymbol{\tau}_h+\boldsymbol{\tau}_h\cdot(\nabla\boldsymbol{a}_h)^T+\nabla\boldsymbol{a}_h\cdot\boldsymbol{\tau}_h\right)\right\|_K\right)\\
&\quad\left(\frac{\lambda\left\|\boldsymbol{a}_h\right\|_K}{h}c_{\text{inv}}+2\lambda\left\|\nabla\boldsymbol{a}_h\right\|_K\right).
\end{aligned}
$$

All the terms have been organized to see that they are bounded by $CE(h)\left\|\boldsymbol{V}_h\right\|_W$, from where (6.35) follows. □

We are finally in a position to prove convergence. The proof is standard, but we include it for completeness.

Theorem 2 (Convergence) *Let $\boldsymbol{U}=(\boldsymbol{u},p,\boldsymbol{\sigma})\in\boldsymbol{\mathcal{X}}$, be the solution of the continuous problem, and suppose that the assumptions of Theorem 1 hold. Then there exist a constant $C>0$ such that*

$$\left\|\boldsymbol{U}-\boldsymbol{U}_h\right\|_W\leq CE(h).$$

Proof. Consider the finite element function $\tilde{\boldsymbol{U}}_h-\boldsymbol{U}_h\in\boldsymbol{\mathcal{X}}_h$ where as in Lemma 2, $\tilde{\boldsymbol{U}}_h\in\boldsymbol{\mathcal{X}}_h$ is the best finite element approximation to $\boldsymbol{U}$. Starting from the inf-sup condition, it follows that there exist $\boldsymbol{V}_h\in\boldsymbol{\mathcal{X}}_h$ such that

$$
\begin{aligned}
C\left\|\tilde{\boldsymbol{U}}_h-\boldsymbol{U}_h\right\|_W\left\|\boldsymbol{V}_h\right\|_W&\leq B_{\text{stab}}\left(\tilde{\boldsymbol{U}}_h-\boldsymbol{U}_h,\boldsymbol{V}_h\right)\\
&=B_{\text{stab}}\left(\tilde{\boldsymbol{U}}_h-\boldsymbol{U},\boldsymbol{V}_h\right)+B_{\text{stab}}\left(\boldsymbol{U}-\boldsymbol{U}_h,\boldsymbol{V}_h\right)\\
&\leq CE(h)\left\|\boldsymbol{V}_h\right\|_W,
\end{aligned}
$$

using Lemma 1 and (6.35) in Lemma 2, from where

$$\left\|\tilde{\boldsymbol{U}}_h-\boldsymbol{U}_h\right\|_W\leq CE(h).$$

The theorem follows using this bound in the triangle inequality

$$\|\boldsymbol{U}-\boldsymbol{U}_h\|_W \leq \left\|\boldsymbol{U}-\tilde{\boldsymbol{U}}_h\right\|_W + \left\|\tilde{\boldsymbol{U}}_h-\boldsymbol{U}_h\right\|_W,$$

and (6.36) in Lemma 2. □

Clearly, this convergence result is optimal.

6.5.3 Stability and convergence in natural norms

The next step will be to prove stability and convergence in a natural norm, that is to say, in the norm of the space where the continuous problem is posed, and not in the mesh dependent norm (6.22). Even though the results to be presented are the expected ones, the analysis presented up to this point has highlighted the role played by the stabilization terms of the formulation. Obviously, since the natural norm does not include any control on the convective terms, stability and convergence in this norm is only meaningful in the case of small cell Reynolds numbers and small cell Weissenberg numbers. This is the situation considered in the following.

Theorem 3 (Stability and convergence in natural norms) *Suppose that the assumptions of Theorem 1 hold and the cell Reynolds numbers and cell Weissenberg numbers are small. Then, the solution of the discrete problem* $\boldsymbol{U}_h=(\boldsymbol{u}_h,p_h,\boldsymbol{\sigma}_h)\in\boldsymbol{\mathcal{X}}_h$ *can be bounded as*

$$\sqrt{\mu}\,\|\boldsymbol{u}_h\|_{H^1(\Omega)}+\frac{1}{\sqrt{\mu}}\,\|\boldsymbol{\sigma}_h\|+\frac{1}{\sqrt{\mu}}\,\|p_h\|\leq\frac{C}{\sqrt{\mu}}\,\|\boldsymbol{f}\|_{H^{-1}(\Omega)}.$$

Moreover, if the solution of the continuous problem $\boldsymbol{U}=(\boldsymbol{u},p,\boldsymbol{\sigma})\in\boldsymbol{\mathcal{X}}$ *is regular enough, the following error estimate holds:*

$$\sqrt{\mu}\,\|\boldsymbol{u}-\boldsymbol{u}_h\|_{H^1(\Omega)}+\frac{1}{\sqrt{\mu}}\,\|\boldsymbol{\sigma}-\boldsymbol{\sigma}_h\|+\frac{1}{\sqrt{\mu}}\,\|p-p_h\|\leq CE(h).$$

Proof. It is clear that

$$\langle\boldsymbol{f},\boldsymbol{v}_h\rangle\leq\frac{C}{\sqrt{\mu}}\,\|\boldsymbol{f}\|_{H^{-1}(\Omega)}\sqrt{\mu}\,\|\boldsymbol{v}_h\|_{H^1(\Omega)}\leq\frac{C}{\sqrt{\mu}}\,\|\boldsymbol{f}\|_{H^{-1}(\Omega)}\,\|\boldsymbol{V}_h\|_W,$$

where $\boldsymbol{V}_h=(\boldsymbol{v}_h,q_h,\boldsymbol{\tau}_h)\in\boldsymbol{\mathcal{X}}_h$ is arbitrary. Therefore the inf-sup condition proved in Theorem 1 implies that:

$$\|\boldsymbol{U}_h\|_W\leq\frac{C}{\sqrt{\mu}}\,\|\boldsymbol{f}\|_{H^{-1}(\Omega)}$$

that is to say,

$$\begin{aligned}
&2\beta\mu(1-\beta)\,\|\nabla^{\mathrm{s}}\boldsymbol{u}_h\|^2+\frac{1}{2\mu}\,\|\boldsymbol{\sigma}_h\|^2+\sum_K\alpha_p\,\|\nabla\cdot\boldsymbol{u}_h\|_K^2+\sum_K\alpha_u\,\|\rho\boldsymbol{a}_h\cdot\nabla\boldsymbol{u}_h+\nabla p_h-\nabla\cdot\boldsymbol{\sigma}_h\|_K^2\\
&+(1-\beta)\sum_K\alpha_u\left\|P_u^{\perp}(\nabla\cdot\boldsymbol{\sigma}_h)\right\|_K^2+\sum_K\alpha_u\left\|P_u^{\perp}(\nabla p_h)\right\|_K^2+\sum_K\alpha_u\left\|P_u^{\perp}(\rho\boldsymbol{a}_h\cdot\nabla\boldsymbol{u}_h)\right\|_K^2\\
&+\frac{\delta_0 h}{2\mu}(1-\beta)\sum_E\|[\![\boldsymbol{n}p_h-\boldsymbol{n}\cdot\boldsymbol{\sigma}_h]\!]\|_E^2+\sum_K\alpha_\sigma\left\|-(1-\beta)\nabla^{\mathrm{s}}\boldsymbol{u}_h+\frac{\lambda}{2\mu}(\boldsymbol{a}_h\cdot\nabla\boldsymbol{\sigma}_h-\dot{\boldsymbol{\sigma}}_h^{**})\right\|_K^2\\
&\leq\frac{C}{\sqrt{\mu}}\,\|\boldsymbol{f}\|_{H^{-1}(\Omega)}.
\end{aligned}\tag{6.37}$$

Using an inverse inequality we can write:

$$\sum_K \alpha_u \left\|\rho \boldsymbol{a}_h \cdot \nabla \boldsymbol{u}_h + \nabla p_h\right\|_K^2 \leq \sum_K \alpha_u \left\|(\rho \boldsymbol{a}_h \cdot \nabla \boldsymbol{u}_h + \nabla p_h) - \nabla \cdot \boldsymbol{\sigma}_h\right\|_K^2 + \sum_K \alpha_u \frac{\mu}{h^2} \frac{C}{\mu} \left\|\boldsymbol{\sigma}_h\right\|_K^2 .$$

In this expression we only have control on $\rho \boldsymbol{a}_h \cdot \nabla \boldsymbol{u}_h + \nabla p_h$. However, we do not have explicit bounds over these two terms (and their errors) separately. Nevertheless, there is the possibility of bounding the pressure gradient making use of the control over the viscous term (viscous dominate case), since

$$\sum_K \alpha_u \left\|\nabla p_h\right\|_K^2 \leq \sum_K \alpha_u \left\|\rho \boldsymbol{a}_h \cdot \nabla \boldsymbol{u}_h + \nabla p_h\right\|_K^2 + \sum_K \alpha_u \frac{\mu}{h^2} \left(\frac{\rho \left\|\boldsymbol{a}_h\right\|_K h}{\mu}\right)^2 \left\|\nabla \boldsymbol{u}_h\right\|_K^2 .$$

Note that this expression explodes with the cell Reynolds number $\mathrm{Re}_h := \rho \left\|\boldsymbol{a}_h\right\|_K h \, \mu^{-1}$. We assume hereafter that this is bounded.

Using the trace inequality we can write

$$(1-\beta) \frac{\delta_0 h}{2\mu} \sum_E \left\|[\![\boldsymbol{n} p_h]\!]\right\|_E^2 \leq (1-\beta) \frac{\delta_0 h}{2\mu} \sum_E \left\|[\![\boldsymbol{n} p_h - \boldsymbol{n} \cdot \boldsymbol{\sigma}_h]\!]\right\|_E^2 + (1-\beta) \frac{\delta_0}{2\mu} 2 c_{\mathrm{tr}} \left\|\boldsymbol{\sigma}_h\right\|^2 .$$

Thus, from (6.37), using Korn's inequality, the expression of α_u and noting that $0 < \beta < 1$, we have

$$\mu \left\|\boldsymbol{u}_h\right\|_{H^1(\Omega)}^2 + \frac{1}{\mu} \left\|\boldsymbol{\sigma}_h\right\|^2 + \frac{h^2}{\mu} \sum_K \left\|\nabla p_h\right\|_K^2 + \frac{h}{\mu} \sum_E \left\|[\boldsymbol{n} p_h]\right\|_E^2 \lesssim \frac{1}{\mu} \left\|\boldsymbol{f}\right\|_{H^{-1}(\Omega)}^2 .$$

To prove the L^2-stability for the pressure we rely on the inf-sup condition between the velocity and pressure spaces that holds for the continuous problem, as in [56]. Details can be found in this reference. This concludes the proof of the first part of the Theorem.

Let us proceed to prove convergence in natural norms. Theorem 2 implies that

$$\mu \left\|\boldsymbol{u} - \boldsymbol{u}_h\right\|_{H^1(\Omega)}^2 + \frac{1}{\mu} \left\|\boldsymbol{\sigma} - \boldsymbol{\sigma}_h\right\|^2 + \sum_K \alpha_u \left\|\rho \boldsymbol{a}_h \cdot \nabla (\boldsymbol{u} - \boldsymbol{u}_h) + \nabla (p - p_h) - \nabla \cdot (\boldsymbol{\sigma} - \boldsymbol{\sigma}_h)\right\|_K^2$$
$$+ \frac{h}{\mu} \sum_E \left\|[\![\boldsymbol{n} (p - p_h) - \boldsymbol{n} \cdot (\boldsymbol{\sigma} - \boldsymbol{\sigma}_h)]\!]\right\|_E^2 + \frac{h}{\mu} \sum_E \left\|[\![\mu \boldsymbol{n} \cdot \nabla^{\mathrm{s}} (\boldsymbol{u} - \boldsymbol{u}_h)]\!]\right\|_E^2 \lesssim E^2(h) .$$

We may use now the same procedure as for proving stability. Assuming the cell Reynolds number to be small, using (6.21) and classical inverse estimates, we obtain

$$\frac{h^2}{\mu} \sum_K \left\|\nabla (p - p_h)\right\|_K^2 \lesssim \sum_K \alpha_u \left\|\rho \boldsymbol{a}_h \cdot \nabla (\boldsymbol{u} - \boldsymbol{u}_h) + \nabla (p - p_h) - \nabla \cdot (\boldsymbol{\sigma} - \boldsymbol{\sigma}_h)\right\|_K^2$$
$$+ \mu \left\|\boldsymbol{u} - \boldsymbol{u}_h\right\|_{H^1(\Omega)}^2 + \frac{1}{\mu} \left\|\boldsymbol{\sigma} - \boldsymbol{\sigma}_h\right\|^2$$
$$\frac{h}{\mu} \sum_E \left\|[\![\boldsymbol{n} (p - p_h)]\!]\right\|_E^2 \lesssim \frac{h}{\mu} \sum_E \left\|[\![\boldsymbol{n} (p - p_h) - \boldsymbol{n} \cdot (\boldsymbol{\sigma} - \boldsymbol{\sigma}_h)]\!]\right\|_E^2 + \frac{1}{\mu} \left\|\boldsymbol{\sigma} - \boldsymbol{\sigma}_h\right\|^2 ,$$

and therefore we have that

$$\mu \left\|\boldsymbol{u} - \boldsymbol{u}_h\right\|_{H^1(\Omega)}^2 + \frac{1}{\mu} \left\|\boldsymbol{\sigma} - \boldsymbol{\sigma}_h\right\|^2 + \frac{h^2}{\mu} \sum_K \left\|\nabla (p - p_h)\right\|_K^2 + \frac{h}{\mu} \sum_E \left\|[\![\boldsymbol{n} (p - p_h)]\!]\right\|_E^2 \lesssim E^2(h) .$$

The error estimate in Theorem 3 can now be obtained using the same procedure as in [56], which relies once again on the inf-sup condition between the velocity and the pressure spaces that holds at the continuous level. □

To complete the analysis of the problem, let us obtain an L^2-error estimate for the velocity field. As usual, this can be proved using a duality argument and an elliptic regularity condition assuming the forcing term to be in $L^2(\Omega)$. The result we have is the following:

Theorem 4 (L^2-error estimate for the velocity) *Assume that the hypothesis of Theorem 3 hold and suppose that the continuous problem satisfies the elliptic regularity condition*

$$\sqrt{\mu}\,\|\boldsymbol{u}\|_{H^2(\Omega)} + \frac{1}{\sqrt{\mu}}\,\|\boldsymbol{\sigma}\|_{H^1(\Omega)} + \frac{1}{\sqrt{\mu}}\,\|p\|_{H^1(\Omega)} \leq \frac{C}{\sqrt{\mu}}\,\|\boldsymbol{f}\|\,,$$

Then

$$\sqrt{\mu}\,\|\boldsymbol{u}-\boldsymbol{u}_h\| \lesssim h\left(\sqrt{\mu}\,\|\boldsymbol{u}-\boldsymbol{u}_h\|_{H^1(\Omega)} + \frac{1}{\sqrt{\mu}}\,\|\boldsymbol{\sigma}-\boldsymbol{\sigma}_h\| + \frac{1}{\sqrt{\mu}}\,\|p-p_h\|\right).$$

Proof. The key point is to set the appropriate adjoint problem in our case. Let $(\boldsymbol{w},\pi,\boldsymbol{S}) \in \boldsymbol{\mathcal{X}}$ be the solution of the following problem:

$$\begin{aligned} -\beta\mu\Delta\boldsymbol{w} - \rho\boldsymbol{a}\cdot\nabla\boldsymbol{w} + (1-\beta)\,\nabla\cdot\boldsymbol{S} - \nabla\pi &= \frac{\mu}{l^2}\,(\boldsymbol{u}-\boldsymbol{u}_h)\,,\\ -\nabla\cdot\boldsymbol{w} &= 0,\\ \frac{1}{2\mu}\boldsymbol{S} + \nabla^{\mathrm{s}}\boldsymbol{w} - \frac{\lambda}{2\mu}\left(\boldsymbol{a}\cdot\nabla\boldsymbol{S} + \boldsymbol{S}\cdot(\nabla\boldsymbol{a})^T + \nabla\boldsymbol{a}\cdot\boldsymbol{S}\right) &= \boldsymbol{0}, \end{aligned}$$

with $\boldsymbol{w}=\boldsymbol{0}$ on $\partial\Omega$ and where l is a characteristic length scale of the problem that has been introduced to keep the dimensionality, but that will play no role in the final result. Let also $\left(\tilde{\boldsymbol{w}}_h,\tilde{\pi}_h,\tilde{\boldsymbol{S}}_h\right)$ be the best approximation to $(\boldsymbol{w},\pi,\boldsymbol{S})$ in $\boldsymbol{\mathcal{X}}_h$. Testing with $(\boldsymbol{u}-\boldsymbol{u}_h, p-p_h, \boldsymbol{\sigma}-\boldsymbol{\sigma}_h)$, $(\boldsymbol{u}_h,p_h,\boldsymbol{\sigma}_h)$ being the solution of the problem, we obtain

$$\begin{aligned} &\frac{\mu}{l^2}\,\|\boldsymbol{u}-\boldsymbol{u}_h\|^2 = B\left((\boldsymbol{u}-\boldsymbol{u}_h,p-p_h,\boldsymbol{\sigma}-\boldsymbol{\sigma}_h),(\boldsymbol{w},\pi,\boldsymbol{S})\right)\\ &\quad= B_{\mathrm{stab}}\left((\boldsymbol{u}-\boldsymbol{u}_h,p-p_h,\boldsymbol{\sigma}-\boldsymbol{\sigma}_h),(\boldsymbol{w},\pi,\boldsymbol{S})\right)\\ &\quad-\sum_K \alpha_\sigma\left\langle P_\sigma^\perp\left(\frac{1}{2\mu}\boldsymbol{S}+\nabla^{\mathrm{s}}\boldsymbol{w}-\frac{\lambda}{2\mu}\left(\boldsymbol{a}\cdot\nabla\boldsymbol{S}+\boldsymbol{S}\cdot(\nabla\boldsymbol{a})^T+\nabla\boldsymbol{a}\cdot\boldsymbol{S}\right)\right),\right.\\ &\quad\left.P_\sigma^\perp\left(\nabla^{\mathrm{s}}(\boldsymbol{u}-\boldsymbol{u}_h)-\frac{\lambda}{2\mu}\left(\boldsymbol{a}_h\cdot\nabla(\boldsymbol{\sigma}-\boldsymbol{\sigma}_h)+(\boldsymbol{\sigma}-\boldsymbol{\sigma}_h)\cdot(\nabla\boldsymbol{a}_h)^T+\nabla\boldsymbol{a}_h\cdot(\boldsymbol{\sigma}-\boldsymbol{\sigma}_h)\right)\right)\right\rangle_K\\ &\quad-\sum_K \alpha_p\left(P_p^\perp(\nabla\cdot\boldsymbol{w}),P_p^\perp(\nabla\cdot(\boldsymbol{u}-\boldsymbol{u}_h))\right)_K\\ &\quad-\sum_K \alpha_u\left\langle P_u^\perp(\nabla\pi),P_u^\perp(\nabla(p-p_h))\right\rangle_K-\sum_K \alpha_u\left\langle P_u^\perp(\rho\boldsymbol{a}_h\cdot\nabla\boldsymbol{w}),P_u^\perp(\rho\boldsymbol{a}_h\cdot\nabla(\boldsymbol{u}-\boldsymbol{u}_h))\right\rangle_K\\ &\quad-\sum_K \alpha_u\left\langle P_u^\perp(\nabla\cdot\boldsymbol{S}),P_u^\perp((1-\beta)\nabla\cdot(\boldsymbol{\sigma}-\boldsymbol{\sigma}_h))\right\rangle_K\\ &\quad-\frac{\delta_0 h}{2\mu}\sum_E\left\langle[\![\boldsymbol{n}(p-p_h)-(1-\beta)\,\boldsymbol{n}\cdot(\boldsymbol{\sigma}-\boldsymbol{\sigma}_h)+2\beta\mu\boldsymbol{n}\cdot\nabla^{\mathrm{s}}(\boldsymbol{u}-\boldsymbol{u}_h)]\!],[\![\boldsymbol{n}\pi-\boldsymbol{n}\cdot(\boldsymbol{S}+2\beta\mu\nabla^{\mathrm{s}}\boldsymbol{w})]\!]\right\rangle_E. \end{aligned}$$

The second and the third row terms are zero because of the definition of the problem. The last term is zero because of the weak continuity of the stresses associated to the problem. Therefore only the first and the fourth terms need to be bounded. We have that

$$\frac{\mu}{l^2}\,\|\boldsymbol{u}-\boldsymbol{u}_h\|^2 = B_{\mathrm{stab}}\left((\boldsymbol{u}-\boldsymbol{u}_h,p-p_h,\boldsymbol{\sigma}-\boldsymbol{\sigma}_h),(\boldsymbol{w},\pi,\boldsymbol{S})\right)$$

$$- \sum_K \alpha_u \left\langle P_u^\perp \left(\nabla \pi\right), P_u^\perp \left(\nabla \left(p - p_h\right)\right)\right\rangle_K - \sum_K \alpha_u \left\langle P_u^\perp \left(\rho \boldsymbol{a}_h \cdot \nabla \boldsymbol{w}\right), P_u^\perp \left(\rho \boldsymbol{a}_h \cdot \nabla \left(\boldsymbol{u} - \boldsymbol{u}_h\right)\right)\right\rangle_K$$
$$- \sum_K \alpha_u \left\langle P_u^\perp \left(\nabla \cdot \boldsymbol{S}\right), P_u^\perp \left(\left(1-\beta\right) \nabla \cdot \left(\boldsymbol{\sigma} - \boldsymbol{\sigma}_h\right)\right)\right\rangle_K \tag{6.38}$$

Using the interpolation properties and the shift assumption it follows that

$$\begin{aligned}
\left\|\boldsymbol{w} - \tilde{\boldsymbol{w}}_h\right\|_{H^1(\Omega)} &\lesssim h \left\|\boldsymbol{w}\right\|_{H^2(\Omega)} \lesssim h \frac{1}{l^2} \left\|\boldsymbol{u} - \boldsymbol{u}_h\right\|, \\
\left\|\boldsymbol{S} - \tilde{\boldsymbol{S}}_h\right\| &\lesssim h \left\|\boldsymbol{S}\right\|_{H^1(\Omega)} \lesssim h \frac{\mu}{l^2} \left\|\boldsymbol{u} - \boldsymbol{u}_h\right\|, \\
\left\|\pi - \tilde{\pi}_h\right\| &\lesssim h \left\|\pi\right\|_{H^1(\Omega)} \lesssim h \frac{\mu}{l^2} \left\|\boldsymbol{u} - \boldsymbol{u}_h\right\|.
\end{aligned}$$

From these expressions we obtain

$$\begin{aligned}
&B_{\text{stab}} \left(\left(\boldsymbol{u} - \boldsymbol{u}_h, p - p_h, \boldsymbol{\sigma} - \boldsymbol{\sigma}_h\right), \left(\boldsymbol{w}, \pi, \boldsymbol{S}\right)\right) \\
&\quad = B_{\text{stab}} \left(\left(\boldsymbol{u} - \boldsymbol{u}_h, p - p_h, \boldsymbol{\sigma} - \boldsymbol{\sigma}_h\right), \left(\boldsymbol{w} - \tilde{\boldsymbol{w}}_h, \pi - \tilde{\pi}_h, \boldsymbol{S} - \tilde{\boldsymbol{S}}_h\right)\right) \\
&\quad - \sum_K \alpha_u \left\langle P_u^\perp \left(\nabla \left(\pi - \tilde{\pi}_h\right)\right), P_u^\perp \left(\nabla \left(p - p_h\right)\right)\right\rangle_K \\
&\quad - \sum_K \alpha_u \left\langle P_u^\perp \left(\rho \boldsymbol{a}_h \cdot \nabla \left(\boldsymbol{w} - \tilde{\boldsymbol{w}}_h\right)\right), P_u^\perp \left(\rho \boldsymbol{a}_h \cdot \nabla \left(\boldsymbol{u} - \boldsymbol{u}_h\right)\right)\right\rangle_K \\
&\quad - \sum_K \alpha_u \left\langle P_u^\perp \left(\nabla \cdot \left(\boldsymbol{S} - \tilde{\boldsymbol{S}}_h\right)\right), P_u^\perp \left(\left(1-\beta\right) \nabla \cdot \left(\boldsymbol{\sigma} - \boldsymbol{\sigma}_h\right)\right)\right\rangle_K .
\end{aligned} \tag{6.39}$$

The following bounds can be easily obtained using inverse estimates and the stability of the adjoint problem:

$$\begin{aligned}
&\sum_K \alpha_u \left\langle P_u^\perp \left(\nabla \left(\pi - \tilde{\pi}_h\right)\right), P_u^\perp \left(\nabla \left(p - p_h\right)\right)\right\rangle_K \lesssim \sum_K \alpha_u \frac{\mu}{l^2} \left\|\boldsymbol{u} - \boldsymbol{u}_h\right\|_K \frac{1}{h} \left\|p - p_h\right\|_K \\
&\sum_K \alpha_u \left\langle P_u^\perp \left(\rho \boldsymbol{a}_h \cdot \nabla \left(\boldsymbol{w} - \tilde{\boldsymbol{w}}_h\right)\right), P_u^\perp \left(\rho \boldsymbol{a}_h \cdot \nabla \left(\boldsymbol{u} - \boldsymbol{u}_h\right)\right)\right\rangle_K \\
&\quad \lesssim \sum_K \alpha_u \left(\rho \left\|\boldsymbol{a}_h\right\|_K\right)^2 \frac{h}{l^2} \left\|\boldsymbol{u} - \boldsymbol{u}_h\right\|_K \left\|\boldsymbol{u} - \boldsymbol{u}_h\right\|_{H^1(K)} \\
&\sum_K \alpha_u \left\langle P_u^\perp \left(\nabla \cdot \left(\boldsymbol{S} - \tilde{\boldsymbol{S}}_h\right)\right), P_u^\perp \left(\left(1-\beta\right) \nabla \cdot \left(\boldsymbol{\sigma} - \boldsymbol{\sigma}_h\right)\right)\right\rangle_K \\
&\quad \lesssim \left(1-\beta\right) \sum_K \alpha_u \frac{\mu}{l^2} \left\|\boldsymbol{u} - \boldsymbol{u}_h\right\|_K \frac{1}{h} \left\|\boldsymbol{\sigma} - \boldsymbol{\sigma}_h\right\|_K .
\end{aligned}$$

Finally we need a bound for

$$B_{\text{stab}} \left(\left(\boldsymbol{u} - \boldsymbol{u}_h, p - p_h, \boldsymbol{\sigma} - \boldsymbol{\sigma}_h\right), \left(\boldsymbol{w} - \tilde{\boldsymbol{w}}_h, \pi - \tilde{\pi}_h, \boldsymbol{S} - \tilde{\boldsymbol{S}}_h\right)\right),$$

in (6.39). It can be bounded in terms of similar bounds as above, again using inverse and error estimates on the boundary, the stability of the adjoint problem and the expression of the stabilization parameters. We omit the details. When all these bounds are combined in (6.39) and finally used in (6.38) we obtain

$$\frac{\mu}{l^2} \left\|\boldsymbol{u} - \boldsymbol{u}_h\right\|^2 \lesssim h \frac{\sqrt{\mu}}{l^2} \left\|\boldsymbol{u} - \boldsymbol{u}_h\right\| \left(\sqrt{\mu} \left\|\boldsymbol{u} - \boldsymbol{u}_h\right\|_{H^1(\Omega)} + \frac{1}{\sqrt{\mu}} \left\|\boldsymbol{\sigma} - \boldsymbol{\sigma}_h\right\|\right.$$

$$+\sum_K \frac{\rho\,\|\boldsymbol{a}_h\|_K\,h}{\mu}\sqrt{\mu}\,\|\boldsymbol{u}-\boldsymbol{u}_h\|_{H^1(K)} + \frac{1}{\sqrt{\mu}}\sum_K\left(\frac{\lambda\,\|\boldsymbol{a}_h\|_K}{h}\right)\|\boldsymbol{\sigma}-\boldsymbol{\sigma}_h\|_K + \frac{1}{\sqrt{\mu}}\,\|p-p_h\|\Bigg),$$

and the theorem follows. Note that the bound obtained explodes with the cell Reynolds and the cell Weissenberg numbers. □

6.6 Conclusions

In this chapter we have presented the numerical analysis of a finite element approximation of the linearized viscoelastic flow problem. The formulation in the nonlinear case was presented in the stationary case in chapter 3. This analysis has confirmed what it was already known from the numerical experiments, namely, that the method provides stable solutions that converge to the exact solutions at an optimal rate of convergence. In particular, we have shown this using a mesh dependent norm especially tailored for the stabilized problem and also the norm of the space where the continuous problem is posed. What is relevant from the analysis presented is that it clearly displays how the estimates obtained deteriorate as the cell Reynolds number and the cell Weissenberg number increase. The former decreases when the mesh size is reduced, but the having a bound on the latter imposes the relaxation time to be very small, which is an indication of the existence of the so called high Weissenberg number problem.

Chapter 7

Numerical Analysis: Nonlinear Time-Dependent Case

7.1 Abstract

In this Chapter we analyze the stabilized finite element formulation proposed in Chapter 3 for the viscoelastic fluid flow problem. The formulation has shown to have accuracy and robustness in the different benchmarks used in the viscoelastic framework and permitting the use of equal interpolation between the unknown fields. This part of the work includes the stability analysis of a linearized time-dependent sub-problem and the study of the existence of a solution for the non-linear case, using the fixed point theory.

7.2 Introduction

The finite element approximation of the flow of viscoelastic fluids presents several numerical difficulties. One the one hand, all the problems inherited from the incompressible Navier-Stokes equations, mainly the compatibility between the velocity-pressure approximation and the treatment of the nonlinear advective term. But, on top of that, now the constitutive equation is highly nonlinear, with an advective term that may lead to both global and local oscillations in the numerical approximation. Moreover, even in the case of smooth solutions it is necessary to meet some additional compatibility conditions between the velocity and the stress interpolation in order to control velocity gradients. Elements that satisfy the compatibility requirements velocity-pressure and stress-velocity are scarce, particularly in the threedimensional case [111, 25]. In [8] one can find a good review of mixed methods that satisfy the two compatibility conditions required.

Viscoelastic fluids are a specific type of non-Newtonian fluids. They are characterized by having complex and high-molecular-weight molecules with many internal degrees of freedom [23]. The classical examples of this type of fluids are the polymer solutions and molten polymers. The basic feature of polymeric fluids is the presence of long chain molecules. In a flow, these chain molecules are stretched out by the drag forces exerted on them by the surrounding fluid [139]. The natural tendency of the molecule to retract from this stretched configuration generates an elastic force which contributes to the macroscopic stress tensor, and for this reason they are called viscoelastic fluids. The interest for fluids of this kind has increased in the last years, due to the connections with the industrial applications. This motivates the numerical, and mathematical analysis of the governing equations [82].

For viscoelastic fluid flows, in contrast to the Navier-Stokes equations, well-posedness for

general models is not well understood. For initial value problems, the existence of solutions has been proved only locally in time. Global existence in time of solutions has been proved only if the initial conditions are small perturbations of the rest state. And for the steady state case, existence of solutions can be proved only for small perturbations of the Newtonian case (see [139] for a comprehensive review).

The existence of slow steady flows of viscoelastic fluids using differential constitutive equations was proved in the work of Renardy [138] for Hilbert spaces. In this work, Renardy used an iterative method to show that the solution is bounded by a certain norm, and then the author proved that all iterates converges in a weaker norm. For the time-dependent case, existence of solutions locally in time, and for small data globally in time, has been proved for Hilbert spaces in the work of Guillopé and Saut [91]. The extension to Banach spaces and a complete review of uniqueness, regularity, well-posedness and stability results can be found in the work of Fernández-Cara et al. [82]. The existence of global weak solutions for general initial conditions using an Oldroyd kind model has been proved by Lions and Masmoudi in [110]. The existence proof in [110] relies upon showing the propagation in time of the compactness of solutions.

In the finite element framework, the work of Baranger and Sandri [16] was one of the first were the existence of an approximate solution and error bounds were given for an Oldroyd-B fluid, using the Brouwer's fixed point theorem, discontinuous interpolation for the elastic stresses and the method of Lesaint-Reviart for the convection of the extra stress tensor in the stationary case. Later, the second author in [146] extended the study for continuous approximation of the stress field, using $P1$-$P2$-$P1$ interpolation for $\boldsymbol{\sigma}$, $\boldsymbol{u}$ and p respectively, and the SUPG method to treat the convective term in the constitutive equation. The time dependent case of the same continuous interpolation problem was analyzed by Baranger and Wardi in [17].

In the same finite element context, Picasso and Rappaz [134] analyzed a stationary non-convective Oldroyd-B problem proving priori and posteriori error estimates. In this work, the authors used the Galerkin Least Square (GLS) method to stabilize the momentum equation and the Elastic Viscous Split Stress (EVSS) scheme for the constitutive equation. The extension for the time-dependent case was treated in [27] for the same simplified Oldroyd-B problem where global existence in time was proved in Banach spaces for small data. For a Stokes/Oldroyd-B linearized problem, Bonito and Burman presented in [26] optimal a priori error estimates using the Interior-Penalty method. A similar problem was studied by Ervin et al. [76] for the steady state case but using the Johnson-Segalman linearized constitutive model, proving existence and uniqueness of the continuous and a finite element approximation under small data assumption. In another work, Ervin and Miles [77] analyzed the Oldroyd-B time-dependent case both in the semi-discrete as in the fully discrete case using the SUPG method and proving existence of a solution and deriving a priori error estimates for the numerical approximation, assuming a Taylor-Hood pair approximation for the velocity and pressure, and a continuous approximation for the viscoelastic stresses. The same authors extended later the analysis to a two-fluid flow problem in [78], giving a priori error estimates for the approximation in terms of the mesh and time discretization parameters.

The stabilized finite element formulation analyzed in this part of the work has its roots in the context of Variational Multiscale Methods (VMS) introduced by Hughes et al. [97] for the scalar convection-diffussion-reaction problem, and extended later to the vectorial Stokes problem in [51], where the space of the sub-grid scales is taken orthogonal to the finite element space. As we shall see, this is an important ingredient in the analyzed method, which consists in a sort of orthogonal term-by-term stabilized formulation. The starting point of a VMS approach consist in splitting the unknowns of the problem in two scales, the finite element one and the unresolvable one, called sub-grid scale. The latter needs to be approximated in a simple manner in terms of the former, so as to capture its main effect and

yield a stable formulation for the finite element unknown, keeping therefore the number of degrees of freedom of the Galerkin method.

The objective of this chapter is to analyze numerically the stabilized finite element formulation proposed in chapter 3 (also in [37]) for the time-dependent viscoelastic flow problem. This formulation has shown to have very good accuracy and robustness in stationary [37] and time-dependent cases [35, 38]. The numerical analysis of a linearized stationary case was performed in chapter 6 (also in [40]) where in addition jump functions were added to permit arbitrary interpolation.

The chapter is organized as follows. Section 7.3 defines some notation statements and general results used in the subsequent analysis. In Section 7.4 we present the problem to be solved and its Galerkin finite element approximation, explaining the sources of the numerical instability. Section 7.5 contains a description of the stabilized finite element formulation analyzed. Section 7.6 is devoted to the numerical analysis of a linearized time-dependent subproblem, where the stability of the method and the existence and uniqueness of the solution in the semi-discrete linearized case are proved. Section 7.7 analyzes the non-linear case, where existence of a solution is proved using a fixed point theorem. Finally, conclusions and some remarks are summarized in Section 7.8.

7.3 Notation and Preliminaries

7.3.1 Notation

In order to write the weak form of the problem, let us introduce some notation used in the chapter. The space of square integrable functions in a domain ω is denoted by $L^2(\omega)$, and the space of functions whose distributional derivatives of order up to $m \in \mathbb{N}$ belong to $L^2(\omega)$ by $H^m(\omega)$. The space $H_0^1(\omega)$ consists on functions in $H^1(\omega)$ vanishing on $\partial\omega$. The topological dual of $H_0^1(\omega)$ is denoted by $H^{-1}(\omega)$, the duality pairing by $\langle\cdot,\cdot\rangle_\omega$, and the L^2 inner product in ω (for scalar, vectors and tensors) is denoted by $(\cdot,\cdot)_\omega$. In this part of the work, when $\omega = \Omega$, the subscript or the domain information are omitted.

Referred to the norms used in the subsequent analysis, $\|\cdot\|$ represents the $L^2(\Omega)$ norm, $\|\cdot\|_{L^4}$ represents the $L^4(\Omega)$ norm, $\|\cdot\|_\infty$ the $L^\infty(\Omega)$ norm, $\|\cdot\|_k$ is the $H^k(\Omega)$-norm, $\|\cdot\|_{1,\infty}$ represents the $W^{1,\infty}(\Omega)$ norm, and $\|\cdot\|_{l,p}$ the norm for the space $W^{l,p}(\Omega)$ where $W^{l,2}(\Omega) = H^l(\Omega)$.

Some symbols used in the work are: $\lesssim$ to refer that the result is independent of h and of the physical parameters and ∇^s to represent the symmetric gradient operator, defined as

$$\nabla^s \boldsymbol{u} = \frac{1}{2}\left(\nabla \boldsymbol{u} + (\nabla \boldsymbol{u})^T\right).$$

7.3.2 Preliminaries

In this subsection, we introduce some mathematical settings and classical theorems used in this part of the work.

The classical form of the Korn's inequality read as

$$\|\boldsymbol{v}\|_1 \leq c_\Omega \|\nabla^s \boldsymbol{v}\| \ \forall \boldsymbol{v} \in \left(H_0^1(\Omega)\right)^d, \tag{7.1}$$

where the existence of the constant c_Ω (dependent of the domain) is guaranteed easily for conforming meshes.

Another useful inequality that bounds the gradient of a function in terms of its symmetrical gradient is the following [48]

$$\|\nabla \boldsymbol{v}\| \leq \sqrt{2}\|\nabla^s \boldsymbol{v}\| \ \forall \boldsymbol{v} \in \left(H_0^1(\Omega)\right)^d. \tag{7.2}$$

The Poincaré-Friedrichs inequality reads as: for $\boldsymbol{v} \in \left(H_0^1(\Omega)\right)^d$, there exists a constant c_{PF} such that

$$\|\boldsymbol{v}\| \leq c_{PF} \|\nabla \boldsymbol{v}\| .$$

From the Sobolev embedding theorems (see [87]), we can bound the $L^4(\Omega)$-norm in terms of the $H^1(\Omega)$-norm as follows

$$\|\boldsymbol{v}\|_{L^4} \leq C_{L^4}^{H^1} \|\boldsymbol{v}\|_1 . \tag{7.3}$$

For the finite element formulation that we shall consider, the discrete velocity field will not be weakly divergence free and the use of the skew symmetric counterpart of the convective term simplifies the analysis. We then define

$$\begin{aligned} \tilde{c}(\boldsymbol{w}, \boldsymbol{u}, \boldsymbol{v}) =& \frac{1}{2} \left(c(\boldsymbol{w}, \boldsymbol{u}, \boldsymbol{v}) - c(\boldsymbol{w}, \boldsymbol{v}, \boldsymbol{u}) \right), \\ c(\boldsymbol{w}, \boldsymbol{u}, \boldsymbol{v}) =& (\boldsymbol{w} \cdot \nabla \boldsymbol{u}, \boldsymbol{v}) . \end{aligned}$$

The following properties are satisfied by this antisymmetric term
i) $\tilde{c}(\boldsymbol{w}, \boldsymbol{u}, \boldsymbol{v}) = c(\boldsymbol{w}, \boldsymbol{u}, \boldsymbol{v})$ when $\nabla \cdot \boldsymbol{u} = 0$ and $\boldsymbol{u} = \boldsymbol{0}$ on Ω
ii) $\tilde{c}(\boldsymbol{w}, \boldsymbol{u}, \boldsymbol{u}) = 0$, for every $\boldsymbol{w}, \boldsymbol{u} \in \left(H_0^1(\Omega)\right)^d$.

Let us consider a finite element partition $\mathcal{T}_h$ of the computational domain Ω. The diameter of an element domain $K \in \mathcal{T}_h$ is denoted by h_K and the diameter of the partition is defined as $h = \max\{h_K \mid K \in \mathcal{T}_h\}$. We will consider quasi-uniform families of meshes, and thus all the element diameters can be bounded above and below by constants multiplying h.

Defining $V_{h,K} := \left\{ \boldsymbol{v}_h \in C^0(\bar{\Omega}) : \boldsymbol{v}_h |_K \in P_k(K) \ \forall K \in \mathcal{T}_h \right\}$, we can write the following inverse inequality: there is a constant c_{inv}, independent of the mesh size h (the maximum of all the element diameters), such that

$$\|v_h\|_{l,p,K} \leq c_{inv} h^{m-l+\min\left(0, \frac{d}{p} - \frac{d}{q}\right)} \|v_h\|_{m,q,K} , \tag{7.4}$$

for all finite element functions v_h defined on $K \in \mathcal{T}_h$ (see [75]).

From the interpolation theory of finite element and Sobolev spaces which we will use in our subsequent analysis, an important inequality is the following. For $\boldsymbol{u} \in W^{l,p}(\Omega)$, there exists a constant C independent of h, for all $0 \leq l \leq k+1$, $1 \leq p \leq \infty$, such that

$$\|\boldsymbol{u} - P[\boldsymbol{u}]\|_p \leq C h^l |\boldsymbol{u}|_{l,p} , \tag{7.5}$$

where $P[\boldsymbol{u}] \in V_h$ is the $L^2(\Omega)$ projection of $\boldsymbol{u}$ in V_h (see [75] for more details).

Based on the interpolation theory it is possible to write the following inequality

$$\|\nabla (\boldsymbol{u} - P[\boldsymbol{u}])\|_\infty \leq C_{\infty,3} \|\boldsymbol{u}\|_3 , \tag{7.6}$$

where, $C_{\infty,3}$, is a positive constant independent of h.

7.4 Problem statement and Galerkin finite element discretization

7.4.1 Boundary Value problem

Let Ω be a bounded, open set of $\mathbb{R}^d$ ($d = 2$ or 3) occupied by the fluid, assumed to be bounded and polyhedral, and let $\partial\Omega$ be its boundary. Aditionally, consider the time interval

$(0,T)$, with $T<\infty$. The incompressible and isothermal viscoelastic fluid flow problem can be written as:

$$\rho\left(\frac{\partial \boldsymbol{u}}{\partial t}+\boldsymbol{u}\cdot\nabla\boldsymbol{u}\right)-\nabla\cdot\left(2\beta\mu\nabla^{s}\boldsymbol{u}+\boldsymbol{\sigma}\right)+\nabla p=\boldsymbol{f}\qquad \text{in }\Omega,\ t\in\left]0,T\right[, \tag{7.7}$$

$$\nabla\cdot\boldsymbol{u}=0\qquad \text{in }\Omega,\ t\in\left]0,T\right[, \tag{7.8}$$

$$\frac{1}{2\mu}\boldsymbol{\sigma}-\left(1-\beta\right)\nabla^{s}\boldsymbol{u}+\frac{\lambda}{2\mu}\left(\frac{\partial\boldsymbol{\sigma}}{\partial t}+\boldsymbol{u}\cdot\nabla\boldsymbol{\sigma}\right)$$
$$-\frac{\lambda}{2\mu}\left(\boldsymbol{\sigma}\cdot\nabla\boldsymbol{u}+\left(\nabla\boldsymbol{u}\right)^{T}\cdot\boldsymbol{\sigma}\right)=\mathbf{0}\qquad \text{in }\Omega,\ t\in\left]0,T\right[, \tag{7.9}$$

$$\boldsymbol{u}=\mathbf{0}\qquad \text{on }\partial\Omega,\ t\in\left]0,T\right[, \tag{7.10}$$

$$\boldsymbol{u}\mid_{t=0}=\boldsymbol{u}_{0}\qquad \text{in }\Omega, \tag{7.11}$$

$$\boldsymbol{\sigma}\mid_{t=0}=\boldsymbol{\sigma}_{0}\qquad \text{in }\Omega. \tag{7.12}$$

The unknowns of the problem are: the velocity field $\boldsymbol{u}\left(\boldsymbol{x},t\right)$, the pressure $p\left(\boldsymbol{x},t\right)$ and the the viscoleastic or elastic part $\boldsymbol{\sigma}\left(\boldsymbol{x},t\right)$ of the extra stress tensor. The physical parameters are the dynamic viscosity μ, the density of the fluid ρ, a real parameter $\beta\in[0,1]$ to define the amount of viscous or solvent viscosity ($\mu_{s}=\beta\mu$) and elastic or polymeric viscosity ($\mu_{p}=\left(1-\beta\right)\mu$) in the fluid, and the relaxation time λ. Finally, $\boldsymbol{f}\in H^{-1}\left(\Omega\right)^{d}$ is the external volume force applied to the fluid confined in Ω.

For viscoelastic fluids, the problem is incomplete without the definition of a constitutive equation for the elastic stresses ($\boldsymbol{\sigma}$). A large variety of approaches exist to define it (see [21, 22] for a complete description). In this work, we use the classical Oldroyd-B constitutive model (7.9) for this purpose. This constitutive law may be used to describe solutions of polymers in a Newtonian solvent, or polymer melts with a fast relaxation time mode.

The conservation laws (7.7)-(7.8) and the Oldroyd-B constitutive equation (7.9) are a mixed parabolic-hyperbolic problem, that need to be complemented with initial (7.11)-(7.12) and boundary (7.10) conditions to close the problem. For simplicity in the exposition, we will consider the simplest boundary condition for the velocity and no boundary conditions for the stress field. With respect to the initial conditions, $\boldsymbol{u}_{0}$ and $\boldsymbol{\sigma}_{0}$ are functions defined on the whole domain Ω. For a complete description of the mathematical structure of the problem we refer to [82, 139].

7.4.2 Variational form

To write the weak form of the problem (7.7)-(7.9) we need to introduce some functional spaces. Let $\boldsymbol{\mathcal{V}}=\left(H_{0}^{1}\left(\Omega\right)\right)^{d}$, $\boldsymbol{\Upsilon}:=\left\{\boldsymbol{\tau}\mid\boldsymbol{\tau}\in\left(L^{2}\left(\Omega\right)\right)_{sym}^{d\times d},\ \boldsymbol{w}\cdot\nabla\boldsymbol{\tau}\in\left(L^{2}\left(\Omega\right)\right)^{d\times d}\ \forall\boldsymbol{w}\in\boldsymbol{\mathcal{V}}\right\}$ and $Q=L_{0}^{2}$, the spaces of the velocity, the elastic stresses and the pressure respectively. If we call $\boldsymbol{U}=\left(\boldsymbol{u},p,\boldsymbol{\sigma}\right)$, $\boldsymbol{\mathcal{X}}:=\boldsymbol{\mathcal{V}}\times Q\times\boldsymbol{\Upsilon}$, the weak form of the problem consists in finding $\boldsymbol{U}:\left]0,T\right[\rightarrow\boldsymbol{\mathcal{X}}$, such that the initial conditions are satisfied and

$$\rho\left(\frac{\partial\boldsymbol{u}}{\partial t}+\boldsymbol{u}\cdot\nabla\boldsymbol{u},\boldsymbol{v}\right)+\left(2\beta\mu\nabla^{s}\boldsymbol{u}+\boldsymbol{\sigma},\nabla^{s}\boldsymbol{v}\right)-\left(p,\nabla\cdot\boldsymbol{v}\right)=\left\langle\boldsymbol{f},\boldsymbol{v}\right\rangle, \tag{7.13}$$

$$\left(\nabla\cdot\boldsymbol{u},q\right)=0, \tag{7.14}$$

$$\left(\frac{1}{2\mu}\boldsymbol{\sigma}-\left(1-\beta\right)\nabla^{s}\boldsymbol{u},\boldsymbol{\tau}\right)+\frac{\lambda}{2\mu}\left(\frac{\partial\boldsymbol{\sigma}}{\partial t}+\boldsymbol{u}\cdot\nabla\boldsymbol{\sigma},\boldsymbol{\tau}\right)-\frac{\lambda}{2\mu}\left(g\left(\boldsymbol{u},\boldsymbol{\sigma}\right),\boldsymbol{\tau}\right)=0, \tag{7.15}$$

for all $\boldsymbol{V}=\left(\boldsymbol{v},q,\boldsymbol{\tau}\right)\in\boldsymbol{\mathcal{X}}$. The last term of the constitutive equation represents the traction or rotational term defined as $g\left(\boldsymbol{u},\boldsymbol{\sigma}\right):=\boldsymbol{\sigma}\cdot\nabla\boldsymbol{u}+\left(\nabla\boldsymbol{u}\right)^{T}\cdot\boldsymbol{\sigma}$.

In a compact form, problem (7.13)-(7.15) can be written as:

$$\left(\mathcal{D}_t\left(\boldsymbol{U}\right),\boldsymbol{V}\right)+B\left(\boldsymbol{u},\boldsymbol{\sigma};\boldsymbol{U},\boldsymbol{V}\right)=\left\langle \boldsymbol{f},\boldsymbol{v}\right\rangle , \tag{7.16}$$

for all $\boldsymbol{V}\in\boldsymbol{\mathcal{X}}$,where

$$\begin{aligned} B\left(\hat{\boldsymbol{u}},\hat{\boldsymbol{\sigma}};\boldsymbol{U},\boldsymbol{V}\right)=&\rho\left(\hat{\boldsymbol{u}}\cdot\nabla\boldsymbol{u},\boldsymbol{v}\right)+2\beta\mu\left(\nabla^{s}\boldsymbol{u},\nabla^{s}\boldsymbol{v}\right)+\left(\boldsymbol{\sigma},\nabla^{s}\boldsymbol{v}\right)-\left(p,\nabla\cdot\boldsymbol{v}\right)+\left(\nabla\cdot\boldsymbol{u},q\right) \\ &+\frac{1}{2\mu}\left(\boldsymbol{\sigma},\boldsymbol{\tau}\right)-\left(1-\beta\right)\left(\nabla^{s}\boldsymbol{u},\boldsymbol{\tau}\right)+\frac{\lambda}{2\mu}\left(\hat{\boldsymbol{u}}\cdot\nabla\boldsymbol{\sigma},\boldsymbol{\tau}\right)-\frac{\lambda}{2\mu}\left(g\left(\hat{\boldsymbol{u}},\hat{\boldsymbol{\sigma}}\right),\boldsymbol{\tau}\right), \end{aligned} \tag{7.17}$$

and

$$\left(\mathcal{D}_t\left(\boldsymbol{U}\right),\boldsymbol{V}\right):=\rho\left(\frac{\partial\boldsymbol{u}}{\partial t},\boldsymbol{v}\right)+\frac{\lambda}{2\mu}\left(\frac{\partial\boldsymbol{\sigma}}{\partial t},\boldsymbol{\tau}\right). \tag{7.18}$$

7.4.3 Galerkin finite element discretization

From $\mathcal{T}_h$ we may construct conforming finite element spaces for the velocity, the pressure and the elastic stress, $\boldsymbol{\mathcal{V}}_h\subset\boldsymbol{\mathcal{V}}$, $Q_h\subset Q$ and $\boldsymbol{\Upsilon}_h\subset\boldsymbol{\Upsilon}$, respectively. Calling $\boldsymbol{\mathcal{X}}_h=\boldsymbol{\mathcal{V}}_h\times Q_h\times\boldsymbol{\Upsilon}_h$, the Galerkin finite element approximation of problem (7.16) consists in finding $\boldsymbol{U}_h:]0,T[\rightarrow\boldsymbol{\mathcal{X}}_h$ such that

$$\left(\mathcal{D}_t\left(\boldsymbol{U}_h\right),\boldsymbol{V}_h\right)+B\left(\boldsymbol{u}_h,\boldsymbol{\sigma}_h;\boldsymbol{U}_h,\boldsymbol{V}_h\right)=\left\langle \boldsymbol{f},\boldsymbol{v}_h\right\rangle , \tag{7.19}$$

for all $\boldsymbol{V}_h\in\boldsymbol{\mathcal{X}}_h$, and satisfying the appropriate initial conditions.

Until now, we have posed no restrictions on the choice of the finite element spaces. However, let us analyze the numerical stability of the problem (7.19). If we take $\boldsymbol{V}_h=\boldsymbol{U}_{h1}=\left(\left(1-\beta\right)\boldsymbol{u}_h,\left(1-\beta\right)p_h,\boldsymbol{\sigma}_h\right)$, it is found that

$$\begin{aligned} B\left(\boldsymbol{U}_h,\boldsymbol{U}_{h1}\right)=&2\left(1-\beta\right)\beta\mu\left\|\nabla^{s}\boldsymbol{u}_h\right\|^{2}+\frac{1}{2\mu}\left\|\boldsymbol{\sigma}_h\right\|^{2} \\ &-\frac{\lambda}{2\mu}\left(\boldsymbol{\sigma}_h\cdot\nabla\boldsymbol{u}_h+\left(\nabla\boldsymbol{u}_h\right)^{T}\cdot\boldsymbol{\sigma}_h,\boldsymbol{\sigma}_h\right). \end{aligned} \tag{7.20}$$

It is seen from (7.20) that $B\left(\cdot,\cdot\right)$ is not coercive in $\boldsymbol{\mathcal{X}}_h$, and we can ensure only control on $\left\|\boldsymbol{\sigma}_h\right\|$ for all β assuming $\lambda\nabla\boldsymbol{u}_h$ to be small enough.

To ensure the control of p_h and $\nabla^{s}\boldsymbol{u}_h$, one has then to choose finite element spaces satisfying:

$$\inf_{q_h\in\mathcal{Q}_h}\sup_{\boldsymbol{v}_h\in\boldsymbol{\mathcal{V}}_h}\frac{\left(q_h,\nabla\cdot\boldsymbol{v}_h\right)}{\left\|\boldsymbol{v}_h\right\|_{\boldsymbol{\mathcal{V}}_h}\left\|q_h\right\|_{\mathcal{Q}_h}}\geq C_1, \tag{7.21}$$

$$\inf_{\boldsymbol{v}_h\in\boldsymbol{\mathcal{V}}_h}\sup_{\boldsymbol{\tau}_h\in\boldsymbol{\Upsilon}_h}\frac{\left(\boldsymbol{\tau}_h,\nabla^{s}\boldsymbol{v}_h\right)}{\left\|\boldsymbol{\tau}_h\right\|_{\boldsymbol{\Upsilon}_h}\left\|\boldsymbol{v}_h\right\|_{\boldsymbol{\mathcal{V}}_h}}\geq C_2, \tag{7.22}$$

where C_1 and C_2 are positive constants. It is therefore required that the finite element spaces satisfy (7.21) and (7.22), which is a stringent requirement inherited from the mixed form of the Navier-Stokes problem [36].

The two compatibility conditions of the viscoelastic flow problem do not allow us the use of an arbitrary interpolation for the different fields because the scheme may become unstable. The implementation of inf-sup stable elements is a possible solution for this problem, however, from the numerical point of view, the spaces that fulfil these conditions are limited and complex, particularly when the problem needs to be solved in three dimensions. See related, the works of Marchal and Crochet [111] and Fortin and Fortin [84] for the 2D case and the work of Bogaerds et al. [25] for the 3D case. The other possibility is to use a stabilized

formulation that permits the use of any interpolation for the variables, which is the approach studied in this work. Note that the constitutive equation is of convective nature, and therefore, some kind of stabilization technique have to be used even if inf-sup stable elements are used, the same for the momentum equation.

In general, a stabilized formulation consists of replacing B in (7.16) by another multi-linear form B_{stab}, possible mesh dependent, designed to enhance stability without upsetting accuracy. This point shall be described in the next Section.

7.5 Stabilized finite element method

In the following section we summarize the stabilized formulation analyzed in this chapter. This formulation was proposed in [37] and tested numerically in [38, 35]. The numerical analysis of the linearized stationary problem was performed in chapter 6 (also in [40]).

Considering $\boldsymbol{\mathcal{X}}_h = \boldsymbol{\mathcal{V}}_h \times Q_h \times \boldsymbol{\Upsilon}_h$ where $\boldsymbol{\mathcal{V}}_h = \left[V_{h,K} \cap H_0^1\right]^d$, $Q_h = V_{h,K}$ and $\boldsymbol{\Upsilon}_h = \left[V_{h,K}\right]_{sym}^{d\times d}$, the method consists in replacing (7.19) by the following problem: find $\boldsymbol{U}_h \in \boldsymbol{\mathcal{X}}_h$, such that

$$\left(\mathcal{D}_t\left(\boldsymbol{U}_h\right), \boldsymbol{V}_h\right) + B_{stab}\left(\boldsymbol{u}_h, \boldsymbol{\sigma}_h; \boldsymbol{U}_h, \boldsymbol{V}_h\right) = \langle \boldsymbol{f}, \boldsymbol{v}\rangle, \tag{7.23}$$

for all $\boldsymbol{V}_h \in \boldsymbol{\mathcal{X}}_h$, where

$$B_{stab}\left(\hat{\boldsymbol{u}}_h, \hat{\boldsymbol{\sigma}}_h; \boldsymbol{U}_h, \boldsymbol{V}_h\right) = B\left(\hat{\boldsymbol{u}}_h, \hat{\boldsymbol{\sigma}}_h; \boldsymbol{U}_h, \boldsymbol{V}_h\right) + B^*\left(\hat{\boldsymbol{u}}_h, \hat{\boldsymbol{\sigma}}_h; \boldsymbol{U}_h, \boldsymbol{V}_h\right), \tag{7.24}$$

and B^*represents the additional stabilization terms added to the Galerkin formulation.

Using the same notation as in [37], we can define B^* as

$$B^*\left(\hat{\boldsymbol{u}}_h, \hat{\boldsymbol{\sigma}}_h; \boldsymbol{U}_h, \boldsymbol{V}_h\right) = S_1^{\perp}\left(\hat{\boldsymbol{u}}_h; \boldsymbol{U}_h, \boldsymbol{V}_h\right) + S_2^{\perp}\left(\boldsymbol{U}_h, \boldsymbol{V}_h\right) + S_3^{\perp}\left(\hat{\boldsymbol{u}}_h, \hat{\boldsymbol{\sigma}}_h; \boldsymbol{U}_h, \boldsymbol{V}_h\right),$$

where

$$\begin{aligned} S_1^{\perp}\left(\hat{\boldsymbol{u}}_h; \boldsymbol{U}_h, \boldsymbol{V}_h\right) =& \alpha_u\left(P_u^{\perp}\left[\rho\hat{\boldsymbol{u}}_h \cdot \nabla \boldsymbol{u}_h\right], P_u^{\perp}\left[\rho\hat{\boldsymbol{u}}_h \cdot \nabla \boldsymbol{v}_h\right]\right) + \alpha_u\left(P_u^{\perp}\left[\nabla p_h\right], P_u^{\perp}\left[\nabla q_h\right]\right) \\ &+ \alpha_u\left(P_u^{\perp}\left[\nabla \cdot \boldsymbol{\sigma}_h\right], P_u^{\perp}\left[(1-\beta)\nabla \cdot \boldsymbol{\tau}_h\right]\right), \end{aligned} \tag{7.25}$$

$$S_2^{\perp}\left(\boldsymbol{U}_h, \boldsymbol{V}_h\right) = \alpha_p\left(P_p^{\perp}\left[\nabla \cdot \boldsymbol{u}_h\right], P_p^{\perp}\left[\nabla \cdot \boldsymbol{v}_h\right]\right), \tag{7.26}$$

$$\begin{aligned} S_3^{\perp}\left(\hat{\boldsymbol{u}}_h, \hat{\boldsymbol{\sigma}}_h; \boldsymbol{U}_h, \boldsymbol{V}_h\right) =& \alpha_\sigma\left(P_\sigma^{\perp}\left[-(1-\beta)\nabla^s \boldsymbol{u}_h + \frac{\lambda}{2\mu}\left(\hat{\boldsymbol{u}}_h \cdot \nabla \boldsymbol{\sigma}_h - g\left(\hat{\boldsymbol{u}}_h, \hat{\boldsymbol{\sigma}}_h\right)\right)\right],\right. \\ &\left. P_\sigma^{\perp}\left[-\nabla^s \boldsymbol{v}_h + \frac{\lambda}{2\mu}\left(\hat{\boldsymbol{u}}_h \cdot \nabla \boldsymbol{\tau}_h + g^*\left(\hat{\boldsymbol{u}}_h, \boldsymbol{\tau}_h\right)\right)\right]\right), \end{aligned} \tag{7.27}$$

and $g^*\left(\hat{\boldsymbol{u}}_h, \boldsymbol{\tau}_h\right)$, represents the adjoint operator of $g\left(\hat{\boldsymbol{u}}_h, \boldsymbol{\tau}_h\right)$, which is defined as $g^*\left(\hat{\boldsymbol{u}}_h, \boldsymbol{\tau}_h\right) := \boldsymbol{\tau}_h \cdot \left(\nabla \hat{\boldsymbol{u}}_h\right)^T + \nabla \hat{\boldsymbol{u}}_h \cdot \boldsymbol{\tau}_h$. Here $P_u^{\perp} = I - P_u$, where $P_u : L^2 \to \boldsymbol{\mathcal{V}}_h$ is the L^2 projection onto $\boldsymbol{\mathcal{V}}_h$ ($P_p^{\perp}$ and $P_\sigma^{\perp}$ are defined in an analogous way).

Note that all the stabilization terms in (7.25)-(7.27) are multiplied by α_i, $i = u, p, \sigma$. These terms are the components of the stabilization parameter matrix, that can be defined as

$$\boldsymbol{\alpha} = \operatorname{diag}\left(\alpha_u \boldsymbol{I}_d, \alpha_p, \alpha_\sigma \boldsymbol{I}_{d\times d}\right),$$

where

$$\alpha_u = \left[c_1 \frac{\mu}{h^2} + c_2 \frac{\rho\left\|\hat{\boldsymbol{u}}_h\right\|_\infty}{h}\right]^{-1}, \tag{7.28}$$

$$\alpha_p = \frac{h^2}{c_1 \alpha_u}, \tag{7.29}$$

$$\alpha_\sigma = \left[c_3 \frac{1}{2\mu} + \frac{\lambda}{2\mu} \left(c_4 \frac{\|\hat{\boldsymbol{u}}_h\|_\infty}{h} + 2c_5 \|\nabla \hat{\boldsymbol{u}}_h\|_\infty \right) \right]^{-1}. \tag{7.30}$$

A general approach to design the terms of the stabilization parameter matrix was proposed in [56] for the three-field Stokes problem. In this work, the author shows as the parameters can be uniquely determined by dimensionality, assuming that this matrix is diagonal.

The stabilizing mechanism introduced by the terms $S_1^\perp$, $S_2^\perp$ and $S_3^\perp$ are the following. The first component of the $S_1^\perp$ gives control on the convective term, the second component gives control on the pressure gradient, and the third term gives control on the divergence of the viscoelastic stress. The term $S_2^\perp$ is not a must but in some cases it improves stability of the problem. Finally, the term $S_3^\perp$ adds stability in the constitutive equation. Note that some of the components of this last term are the convective-convective term of the viscoelastic stress tensor and an equivalent EVSS-structure component, among others cross local inner-product terms (see [37] for more details of this spatial stabilized formulation). The addition of these three terms permit the resolution of convection dominant problems both in velocity and in stress, and the implementation of equal order interpolation for all the unknowns. The orthogonal projections introduce consistency errors, but of optimal order, a key point in the design of accurate non-residual based methods. For stationary problems, the resulting formulation turns out to have optimal order of convergence, as checked numerically in [37] for linear and quadratic elements.

The term-by-term form of $S_1^\perp$ was proposed instead of a residual one, because the first has shown a better numerical behavior in problems where high gradients in pressure and stress are presented, see [39] for more details of this idea.

7.6 Linearized time-dependent case

The numerical analysis of the stabilized formulation performed in the chapter is divided in two steps. In this Section we present the stability analysis of the linearized case. The second part (Section 7.7), is devoted to the nonlinear analysis.

7.6.1 Linearized stabilized Semi-discrete problem

The equations for incompressible viscoelastic flows have several nonlinear terms, both in the momentum and in the constitutive equation. In the former we have the convective term, and in the latter we have the term corresponding to convection of stresses and the rotational term arising from the objective derivative of stresses. On top of that, the stabilization terms depend also on the velocity, introducing therefore additional nonlinearities.

As it is usual for incompressible flow problems, for the convective term of the momentum equation we can use a Picard scheme, taking the advection velocity of the previous iteration. This leads only to first order convergence, but is a robust option. The constitutive equation is rather more complex and many times is recomended the implementation combined algorithms. See for example the work of Castillo and Codina [37] where a Newton scheme was combined with a continuation method, or the work of Howell [95] where different types of continuation methods were proposed. For simplicity in the numerical analysis we will use only the fixed point scheme for all the nonlinear terms, including the terms associated to the matrix of stabilization parameters $\boldsymbol{\alpha}$. The extended form of the equations after linearization is presented in Eq. (7.31)-(7.33).

Given $\hat{\boldsymbol{u}}_h \in \boldsymbol{\mathcal{V}}_h$ and $\hat{\boldsymbol{\sigma}}_h \in \boldsymbol{\Upsilon}_h$, we analyze the following semi-discrete linearized problem: find $\boldsymbol{U}_h :]0,T[\to \boldsymbol{\mathcal{X}}_h$ such that

$$\rho\left(\frac{\partial \boldsymbol{u}_h}{\partial t}, \boldsymbol{v}_h\right) + \rho\tilde{c}\left(\hat{\boldsymbol{u}}_h, \boldsymbol{u}_h, \boldsymbol{v}_h\right) + \left(2\beta\mu\nabla^s\boldsymbol{u}_h + \boldsymbol{\sigma}_h, \nabla^s\boldsymbol{v}_h\right) - \left(p_h, \nabla\cdot\boldsymbol{v}_h\right) \tag{7.31}$$
$$+\alpha_u\left(P_u^{\perp}\left[\rho\hat{\boldsymbol{u}}_h\cdot\nabla\boldsymbol{u}_h\right], P_u^{\perp}\left[\rho\hat{\boldsymbol{u}}_h\cdot\nabla\boldsymbol{v}_h\right]\right) + \alpha_p\left(P_p^{\perp}\left[\nabla\cdot\boldsymbol{u}_h\right], P_p^{\perp}\left[\nabla\cdot\boldsymbol{v}_h\right]\right)$$
$$+\alpha_\sigma\left(P_\sigma^{\perp}\left[\left(1-\beta\right)\nabla^s\boldsymbol{u}_h - \frac{\lambda}{2\mu}\left(\hat{\boldsymbol{u}}_h\cdot\nabla\boldsymbol{\sigma}_h - g\left(\hat{\boldsymbol{u}}_h, \hat{\boldsymbol{\sigma}}_h\right)\right)\right], P_\sigma^{\perp}\left[\nabla^s\boldsymbol{v}_h\right]\right) = \left\langle \boldsymbol{f}, \boldsymbol{v}_h\right\rangle,$$
$$\left(\nabla\cdot\boldsymbol{u}_h, q_h\right) + \alpha_u\left(P_u^{\perp}\left[\nabla p_h\right], P_u^{\perp}\left[\nabla q_h\right]\right) = 0, \tag{7.32}$$
$$\left(\frac{1}{2\mu}\boldsymbol{\sigma}_h - \left(1-\beta\right)\nabla^s\boldsymbol{u}_h, \boldsymbol{\tau}_h\right) + \frac{\lambda}{2\mu}\left(\frac{\partial\boldsymbol{\sigma}_h}{\partial t}, \boldsymbol{\tau}_h\right) + \frac{\lambda}{2\mu}\tilde{c}\left(\hat{\boldsymbol{u}}_h, \boldsymbol{\sigma}_h, \boldsymbol{\tau}_h\right) \tag{7.33}$$
$$-\frac{\lambda}{2\mu}\left(g\left(\hat{\boldsymbol{u}}_h, \hat{\boldsymbol{\sigma}}_h\right), \boldsymbol{\tau}_h\right) + \left(1-\beta\right)\alpha_u\left(P_u^{\perp}\left[\nabla\cdot\boldsymbol{\sigma}_h\right], P_u^{\perp}\left[\nabla\cdot\boldsymbol{\tau}_h\right]\right)$$
$$+\alpha_\sigma\left(P_\sigma^{\perp}\left[-\left(1-\beta\right)\nabla^s\boldsymbol{u}_h + \frac{\lambda}{2\mu}\left(\hat{\boldsymbol{u}}_h\cdot\nabla\boldsymbol{\sigma}_h - g\left(\hat{\boldsymbol{u}}_h, \hat{\boldsymbol{\sigma}}_h\right)\right)\right],$$
$$P_\sigma^{\perp}\left[\frac{\lambda}{2\mu}\left(\hat{\boldsymbol{u}}_h\cdot\nabla\boldsymbol{\tau}_h + g^*\left(\hat{\boldsymbol{u}}_h, \boldsymbol{\tau}_h\right)\right)\right]\right) = 0,$$

for all $\boldsymbol{V}_h = (\boldsymbol{v}_h, q_h, \boldsymbol{\tau}_h) \in \boldsymbol{\mathcal{X}}_h$. The initial conditions are set as appropriate projections of $\boldsymbol{u}_0$ and $\boldsymbol{\sigma}_0$.

7.6.2 Existence and uniqueness of the semi-discrete solution

The following existence and uniqueness analysis of the discrete solution was motivated by the procedure followed by Burman and Fernández in [32] for the two-field Navier-Stokes problem.

To prove existence and uniqueness of the discrete linearized problem (7.31)-(7.33), we shall make use of the following pressure and velocity subspaces:

$$Q_h^{\star} = \left\{q_h \in Q_h : \left(P_u^{\perp}\left[\nabla q_h\right], P_u^{\perp}\left[\nabla q_h\right]\right) = 0\right\},$$
$$\boldsymbol{\mathcal{V}}_h^{div} = \left\{\boldsymbol{v}_h \in \boldsymbol{\mathcal{V}}_h : \left(q_h, \nabla\cdot\boldsymbol{v}_h\right) = 0,\ \forall q_h \in Q_h^{\star}\right\}.$$

In addition, $Q_h \backslash Q_h^{\star}$ will stand for the supplementary of $Q_h^{\star}$ in Q_h, i.e., $Q_h = (Q_h \backslash Q_h^{\star}) \oplus Q_h^{\star}$.

To ensure that $\boldsymbol{\mathcal{V}}_h^{div}$ is not trivial, we use the following lemma.

Lemma 1 *There exists a constant $\gamma > 0$, independent of h, such that*

$$\inf_{q_h \in \mathcal{Q}_h^{\star}} \sup_{\boldsymbol{v}_h \in \boldsymbol{\mathcal{V}}_h} \frac{\left(q_h, \nabla\cdot\boldsymbol{v}_h\right)}{\left\|\boldsymbol{v}_h\right\|_{\boldsymbol{\mathcal{V}}_h}\left\|q_h\right\|_{\mathcal{Q}_h^{\star}}} \geq \gamma.$$

Proof. Let $q_h \in Q_h^{\star}$. From inf-sup theory (see for example [87]), there exists $\boldsymbol{v}_q \in H_0^1$ such that

$$\nabla\cdot\boldsymbol{v}_q = q_h,\ \left\|\boldsymbol{v}_q\right\|_1 \leq c\left\|q_h\right\|.$$

Integrating by parts, we have

$$\begin{aligned}\left\|q_h\right\|^2 &= \left(q_h, \nabla\cdot\boldsymbol{v}_p\right)\\ &= -\left(\nabla q_h, \boldsymbol{v}_p - P_u\left[\boldsymbol{v}_p\right]\right) + \left(q_h, \nabla\cdot P_u\left[\boldsymbol{v}_p\right]\right)\\ &= \left(q_h, \nabla\cdot P_u\left[\boldsymbol{v}_p\right]\right),\end{aligned}$$

since, as $q_h \in \mathcal{Q}_h^\star$, then $\nabla q_h \in \boldsymbol{\mathcal{V}}_h$. In addition, we have

$$\|\nabla \cdot P_u[\boldsymbol{v}_p]\|^2 \leq d\,\|P_u[\boldsymbol{v}_p]\|_1^2 \leq c\,\|\nabla \boldsymbol{v}_p\|_1^2 \leq c\,\|q_h\|^2,$$

which completes the proof. □

Theorem 2 *The semi discrete problem (7.31)-(7.33) has a unique solution*

Proof. Problem (7.31)-(7.33), satisfying the initial and boundary conditions, can be written in operator form, as

$$M_u \partial_t \boldsymbol{u}_h + K_u(\hat{\boldsymbol{u}}_h)\,\boldsymbol{u}_h + G p_h - D_\sigma \boldsymbol{\sigma}_h = M_u \boldsymbol{f} \text{ in } \boldsymbol{\mathcal{V}}_h, \tag{7.34}$$

$$D\boldsymbol{u}_h = S_{1,p}^{\perp} p_h \text{ in } Q_h, \tag{7.35}$$

$$M_\sigma \partial_t \boldsymbol{\sigma}_h + K_\sigma(\hat{\boldsymbol{u}}_h, \hat{\boldsymbol{\sigma}}_h)\,\boldsymbol{\sigma}_h - S\boldsymbol{u}_h = 0 \text{ in } \boldsymbol{\Upsilon}_h, \tag{7.36}$$

where

$$\begin{aligned}
M_u \partial_t \boldsymbol{u}_h =& \rho\left(\frac{\partial \boldsymbol{u}_h}{\partial t}, \boldsymbol{v}_h\right),\\
K_u(\hat{\boldsymbol{u}}_h)\,\boldsymbol{u}_h =& \rho\tilde{c}(\hat{\boldsymbol{u}}_h, \boldsymbol{u}_h, \boldsymbol{v}_h) + 2\beta\mu(\nabla^s \boldsymbol{u}_h \nabla^s \boldsymbol{v}_h) + \alpha_u\left(P_u^{\perp}[\rho\hat{\boldsymbol{u}}_h \cdot \nabla \boldsymbol{u}_h], P_u^{\perp}[\rho\hat{\boldsymbol{u}}_h \cdot \nabla \boldsymbol{v}_h]\right)\\
&+ \alpha_p\left(P_p^{\perp}[\nabla \cdot \boldsymbol{u}_h], P_p^{\perp}[\nabla \cdot \boldsymbol{v}_h]\right)\\
&+ (1-\beta)\,\alpha_\sigma\left(P_\sigma^{\perp}\left[(1-\beta)\nabla^s \boldsymbol{u}_h - \frac{\lambda}{2\mu}(\hat{\boldsymbol{u}}_h \cdot \nabla \boldsymbol{\sigma}_h - g(\hat{\boldsymbol{u}}_h, \boldsymbol{\sigma}_h))\right], P_\sigma^{\perp}[\nabla^s \boldsymbol{v}_h]\right),\\
G p_h =& -(p_h, \nabla \cdot \boldsymbol{v}_h),\\
D_\sigma \boldsymbol{\sigma}_h =& (\boldsymbol{\sigma}_h, \nabla^s \boldsymbol{v}_h),\\
D\boldsymbol{u}_h =& (\nabla \cdot \boldsymbol{u}_h, q_h),\\
S_{1,p}^{\perp} p_h =& -\alpha_u\left(P_u^{\perp}[\nabla q_h], P_u^{\perp}[\nabla q_h]\right),\\
M_\sigma \partial_t \boldsymbol{\sigma}_h =& \frac{\lambda}{2\mu}\left(\frac{\partial \boldsymbol{\sigma}_h}{\partial t}, \boldsymbol{\tau}_h\right),\\
K_\sigma(\hat{\boldsymbol{u}}_h, \hat{\boldsymbol{\sigma}}_h)\,\boldsymbol{\sigma}_h =& \frac{1}{2\mu}(\boldsymbol{\sigma}_h, \boldsymbol{\tau}_h) + \frac{\lambda}{2\mu}\tilde{c}(\hat{\boldsymbol{u}}_h, \boldsymbol{\sigma}_h, \boldsymbol{\tau}_h) + (1-\beta)\,\alpha_u\left(P_u^{\perp}[\nabla \cdot \boldsymbol{\sigma}_h], P_u^{\perp}[\nabla \cdot \boldsymbol{\tau}_h]\right)\\
&+ \alpha_\sigma\left(P_\sigma^{\perp}\left[-(1-\beta)\nabla^s \boldsymbol{u}_h + \frac{\lambda}{2\mu}(\hat{\boldsymbol{u}}_h \cdot \nabla \boldsymbol{\sigma}_h - g(\hat{\boldsymbol{u}}_h, \hat{\boldsymbol{\sigma}}_h))\right],\right.\\
&\left. P_\sigma^{\perp}\left[\frac{\lambda}{2\mu}(\hat{\boldsymbol{u}}_h \cdot \nabla \boldsymbol{\tau}_h + g^*(\hat{\boldsymbol{u}}_h, \boldsymbol{\tau}_h))\right]\right),\\
S\boldsymbol{u}_h =& -(1-\beta)(\nabla^s \boldsymbol{u}_h, \boldsymbol{\tau}_h).
\end{aligned}$$

We also introduce the operator D^1, defined by

$$D^1 \boldsymbol{v}_h = (D\boldsymbol{v}_h)_{Q_h^\star}, \quad \forall \boldsymbol{v}_h \in \boldsymbol{\mathcal{V}}_h.$$

From Lemma 1, it follows that D^1 is surjective and $\left(D^1\right)^T$ is injective, and therefore, $\boldsymbol{\mathcal{V}}_h^{div} := \ker\left(D^1\right) \neq \{0\}$.

Let us consider the following reduced formulation, derived from (7.31)-(7.33) with $\boldsymbol{V}_h \in \boldsymbol{\mathcal{X}}_h^\star = \boldsymbol{\mathcal{V}}_h^{div} \times (Q_h \backslash Q_h^\star) \times \boldsymbol{\Upsilon}_h$: find $\boldsymbol{U}_h :]0, T[\to \boldsymbol{\mathcal{X}}_h^\star$ such that

$$M_u \partial_t \boldsymbol{u}_h + K_u(\hat{\boldsymbol{u}}_h)\,\boldsymbol{u}_h + G\tilde{p}_h - D_\sigma \boldsymbol{\sigma}_h = M_u \boldsymbol{f} \text{ in } \boldsymbol{\mathcal{V}}_h^{div}, \tag{7.37}$$

$$D\boldsymbol{u}_h = S_{1,p}^{\perp}\tilde{p}_h \text{ in } (Q_h \backslash Q_h^\star), \tag{7.38}$$

$$M_\sigma \partial_t \boldsymbol{\sigma}_h + K_\sigma(\hat{\boldsymbol{u}}_h, \hat{\boldsymbol{\sigma}}_h)\,\boldsymbol{\sigma}_h - S\boldsymbol{u}_h = 0 \text{ in } \boldsymbol{\Upsilon}_h. \tag{7.39}$$

Since, by construction, $Q_h^\star = \mathrm{Ker}\left(S_{1,p}^\perp\right)$, we conclude that $S_{1,p}^\perp$ is invertible in $Q_h \backslash Q_h^\star$, and therefore, from (7.38) we obtain

$$\tilde{p}_h = \left(S_{1,p}^\perp\right)_{Q_h \backslash Q_h^\star}^{-1} D\boldsymbol{u}_h$$

By plugging this expression into (7.37), we obtain the following equivalent problem

$$M_u \partial_t \boldsymbol{u}_h + K_u\left(\hat{\boldsymbol{u}}_h\right)\boldsymbol{u}_h + G\left(S_{1,p}^\perp\right)_{Q_h \backslash Q_h^\star}^{-1} D\boldsymbol{u}_h - D_\sigma \boldsymbol{\sigma}_h = M_u \boldsymbol{f} \ \text{ in } \boldsymbol{\mathcal{V}}_h^{div}, \tag{7.40}$$

$$M_\sigma \partial_t \boldsymbol{\sigma}_h + K_\sigma\left(\hat{\boldsymbol{u}}_h, \hat{\boldsymbol{\sigma}}_h\right)\boldsymbol{\sigma}_h - S\boldsymbol{u}_h = 0 \ \text{ in } \boldsymbol{\Upsilon}_h, \tag{7.41}$$

which is a standard Cauchy problem for $\boldsymbol{u}_h$ and $\boldsymbol{\sigma}_h$. Existence and uniqueness for $\boldsymbol{u}_h$ and $\boldsymbol{\sigma}_h$ follows by the Lipschitz continuity of $K_u\left(\hat{\boldsymbol{u}}_h\right)$ and $K_\sigma\left(\hat{\boldsymbol{u}}_h, \hat{\boldsymbol{\sigma}}_h\right)$. We may then recover $\tilde{p}_h$ uniquely from (7.38). Therefore, the reduced problem (7.37)-(7.39) has a unique solution. On the other hand, from (7.37), it follows that

$$M_u \partial_t \boldsymbol{u}_h + K_u\left(\hat{\boldsymbol{u}}_h\right)\boldsymbol{u}_h + G\tilde{p}_h - D_\sigma \boldsymbol{\sigma}_h - M_u \boldsymbol{f} \in \left(\mathrm{Ker}\left(D^1\right)\right)^0,$$

with $\left(\mathrm{Ker}\left(D^1\right)\right)^0$ standing for the polar set of $\mathrm{Ker}\left(D^1\right)$. From Lemma 1, it follows that D^1 is an isomorphism from $Q_h^\star$ onto $\left(\mathrm{Ker}\left(D^1\right)\right)^0$. Thus, there exists a unique $p^1 \in Q_h^\star$ such that

$$M_u \partial_t \boldsymbol{u}_h + K_u\left(\hat{\boldsymbol{u}}_h\right)\boldsymbol{u}_h + G\tilde{p}_h - D_\sigma \boldsymbol{\sigma}_h - M_u \boldsymbol{f} = Gp^1 \ \text{ in } \boldsymbol{\mathcal{V}}_h. \tag{7.42}$$

Therefore, from (7.42) and the reduced problem (7.37)-(7.39), it follows that the discrete problem (7.31)-(7.33) has a unique solution, given by $\left(\boldsymbol{u}_h, \tilde{p}_h - p^1, \boldsymbol{\sigma}_h\right)$. □

7.6.3 Stability of the linearized semi-discrete problem

We will use the following norm in the subsequent analysis:

$$\begin{aligned}
\|\boldsymbol{V}_h\|_W^2 =& 2\beta\mu\left(1-\beta\right)\left\|\nabla^s \boldsymbol{v}_h\right\|^2 + \frac{1}{2\mu}\left\|\boldsymbol{\tau}_h\right\|^2 + \left(1-\beta\right)\alpha_u\left\|P_u^\perp\left[\rho\hat{\boldsymbol{u}}_h \cdot \nabla \boldsymbol{v}_h\right]\right\|^2 \\
&+ \left(1-\beta\right)\alpha_u\left\|\rho\frac{\partial \boldsymbol{v}_h}{\partial t} + \rho\hat{\boldsymbol{u}}_h \cdot \nabla \boldsymbol{v}_h + \nabla q_h - \nabla \cdot \boldsymbol{\tau}_h\right\|^2 \\
&+ \left(1-\beta\right)\alpha_p\left\|\nabla \cdot \boldsymbol{v}_h\right\|^2 + \left(1-\beta\right)\alpha_u\left\|P_u^\perp\left[\nabla q_h\right]\right\|^2 + \left(1-\beta\right)\alpha_u\left\|P_u^\perp\left[\nabla \cdot \boldsymbol{\tau}_h\right]\right\|^2 \\
&+ \alpha_\sigma\left\|\frac{\lambda}{2\mu}\frac{\partial \boldsymbol{\tau}_h}{\partial t} - \left(1-\beta\right)\nabla^s \boldsymbol{v}_h + \frac{\lambda}{2\mu}\hat{\boldsymbol{u}}_h \cdot \nabla \boldsymbol{\tau}_h\right\|^2.
\end{aligned} \tag{7.43}$$

Remark 1. The term multiplied by α_p is strictly unnecessary, since it already is contained in $\|\nabla^s \boldsymbol{v}_h\|$,but sometimes could reinforce this stability. We will keep it for generality, to see the effect of the subscale associated to the pressure.

The next result stats the stability of the proposed semi-discrete formulation defined in (7.31)-(7.33).

Theorem 3 *Let $\left(\boldsymbol{u}_h, p_h, \boldsymbol{\sigma}_h\right)$ be the solution of (7.31)-(7.33). Then, the following stability holds, for all $t \in [0,T]$*

$$\left(1-\beta\right)\frac{\rho}{2}\left\|\boldsymbol{u}_h\left(t\right)\right\|^2 + \frac{\lambda}{4\mu}\left\|\boldsymbol{\sigma}_h\left(t\right)\right\|^2 + \int_0^t \|\boldsymbol{V}_h\|_W^2 \lesssim$$

$$\frac{c_\Omega^2}{2\mu}\int_0^t \|\boldsymbol{f}\|_{H^{-1}}^2 + \frac{\lambda^2}{2\mu}\int_0^t \left\|g\left(\hat{\boldsymbol{u}}_h, \hat{\boldsymbol{\sigma}}_h\right)\right\|^2 + \left(1-\beta\right)\frac{\rho}{2}\left\|\boldsymbol{u}_h\right\|^2\left(0\right) + \frac{\lambda}{4\mu}\left\|\boldsymbol{\sigma}_h\right\|^2\left(0\right).$$

Proof. In this proof $\varepsilon_1, \varepsilon_2, ...$ are positive constants used in the application of Young inequalities. The values will be chosen at the end of the proof.

Taking $(\boldsymbol{v}_h, q_h, \boldsymbol{\tau}_h) = \boldsymbol{U}_{h1} = ((1-\beta)\,\boldsymbol{u}_h, (1-\beta)\,p_h, \boldsymbol{\sigma}_h)$ in (7.31)-(7.33) and adding, we can write

$$
\begin{aligned}
&\left(\rho\frac{\partial \boldsymbol{u}_h}{\partial t}, (1-\beta)\,\boldsymbol{u}_h\right) - (1-\beta)\,(p_h, \nabla\cdot\boldsymbol{u}_h) + (1-\beta)\,(2\beta\mu\nabla^s\boldsymbol{u}_h + \boldsymbol{\sigma}_h, \nabla^s\boldsymbol{u}_h)\\
&\quad +\rho\,(1-\beta)\,\tilde{c}\,(\hat{\boldsymbol{u}}_h, \boldsymbol{u}_h, \boldsymbol{u}_h) + (1-\beta)\,\alpha_u\left(P_u^{\perp}\left[\rho\hat{\boldsymbol{u}}_h\cdot\nabla\boldsymbol{u}_h\right], P_u^{\perp}\left[\rho\hat{\boldsymbol{u}}_h\cdot\nabla\boldsymbol{u}_h\right]\right)\\
&+(1-\beta)\,\alpha_p\left(P_p^{\perp}\left[\nabla\cdot\boldsymbol{u}_h\right], P_p^{\perp}\left[\nabla\cdot\boldsymbol{u}_h\right]\right) + (1-\beta)\,\alpha_u\left(P_u^{\perp}\left[\nabla p_h\right], P_u^{\perp}\left[\nabla p_h\right]\right)\\
&\quad +\left(\frac{1}{2\mu}\boldsymbol{\sigma}_h - (1-\beta)\,\nabla^s\boldsymbol{u}_h, \boldsymbol{\sigma}_h\right) + \frac{\lambda}{2\mu}\left(\frac{\partial\boldsymbol{\sigma}_h}{\partial t}, \boldsymbol{\sigma}_h\right) + \frac{\lambda}{2\mu}\tilde{c}\,(\hat{\boldsymbol{u}}_h, \boldsymbol{\sigma}_h, \boldsymbol{\sigma}_h)\\
&\quad +(1-\beta)\,\alpha_u\left(P_u^{\perp}\left[\nabla\cdot\boldsymbol{\sigma}_h\right], P_u^{\perp}\left[\nabla\cdot\boldsymbol{\sigma}_h\right]\right) + (1-\beta)\,(\nabla\cdot\boldsymbol{u}_h, p_h)\\
&\quad +\alpha_\sigma\left(P_\sigma^{\perp}\left[\frac{\lambda}{2\mu}\frac{\partial\boldsymbol{\sigma}_h}{\partial t} - (1-\beta)\,\nabla^s\boldsymbol{u}_h + \frac{\lambda}{2\mu}\left(\hat{\boldsymbol{u}}_h\cdot\nabla\boldsymbol{\sigma}_h - g\,(\hat{\boldsymbol{u}}_h, \hat{\boldsymbol{\sigma}}_h)\right)\right],\right.\\
&\qquad \left.P_\sigma^{\perp}\left[\frac{\lambda}{2\mu}\frac{\partial\boldsymbol{\sigma}_h}{\partial t} - (1-\beta)\,\nabla^s\boldsymbol{u}_h + \frac{\lambda}{2\mu}\left(\hat{\boldsymbol{u}}_h\cdot\nabla\boldsymbol{\sigma}_h + g^*\,(\hat{\boldsymbol{u}}_h, \boldsymbol{\sigma}_h)\right)\right]\right) = (1-\beta)\,\langle\boldsymbol{f}, \boldsymbol{u}_h\rangle\\
&\qquad\qquad + \frac{\lambda}{2\mu}\,(g\,(\hat{\boldsymbol{u}}_h, \hat{\boldsymbol{\sigma}}_h), \boldsymbol{\sigma}_h)\,.
\end{aligned}
$$

We have also includes in the result above the term $P_\sigma^{\perp}\left[\frac{\lambda}{2\mu}\frac{\partial\boldsymbol{\sigma}_h}{\partial t}\right]$ (which is zero). Next using Cauchy-Schwarz and Young inequalities we arrive at

$$
\begin{aligned}
&(1-\beta)\,\frac{\rho}{2}\frac{d}{dt}\left\|\boldsymbol{u}_h\right\|^2 + 2\mu\beta\,(1-\beta)\left\|\nabla^s\boldsymbol{u}_h\right\|^2 + \frac{\lambda}{4\mu}\frac{d}{dt}\left\|\boldsymbol{\sigma}_h\right\|^2 \qquad (7.44)\\
&+(1-\beta)\,\alpha_p\left\|P_p^{\perp}\left[\nabla\cdot\boldsymbol{u}_h\right]\right\|^2 + (1-\beta)\,\alpha_u\left\|P_u^{\perp}\left[\nabla\cdot\boldsymbol{\sigma}_h\right]\right\|^2\\
&+\frac{1}{2\mu}\left(1 - \frac{\varepsilon_1}{2} - 4\frac{\alpha_\sigma}{2\mu}\lambda^2\left\|\nabla\hat{\boldsymbol{u}}_h\right\|_\infty^2\left(\frac{1}{2\varepsilon_2} + \frac{1}{2\varepsilon_4}\right)\right)\left\|\boldsymbol{\sigma}_h\right\|^2\\
&+(1-\beta)\,\alpha_u\left\|P_u^{\perp}\left[\rho\hat{\boldsymbol{u}}_h\cdot\nabla\boldsymbol{u}_h\right]\right\|^2 + (1-\beta)\,\alpha_u\left\|P_u^{\perp}\left[\nabla p_h\right]\right\|^2\\
&+\alpha_\sigma\left(1 - \frac{\varepsilon_2}{2} - \frac{\varepsilon_3}{2}\right)\left\|P_\sigma^{\perp}\left[-(1-\beta)\,\nabla^s\boldsymbol{u}_h + \frac{\lambda}{2\mu}\left(\frac{\partial\boldsymbol{\sigma}_h}{\partial t} + \hat{\boldsymbol{u}}_h\cdot\nabla\boldsymbol{\sigma}_h\right)\right]\right\|^2\\
&\leq (1-\beta)\,\langle\boldsymbol{f}, \boldsymbol{u}_h\rangle + \frac{\lambda^2}{4\mu}\left[\frac{1}{\varepsilon_1}\left\|g\,(\hat{\boldsymbol{u}}_h, \hat{\boldsymbol{\sigma}}_h)\right\|^2 + \frac{\alpha_\sigma}{\mu}\left(\frac{1}{2\varepsilon_3} + \frac{\varepsilon_4}{2}\right)\left\|P_\sigma^{\perp}\left[g\,(\hat{\boldsymbol{u}}_h, \hat{\boldsymbol{\sigma}}_h)\right]\right\|^2\right].
\end{aligned}
$$

If we compare the bounded terms of the expression (7.44) with the terms of the working norm (7.43), we can see that the missing terms are all of them associated to the finite element space. The key point is that this missing control comes from the Galerkin part of the multilinear form B_{stab} in Eq. (7.24).

Let us take $\boldsymbol{V}_{h1} = (\boldsymbol{v}_h, q_h, \boldsymbol{\tau}_h) = \alpha_u\,((1-\beta)\,\boldsymbol{v}_1, 0, \boldsymbol{0})$ with

$$
\boldsymbol{v}_1 \equiv P_u\left[\rho\frac{\partial\boldsymbol{u}_h}{\partial t} + \rho\hat{\boldsymbol{u}}_h\cdot\nabla\boldsymbol{u}_h + \nabla p_h - \nabla\cdot\boldsymbol{\sigma}_h\right].
$$

Then in the same way than in the $\boldsymbol{U}_{h1}$ case, we can write

$$
\begin{aligned}
&(1-\beta)\,\alpha_u\left(\rho\frac{\partial\boldsymbol{u}_h}{\partial t}, \boldsymbol{v}_1\right) + (1-\beta)\,\alpha_u\rho\tilde{c}\,(\hat{\boldsymbol{u}}_h, \boldsymbol{u}_h, \boldsymbol{v}_1)\\
&+(1-\beta)\,\alpha_u\,(2\beta\mu\nabla^s\boldsymbol{u}_h + \boldsymbol{\sigma}_h, \nabla^s\boldsymbol{v}_1) - (1-\beta)\,\alpha_u\,(p_h, \nabla\cdot\boldsymbol{v}_1)\\
&\quad +(1-\beta)\,\alpha_u^2\left(P_u^{\perp}\left[\rho\hat{\boldsymbol{u}}_h\cdot\nabla\boldsymbol{u}_h\right], P_u^{\perp}\left[\rho\hat{\boldsymbol{u}}_h\cdot\nabla\boldsymbol{v}_1\right]\right)
\end{aligned}
$$

$$
\begin{aligned}
&+(1-\beta)\,\alpha_u\alpha_p\left(P_p^{\perp}\left[\nabla\cdot\boldsymbol{u}_h\right],P_p^{\perp}\left[\nabla\cdot\boldsymbol{v}_1\right]\right)\\
+\alpha_u\alpha_\sigma\Bigg(&P_\sigma^{\perp}\left[-\frac{\lambda}{2\mu}\frac{\partial\boldsymbol{\sigma}_h}{\partial t}+(1-\beta)\,\nabla^s\boldsymbol{u}_h-\frac{\lambda}{2\mu}\left(\hat{\boldsymbol{u}}_h\cdot\nabla\boldsymbol{\sigma}_h+g\left(\hat{\boldsymbol{u}}_h,\hat{\boldsymbol{\sigma}}_h\right)\right)\right],\\
&P_\sigma^{\perp}\left[(1-\beta)\,\nabla^s\boldsymbol{v}_1\right]\Bigg)=(1-\beta)\,\alpha_u\left\langle\boldsymbol{f},\boldsymbol{v}_1\right\rangle,
\end{aligned}
$$

integrating by parts the terms arising from the divergence of the total stress and the gradient of the pressure, and using the fact that $\hat{\boldsymbol{u}}_h=\boldsymbol{0}$ on $\partial\Omega$, we can write

$$
\begin{aligned}
&-2\beta\mu\,(1-\beta)\,\alpha_u\left(\nabla^s\boldsymbol{u}_h,\nabla^s\boldsymbol{v}_1\right)\\
&+(1-\beta)\,\alpha_u\left(\rho\frac{\partial\boldsymbol{u}_h}{\partial t}+\rho\hat{\boldsymbol{u}}_h\cdot\nabla\boldsymbol{u}_h+\nabla p_h-\nabla\cdot\boldsymbol{\sigma}_h,\boldsymbol{v}_1\right)\\
&+(1-\beta)\,\alpha_u^2\left(P_u^{\perp}\left[\rho\hat{\boldsymbol{u}}_h\cdot\nabla\boldsymbol{u}_h\right],P_u^{\perp}\left[\rho\hat{\boldsymbol{u}}_h\cdot\nabla\boldsymbol{v}_1\right]\right)\\
&+(1-\beta)\,\alpha_u\alpha_p\left(P_p^{\perp}\left[\nabla\cdot\boldsymbol{u}_h\right],P_p^{\perp}\left[\nabla\cdot\boldsymbol{v}_1\right]\right)\\
+\alpha_u\alpha_\sigma\Bigg(&P_\sigma^{\perp}\left[-\frac{\lambda}{2\mu}\frac{\partial\boldsymbol{\sigma}_h}{\partial t}+(1-\beta)\,\nabla^s\boldsymbol{u}_h-\frac{\lambda}{2\mu}\hat{\boldsymbol{u}}_h\cdot\nabla\boldsymbol{\sigma}_h\right],P_\sigma^{\perp}\left[(1-\beta)\,\nabla^s\boldsymbol{v}_1\right]\Bigg)\\
&-\alpha_u\alpha_\sigma\left(P_\sigma^{\perp}\left[\frac{\lambda}{2\mu}g\left(\hat{\boldsymbol{u}}_h,\hat{\boldsymbol{\sigma}}_h\right)\right],P_\sigma^{\perp}\left[(1-\beta)\,\nabla^s\boldsymbol{v}_1\right]\right)\\
&-(1-\beta)\,\frac{1}{2}\alpha_u\rho\left\|\nabla\cdot\hat{\boldsymbol{u}}_h\right\|_\infty\left\|\boldsymbol{v}_1\right\|\left\|\boldsymbol{u}_h\right\|=(1-\beta)\,\alpha_u\left\langle\boldsymbol{f},\boldsymbol{v}_1\right\rangle,
\end{aligned}
$$

applying Cauchy-Schwarz, the Young inequalities and inverse inequalities in all the products above, we obtain the following result

$$
\begin{aligned}
&+(1-\beta)\,\alpha_u\left(1-\alpha_u c_{\mathrm{inv}}^2\left[\frac{\alpha_p}{h^2}\frac{\varepsilon_6}{2}+\frac{\rho\left\|\hat{\boldsymbol{u}}_h\right\|_\infty}{h}\frac{\varepsilon_7}{2}+\frac{\alpha_\sigma}{h^2}\left(\frac{\varepsilon_8}{2}+\frac{\varepsilon_9}{2}\right)\right]\right.\\
&\left.-\beta\alpha_u\frac{2\mu}{h^2}c_{inv}^2\frac{\varepsilon_5}{2}-\alpha_u\frac{d}{4\varepsilon_{10}}\frac{c_\Omega^2}{2\mu}\rho^2\left\|\nabla\hat{\boldsymbol{u}}_h\right\|_\infty^2\right)\left\|\boldsymbol{v}_1\right\|^2\\
&-2\mu\,(1-\beta)\left(\beta\frac{1}{2\varepsilon_5}+\frac{\varepsilon_{10}}{2}\right)\left\|\nabla^s\boldsymbol{u}_h\right\|^2-(1-\beta)\,\alpha_p\frac{1}{2\varepsilon_6}\left\|P_p^{\perp}\left[\nabla\cdot\boldsymbol{u}_h\right]\right\|^2\\
&-(1-\beta)\,\alpha_u^2\frac{\rho\left\|\hat{\boldsymbol{u}}_h\right\|_\infty}{h}\frac{1}{2\varepsilon_7}\left\|P_u^{\perp}\left[\rho\hat{\boldsymbol{u}}_h\cdot\nabla\boldsymbol{u}_h\right]\right\|^2\\
&-(1-\beta)\,\alpha_\sigma\frac{1}{2\varepsilon_8}\left\|P_\sigma^{\perp}\left[\frac{\lambda}{2\mu}\frac{\partial\boldsymbol{\sigma}_h}{\partial t}-(1-\beta)\,\nabla^s\boldsymbol{u}_h+\frac{\lambda}{2\mu}\hat{\boldsymbol{u}}_h\cdot\nabla\boldsymbol{\sigma}_h\right]\right\|^2\\
&\leq(1-\beta)\,\alpha_u\left\langle\boldsymbol{f},\boldsymbol{v}_1\right\rangle+\frac{(1-\beta)}{2\varepsilon_9}\frac{\lambda^2}{2\mu}\frac{\alpha_\sigma}{2\mu}\left\|P_\sigma^{\perp}\left[g\left(\hat{\boldsymbol{u}}_h,\hat{\boldsymbol{\sigma}}_h\right)\right]\right\|^2.
\end{aligned}
\tag{7.45}
$$

To obtain the control of $P_p\left[\nabla\cdot\boldsymbol{u}_h\right]$, we proceed taking $\boldsymbol{V}_{h2}=(1-\beta)\,\alpha_p\left(\boldsymbol{0},q_2,\boldsymbol{0}\right)$ with $q_2\equiv P_p\left[\nabla\cdot\boldsymbol{u}_h\right]$.

$$
\begin{aligned}
(1-\beta)\,\alpha_p\left(\left(\nabla\cdot\boldsymbol{u}_h,q_2\right)+\alpha_u\left(P_u^{\perp}\left[\nabla p_h\right],\nabla q_2\right)\right)\geq&(1-\beta)\,\alpha_p\left(1-c_{\mathrm{inv}}^2\alpha_u\frac{\alpha_p}{h^2}\frac{\varepsilon_{11}}{2}\right)\left\|P_p\left[\nabla\cdot\boldsymbol{u}_h\right]\right\|^2\\
&-(1-\beta)\,\alpha_u\frac{1}{2\varepsilon_{11}}\left\|P_u^{\perp}\left[\nabla p_h\right]\right\|^2.
\end{aligned}
\tag{7.46}
$$

Finally, taking: $\boldsymbol{V}_{h3}=\alpha_\sigma\left(\boldsymbol{0},0,\boldsymbol{\sigma}_3\right)$ with $\boldsymbol{\sigma}_3\equiv P_\sigma\left[\frac{\lambda}{2\mu}\frac{\partial\boldsymbol{\sigma}_h}{\partial t}-(1-\beta)\,\nabla^s\boldsymbol{u}_h+\frac{\lambda}{2\mu}\hat{\boldsymbol{u}}_h\cdot\nabla\boldsymbol{\sigma}_h\right]$, we obtain

$$
\frac{1}{2\mu}\alpha_\sigma\left(\boldsymbol{\sigma}_h,\boldsymbol{\sigma}_3\right)+\frac{1}{2}\frac{\lambda}{2\mu}\alpha_\sigma\left(\nabla\cdot\hat{\boldsymbol{u}}_h\boldsymbol{\sigma}_h,\boldsymbol{\sigma}_3\right)
$$

$$
\begin{aligned}
&+\alpha_\sigma\left(\frac{\lambda}{2\mu}\frac{\partial\boldsymbol{\sigma}_h}{\partial t}-(1-\beta)\nabla^s\boldsymbol{u}_h+\frac{\lambda}{2\mu}\hat{\boldsymbol{u}}_h\cdot\nabla\boldsymbol{\sigma}_h,\boldsymbol{\sigma}_3\right)\\
&-\alpha_\sigma\left(\frac{\lambda}{2\mu}g\left(\hat{\boldsymbol{u}}_h,\hat{\boldsymbol{\sigma}}_h\right),\boldsymbol{\sigma}_3\right)+\alpha_u\alpha_\sigma\left(P_u^\perp\left[\nabla\cdot\boldsymbol{\sigma}_h\right],P_u^\perp\left[(1-\beta)\nabla\cdot\boldsymbol{\sigma}_3\right]\right)\\
&+\alpha_\sigma^2\left(P_\sigma^\perp\left[-(1-\beta)\nabla^s\boldsymbol{u}_h+\frac{\lambda}{2\mu}\left(\hat{\boldsymbol{u}}_h\cdot\nabla\boldsymbol{\sigma}_h-g\left(\hat{\boldsymbol{u}}_h,\hat{\boldsymbol{\sigma}}_h\right)\right)\right],\right.\\
&\left.P_\sigma^\perp\left[\frac{\lambda}{2\mu}\left(\hat{\boldsymbol{u}}_h\cdot\nabla\boldsymbol{\sigma}_3+g^*\left(\hat{\boldsymbol{u}}_h,\boldsymbol{\sigma}_3\right)\right)\right]\right)=0,
\end{aligned}
$$

$$
\begin{aligned}
&-\frac{1}{2\mu}\left(\frac{1}{2\varepsilon_{12}}+\frac{1}{2}\frac{1}{2\varepsilon_{17}}\right)\left\|\boldsymbol{\sigma}_h\right\|^2-\frac{(1-\beta)}{2\varepsilon_{14}}\alpha_u\left\|P_u^\perp\left[\nabla\cdot\boldsymbol{\sigma}_h\right]\right\|^2\\
&+\alpha_\sigma\left(1-\frac{\alpha_\sigma}{2\mu}\frac{\varepsilon_{12}}{2}-\frac{\varepsilon_{13}}{2}-\frac{\varepsilon_{17}}{4}\frac{\alpha_\sigma}{2\mu}d\left(\lambda\left\|\nabla\hat{\boldsymbol{u}}_h\right\|_\infty\right)^2-c_{inv}^2(1-\beta)\alpha_u\frac{\alpha_\sigma}{h^2}\frac{\varepsilon_{14}}{2}\right.\\
&\left.-c_{inv}^2 2\alpha_\sigma^2\left[\left(\frac{\lambda\left\|\hat{\boldsymbol{u}}_h\right\|_\infty}{2\mu h}\right)^2+4\left(\frac{\lambda\left\|\nabla\hat{\boldsymbol{u}}_h\right\|_\infty}{2\mu}\right)^2\right]\left(\frac{1}{2\varepsilon_{15}}+\frac{1}{2\varepsilon_{16}}\right)\right)\left\|\boldsymbol{\sigma}_3\right\|^2\\
&-\alpha_\sigma\frac{\varepsilon_{15}}{2}\left\|P_\sigma^\perp\left[\frac{\lambda}{2\mu}\frac{\partial\boldsymbol{\sigma}_h}{\partial t}-(1-\beta)\nabla^s\boldsymbol{u}_h+\frac{\lambda}{2\mu}\left(\hat{\boldsymbol{u}}_h\cdot\nabla\boldsymbol{\sigma}_h\right)\right]\right\|^2\\
\leq&\frac{\lambda^2}{4\mu}\frac{\alpha_\sigma}{\mu}\left(\frac{1}{2\varepsilon_{13}}\left\|g\left(\hat{\boldsymbol{u}}_h,\hat{\boldsymbol{\sigma}}_h\right)\right\|^2+\frac{\varepsilon_{16}}{2}\left\|P_\sigma^\perp\left[g\left(\hat{\boldsymbol{u}}_h,\hat{\boldsymbol{\sigma}}_h\right)\right]\right\|^2\right).
\end{aligned}
\tag{7.47}
$$

Let $\boldsymbol{V}_h^*=\boldsymbol{U}_{h1}+\theta_1\boldsymbol{V}_{h1}+\theta_2\boldsymbol{V}_{h2}+\theta_3\boldsymbol{V}_{h3}$, with $\boldsymbol{V}_{hi}$, $i=1,...,3$ introduced above. Adding (7.45)-(7.47) multiplied by θ_i, $i=1,...,3$, and adding also (7.44), we arrive at an expresion of the form

$$
LHS\left(\boldsymbol{V}_h^*\right)\leq RHS\left(\boldsymbol{V}_h^*\right).
$$

For the right hand side term, applying Young inequalities and the inverse inequality, we obtain

$$
\begin{aligned}
RHS\left(\boldsymbol{V}_h^*\right)\leq&(1-\beta)\left(\frac{1}{2\mu}\left(\frac{1}{2\varepsilon_{17}}+\theta_1\frac{1}{2\varepsilon_{18}}\right)c_\Omega^2\left\|\boldsymbol{f}\right\|_{H^{-1}}^2\right.\\
&+2\mu\frac{\varepsilon_{17}}{2}\left\|\nabla^s\boldsymbol{u}_h\right\|^2+\theta_1\alpha_u\left(\alpha_u\frac{2\mu}{h^2}\right)c_{inv}^2\frac{\varepsilon_{18}}{2}\left\|\boldsymbol{v}_1\right\|^2\Big)\\
&+\frac{\lambda^2}{2\mu}\left(\frac{1}{2\varepsilon_1}+\theta_3\frac{\alpha_\sigma}{2\mu}+\frac{\alpha_\sigma}{2\mu}\left(\frac{1}{2\varepsilon_3}+\frac{\varepsilon_4}{2}+\theta_1\frac{(1-\beta)}{2\varepsilon_9}+\theta_3\frac{\varepsilon_{16}}{2}\right)\right)\left\|g\left(\hat{\boldsymbol{u}}_h,\hat{\boldsymbol{\sigma}}_h\right)\right\|^2.
\end{aligned}
\tag{7.48}
$$

And for the left hand side, integrating the inequalities (7.44),(7.45),(??), (7.47) and (7.48) from 0 to t , we obtain

$$
\begin{aligned}
&(1-\beta)\frac{\rho}{2}\left\|\boldsymbol{u}_h\right\|^2(t)+\frac{\lambda}{4\mu}\left\|\boldsymbol{\sigma}_h\right\|^2(t)+2\mu(1-\beta)\beta C_1\int_0^t\left\|\nabla^s\boldsymbol{u}_h\right\|^2\\
&+\frac{1}{2\mu}C_2\int_0^t\left\|\boldsymbol{\sigma}_h\right\|^2+(1-\beta)C_3\alpha_u\int_0^t\left\|P_u^\perp\left[\rho\hat{\boldsymbol{u}}_h\cdot\nabla\boldsymbol{u}_h\right]\right\|^2\\
&+(1-\beta)C_4\alpha_p\int_0^t\left\|P_p^\perp\left[\nabla\cdot\boldsymbol{u}_h\right]\right\|^2+(1-\beta)C_5\alpha_u\int_0^t\left\|P_u^\perp\left[\nabla\cdot\boldsymbol{\sigma}_h\right]\right\|^2\\
&+(1-\beta)C_6\alpha_u\int_0^t\left\|P_u^\perp\left[\nabla p_h\right]\right\|^2+C_7\alpha_\sigma\int_0^t\left\|P_\sigma^\perp\left[-(1-\beta)\nabla^s\boldsymbol{u}_h+\frac{\lambda}{2\mu}\left(\hat{\boldsymbol{u}}_h\cdot\nabla\boldsymbol{\sigma}_h\right)\right]\right\|^2\\
&+(1-\beta)C_8\alpha_u\int_0^t\left\|P_u\left[\rho\frac{\partial\boldsymbol{u}_h}{\partial t}+\rho\hat{\boldsymbol{u}}_h\cdot\nabla\boldsymbol{u}_h+\nabla p_h-\nabla\cdot\boldsymbol{\sigma}_h\right]\right\|^2
\end{aligned}
\tag{7.49}
$$

$$
\begin{aligned}
&+ (1-\beta)\, C_9 \alpha_p \int_0^t \|P_p\left[\nabla \cdot \boldsymbol{u}_h\right]\|^2 \\
&+ C_{10}\alpha_\sigma \int_0^t \left\| P_\sigma \left[\frac{\lambda}{2\mu}\frac{\partial \boldsymbol{\sigma}_h}{\partial t} - (1-\beta)\,\nabla^s \boldsymbol{u}_h + \frac{\lambda}{2\mu}\hat{\boldsymbol{u}}_h \cdot \nabla \boldsymbol{\sigma}_h \right] \right\|^2 \\
&\leq (1-\beta)\,\frac{c_\Omega^2}{2\mu} C_{11} \int_0^t \|\boldsymbol{f}\|_{H^{-1}}^2 + \frac{\lambda^2}{2\mu} C_{12} \int_0^t \|g\left(\hat{\boldsymbol{u}}_h, \hat{\boldsymbol{\sigma}}_h\right)\|^2 + (1-\beta)\,\frac{\rho}{2}\left\|\boldsymbol{u}_h\left(0\right)\right\|^2 + \frac{\lambda}{4\mu}\left\|\boldsymbol{\sigma}_h\left(0\right)\right\|^2,
\end{aligned}
$$

where C_i, $i = 1, ..., 12$, given by

$$
\begin{aligned}
C_1 &= \left(\beta - \frac{\varepsilon_{17}}{2} - \theta_1\left(\beta\frac{1}{2\varepsilon_5} + \frac{\varepsilon_{10}}{2}\right)\right), \\
C_2 &= \left(1 - \frac{\varepsilon_1}{2} - 4\frac{\alpha_\sigma}{2\mu}\lambda^2 \|\nabla \hat{\boldsymbol{u}}_h\|_\infty^2 \left(\frac{1}{2\varepsilon_2} + \frac{1}{2\varepsilon_4}\right) - \theta_3\left(\frac{1}{2\varepsilon_{12}} + \frac{1}{2}\frac{1}{2\varepsilon_{17}}\right)\right), \\
C_3 &= \left(1 - \theta_1\alpha_u \frac{\rho\|\hat{\boldsymbol{u}}_h\|_\infty}{h}\frac{1}{2\varepsilon_7}\right), \\
C_4 &= \left(1 - \theta_1\frac{1}{2\varepsilon_6}\right), \\
C_5 &= \left(1 - \theta_3\frac{(1-\beta)}{2\varepsilon_{14}}\right), \\
C_6 &= \left(1 - \theta_2\frac{1}{2\varepsilon_{11}}\right), \\
C_7 &= \left(1 - \frac{\varepsilon_2}{2} - \frac{\varepsilon_3}{2} - \theta_1\frac{(1-\beta)}{2\varepsilon_8} - \theta_3\frac{\varepsilon_{15}}{2}\right), \\
C_8 &= \theta_1\left(1 - \alpha_u c_{\text{inv}}^2\left[\frac{2\mu}{h^2}\left(\beta\frac{\varepsilon_5}{2} + \frac{\varepsilon_{18}}{2}\right) + \frac{\alpha_p}{h^2}\frac{\varepsilon_6}{2} + \frac{\rho\|\hat{\boldsymbol{u}}_h\|_\infty}{h}\frac{\varepsilon_7}{2} + \frac{\alpha_\sigma}{h^2}\left(\frac{\varepsilon_8}{2} + \frac{\varepsilon_9}{2}\right)\right.\right. \\
&\quad \left.\left. + \alpha_u\frac{d}{8\varepsilon_{10}}\frac{c_\Omega^2}{\mu}\rho^2\|\nabla\hat{\boldsymbol{u}}_h\|_\infty^2\right]\right), \\
C_9 &= \theta_2\left(1 - c_{\text{inv}}^2\alpha_u\frac{\alpha_p}{h^2}\frac{\varepsilon_{11}}{2}\right), \\
C_{10} &= \theta_3\left(1 - \frac{\alpha_\sigma}{2\mu}\frac{\varepsilon_{12}}{2} - \frac{\varepsilon_{13}}{2} - \frac{\varepsilon_{17}}{4}\frac{\alpha_\sigma}{2\mu}d\left(\lambda\|\nabla\hat{\boldsymbol{u}}_h\|_\infty\right)^2\right. \\
&\quad \left. - c_{inv}^2\left[\left(1-\beta\right)\alpha_u\frac{\alpha_\sigma}{h^2}\frac{\varepsilon_{14}}{2} + 2\alpha_\sigma^2\left(\left(\frac{\lambda\|\hat{\boldsymbol{u}}_h\|_\infty}{2\mu h}\right)^2 + 4\left(\frac{\lambda\|\nabla\hat{\boldsymbol{u}}_h\|_\infty}{2\mu}\right)^2\right)\left(\frac{1}{2\varepsilon_{15}} + \frac{1}{2\varepsilon_{16}}\right)\right]\right), \\
C_{11} &= \left(\frac{1}{2\varepsilon_{17}} + \theta_1\frac{1}{2\varepsilon_{18}}\right), \\
C_{12} &= \left(\frac{1}{2\varepsilon_1} + \theta_3\frac{\alpha_\sigma}{2\mu} + \frac{\alpha_\sigma}{2\mu}\left(\frac{1}{2\varepsilon_3} + \frac{\varepsilon_4}{2} + \theta_1\frac{(1-\beta)}{2\varepsilon_9} + \theta_3\frac{\varepsilon_{16}}{2}\right)\right).
\end{aligned}
$$

The result then follow by choosing $\varepsilon_1, ..., \varepsilon_{18}$ and $\theta_1, ..., \theta_3$, in such a way that $C_i > 0$ for all i. □

7.7 Analysis of the nonlinear problem

In this section, based on the fixed point theory, we show that under suitable conditions, a unique solution to the discretized system exists. Using the same procedure proposed by [77], the proof can be subdivided in the following four steps:

1. Define an iterative map in such a way that a fixed point of the map is a solution to the original problem.

2. Show that the map is well defined and bounded on bounded sets.

3. Show that there exists an invariant ball of the map.

4. Apply the Schauder's fixed point theorem to conclude there exists a discrete solution $\boldsymbol{U}_h$ in this ball.

Theorem 4 *Assume that the system (7.23) has a solution* $(\boldsymbol{u}, p, \boldsymbol{\sigma}) \in L^\infty\left(0,T;W^{1,\infty}(\Omega)\right) \cap H^1\left(0,T;H^{k+1}(\Omega)\right) \times L^2\left(0,T;H^{k+1}(\Omega)\right) \times \left(L^\infty\left(0,T;W^{1,\infty}(\Omega)\right) \cap H^1\left(0,T;H^{k+1}(\Omega)\right)\right)$. *In addition assume that* $k \geq {}^d/_2$, *and*

$$\begin{aligned} \|\boldsymbol{u}\|_\infty \leq D_1,\ \|\nabla \boldsymbol{u}\|_\infty, \leq D_2,\ \|\boldsymbol{u}\|_{k+1} \leq D_3, \\ \|\boldsymbol{\sigma}\|_\infty \leq D_4,\ \|\nabla \boldsymbol{\sigma}\|_\infty, \leq D_5,\ \|\boldsymbol{\sigma}\|_{k+1} \leq D_6, \\ \|p\|_k \leq D_7,\ \|\partial_t \boldsymbol{u}\|_k \leq D_8,\ \|\partial_t \boldsymbol{\sigma}\|_k \leq D_9, \end{aligned} \tag{7.50}$$

almost for all $t \in [0,T]$, where $\partial_t := \dfrac{\partial}{\partial t}$.

Then for D_i $i = 1, ..., 9$ *and* h *sufficiently small, there exists a unique solution to* (7.31)-(7.33) satisfying

$$\begin{aligned} \sup_{0\leq t\leq T} \|\boldsymbol{u} - \boldsymbol{u}_h\|^2 + \int_0^t \left(L_d \|\nabla(\boldsymbol{u} - \boldsymbol{u}_h)\|\right)^2 dt \leq & u_\star^2 h^{2k}, \\ \sup_{0\leq t\leq T} \|\boldsymbol{\sigma} - \boldsymbol{\sigma}_h\|^2 \leq & \sigma_\star^2 h^{2k}, \\ \int_0^t \left(\frac{h^2}{\mu + \rho u_\star^2 h^{k+1-\frac{d}{6}} + \rho h \|\boldsymbol{u}\|_1} \right) \left\|P_u^\perp\left[\nabla(p - p_h)\right]\right\|^2 dt \leq & p_\star^2 h^{2k}, \end{aligned} \tag{7.51}$$

being k *the order of interpolation of the unknowns (we are focused on equal interpolation) and* L_d *represents a characteristic length. The terms* $u_\star$, $\sigma_\star$ *and* $p_\star$ *give dimensional consistency.*

Proof.

Step 1. The iterative map. A mapping $\delta : L^2\left(0,T;\boldsymbol{\mathcal{V}}_h\right) \times L^2\left(0,T;Q_h\right) \times L^\infty\left(0,T;\boldsymbol{\Upsilon}_h\right) \to L^2\left(0,T;\boldsymbol{\mathcal{V}}_h\right) \times L^2\left(0,T;Q_h\right) \times L^\infty\left(0,T;\boldsymbol{\Upsilon}_h\right)$ is defined via $(\boldsymbol{u}_h, p_h, \boldsymbol{\sigma}_h) = \delta\left(\hat{\boldsymbol{u}}_h, \hat{p}_h, \hat{\boldsymbol{\sigma}}_h\right)$, where $(\boldsymbol{u}_h, p_h, \boldsymbol{\sigma}_h)$ satisfies:

$$\begin{aligned} &\rho\left(\partial_t \boldsymbol{u}_h, \boldsymbol{v}_h\right) + \rho\tilde{c}\left(\hat{\boldsymbol{u}}_h, \boldsymbol{u}_h, \boldsymbol{v}_h\right) + \left(2\beta\mu\nabla^s \boldsymbol{u}_h + \boldsymbol{\sigma}_h, \nabla^s \boldsymbol{v}_h\right) - \left(p_h, \nabla\cdot\boldsymbol{v}_h\right) \\ &+\alpha_u\left(P_u^\perp\left[\rho\hat{\boldsymbol{u}}_h\cdot\nabla\boldsymbol{u}_h\right], P_u^\perp\left[\rho\hat{\boldsymbol{u}}_h\cdot\nabla\boldsymbol{v}_h\right]\right) + \alpha_p\left(P_p^\perp\left[\nabla\cdot\boldsymbol{u}_h\right], P_p^\perp\left[\nabla\cdot\boldsymbol{v}_h\right]\right) \\ &+(1-\beta)\,\alpha_\sigma\left(P_\sigma^\perp\left[(1-\beta)\nabla^s\boldsymbol{u}_h - \frac{\lambda}{2\mu}\left(\hat{\boldsymbol{u}}_h\cdot\nabla\boldsymbol{\sigma}_h - g\left(\hat{\boldsymbol{u}}_h, \hat{\boldsymbol{\sigma}}_h\right)\right)\right], P_\sigma^\perp\left[\nabla^s\boldsymbol{v}_h\right]\right) = \left\langle \boldsymbol{f}, \boldsymbol{v}_h\right\rangle, \end{aligned} \tag{7.52}$$

$$\left(\nabla\cdot\boldsymbol{u}_h, q_h\right) + \alpha_u\left(P_u^\perp\left[\nabla p_h\right], P_u^\perp\left[\nabla q_h\right]\right) = 0, \tag{7.53}$$

$$\begin{aligned} &\left(\frac{1}{2\mu}\boldsymbol{\sigma}_h - (1-\beta)\nabla^s\boldsymbol{u}_h, \boldsymbol{\tau}_h\right) + \frac{\lambda}{2\mu}\left(\partial_t\boldsymbol{\sigma}_h, \boldsymbol{\tau}_h\right) + \frac{\lambda}{2\mu}\tilde{c}\left(\hat{\boldsymbol{u}}_h, \boldsymbol{\sigma}_h, \boldsymbol{\tau}_h\right) \\ &+(1-\beta)\,\alpha_u\left(P_u^\perp\left[\nabla\cdot\boldsymbol{\sigma}_h\right], P_u^\perp\left[\nabla\cdot\boldsymbol{\tau}_h\right]\right) \\ &+\alpha_\sigma\left(P_\sigma^\perp\left[-(1-\beta)\nabla^s\boldsymbol{u}_h + \frac{\lambda}{2\mu}\left(\hat{\boldsymbol{u}}_h\cdot\nabla\boldsymbol{\sigma}_h - g\left(\hat{\boldsymbol{u}}_h, \hat{\boldsymbol{\sigma}}_h\right)\right)\right],\right. \\ &\left. P_\sigma^\perp\left[\frac{\lambda}{2\mu}\left(\hat{\boldsymbol{u}}_h\cdot\nabla\boldsymbol{\tau}_h + g^*\left(\hat{\boldsymbol{u}}_h, \boldsymbol{\tau}_h\right)\right)\right]\right) = \frac{\lambda}{2\mu}\left[g\left(\hat{\boldsymbol{u}}_h, \hat{\boldsymbol{\sigma}}_h\right), \boldsymbol{\tau}_h\right], \end{aligned} \tag{7.54}$$

for all $\boldsymbol{V}_h = (\boldsymbol{v}_h, q_h, \boldsymbol{\tau}_h) \in \boldsymbol{\mathcal{X}}_h$. Thus, given an initial guess for the three unknowns $(\hat{\boldsymbol{u}}_h, \hat{p}_h, \hat{\boldsymbol{\sigma}}_h)$, solving the above system for $(\boldsymbol{u}_h, p_h, \boldsymbol{\sigma}_h)$ gives a new approximation to the

solution. Also, it is clear that the fixed point of (7.52)-(7.54), is a solution to the approximating system (7.31)-(7.33) (i.e, $\delta\left(\hat{\boldsymbol{u}}_h, \hat{p}_h, \hat{\boldsymbol{\sigma}}_h\right) = \left(\hat{\boldsymbol{u}}_h, \hat{p}_h, \hat{\boldsymbol{\sigma}}_h\right)$ implies that $\left(\hat{\boldsymbol{u}}_h, \hat{p}_h, \hat{\boldsymbol{\sigma}}_h\right)$ is a solution to (7.31)-(7.33)).

Step 2. *Show that the mapping δ is well defined and bounded on bounded sets.*

The existence and uniqueness of the discrete solution was proved in subsection 7.6.2 for a linearized problem, that can be associated to the solution of the fixed point problem.

The stability result proved in subsection 7.6.3 ensures that the linearized problem, that can be viewed as a fixed point iteration of the nonlinear case, is stable and bounded under suitable regularity assumptions. Note that this step is crucial in the definition of the contraction and can be used to establish that the mapping δ is bounded on bounded sets.

Step 3. *Existence of an invariant ball on which the map is a contraction.* We begin defining an invariant ball. Let $R = c^* h^{2k}$ for $0 \leq c^* \leq 1$, and defining the ball $\mathcal{B}_h$ as

$$\begin{aligned}\mathcal{B}_h = \Big\{ & \left(\boldsymbol{v}_h, q_h, \boldsymbol{\tau}_h\right) \in \left(L^\infty\left(0,T;L^2\left(\Omega\right)\right) \cap L^2\left(0,T;\boldsymbol{\mathcal{V}}_h\right)\right) \times L^2\left(0,T;Q_h\right) \times L^2\left(0,T;\boldsymbol{\Upsilon}_h\right) : \\ & \sup_{0\leq t\leq T} \left\|\boldsymbol{u}-\boldsymbol{v}_h\right\|^2 + \int_0^t \left(L_d \left\|\nabla\left(\boldsymbol{u}-\boldsymbol{v}_h\right)\right\|\right)^2 dt \leq u_\star^2 R^2, \\ & \sup_{0\leq t\leq T} \left\|\boldsymbol{\sigma}-\boldsymbol{\tau}_h\right\|^2 \leq \sigma_\star^2 R^2, \\ & \int_0^t \left(\frac{h^2}{\mu + \rho u_\star^2 h^{k+1-\frac{d}{6}} + \rho h \left\|\boldsymbol{u}\right\|_1} \right) \left\|P_u^\perp\left[\nabla\left(p-q_h\right)\right]\right\|^2 dt \leq p_\star^2 R^2 \Big\}, \end{aligned} \tag{7.55}$$

where $(\boldsymbol{u}, p, \boldsymbol{\sigma})$ is the solution of (7.19). This solution satisfies

$$\begin{aligned} & \rho\left(\partial_t \boldsymbol{u}, \boldsymbol{v}_h\right) + \rho\tilde{c}\left(\boldsymbol{u},\boldsymbol{u},\boldsymbol{v}_h\right) + \left(2\beta\mu\nabla^s\boldsymbol{u}+\boldsymbol{\sigma}, \nabla^s\boldsymbol{v}_h\right) - \left(p, \nabla\cdot\boldsymbol{v}_h\right) \\ & \qquad + \left(\nabla\cdot\boldsymbol{u}, q_h\right) + \left(\frac{1}{2\mu}\boldsymbol{\sigma} - \left(1-\beta\right)\nabla^s\boldsymbol{u}, \boldsymbol{\tau}_h\right) \\ & + \frac{\lambda}{2\mu}\left(\partial_t\boldsymbol{\sigma}, \boldsymbol{\tau}_h\right) + \frac{\lambda}{2\mu}\tilde{c}\left(\boldsymbol{u},\boldsymbol{\sigma},\boldsymbol{\tau}_h\right) - \frac{\lambda}{2\mu}\left(g\left(\boldsymbol{u},\boldsymbol{\sigma}\right),\boldsymbol{\tau}_h\right) = \left\langle \boldsymbol{f}, \boldsymbol{v}_h\right\rangle. \end{aligned} \tag{7.56}$$

Let now $\left(\hat{\boldsymbol{u}}_h, \hat{p}_h, \hat{\boldsymbol{\sigma}}_h\right) \in \mathcal{B}_h$. Then $\left(\boldsymbol{u}_h, p_h, \boldsymbol{\sigma}_h\right) = \delta\left(\hat{\boldsymbol{u}}_h, \hat{p}_h, \hat{\boldsymbol{\sigma}}_h\right)$ satisfies

$$\begin{aligned} & \rho\left(\partial_t \boldsymbol{u}_h, \boldsymbol{v}_h\right) + \rho\tilde{c}\left(\hat{\boldsymbol{u}}_h,\boldsymbol{u}_h,\boldsymbol{v}_h\right) + \left(2\beta\mu\nabla^s\boldsymbol{u}_h+\boldsymbol{\sigma}_h, \nabla^s\boldsymbol{v}_h\right) - \left(p_h, \nabla\cdot\boldsymbol{v}_h\right) \\ & + \alpha_u\left(P_u^\perp\left[\rho\hat{\boldsymbol{u}}_h\cdot\nabla\boldsymbol{u}_h\right], P_u^\perp\left[\rho\hat{\boldsymbol{u}}_h\cdot\nabla\boldsymbol{v}_h\right]\right) + \alpha_p\left(P_p^\perp\left[\nabla\cdot\boldsymbol{u}_h\right], P_p^\perp\left[\nabla\cdot\boldsymbol{v}_h\right]\right) \\ & + \left(1-\beta\right)\alpha_\sigma\left(P_\sigma^\perp\left[\left(1-\beta\right)\nabla^s\boldsymbol{u}_h - \frac{\lambda}{2\mu}\left(\hat{\boldsymbol{u}}_h\cdot\nabla\boldsymbol{\sigma}_h - g\left(\hat{\boldsymbol{u}}_h,\boldsymbol{\sigma}_h\right)\right)\right], P_\sigma^\perp\left[\nabla^s\boldsymbol{v}_h\right]\right) \\ & + \left(\nabla\cdot\boldsymbol{u}_h, q_h\right) + \alpha_u\left(P_u^\perp\left[\nabla p_h\right], P_u^\perp\left[\nabla q_h\right]\right) + \left(\frac{1}{2\mu}\boldsymbol{\sigma}_h - \left(1-\beta\right)\nabla^s\boldsymbol{u}_h, \boldsymbol{\tau}_h\right) \\ & + \frac{\lambda}{2\mu}\left(\partial_t\boldsymbol{\sigma}_h, \boldsymbol{\tau}_h\right) + \frac{\lambda}{2\mu}\tilde{c}\left(\hat{\boldsymbol{u}}_h,\boldsymbol{\sigma}_h,\boldsymbol{\tau}_h\right) - \frac{\lambda}{2\mu}\left(g\left(\hat{\boldsymbol{u}}_h,\hat{\boldsymbol{\sigma}}_h\right),\boldsymbol{\tau}_h\right) \\ & + \left(1-\beta\right)\alpha_u\left(P_u^\perp\left[\nabla\cdot\boldsymbol{\sigma}_h\right], P_u^\perp\left[\nabla\cdot\boldsymbol{\tau}_h\right]\right) \\ & + \alpha_\sigma\left(P_\sigma^\perp\left[-\left(1-\beta\right)\nabla^s\boldsymbol{u}_h + \frac{\lambda}{2\mu}\left(\hat{\boldsymbol{u}}_h\cdot\nabla\boldsymbol{\sigma}_h - g\left(\hat{\boldsymbol{u}}_h,\hat{\boldsymbol{\sigma}}_h\right)\right)\right],\right. \\ & \left. P_\sigma^\perp\left[\frac{\lambda}{2\mu}\left(\hat{\boldsymbol{u}}_h\cdot\nabla\boldsymbol{\tau}_h + g^*\left(\hat{\boldsymbol{u}}_h,\boldsymbol{\tau}_h\right)\right)\right]\right) = \left\langle \boldsymbol{f}, \boldsymbol{v}_h\right\rangle. \end{aligned} \tag{7.57}$$

Subtracting (7.57) from (7.56) give

$$
\begin{aligned}
&\rho\left(\partial_t\left(\boldsymbol{u}-\boldsymbol{u}_h\right),\boldsymbol{v}_h\right)+\rho\left(\tilde{c}\left(\boldsymbol{u},\boldsymbol{u},\boldsymbol{v}_h\right)-\tilde{c}\left(\hat{\boldsymbol{u}}_h,\boldsymbol{u}_h,\boldsymbol{v}_h\right)\right) \\
&+2\beta\mu\left(\nabla^s\left(\boldsymbol{u}-\boldsymbol{u}_h\right),\nabla^s\boldsymbol{v}_h\right)+\left(\boldsymbol{\sigma}-\boldsymbol{\sigma}_h,\nabla^s\boldsymbol{v}_h\right)-\left(p-p_h,\nabla\cdot\boldsymbol{v}_h\right) \\
&-\alpha_u\left(P_u^{\perp}\left[\rho\hat{\boldsymbol{u}}_h\cdot\nabla\boldsymbol{u}_h\right],P_u^{\perp}\left[\rho\hat{\boldsymbol{u}}_h\cdot\nabla\boldsymbol{v}_h\right]\right)+\alpha_p\left(P_p^{\perp}\left[\nabla\cdot\boldsymbol{u}_h\right],P_p^{\perp}\left[\nabla\cdot\boldsymbol{v}_h\right]\right) \\
&-\alpha_\sigma\left(P_\sigma^{\perp}\left[\left(1-\beta\right)\nabla^s\boldsymbol{u}_h-\frac{\lambda}{2\mu}\left(\hat{\boldsymbol{u}}_h\cdot\nabla\boldsymbol{\sigma}_h-g\left(\hat{\boldsymbol{u}}_h,\hat{\boldsymbol{\sigma}}_h\right)\right)\right],P_\sigma^{\perp}\left[\nabla^s\boldsymbol{v}_h\right]\right) \\
&+\left(\nabla\cdot\left(\boldsymbol{u}-\boldsymbol{u}_h\right),q_h\right)-\alpha_u\left(P_u^{\perp}\left[\nabla p_h\right],P_u^{\perp}\left[\nabla q_h\right]\right) \\
&+\frac{1}{2\mu}\left(\boldsymbol{\sigma}-\boldsymbol{\sigma}_h,\boldsymbol{\tau}_h\right)-\left(1-\beta\right)\left(\nabla^s\left(\boldsymbol{u}-\boldsymbol{u}_h\right),\boldsymbol{\tau}_h\right)+\frac{\lambda}{2\mu}\left(\partial_t\left(\boldsymbol{\sigma}-\boldsymbol{\sigma}_h\right),\boldsymbol{\tau}_h\right) \\
&+\frac{\lambda}{2\mu}\left(\tilde{c}\left(\boldsymbol{u},\boldsymbol{\sigma},\boldsymbol{\tau}_h\right)-\tilde{c}\left(\hat{\boldsymbol{u}}_h,\boldsymbol{\sigma}_h,\boldsymbol{\tau}_h\right)\right)-\frac{\lambda}{2\mu}\left(g\left(\boldsymbol{u},\boldsymbol{\sigma}\right),\boldsymbol{\tau}_h\right)+\frac{\lambda}{2\mu}\left(g\left(\hat{\boldsymbol{u}}_h,\hat{\boldsymbol{\sigma}}_h\right),\boldsymbol{\tau}_h\right) \\
&-\left(1-\beta\right)\alpha_u\left(P_u^{\perp}\left[\nabla\cdot\boldsymbol{\sigma}_h\right],P_u^{\perp}\left[\nabla\cdot\boldsymbol{\tau}_h\right]\right) \\
&-\alpha_\sigma\left(P_\sigma^{\perp}\left[-\left(1-\beta\right)\nabla^s\boldsymbol{u}_h+\frac{\lambda}{2\mu}\left(\hat{\boldsymbol{u}}_h\cdot\nabla\boldsymbol{\sigma}_h-g\left(\hat{\boldsymbol{u}}_h,\hat{\boldsymbol{\sigma}}_h\right)\right)\right],\right. \\
&\left.P_\sigma^{\perp}\left[\frac{\lambda}{2\mu}\left(\hat{\boldsymbol{u}}_h\cdot\nabla\boldsymbol{\tau}_h+g^*\left(\hat{\boldsymbol{u}}_h,\boldsymbol{\tau}_h\right)\right)\right]\right)=0.
\end{aligned}
\tag{7.58}
$$

Defining the following approximation and interpolation errors:

$$
\begin{aligned}
\boldsymbol{\Lambda}=\boldsymbol{u}-\boldsymbol{\mathcal{U}} &\text{ and } \boldsymbol{E}=\boldsymbol{\mathcal{U}}-\boldsymbol{u}_h, \\
\boldsymbol{\Gamma}=\boldsymbol{\sigma}-\boldsymbol{\Sigma} &\text{ and } \boldsymbol{F}=\boldsymbol{\Sigma}-\boldsymbol{\sigma}_h, \\
\Pi=p-\mathcal{P} &\text{ and } G=\mathcal{P}-p_h,
\end{aligned}
$$

where $\boldsymbol{\mathcal{U}}=P_u\left[\boldsymbol{u}\right]$, $\boldsymbol{\Sigma}=P_\sigma\left[\boldsymbol{\sigma}\right]$ and $\mathcal{P}=P_p\left[p\right]$. Taking into account that the total error can be decomposed in terms of its approximation and the interpolation part as, then

$$
\begin{aligned}
\boldsymbol{e}_u=&\boldsymbol{u}-\boldsymbol{u}_h=\boldsymbol{\Lambda}+\boldsymbol{E}, \\
\boldsymbol{e}_\sigma=&\boldsymbol{\sigma}-\boldsymbol{\sigma}_h=\boldsymbol{\Gamma}+\boldsymbol{F}, \\
e_p=&p-p_h=\Pi+G.
\end{aligned}
$$

Taking: $\boldsymbol{v}_h=\left(1-\beta\right)\boldsymbol{E}$, $\boldsymbol{\tau}_h=\boldsymbol{F}$ and $p_h=\left(1-\beta\right)G$ in (7.58), we obtain

$$
\begin{aligned}
&\rho\left(1-\beta\right)\frac{1}{2}\int_0^T\frac{d}{dt}\left\|\boldsymbol{E}\right\|^2+\frac{\lambda}{2\mu}\frac{1}{2}\int_0^t\frac{d}{dt}\left\|\boldsymbol{F}\right\|^2+2\beta\left(1-\beta\right)\mu\left\|\nabla^s\boldsymbol{E}\right\|^2 \\
&+\frac{1}{2\mu}\left\|\boldsymbol{F}\right\|^2+\left(1-\beta\right)\alpha_u\left\|P_u^{\perp}\left[\rho\hat{\boldsymbol{u}}_h\cdot\nabla\boldsymbol{E}\right]\right\|^2+\left(1-\beta\right)\alpha_p\left\|P_p^{\perp}\left[\nabla\cdot\boldsymbol{E}\right]\right\|^2 \\
&+\left(1-\beta\right)\alpha_u\left\|P_u^{\perp}\left[\nabla G\right]\right\|^2+\left(1-\beta\right)\alpha_u\left\|P_u^{\perp}\left[\nabla\cdot\boldsymbol{F}\right]\right\|^2 \\
&\rho\left(1-\beta\right)\left(\tilde{c}\left(\boldsymbol{u},\boldsymbol{u},\boldsymbol{E}\right)-\tilde{c}\left(\hat{\boldsymbol{u}}_h,\boldsymbol{u}_h,\boldsymbol{E}\right)\right)+\frac{\lambda}{2\mu}\left(\tilde{c}\left(\boldsymbol{u},\boldsymbol{\sigma},\boldsymbol{F}\right)-\tilde{c}\left(\hat{\boldsymbol{u}}_h,\boldsymbol{\sigma}_h,\boldsymbol{F}\right)\right) \\
&+\alpha_\sigma\left(P_\sigma^{\perp}\left[-\left(1-\beta\right)\nabla^s\boldsymbol{E}+\frac{\lambda}{2\mu}\left(\hat{\boldsymbol{u}}_h\cdot\nabla\boldsymbol{F}\right)\right],\right. \\
&\left.P_\sigma^{\perp}\left[-\left(1-\beta\right)\nabla^s\boldsymbol{E}+\frac{\lambda}{2\mu}\left(\hat{\boldsymbol{u}}_h\cdot\nabla\boldsymbol{F}+g^*\left(\hat{\boldsymbol{u}}_h,\boldsymbol{F}\right)\right)\right]\right)=\sum_{j=1}^{15}R_j.
\end{aligned}
\tag{7.59}
$$

The objective of this step is to find a bound for the approximation error in terms of the interpolation error and the error arising from the linearization of the original problem.

We will start with the right hand side terms of (7.59). Using Young inequalities, Cauchy-Schwarz, the Poincare-Friedrichs inequality and the relationship between the gradient and the symmetrical gradient (7.2), we can write

$$\begin{aligned}
R_1 = &-(1-\beta)\,\rho\,(\partial_t \boldsymbol{\Lambda}, \boldsymbol{E}) \leq (1-\beta)\,\rho\,\|\partial_t \boldsymbol{\Lambda}\|\,\|\boldsymbol{E}\| \\
&\leq 2\mu\,(1-\beta)\,\frac{\varepsilon_1}{2}\,\|\nabla^s \boldsymbol{E}\|^2 + \frac{\rho^2}{2\mu}\,(1-\beta)\,2c_{PF}^2\,\frac{1}{2\varepsilon_1}\,\|\partial_t \boldsymbol{\Lambda}\|^2\,, \\
R_2 = &-\frac{\lambda}{2\mu}\,(\partial_t \boldsymbol{\Gamma}, \boldsymbol{F}) \leq \frac{1}{2\mu}\,\frac{\varepsilon_2}{2}\,\|\boldsymbol{F}\|^2 + \frac{\lambda^2}{2\mu}\,\frac{1}{2\varepsilon_2}\,\|\partial_t \boldsymbol{\Gamma}\|^2\,, \\
R_3 = &\,(1-\beta)\,(\mathit{\Pi}, \nabla\cdot\boldsymbol{E}) \leq 2\mu\,(1-\beta)\,\frac{\varepsilon_3}{2} 2d\,\|\nabla^s \boldsymbol{E}\|^2 + \frac{1}{2\mu}\,\frac{(1-\beta)}{2\varepsilon_3}\,\|\mathit{\Pi}\|^2\,.
\end{aligned}$$

The term that involve the discrete error of the pressure needs a special treatment. Note that we are using the L^2 orthogonal projection operator. Using the properties of this operator, we can write

$$\begin{aligned}
R_4 = &-(1-\beta)\,(\nabla\cdot\boldsymbol{\Lambda}, G) = -(1-\beta)\,(\boldsymbol{u}-\boldsymbol{\mathcal{U}}, \nabla G) \\
&= -(1-\beta)\,(\boldsymbol{u} - P_u[\boldsymbol{u}]\,, \nabla G - P_u[\nabla G]) \\
&= -(1-\beta)\,\left(\boldsymbol{u} - P_u[\boldsymbol{u}]\,, P_u^{\perp}[\nabla G]\right) \\
&\leq \alpha_u^{-1}\,\frac{(1-\beta)}{2\varepsilon_4}\,\|\boldsymbol{\Lambda}\|^2 + (1-\beta)\,\frac{\varepsilon_4}{2}\alpha_u\left\|P_u^{\perp}[\nabla G]\right\|^2\,.
\end{aligned}$$

The following three terms only need Cauchy-Schwarz and Young inequalities:

$$\begin{aligned}
R_5 = -2\beta\,(1-\beta)\,\mu\,(\nabla^s \boldsymbol{\Lambda}, \nabla^s \boldsymbol{E}) \leq &\,2\beta\,(1-\beta)\,\mu\frac{\varepsilon_5}{2}\,\|\nabla^s \boldsymbol{E}\|^2 + 2\beta\,(1-\beta)\,\mu\frac{1}{2\varepsilon_5}\,\|\nabla^s \boldsymbol{\Lambda}\|^2\,, \\
R_6 = -(1-\beta)\,(\boldsymbol{\Gamma}, \nabla^s \boldsymbol{E}) \leq &\,2\mu\,(1-\beta)\,\frac{\varepsilon_6}{2}\,\|\nabla^s \boldsymbol{E}\|^2 + \frac{1}{2\mu}\,(1-\beta)\,\frac{1}{2\varepsilon_6}\,\|\boldsymbol{\Gamma}\|^2\,, \\
R_7 = -\frac{1}{2\mu}\,(\boldsymbol{\Gamma}, \boldsymbol{F}) \leq &\,\frac{1}{2\mu}\,\frac{1}{2\varepsilon_7}\,\|\boldsymbol{\Gamma}\|^2 + \frac{1}{2\mu}\,\frac{\varepsilon_7}{2}\,\|\boldsymbol{F}\|^2\,, \\
R_8 = (1-\beta)\,(\nabla^s \boldsymbol{\Lambda}, \boldsymbol{F}) \leq &\,2\mu\,(1-\beta)\,\frac{1}{2\varepsilon_8}\,\|\nabla^s \boldsymbol{\Lambda}\|^2 + \frac{1}{2\mu}\,(1-\beta)\,\frac{\varepsilon_8}{2}\,\|\boldsymbol{F}\|^2\,.
\end{aligned}$$

For the stabilization terms of the right hand side of (7.59), we only need to use Cauchy-Schwarz and Young inequalities:

$$\begin{aligned}
R_9 &= (1-\beta)\,\alpha_u\left(P_u^{\perp}[\rho\hat{\boldsymbol{u}}_h\cdot\nabla\boldsymbol{\mathcal{U}}]\,, P_u^{\perp}[\rho\hat{\boldsymbol{u}}_h\cdot\nabla\boldsymbol{E}]\right) \\
&\leq (1-\beta)\,\alpha_u\left(\frac{1}{2\varepsilon_9}\left\|P_u^{\perp}[\rho\hat{\boldsymbol{u}}_h\cdot\nabla\boldsymbol{\mathcal{U}}]\right\|^2 + \frac{\varepsilon_9}{2}\left\|P_u^{\perp}[\rho\hat{\boldsymbol{u}}_h\cdot\nabla\boldsymbol{E}]\right\|^2\right), \\
R_{10} &= (1-\beta)\,\alpha_p\left(P_p^{\perp}[\nabla\cdot\boldsymbol{\mathcal{U}}]\,, P_p^{\perp}[\nabla\cdot\boldsymbol{E}]\right) \\
&\leq (1-\beta)\,\alpha_p\left(\frac{1}{2\varepsilon_{10}}\left\|P_p^{\perp}[\nabla\cdot\boldsymbol{\mathcal{U}}]\right\|^2 + \frac{\varepsilon_{10}}{2}\left\|P_p^{\perp}[\nabla\cdot\boldsymbol{E}]\right\|^2\right), \\
R_{11} &= (1-\beta)\,\alpha_u\left(P_u^{\perp}[\nabla\mathcal{P}]\,, P_u^{\perp}[\nabla G]\right) \\
&\leq (1-\beta)\,\alpha_u\left(\frac{1}{2\varepsilon_{11}}\left\|P_u^{\perp}[\nabla\mathcal{P}]\right\|^2 + \frac{\varepsilon_{11}}{2}\left\|P_u^{\perp}[\nabla G]\right\|^2\right), \\
R_{12} &= (1-\beta)\,\alpha_u\left(P_u^{\perp}[\nabla\cdot\boldsymbol{\Sigma}]\,, P_u^{\perp}[\nabla\cdot\boldsymbol{F}]\right) \\
&\leq (1-\beta)\,\alpha_u\left(\frac{1}{2\varepsilon_{12}}\left\|P_u^{\perp}[\nabla\cdot\boldsymbol{\Sigma}]\right\|^2 + \frac{\varepsilon_{12}}{2}\left\|P_u^{\perp}[\nabla\cdot\boldsymbol{F}]\right\|^2\right),
\end{aligned}$$

$$
\begin{aligned}
R_{13} =& \alpha_\sigma \left(P_\sigma^\perp \left[-(1-\beta)\nabla^s \boldsymbol{\mathcal{U}} + \frac{\lambda}{2\mu}(\hat{\boldsymbol{u}}_h \cdot \nabla \boldsymbol{\Sigma}) \right], P_\sigma^\perp \left[-(1-\beta)\nabla^s \boldsymbol{E} + \frac{\lambda}{2\mu}(\hat{\boldsymbol{u}}_h \cdot \nabla \boldsymbol{F} + g^*(\hat{\boldsymbol{u}}_h, \boldsymbol{F})) \right] \right) \\
\leq & \alpha_\sigma \frac{1}{2\varepsilon_{13}} \left\| P_\sigma^\perp \left[-(1-\beta)\nabla^s \boldsymbol{\mathcal{U}} + \frac{\lambda}{2\mu}(\hat{\boldsymbol{u}}_h \cdot \nabla \boldsymbol{\Sigma}) \right] \right\|^2 \\
& + 2\alpha_\sigma \frac{\varepsilon_{13}}{2} \left\| P_\sigma^\perp \left[-(1-\beta)\nabla^s \boldsymbol{E} + \frac{\lambda}{2\mu}(\hat{\boldsymbol{u}}_h \cdot \nabla \boldsymbol{F}) \right] \right\|^2 + 2\frac{\lambda^2}{2\mu}\frac{\alpha_\sigma}{2\mu}\frac{\varepsilon_{13}}{2} \left\| P_\sigma^\perp \left[g^*(\hat{\boldsymbol{u}}_h, \boldsymbol{F}) \right] \right\|^2, \\
R_{14} =& \alpha_\sigma \left(P_\sigma^\perp \left[-\frac{\lambda}{2\mu} g(\hat{\boldsymbol{u}}_h, \hat{\boldsymbol{\sigma}}_h) \right], P_\sigma^\perp \left[-(1-\beta)\nabla^s \boldsymbol{E} + \frac{\lambda}{2\mu}(\hat{\boldsymbol{u}}_h \cdot \nabla \boldsymbol{F} + g^*(\hat{\boldsymbol{u}}_h, \boldsymbol{F})) \right] \right) \\
\leq & \frac{\lambda^2}{2\mu}\frac{\alpha_\sigma}{2\mu}\frac{1}{2\varepsilon_{14}} \left\| P_\sigma^\perp \left[g(\hat{\boldsymbol{u}}_h, \hat{\boldsymbol{\sigma}}_h) \right] \right\|^2 \\
& + 2\alpha_\sigma \frac{\varepsilon_{14}}{2} \left\| P_\sigma^\perp \left[-(1-\beta)\nabla^s \boldsymbol{E} + \frac{\lambda}{2\mu}(\hat{\boldsymbol{u}}_h \cdot \nabla \boldsymbol{F}) \right] \right\|^2 + 2\frac{\lambda^2}{2\mu}\frac{\alpha_\sigma}{2\mu}\frac{\varepsilon_{14}}{2} \left\| P_\sigma^\perp \left[g^*(\hat{\boldsymbol{u}}_h, \boldsymbol{F}) \right] \right\|^2.
\end{aligned}
$$

The last term of the right hand side of (7.59) corresponds to the traction or rotational term of the Oldroyd-B constitutive model, that can be written in convenient form as

$$
\begin{aligned}
R_{15} = -\frac{\lambda}{2\mu} g(\boldsymbol{u}, \boldsymbol{\sigma}) + \frac{\lambda}{2\mu} g(\hat{\boldsymbol{u}}_h, \hat{\boldsymbol{\sigma}}_h) =& -\frac{\lambda}{2\mu} g(\boldsymbol{u}, \boldsymbol{\sigma} - \hat{\boldsymbol{\sigma}}_h) + \frac{\lambda}{2\mu} g(\boldsymbol{u} - \hat{\boldsymbol{u}}_h, \boldsymbol{\sigma} - \hat{\boldsymbol{\sigma}}_h) \\
& - \frac{\lambda}{2\mu} g(\boldsymbol{u} - \hat{\boldsymbol{u}}_h, \boldsymbol{\sigma}).
\end{aligned} \tag{7.60}
$$

The three terms in the right of (7.60) are bounded using Cauchy-Schwarz, Young inequalities and the inverse inequality (7.4), giving :

$$
\begin{aligned}
\frac{\lambda}{2\mu}(g(\boldsymbol{u}, \boldsymbol{\sigma} - \hat{\boldsymbol{\sigma}}_h), \boldsymbol{F}) &\leq 2\frac{\lambda}{2\mu} \|\nabla \boldsymbol{u}\|_\infty \|\boldsymbol{\sigma} - \hat{\boldsymbol{\sigma}}_h\| \|\boldsymbol{F}\| \\
&\leq 4\frac{\lambda^2}{2\mu}\frac{1}{2\varepsilon_{15}} \|\nabla \boldsymbol{u}\|_\infty^2 \|\boldsymbol{\sigma} - \hat{\boldsymbol{\sigma}}_h\|^2 + \frac{1}{2\mu}\frac{\varepsilon_{15}}{2} \|\boldsymbol{F}\|^2, \\
\frac{\lambda}{2\mu}(g(\boldsymbol{u} - \hat{\boldsymbol{u}}_h, \boldsymbol{\sigma} - \hat{\boldsymbol{\sigma}}_h), \boldsymbol{F}) &\leq 2\frac{\lambda}{2\mu} \|\boldsymbol{\sigma} - \hat{\boldsymbol{\sigma}}_h\| \|\nabla(\boldsymbol{u} - \hat{\boldsymbol{u}}_h)\| \|\boldsymbol{F}\|_\infty \\
&\leq 4\frac{\lambda^2}{2\mu}\frac{1}{2\varepsilon_{16}} h^{-d} \|\nabla(\boldsymbol{u} - \hat{\boldsymbol{u}}_h)\|^2 \|\boldsymbol{\sigma} - \hat{\boldsymbol{\sigma}}_h\|^2 + \frac{1}{2\mu}\frac{\varepsilon_{16}}{2} \|\boldsymbol{F}\|^2, \\
\frac{\lambda}{2\mu}(g(\boldsymbol{u} - \hat{\boldsymbol{u}}_h, \boldsymbol{\sigma}), \boldsymbol{F}) &\leq 2\frac{\lambda}{2\mu} \|\boldsymbol{\sigma}\|_\infty \|\nabla(\boldsymbol{u} - \hat{\boldsymbol{u}}_h)\| \|\boldsymbol{F}\| \\
&\leq 4\frac{\lambda^2}{2\mu}\frac{1}{2\varepsilon_{17}} \|\nabla(\boldsymbol{u} - \hat{\boldsymbol{u}}_h)\|^2 \|\boldsymbol{\sigma}\|_\infty^2 + \frac{1}{2\mu}\frac{\varepsilon_{17}}{2} \|\boldsymbol{F}\|^2.
\end{aligned}
$$

With the terms of the left hand side of (7.59), that not have a quadratic form, we apply a similar procedure. We will start with the convective terms. From the momentum equation, we have the following term

$$
\begin{aligned}
& \rho(1-\beta)(\tilde{c}(\boldsymbol{u}, \boldsymbol{u}, \boldsymbol{E}) - \tilde{c}(\hat{\boldsymbol{u}}_h, \boldsymbol{u}_h, \boldsymbol{E})) \\
=& \rho(1-\beta)(\tilde{c}((\boldsymbol{u} - \hat{\boldsymbol{u}}_h), \boldsymbol{u}, \boldsymbol{E}) - \tilde{c}((\boldsymbol{u} - \hat{\boldsymbol{u}}_h), \boldsymbol{\Lambda}, \boldsymbol{E}) + \tilde{c}(\boldsymbol{u}, \boldsymbol{\Lambda}, \boldsymbol{E})).
\end{aligned} \tag{7.61}
$$

The three right hand side terms of the above equation can be bounded as before, giving

$$
\begin{aligned}
\rho(1-\beta)\tilde{c}((\boldsymbol{u} - \hat{\boldsymbol{u}}_h), \boldsymbol{u}, \boldsymbol{E}) \leq & \frac{1}{2}\rho(1-\beta)\left(\|\boldsymbol{u} - \hat{\boldsymbol{u}}_h\| \|\nabla \boldsymbol{u}\|_\infty c_\Omega \|\nabla^s \boldsymbol{E}\| + \|\boldsymbol{u} - \hat{\boldsymbol{u}}_h\| \|\nabla \boldsymbol{E}\| \|\boldsymbol{u}\|_\infty \right) \\
\leq & \frac{1}{2}(1-\beta)\|\boldsymbol{u} - \hat{\boldsymbol{u}}_h\|^2 \frac{\rho^2}{2\mu}\left(c_\Omega^2 \frac{1}{2\varepsilon_{18}} \|\nabla \boldsymbol{u}\|_\infty^2 + \frac{1}{2\varepsilon_{19}} \|\boldsymbol{u}\|_\infty^2 \right) \\
& + \frac{(1-\beta)}{2} 2\mu \left(\frac{\varepsilon_{18}}{2} + 2\frac{\varepsilon_{19}}{2} \right) \|\nabla^s \boldsymbol{E}\|^2,
\end{aligned}
$$

$$\begin{aligned}\rho(1-\beta)\tilde{c}((\boldsymbol{u}-\hat{\boldsymbol{u}}_h),\boldsymbol{\Lambda},\boldsymbol{E}) \leq & \frac{1}{2}\rho(1-\beta)\left(\|\boldsymbol{u}-\hat{\boldsymbol{u}}_h\|_{L^4}\|\nabla\boldsymbol{\Lambda}\|\|\boldsymbol{E}\|_{L^4}+\|\boldsymbol{u}-\hat{\boldsymbol{u}}_h\|_{L^4}\|\nabla\boldsymbol{E}\|\|\boldsymbol{\Lambda}\|_{L^4}\right)\\ \leq & \frac{1}{2}\rho(1-\beta)\left(C_{L^4}^{H^1}\right)^2\left(\|\boldsymbol{u}-\hat{\boldsymbol{u}}_h\|_1\|\nabla\boldsymbol{\Lambda}\|\|\boldsymbol{E}\|_1+\|\boldsymbol{u}-\hat{\boldsymbol{u}}_h\|_1\|\boldsymbol{\Lambda}\|_1\|\nabla\boldsymbol{E}\|\right)\\ \leq & \frac{1}{2}\frac{\rho^2}{2\mu}(1-\beta)\left(c_\Omega^2\|\nabla\boldsymbol{\Lambda}\|^2\frac{1}{2\varepsilon_{20}}+2\|\boldsymbol{\Lambda}\|_1^2\frac{1}{2\varepsilon_{21}}\right)\left(C_{L^4}^{H^1}\right)^4\|\boldsymbol{u}-\hat{\boldsymbol{u}}_h\|_1^2\\ & +\frac{(1-\beta)}{2}2\mu\left(\frac{\varepsilon_{20}}{2}+2\frac{\varepsilon_{21}}{2}\right)\|\nabla^s\boldsymbol{E}\|^2.\end{aligned}$$

For the last term that defines (7.61),we use integration by parts and the Young inequality

$$\begin{aligned}\rho(1-\beta)\tilde{c}(\boldsymbol{u},\boldsymbol{\Lambda},\boldsymbol{E}) = & -\rho(1-\beta)(\boldsymbol{u}\cdot\nabla\boldsymbol{E},\boldsymbol{\Lambda})\\ \leq & \rho(1-\beta)\|\boldsymbol{u}\|_\infty\|\nabla\boldsymbol{E}\|\|\boldsymbol{\Lambda}\|\\ \leq & 2(1-\beta)\frac{\varepsilon_{22}}{2}2\mu\|\nabla^s\boldsymbol{E}\|^2+\rho^2(1-\beta)\frac{1}{2\mu}\frac{1}{2\varepsilon_{22}}\|\boldsymbol{u}\|_\infty^2\|\boldsymbol{\Lambda}\|^2.\end{aligned}$$

A similar procedure can be applied to the convective term of the constitutive equation

$$\begin{aligned}&\frac{\lambda}{2\mu}\left(\tilde{c}(\boldsymbol{u},\boldsymbol{\sigma},\boldsymbol{F})-\tilde{c}(\hat{\boldsymbol{u}}_h,\boldsymbol{\sigma}_h,\boldsymbol{F})\right)\\ =&\frac{\lambda}{2\mu}\left(\tilde{c}((\boldsymbol{u}-\hat{\boldsymbol{u}}_h),\boldsymbol{\sigma},\boldsymbol{F})-\tilde{c}((\boldsymbol{u}-\hat{\boldsymbol{u}}_h),\boldsymbol{\Gamma},\boldsymbol{F})+\tilde{c}(\boldsymbol{u},\boldsymbol{\Gamma},\boldsymbol{E})\right),\end{aligned}$$

where the three right hand side terms of the above equation are bounded as:

$$\begin{aligned}\frac{\lambda}{2\mu}\tilde{c}((\boldsymbol{u}-\hat{\boldsymbol{u}}_h),\boldsymbol{\sigma},\boldsymbol{F}) \leq & \frac{1}{2}\frac{\lambda}{2\mu}\left(2\|\boldsymbol{u}-\hat{\boldsymbol{u}}_h\|\|\nabla\boldsymbol{\sigma}\|_\infty\|\boldsymbol{F}\|+\sqrt{d}\|\nabla(\boldsymbol{u}-\hat{\boldsymbol{u}}_h)\|\|\boldsymbol{F}\|\|\boldsymbol{\sigma}\|_\infty\right)\\ \leq & \frac{1}{2}\frac{\lambda^2}{2\mu}\left(2\frac{1}{2\varepsilon_{23}}\|\boldsymbol{u}-\hat{\boldsymbol{u}}_h\|^2\|\nabla\boldsymbol{\sigma}\|_\infty^2+\frac{1}{2\varepsilon_{24}}d\|\nabla(\boldsymbol{u}-\hat{\boldsymbol{u}}_h)\|^2\|\boldsymbol{\sigma}\|_\infty^2\right)\\ & +\frac{1}{2}\frac{1}{2\mu}\left(\frac{\varepsilon_{23}}{2}+\frac{\varepsilon_{24}}{2}\right)\|\boldsymbol{F}\|^2,\\ \frac{\lambda}{2\mu}\tilde{c}((\boldsymbol{u}-\hat{\boldsymbol{u}}_h),\boldsymbol{\Gamma},\boldsymbol{F}) \leq & \frac{1}{2}\frac{\lambda}{2\mu}\left(\|\boldsymbol{u}-\hat{\boldsymbol{u}}_h\|_{L^4}\|\nabla\boldsymbol{\Gamma}\|\|\boldsymbol{F}\|_{L^4}+\|\boldsymbol{u}-\hat{\boldsymbol{u}}_h\|_{L^4}\|\nabla\boldsymbol{F}\|\|\boldsymbol{\Gamma}\|_{L^4}\right)\\ \leq & \frac{1}{2}\frac{\lambda}{2\mu}C_{L^4}^{H^1}\left(h^{-\frac{d}{4}}\|\boldsymbol{u}-\hat{\boldsymbol{u}}_h\|_1\|\nabla\boldsymbol{\Gamma}\|\|\boldsymbol{F}\|+C_{L^4}^{H^1}\|\boldsymbol{u}-\hat{\boldsymbol{u}}_h\|_1 c_{inv}h^{-1}\|\boldsymbol{\Gamma}\|_1\|\boldsymbol{F}\|\right)\\ \leq & \frac{\lambda^2}{4\mu}\left(C_{L^4}^{H^1}\right)^2\left(\frac{h^{-\frac{d}{2}}}{2\varepsilon_{25}}\|\nabla\boldsymbol{\Gamma}\|^2+\left(C_{L^4}^{H^1}\right)^2\frac{c_{inv}^2}{h^2}\|\boldsymbol{\Gamma}\|_1^2\frac{1}{2\varepsilon_{26}}\right)\|\boldsymbol{u}-\hat{\boldsymbol{u}}_h\|_1^2\\ & +\frac{1}{4\mu}\left(\frac{\varepsilon_{25}}{2}+\frac{\varepsilon_{26}}{2}\right)\|\boldsymbol{F}\|^2,\\ \frac{\lambda}{2\mu}\tilde{c}(\boldsymbol{u},\boldsymbol{\Gamma},\boldsymbol{F}) \leq & \frac{\lambda^2}{2\mu}\frac{1}{2\varepsilon_{27}}\|\boldsymbol{u}\|_\infty^2\|\nabla\boldsymbol{\Gamma}\|^2+\frac{\varepsilon_{27}}{2}\frac{1}{2\mu}\|\boldsymbol{F}\|^2.\end{aligned}$$

For the remaining left hand side term of (7.59) we have

$$\begin{aligned}&\alpha_\sigma\left(P_\sigma^\perp\left[-(1-\beta)\nabla^s\boldsymbol{E}+\frac{\lambda}{2\mu}(\hat{\boldsymbol{u}}_h\cdot\nabla\boldsymbol{F})\right],P_\sigma^\perp\left[-(1-\beta)\nabla^s\boldsymbol{E}+\frac{\lambda}{2\mu}(\hat{\boldsymbol{u}}_h\cdot\nabla\boldsymbol{F}+g^*(\hat{\boldsymbol{u}}_h,\boldsymbol{F}))\right]\right)\\ =&\alpha_\sigma\left\|P_\sigma^\perp\left[-(1-\beta)\nabla^s\boldsymbol{E}+\frac{\lambda}{2\mu}(\hat{\boldsymbol{u}}_h\cdot\nabla\boldsymbol{F})\right]\right\|^2\\ &+\alpha_\sigma\left(P_\sigma^\perp\left[-(1-\beta)\nabla^s\boldsymbol{E}+\frac{\lambda}{2\mu}(\hat{\boldsymbol{u}}_h\cdot\nabla\boldsymbol{F})\right],P_\sigma^\perp\left[\frac{\lambda}{2\mu}g^*(\hat{\boldsymbol{u}}_h,\boldsymbol{F})\right]\right)\end{aligned}$$

$$\geq \alpha_\sigma \left(1-\frac{\varepsilon_{28}}{2}\right)\left\|P_\sigma^\perp\left[-(1-\beta)\nabla^s \boldsymbol{E}+\frac{\lambda}{2\mu}(\hat{\boldsymbol{u}}_h\cdot\nabla\boldsymbol{F})\right]\right\|^2-\frac{\lambda^2}{2\mu}\frac{\alpha_\sigma}{2\mu}\frac{1}{2\varepsilon_{28}}\left\|P_\sigma^\perp\left[g^*\left(\hat{\boldsymbol{u}}_h,\boldsymbol{F}\right)\right]\right\|^2.$$

where the last term can be written using the inverse inequality (7.4) as

$$\begin{aligned}\frac{\lambda^2}{2\mu}\frac{\alpha_\sigma}{2\mu}\frac{1}{2\varepsilon_{28}}\left\|P_\sigma^\perp\left[g^*\left(\hat{\boldsymbol{u}}_h,\boldsymbol{F}\right)\right]\right\|^2 \leq & 2\frac{\lambda^2}{2\mu}\frac{\alpha_\sigma}{2\mu}\left(\frac{1}{2\varepsilon_{28}}\left\|P_\sigma^\perp\left[g^*\left(\left(\hat{\boldsymbol{u}}_h-\boldsymbol{u}\right),\boldsymbol{F}\right)\right]\right\|^2+\frac{1}{2\varepsilon_{28}}\left\|P_\sigma^\perp\left[g^*\left(\boldsymbol{u},\boldsymbol{F}\right)\right]\right\|^2\right)\\ \leq & 8\frac{\lambda^2}{2\mu}\frac{\alpha_\sigma}{2\mu}\frac{1}{2\varepsilon_{28}}\left(\left\|\nabla\left(\hat{\boldsymbol{u}}_h-\boldsymbol{u}\right)\right\|^2\left\|\boldsymbol{F}\right\|_\infty^2+\left\|\nabla\boldsymbol{u}\right\|_\infty^2\left\|\boldsymbol{F}\right\|^2\right)\\ \leq & 8\frac{\lambda^2}{2\mu}\frac{\alpha_\sigma}{2\mu}\frac{1}{2\varepsilon_{28}}\left(h^{-d}\left\|\nabla\left(\hat{\boldsymbol{u}}_h-\boldsymbol{u}\right)\right\|^2+\left\|\nabla\boldsymbol{u}\right\|_\infty^2\right)\left\|\boldsymbol{F}\right\|^2.\end{aligned}$$

Collecting all the terms that involve $\boldsymbol{F}$, $\boldsymbol{E}$ and G in (7.59), that represent the approximation error, we can construct the following result

$$\begin{aligned}&\rho(1-\beta)\frac{1}{2}\int_0^t\frac{d}{dt}\left\|\boldsymbol{E}\right\|^2+\frac{\lambda}{2\mu}\frac{1}{2}\int_0^t\frac{d}{dt}\left\|\boldsymbol{F}\right\|^2 \qquad (7.62)\\ &+\frac{1}{2\mu}\int_0^t\left(1-\frac{\varepsilon_2}{2}-\frac{\varepsilon_7}{2}-\frac{\varepsilon_8}{2}-\frac{\varepsilon_{15}}{2}-\frac{\varepsilon_{16}}{2}-\frac{\varepsilon_{17}}{2}-\frac{\varepsilon_{23}}{4}-\frac{\varepsilon_{24}}{4}-\frac{\varepsilon_{25}}{4}-\frac{\varepsilon_{26}}{4}-\frac{\varepsilon_{27}}{2}\right.\\ &\left.-8\frac{\alpha_\sigma}{2\mu}\left(\lambda^2\left(h^{-d}\left\|\nabla\left(\hat{\boldsymbol{u}}_h-\boldsymbol{u}\right)\right\|^2+\left\|\nabla\boldsymbol{u}\right\|_\infty^2\right)\right)\left(2\left(\frac{\varepsilon_{13}}{2}+\frac{\varepsilon_{14}}{2}\right)+\frac{1}{2\varepsilon_{28}}\right)\right)\left\|\boldsymbol{F}\right\|^2\\ &+2\mu(1-\beta)\int_0^t\left(\beta-\frac{\varepsilon_1}{2}-2d\frac{\varepsilon_3}{2}-\beta\frac{\varepsilon_5}{2}-\frac{\varepsilon_6}{2}-\frac{\varepsilon_{18}}{4}-\frac{\varepsilon_{19}}{2}-\frac{\varepsilon_{20}}{4}-\frac{\varepsilon_{21}}{2}-2\frac{\varepsilon_{22}}{2}\right)\left\|\nabla^s\boldsymbol{E}\right\|^2\\ &+(1-\beta)\int_0^t\alpha_u\left(1-\frac{\varepsilon_9}{2}\right)\left\|P_u^\perp\left[\rho\hat{\boldsymbol{u}}_h\cdot\nabla\boldsymbol{E}\right]\right\|^2\\ &+(1-\beta)\int_0^t\alpha_p\left(1-\frac{\varepsilon_{10}}{2}\right)\left\|P_p^\perp\left[\nabla\cdot\boldsymbol{E}\right]\right\|^2\\ &+(1-\beta)\int_0^t\alpha_u\left(1-\frac{\varepsilon_{11}}{2}-\frac{\varepsilon_4}{2}\right)\left\|P_u^\perp\left[\nabla G\right]\right\|^2\\ &+(1-\beta)\int_0^t\alpha_u\left(1-\frac{\varepsilon_{12}}{2}\right)\left\|P_u^\perp\left[\nabla\cdot\boldsymbol{F}\right]\right\|^2\\ &+\int_0^t\alpha_\sigma\left(1-\frac{\varepsilon_{28}}{2}-2\left(\frac{\varepsilon_{13}}{2}+\frac{\varepsilon_{14}}{2}\right)\right)\left\|P_\sigma^\perp\left[-(1-\beta)\nabla^s\boldsymbol{E}+\frac{\lambda}{2\mu}(\hat{\boldsymbol{u}}_h\cdot\nabla\boldsymbol{F})\right]\right\|^2\leq RHS.\end{aligned}$$

Taking $\varepsilon_9=2$, $\varepsilon_{13}=\varepsilon_{14}=\dfrac{1}{4}$, $\varepsilon_{28}=1$, the remaining ε's small enough to guarantee that the constants in the LHS of (7.62) are positive, and using (7.50) and $(\hat{\boldsymbol{u}}_h,\hat{p}_h,\hat{\boldsymbol{\sigma}}_h)\in\mathcal{B}_h$, we arrive at

$$\begin{aligned}&(1-\beta)\rho\left\|\boldsymbol{E}(t)\right\|^2+\frac{\lambda}{\mu}\left\|\boldsymbol{F}(t)\right\|^2+\frac{1}{2\mu}\int_0^t\left\|\boldsymbol{F}\right\|^2+2\mu(1-\beta)\beta\int_0^t\left\|\nabla^s\boldsymbol{E}\right\|^2 \qquad (7.63)\\ &+(1-\beta)\alpha_p\int_0^t\left\|P_p^\perp\left[\nabla\cdot\boldsymbol{E}\right]\right\|^2+(1-\beta)\alpha_u\int_0^t\left\|P_u^\perp\left[\nabla G\right]\right\|^2+(1-\beta)\alpha_u\int_0^t\left\|P_u^\perp\left[\nabla\cdot\boldsymbol{F}\right]\right\|^2\lesssim RHS.\end{aligned}$$

Now, for the right hand side term we can collect all the other terms that involve interpolation and linearization errors, such that

$$\begin{aligned}RHS=&\frac{\rho^2}{2\mu}2c_{PF}^2\frac{(1-\beta)}{2\varepsilon_1}\int_0^t\left\|\boldsymbol{\Lambda}_t\right\|^2+\frac{\lambda^2}{2\mu}\frac{1}{2\varepsilon_2}\int_0^t\left\|\boldsymbol{\Gamma}_t\right\|^2+\frac{1}{2\mu}\frac{(1-\beta)}{2\varepsilon_3}\int_0^t\left\|\Pi\right\|^2 \qquad (7.64)\\ &+\alpha_u^{-1}\frac{(1-\beta)}{2\varepsilon_4}\int_0^t\left\|\boldsymbol{\Lambda}\right\|^2+2\mu\frac{\beta(1-\beta)}{2\varepsilon_5}\int_0^t\left\|\nabla^s\boldsymbol{\Lambda}\right\|^2\\ &+\frac{1}{2\mu}\frac{(1-\beta)}{2\varepsilon_6}\int_0^t\left\|\boldsymbol{\Gamma}\right\|^2+\frac{1}{2\mu}\frac{1}{2\varepsilon_7}\int_0^t\left\|\boldsymbol{\Gamma}\right\|^2+2\mu\frac{(1-\beta)}{2\varepsilon_8}\int_0^t\left\|\nabla^s\boldsymbol{\Lambda}\right\|^2\end{aligned}$$

$$
\begin{aligned}
&+\alpha_u\frac{(1-\beta)}{2\varepsilon_9}\int_0^t\left\|P_u^{\perp}\left[\rho\hat{\boldsymbol{u}}_h\cdot\nabla\boldsymbol{\mathcal{U}}\right]\right\|^2+\alpha_p\frac{(1-\beta)}{2\varepsilon_{10}}\int_0^t\left\|P_p^{\perp}\left[\nabla\cdot\boldsymbol{\mathcal{U}}\right]\right\|^2\\
&+\alpha_u\frac{(1-\beta)}{2\varepsilon_{11}}\int_0^t\left\|P_u^{\perp}\left[\nabla\mathcal{P}\right]\right\|^2+\alpha_u\frac{(1-\beta)}{2\varepsilon_{12}}\int_0^t\left\|P_u^{\perp}\left[\nabla\cdot\boldsymbol{\Sigma}\right]\right\|^2\\
&+\alpha_\sigma\frac{1}{\varepsilon_{13}}\int_0^t\left\|P_\sigma^{\perp}\left[-\left(1-\beta\right)\nabla^s\boldsymbol{\mathcal{U}}\right]\right\|^2+\alpha_\sigma\frac{1}{\varepsilon_{13}}\int_0^t\left\|P_\sigma^{\perp}\left[\frac{\lambda}{2\mu}\left(\hat{\boldsymbol{u}}_h\cdot\nabla\boldsymbol{\Sigma}\right)\right]\right\|^2\\
&+\alpha_\sigma\frac{1}{2\varepsilon_{14}}\int_0^t\left\|P_\sigma^{\perp}\left[\frac{\lambda}{2\mu}g\left(\hat{\boldsymbol{u}}_h,\hat{\boldsymbol{\sigma}}_h\right)\right]\right\|^2\\
&+\frac{\lambda^2}{2\mu}\frac{2}{\varepsilon_{15}}\int_0^t\left\|\nabla\boldsymbol{u}\right\|_\infty^2\left\|\boldsymbol{\sigma}-\hat{\boldsymbol{\sigma}}_h\right\|^2+\frac{\lambda^2}{2\mu}\frac{2}{\varepsilon_{16}}h^{-d}\int_0^t\left\|\nabla\left(\boldsymbol{u}-\hat{\boldsymbol{u}}_h\right)\right\|^2\left\|\boldsymbol{\sigma}-\hat{\boldsymbol{\sigma}}_h\right\|^2\\
&+\frac{\lambda^2}{2\mu}\frac{2}{\varepsilon_{17}}\int_0^t\left\|\nabla\left(\boldsymbol{u}-\hat{\boldsymbol{u}}_h\right)\right\|^2\left\|\boldsymbol{\sigma}\right\|_\infty^2\\
&+\frac{(1-\beta)}{2}\int_0^t\left\|\boldsymbol{u}-\hat{\boldsymbol{u}}_h\right\|^2\frac{\rho^2}{2\mu}\left(c_\Omega^2\frac{1}{2\varepsilon_{18}}\left\|\nabla\boldsymbol{u}\right\|_\infty^2+\frac{1}{2\varepsilon_{19}}\left\|\boldsymbol{u}\right\|_\infty^2\right)\\
&+\frac{(1-\beta)}{2}\frac{\rho^2}{2\mu}\int_0^t\left(c_\Omega^2\left\|\nabla\boldsymbol{\Lambda}\right\|^2\frac{1}{2\varepsilon_{20}}+2\left\|\boldsymbol{\Lambda}\right\|_1^2\frac{1}{2\varepsilon_{21}}\right)\left(C_{L^4}^{H^1}\right)^4\left\|\boldsymbol{u}-\hat{\boldsymbol{u}}_h\right\|_1^2\\
&+\rho^2\frac{1}{2\mu}\frac{(1-\beta)}{2\varepsilon_{22}}\int_0^t\left\|\boldsymbol{u}\right\|_\infty^2\left\|\boldsymbol{\Lambda}\right\|^2\\
&+\frac{1}{2}\frac{\lambda^2}{2\mu}\int_0^t\left(2\frac{1}{2\varepsilon_{23}}\left\|\boldsymbol{u}-\hat{\boldsymbol{u}}_h\right\|^2\left\|\nabla\boldsymbol{\sigma}\right\|_\infty^2+\frac{1}{2\varepsilon_{24}}d\left\|\nabla\left(\boldsymbol{u}-\hat{\boldsymbol{u}}_h\right)\right\|^2\left\|\boldsymbol{\sigma}\right\|_\infty^2\right)\\
&+\frac{\lambda^2}{4\mu}\left(C_{L^4}^{H^1}\right)^2\int_0^t\left(\frac{h^{-\frac{d}{2}}}{2\varepsilon_{25}}\left\|\nabla\boldsymbol{\Gamma}\right\|^2+\left(C_{L^4}^{H^1}\right)^2\frac{c_{inv}^2}{h^2}\left\|\boldsymbol{\Gamma}\right\|_1^2\frac{1}{2\varepsilon_{26}}\right)\left\|\boldsymbol{u}-\hat{\boldsymbol{u}}_h\right\|_1^2\\
&+\frac{\lambda^{^2}}{2\mu}\frac{1}{2\varepsilon_{27}}\int_0^t\left\|\boldsymbol{u}\right\|_\infty^2\left\|\nabla\boldsymbol{\Gamma}\right\|^2,
\end{aligned}
$$

in (7.64) we have three terms that need some additional treatment. The first one is

$$
\begin{aligned}
\alpha_u\left\|P_u^{\perp}\left[\rho\hat{\boldsymbol{u}}_h\cdot\nabla\boldsymbol{\mathcal{U}}\right]\right\|^2\lesssim&\alpha_u\rho^2\left\|P_u^{\perp}\left[\left(\hat{\boldsymbol{u}}_h-\boldsymbol{u}\right)\cdot\nabla\left(\boldsymbol{\mathcal{U}}-\boldsymbol{u}\right)\right]\right\|^2+\alpha_u\rho^2\left\|P_u^{\perp}\left[\boldsymbol{u}\cdot\nabla\left(\boldsymbol{\mathcal{U}}-\boldsymbol{u}\right)\right]\right\|^2\\
&+\alpha_u\rho^2\left\|P_u^{\perp}\left[\boldsymbol{u}\cdot\nabla\boldsymbol{u}\right]\right\|^2+\alpha_u\rho^2\left\|P_u^{\perp}\left[\left(\hat{\boldsymbol{u}}_h-\boldsymbol{u}\right)\cdot\nabla\boldsymbol{u}\right]\right\|^2,
\end{aligned}
$$

where the four terms of the right hand side can be bounded as

$$
\begin{aligned}
\alpha_u\rho^2\left\|P_u^{\perp}\left[\left(\hat{\boldsymbol{u}}_h-\boldsymbol{u}\right)\cdot\nabla\left(\boldsymbol{\mathcal{U}}-\boldsymbol{u}\right)\right]\right\|^2\leq&\alpha_u\rho^2\left\|\boldsymbol{u}-\hat{\boldsymbol{u}}_h\right\|^2\left\|\nabla\left(\boldsymbol{u}-\boldsymbol{\mathcal{U}}\right)\right\|_{L^\infty}^2\\
\leq&\left(C_{\infty,3}\right)^2\alpha_u\rho^2\left\|\boldsymbol{u}-\hat{\boldsymbol{u}}_h\right\|^2\left\|\boldsymbol{u}\right\|_3^2,\\
\alpha_u\rho^2\left\|P_u^{\perp}\left[\boldsymbol{u}\cdot\nabla\left(\boldsymbol{\mathcal{U}}-\boldsymbol{u}\right)\right]\right\|^2\leq&\alpha_u\rho^2\left\|\boldsymbol{u}\right\|_\infty^2\left\|\nabla\left(\boldsymbol{u}-\boldsymbol{\mathcal{U}}\right)\right\|^2\\
\leq&\alpha_u\rho^2\left\|\boldsymbol{u}\right\|_\infty^2\left\|\boldsymbol{u}\right\|_{k+1}^2h^{2k},\\
\alpha_u\rho^2\left\|P_u^{\perp}\left[\boldsymbol{u}\cdot\nabla\boldsymbol{u}\right]\right\|^2\leq&\alpha_u\rho^2h^{2k}\left\|\boldsymbol{u}\cdot\nabla\boldsymbol{u}\right\|_k^2\\
\lesssim&\alpha_u\rho^2\left(\left\|\boldsymbol{u}\right\|_{k+1}^2\left\|\boldsymbol{u}\right\|_{1,\infty}^2+\sum_{i=1}^{k-1}\left\|\partial^{i+1}\boldsymbol{u}\right\|^2\left\|\partial^{k-i-1}\nabla\boldsymbol{u}\right\|^2\right)h^{2k},\\
\alpha_u\rho^2\left\|P_u^{\perp}\left[\left(\hat{\boldsymbol{u}}_h-\boldsymbol{u}\right)\cdot\nabla\boldsymbol{u}\right]\right\|^2\leq&\alpha_u\rho^2\left\|\nabla\boldsymbol{u}\right\|_\infty^2\left\|\hat{\boldsymbol{u}}_h-\boldsymbol{u}\right\|^2.
\end{aligned}
$$

The second is term is

$$\begin{aligned}\alpha_\sigma\left(\frac{\lambda}{2\mu}\right)^2\left\|P_u^\perp\left[\rho\hat{\boldsymbol{u}}_h\cdot\nabla\boldsymbol{\Sigma}\right]\right\|^2\lesssim&\alpha_\sigma\left(\frac{\lambda}{2\mu}\right)^2\left\|P_u^\perp\left[\left(\hat{\boldsymbol{u}}_h-\boldsymbol{u}\right)\cdot\nabla\left(\boldsymbol{\Sigma}-\boldsymbol{\sigma}\right)\right]\right\|^2\\&+\alpha_\sigma\left(\frac{\lambda}{2\mu}\right)^2\left\|P_u^\perp\left[\boldsymbol{u}\cdot\nabla\left(\boldsymbol{\Sigma}-\boldsymbol{\sigma}\right)\right]\right\|^2\\&+\alpha_\sigma\left(\frac{\lambda}{2\mu}\right)^2\left\|P_u^\perp\left[\boldsymbol{u}\cdot\nabla\boldsymbol{\sigma}\right]\right\|^2\\&+\alpha_\sigma\left(\frac{\lambda}{2\mu}\right)^2\left\|P_u^\perp\left[\left(\hat{\boldsymbol{u}}_h-\boldsymbol{u}\right)\cdot\nabla\boldsymbol{\sigma}\right]\right\|^2,\end{aligned}$$

where the four terms of the right hand side can be bounded as

$$\begin{aligned}\alpha_\sigma\left(\frac{\lambda}{2\mu}\right)^2\left\|P_u^\perp\left[\left(\hat{\boldsymbol{u}}_h-\boldsymbol{u}\right)\cdot\nabla\left(\boldsymbol{\sigma}-\boldsymbol{\Sigma}\right)\right]\right\|^2\leq&\alpha_\sigma\left(\frac{\lambda}{2\mu}\right)^2\left\|\boldsymbol{u}-\hat{\boldsymbol{u}}_h\right\|^2\left\|\nabla\left(\boldsymbol{\sigma}-\boldsymbol{\Sigma}\right)\right\|_{L^\infty}^2\\\lesssim&\left(C_{\infty,3}\right)^2\alpha_\sigma\left(\frac{\lambda}{2\mu}\right)^2\left\|\boldsymbol{u}-\hat{\boldsymbol{u}}_h\right\|^2\left\|\boldsymbol{\sigma}\right\|_3^2,\\\alpha_\sigma\left(\frac{\lambda}{2\mu}\right)^2\left\|P_u^\perp\left[\boldsymbol{u}\cdot\nabla\left(\boldsymbol{\sigma}-\boldsymbol{\Sigma}\right)\right]\right\|^2\leq&\alpha_\sigma\left(\frac{\lambda}{2\mu}\right)^2\left\|\boldsymbol{u}\right\|_\infty^2\left\|\nabla\left(\boldsymbol{\sigma}-\boldsymbol{\Sigma}\right)\right\|^2\\\leq&\alpha_\sigma\left(\frac{\lambda}{2\mu}\right)^2\left\|\boldsymbol{u}\right\|_\infty^2\left\|\boldsymbol{\sigma}\right\|_{k+1}^2h^{2k},\\\alpha_\sigma\left(\frac{\lambda}{2\mu}\right)^2\left\|P_u^\perp\left[\boldsymbol{u}\cdot\nabla\boldsymbol{\sigma}\right]\right\|^2\leq&\alpha_\sigma\left(\frac{\lambda}{2\mu}\right)^2h^{2k}\left\|\boldsymbol{u}\cdot\nabla\boldsymbol{\sigma}\right\|_k^2\\\lesssim&\alpha_\sigma\left(\frac{\lambda}{2\mu}\right)^2\left(\left\|\boldsymbol{u}\right\|_k^2\left\|\nabla\boldsymbol{\sigma}\right\|_\infty^2\right.\\&\left.+\sum_{i=1}^{k-1}\left\|\partial^{i+1}\boldsymbol{u}\right\|^2\left\|\partial^{k-i-1}\nabla\boldsymbol{\sigma}\right\|^2+\left\|\boldsymbol{u}\right\|_\infty^2\left\|\boldsymbol{\sigma}\right\|_{k+1}^2\right)h^{2k},\\\alpha_\sigma\left(\frac{\lambda}{2\mu}\right)^2\left\|P_u^\perp\left[\left(\hat{\boldsymbol{u}}_h-\boldsymbol{u}\right)\cdot\nabla\boldsymbol{\sigma}\right]\right\|^2\leq&\alpha_\sigma\left(\frac{\lambda}{2\mu}\right)^2\left\|\nabla\boldsymbol{\sigma}\right\|_\infty^2\left\|\hat{\boldsymbol{u}}_h-\boldsymbol{u}\right\|^2.\end{aligned}$$

And the the last term is

$$\begin{aligned}\alpha_\sigma\left(\frac{\lambda}{2\mu}\right)^2\left\|P_\sigma^\perp\left[g\left(\hat{\boldsymbol{u}}_h,\hat{\boldsymbol{\sigma}}_h\right)\right]\right\|^2\lesssim&\alpha_\sigma\left(\frac{\lambda}{2\mu}\right)^2\left\|P_u^\perp\left[g\left(\left(\hat{\boldsymbol{u}}_h-\boldsymbol{u}\right),\left(\hat{\boldsymbol{\sigma}}_h-\boldsymbol{\sigma}\right)\right)\right]\right\|^2\\&+\alpha_\sigma\left(\frac{\lambda}{2\mu}\right)^2\left\|P_u^\perp\left[g\left(\boldsymbol{u},\left(\hat{\boldsymbol{\sigma}}_h-\boldsymbol{\sigma}\right)\right)\right]\right\|^2\\&+\alpha_\sigma\left(\frac{\lambda}{2\mu}\right)^2\left\|P_u^\perp\left[g\left(\boldsymbol{u},\boldsymbol{\sigma}\right)\right]\right\|^2+\alpha_\sigma\left(\frac{\lambda}{2\mu}\right)^2\left\|P_u^\perp\left[g\left(\left(\hat{\boldsymbol{u}}_h-\boldsymbol{u}\right),\boldsymbol{\sigma}\right)\right]\right\|^2,\end{aligned}$$

where the four terms of the right hand side can be bounded as

$$\begin{aligned}\left\|P_u^\perp\left[g\left(\left(\hat{\boldsymbol{u}}_h-\boldsymbol{u}\right),\left(\hat{\boldsymbol{\sigma}}_h-\boldsymbol{\sigma}\right)\right)\right]\right\|^2\lesssim&\left\|\nabla\left(\boldsymbol{u}-\boldsymbol{\mathcal{U}}\right)\cdot\left(\boldsymbol{\sigma}-\hat{\boldsymbol{\sigma}}_h\right)\right\|^2\\&+\left\|\nabla\left(\boldsymbol{\mathcal{U}}-\hat{\boldsymbol{u}}_h\right)\cdot\left(\boldsymbol{\sigma}-\hat{\boldsymbol{\sigma}}_h\right)\right\|^2\\\lesssim&\left(\left\|\boldsymbol{u}\right\|_3^2+h^{-d}\left\|\nabla\left(\boldsymbol{\mathcal{U}}-\hat{\boldsymbol{u}}_h\right)\right\|^2\right)\left\|\boldsymbol{\sigma}-\hat{\boldsymbol{\sigma}}_h\right\|^2\\\lesssim&\left(\left\|\boldsymbol{u}\right\|_3^2+h^{-d}\left(\left\|\nabla\left(\boldsymbol{\mathcal{U}}-\boldsymbol{u}\right)\right\|^2+\left\|\nabla\left(\boldsymbol{u}-\hat{\boldsymbol{u}}_h\right)\right\|^2\right)\right)\left\|\boldsymbol{\sigma}-\hat{\boldsymbol{\sigma}}_h\right\|^2\\\lesssim&\left(\left\|\boldsymbol{u}\right\|_3^2+h^{-d}\left(h^{2k}\left\|\boldsymbol{u}\right\|_{k+1}^2+\left\|\nabla\left(\boldsymbol{u}-\hat{\boldsymbol{u}}_h\right)\right\|^2\right)\right)\left\|\boldsymbol{\sigma}-\hat{\boldsymbol{\sigma}}_h\right\|^2,\\\left\|P_u^\perp\left[g\left(\boldsymbol{u},\left(\hat{\boldsymbol{\sigma}}_h-\boldsymbol{\sigma}\right)\right)\right]\right\|^2\lesssim&\left\|\nabla\boldsymbol{u}\right\|_\infty^2\left\|\boldsymbol{\sigma}-\hat{\boldsymbol{\sigma}}_h\right\|^2,\end{aligned}$$

$$\begin{aligned}
\left\|P_u^{\perp}\left[g\left(\boldsymbol{u},\boldsymbol{\sigma}\right)\right]\right\|^2 \lesssim & h^{2k}\left\|\nabla\boldsymbol{u}\cdot\boldsymbol{\sigma}\right\|_k^2 \\
\lesssim & \left(\left\|\boldsymbol{u}\right\|_{k+1}^2\left\|\boldsymbol{\sigma}\right\|_{\infty}^2\right. \\
& \left.+\sum_{i=1}^{k-1}\left\|\partial^{i+1}\nabla\boldsymbol{u}\right\|^2\left\|\partial^{k-i-1}\boldsymbol{\sigma}\right\|^2+\left\|\nabla\boldsymbol{u}\right\|_{\infty}^2\left\|\boldsymbol{\sigma}\right\|_k^2\right)h^{2k}, \\
\left\|P_u^{\perp}\left[g\left(\left(\hat{\boldsymbol{u}}_h-\boldsymbol{u}\right),\boldsymbol{\sigma}\right)\right]\right\|^2 \lesssim & \left\|\nabla\left(\hat{\boldsymbol{u}}_h-\boldsymbol{u}\right)\right\|^2\left\|\boldsymbol{\sigma}\right\|_{\infty}^2,
\end{aligned}$$

replacing this results in (7.64) and using (7.5), we have

$$\begin{aligned}
RHS \lesssim & \frac{\rho^2}{\mu}c_{PF}^2\int_0^t\left\|\partial_t\boldsymbol{\Lambda}\right\|^2+\frac{\lambda^2}{\mu}\int_0^t\left\|\partial_t\boldsymbol{\Gamma}\right\|^2+\frac{1}{\mu}\int_0^t\left\|\Pi\right\|^2 \\
& +\alpha_u^{-1}\int_0^t\left\|\boldsymbol{\Lambda}\right\|^2+\mu\int_0^t\left\|\nabla^s\boldsymbol{\Lambda}\right\|^2 \\
& +\frac{1}{\mu}\int_0^t\left\|\boldsymbol{\Gamma}\right\|^2+\frac{1}{\mu}\int_0^t\left\|\boldsymbol{\Gamma}\right\|^2+\mu\int_0^t\left\|\nabla^s\boldsymbol{\Lambda}\right\|^2 \\
& +\alpha_{\sigma}\int_0^t\left\|P_{\sigma}^{\perp}\left[\nabla^s\boldsymbol{\mathcal{U}}\right]\right\|^2+\alpha_p\int_0^t\left\|P_p^{\perp}\left[\nabla\cdot\boldsymbol{\mathcal{U}}\right]\right\|^2 \\
& +\alpha_u\int_0^t\left\|P_u^{\perp}\left[\nabla\mathcal{P}\right]\right\|^2+\alpha_u\int_0^t\left\|P_u^{\perp}\left[\nabla\cdot\boldsymbol{\Sigma}\right]\right\|^2 \\
& +\alpha_u\rho^2\int_0^t\left(\left\|\boldsymbol{u}-\hat{\boldsymbol{u}}_h\right\|^2C_{\infty,3}^2\left\|\boldsymbol{u}\right\|_3^2+\left(\left\|\boldsymbol{u}\right\|_{1,\infty}^2+\left\|\boldsymbol{u}\right\|_{\infty}^2\right)\left\|\boldsymbol{u}\right\|_{k+1}^2h^{2k}+\left\|\nabla\boldsymbol{u}\right\|_{\infty}^2\left\|\boldsymbol{u}-\hat{\boldsymbol{u}}_h\right\|^2\right) \\
& +\alpha_{\sigma}\left(\frac{\lambda}{\mu}\right)^2\int_0^t\left(\left\|\boldsymbol{u}-\hat{\boldsymbol{u}}_h\right\|^2C_{\infty,3}^2\left\|\boldsymbol{\sigma}\right\|_3^2+\left(\left\|\boldsymbol{u}\right\|_{1,\infty}^2+\left\|\boldsymbol{u}\right\|_{\infty}^2\right)\left\|\boldsymbol{\sigma}\right\|_{k+1}^2h^{2k}+\left\|\nabla\boldsymbol{\sigma}\right\|_{\infty}^2\left\|\boldsymbol{u}-\hat{\boldsymbol{u}}_h\right\|^2\right) \\
& +\alpha_{\sigma}\left(\frac{\lambda}{\mu}\right)^2\int_0^t\left(\left\|\boldsymbol{\sigma}\right\|_{\infty}^2\left\|\nabla\left(\boldsymbol{u}-\hat{\boldsymbol{u}}_h\right)\right\|^2+\left\|\nabla\boldsymbol{u}\right\|_{\infty}^2\left\|\boldsymbol{\sigma}-\hat{\boldsymbol{\sigma}}_h\right\|^2\right) \\
& +\alpha_{\sigma}\left(\frac{\lambda}{\mu}\right)^2\int_0^t\left(C_{\infty,3}^2\left\|\boldsymbol{u}\right\|_3^2+h^{-d}\left(h^{2k}\left\|\boldsymbol{u}\right\|_{k+1}^2+\left\|\nabla\left(\boldsymbol{u}-\hat{\boldsymbol{u}}_h\right)\right\|^2\right)\right)\left\|\boldsymbol{\sigma}-\hat{\boldsymbol{\sigma}}_h\right\|^2 \\
& +\alpha_{\sigma}\left(\frac{\lambda}{\mu}\right)^2\int_0^t\left(\left\|\boldsymbol{u}\right\|_{k+1}^2\left(\left\|\boldsymbol{\sigma}\right\|_{\infty}^2+h^2\left\|\nabla\boldsymbol{\sigma}\right\|_{\infty}^2\right)\right)h^{2k} \\
& +\frac{\lambda^2}{\mu}\int_0^t\left\|\nabla\boldsymbol{u}\right\|_{\infty}^2\left\|\boldsymbol{\sigma}-\hat{\boldsymbol{\sigma}}_h\right\|^2+\frac{\lambda^2}{\mu}h^{-d}\int_0^t\left\|\nabla\left(\boldsymbol{u}-\hat{\boldsymbol{u}}_h\right)\right\|^2\left\|\boldsymbol{\sigma}-\hat{\boldsymbol{\sigma}}_h\right\|^2 \\
& +\frac{\lambda^2}{\mu}\int_0^t\left\|\nabla\left(\boldsymbol{u}-\hat{\boldsymbol{u}}_h\right)\right\|^2\left\|\boldsymbol{\sigma}\right\|_{\infty}^2 \\
& +\int_0^t\left\|\boldsymbol{u}-\hat{\boldsymbol{u}}_h\right\|^2\frac{\rho^2}{\mu}\left(c_{\Omega}^2\left\|\nabla\boldsymbol{u}\right\|_{\infty}^2+\left\|\boldsymbol{u}\right\|_{\infty}^2\right) \\
& +\frac{\rho^2}{\mu}\int_0^t\left(c_{\Omega}^2\left\|\nabla\boldsymbol{\Lambda}\right\|^2+\left\|\boldsymbol{\Lambda}\right\|_1^2\right)\left(C_{L^4}^{H^1}\right)^4\left\|\boldsymbol{u}-\hat{\boldsymbol{u}}_h\right\|_1^2 \\
& +\rho^2\frac{1}{\mu}\int_0^t\left\|\boldsymbol{u}\right\|_{\infty}^2\left\|\boldsymbol{\Lambda}\right\|^2 \\
& +\frac{\lambda^2}{\mu}\int_0^t\left(\left\|\boldsymbol{u}-\hat{\boldsymbol{u}}_h\right\|^2\left\|\nabla\boldsymbol{\sigma}\right\|_{\infty}^2+\left\|\nabla\left(\boldsymbol{u}-\hat{\boldsymbol{u}}_h\right)\right\|^2\left\|\boldsymbol{\sigma}\right\|_{\infty}^2\right) \\
& +\frac{\lambda^2}{\mu}\left(C_{L^4}^{H^1}\right)^2\int_0^t\left(h^{-\frac{d}{2}}\left\|\nabla\boldsymbol{\Gamma}\right\|^2+\left(C_{L^4}^{H^1}\right)^2\frac{c_{inv}^2}{h^2}\left\|\boldsymbol{\Gamma}\right\|_1^2\right)\left\|\boldsymbol{u}-\hat{\boldsymbol{u}}_h\right\|_1^2 \\
& +\frac{\lambda^2}{\mu}\int_0^t\left\|\boldsymbol{u}\right\|_{\infty}^2\left\|\nabla\boldsymbol{\Gamma}\right\|^2 \\
& +\alpha_u\rho^2\int_0^t\left(\sum_{i=1}^{k-1}\left\|\partial^{i+1}\boldsymbol{u}\right\|^2\left\|\partial^{k-i-1}\nabla\boldsymbol{u}\right\|^2\right)h^{2k}
\end{aligned}$$

$$+\alpha_\sigma\left(\frac{\lambda}{2\mu}\right)^2\int_0^t\left(\sum_{i=1}^{k-1}\left\|\partial^{i+1}\boldsymbol{u}\right\|^2\left\|\partial^{k-i-1}\nabla\boldsymbol{\sigma}\right\|^2\right)h^{2k}$$
$$+\alpha_\sigma\left(\frac{\lambda}{2\mu}\right)^2\int_0^t\left(\sum_{i=1}^{k-1}\left\|\partial^{i+1}\nabla\boldsymbol{u}\right\|^2\left\|\partial^{k-i-1}\boldsymbol{\sigma}\right\|^2\right)h^{2k},$$

regrouping terms, using the definition of the ball (7.55) and the interpolation inequality (7.6), we can write the final result for the right hand side terms

$$\begin{aligned}
RHS\lesssim&\frac{\rho^2}{\mu}c_{PF}^2\int_0^t\|\partial_t\boldsymbol{u}\|_k^2h^{2k}+\frac{\lambda^2}{\mu}\int_0^t\|\partial_t\boldsymbol{\sigma}\|_k^2h^{2k}\\
&+\frac{1}{\mu}\left(1+\alpha_u\frac{\mu}{h^2}\right)\int_0^t\|p\|_k^2h^{2k}\\
&+\mu\left(\alpha_u^{-1}\frac{h^2}{\mu}+\frac{\alpha_p}{\mu}+\left(\frac{\rho\|\boldsymbol{u}\|_\infty h}{\mu}\right)^2+\frac{\alpha_\sigma}{\mu}\left(\lambda\|\boldsymbol{\sigma}\|_{1,\infty}\right)^2+\alpha_u\frac{\mu}{h^2}\left(\frac{\rho h\|\boldsymbol{u}\|_{1,\infty}}{\mu}\right)^2\right)\int_0^t\|\boldsymbol{u}\|_{k+1}^2h^{2k}\\
&+\frac{1}{\mu}h^2\left(1+\alpha_u\frac{\mu}{h^2}+\left(\frac{\lambda\|\boldsymbol{u}\|_\infty}{h}\right)^2+\frac{\alpha_\sigma}{\mu}\left(\frac{\lambda}{h}\right)^2\|\boldsymbol{u}\|_{1,\infty}^2\right)\int_0^t\|\boldsymbol{\sigma}\|_{k+1}^2h^{2k}\\
&+\frac{\rho^2}{\mu}\left(\mu\alpha_u\left(\left(C_{\infty,3}\|\boldsymbol{u}\|_3\right)^2+\|\nabla\boldsymbol{u}\|_\infty^2\right)+\left(c_\Omega^2\|\nabla\boldsymbol{u}\|_\infty^2+\|\boldsymbol{u}\|_\infty^2\right)\right)\int_0^t u_\star^2R^2\\
&+\alpha_\sigma\left(\frac{\lambda}{\mu}\right)^2\left(\left(C_{\infty,3}\|\boldsymbol{\sigma}\|_3\right)^2+\|\nabla\boldsymbol{\sigma}\|_\infty^2+\frac{1}{L_d^2}\|\boldsymbol{\sigma}\|_\infty^2\right)\int_0^t u_\star^2R^2\\
&+\frac{1}{\mu}\left[\left(1+\frac{\alpha_\sigma}{\mu}\right)\left(\lambda\|\nabla\boldsymbol{u}\|_\infty\right)^2+\frac{\alpha_\sigma}{\mu}\left(\lambda C_{\infty,3}\|\boldsymbol{u}\|_3\right)^2\right]\int_0^t\sigma_\star^2R^2\\
&+\alpha_\sigma\left(\frac{\lambda}{\mu}\right)^2\int_0^t\|\boldsymbol{u}\|_{k+1}^2\sigma_\star^2\left(h^{2k-d}\right)R^2\\
&+\frac{\lambda^2}{\mu}\left(1+\frac{\alpha_\sigma}{\mu}\right)\int_0^t\frac{1}{L_d^2}u_\star^2\sigma_\star^2\left(h^{-d}R^2\right)R^2\\
&+\mu\int_0^t\left(\frac{\rho\|\boldsymbol{u}\|_{k+1}c_\Omega}{\mu}\right)^2u_\star^2\left(\left(C_{L^4}^{H^1}\right)^4h^{2k}\right)R^2\\
&+\frac{1}{\mu}\int_0^t\lambda^2\|\boldsymbol{\sigma}\|_{k+1}^2u_\star^2\left(\left(C_{L^4}^{H^1}\right)^2h^{2k-\frac{d}{2}}+\left(C_{L^4}^{H^1}\right)^4c_\Omega^2h^{2k-2}\right)R^2\\
&+\alpha_u\rho^2\int_0^t\left(\sum_{i=1}^{k-1}\left\|\partial^{i+1}\boldsymbol{u}\right\|^2\left\|\partial^{k-i-1}\nabla\boldsymbol{u}\right\|^2\right)h^{2k}\\
&+\alpha_\sigma\left(\frac{\lambda}{2\mu}\right)^2\int_0^t\left(\sum_{i=1}^{k-1}\left\|\partial^{i+1}\boldsymbol{u}\right\|^2\left\|\partial^{k-i-1}\nabla\boldsymbol{\sigma}\right\|^2+\sum_{i=1}^{k-1}\left\|\partial^{i+1}\nabla\boldsymbol{u}\right\|^2\left\|\partial^{k-i-1}\boldsymbol{\sigma}\right\|^2\right)h^{2k}.
\end{aligned}\tag{7.65}$$

As we can see, five types of terms that involve h power are involved in (7.65). The first group is multiplied by h^{2k}, the second group by R^2, a third group is multiplied by $h^{2k-\frac{d}{2}}$ and the last two are multiplied by $\left(h^{2k-d}\right)R^2$ and $\left(h^{-d}R^2\right)R^2$, respectively. Since $k\geq 2$, then all the terms are, al least, of the order h^{2k}.

Step 4. Since $k\geq 2$, we can take $D_1,...,D_9$ in (7.50) and h small enough in such a way that

$$\sup_{0\leq t\leq T}\|\boldsymbol{u}-\boldsymbol{u}_h\|^2+\int_0^t\left(L_d\|\nabla\left(\boldsymbol{u}-\boldsymbol{u}_h\right)\|\right)^2dt\lesssim\tilde{C}h^{2k}$$

where $\tilde{C}<c^*u_\star$,

$$\sup_{0\leq t\leq T}\|\boldsymbol{\sigma}-\boldsymbol{\sigma}_h\|^2\lesssim\hat{C}h^{2k},$$

where $\hat{C} < c^* \sigma_\star$, and

$$\int_0^t \left(\frac{h^2}{\mu + \rho u_\star^2 h^{k+1-\frac{d}{6}} + \rho h \|\boldsymbol{u}\|_1} \right) \left\| P_u^\perp \left[\nabla \left(p - p_h \right) \right] \right\|^2 dt \lesssim \check{C} h^{2k}$$

where $\check{C} < c^* p_\star$. This shows that $\delta\left(\mathcal{B}_h\right) \subset \mathcal{B}_h$, and then appliying Schauder's fixed point theorem, there exist $(\boldsymbol{u}_h, p_h, \boldsymbol{\sigma}_h) \in \mathcal{B}_h$, solution of (7.23). This prove the error estimate since the definition of the ball is exactly the error estimate (7.51).□

7.8 Conclusions

In this chapter we have presented the numerical analysis of the finite element approximation proposed in Chapter 3 for the nonlinear time-dependent case. This analysis has confirmed the numerical results obtained in Chapter 3, where the method was proposed and tested numerically using nonlinear examples. In particular, we have shown this using a fixed point theorem under suitable regularity conditions in velocity, stress and pressure. What is relevant from the analysis presented is that it clearly displays how the estimates obtained deteriorate as the Reynolds number and the elasticity of the fluid increase, which is the expected result in this type of fluids.

Chapter 8

Conclusions

In this chapter we present the achievements and conclusions obtained during the preparation of the present work, and we state some of the possible future research lines.

8.1 Achievements

In the above chapters, we have presented a series of works in the context of stabilized finite element methods applied to non-Newtonian fluid flows. An important point of these works resides in the fact that in all of them, a mixed or a three-field formulation is used.

- In Chapter 2, two stabilized numerical formulation of sub-grid-scale (SGS) type were proposed and tested numerically for the three-field (velocity-pressure-stress) Navier-Stokes problem considering nonlinear viscosity models. Both formulations present optimal convergence properties for linear and quadratic elements, also evidencing a clear reduction in the L^2-norm of the error when approximating a problem with analytical solution with respect to the two-field (velocity-pressure) formulation. The numerical results presented in this chapter serve to demonstrate the feasibility of the finite element formulation proposed to approximate the three-field Navier-Stokes problem, both in situations in which the viscosity is highly nonlinear and in convection dominated flows, using equal interpolation spaces for all the unknowns.

- In Chapter 3, we have introduced stabilized finite element methods for the viscoelastic flow problem based on the sub-grid-scale concept. Starting from residual-based formulations for the momentum and the continuity equations, we have moved to the use of a split orthogonal sub-grid scale technique for them. We have observed a better behavior of this approach in regions where the solution displays high gradients. For the approximation of the constitutive equation, classical residual-based stabilization works well. Although stabilized methods allow one to obtain globally stable solutions using equal interpolation for all the unknowns and to treat convection-dominated problems, node-to-node oscillations in the viscoelastic stress components and the pressure in regions of high gradients may still remain. A discontinuity-capturing technique has been introduced to remove them. The resulting formulations are accurate, showing optimal convergence properties for smooth solutions, and robust, able to deal with high gradients of the unknowns appearing at geometrical singularities in viscoelastic flow problems.

- In Chapter 4, we have presented three different fractional step methods of first, second and third order in time to solve the viscoelastic fluid flow problem. The final schemes

allow one to solve the problem in a fully decoupled form, where each equation is solved separately. The efficiency of the fractional step formulations has been tested in dynamic problems in 2D and 3D, showing an important reduction in the CPU time with respect to the monolithic case for the three formulations. The splitting of the equations yields a problem that requires less nonlinear iterations per time step than the monolithic method, and the maximum number of linear solver iterations is only needed for the slowest variable, pressure in the incompressible flows considered.

- In Chapter 5, all the numerical ingredients proposed in the above chapters were tested in a complex problem. In this chapter, we have presented a stabilized finite element method to solve the two immiscible fluid flow problem by the level set method for Oldroyd-B and Giesekus fluids. The method shows very good stability and robustness even using the standard formulation of the elastic stress tensor, instead of a logarithmic one. For the case of two immiscible fluids, the discontinuity in the material properties when the interface cuts an element leads to discontinuities in the gradients of the unknowns that standard interpolations cannot capture. A local pressure enriched function was tested to solve the interaction of viscoelastic and Newtonian fluids with very good results, correcting the amount of lost mass, and permitting the exact resolution of the hydrostatic rest state that standard formulations cannot solve. The fractional step approach proposed in Chapter 4 was used to solve the two immiscible fluid flow problem, showing an important reduction in computational resources with respect to the monolithic case. The discontinuity-capturing technique for the constitutive equation, proposed in Chapter 3, was tested in order to eliminate non-physical peaks that can appear when the flow hits an obstacle with very satisfactory results.

- In Chapter 6, we have presented the numerical analysis of the finite element approximation proposed in Chapter 3 for the linearized stationary viscoelastic flow problem. This analysis has confirmed what it was already known from the numerical experiments, namely, that the method provides stable solutions that converge to the exact solutions at an optimal rate of convergence. In particular, we have shown this using a mesh dependent norm especially tailored for the stabilized problem and also the norm of the space where the continuous problem is posed. What is relevant from the analysis presented is that it clearly displays how the estimates obtained deteriorate as the cell Reynolds number and the cell Weissenberg number increase. The former decreases when the mesh size is reduced, but the having a bound on the latter imposes the relaxation time to be very small, which is an indication of the existence of the so called high Weissenberg number problem.

- In Chapter 7, we have presented the numerical analysis of the finite element approximation proposed in Chapter 3 for the nonlinear time-dependent case. This analysis has confirmed the numerical results obtained in Chapter 3, where the method was proposed and tested numerically using nonlinear examples. In particular, we have shown this using a fixed point theorem under suitable regularity conditions in velocity, stress and pressure. What is relevant from the analysis presented is that it clearly displays how the estimates obtained deteriorate as the Reynolds number and the elasticity of the fluid increase, which is the expected result in this type of fluids.

8.2 Future work

Viscoelastic fluids have very advantageous properties for heat transfer and transport, because they have an increased mixing capacity and as a consequence heat transfer coefficients are increased. Also, pressure losses are reduced in the transport of viscoelastic fluids, which

allows to diminish the cost associated to the pumping or transport of the fluid. In this framework, many developments can be done could be developed starting from the work presented in this thesis to attempt to exploit this properties from the numerical point of view and apply them in the optimization of industrial processes.

Possible future research lines are:

Thermal Coupling

In general, viscoelastic flows can be considered as incompressible, the most widely used model in the context of thermally coupled flows is the so called Boussinesq approximation. The extension to the thermally coupled problem could perfectly be the first future research line, and many applications framed in the context of thermal radiators are interesting both in the numerical framework and in the applied world.

Elastic-Turbulence

In general, two parallel research lines have been followed in the development of mathematical models for viscous turbulence and in their numerical approximation. On the one hand, the so called "large eddy simulation" (LES) models are based on a decomposition of the unknown into a "macroscopic" scale and another one that can be called *microscopic*, often called subscale. An equation for the former is then set, although accounting for the effects of the latter. However, precisely the same idea is the ground for some of the so called "stabilisation methods" based on the VMS concept. In recent works [60, 62] these two theories were unified for the problem of viscous turbulence by using a series of stabilized finite element formulations capable of accurately reproducing the Kolmogorov energy cascade in Newtonian fluids. The same ideas can be applied to the problem of elastic turbulence extending the proposed formulations.

Two-fluids problems

In typical finite element methods, the gradient of the shape functions is continuous within each element and therefore the gradient of the unknown is also continuous. If the interface cuts an element, the discontinuity in the material properties when solving a two immiscible fluid flow problems leads to discontinuities in the gradients of the unknowns which cannot be captured with standard finite element interpolations. In Chapter 5, an enrichment for the pressure field was implemented to deal with different density fluids. A similar approach could be developed to deal with the stress discontinuities associated to different viscosity values.

Log-conformation tensor approach

The high Weissenberg number problem (HWNP) has been the major stumbling block in computational rheology in the last few years. In essence, it is a numerical instability caused by the failure to balance the exponential growth of the stress with convection. The failure, is common to all methods that approximate the elastic stresses by polynomial base functions. A possible remedy to this situation, proposed by Fattal and Kupferman [80] is associated to a change of variables into new variables that scale logarithmically with the stress tensor. Specifically, the constitutive relations must be reformulated as equations for the matrix logarithm of the conformation tensor, using the fact that this tensor is symmetric positive definite. A natural future work, would be to extend our variational multiscale formulations to the log-conformation case.

Fractional step: velocity correction schemes

In Chapter 4, three different fractional step schemes were proposed. All of them can be understood as pressure extrapolation algorithms. Another family of fractional step schemes can be designed using the velocity segregation approach, which permits a second order extrapolation of the velocity, thus avoiding the unstable pressure extrapolation. A comprehensive review of this type of fractional step methods can be found in the work of Badia and Codina [11] in the context of Newtonian fluids.

Numerical Analysis

In Chapters 6 and 7, some results from the numerical analysis were presented for the stationary linearized case and for the time-dependent non-linear semi-discrete one. However, the fully-discrete analysis is still remaining. Another interesting work would be the study of long-term stability estimates and the existence of some global attractor associated to the stabilized finite element approximation, following an approach similar to the used in [14] for the Navier-Stokes problem.

Bibliography

[1] M. Aboubacar and M. Webster. A cell-vertex finite volume/element method on triangles for abrupt contraction viscoelastic flows. *Journal of Non-Newtonian Fluid Mechanics*, 98(2-3):83–106, 2001.

[2] A. Afonso, P. Oliveira, F. Pinho, and M. Alves. The log-conformation tensor approach in the finite-volume method framework. *Journal of Non-Newtonian Fluid Mechanics*, 157(1-2):55–65, 2009.

[3] M. Alves, F. Pinho, and P. Oliveira. Effect of a high-resolution differencing scheme on finite-volume predictions of viscoelastic flows. *Journal of Non-Newtonian Fluid Mechanics*, 93(2-3):287–314, 2000.

[4] M. Alves, F. Pinho, and P. Oliveira. The flow of viscoelastic fluids past a cylinder: finite-volume high-resolution methods. *Journal of Non-Newtonian Fluid Mechanics*, 97(2-3):207–232, 2001.

[5] M. A. Alves, P. J. Oliveira, and F. T. Pinho. Benchmark solutions for the flow of Oldroyd-B and PTT fluids in planar contractions. *Journal of Non-Newtonian Fluid Mechanics*, 110(1):45–75, 2003.

[6] M. Avila, J. Principe, and R. Codina. A finite element dynamical nonlinear subscale approximation for the low Mach number flow equations. *Journal of Computational Physics*, 230(22):7988–8009, 2011.

[7] F. P. Baaijens. Application of low-order Discontinuous Galerkin methods to the analysis of viscoelastic flows. *Journal of Non-Newtonian Fluid Mechanics*, 52:37–57, 1994.

[8] F. P. Baaijens. Mixed finite element methods for viscoelastic flow analysis: a review. *Journal of Non-Newtonian Fluid Mechanics*, 79(2-3):361–385, 1998.

[9] F. P. T. Baaijens, M. A. Hulsen, and P. D. Anderson. *The Use of Mixed Finite Element Methods for Viscoelastic Fluid Flow Analysis*. John Wiley & Sons, Ltd, 2004.

[10] S. Badia. On stabilized finite element methods based on the Scott-Zhang projector. Circumventing the inf-sup condition for the Stokes problem. *Computer Methods in Applied Mechanics and Engineering*, 247-248(0):65–72, 2012.

[11] S. Badia and R. Codina. Algebraic pressure segregation methods for the incompressible Navier-Stokes equations. *Archives of Computational Methods in Engineering*, 15:343–369, 2008.

[12] S. Badia and R. Codina. Pressure segregation methods based on a discrete pressure Poisson equation. An algebraic approach. *International Journal for Numerical Methods in Fluids*, 56:351–382, 2008.

[13] S. Badia and R. Codina. On a multiscale approach to the transient Stokes problem: Dynamic subscales and anisotropic space-time discretization. *Applied Mathematics and Computation*, 207(2):415–433, 2009.

[14] S. Badia, R. Codina, and J. V. Gutiérrez-Santacreu. Long-term stability estimates and existence of a global attractor in a finite element approximation of the Navier-Stokes equations with numerical subgrid scale modeling. *SIAM Journal on Numerical Analysis*, 48(3):1013–1037, 2010.

[15] T. K. Bandyopadhyay and S. K. Das. Non-Newtonian pseudoplastic liquid flow through small diameter piping components. *Journal of Petroleum Science and Engineering*, 55(1-2):156–166, 2007.

[16] J. Baranger and D. Sandri. Finite element approximation of viscoelastic fluid flow: Existence of approximate solutions and error bounds. *Numerische Mathematik*, 63(1):13–27, 1992.

[17] J. Baranger and S. Wardi. Numerical analysis of a FEM for a transient viscoelastic flow. *Computer Methods in Applied Mechanics and Engineering*, 125(1-4):171–185, 1995.

[18] R. Becker and M. Braack. A finite element pressure gradient stabilization for the Stokes equations based on local projections. *CALCOLO*, 38(4):173–199, 2001.

[19] M. A. Behr, L. P. Franca, and T. E. Tezduyar. Stabilized finite element methods for the velocity-pressure-stress formulation of incompressible flows. *Computer Methods in Applied Mechanics and Engineering*, 104(1):31–48, 1993.

[20] R. P. Bharti, R. P. Chhabra, and V. Eswaran. Steady flow of power law fluids across a circular cylinder. *The Canadian Journal of Chemical Engineering*, 84(4):406–421, 2006.

[21] R. B. Bird, R. C. Amstrong, and O. Hassager. *Dynamics of Polymeric Liquids, vol.1: Fluid Mechanics*. Wiley, New York, 2nd edition, 1987.

[22] R. B. Bird, R. C. Amstrong, and O. Hassager. *Dynamics of Polymeric Liquids, vol.2: Kinetic Theory*. Wiley, New York, 2nd edition, 1987.

[23] R. B. Bird, W. E. Stewart, and E. N. Lightfoot. *Transport Phenomena*. Wiley, New York, 2002.

[24] J. Blasco and R. Codina. Error estimates for an operator splitting method for incompressible flows. *Applied Numerical Mathematics*, 51:1–17, 2004.

[25] A. C. Bogaerds, W. M. Verbeeten, G. W. Peters, and F. P. Baaijens. 3d viscoelastic analysis of a polymer solution in a complex flow. *Computer Methods in Applied Mechanics and Engineering*, 180(3-4):413–430, 1999.

[26] A. Bonito and E. Burman. A continuous interior penalty method for viscoelastic flows. *SIAM Journal on Scientific Computing*, 30(3):1156–1177, 2007.

[27] A. Bonito, P. Clément, and M. Picasso. Mathematical and numerical analysis of a simplified time-dependent viscoelastic flow. *Numerische Mathematik*, 107(2):213–255, 2007.

[28] A. Bonito, M. Picasso, and M. Laso. Numerical simulation of 3D viscoelastic flows with free surfaces. *Journal of Computational Physics*, 215(2):691–716, 2006.

[29] J. Bonvin, M. Picasso, and R. Stenberg. GLS and EVSS methods for a three-field Stokes problem arising from viscoelastic flows. *Computer Methods in Applied Mechanics and Engineering*, 190(29-30):3893–3914, 2001.

[30] F. Brezzi and M. Fortin. Variational formulations and finite element methods. In F. Brezzi and M. Fortin, editors, *Mixed and Hybrid Finite Element Methods*, volume 15 of *Springer Series in Computational Mathematics*, pages 1–35. Springer New York, 1991.

[31] A. N. Brooks and T. J. Hughes. Streamline Upwind/Petrov-Galerkin formulations for convection dominated flows with particular emphasis on the incompressible Navier-Stokes equations. *Computer Methods in Applied Mechanics and Engineering*, 32(1-3):199–259, 1982.

[32] E. Burman and M. A. Fernández. Continuous interior penalty finite element method for the time-dependent Navier-Stokes equations: space discretization and convergence. *Numerische Mathematik*, 107(1):39–77, 2007.

[33] E. Carew, P. Townsend, and M. Webster. On a discontinuity capturing technique for Oldroyd-B fluids. *Journal of Non-Newtonian Fluid Mechanics*, 51(2):231–238, 1994.

[34] P. J. Carreau and R. P. Chhabra. In *Rheology of Polymeric Systems: Principles and Applications*. Hanser, Munich, second edition, 1997.

[35] E. Castillo, J. Baiges, and R. Codina. Approximation of the two-fluid flow problem for viscoelastic fluids using the level set method and pressure enriched finite element shape functions. *Journal of Non-Newtonian Fluid Mechanics*, 225:37–53, 2015.

[36] E. Castillo and R. Codina. Stabilized stress-velocity-pressure finite element formulations of the Navier-Stokes problem for fluids with non-linear viscosity. *Computer Methods in Applied Mechanics and Engineering*, 279:554–578, 2014.

[37] E. Castillo and R. Codina. Variational multi-scale stabilized formulations for the stationary three-field incompressible viscoelastic flow problem. *Computer Methods in Applied Mechanics and Engineering*, 279:579–605, 2014.

[38] E. Castillo and R. Codina. First, second and third order fractional step methods for the three-field viscoelastic flow problem. *Journal of Computational Physics*, 296:113–137, 2015.

[39] E. Castillo and R. Codina. Finite element approximation of the viscoelastic flow problem: A non-residual based stabilized formulation. *Computers & Fluids*, 2016. Accepted for publication.

[40] E. Castillo and R. Codina. Numerical analysis of a stabilized finite element approximation for the three-field linearized viscoelastic fluid problem using arbitrary interpolations. 2016. Submitted.

[41] M. Cervera, M. Chiumenti, and R. Codina. Mixed stabilized finite element methods in nonlinear solid mechanics. Part I: Formulation. *Computer Methods in Applied Mechanics and Engineering*, 199:2559–2570, 2010.

[42] J. Chen, X.-Y. Lu, and W. Wang. Non-Newtonian effects of blood flow on hemodynamics in distal vascular graft anastomoses. *Journal of Biomechanics*, 39(11):1983–1995, 2006.

[43] J. Chessa and T. Belytschko. An Extended Finite Element Method for Two-Phase Fluids. *Journal of Applied Mechanics*, 70:10–17, 2003.

[44] R. P. Chhabra and J. F. Richardson. In *Non-Newtonian Flow and Applied Rheology*. Elsevier Butterworth-Heinemann, second edition, 2008.

[45] H. Choi, H. Choi, and J. Yoo. A fractional four-step finite element formulation of the unsteady incompressible Navier-Stokes equations using SUPG and linear equal-order element methods. *Computer Methods in Applied Mechanics and Engineering*, 143:333–348, 1997.

[46] A. J. Chorin. A numerical method for solving incompressible viscous flow problems. *Journal of Computational Physics*, 2:12–26, 1967.

[47] J. Chrispell, V. Ervin, and E. Jenkins. A fractional step θ-method approximation of time-dependent viscoelastic fluid flow. *Journal of Computational and Applied Mathematics*, 232:159–175, 2009.

[48] P. G. Ciarlet. *Linear and Nonlinear Functional Analysis with Applications*. Society for Industrial and Applied Mathematics (SIAM), Philadelphia, PA, USA, 2013.

[49] R. Codina. A discontinuity-capturing crosswind-dissipation for the finite element solution of the convection-diffusion equation. *Computer Methods in Applied Mechanics and Engineering*, 110(3-4):325–342, 1993.

[50] R. Codina. Comparison of some finite element methods for solving the diffusion-convection-reaction equation. *Computer Methods in Applied Mechanics and Engineering*, 156(1-4):185–210, 1998.

[51] R. Codina. Stabilization of incompressibility and convection through orthogonal subscales in finite element methods. *Computer Methods in Applied Mechanics and Engineering*, 190(13-14):1579–1599, 2000.

[52] R. Codina. Pressure stability in fractional step finite element methods for incompressible flows. *Journal of Computational Physics*, 170:112–140, 2001.

[53] R. Codina. A stabilized finite element method for generalized stationary incompressible flows. *Computer Methods in Applied Mechanics and Engineering*, 190(20-21):2681–2706, 2001.

[54] R. Codina. Stabilized finite element approximation of transient incompressible flows using orthogonal subscales. *Computer Methods in Applied Mechanics and Engineering*, 191(39-40):4295–4321, 2002.

[55] R. Codina. Analysis of a stabilized finite element approximation of the Oseen equations using orthogonal subscales. *Applied Numerical Mathematics*, 58(3):264–283, 2008.

[56] R. Codina. Finite element approximation of the three-field formulation of the Stokes problem using arbitrary interpolations. *SIAM Journal on Numerical Analysis*, 47(1):699–718, 2009.

[57] R. Codina and S. Badia. On some pressure segregation methods of fractional-step type for the finite element approximation of incompressible flow problems. *Computer Methods in Applied Mechanics and Engineering*, 195(23-24):2900–2918, 2006.

[58] R. Codina and J. Principe. Dynamic subscales in the finite element approximation of thermally coupled incompressible flows. *International Journal for Numerical Methods in Fluids*, 54:707–730, 2007.

[59] R. Codina, J. Principe, and J. Baiges. Subscales on the element boundaries in the variational two-scale finite element method. *Computer Methods in Applied Mechanics and Engineering*, 198(5-8):838–852, 2009.

[60] R. Codina, J. Principe, O. Guasch, and S. Badia. Time dependent subscales in the stabilized finite element approximation of incompressible flow problems. *Computer Methods in Applied Mechanics and Engineering*, 196(21-24):2413–2430, 2007.

[61] R. Codina and O. Soto. A numerical model to track two-fluid interfaces based on a stabilized finite element method and the level set technique. *International Journal for Numerical Methods in Fluids*, 4:293–301, 2002.

[62] O. Colomés, S. Badia, R. Codina, and J. Principe. Assessment of variational multiscale models for the large eddy simulation of turbulent incompressible flows. *Computer Methods in Applied Mechanics and Engineering*, 285:32–63, 2015.

[63] A. H. Coppola-Owen and R. Codina. Improving Eulerian two-phase flow finite element approximation with discontinuous gradient pressure shape functions. *International Journal for Numerical Methods in Fluids*, 49(12):1287–1304, 2005.

[64] O. M. Coronado, D. Arora, M. Behr, and M. Pasquali. Four-field Galerkin/least-squares formulation for viscoelastic fluids. *Journal of Non-Newtonian Fluid Mechanics*, 140(1-3):132–144, 2006.

[65] M. Cruchaga, L. Battaglia, M. Storti, and J. D'Elía. Numerical modeling and experimental validation of free surface flow problems. *Archives of Computational Methods in Engineering*, pages 1–31, 2014.

[66] M. Cruchaga, D. Celentano, and T. Tezduyar. Collapse of a liquid column: Numerical simulation and experimental validation. *Computational Mechanics*, 39(4):453–476, 2007.

[67] M. A. Cruchaga, D. J. Celentano, and R. W. Lewis. Modelling of twin-roll strip casting processes. *Communications in Numerical Methods in Engineering*, 19(8):623–635, 2003.

[68] J. O. Cruickshank and B. R. Munson. Viscous fluid buckling of plane and axisymmetric jets. *Journal of Fluid Mechanics*, 113:221–239, 12 1981.

[69] H. Damanik, J. Hron, A. Ouazzi, and S. Turek. A monolithic FEM approach for the log-conformation reformulation LCR of viscoelastic flow problems. *Journal of Non-Newtonian Fluid Mechanics*, 165:1105–1113, 2010.

[70] G. D'Avino and M. Hulsen. Decoupled second-order transient schemes for the flow of viscoelastic fluids without a viscous solvent contribution. *Journal of Non-Newtonian Fluid Mechanics*, 165:1602–1612, 2010.

[71] G. D'Avino, M. Hulsen, and P. Maffettone. Decoupled transient schemes for viscoelastic fluid flow with inertia. *Computers & Fluids*, 66:183–193, 2012.

[72] J. Donea. A Taylor-Galerkin method for convective transport problems. *International Journal for Numerical Methods in Engineering*, 20(1):101–119, 1984.

[73] H.-S. Dou and N. Phan-Thien. The flow of an Oldroyd-B fluid past a cylinder in a channel: adaptive viscosity vorticity DAVSS-w formulation. *Journal of Non-Newtonian Fluid Mechanics*, 87:47–73, 1999.

[74] J. Douglas, Jr. and T. Russell. Numerical methods for convection-dominated diffusion problems based on combining the method of characteristics with finite element or finite difference procedures. *SIAM Journal on Numerical Analysis*, 19(5):871–885, 1982.

[75] A. Ern and J.-L. Guermond. *Theory and Practice of Finite Elements*, volume 159 of *Applied Mathematical Sciences*. Springer-Verlag New York, 1st edition, 2004.

[76] V. J. Ervin, H. K. Lee, and L. N. Ntasin. Analysis of the Oseen-viscoelastic fluid flow problem. *Journal of Non-Newtonian Fluid Mechanics*, 127(2-3):157–168, 2005.

[77] V. J. Ervin and W. W. Miles. Approximation of time-dependent viscoelastic fluid flow: SUPG approximation. *SIAM Journal on Numerical Analysis*, 41(2):457–486, 2003.

[78] V. J. Ervin and W. W. Miles. Approximation of time-dependent, multi-component, viscoelastic fluid flow. *Computer Methods in Applied Mechanics and Engineering*, 194(18-20):2229–2255, 2005.

[79] Y. Fan, R. Tanner, and N. Phan-Thien. Galerkin/least-square finite-element methods for steady viscoelastic flows. *Journal of Non-Newtonian Fluid Mechanics*, 84(2-3):233–256, 1999.

[80] R. Fattal and R. Kupferman. Constitutive laws for the matrix-logarithm of the conformation tensor. *Journal of Non-Newtonian Fluid Mechanics*, 123(2-3):281–285, 2004.

[81] R. Fattal and R. Kupferman. Time-dependent simulation of viscoelastic flows at high Weissenberg number using the log-conformation representation. *Journal of Non-Newtonian Fluid Mechanics*, 126(1):23–37, 2005.

[82] E. Fernández-Cara, F. Guillén, and R. Ortega. *Mathematical modeling and analysis of viscoelastic fluids of the Oldroyd kind,* in Handbook of Numerical Analysis, VIII. North-Holland, 2002.

[83] R. Figueiredo, C. Oishi, J. Cuminato, and M. Alves. Three-dimensional transient complex free surface flows: Numerical simulation of XPP fluid. *Journal of Non-Newtonian Fluid Mechanics*, 195(0):88–98, 2013.

[84] M. Fortin and A. Fortin. A new approach for the FEM simulation of viscoelastic flows. *Journal of Non-Newtonian Fluid Mechanics*, 32(3):295–310, 1989.

[85] M. Fortin and R. Pierre. On the convergence of the mixed method of Crochet and Marchal for viscoelastic flows. *Computer Methods in Applied Mechanics and Engineering*, 73(3):341–350, 1989.

[86] P. Gervasio, F. Saleri, and A. Veneziani. Algebraic fractional-step schemes with spectral methods for the incompressible Navier-Stokes equations. *Journal of Computational Physics*, 214:347–365, 2006.

[87] V. Girault and P.-A. Raviart. *Finite Elements for the Navier Stokes Equations.* Springer-Verlag Berlin, 1986.

[88] R. Glowinsky and O. Pironneau. Finite-element methods for Navier-Stokes equations. *Ann. Rev. Fluid Mech.*, 24:164–204, 1992.

[89] R. Guénette and M. Fortin. A new mixed finite element method for computing viscoelastic flows. *Journal of Non-Newtonian Fluid Mechanics*, 60(1):27–52, 1995.

[90] J. Guermond, P. Minev, and J. Shen. An overview of projection methods for incompressible flows. *Computer Methods in Applied Mechanics and Engineering*, 195:6011–6045, 2006.

[91] C. Guillopé and J. Saut. Existence results for the flow of viscoelastic fluids with a differential constitutive law. *Nonlinear Analysis: Theory, Methods & Applications*, 15(9):849–869, 1990.

[92] F. Habla, M. W. Tan, J. Haßlberger, and O. Hinrichsen. Numerical simulation of the viscoelastic flow in a three-dimensional lid-driven cavity using the log-conformation reformulation in OpenFOAM. *Journal of Non-Newtonian Fluid Mechanics*, 212(0):47–62, 2014.

[93] D. M. Hall, T. Lookman, G. H. Fredrickson, and S. Banerjee. Numerical method for hydrodynamic transport of inhomogeneous polymer melts. *Journal of Computational Physics*, 224(2):681–698, 2007.

[94] J. S. Howell. Computation of viscoelastic fluid flows using continuation methods. *Journal of Computational and Applied Mathematics*, 225(1):187–201, 2009.

[95] J. S. Howell. Dual-mixed finite element approximation of Stokes and nonlinear Stokes problems using trace-free velocity gradients. *Journal of Computational and Applied Mathematics*, 231(2):780–792, 2009.

[96] T. J. Hughes. Multiscale phenomena: Green's functions, the Dirichlet-to-Neumann formulation, subgrid scale models, bubbles and the origins of stabilized methods. *Computer Methods in Applied Mechanics and Engineering*, 127(1-4):387–401, 1995.

[97] T. J. Hughes, G. R. Feijóo, L. Mazzei, and J.-B. Quincy. The variational multiscale method-a paradigm for computational mechanics. *Computer Methods in Applied Mechanics and Engineering*, 166(1-2):3–24, 1998.

[98] T. J. Hughes, L. P. Franca, and G. M. Hulbert. A new finite element formulation for computational fluid dynamics: VIII The Galerkin/Least-Squares method for advective-diffusive equations. *Computer Methods in Applied Mechanics and Engineering*, 73(2):173–189, 1989.

[99] M. A. Hulsen, R. Fattal, and R. Kupferman. Flow of viscoelastic fluids past a cylinder at high Weissenberg number: Stabilized simulations using matrix logarithms. *Journal of Non-Newtonian Fluid Mechanics*, 127(1):27–39, 2005.

[100] B. M. Johnston, P. R. Johnston, S. Corney, and D. Kilpatrick. Non-Newtonian blood flow in human right coronary arteries: steady state simulations. *Journal of Biomechanics*, 37(5):709–720, 2004.

[101] J. M. Kim, C. Kim, J. H. Kim, C. Chung, K. H. Ahn, and S. J. Lee. High-resolution finite element simulation of 4:1 planar contraction flow of viscoelastic fluid. *Journal of Non-Newtonian Fluid Mechanics*, 129(1):23–37, 2005.

[102] P. Knobloch and L. Tobiska. On Korn's first inequality for quadrilateral nonconforming finite elements of first order approximation properties. *International Journal of Numerical Analysis and Modelling*, 2(4):439–458, 2005.

[103] J. Kwack and A. Masud. A three-field formulation for incompressible viscoelastic fluids. *International Journal of Engineering Science*, 48(11):1413–1432, 2010. Special Issue in Honor of K.R. Rajagopal.

[104] Y. Kwon. Numerical aspects in modeling high Deborah number flow and elastic instability. *Journal of Computational Physics*, 265:128–144, 2014.

[105] H. Lee. A multigrid method for viscoelastic fluid flow. *SIAM Journal on Numerical Analysis*, 42(1):109–129, 2004.

[106] H.-C. Lee. A nonlinear weighted least-squares finite element method for the Oldroyd-B viscoelastic flow. *Applied Mathematics and Computation*, 219(1):421–434, 2012.

[107] R. A. Lemus-Mondaca, N. O. Moraga, and J. Riquelme. Unsteady 2D conjugate natural non-Newtonian convection with non-Newtonian liquid sterilization in square cavity. *International Journal of Heat and Mass Transfer*, 61(0):73–81, 2013.

[108] X. Li, X. Han, and X. Wang. Numerical modeling of viscoelastic flows using equal low-order finite elements. *Computer Methods in Applied Mechanics and Engineering*, 199(9-12):570–581, 2010.

[109] F. Lien and P. Durbin. *Non-linear modeling with application to high-lift,* in Proceeding of the Summer Program. Stanford University, 1996.

[110] P. L. Lions and N. Masmoudi. Global solutions for some Oldroyd models of non-Newtonian flows. *Chinese Annals of Mathematics*, 21(3):131–146, 2000.

[111] J. Marchal and M. Crochet. A new mixed finite element for calculating viscoelastic flow. *Journal of Non-Newtonian Fluid Mechanics*, 26(1):77–114, 1987.

[112] M. Masoudian, K. Kim, F. Pinho, and R. Sureshkumar. A viscoelastic turbulent flow model valid up to the maximum drag reduction limit. *Journal of Non-Newtonian Fluid Mechanics*, 202:99–111, 2013.

[113] H. Matallah, P. Townsend, and M. Webster. Recovery and stress-splitting schemes for viscoelastic flows. *Journal of Non-Newtonian Fluid Mechanics*, 75(2-3):139–166, 1998.

[114] G. Matthies, P. Skrzypacz, and L. Tobiska. A unified convergence analysis for local projection stabilisations applied to the Oseen problem. *ESAIM: Mathematical Modelling and Numerical Analysis*, 41:713–742, 7 2007.

[115] S. McKee, M. Tomé, V. Ferreira, J. Cuminato, A. Castelo, F. Sousa, and N. Mangiavacchi. The MAC method. *Computers & Fluids*, 37(8):907–930, 2008.

[116] S. S. Mendu and P. Das. Flow of power-law fluids in a cavity driven by the motion of two facing lids - A simulation by lattice Boltzmann method. *Journal of Non-Newtonian Fluid Mechanics*, 175-176(0):10–24, 2012.

[117] J. Mewis and N. J. Wagner. Current trends in suspension rheology. *Journal of Non-Newtonian Fluid Mechanics*, 157(3):147–150, 2009.

[118] P. Minev, T. Chen, and K. Nandakumar. A finite element technique for multifluid incompressible flow using Eulerian grids. *Journal of Computational Physics*, 187(1):255–273, 2003.

[119] T. S. Montgomery and W. MacKnight. In *Introduction to Polymer Viscoelasticity.* Wiley, New Jersey, third edition, 2005.

[120] N. Moraga, E. Castillo, and C. Garrido. Non Newtonian annular alloy solidification in mould. *Heat and Mass Transfer*, 48(8):1415–1424, 2012.

[121] N. O. Moraga, L. A. Lemus, M. A. Saavedra, and R. A. Lemus-Mondaca. VOF/FVM prediction and experimental validation for shear-thinning fluid column collapse. *Computers & Mathematics with Applications*, 69(2):89–100, 2015.

[122] Y. Mu, G. Zhao, X. Wu, and J. Zhai. Modeling and simulation of three-dimensional planar contraction flow of viscoelastic fluids with PTT, Giesekus and FENE-P constitutive models. *Applied Mathematics and Computation*, 218(17):8429–8443, 2012.

[123] P. Nithiarasu. A fully explicit characteristic based split CBS scheme for viscoelastic flow calculations. *International Journal for Numerical Methods in Engineering*, 60(5):949–978, 2004.

[124] P. Nithiarasu, O. C. Zienkiewicz, B. V. K. S. Sai, K. Morgan, R. Codina, and M. Vázquez. Shock capturing viscosities for the general fluid mechanics algorithm. *International Journal for Numerical Methods in Fluids*, 28(9):1325–1353, 1998.

[125] W. Noh and P. Woodward. SLIC (Simple Line Interface Calculation). volume 59 of *Lecture Notes in Physics*, pages 330–340. Springer Berlin Heidelberg, 1976.

[126] P. Oliveira and F. Pinho. Plane contraction flows of upper convected Maxwell and Phan-Thien-Tanner fluids as predicted by a finite-volume method. *Journal of Non-Newtonian Fluid Mechanics*, 88:63–88, 1999.

[127] E. Olsson and G. Kreiss. A conservative level set method for two phase flow. *Journal of Computational Physics*, 210(1):225–246, 2005.

[128] S. Osher and R. Fedkiwr. In *Level Set Methods and Dynamic Implicit Surfaces*. Springer-Verlag, 2003.

[129] H. Owen and R. Codina. A third-order velocity correction scheme obtained at the discrete level. *International Journal for Numerical Methods in Fluids*, 69:57–72, 2012.

[130] T.-W. Pan, J. Hao, and R. Glowinski. On the simulation of a time-dependent cavity flow of an Oldroyd-B fluid. *International Journal for Numerical Methods in Fluids*, 60:791–808, 2009.

[131] V. K. Patnana, R. P. Bharti, and R. P. Chhabra. Two-dimensional unsteady flow of power-law fluids over a cylinder. *Chemical Engineering Science*, 64(12):2978–2999, 2009.

[132] J. Perot. An analysis of the fractional step method. *Journal of Computational Physics*, 108:51–58, 1993.

[133] T. Phillips and A. Williams. Viscoelastic flow through a planar contraction using a semi-Lagrangian finite volume method. *Journal of Non-Newtonian Fluid Mechanics*, 87(2-3):215–246, 1999.

[134] M. Picasso and J. Rappaz. Existence, a priori and a posteriori error estimates for a nonlinear three-field problem arising from Oldroyd-B viscoelastic flows. *ESAIM: Mathematical Modelling and Numerical Analysis*, 35(5):879–897, 2001.

[135] S. Pillapakkam and P. Singh. A Level-Set Method for Computing Solutions to Viscoelastic Two-Phase Flow. *Journal of Computational Physics*, 174(2):552–578, 2001.

[136] J. Principe, R. Codina, and F. Henke. The dissipative structure of variational multiscale methods for incompressible flows. *Computer Methods in Applied Mechanics and Engineering*, 199:791–801, 2010.

[137] A. Quarteroni, F. Saleri, and A. Veneziani. Analysis of the Yosida method for the incompressible Navier-Stokes equations. *Journal de Mathématiques Pures et Appliquées*, 78:473–503, 1999.

[138] M. Renardy. Existence of slow steady flows of viscoelastic fluids with differential constitutive equations. *ZAMM Journal of Applied Mathematics and Mechanics*, 65(9):449–451, 1985.

[139] M. Renardy. *Mathematical Analysis of Viscoelastic Flows.* CBMS-NSF Regional Conference Series in Applied Mathematics, 1989.

[140] M. Renardy. Asymptotic structure of the stress field in flow past a cylinder at high Weissenberg number. *Journal of Non-Newtonian Fluid Mechanics*, 90(1):13–23, 2000.

[141] M. Renardy, W. Hrusa, and J. Nohel. In *Mathematical Problems in Viscoelasticity.* John Wiley & Sons, Inc., New York, 1987.

[142] R. C. J. Richardson. *Non-Newtonian Flow and Applied Rheology (Second Edition).* Butterworth-Heinemann, second edition edition, 2008.

[143] V. Ruas. An optimal three-field finite element approximation of the Stokes system with continuous extra stresses. *Japan Journal of Industrial and Applied Mathematics*, 11(1):113–130, 1994.

[144] Y. Saad and M. H. Schultz. GMRES: A Generalized Minimal Residual Algorithm for Solving Nonsymmetric Linear Systems. *SIAM Journal on Scientific and Statistical Computing*, 7(3):856–869, 1983.

[145] D. Sandri. Analyse d'une formulation à trois champs du problème de Stokes. *ESAIM: Mathematical Modelling and Numerical Analysis - Modélisation Mathématique et Analyse Numérique*, 27(7):817–841, 1993.

[146] D. Sandri. Finite element approximation of viscoelastic fluid flow: existence of approximate solutions and error bounds. continuous approximation of the stress. *SIAM Journal on Numerical Analysis*, 31(2):362–377, 1994.

[147] D. Sandri. On a FEM method for a linearized version of the Oldroyd's problem. *Computer Methods in Applied Mechanics and Engineering*, 191(44):5045–5065, 2002.

[148] D. Sandri. Numerical study of a new finite element method for the approximation of viscoelastic fluid flow problems. *Journal of Non-Newtonian Fluid Mechanics*, 118(2-3):103–120, 2004.

[149] P. Saramito. A new θ-scheme algorithm and incompressible fem for viscoelastic fluid flows. *ESAIM: Mathematical Modelling and Numerical Analysis - Modélisation Mathématique et Analyse Numérique*, 28:1–35, 1994.

[150] T. Sato and S. M. Richardson. Explicit numerical simulation of time-dependent viscoelastic flow problems by a finite element/finite volume method. *Journal of Non-Newtonian Fluid Mechanics*, 51(3):249–275, 1994.

[151] J. Shen. On error estimates of some higher order projection and penalty-projection methods. *Numerische Mathematik*, 62:49–73, 1992.

[152] P. Singh, D. Joseph, T. Hesla, R. Glowinski, and T.-W. Pan. A distributed Lagrange multiplier/fictitious domain method for viscoelastic particulate flows. *Journal of Non-Newtonian Fluid Mechanics*, 91:165 – 188, 2000.

[153] P. Singh and L. Leal. Finite-element simulation of the start-up problem for a viscoelastic fluid in an eccentric rotating cylinder geometry using a third-order upwind scheme. *Theoretical and Computational Fluid Dynamics*, 5:107–137, 1993.

[154] A. A. Soares, J. M. Ferreira, and R. P. Chhabra. Flow and forced convection heat transfer in crossflow of non-Newtonian fluids over a circular cylinder. *Industrial & Engineering Chemistry Research*, 44(15):5815–5827, 2005.

[155] P. Sousa, P. Coelho, M. Oliveira, and M. Alves. Effect of the contraction ratio upon viscoelastic fluid flow in three-dimensional square-square contractions. *Chemical Engineering Science*, 66(5):998–1009, 2011.

[156] J. Su, J. Ouyang, X. Wang, B. Yang, and W. Zhou. Lattice Boltzmann method for the simulation of viscoelastic fluid flows over a large range of Weissenberg numbers. *Journal of Non-Newtonian Fluid Mechanics*, 194:42–59, 2013.

[157] M. Sussman. A second order coupled level set and volume-of-fluid method for computing growth and collapse of vapor bubbles. *Journal of Computational Physics*, 187(1):110–136, 2003.

[158] M. Sussman and E. G. Puckett. A Coupled Level Set and Volume-of-Fluid Method for Computing 3D and Axisymmetric Incompressible Two-Phase Flows. *Journal of Computational Physics*, 162(2):301–337, 2000.

[159] R. Temam. Sur l'approximation de la solution des équations de Navier-Stokes par la méthode des pas fractionaires (I). *Arch. Rational Mech. Anal.*, 32:135–153, 1969.

[160] M. Tomé, A. Castelo, A. Afonso, M. Alves, and F. Pinho. Application of the log-conformation tensor to three-dimensional time-dependent free surface flows. *Journal of Non-Newtonian Fluid Mechanics*, 175-176(0):44–54, 2012.

[161] M. Tomé, A. Filho, J. Cuminato, N. Mangiavacchi, and S. McKee. GENSMAC3D: a numerical method for solving unsteady three-dimensional free surface flows. *International Journal for Numerical Methods in Fluids*, 37(7):747–796, 2001.

[162] M. F. Tomé and S. McKee. GENSMAC: A Computational Marker and Cell Method for Free Surface Flows in General Domains. *Journal of Computational Physics*, 110(1):171–186, 1994.

[163] M. F. Tomé and S. McKee. Numerical simulation of viscous flow: Buckling of planar jets. *International Journal for Numerical Methods in Fluids*, 29(6):705–718, 1999.

[164] S. P. van der Pijl, A. Segal, C. Vuik, and P. Wesseling. A mass-conserving Level-Set method for modelling of multi-phase flows. *International Journal for Numerical Methods in Fluids*, 47(4):339–361, 2005.

[165] H. A. van der Vorst. BI-CGSTAB: A Fast and Smoothly Converging Variant of BI-CG for the solution of Nonsymmetric Linear Systems. *SIAM J. Sci. Stat. Comput.*, 13(2):631–644, Mar. 1992.

[166] D. Wang and J. Bernsdorf. Lattice Boltzmann simulation of steady non-Newtonian blood flow in a 3D generic stenosis case. *Computers & Mathematics with Applications*, 58(5):1030–1034, 2009.

[167] K. Yapici, B. Karasozen, and Y. Uludag. Finite volume simulation of viscoelastic laminar flow in a lid-driven cavity. *Journal of Non-Newtonian Fluid Mechanics*, 164:51–65, 2009.

[168] J. Y. Yoo and Y. Na. A numerical study of the planar contraction flow of a viscoelastic fluid using the SIMPLER algorithm. *Journal of Non-Newtonian Fluid Mechanics*, 39(1):89–106, 1991.

[169] J.-D. Yu, S. Sakai, and J. Sethian. Two-phase viscoelastic jetting. *Journal of Computational Physics*, 220(2):568–585, 2007.

[170] Z. Yu, N. Phan-Thien, Y. Fan, and R. I. Tanner. Viscoelastic mobility problem of a system of particles. *Journal of Non-Newtonian Fluid Mechanics*, 104:87–124, 2002.

[171] J.-B. Zhang and Z.-B. Kuang. Study on blood constitutive parameters in different blood constitutive equations. *Journal of Biomechanics*, 33(3):355–360, 2000.

[172] O. C. Zienkiewicz and R. Codina. A general algorithm for compressible and incompressible flow-part i. the split, characteristic-based scheme. *International Journal for Numerical Methods in Fluids*, 20(8-9):869–885, 1995.

[173] O. C. Zienkiewicz, R. L. Taylor, and P. Nithiarasu. In *The Finite Element Method for Fluid Dynamics*, volume 3. Elsevier Butterworth-Heinemann, sixth edition, 2005.